

QUARTERLY PROGRESS REPORT

No. 85

APRIL 15, 1967

GPO PRICE \$ _____

CFSTI PRICE(S) \$ _____

Hard copy (HC) 3.00

Microfiche (MF) .65

ff 653 July 65

MASSACHUSETTS INSTITUTE OF TECHNOLOGY
RESEARCH LABORATORY OF ELECTRONICS
CAMBRIDGE, MASSACHUSETTS

N67-27081

N67-57105

FACILITY FORM 602

(ACCESSION NUMBER)

(THRU)

369
(PAGES)

1
(CODE)

CR-84300
(NASA CR OR TMX OR AD NUMBER)

23
(CATEGORY)

The Research Laboratory of Electronics is an interdepartmental laboratory in which faculty members and graduate students from numerous academic departments conduct research.

The research reported in this document was made possible by support extended the Massachusetts Institute of Technology, Research Laboratory of Electronics, by the following agencies.

Joint Services Electronics Programs (U.S. Army, U.S. Navy, U.S. Air Force)

Contract DA 28-043-AMC-02536 (E)

U.S. Air Force—Aerospace Medical Division

Contract AF 33 (615)-3885

U.S. Air Force—Electronic Systems Division

Contract AF 19 (628)-5661

Contract AF 19 (628)-2487

Contract AF 19 (628)-6066

U.S. Air Force—Research and Technology Division

Contract F33615-67-C-1148

National Aeronautics and Space Administration

Grant NsG-496

Grant NGR-22-009-163

Grant NGR-22-009-114

Grant NGR-22-009-131

Grant NsG-334

Grant NsG-419

Contract NSR-22-009-120

National Institutes of Health

Grant 2 PO1 MH-04737-06

Grant 5 RO1 NB-04332-04

Grant 1 505 FR-07047-01

Grant 5 RO1 NB-04985-04

National Science Foundation

Grant GK-835

Grant GK-57

Grant GK-1165

U.S. Atomic Energy Commission

Contract AT (30-1)-3581

Contract AT (30-1)-3285

Contract AT (30-1)-1842

M.I.T. Sloan Fund for Basic Research

Support of projects is acknowledged in footnotes to the appropriate sections.

Reproduction in whole or in part is permitted for any purpose of the United States Government.

MASSACHUSETTS INSTITUTE OF TECHNOLOGY
RESEARCH LABORATORY OF ELECTRONICS

QUARTERLY PROGRESS REPORT No. 85

April 15, 1967

Submitted by: H. J. Zimmermann
G. G. Harvey
S. J. Mason

PRECEDING PAGE BLANK NOT FILMED.

TABLE OF CONTENTS

Personnel	vi
Publications and Reports	xv
Introduction	xx

GENERAL PHYSICS

I.	Molecular Beams	1 ✓
	Cesium Beam Atomic Clock	1
II.	Microwave Spectroscopy	5 ✓
	Velocity Surfaces in Lithium Niobate	5
III.	Electron Magnetic Resonance	13 ✓
	Radicals in the Gas Phase	13
	Construction of a Rapid-Scanning EPR Spectrometer Coupled with a Flash-Discharge Source	14
IV.	Radio Astronomy	15 ✓
	Interpretation of Spectral Data	15
	Results Obtained from the Inversion of Simulated Atmo- spheric Water-Vapor Spectra	16
	Microwave Dielectric Constant and Emissivity of a Solu- tion Approximating Sea Water	19
	Hydrogen Recombination Line Observations	22
	Observations of OH Emission	23
V.	Solid-State Microwave Electronics	27 ✓
	High Dynamic Range Techniques	27
	High-Power Varactor Multipliers	27
	Device Characterization	28
	Computer Design of Varactor Circuits	28
VI.	Electronic Instrumentation	33 ✓
	Shielded Room Facility	33
	Mass Spectrometer Detector	34
	Resolution of Mass Spectrometer	36
	Sampling and Retrieval of the Spectrum	37
VII.	Optical and Infrared Spectroscopy	39 ✓
	Reflection Measurements on Potassium Halides in the Far Infrared Region	39
	Lattice Vibrations in CdS/Se Mixed Crystals	42
VIII.	Geophysical Research	49 ✓
	Optical Radar and Airglow Observations in Norway during the Presence of Noctilucent Clouds	49

CONTENTS

IX.	Electrodynamics of Media	51 ✓
	Electrodynamics of Quadrupolar Media	51
	Pulse Distortion in Nonlinear Optics	56
X.	Physical Optics of Invertebrate Eyes	69 ✓
	Optics of the Tobacco Hornworm Moth	69
PLASMA DYNAMICS		
XI.	Plasma Physics	71 ✓
	Computer Programmed "Basic Data of Plasma Physics"	71
	Far Infrared Plasma Diagnostics	73
	Electron Density Measurements with a Narrow-Band Far Infrared Interferometer	87
	Microwave Scattering from Warm Plasma Waves near the Electron-Cyclotron Frequency	98
	Nonlinear Harmonic Generation at Plasma Resonance	103
	Laser Breakdown Experiment	108
	Microwave Emission from n-type Indium Antimonide at 4.2°K and 77°K	128
XII.	Gaseous Electronics	135 ✓
	Electron Collisional Effects on Wave Propagation in a Non-magnetized Plasma	135
XIII.	Plasmas and Controlled Nuclear Fusion	141 ✓
	Active Plasma Systems	141
	System C: Excitation of an Ion-Cyclotron Resonance	141
	Beam-Plasma Discharge: System D	146
	Cross-Field Beam-Plasma Experiments	150
	Experimental Investigation of a Beam-Plasma Interaction in a Minimum-B Field	154
	Anomalous Millimeter Microwave Plasma Density Measurements	157
	Theory of Beam-Plasma Interactions	163
	Dispersion Relations for Beam-Plasma Interactions	168
	Sheet Models of the Beam-Plasma Discharge	178
	Effect of Essential Singularities on Stability Criteria	183
	Motion of Charged Particles in Magnetic Mirror Field in the Presence of a Radial Time-Variant Electric Field	186
	Applied Plasma Physics Related to Controlled Nuclear Fusion	193
	Experimental Study of Hollow-Cathode Discharge Arc Plasma	193
	Plasma Magnetohydrodynamic Flows, Waves, and Instabilities	201
	Magnetohydrodynamic Wave Propagation Transverse to Magnetic Field	201
XIV.	Energy Conversion Research	217 ✓
	Status of Research	217

CONTENTS

XV.	Spontaneous Radiofrequency Emission from Hot-Electron Plasmas	219 ✓
	Enhanced Cyclotron Radiation from an Electron-Cyclotron Resonance Discharge	219
XVI.	Interaction of Laser Radiation with Plasmas and Nonadiabatic Motion of Particles in Magnetic Fields	223 ✓
	Incoherent Scattering of Light from a Plasma IV	223
	Electron Diffusion in a Helically Perturbed Magnetic Field of the M. I. T. Stellarator	225
COMMUNICATION SCIENCES AND ENGINEERING		
XVII.	Statistical Communication Theory	231 ✓
	Discrete Analysis of Homomorphic Deconvolution	231
	Unity Feedback Two-State Modular Configurations	234
XVIII.	Processing and Transmission of Information	239 ✓
	Shift-Register Synthesis and Applications	239
	Coding Theorems for Source-Channel Pairs	241
XIX.	Detection and Estimation Theory	249 ✓
	Nonlinear Map Interval Estimation	249
	Performance Bounds for Optimum Detection for Gaussian Signals	253
XX.	Speech Communication	267 ✓
	On the Mechanism of Glottal Vibration for Vowels and Consonants	267
	Homomorphic Speech Processing	271
XXI.	Linguistics	279 ✓
	On Noncyclic Transformational Grammars	279
	Lithuanian Morphophonemics	284
	Inward and Upward – Directionals in English	297
	On Problems Implied by the Concept 'Performance'	301
XXII.	Cognitive Information Processing	305 ✓
	Acquired Asymmetry of Shape Learning	305
	Transmission and Coding of Color Pictures	307
	Subjective Effects of Additive White Pictorial Noise with Various Probability Distributions	317
	Stochastic Model for Weather Maps	320
XXIII.	Neurophysiology	312 ✓ 321
	Contrast Detectors	312 321
	Insight into Neuronal Closed Loops from Shift-Register Theory	325
XXIV.	Computation Research	329 ✓
	Finding the Roots of an Analytic Function	329
	Author Index	331

PERSONNEL

Administration

Prof. H. J. Zimmermann, Director
Prof. G. G. Harvey, Associate Director
Prof. S. J. Mason, Associate Director
Mr. R. A. Sayers, Assistant Director

Advisory Committee

Dean R. A. Alberty
Dean R. L. Bishop
Dean G. S. Brown
Prof. G. G. Harvey
Prof. A. G. Hill
Prof. S. J. Mason
Prof. J. Ross
Prof. I. W. Sizer
Prof. L. D. Smullin
Prof. V. S. Weisskopf
Prof. H. J. Zimmermann
(Chairman)

Research Committee

Dean S. C. Brown
Prof. L. J. Chu
Prof. M. Eden
Prof. M. Halle
Prof. G. G. Harvey
Prof. J. G. King
Prof. S. J. Mason
Prof. D. J. Rose
Prof. W. A. Rosenblith
Mr. R. A. Sayers
Prof. W. M. Siebert
Prof. M. W. P. Strandberg
Prof. P. D. Wall
Prof. J. R. Zacharias
Prof. H. J. Zimmermann
(Chairman)

Professors

Allis, W. P.
Barrett, A. H.
Bitter, F.
Bose, A. G.
Brown, S. C.
Burke, B. F.
Chomsky, N. A.
Chu, L. J.
Eden, M.
Edgerton, H. E.
Elias, P.
Gross, P. L.
Gyftopoulos, E. P.
Halle, M.

Harvey, G. G.
Haus, H. A.
Hill, A. G.
Huffman, D. A.
Ingard, K. U.
Jakobson, R.
Kerrebrock, J. L.
King, J. G.
Lee, Y. W.
Lettvin, J. Y.
Levinthal, C.
Mason, S. J.
Minsky, M. L.
Rose, D. J.
Rosenblith, W. A.

Ross, J.
Shannon, C. E.
Shu, C. G. (Visiting)
Siebert, W. M.
Sledd, J. H. (Visiting)
Smullin, L. D.
Stevens, K. N.
Strandberg, M. W. P.
Wall, P. D.
Warren, B. E.
Waugh, J. S.
Wozencraft, J. M. (Absent)
Zacharias, J. R.
Zimmermann, H. J.

PERSONNEL

Associate Professors

Bekefi, G.	Hoffman, M. A.	Mortenson, E. (Visiting)
Bers, A.	Katz, J. J.	Oates, G. C.
Dennis, J. B.	Kleppner, D.	Peake, W. T.
Dupree, T. H.	Klima, E. S. (Absent)	Pomorska, Krystyna
Fodor, J. A.	Kyhl, R. L.	Rafuse, R. P.
Gallager, R. G.	Lee, F. F.	Schreiber, W. F.
Garland, C. W.	Massey, J. L. (Visiting)	Searle, C. L.
Hennie, F. C., III	Matthews, G. H.	Van Trees, H. L.

Assistant Professors

Andersen, J. (1)	Henke, W. L.	Penman, S.
Bernard, G. D.	Hoversten, E. V. (1)	Perry, C. H.
Billman, K. W.	Huang, T. S.	Pomeranz, B.
Black, W. L. (1)	Ingraham, J. C.	Ross, J. R.
Blum, M.	Katona, P. G.	Siambis, J. G. (1)
Bowers, K. W.	Kennedy, R. S.	Snyder, D. L.
Briggs, R. J.	Kinsey, J. L.	Spann, R. N.
Bromberger, S.	Kiparsky, R. P. V.	Staelin, D. H. (1)
Brown, J. E.	Klatt, D. H. (1)	Steinfeld, J. I.
Bruce, J. D.	Kolenkow, R. J.	Stickney, R. E.
Dean, L. W., III	Lee, H. B.	Troxel, D. E.
Fiocco, G.	Lenoir, W. B. (1)	Weiss, R.
Goutmann, M. M.	Lidsky, L. M.	Weiss, T. F.
Gray, P. R. (Absent)	Nelsen, D. E.	Yip, S.
	Oppenheim, A. V.	

Lecturers

Bever, T. G.	Ferretti, E.	Rines, R. H.
Brown, G. A.	Mark, R. G.	Teager, H. M.
	Pitts, W. H.	

Instructors

Baggeroer, A. B.	Glaser, J.	Schafer, R. W.
Blessner, B.	Kukolich, S. G.	Schindall, J. E.
Burns, S. K.	McEnally, T. E., Jr.	Schneider, H. M.
Eisenberg, M.	Nahvi, M.	Speck, C. E.
Evans, J. E.	Parker, R. R.	Tripp, A. P.

Research Associates

Barnett, G. O.	Garrett, M. F. (2)	Ingham, K. R.
Canfield, J. V.	Gerschenfeld, Dora J.	Kittelberger, J. S.
Chung, K.	Grams, G. W.	Kolers, P. A.
Dilly, P. N.	Hall, R. D.	Kornacker, K.
Durlach, N. I.	Hoffman, R. A.	Liss, P. H.

(1) Engineering Postdoctoral Fellow

(2) NIH Postdoctoral Trainee

PERSONNEL

Research Associates (continued)

Novotny, D. B.
Papert, S. A.

Sears, R. E. J.
Shepherd, G. M.
Steinbrecher, D. H.

Zisk, S. H.
Zupancic, I.

Guests

Bailey, C-J. N.
Fraser, J. B.
Kessler, A. R.
Kim, C. K.

Lieberman, P.
Paik, S. F.
Pritchard, D. E.

Ruddick, W. M.
Walker, D. E.
Winkler, P. F., Jr.
Zurer, Barbara L.

Visiting Scientists

Da Fonseca, J. S.
Koide, F.

Moreno-Diaz, R.

Nomoto, M. (1)
Suzuki, J.

Research Affiliates

Barlow, J. S.
Brodey, W. M.
Brown, R. M.

Bullowa, Margaret
Crist, A. H.
Howland, B. (2)
Langbein, D.

McLardy, T.
Miller, W. H.
Ozier, I.

Postdoctoral Fellows

Binford, T. O. (3)
Borbely, A. A.
Fokkens, N.
Franzen, O.
Gruber, J. S. (5)

Hartman, H. (4)
Hellekant, B. C.
Milner, J-C. G.
Natapoff, A. (4)
Offenloch, K.

Schwartz, A. (4)
Smith, N. V.
Songster, G. F. (4)
Taub, A. (4)
Wierzbicka, Anna

R. L. E. Research Staff

Babitch, D.
Barrett, J. W.
Benhaim, N.
Brown, Elaine S.
Burgess, R. G.
Burnham, D. C.
Cattell, N. R.
Chung, S-H.
Crowther, Patricia P.
Cunningham, A. W. B.
Davis, Heather S.
Fontaine, C. L.
Gambardella, G.
Harwitt, Joan

Ingersoll, J. G.
Isaacs, Elaine C.
Jensen, E. R.
Kelley, W. F.
Kiang, N. Y. S.
Kierstead, J. D.
Kim, C-W.
McCaffrey, A.
McCarthy, J. J.
McCulloch, W. S.
Menyuk, Paula
Mulligan, W. J.
Myint, M. T.
O'Brien, F. J.
Pennell, Martha M.

Perkell, J. S.
Pitts, W. H.
Plummer, W. W.
River, Eleanor C.
Rojas-Corona, R. R.
Rosebury, F.
Ryan, L. W.
Sanchez-Felipe, O.
Shaw, Marion L.
Smith, T. B.
Tretiak, O. J.
Viertel, J. J.
Ward, S. A.
Wickelgren, G. L.

- (1) NIH International Postdoctoral Fellow
(2) Lincoln Laboratory Staff Member
(3) NIH Training Grant

- (4) NIH Fellow
(5) NIH Postdoctoral Trainee

PERSONNEL

Research Assistants

Baran, R. J.	Frediani, J. K.	Moran, J. M., Jr.
Bartsch, R. R.	Gabrielian, A.	Moses, J.
Brown, T. S.	Gadzuk, J. W.	Ng, L. C.
Chan, S. W-C.	Granek, H.	Offenberger, A. A.
Chandra, A. N.	Greenspan, R. L.	Papadopoulos, G. D.
Chase, D.	Gustafson, K. T.	Perozek, D. M.
Chen, K. R-S.	Ham, D. O.	Peterson, D. L.
Chou, S.	Herba, F.	Poulo, R. L.
Citron, A.	Hoff, P. W.	Poussart, D. J-M.
Colombant, D. G.	Hougen, M. L.	Richters, J. S.
Davis, J. A.	Huang, T.	Rogers, A. E. E.
Davis, T. G.	Kirk, R.	Schumaker, N. E.
Dean, Janet P.	Kitrosser, D. F.	Snyder, D. D.
DeRijk, R. P. G.	Klumpp, Marion H.	Sugawara, A.
DeWolf, J. B.	Kurth, R. R.	Tomlinson, R. S.
Ditz, J. Merle	Kusse, B. R.	Wang, C. H.
Eberle, F. W.	Levy, E. K.	Ward, M. J.
Edwards, K. R.	Liu, Jane W-S.	Wawzonek, J. J.
English, R. P.	Makhoul, J. J.	Weidner, M. Y.
Espino, R. L.	Mangano, J. A.	Weigand, R. M.
Ezekiel, S.	Maul, M. K.	Weiner, B. B.
Fehrs, D. L.	McNary, C. A.	Wong, Y-M.
Fisher, C. H.	Melnick, M.	Yamamoto, S.
Flannery, D. L.	Moir, R. W.	Young, R. A.
Flynn, R. W.	Moldon, J. C.	Zeiders, G. W., Jr.

Graduate Assistants

Brown, T. R.	Free, J. U., Jr.	Reznek, S. R.
Davis, W. B.	Garosi, G. A.	Schwartz, P. R.
Ewing, H.	Gschwendtner, A. B.	Silk, J. K.
Fertel, Jeanne H.	Langdon, R. M., Jr.	Vellenga, J. H.
Forrester, V. G.	Oates, D. E.	Wilheit, T. T., Jr.
Fox, R. L.	Pleasance, D. E.	Yung, B. N.
	Reifenstein, E. C., III	

Teaching Assistants

Anderson, G. B.	Khanna, M.	Nelson, A. C.
Bice, P. K.	Kinsley, R. W., Jr.	Olsen, R. E.
Bless, S. J.	Koehler, R.	Patterson, J. T.
Catto, P. J.	Kosowski, J. F.	Portner, E. M., Jr.
Ching, H.	Lee, W-H.	Schaefer, D. W.
Freeman, J. A. (1)	Levitt, B. K.	Seitz, C. L.
Greenwood, R. E.	Mattison, D. R.	Tuhy, F. P., Jr.
Harris, R. V., III	Mazza, C. (2)	Williams, J. A.
Hartmann, H. P.	Medress, M. F.	Woods, J. W.
Hill, R. A.	Moxon, E. C.	Yamanashi, B. S.
Johnson, L. G.	Nedzelnitsky, V.	Young, I. T.

(1) United States Air Force

(2) Sci. Teach. Ctr. Grant

PERSONNEL

Graduate Students

Akmajian, A. (6)	DeWan, D. P. (4)	Kronquist, R. L.
Allen, J. (9)	Dougherty, R. C. (8)	Lackner, J. R. (6)
Allen, J. L. (15)	Ehrenberg, J. E. (9)	Lawter, J. R. (4)
Anderson, S. R. (8)	Ellett, J. D., Jr. (4)	Leonardi-Cattolica, A. M. (19)
Andrews, M. L.	Emonds, J. E. (8)	Linford, R. (4)
Arnstein, D. S. (15)	Fidelholtz, J. L. (10)	Lopez, O. (12)
Austin, M. E.	Gaut, N. E. (7)	Lubin, M. D.
Balcewicz, J. F. (9)	George, E. V. (11)	Manheimer, W. M. (4)
Barnwell, T. P., III (4)	Goddard, G. W. (4)	Matthiesen, D. J. (11)
Barron, M. E. (4)	Goldberg, A. J. (12)	Max, J. (15)
Bedell, G. D., IV (6)	Goldfield, R. (6)	Merrill, E. G. (20)
Bell, C. M. (31)	Golub, R.	Mohajeri, M. (33)
Beltran-B., F. (24)	Good, W. E. (13)	Mozzi, R. L. (21)
Berliner, J. E. (4)	Greaves, W. (14)	Muehlner, D. J. (4)
von Bismarck, G.	Gross, L. N. (8)	Mueller, P. E. (22)
Blum, G. D. (4)	Guinan, J. J., Jr. (4)	Myers, Amy E. (6)
Bowers, J. S. (6)	Halme, S. J. (16)	Naro, A. J. (8)
Bradley, W. C.	Harris, J. W. (10)	Nelson, G. P. (10)
Braida, L. D. (4)	Hartman, D. W. (4)	Odette, G. (5)
Brame, M. K. (25)	Heggestad, H. M. (15)	Ohuri, D. A. (18)
Browne, E. W. (6)	Heller, J. A. (17)	Parrish, J. H. (4)
Brueck, S. R. J. (4)	Hershkowitz, R. (4)	Perkins, P. E. (7)
Bucher, E. A. (4)	Hofmann, T. R. (8)	Perlmutter, D. M. (23)
Cahn, M. F. (4)	Howard, I. J. (6)	Pinkston, J. T., III (4)
Callen, J. D. (5)	Hsiao, H. S.	Pittenger, L. C. (5)
Carter, R. J. (32)	Hudis, M. (5)	Platts, D. A. (4)
Carvey, P. P.	Jackendoff, R. S. (6)	Portny, S. E. (28)
Chapin, P. G. (1)	Jameson, P. W.	Prerau, D. S. (4)
Cohen, A. J. (2)	Jamin, E. (29)	Rabiner, L. R. (4)
Colburn, S. H. (3)	Kalan, G. R. (18)	Ramshaw, J. D. (4)
Collins, L. D. (4)	Katyl, R. H. (4)	Raymond, S. A. (12)
Cornew, R. W.	Kayne, R. S. (6)	Ritter, J. T. (25)
Crane, D. E. (5)	Kimball, J. P. (8)	Robbins, G. M. (9)
Cruise, T. J. (4)	Kolodny, Nancy H. (8)	Rogoff, G. L.
Culicover, P. W. (6)	Kolor, R. W. (9)	Rolland, A. E. (26)
Decher, R. (7)	Koons, H. C. (12)	Sheena, D. (4)
Demko, P., Jr. (12)	Krischer, C.	Sheinson, R. S. (10)

- | | |
|---|---|
| (1) Danforth Foundation Fellow | (18) Jonathan Whitney Fellow |
| (2) Shell Oil Co. Fellow | (19) Whitney Predoctoral Fellow |
| (3) Sperry-Rand Fellow | (20) Public Health Service Trainee |
| (4) NSF Fellow | (21) Raytheon Fellow |
| (5) U.S. AEC Fellow | (22) American Can Co. Fellow |
| (6) National Defense Education Act Fellow | (23) American Council of Learned Sciences |
| (7) NASA Fellow | (24) O.A.S. Fellow |
| (8) NIH Trainee | (25) Woodrow Wilson Fellow |
| (9) Bell Telephone Laboratories Fellow | (26) United States Coast Guard |
| (10) NIH Fellow | (27) Hertz Foundation Fellow |
| (11) RCA Fellow | (28) NASA Trainee |
| (12) NSF Trainee | (29) Belgium American Foundation |
| (13) U.S. Rubber Corporation Fellow | (30) General Electric Fellow |
| (14) Kennedy Fellow | (31) M.I.T. Fellow |
| (15) Lincoln Laboratory Associate | (32) Sci. Teach. Ctr. Grant |
| (16) American Scandinavian Foundation | (33) American Friends of Middle East Fellow |
| (17) Xerox Fellow | |

PERSONNEL

Graduate Students (continued)

Shupe, D. S. (1)	Tin, N. T. (6)	Weinstein, C. J. (9)
Simpson, J. I. (1)	Tornberg, N. E. (1)	Wiederhold, M. L. (10)
Sirbu, M. A. (1)	Tremain, R. E. (1)	Wilder, W. C. (9)
Snow, M. S. (1)	Urquizo-B, C.	Wilson, T. L. (1)
Sokoloff, D. R. (1)	Vandamme, F. J. (7)	Winston, P. (1)
Stanley, R. J. (2)	Vanderbilt, D. H. (1)	Wolaver, D. H. (1)
Strong, R. M. (3)	Walker, J. L. (8)	Wolf, J. J.
Suchard, S. N. (4)	Wallace, R. N. (1)	Woo, Nancy (2)
Swain, D. W. (4)	Walpert, G. A. (9)	Wright, B. L.
Thiersch, C. L. (1)	Ware, R. W. (10)	Wright, D. A. (12)
Thomae, I. H. (5)	Watanabe, A. (11)	Wright, W. A.

Undergraduates (Thesis or Special Problems)

Ashton, B.	Immerman, E. M.	Postol, T. A.
Bayer, S. J.	Jeffrey, W. H.	Puls, J. H.
Boxman, R. L.	Jerrell, J. G.	Rible, J. W.
Bright, K. S.	Juvkam-Wold, H. C.	Rosenfeld, E.
Bryant, R. W.	King, P. A.	Samsam, S.
Chappell, R. F.	Kohn, M. S.	Schaffner, S. C.
Cohen, M. H.	Kolb, C. E., Jr.	Schoman, K. E., Jr.
Cohen, S. A.	Kutner, S. R.	Sevick, G. E.
Collins, T. L.	Lange, J. H., Jr.	Silvert, M. A.
Cooper, C. M., Jr.	Law, Sara	Small, J. G.
Davidow, J. E.	Leary, A. R.	Smith, R. R.
DeBonte, R. J.	Leighninger, Diana M.	Solomon, G. S.
Eckberg, A. E., Jr.	Malgari, S.	Sorensen, K.
Eckstein, P. F.	Malpelli, J. G.	Spann, C. W.
Eldridge, D. P.	Marandino, G. F.	Sullivan, K. J.
Evans, H. D., III	Mase, J. Z.	Toong, H-M. D.
Fairbanks, J. T.	Mauer, J. L., IV	Vail, W. B., III
Farrell, R. M.	Mechler, D. H.	Walker, J. D.
Franz, J. M.	Morrey, W. T.	Wandzilak, M.
Galiger, P. E.	Neuendorffer, A. C.	Warshaw, A. S.
Getting, P. A.	Ogan, K. L.	Weatherly, W. P.
Gill, T. A.	Partridge, L. D.	Weber, W. J.
Grubic, L. R., Jr.	Peruggi, R. E.	Wheeler, G. M.
Henckels, L. P. A.	Pfister, G. F.	Wolfe, P. D.
Huie, J. L.	Pitegoff, A. D.	Wrigley, J. D., Jr.

Student Employees

Ackerman, W. B.	DeRodeff, S. III	Gibb, B. C.
Bennett, D. W.	Dreher, S. III	Howell, R. P.
Bosel, J. P.	Drobak, J. N.	Kinnaman, W. A.
Chan, M-L.	Engle, R. H.	Laurino, J. A., Jr.

- | | |
|--------------------------------|---------------------------------|
| (1) NSF Fellow | (7) Belgium American Foundation |
| (2) NIH Trainee | (8) United States Coast Guard |
| (3) Hertz Foundation Fellow | (9) NSF Trainee |
| (4) NASA Trainee | (10) NIH Fellow |
| (5) Danforth Foundation Fellow | (11) General Electric Fellow |
| (6) A.I.D. Fellow | (12) RCA Fellow |

PERSONNEL

Student Employees (continued)

Malek, P. S.	Pozgay, J. H.	Sturges, R. H., Jr.
Masiello, R. D.	Ruderman, G. S.	Trunek, R. J.
Michel, A.	Solarz, R. W.	Waters, J. W.
Ostrach, S. S.		Welch, D. R.

R. L. E. Administrative Staff

Duffy, D. F.	Sayers, R. A.
Hewitt, J. H.	Smith, P. L.
Keyes, R. V., Jr.	Thomas, Helen L.

Administrative Assistant

Bella, C. J.

Office Clerks

Barron, Gladys G.	Gregor, C. A.	Peck, J. S.
Butler, D. F.	Ippolito, Dorothy A.	Scalleri, Mary B.
Chase, Arbella P.	Mulligan, Maureen F.	Simon, E.
Engler, R. R.	O'Toole, J. P.	Toebe, Rita K.

Typists

Dilworth, Doris L.	Murphy, Mary R.	Olasz, Irene A.
Foley, Ruth E.	O'Brien, Geneva	Young, Nancy E.

Technical Typists

Anderson, Linda	Kliphan, Evelyn C.	Mullin, Priscilla A.
Jones, Elizabeth		Schröder, Gertraude L.

Secretaries

Bacon, Carolyn L. P.	Hamilton, Martha C.	Paige, Okella M.
Baumann, Irene H. E.	Hurley, Denise B.	Reid, Gloria C.
Carbone, Angelina	Hurvitz, Rose S.	Ricker, Barbara J.
Cataldo, Donna L.	Illiscavitch, Patricia A.	Robbins, Toni R.
Cohen, Phyllis J.	Ingersoll, Nancy L. B.	Skewes, Anne
Conwicke, Vera	Kaloyanides, Venetia	Smith, Clare F.
Cook, Elaine J.	Kirk, Marsha A.	Stagliola, Eleanor E.
Cosgrove, Mary J.	Loeb, Charlotte G.	Tortorici, Camille A.
Dunn, Eleanor I.	Lorthrop, Helena	Van Wezel, Ruth
Fernandez, Teresita M.	McCarthy, Barbara L.	Wanner, Patricia A.
Gatton, Tonya K.	McEntee, Doris C.	Wright, Ruth L.

Engineering Assistants

Alpert, M.	McKenzie, J. A.	Stevens, J. A.
Berg, A. E.	Papa, D. C.	Thompson, J. B.

PERSONNEL

Technical Assistants

Austin, Susan G.
Barger, Z. O.
Byers, F. H.
Grande, Esther D.

Hall, Kyra M.
Major, Diane
McClellan, Suzan E.
Newman, Charlotte M.
Rabin, Sylvia G.

Seymour, P. L.
Swenson, Judith E.
Toop, R. W.
Yaffee, M. A.

Technicians

Aucella, Alice G.
Barrows, F. W.
Beaton, Catherine M.
Butler, R. E., Jr.
Cardia, P. F.
Connolly, J. T.
DiPietro, P. J.
Ferrogamo, A. A.
Fitzgerald, E. W., Jr.
Gage, R. B., Jr.

Gay, H. D.
Goodman, L.
Hill, R. F.
Iovine, M. A.
Kaufman, D. E.
Kelly, M. A.
Lewis, R. R.
McLean, J. J.
Neal, R. W.
North, D. K.

Rodrigues, G. D.
Schwabe, W. J.
Sears, A. R.
Sholder, J. A.
Speredelozzi, A. J.
Sprague, L. E.
Summers, C. L.
Tortolano, A. J.
Varney, R. J.
Wentworth, A. G., Jr.

Technicians' Shop

Lorden, G. J., Foreman

Fownes, Marilyn R.
MacDonald, K. R.

Pyle, S. C.

Laboratory Assistants

Barrows, Helene G.

Drafting Room

Navedonsky, C. P. Foreman
DeCesare, Olive J.

Porter, Jean M.

Rollins, I. E.
Zeleznik, Fran X.

Photographic Shop

Cook, J. F.
Geraigery, R. J.
Karas, P.

Machine Shop

Keefe, J. B. Foreman
Aalrud, R. W.
Alvarez, R. C.
Bletzer, P. W.
Brennan, J.

Bunick, F. J.
Cabral, M., Jr.
Carter, C. E.
Harvey, A. O.
Liljeholm, F. H.

Muse, W. J.
Reimann, W.
Ryan, J. F.
Sanromá, J. B.
Wheaton, K. E.

PERSONNEL

Tube Laboratory

Rosebury, F.

Leach, G. H., Jr.
MacDonald, A. A.
Thibodeau, D. S.

Glass Shop

Ryan, L. W.

DiGiacomo, R. M.
Doucette, W. F.

Stock Clerks

Haggerty, R. H.

Legier, D. O.
Ridge, P. A.

Sharib, G.

Utility and Maintenance

Doiron, E. J. Foreman
Audette, A. G.
Lucas, W. G.

McAteer, T. F., Jr.
McDermott, J. F.

Riley, J. F.
Severino, E.
Sincul, J. Jr.

PUBLICATIONS AND REPORTS
MEETING PAPERS PRESENTED

NEREM-66, Boston, Massachusetts

November 2-4, 1966

D. H. Staelin and E. C. Reifstein, K-band Observations of Venus and Jupiter during 1966

1966 Fall URSI-IEEE Meeting, Palo Alto, California

December 6-9, 1966

S. Zisk, Maximum Information and Other Effects of Baseline Parameters on Interferometers Used for Radio Astronomy

Department of Electrical Engineering Colloquium, University of Notre Dame, Notre Dame, Indiana

December 9, 1966

A. Bers, Instabilities of Plasmas in Solids (invited)

Conference on Fundamentals of Gas-Surface Interactions, San Diego, California

December 13-16, 1966

R. E. Stickney, R. M. Logan, S. Yamamoto, and J. C. Keck, Simple Classical Model for the Scattering of Gas Atoms from a Solid Surface : III. Analyses for Monoenergetic Beams and Lock-in Detector Signals

American Philosophical Society Meeting, Philadelphia, Pennsylvania

December 21, 1966

S. Bromberger, Questions

41st Annual Meeting, Linguistic Society of America, New York

December 28-30, 1966

C-W. Kim, On the Notion "Optimal Opposition"

Symposium on the Engineering Significance of the Biological Sciences, Carnegie Institute of Technology, Pittsburgh, Pennsylvania

January 25-27, 1967

W. A. Rosenblith, Communications Engineering Views the Brain : Anno 1967

International Symposium on Zodiacal Light and the Interplanetary Medium, Honolulu, Hawaii

January 29-February 3, 1967

G. Fiocco, Possibility of Continuously Measuring the Influx of Extraterrestrial Dust by Optical Radar (invited)

American Physical Society Meeting, New York

January 30-February 2, 1967

K. U. Ingard and M. Schulz, Role of Electrons and Ions in a Sound Wave in a Weakly Ionized Gas

MEETING PAPERS PRESENTED (continued)

Third Annual Informal Conference on Active Microwave Effects in Bulk Semiconductors,
IEEE Headquarters, New York

February 2-3, 1967

G. Bekefi and A. Bers, Microwave Emission from n-Type Indium Antimonide
at 4.2°K and 78°K

R. N. Wallace and A. Bers, Microwave Emission from 'Contactless' Indium
Antimonide Samples

1967 International Solid-State Circuits Conference, Philadelphia, Pennsylvania

February 15-17, 1967

D. H. Steinbrecher, Efficiency Limits for Tuned Harmonic Multipliers with
Punch-through Varactors

Colloquium, Rockefeller University, New York

February 16, 1967

W. A. Rosenblith, Computer Processing of Neuroelectric Data (invited)

Symposium "Psycholinguistic Insights into the Reading Process," New York

February 16-18, 1967

P. A. Kolers, Linguistic Analysis of Reading Errors (invited)

Demonstration Lecture, Dartmouth College, Hanover, New Hampshire

February 17, 1967

S. C. Brown, Computer-Aided Search for Scientific Literature (invited)

JOURNAL PAPERS ACCEPTED FOR PUBLICATIONS

(Reprints, if available, may be obtained from the Document Room,
26-327, Research Laboratory of Electronics, Massachusetts Insti-
tute of Technology, Cambridge, Massachusetts 02139.)

R. J. Allen and A. H. Barrett, Intensity and Linear Polarization Observations of
Cassiopeia A, Cygnus A, and Taurus A at 1.97 cm (Abstract) (Astron. J.)

A. H. Barrett, Radio Observations of Interstellar OH (Science)

K. W. Gentle, Moving Striations in the Argon Positive Column I. Theory (Phys. Fluids)

K. W. Gentle, Moving Striations in the Argon Positive Column II. Experiments (Phys.
Fluids)

R. D. Hall and R. G. Mark, Fear and the Modification of Acoustically Evoked Poten-
tials during Conditioning (J. Neurophysiol.)

T. S. Huang and M. T. Chikhaoui, The Effect of BSC on PCM Picture Quality
(IEEE Trans. (IT))

T. S. Huang, O. J. Tretiak, B. Prasada, and Y. Yamaguchi, Design Considerations in
in PCM Transmission of Low-Resolution Monochrome Still Pictures (Proc. IEEE)

W-D. Heiss and D. C. Milne, Single Fibers of Cat Optic Nerve : Thresholds to Light
(Science)

JOURNAL PAPERS ACCEPTED FOR PUBLICATION (continued)

- U. Ingard and H. Ising, Acoustic Nonlinearity of an Orifice (J. Acoust. Soc. Am.)
- U. Ingard and M. Schulz, The Acoustic Wave Mode in a Weakly Ionized Gas (Phys. Rev.)
- J. J. Katz, Some Remarks on Quine on Analyticity (J. Philos.)
- J. J. Katz, Recent Issues in Semantic Theory (Foundations of Language)
- J. P. Kimball, Predicates Definable over Transformational Derivations by Intersection with Regular Languages (Inform. Contr.)
- S. G. Kukolich, Measurement of Ammonia Hyperfine Structure with a Two-Cavity Maser (Phys. Rev.)
- S. G. Kukolich and K. W. Billman, Square-Wave Phase Modulation in Ramsey-type Molecular Beam Resonance Experiments (J. Appl. Phys.)
- R. G. Mark and R. D. Hall, Acoustically Evoked Potentials in the Rat during Conditioning (J. Neurophysiol.)
- A. Natapoff, The Consideration of Evolutionary Conservatism Toward a Theory of the Human Brain (Perspectives in Biology and Medicine)
- R. A. Newmark, J. C. Stephenson, and J. S. Waugh, Proton Relaxation in Potassium-Ammonia Solutions (J. Chem. Phys.)
- W. F. Schreiber, Picture Coding (Proc. IEEE)
- M. Schulz and U. Ingard, Acoustic Kink Instability in an Argon Discharge (Phys. Fluids)
- Shardanand and Y. Mikawa, Photon Scattering Cross Sections at Lyman-Alpha (1215.7 \AA) for He and Ne (J. Quant. Spectry. Radiat. Transfer.)

LETTERS TO THE EDITOR ACCEPTED FOR PUBLICATION

- J. S. Barlow, Automatic Curve Reading by Phase-Modulated Analog Sampling (Proc. IEEE)
- R. A. Hoffman, Chemical Rate Processes and Magnetic Resonance Linewidths (J. Chem. Phys.)
- J. D. Macomber, N. S. Ham, and J. S. Waugh, Upper Limit to the Electric-Field Effect on the NMR Spectrum of Nitromethane (J. Chem. Phys.)
- J. M. Moran, B. F. Burke, B. Zuckerman, H. Penfield, and M. L. Meeks, Observations of OH Emission in the H II Region W3 with a $74,400\lambda$ Interferometer (Astrophys. J.)
- C. H. Perry and J. D. Wrigley, Jr., Infrared Reflectance and Optical Constants of Tektites (Appl. Opt.)
- J. A. Ross and U. Ingard, Generation of Vorticity by Waves in a Plasma (Phys. Fluids)
- J. C. Woo and D. J. Rose, Generation of a Quiescent, Variable Parameter Arc Plasma (Phys. Fluids)

SPECIAL PUBLICATIONS

- W. H. Glenn, D. R. Whitehouse, and S. C. Brown, Ion-Cyclotron Oscillations in a Plasma (Proc. Seventh International Conference on Phenomena in Ionized Gases, Beograd, 22-27 August 1965, Vol. II, pp. 370-373)
- E. B. Hooper and G. Bekefi, Electron Density Measurements with a Laser Interferometer (Proc. Seventh International Conference on Phenomena in Ionized Gases, Beograd, 22-27 August 1965, Vol. III, pp. 209-213)
- W. S. McCulloch, Cybernetic Problems of Learning (Conditional Reflex, J. B. Lippincott Co., Philadelphia, 1967)
- D. H. Staelin and E. C. Reifenstein, K-band Observations of Venus and Jupiter during 1966 (NEREM Record 1966) (pp. 138-139)
- J. S. Waugh, Nuclear Relaxation in Liquids and Gases, in Proc. International Conference on Magnetic Resonance and Relaxation, XIVth Colloque Ampère (North-Holland Publishing Co., Amsterdam, The Netherlands, 1967)

TECHNICAL REPORTS PUBLISHED

(These and previously published technical reports, if available, may be obtained from the Document Room, 26-327, Research Laboratory of Electronics, Massachusetts Institute of Technology, Cambridge, Massachusetts 02139)

INTRODUCTION

This report, the eighty-fifth in a series of quarterly progress reports issued by the Research Laboratory of Electronics, contains a review of the research activities of the Laboratory for the three-month period ending February 28, 1967. Since this is a report on work in progress, some of the results may not be final.

GENERAL PHYSICS

I. MOLECULAR BEAMS*

Academic and Research Staff

Prof. J. R. Zacharias
Prof. K. W. Billman
Prof. J. G. King

Prof. C. L. Searle
Dr. K. Fokkens
Dr. S. G. Kukolich

D. Babitch
F. J. O'Brien
M. A. Yaffee

Graduate Students

R. Golub
C. M. Bell
D. E. Oates

A. CESIUM BEAM ATOMIC CLOCK

N67-27082

A new beam tube, which was last mentioned in Quarterly Progress Report No. 80 (page 2), that differs in design from previous clocks, primarily in possessing a recirculating oven,¹ and in detail in magnet and cavity design, has been completed. The construction of the associated low-frequency electronics system is nearly complete.

The proposed system for the new clock is shown in Fig. I-1. The theoretical clock

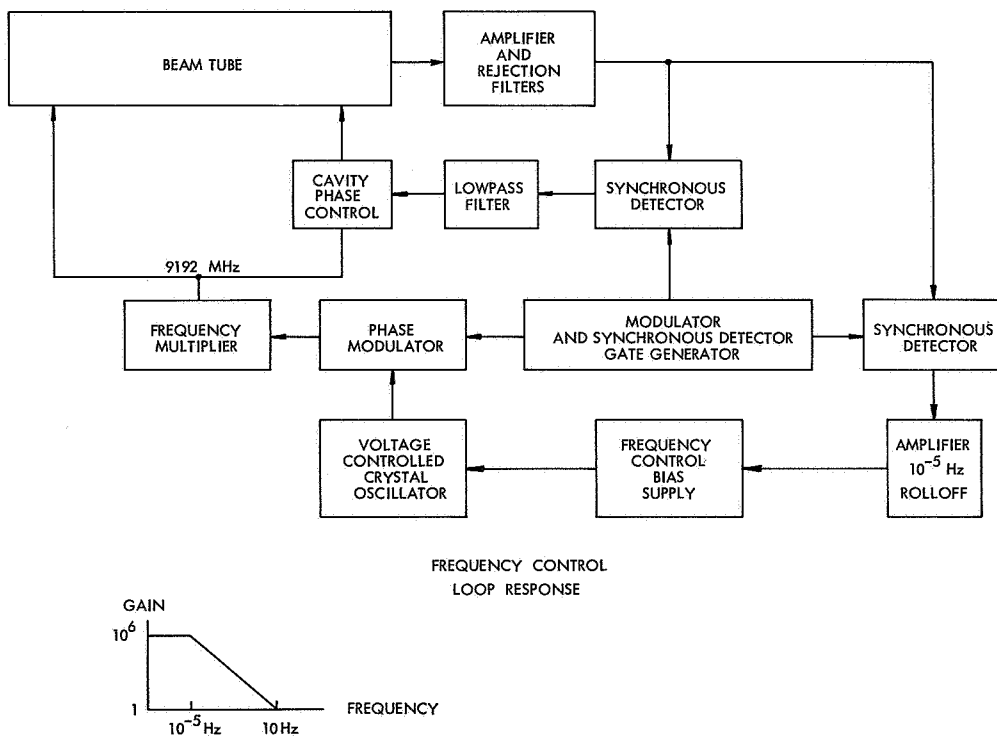


Fig. I-1. Atomic clock diagram and frequency-control loop response.

*This work was supported by the Joint Services Electronics Programs (U. S. Army, U. S. Navy, and U. S. Air Force) under Contract DA 28-043-AMC-02536(E).

(I. MOLECULAR BEAMS)

stability for beam shot noise only is

$$\frac{\sigma[\langle \phi \rangle_{t, \tau}]}{\omega_0} = \frac{5 \times 10^{-13}}{\tau^{1/2}}, \quad \tau \leq 10^6 \text{ sec,}$$

where $\sigma[\langle \phi \rangle_{t, \tau}]$ is the variance of the average frequency departure from the undisturbed cesium resonance frequency ω_0 for an averaging time τ . We hope that this shot-noise limitation can be reached by utilizing the high beam current provided by a recirculating oven and by making use of the cavity phase-error correction capabilities of frequency impulse modulation.² It has been found that the noise of a cesium beam detected by a niobium hot wire is approximately the theoretical shot noise attributable to pressure fluctuations in the region of the modulation frequency.

1. Theoretical Work

Following the lines developed by Cutler,³ work has been carried out on calculating the effects of various types of noise on clock stability. Explicit expressions for noise sensitivity have been obtained for a simplified (linearly additive noise) loop equation, and work on a more complete power spectral density (vectorially additive noise) theory is now in progress. The effects of distortion of the modulation signal and imperfect synchronous detection are also of extreme importance to clock stability; these problems are being investigated at the present time. A system analysis, which has resulted in clarification of how frequency and phase errors are generated and transmitted through the loop, has been carried out.

2. Recirculating Oven

It is a fundamental theorem of cesium beam resonance apparatus that larger beam currents lead to larger signal-to-noise ratios, and consequently to better stability. Unfortunately, in most devices the amount of cesium which forms a collimated beam is small compared with the total cesium lost from the oven, because of the $\cos^2 \theta$ intensity distribution of atoms emerging from a slit. Thus impractically large amounts of cesium would be needed to provide an intense beam during a long running period. It was proposed that a recirculating oven be built on the plan sketched in Fig. I-2.

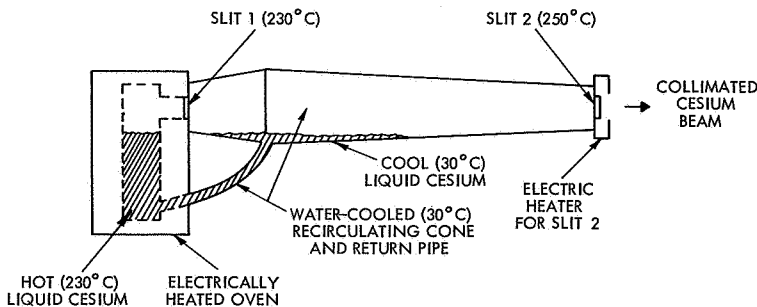


Fig. I-2. Recirculating oven.

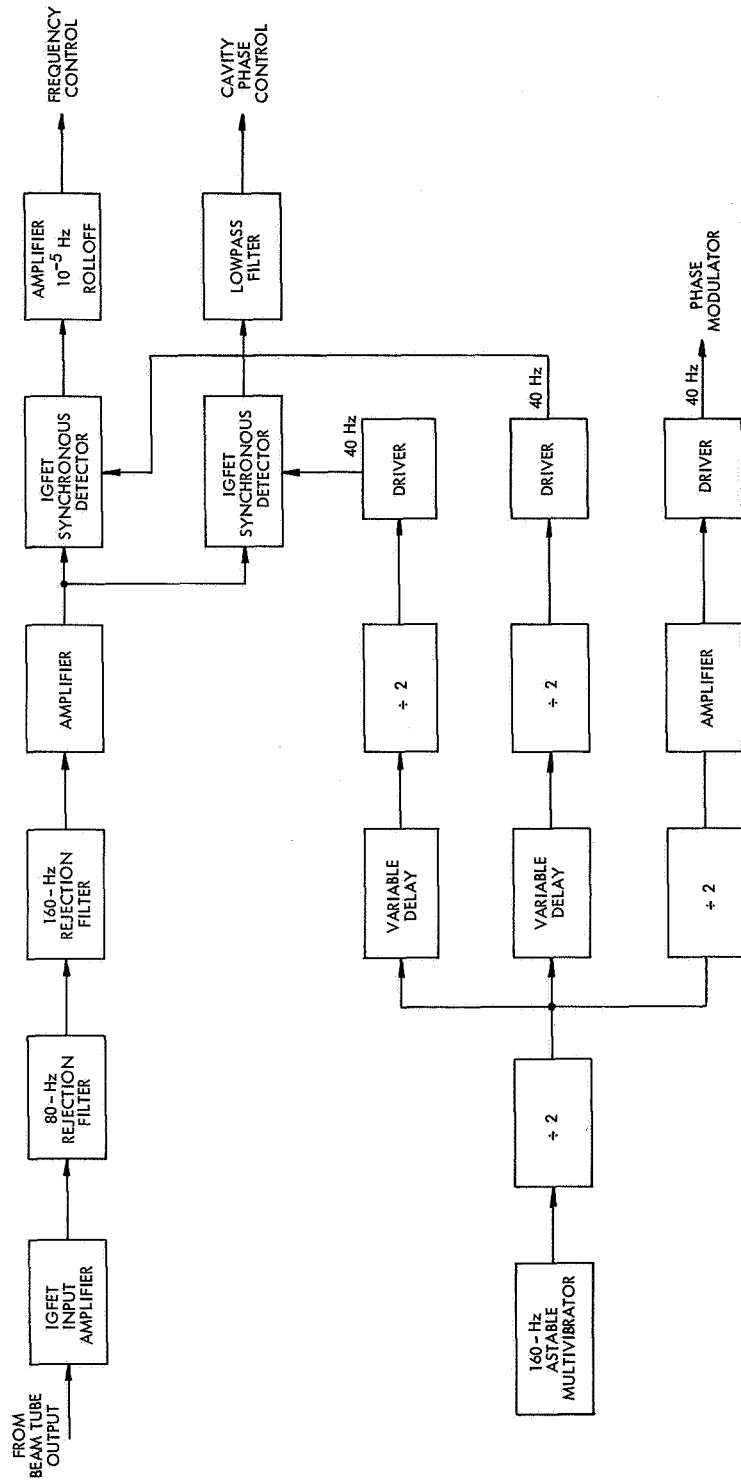


Fig. I-3. Low-frequency electronics system.

(I. MOLECULAR BEAMS)

The oven was constructed, but it was found subsequently that large amounts of background gas emerging from the hot oven walls and failing to exit through the small slits 1 and 2 caused the recirculating cone to act as a long scattering chamber, thereby reducing beam intensity. A suitable pumpout device for the cone was made, and the beam intensity was restored to expected values. In a different earlier experiment⁴ it was shown that vigorous outgassing of the oven, before filling with cesium, without the flow-restricting slits also cured the problem. Examination of the distribution of cesium in an oven frozen by application of dry ice indicated that recirculation may have been taking place. Not enough running time at high intensities has been accumulated yet to prove in the direct manner that recirculation must be taking place.

3. Low-Frequency Electronics

The proposed low-frequency electronics system is shown in Fig. I-3. Digital techniques have been used to produce a symmetrical (small even harmonic content) modulator signal, and to produce synchronous detector gate waveforms of variable delay that have a 90° phase difference when the variable delays are zero. Integrated circuits were found useful in both digital and linear circuitry, and were used to make active notch filters of high rejection and narrow stopband [the 80-Hz and 160-Hz notch filters are used to prevent saturation by even harmonics of the amplifier following them, since the even harmonics of the beam tube output are not zero when the phase and frequency errors of the loop are zero]. Use has also been made of recently available complementary insulated gate field-effect transistors to make extremely low-error synchronous detectors that are now undergoing testing.

D. Babitch, C. M. Bell

Footnotes and References

1. Proposed by C. O. Thornburg (1966).
2. The original paper on the subject of frequency impulse modulation is by R. S. Badessa, V. J. Bates, and C. L. Searle, "Frequency Impulse Modulation as a Means of Attaining Accuracy in Cesium Atomic Clocks," *IEEE Trans.*, Vol. IM-13, No. 4, pp. 175-180, December 1964. In his Ph.D. thesis, C. O. Thornburg considerably expanded the theory, and recently S. G. Kukolich and K. W. Billman have carried out computer calculations and performed experiments (to be published in *J. Appl. Phys.*) proving the validity of the theory.
3. A fundamental work on noise in frequency sources is the paper by L. S. Cutler and C. L. Searle, "Some Aspects of the Theory and Measurement of Frequency Fluctuations in Frequency Standards," *Proc. IEEE* 54, 2 (1966).
4. T. R. Brown, Private communication, Research Laboratory of Electronics, M.I.T., 1966.

II. MICROWAVE SPECTROSCOPY*

Academic and Research Staff

Prof. M. W. P. Strandberg
Prof. R. L. Kyhl

Dr. T. E. McEnally, Jr.

J. G. Ingersoll
J. D. Kierstead

Graduate Students

J. M. Ditz
R. L. Espino
L. R. Fox

J. U. Free
R. M. Langdon, Jr.

M. K. Maul
S. R. Reznick
B. N. Yung

A. VELOCITY SURFACES IN LITHIUM NIOBATE

N67-27083

The method for determining an analytical approximation for the velocity of sound surfaces for previously reported crystals¹ has been applied to lithium niobate. This method expresses an approximation to each of the three surfaces as a sum over functions of the appropriate symmetries. The method determines the coefficients in the sum by a least-squares fit to the exact surface. Lithium niobate has the symmetry of quartz or sapphire. The basis functions are those listed in Quarterly Progress Report No. 84. Table II-1 lists the coefficients in the expansion $V(\theta, \phi) = \sum C_n^\sigma W_n^\sigma(\theta, \phi)$. ($\sigma = 1, 2, 3$ for each of the three surfaces.)

Table II-1. Coefficients C_n^σ .

n	$\sigma = 1$	$\sigma = 2$	$\sigma = 3$
1	.7920	.8610	1.4484
2	-.003786	-.02802	.07939
3	-.06458	-.01514	.04267
4	.04947	-.04637	-.001434
5	.04148	-.03404	-.004503
6	.02470	-.02417	-.006694
7	$-.1190 \times 10^{-6}$	$.1117 \times 10^{-6}$	$.3242 \times 10^{-8}$
8	.009004	-.008396	-.001100
9	.006779	-.006630	-.001841
10	$.70618 \times 10^{-8}$	$-.6717 \times 10^{-8}$	$-.9156 \times 10^{-9}$
11	.0003993	-.0007653	.0004249
12	.0007973	-.0007792	-.0002178
13	$.1125 \times 10^{-8}$	$-.8639 \times 10^{-9}$	$-.2138 \times 10^{-9}$
14	$.1676 \times 10^{-10}$	$-.1638 \times 10^{-10}$	$.1692 \times 10^{-12}$

*This work was supported by the Joint Services Electronics Programs (U.S. Army, U.S. Navy, and U.S. Air Force) under Contract DA 28-043-AMC-02536(E).

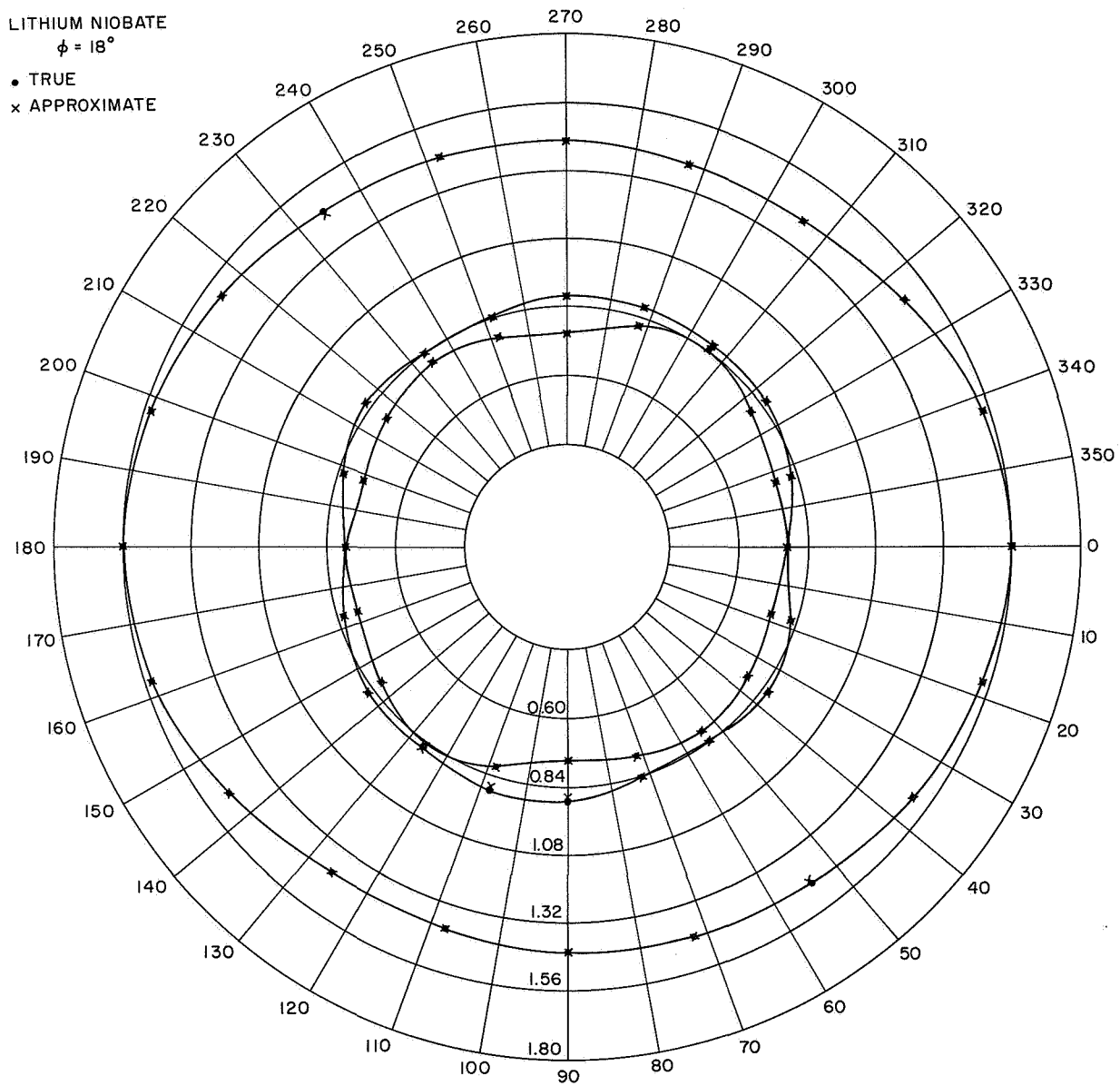


Fig. II-1. True and approximate values for the velocity of sound in Lithium Niobate.

LITHIUM NIOBATE
 $\phi = 24^\circ$

• TRUE
x APPROXIMATE

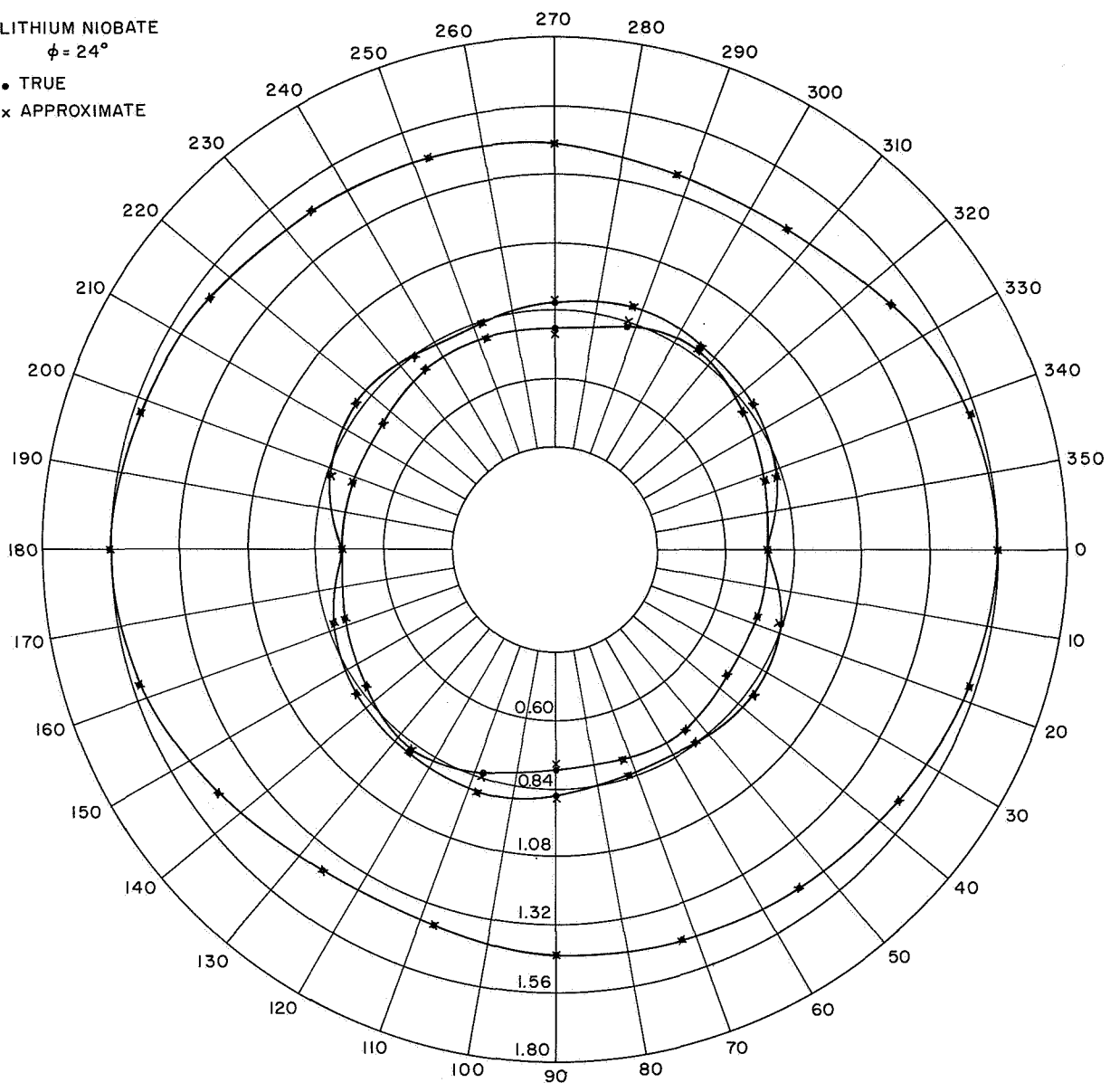


Fig. II-1. Continued.

LITHIUM NIOBATE
 $\phi = 6^\circ$
 • TRUE
 x APPROXIMATE

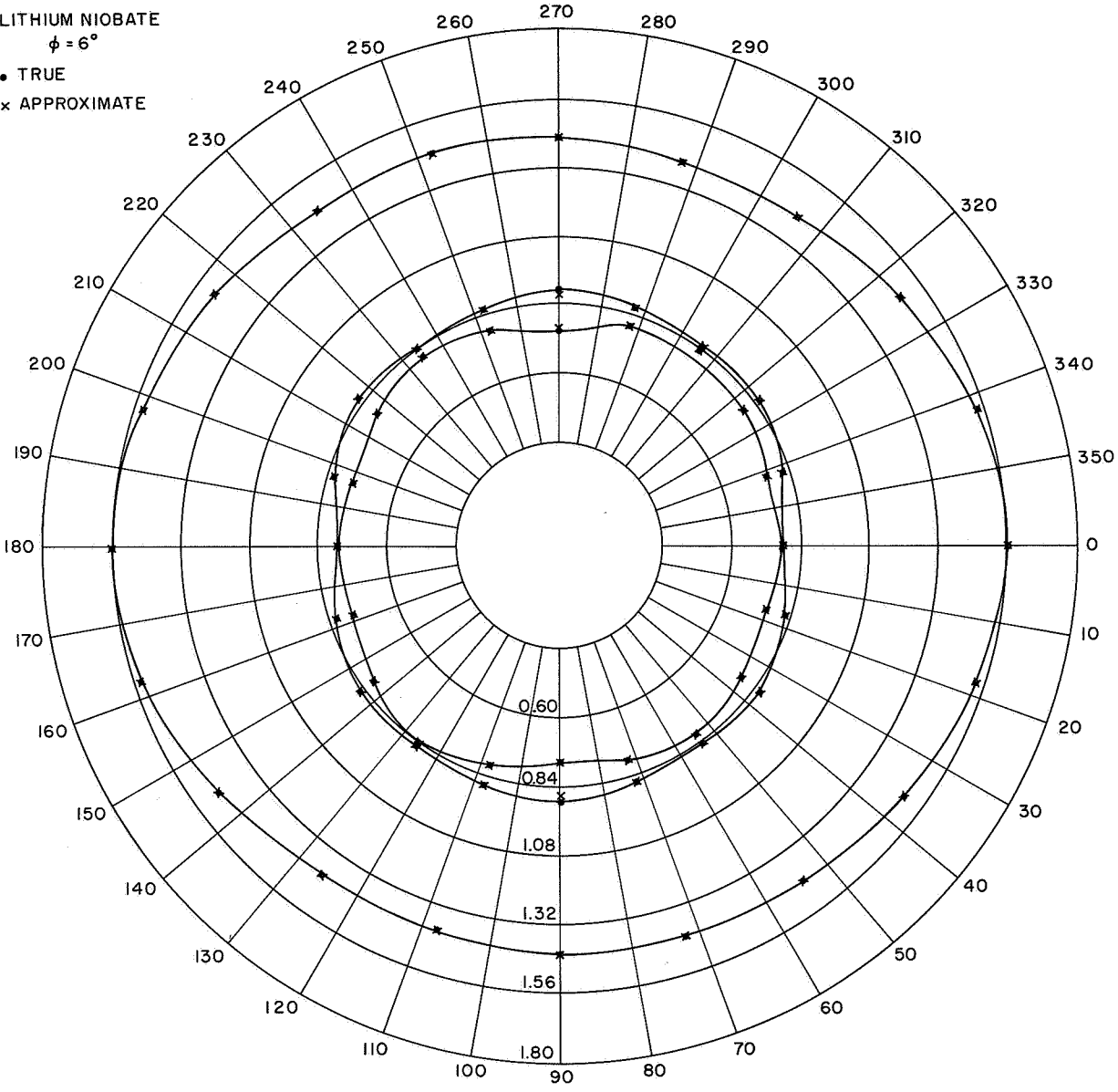


Fig. II-1. Continued.

LITHIUM NIOBATE
 $\phi = 12^\circ$

• TRUE
x APPROXIMATE

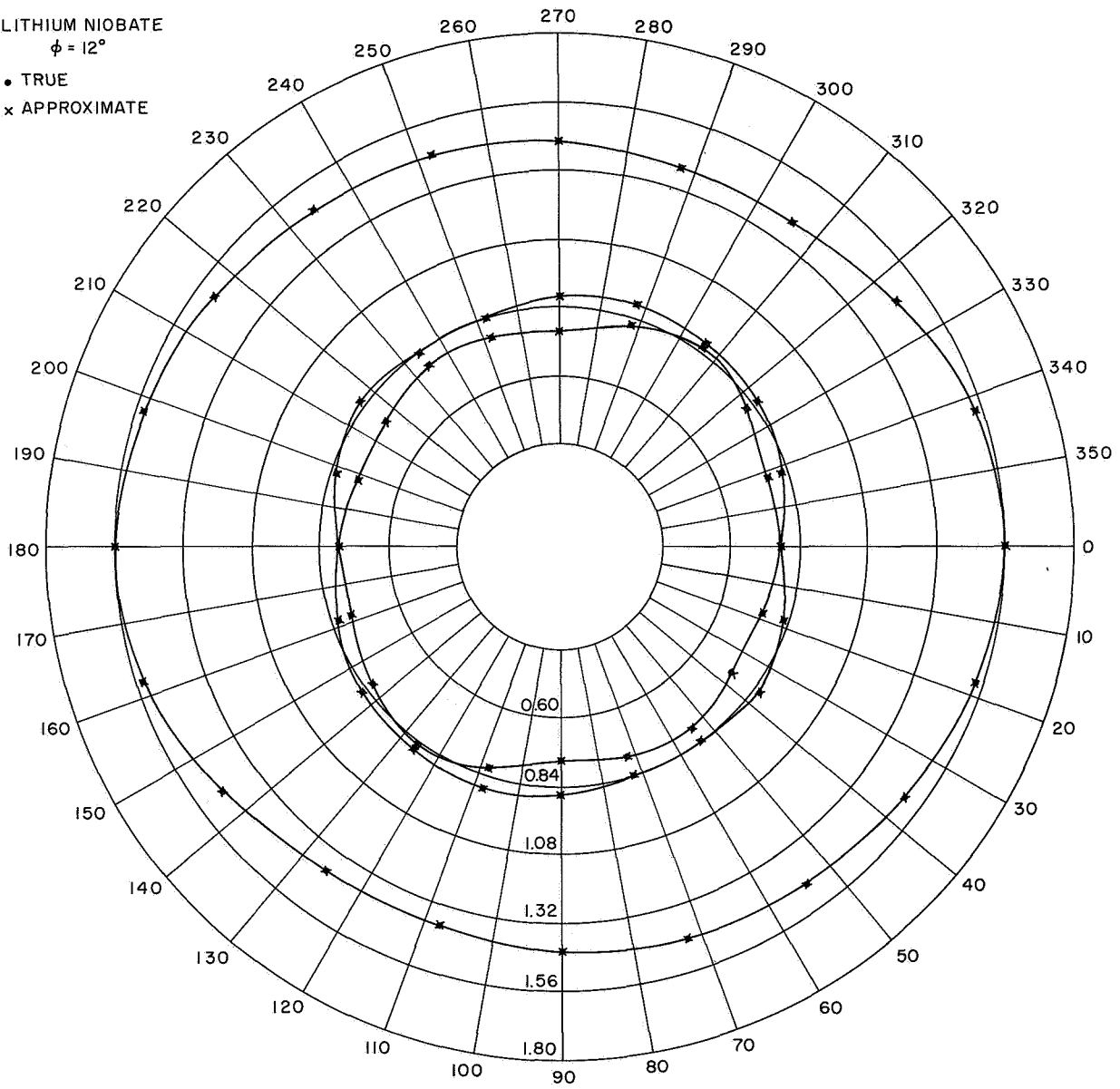


Fig. II-1. Continued.

LITHIUM NIOBATE

$\phi = 30^\circ$

• TRUE
x APPROXIMATE

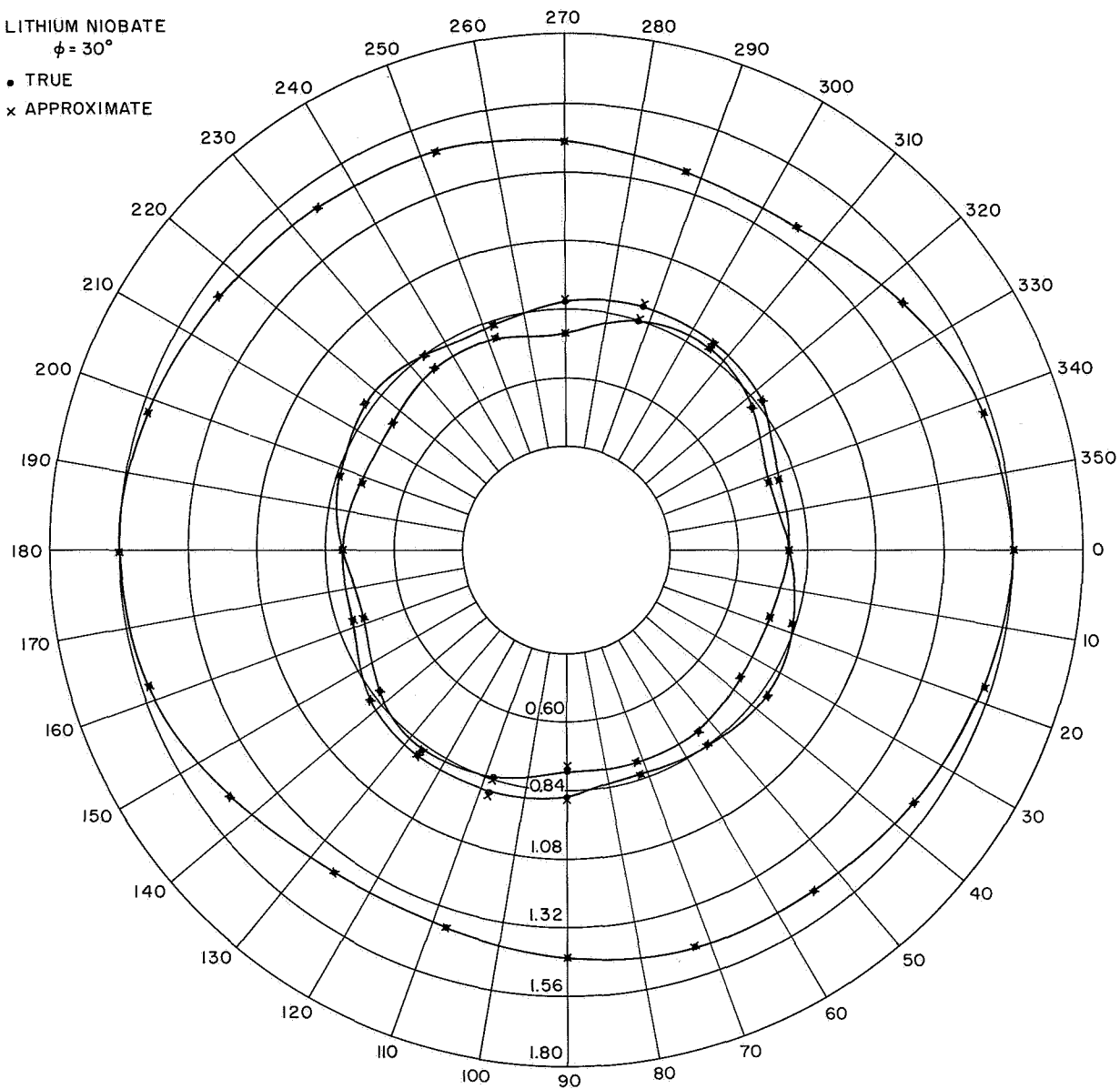


Fig. II-1. Continued.

LITHIUM NIOBATE

$\phi = 0^\circ$

• TRUE

x APPROXIMATE

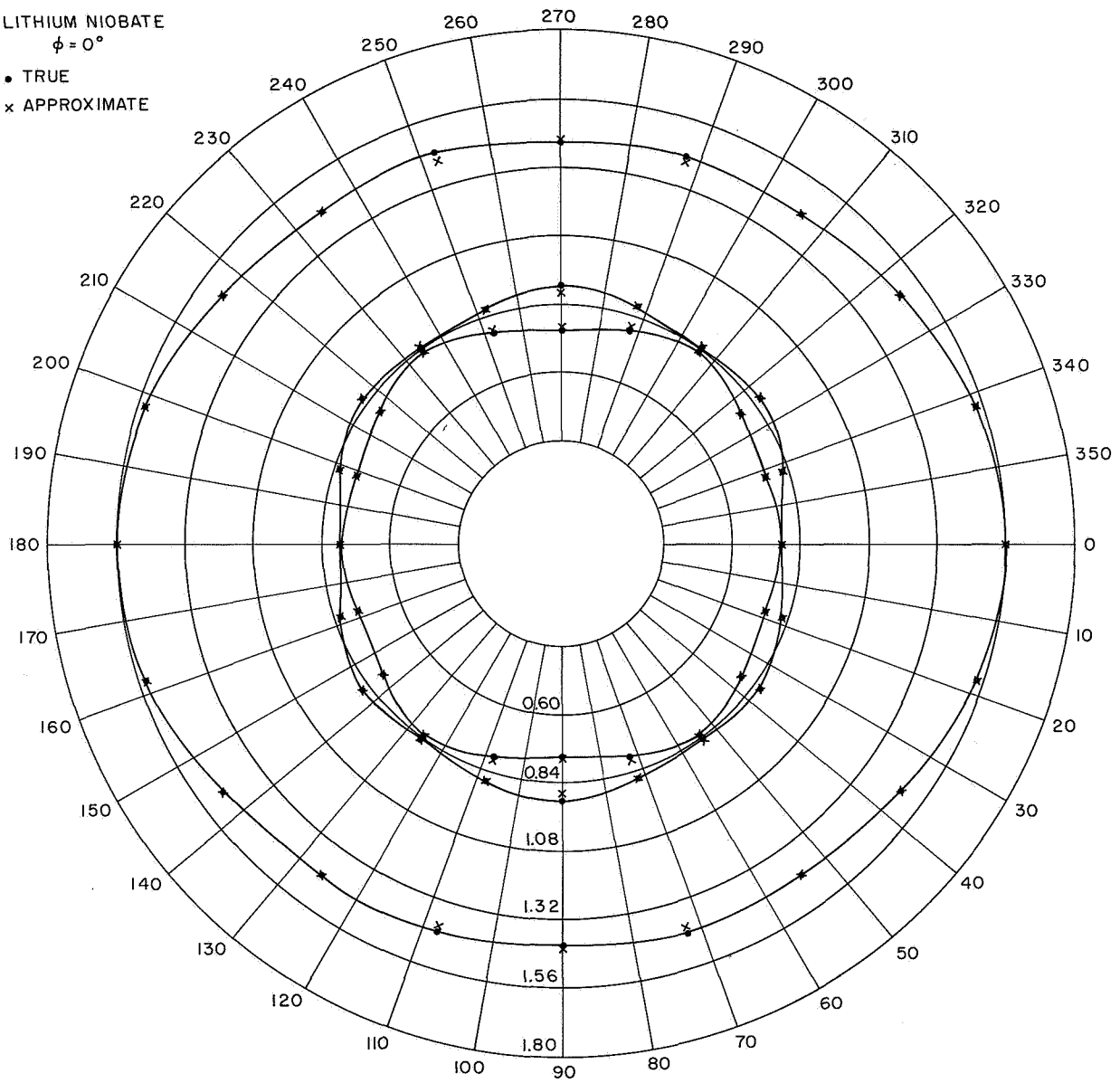


Fig. II-1. Concluded.

(II. MICROWAVE SPECTROSCOPY)

Figure II-1 shows the surfaces computed exactly and those computed by using the analytical approximations.

S. R. Reznek

References

1. S. R. Reznek, "Expansion of Velocity Surfaces in Spherical Harmonics," Quarterly Progress Report No. 84, Research Laboratory of Electronics, M.I.T., January 15, 1967, pp. 17-26.

III. ELECTRON MAGNETIC RESONANCE*

Academic and Research Staff

Prof. K. W. Bowers

Graduate Students

Nancy H. Kolodny
C. Mazza

A. C. Nelson
R. S. Sheinson
S. N. Suchard

Y.-M. Wong
B. S. Yamanashi

A. RADICALS IN THE GAS PHASE

N67-27084

Paramagnetic species in the gas phase are of special interest, because of their unusual physical and chemical properties. In the past few years, detection of a few simple radicals has been reported (NO^1 , OH^2 , ClO^3 , BrO^3). These successes make us considerably optimistic about the detectability of more complex but much less stable radicals, such as CH_3 and C_2H_5 . We hope that study of these species in the gas phase may lead to an understanding of their internal molecular dynamics. In the past few months, two methods have been explored for generating ethyl radicals. In both cases, hydrogen atoms were produced by a microwave discharge of hydrogen gas at $\sim 100\text{-}\mu$ pressure. In one case, ethylene was added to the stream of hydrogen atoms; in the other, ethyl iodide was used as reactant. The choice of ethyl iodide was suggested by the fact that the activation energy of the reaction



is very small. Present results favor the use of ethyl iodide.

Production and detection of the radicals is carried out in a flow system through an Electron Magnetic Resonance spectrometer. Throughout the process, the system is maintained at constant pressure between $100\ \mu$ and $300\ \mu$. Numerous lines have been observed, but at very poor signal-to-noise ratios. Current work is directed toward improving the signal-to-noise ratio with improved flow systems and better resonant-cavity design. Also, a small mass spectrometer is being constructed to monitor the concentrations of the various species that are formed. Work is also under way to produce enough CH to work with (by different means).

K. W. Bowers

References

1. R. Beringer, *Phys. Rev.* **78**, 581 (1950).
2. H. E. Radford, *Phys. Rev.* **122**, 114 (1960).
3. A. Carrington and P. H. Levy, *J. Chem. Phys.* **44**, 1298 (1966).

*This work was supported by the Joint Services Electronics Programs (U.S. Army, U.S. Navy, and U.S. Air Force) under Contract DA 28-043-AMC-02536(E).

(III. ELECTRON MAGNETIC RESONANCE)

B. CONSTRUCTION OF A RAPID-SCANNING EPR SPECTROMETER COUPLED WITH A FLASH-DISCHARGE SOURCE

The use of high-intensity, short-duration flash-discharge lamps for the production and study of transient species and excited states of molecules by optical means is well known. The power of magnetic resonance methods has not yet been applied to such methods, because of a large number of difficulties that we now seem to have overcome. Our system behaves as follows: A 1-mfd, 3000-volt capacitor bank is discharged through a specially designed Xenon flash tube that is focused on the sample of interest in the resonant cavity of an EPR spectrometer; the flash triggers a series of pulses, which (i) triggers a ramp used for field sweep, (ii) initiates the recording of the spectrum by a small digital computer (1000 points at 25 μ sec per point), (iii) shuts off the computer, (iv) shuts off the ramp, (v) recharges the capacitor bank, and (vi) begins the cycle over again, adding the new signal to the old for a predetermined number of cycles; the initial magnetic field is shifted and the whole process is repeated. At present, we are involved in the optimization of the various components of this apparatus, and we hope to present a complete description in the next progress report.

K. W. Bowers

IV. RADIO ASTRONOMY*

Academic and Research Staff

Prof. A. H. Barrett
Prof. B. F. Burke
Prof. L. B. Lenoir

Prof. D. H. Staelin
Dr. S. H. Zisk

J. W. Barrett
Patricia P. Crowther
P. L. Seymour

Graduate Students

M. S. Ewing
N. E. Gaut
M. Melnick

J. M. Moran, Jr.
G. D. Papadopoulos

E. C. Reifenstein III
A. E. E. Rogers
T. L. Wilson

A. INTERPRETATION OF SPECTRAL DATA

N67-27085

A microwave spectrum contains information about the temperature, pressure, and composition of the spectrum source. A basic problem in microwave observations is the optimum interpretation of observed spectra in terms of source parameters.

A good example is the problem of estimating the water-vapor profile in the terrestrial atmosphere by using observed atmospheric absorption spectra. This example is interesting because considerable use of a priori statistics must be made to obtain good performance.

A successful approach has been to assume a linear form for the optimum estimation procedure, and then to minimize the mean-square error. The estimate is

$$p^* = \underline{\underline{D}} d,$$

where p^* is a column matrix representing the estimated water-vapor profile, $\underline{\underline{D}}$ is the linear operator matrix, and d is the data column matrix. The optimum matrix $\underline{\underline{D}}$ is a function of the known a priori statistics and relationships governing the true water-vapor profile p and the data matrix d .

It can be shown¹ that $\underline{\underline{D}}$ is

$$\underline{\underline{D}}^t = \underline{\underline{C}}_d^{-1} E[d p^t],$$

where $\underline{\underline{C}}_d$, the correlation matrix of the data vector d , = $E[d d^t]$. Only second-order a priori statistics are required to minimize the mean-square error if a linear matrix estimation procedure is used. This basic method has been applied to simulated water-vapor spectral data; the results are described in Section IV-A. 1.

*This work was supported principally by the National Aeronautics and Space Administration (Grant NsG-419 and Contract NSR-22-009-120); and in part by the Joint Services Electronics Programs (U. S. Army, U. S. Navy, and U. S. Air Force, under Contract DA 28-043-AMC-02536(E)).

(IV. RADIO ASTRONOMY)

Since microwave emission data are inherently nonlinear, it is reasonable to seek a nearly optimum nonlinear estimation procedure. A form of Baye's estimate was applied to this problem, but required inordinate amounts of computer time for any but relatively simple estimations. An extension of the linear operator technique appears more promising. Here the linear operator $\underline{\underline{D}}$ operates not only on the raw data d , but also on cross products and higher powers of the raw-data values. Thus an augmented data matrix d_a might include $(1, d_1, d_2, d_1^2, d_2^3, d_1 d_2)$, or several more elements than the original d matrix (d_1, d_2) . The method for deriving the new D is essentially the same as before. The nonlinear result is

$$\underline{\underline{D}}^t = \underline{\underline{C}}_{d_a}^{-1} E[d_a p^t],$$

where d_a is the data vector augmented as illustrated above, and $\underline{\underline{C}}_{d_a}$ is the correlation matrix for the augmented data vector. The nonlinearity of the estimation procedure may be controlled by the degree to which d_a is augmented.

An interesting feature of this estimation procedure is the way that the optimum estimate requires higher order statistics in $\underline{\underline{C}}_{d_a}$ for higher order nonlinearities in the estimation procedure. If d_a includes elements like $d_i d_j$, then $\underline{\underline{C}}_{d_a}$ may include elements like $E[d_i d_j d_k d_l]$. This nonlinear estimation procedure appears to be practical for many problems involving interpretation of spectra, and could probably be applied in many other areas.

D. H. Staelin

References

1. C. D. Rogers, "Satellite Infrared Radiometer, A Discussion of Inversion Methods," Memorandum No. 66.13, Oxford University, 1966.

1. RESULTS OBTAINED FROM THE INVERSION OF SIMULATED ATMOSPHERIC WATER-VAPOR SPECTRA

An optimum linear estimator for inverting spectral data has been outlined in Section IV-A. Its form is

$$p^* = \underline{\underline{D}} d,$$

in which p^* is the estimated column vector for the parameter of interest; d , the column vector representing spectral and other, if any, related data; and $\underline{\underline{D}}$, the linear operator matrix relating p^* and d .

Minimizing the mean-square error between p^* and the true profile p leads to an expression from which \underline{D} may be computed. In the vertical profile of atmospheric water vapor, for which the water-vapor density is the parameter of interest, it can be shown that this expression becomes

$$\underline{D}^t = \underline{C}_d^{-1} E[d \rho^t] = [\underline{C}_o + \underline{C}_n]^{-1} \underline{W} \underline{C}_\rho.$$

Here, \underline{W} is the modified weighting-function matrix for atmospheric absorption, and \underline{C}_o is the noiseless data correlation matrix defined by

$$\underline{C}_o = E[d_o d_o^t] = \underline{W} \underline{C}_\rho \underline{W}^t,$$

in which \underline{C}_ρ is the atmospheric water-vapor correlation matrix given by

$$\underline{C}_\rho = E[\rho \rho^t],$$

and \underline{C}_n is the noise correlation matrix defined by

$$\underline{C}_n = E[n n^t].$$

Preliminary inversions have been completed. We have used as input computed absorption spectra from each radiosonde at the following frequencies: 21.9, 23.5, and 29.45 GHz. As an additional data point, we have used the water vapor density at

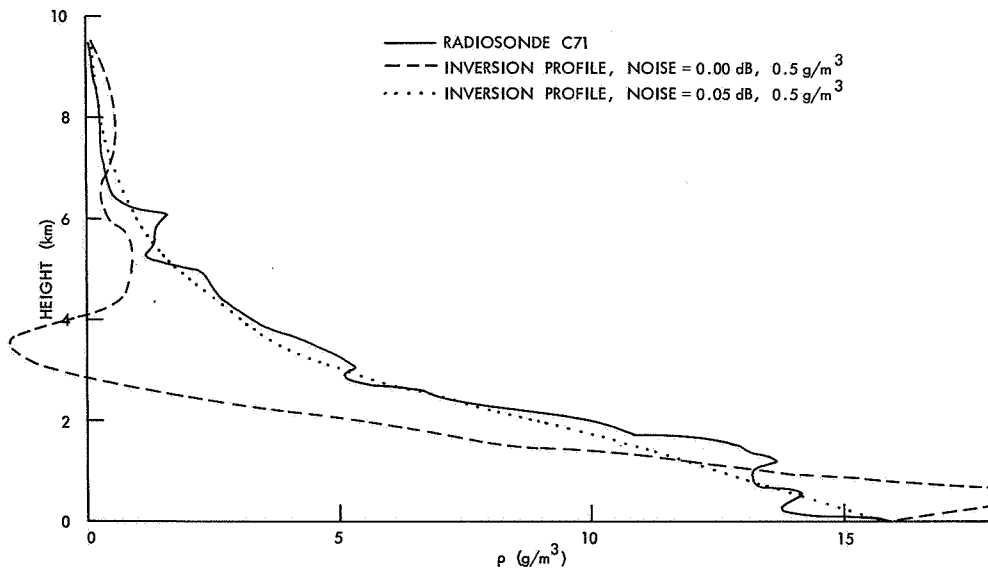


Fig. IV-1. Radiosonde C71 results.

(IV. RADIO ASTRONOMY)

the surface. Two radiosondes with their corresponding inversion profiles are illustrated in Figs. IV-1 and IV-2.

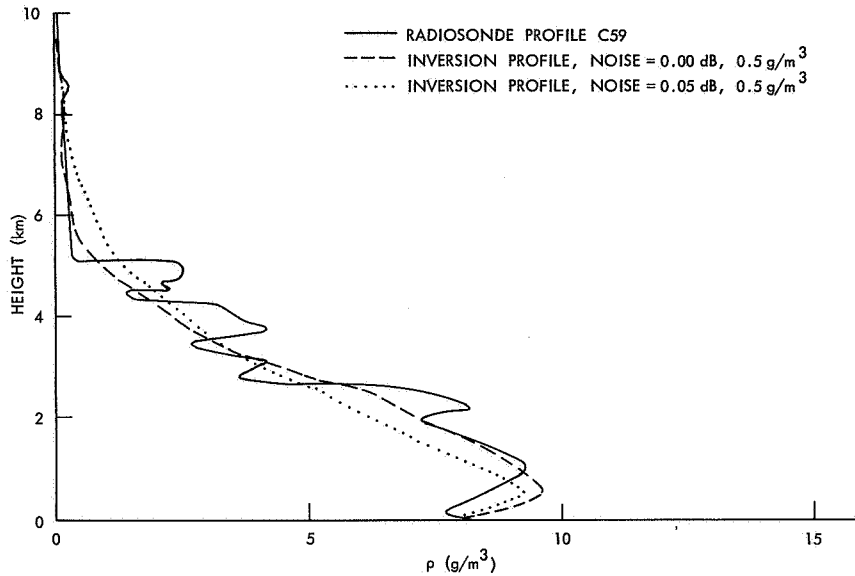


Fig. IV-2. Radiosonde C59 results.

Figure IV-1 best illustrates the effect of noise on inversion. The solid profile is the water-vapor density as recorded by radiosonde C71, which was launched 10 August 1965. The dashed profile represents the inversion when there is assumed to be no noise in the spectral data, but that surface water-vapor density is uncertain to the extent of $0.5 \text{ g}/\text{m}^3$. A grossly unstable inversion results. When the spectral data are assumed to have an rms error of 0.05 db, the inversion is stabilized and represents the true profile quite well. The zero noise case, however, represents an integrated water vapor that differs only -0.2% from the integrated water vapor derived from the radiosonde, whereas the noise case differs by -2.8% .

This latter effect is a general feature of the inversion scheme. Noise stabilizes the solution but also drives the inversion toward the mean profile as defined by the a priori statistics. In this case, the mean represents less integrated water vapor than the true profile, and therefore the estimated total water vapor is driven toward smaller values in the noise case.

Figure IV-2 is included to show that strong inversions of moisture near the surface of the earth can be indicated, if not faithfully reproduced, by this scheme. The radiosonde illustrated here was taken 14 July 1965. The dashed profile is the noiseless case, and, for this radiosonde, is a better representation of the true

profile than the noise case. The other oscillations of the true profile will not be recoverable by using the present data input, unless they appear in the a priori statistics. The integrated water vapor for the noiseless case differs from the true value by -1.3% . The noisy inversion differs by -4.3% .

Figure IV-3 is a histogram showing the distribution of percentage errors between

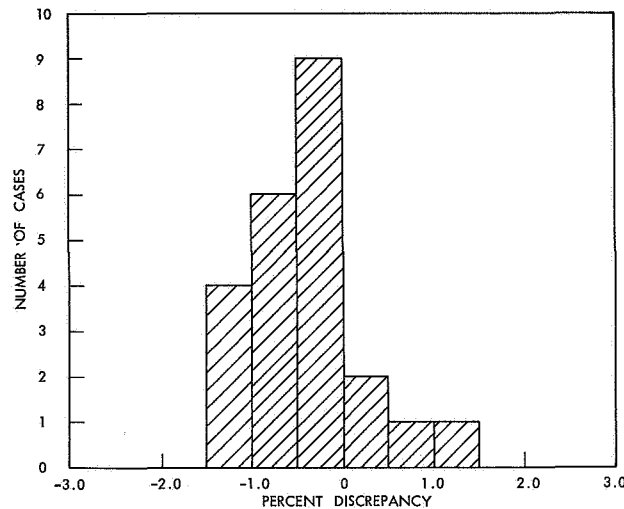


Fig. IV-3. Integrated water vapor percentage of errors.

the integrated water vapor as computed from the inversion profiles and the corresponding radiosonde profiles. The noise for these inversions was taken to be 0.005 db and 0.5 g/m^3 . The errors are skewed toward negative values, with the mean near -0.5%

Further analysis using simulated data will be conducted to understand completely the roles of noise, sampling intervals, and the a priori statistics. An analysis with observed atmospheric absorption spectra is being prepared.

N. E. Gaut, A. H. Barrett, D. H. Staelin

2. MICROWAVE DIELECTRIC CONSTANT AND EMISSIVITY OF A SOLUTION APPROXIMATING SEA WATER

For staellite-borne microwave radiometers looking at the Earth, much of the background radiation will originate from sea water at various temperatures. In order to better understand this source of radiation, the complex dielectric constant and emissivity for sea water as a function of wavelength, temperature, and angle of incidence was studied. The real part of the dielectric constant, and that portion of the imaginary part

(IV. RADIO ASTRONOMY)

which is due to losses from the oscillations of polar molecules, came from work on 0.66 normal aqueous solutions of NaCl.¹ That portion of the imaginary part of the dielectric constant which is due to ohmic losses was computed from tables of the DC conductivity of sea water.² The use of the DC conductivity for high-frequency work appears to be justified from the measurements made on the salt solutions referred to above.

Details of the real part of the dielectric constant for the salt solution at various temperatures and over the wavelength interval 0.5-22 cm are presented in Fig. IV-4.

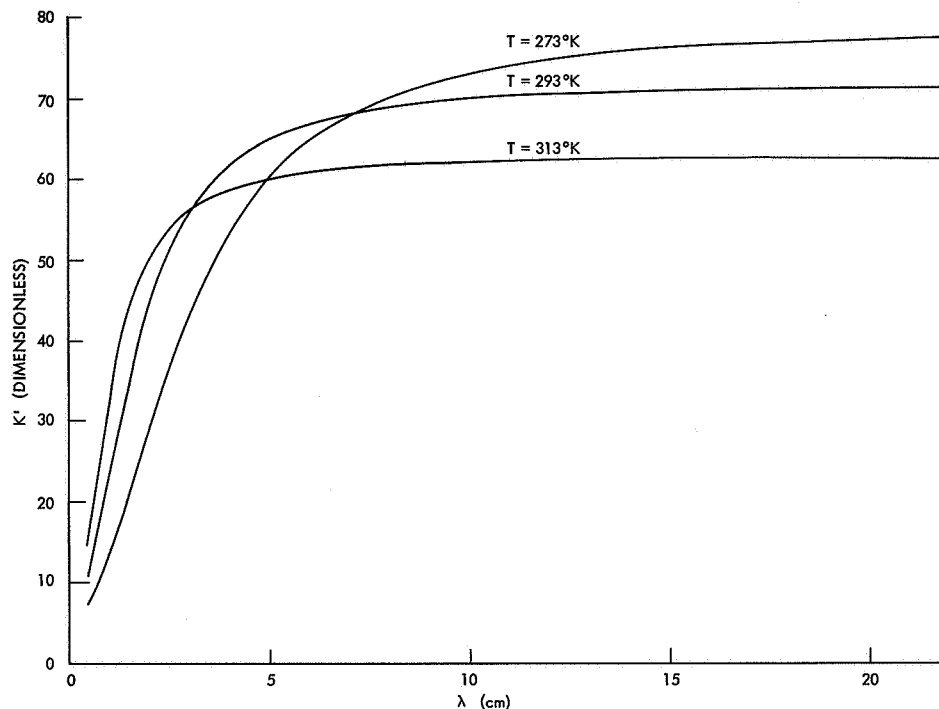


Fig. IV-4. Sea water (0.66N NaCl). Real part of the dielectric constant (K') vs wavelength.

It is important to notice the reversal of the temperature effect between the shortest and longest wavelengths depicted, with an anomalous region in the vicinity of 3-5 cm.

The complex part of the dielectric constant for the solution is shown in Fig. IV-5, again as a function of temperature and wavelength. It can be seen that the sense of the temperature effect is similar at the shortest and longest wavelengths; however, between approximately 2 cm and 6 cm, the temperature effect is reversed. This is understandable because the dielectric losses predominate in this region, and their temperature dependence completely reverses near 2 cm. Beyond 9 cm, the conduction losses dominate and the temperature effect is restored to its short-wavelength sense.

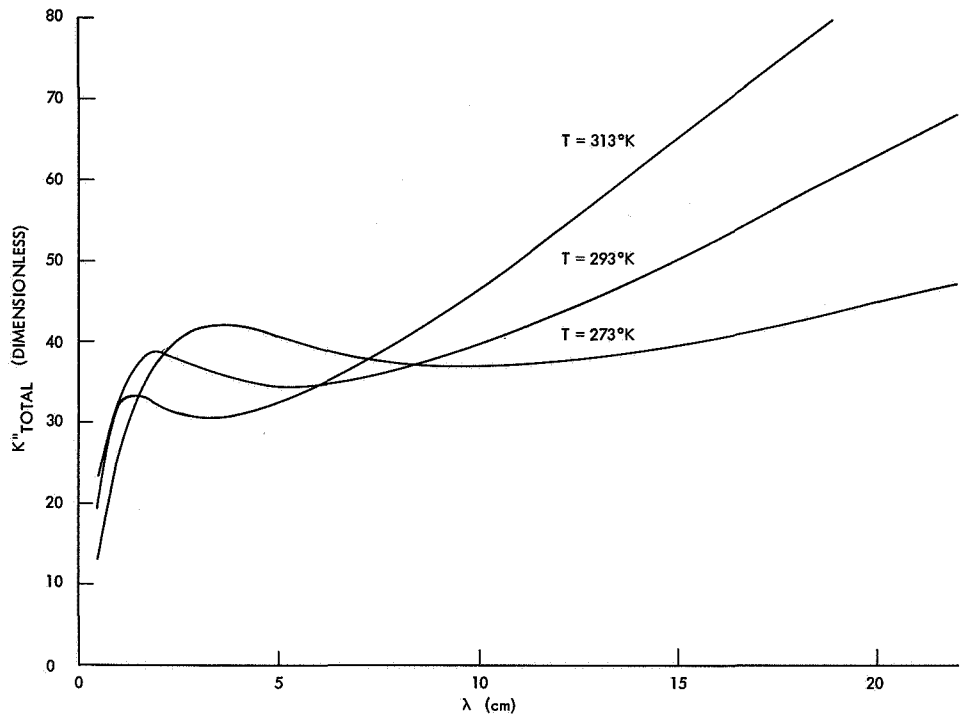


Fig. IV-5. Sea water. Imaginary part of the dielectric constant (K''_{total}) vs wavelength.

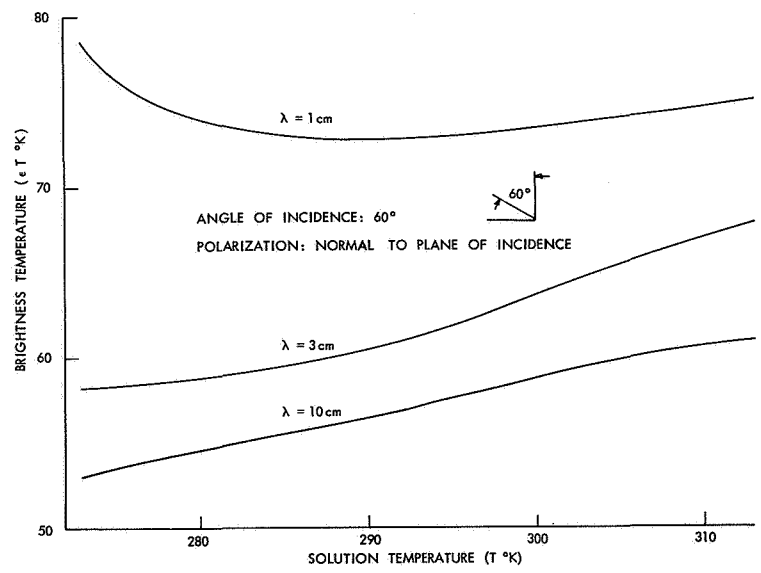


Fig. IV-6. Sea Water. Brightness temperature vs solution temperature.

(IV. RADIO ASTRONOMY)

Anomalous transition regions occur between approximately 0.8 cm and 2 cm, and between approximately 6 cm and 9 cm.

Figure IV-6 incorporates information from Figs. IV-4 and IV-5, and represents the brightness temperature as a function of thermometric temperature of the solution at wavelengths of 1, 3, and 10 cm, for an angle of incidence of 60° and for polarization normal to the plane of incidence. This figure is a corrected version of Fig. II-1 in Quarterly Progress Report No. 81 (page 11). The computations for that figure did not include losses attributable to conduction currents. The essential features of the original figure are retained in Fig. IV-6.

N. E. Gaut

References

1. J. B. Hasted, D. M. Ritson, and C. H. Collie, J. Chem. Phys. 16, 1 (1948).
2. American Institute of Physics Handbook, 2d edition, 1963.

B. HYDROGEN RECOMBINATION LINE OBSERVATIONS

The first observational phase of a program to make a survey of radial velocities of H II regions throughout the galaxy has been completed. The 140-ft telescope and 6-cm front end of the National Radio Astronomy Observatory was used, together with the Harvard multichannel spectral analyzer, to observe the 109α hydrogen recombination line. The system temperature (70°K) permits observation of lines as weak as 0.05°K in 30 minutes, with 100-kHz resolution. The recombination lines have been observed in 52 of the H II regions that have been reduced thus far, and several more identifications are expected when data analysis has been completed. There are several high-velocity regions among those observed, the highest velocity observed being 119 km/sec.

The general survey will be used to construct a dynamical model of the galaxy, analogous to the well-known 21-cm model of the Leiden and Sydney groups, which shows the distribution of neutral hydrogen in the galaxy. The new model will show the distribution of O-associations which form the H II regions, and hence should be closely related to optically derived galactic models. From the observations, a rotation law should eventually be derived, although further observations will be required to improve our statistics.

The region of the galactic center has also been examined closely, and we have been able to correct the early observations of Hoglund and Mezger, who incorrectly attributed the lines from the sources G 0.5, -0.0 and G 0.7, -0.1 to G 0.2, 0.0, and G 0.5, -0.5 , respectively. We have been unable to detect a line of normal linewidth (30 km/sec, or so) in G 0.0, 0.0 and G 0.2, 0.0, but the existence of a broad feature in these sources cannot

be excluded.

Cygnus X is an especially interesting region, and all of the major sources identified by Downes and Rinehart have been observed. Several of these sources, although they are believed to be thermal, show no line of the expected intensity, and the possibility that a number of the "thermal" sources are really old supernovae remnants with rather flat spectra is now being examined.

B. F. Burke, T. L. Wilson, E. C. Reifenstein III

C. OBSERVATIONS OF OH EMISSION

Observation of the ground-state emission lines of $O^{16}H^1$ at 18 cm near galactic H II regions have shown that the apparent diameters of the emitting regions are very small.¹⁻³ The sources associated with individual spectral features in W3, W49, and W24 (Sgr B₂) were all unresolved by an interferometer having a baseline of 3800 λ . In particular, an upper limit of 20" of arc was found for the size of the 4 strongest features in W3. All features were reported to be at the same position within 3" of arc near the edge of the optical nebulosity of the H II region. The size limits imply brightness temperatures in excess of 10^6 °K, although the linewidths of the features were characteristic of kinetic temperatures of approximately 100°K. All emission sources were polarized and exhibited anomalous multiplet intensity ratios. A quantitative explanation for the emission mechanism has not been found.

Increased angular resolution has been obtained with a new interferometer, by using the 84-ft Millstone antenna at Lincoln Laboratory and the 60-ft antenna at the Agassiz Field Station of Harvard College Observatory. The baseline was 74,400 λ at 18 cm along a bearing of 24° East of North, which gives a minimum fringe spacing of approximately 3" of arc. An effective system temperature of 300°K was achieved with the Agassiz maser amplifier and a tunnel-diode amplifier at the Millstone antenna. The strongest spectral feature of W3 yielded a signal-to-noise ratio of 8:1, with only 1 minute of integration. The measurements were made with linearly or circularly polarized feeds on the Millstone antenna and a linearly polarized feed on the Agassiz antenna. The polarizations were almost always nonorthogonal, since the Millstone antenna is altazimuth-mounted and the Agassiz antenna is polar-mounted.

The two stations were connected by a 7-GHz microwave link which carried a 5-MHz local-oscillator reference signal and an IF channel having a 400-kHz bandwidth from the Agassiz site to the Millstone site. The IF signals were effectively crosscorrelated by the use of a phase-switching technique and a digital autocorrelator. A computer was programmed to obtain the fringe amplitude and phase information as a function of frequency from the correlation functions. The phase stability of the system permitted integration periods of 1 minute. Longer integration periods were achieved by averaging

(IV. RADIO ASTRONOMY)

vectorially the fringe amplitude and phase for each frequency, by using the phase of the strongest feature as a reference phase. Hence, relative fringe phases among the various spectral components were obtained.

Observations were made of the 1665-MHz transition in source W3, during November 1966 and January 1967. The fringe amplitudes of the features at -43.7 km/sec and -46.5 km/sec were found to be unity over a local hour-angle coverage of 16 hours. The feature at -45.1 km/sec also gave unity fringe amplitude when observed with right-circular polarization. The normalizations were made by using single-antenna flux measurements of the source. Under the assumption of uniformly bright circular disks as a source model, the features were found to be smaller than $2''$ of arc in diameter. Recent observations by Davies, Rowson, Booth, Cooper, Gent, Adgie, Crowther⁴ have reduced these size limits to $0.1''$, or smaller, for the individual features in this region.

The right-elliptical and left-elliptical features at -45.1 and -45.5 km/sec, respectively, when observed, were blended with linear polarization. The fringe amplitude function of this superposition did not follow the local hour-angle dependence expected for a single point source with the polarization parameters given by Meeks, Ball, Carter, and Ingalls.⁵ A model that fits the observations can be constructed of two components separated approximately $1''$ of arc. Further observations are planned with improved sensitivity and with orthogonally polarized feeds, which should yield further information about the angular distributions of polarization and brightness.

The relative fringe phases between the strong features are shown in Fig. IV-7.

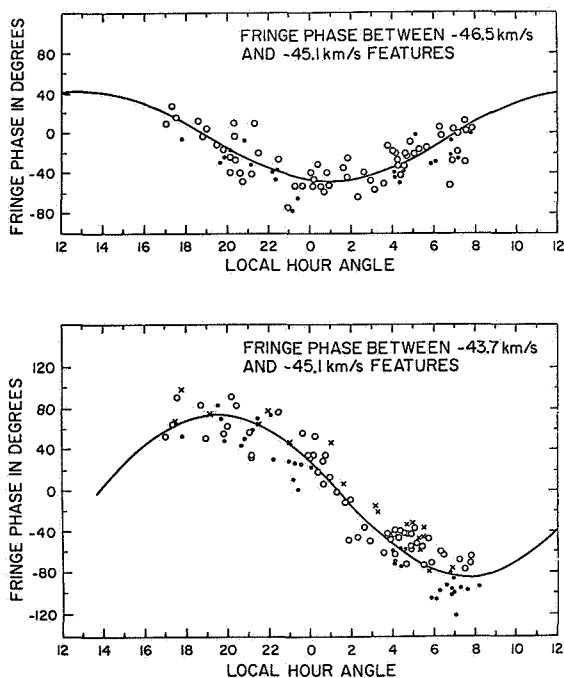


Fig. IV-7

Fringe phase between -43.7 and -45.1 km/sec features and between -46.5 and -45.1 km/sec features as a function of Local Hour Angle for the 1665-MHz OH transition in W3. Each data point represents 10 minutes of integration. Horizontal, vertical, and circular polarization points are represented by the symbols o, ●, and x. The velocities are based on a rest frequency of 1665.401 MHz for the $F = 1 \rightarrow F = 1$ transition of the $^2\Pi_{3/2}$ state.

(IV. RADIO ASTRONOMY)

The expected phase difference, $\Delta\phi$, for point sources separated by $\Delta\alpha$ in Right Ascension and by $\Delta\delta$ in Declination is given by

$$\Delta\alpha = \omega_0 \frac{D}{c} \{ [\sin \delta_B \cos \delta_S - \cos \delta_B \sin \delta_S \cos (L_S - L_B)] \Delta\delta + [\cos \delta_B \cos \delta_S \sin (L_S - L_B)] \Delta\alpha \},$$

where δ_B , L_B , δ_S are the Declination and Local Hour Angle of the baseline and the source, respectively, $\omega_0/2\pi$ is the frequency, D is the baseline length, and c is the

Table IV-1. Sizes and separations of features in 1665-MHz OH spectra of W3.

Feature	Polarization	Fringe Amplitude	Size	$\Delta\alpha$	$\Delta\delta$
-43.7 km/s	R. E.	$1 \pm .2$	2"	$.12^S \pm .04$	$-.15'' \pm .3$
-45.1	R. E.	$1 \pm .1$	1"	0	0
-46.5	L.	$1 \pm .2$	2"	$-.01^S \pm .04$	$-.45'' \pm .3$

The quoted uncertainties represent two standard deviations for the parameter estimates made from the data in Fig. IV-7.

velocity of light. The data were found to follow this relation and yielded the position offsets listed in Table IV-1, with the -45.1 km/sec feature used as a reference position. The position errors were limited by the noise level in the relative phase measurements. A sketch of the source model is given in Fig. IV-8. Solid lines indicate

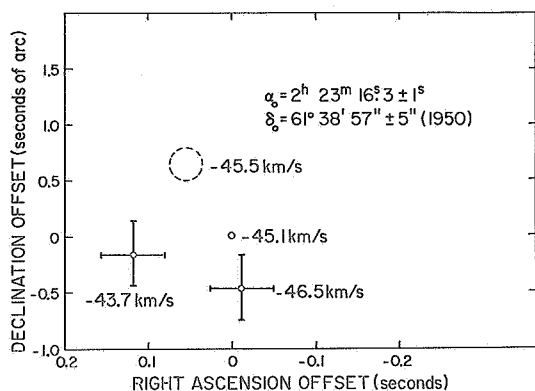


Fig. IV-8. Map of the relative positions of the centers of the 4 strongest features in the W3 OH source. The coordinates are the absolute position derived from the short baseline interferometer measurements of Rogers, Moran, and Crowther.²

the positions for the -43.7 and -46.5 km/sec features, while the position for the -45.5 km/sec feature is model-dependent, and hence is shown by dotted lines.

An angular size of 2" of arc corresponds to a linear dimension of 3400 astronomical

(IV. RADIO ASTRONOMY)

units, or 0.016 parsecs if the distance to W3 is taken to be 1700 parsecs. This implies that the radio brightness temperatures of these regions must be greater than 10^9 °K from our measurements or 10^{11} °K from the recent results of Davies and co-workers.⁴ The angular size determined by these observations may be an apparent size only. If a coherent phenomenon such as maser action is occurring, the dimension of the region can be much larger than the size inferred from our measurements.

J. M. Moran, Jr., A. H. Barrett, A. E. E. Rogers, B. F. Burke

References

1. A. E. E. Rogers, J. M. Moran, P. P. Crowther, B. F. Burke, M. L. Meeks, J. A. Ball, and G. M. Hyde, *Astrophys. J.* 147, 369-377 (1967).
2. A. E. E. Rogers, J. M. Moran, and P. P. Crowther, *Phys. Rev. Letters* 17, 450-452 (1966).
3. D. D. Cudaback, R. B. Read, and G. W. Rougoor, *Phys. Rev. Letters* 17, 452 (1966).
4. R. D. Davies, B. Rowson, R. S. Booth, A. J. Cooper, H. Gent, R. L. Adgie, and J. H. Crowther (to appear in *Nature*).
5. M. L. Meeks, J. A. Ball, J. C. Carter, and R. P. Ingalls, *Science* 153, 978 (1966).

V. SOLID-STATE MICROWAVE ELECTRONICS*

Academic and Research Staff

Prof. R. P. Rafuse
Dr. D. H. Steinbrecher

Graduate Students

J. Balecewicz
M. J. Ward

N67-27086

A. HIGH DYNAMIC RANGE TECHNIQUES

Several projects are now under way. They include mixers, linear amplifiers, detectors, filters, and log-amplifiers designed and built to have the widest possible dynamic range. During the last quarter, a phase detector with nearly 140 db of dynamic range was completed, and preliminary results are available on both a linear and a logarithmic amplifier.

The linear amplifier utilized a push-pull MOSFET stage with 10-db gain and a bandwidth of 2-20 MHz. A +13 dbm two-tone signal applied to the input gave third-order intermodulation products more than 45 db down from the two-tone signal. A simple low-frequency logarithmic amplifier with 11-decade range has been constructed in order to test theoretical calculations.

A crystal filter using high dynamic range interstage and output amplifiers is now under construction. We hope that the completed amplifier-filter will have 20-db gain, a 2-to-1 shape factor, 10-kHz bandwidth (center frequency of 30 MHz), and an out-of-band response 150 db down from the passband behavior. Considerable care during the construction phase will be necessary in order that grounding, shielding, and filtering be sufficient to maintain the 150-db out-of-band attenuation.

Wideband high dynamic range phase detectors have been built in the past by our group. At the present time, the same technology is being investigated, in order to provide similar dynamic range for square-law and peak detectors.

R. P. Rafuse

B. HIGH-POWER VARACTOR MULTIPLIERS

Devices that have theoretical power-handling capabilities of 12 watts per diode have been purchased and characterized (see Sec. V-C). Results of the characterization indicate that these diodes will be "circuit-limited" in terms of efficiency and the design frequency of 250-1500 GHz. An interdigital output filter has been designed and is under construction. An input filter is being designed. Idler circuit synthesis awaits

*This work was supported by the National Aeronautics and Space Administration (Grant NGR-22-009-163).

(V. SOLID-STATE MICROWAVE ELECTRONICS)

construction and measurement of the input and output filters.

In addition to the single diode, times-6 multiplier, a four-diode, 100-watt doubler is being designed as the first stage of a times-8 chain to S-band. The output power of this chain is expected to be greater than 60 watts.

D. H. Steinbrecher

C. DEVICE CHARACTERIZATION

Preliminary measurement of high-power, punch-through varactors in a new test jig at 500 MHz indicate cutoff frequencies of as much as a factor of 2 higher than those reported by the manufacturer. The measurements indicate that the high-power high-efficiency transmitter for 2 GHz will be relatively easy to realize. A selected and modified General Radio Series 900 slotted line has been received and will soon be in operation as a 3-GHz varactor (and other two-port device) measurement arrangement. All of the measurements now being carried out on varactors, Schottky-barrier diodes, MOSFETS and other solid-state devices are being analyzed by computer programs generated by the group and run on the M.I.T. Computation Center's CTSS system.

R. P. Rafuse

D. COMPUTER DESIGN OF VARACTOR CIRCUITS

Two analysis programs for high-order punch-through varactor multipliers were developed during the past quarter. One program, called SAMPLE, operates on a measured varactor current waveform to recover the instantaneous varactor voltage, the power flow at each harmonic, and the network impedance seen by the varactor junction at each harmonic. The other program, called MULTAN, works from the imbedding impedances and the junction characteristics to synthesize the junction voltage and current waveforms, and, consequently, the complete power distribution for the multiplier.

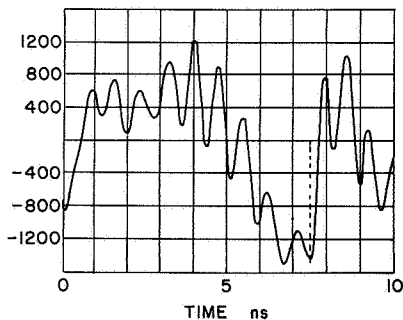


Fig. V-1. Diode current.
[Reprinted from "hpa Application Note No. 8," Fig. 7, p. 3.]

MULTAN allows a designer to test a theory before construction, while SAMPLE permits a complete diagnostic of a working multiplier. Both programs are intimately related to the High Power Varactor Multiplier project.

MULTAN is not completely operational, because of its idealized concepts. During the next quarter methods for including discontinuity susceptances, line loss, and other nonideal

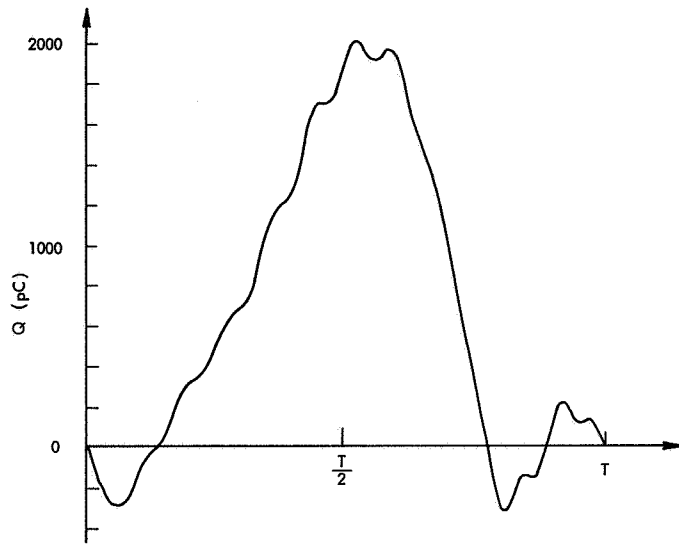


Fig. V-2. Charge waveform.

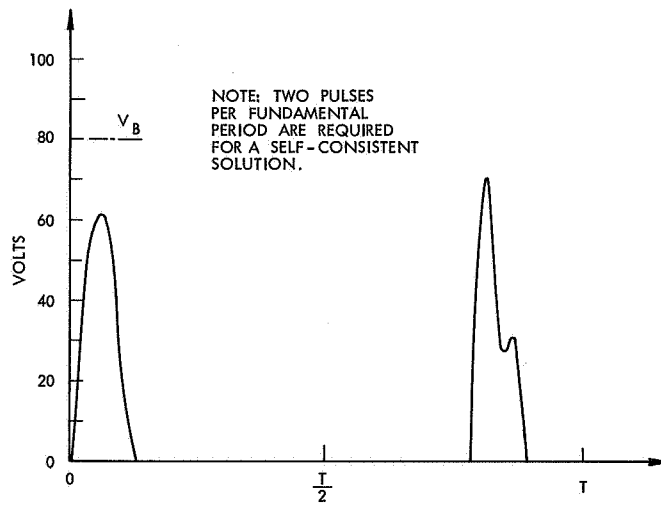


Fig. V-3. Voltage waveform (HP X-13 multiplier).

(V. SOLID-STATE MICROWAVE ELECTRONICS)

circuit properties will be investigated.

SAMPLE has been tested on a current waveform published by Hewlett-Packard Associates.¹ The results were very interesting. They described the current waveform as that of a times-14 multiplier with 1.5 watts input at 100 MHz and approximately 200 mW output at the 14th harmonic. SAMPLE revealed that the order of multiplication was actually times-13 (which was confirmed later by a Hewlett-Packard spokesman) and that 40% of the input power was being dissipated in network losses at the 4th harmonic. The current waveform, from which all of the following information was obtained, is illustrated in Fig. V-1. The varactor charge and voltage waveforms, obtained by

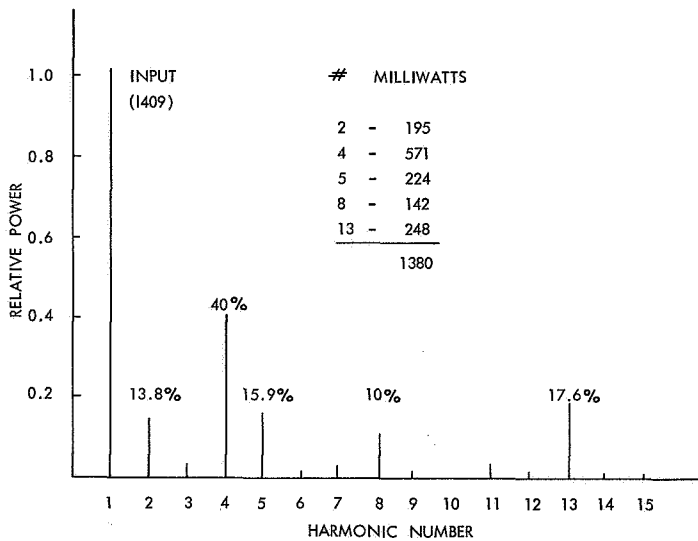


Fig. V-4.
Harmonic power distribution.
(HP X-13 Multiplier.)

SAMPLE are shown in Figs. V-2 and V-3. Figure V-4 illustrates the harmonic power distribution for the Hewlett-Packard X-13 multiplier.

This project led to the preparation of a joint paper. A summary of this paper appears in Section V-E.

D. H. Steinbrecher

References

1. "Frequency Multiplication with the Step Recovery Diode," hpa Application Note No. 8, Hewlett-Packard Associates, Palo Alto, California, July 1965.

E. ITERATIVE SYNTHESIS OF VARACTOR-MULTIPLIER MICROWAVE NETWORKS AND A DOUBLER WITH 0.17-WATT OUTPUT AT 47 GHz

[This report summarizes a paper that will be presented at the International Symposium on Microwave Theory and Techniques (sponsored by the IEEE Professional Group on Microwave Theory and Techniques), Boston, Massachusetts, May 10, 1967.]

A method for the design and evaluation of the input and output networks of microwave

(V. SOLID-STATE MICROWAVE ELECTRONICS)

frequency varactor multiplier circuits will be presented. This method permits a quantitative measure of circuit loss, input-output isolation and effective diode cutoff frequency. Furthermore, it enables the designer to establish the boundary conditions at the varactor junction which are required for optimum efficiency, independent of any specific knowledge of package parasitics, transmission-line characteristic impedances, or other difficult-to-quantize microwave circuit parameters. By using this method, a doubler from 23.5 GHz to 47 GHz has been designed and tested. Output power of 173 mW was obtained with an efficiency of 33%. The measured efficiency was within 0.5 db of the calculated value.

D. H. Steinbrecher, M. E. Goff, A. H. Solomon

[M. E. Goff and A. H. Solomon are with Sylvania Electric Products, Inc. Their work was supported in part by the U. S. Air Force Avionics Laboratory (Research and Technology Division) under Contract AF33(615)-3518.]

VI. ELECTRONIC INSTRUMENTATION*

Academic and Research Staff

Dr. D. H. Steinbrecher
Prof. K. Biemann†

Dr. J. I. Glaser

Dr. R. E. Lovins†
Dr. S. H. Zisk

Graduate Students

J. M. Steele
N. T. Tin

RESEARCH OBJECTIVES

N67-27087

Electronic instrumentation plays a significant role in almost every branch of scientific research. Similarly, progress in electronic instrumentation is increasingly dependent on advances in chemistry and physics. The formation of the Electronic Instrumentation Group is an effort to stimulate instrumentation research and development with state-of-the-art needs in other areas of science.

The activities now under way in our group are centered on instrumentation for mass spectrography. Profile analyses and spectrographic data-reduction methods already require extensive use of high-speed digital computers. Data from a Mass Spectrograph are collected, however, on photographic plates that must be processed by time-consuming methods to achieve a form acceptable to a computer. Many experiments, which are impossible to perform with present methods, could be conducted with the addition of a real-time interface between a Mass Spectrograph and a computer with on-line processing capability. Reports on progress in areas related to the development of suitable interface hardware and software appear in Sections VI-B, -C, and -D.

Since much of the present and future Mass Spectrograph instrumentation is and will be environmentally sensitive, a semiclean, temperature- and humidity-controlled shielded room is being provided. The instrument will be mounted within the room on a 1-Hz air piston antishock and vibration assembly. Nearly complete environmental control will permit an investigation of system-produced instabilities that can be corrected by sophisticated instrumentation. The resulting influence on next generation equipments will allow spectrographic analyses to be carried out on low-vapor-pressure compounds that require very long (several hours) exposures. It is virtually impossible to make analyses of some of these compounds with present methods. Progress on the shielded room facility is discussed in Section VI-A.

D. H. Steinbrecher, K. Biemann

A. SHIELDED ROOM FACILITY

This report outlines briefly the current status and the rest of the work to be done on the wrought-iron screen room that is being constructed in Room 56-031, M.I.T. The iron walls, floor, and ceiling have been erected and the continuous seam welds are

*This work was supported principally by the National Institutes of Health (Grant 1 505 FR07047-01).

†Professor K. Biemann and Dr. R. E. Lovins, of the Department of Chemistry, M.I.T., are collaborating with the Electronic Instrumentation Group of the Research Laboratory of Electronics in research under NIH Grant 1 505 FR07047-01.

(VI. ELECTRONIC INSTRUMENTATION)

approximately 80% complete. Also, the electrical ground for the room has been completed.

We estimate that the completion of the basic room (i. e. , welding of iron) will soon be accomplished. In addition to the basic-room design, additional time will be needed for (a) installation of an air-conditioning system, (b) interior finishing of the room (i. e. , acoustical walls, ceiling, etc.), (c) making available electrical power and water to the room through pierce points in the roof of the room, (d) exterior finishing of the area surrounding the room (i. e. , block wall in the corridor, etc.), (e) installation of a motor generator set for the mass spectrometer primary power, (f) installation of line filters and other accessories to provide services for the room.

R. E. Lovins

B. MASS SPECTROMETER DETECTOR

The simplest detection scheme, that of collecting each ion beam on a metal plate and amplifying the resulting current, would require that we push the present capability to measure low current levels downward by at least two orders of magnitude. There is an alternative, on the other hand, which involves use of state-of-the-art components, and thus affords a better chance of success in building the final instrument.

We are considering replacement of the photographic plate by a slit mask containing 300-1000 slits, each 1 mm long and with an expected width of 5 microns. The mask could be made of metal foil on a rigid frame, with slits formed either by high-resolution photo-etching (by Bendix Research Laboratories) or by multiple drilling with a pulsed laser (Raytheon Company, among others). Since the slits would have fixed positions on the mask, either the beam of the spectrometer or the mask itself could be scanned in steps through a total distance somewhat greater than the spacing between adjacent slits. The ions issuing from the slits would be counted by continuous-channel photomultipliers mounted behind each slit. These novel devices are made by the Bendix Corporation, and consist of a glass tube (as small as 0.25 mm O.D. by 1 cm long) coated on the inner surface with a secondary-emitting film of high resistivity. A high-voltage applied across the ends of the tube accelerates the electrons as they carom down the tube and build up their numbers to produce, finally, a constant-amplitude space-charge-limited output pulse for each incident ion (with at least 60% ion-collection efficiency).

1. Block Diagram

The essential components of the interface system between computer and ion beams are sketched in Fig. VI-1. The diagram is a preliminary description of one form of logic that transfers the complete spectrum from the focal plane of the spectrograph into

(VI. ELECTRONIC INSTRUMENTATION)

the computer. The ion counts are accumulated in the scaler until the time t_0 , at which time the counting is stopped; the sum is transferred to the buffer an instant later, at t_1 , and, if it is desired, the beam is shifted to align the next samples of the spectrum with the slits. The scaler is disconnected from the buffer and is reset at t_2 ; and the counting begins at t_3 , after a total delay of a few milliseconds. Meanwhile, the count in the buffer remains available, for transfer to the computer memory, until the beginning of the next cycle at $(t_0 + T)$.

2. Sampling and Retrieval of the Spectrum

The interactions among timing, slit width, and resolving power can be solved by considering that the ion beam intensity is an unknown function of the distance x along the focal plane. The profile of an isolated line is approximately Gaussian with a well-defined half-width. We may therefore consider the whole spectrum to be a function that consists of a sequence of Dirac delta functions with different areas and x coordinates, which has been convolved as a whole with a Gaussian. (In reality, the width of the profile changes by approximately 5 times from one end to the other of the 30-cm focal plane, so that a one-dimensional transformation of the spectrum must be performed first if mathematical rigor is to be preserved.) In this way, the problem is reduced to classical terms. Ideally, then, each slit in the mask obtains a sample of the smoothed spectrum; however, because of the nonzero width of the slit, we must consider that the smoothed spectrum is convolved again by the slit, and the output from an electron multiplier then represents a sample (in the mathematical sense) of the resulting spectrum.

3. Anticipated Difficulties

The assembly of slits and multipliers must be located at the edge of the magnet gap, within a magnetic field of approximately 10,000 Gauss. We do not yet know whether the multiplier tubes can be operated in such a high field. In order to prevent the first emitted electron from striking the wall too soon, before it has acquired enough energy from the electric field to dislodge secondaries, we shall probably align the axes of the multipliers with the magnetic field; other problems and/or experimental solutions will undoubtedly turn up.

The second problem is the unknown response of the active film in the electron multipliers to ions at the heavy (hence low-velocity) end of the spectrum.

S. H. Zisk

C. RESOLUTION OF MASS SPECTROMETER

A proposed analog-to-digital converter for the ion-beam outputs should not significantly decrease the mass spectrometer's resolution.¹ It is important, then, to determine quantitatively the factors that degrade the resolution: (i) energy dispersion in the

(VI. ELECTRONIC INSTRUMENTATION)

ion source; (ii) defocussing in the ion-optics systems; and (iii) electronic noise in the detector. A search is being made for an electrical equivalent circuit for an ion-beam output in which these 3 factors will be lumped in noise sources.

J. I. Glaser

References

1. K. Biemann, Mass Spectrometry: Organic Chemical Applications (McGraw-Hill Book Company, Inc., New York, 1962).

D. SAMPLING AND RETRIEVAL OF THE SPECTRUM

To increase the speed with which results may be obtained from the Mass Spectrometer, the data will be gathered digitally and processed in a computer. The ions will be detected by electron multipliers, on related devices, and the pulses counted and stored for transfer to the computer.

Digital acquisition of data from the Mass Spectrometer poses the problem of how well a discrete number of digital samples characterizes the continuous spectrum. A computer program has been written to simulate the sampling process on a normal Gaussian curve and to reconstruct the curve from the samples for comparison.

J. M. Steele

VII. OPTICAL AND INFRARED SPECTROSCOPY*

Academic and Research Staff

Prof. C. H. Perry

Graduate Students

T. G. Davis
Jeanne H. Fertel

D. J. Muehlner

J. F. Parrish
N. E. Tornberg

A. REFLECTION MEASUREMENTS ON POTASSIUM HALIDES
IN THE FAR INFRARED REGION

1. Introduction

Most ionic crystals have strong reflection bands, known as Reststrahlen bands, in the far infrared region. These are due to lattice vibrations. The lattice resonances have been observed at temperatures down to 5°K for several potassium halides, by measuring the reflection from single crystals at an incident angle of 10°.

The following crystals have been investigated: KCl, KBr, and KI.

2. Experimental Procedure

The interferometer and detector used for this measurement have been described elsewhere.¹ The reflectivity values indicated below are relative to the reflectivity of a front-aluminized reference mirror.

3. Experimental Results

The measured reflectivity spectral profiles are shown in Fig. VII-1 for T = 5°, 80°, 195°, and 300°K, except for KCl which was not investigated at 195°K. The main absorption peak can be identified as the transverse optical fundamental of frequency, ω_T , at the zone center. Also, all of the alkali halides show a sideband on the high-frequency side of the main peak.

The Reststrahlen bands of KCl, KBr, KI have been fitted to a classical dispersion formula by machine programming. We found that this could not be done without assuming the existence of a second sideband between the main peak and observed sideband. The dispersion constants obtained in this way are tabulated in Table VII-1.

Here, S_i denotes the oscillator strength, and γ_i the damping constant of oscillator i . All frequencies are in cm^{-1} ; ω_L is the frequency of the longitudinal optical fundamental

*This work was supported in part by the Joint Services Electronics Programs (U.S. Army, U.S. Navy, and U.S. Air Force) under Contract DA 28-043-AMC-02536(E), the U.S. Air Force (ESD Contract AF19(628)-6066), and the Sloan Found for Basic Research (M.I.T. Grant).

N67-27088

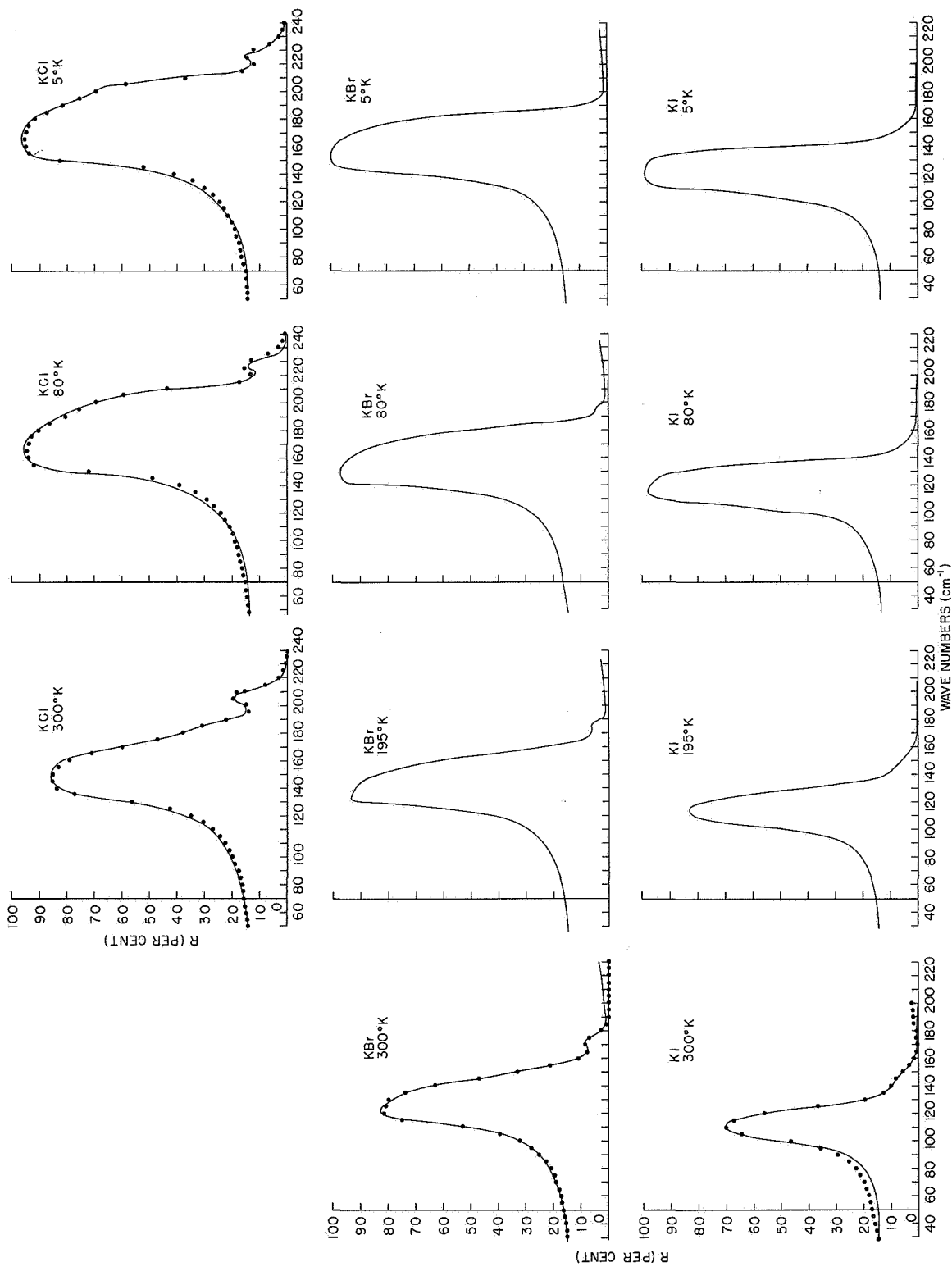


Fig. VII-1. Reflectivity of potassium halides at various temperatures.
 Measured.
 Calculated by using the classical dispersion analysis.

Table VII-1. Dispersion constants obtained from the classical oscillator model.

	S_T	ω_T	γ_T	S_1	ω_1	γ_1	S_2	ω_2	γ_2	ϵ_∞	ϵ_0	ω_L	ω_{LST}	e^*/e
KCl (300°)	215	143	5	55	189.5	31	41	210.5	14.5	2.22	4.6	203	206	.77
KCl (90)	230	151	2	35	193	30	40	222	17	2.22	4.61	216	216	
KCl (10)	230	150	1.0	35	193	30	40	222	17	2.22	4.64	215	216	
KBr (300°)	172	113	5	42	150	28	36.5	169	15	2.43	4.9	158	161	.74
KBr (195)	170	117	1.5	39	147	30	30	172	15	2.43				
KBr (90)	173	120	0.8	30	152	28	25	174	15	2.43				
KBr (10)	178	122	0.1	24	157	28	28	178	23	2.43				
KI (300°)	147	103.5	6.6	50	136	28	48	148	36	2.82	5.08	135	138	.71
KI (195)	151	106	3.5	44	138	27	38	149	25	2.82				
KI (90)	155	108	0.5	24	141	28	38	151	25	2.82				
KI (10)	161	110	0.2	15	144	28	41	153	25	2.82				

(VII. OPTICAL AND INFRARED SPECTROSCOPY)

at the zone center, and ω_L (LST) is that same quantity calculated from the Lyddane-Sacks-Teller relation:

$$\omega_L \text{ (LST)} = \sqrt{\epsilon_0 / \epsilon_\infty} \omega_T \quad (1)$$

The effective charge on an ion, e^* , is obtained from the Szigetti relation

$$\omega_T^2 = \frac{4\pi N}{9m} e^{*2} \frac{(\epsilon_\infty + 2)^2}{\epsilon_0 - \epsilon_\infty}, \quad (2)$$

where N is the number of ion pairs per unit volume, and m is the reduced mass of an ion pair.

We have tentatively identified the frequency ω_1 with the multiphonon compensation TO + TA at the zone boundary, and ω_2 with TO + LA.

All of the values of ϵ_∞ that we used were obtained from the CRC tables. The values of ϵ_0 were obtained from the reflectivity spectra extrapolated to $\omega = 0$.

We would like to thank Professor Alexander Smakula and Mr. J. Kalnajs, of the Center for Materials Science and Engineering, M.I.T., for the samples.

Jeanne H. Fertel, C. H. Perry

References

1. C. H. Perry, R. Geick, and E. F. Young, *J. Appl. Opt.* **5**, 1171 (1966).

B. LATTICE VIBRATIONS IN CdS/Se MIXED CRYSTALS

1. Introduction

The infrared transmittance and reflectance of pure crystals of CdS and CdSe have been studied and reported several years ago. More recently, the infrared transmittance and reflectance of the hexagonal mixed crystals of CdS/Se have been studied, and several preliminary reports have been published or informally exchanged between researchers at the Massachusetts Institute of Technology and elsewhere. At M.I.T, several mixed crystals of $\text{CdS}_x\text{Se}_{(1-x)}$ ($.29 < x < .93$) were studied in transmission at temperatures down to that of liquid Helium, and in reflection at temperatures down to that of liquid nitrogen, with the use of the FS520 Fourier spectrophotometer. A preliminary analysis of these results is presented here.

2. Discussion of Results

The CdS/Se systems appear to form good mixed crystals with hexagonal unit cells like pure CdS and CdSe. Such a unit cell for CdS with the lattice constants "a" and "c"

(VII. OPTICAL AND INFRARED SPECTROSCOPY)

labeled is shown in Fig. VII-2. A quantitative analysis of 7 samples of CdS/Se determined the relative weights of Cd and Se in each sample. These two weights for each sample

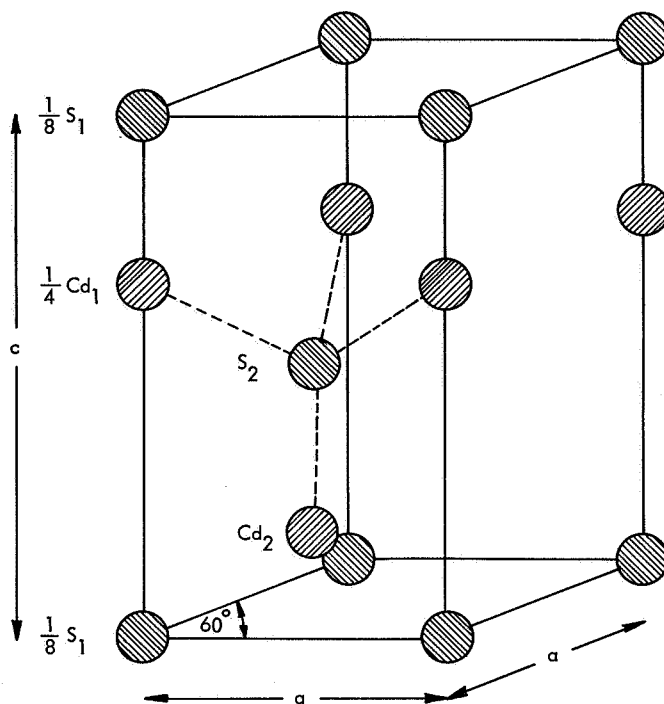


Fig. VII-2. Hexagonal CdS.

were then used to calculate independent values of "x" in the empirical formula $CdS_xSe_{(1-x)}$. For all but one sample (sample H), these two values of x agreed within 1% of each other, thereby showing that the crystals were indeed stoichiometric mixtures of CdS and CdSe. X-ray measurements on 5 of these samples were performed to obtain the lattice constants "a" and "c". All of the diffraction peaks were sharp, indicating unique lattice constants and no evidence of clustering, thereby confirming that the CdS/CdSe systems formed good mixed crystals for the range of concentrations studied. Plots of a, c, and a^2c (volume of unit cell) against x are shown in Figs. VII-3, VII-4, and VII-5, established for the pure samples; thus it is shown that the lattice parameters vary uniformly and nearly linearly with concentration. Moreover, the conclusion that CdS/Se does form good mixed crystals has also been confirmed by other researchers who measured these and other properties such as fluorescence of the CdS/Se system.^{1-6, 8-10}

The reflection spectra of the mixed crystals of CdS/Se show at least two optically active lattice vibrations. Figure VII-6 shows the reflectivity of one of the samples

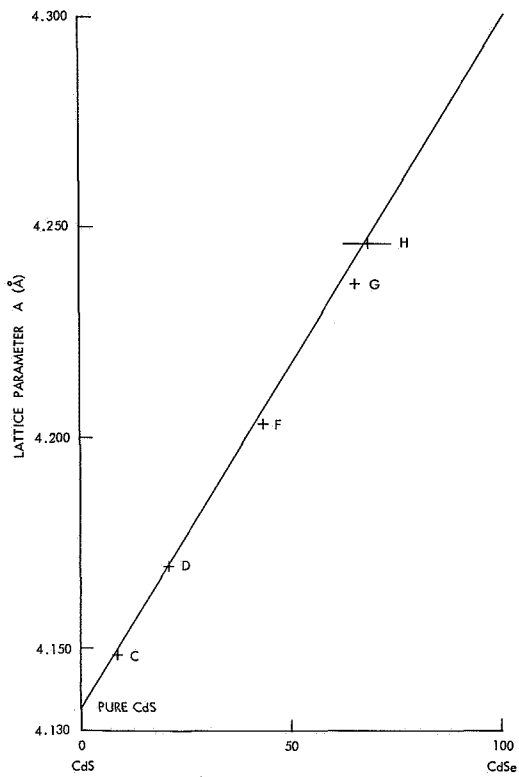


Fig. VII-3. Plot of a against x .

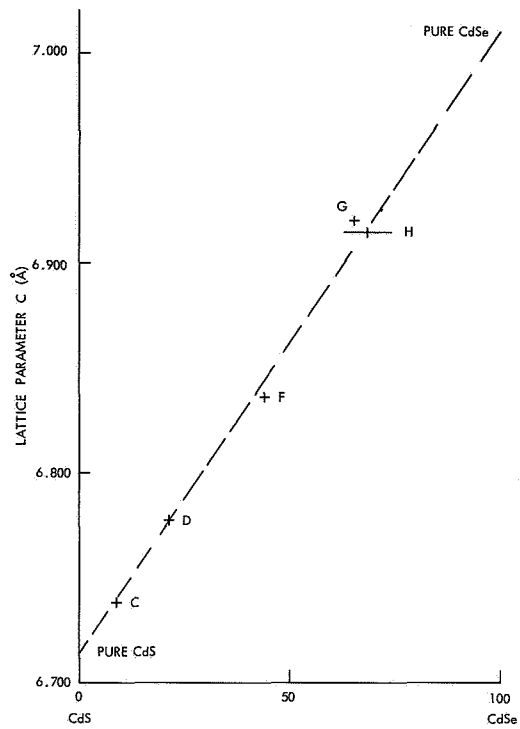


Fig. VII-4. Plot of c against x .

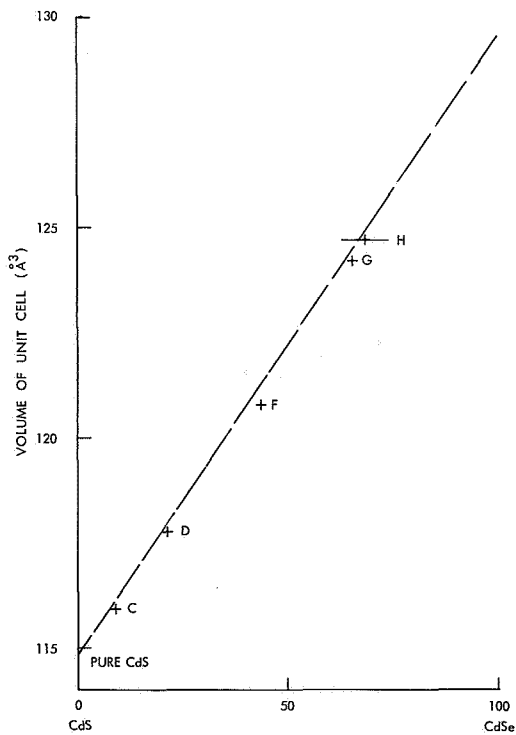


Fig. VII-5. Plot of $a^2 c$ (volume of unit cell) against x .

(VII. OPTICAL AND INFRARED SPECTROSCOPY)

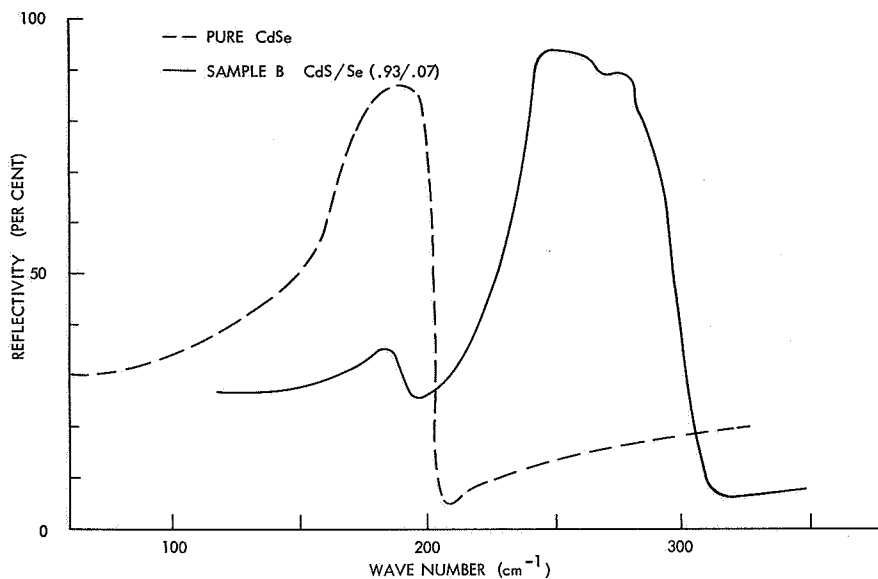


Fig. VII-6. Reflectivity vs frequency at room temperature.

compared with pure CdSe at room temperature. Whereas the reflectivity of mixed crystals of the alkali halides and NiO/CoO show only a single peak whose frequency varies with the atomic concentration of the crystal's constituents⁵⁻⁷; the reflectivity of CdS/Se shows two distinct peaks whose frequencies remain nearly constant but whose intensities vary with the atomic concentration parameter x . Thus, the mixed II-VI compound shows some of the properties of the covalent-type bonding characteristic of the mixed III-V compounds like GaAs/P, but without the clustering found in GaAs/P.^{3,9} Also, Verleur and Barker¹⁰ have shown that some of the theoretical tools used to analyze the GaAs/P system may also be applied to the CdS/Se system.

Table VII-2 shows the principal room-temperature multiphonon absorption bands of

Table VII-2. Principal absorption bands, $\nu > 300 \text{ cm}^{-1}$.

CdS	CdSe
334 cm^{-1}	310 cm^{-1}
345-355	360
388	405
404	470
415	
498	
518	

(VII. OPTICAL AND INFRARED SPECTROSCOPY)

pure CdS and CdSe above 300 cm^{-1} . Figure VII-7 shows the room-temperature absorption spectrum of one of the typical mixed crystals of CdS/Se. As can be seen by

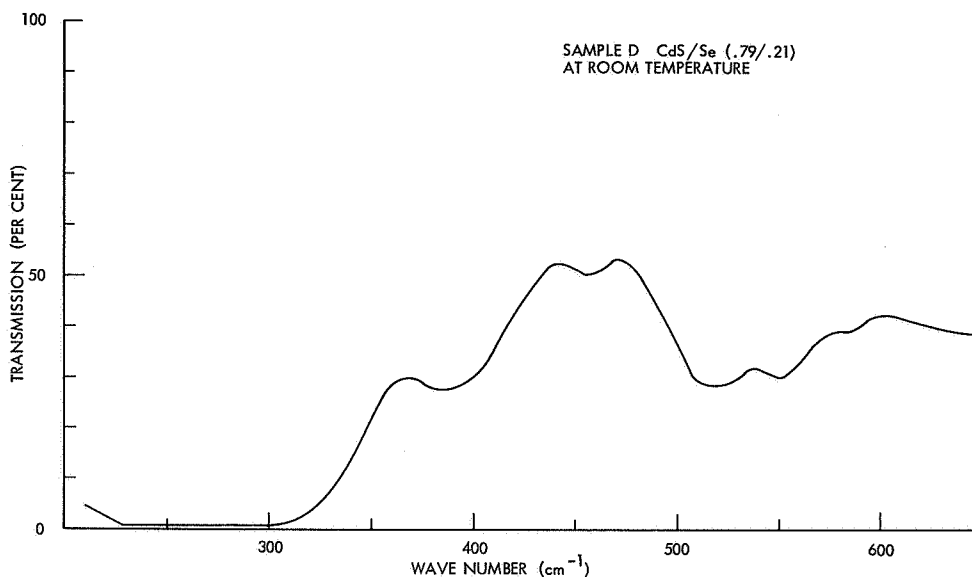


Fig. VII-7. Sample D CdS/Se (.79/.21) at room temperature.

comparing this graph with Table VII-2, the absorption of the mixed crystal looks much like the product of the two pure absorption curves.

Although the experimental evidence shows that CdS and CdSe do form good, uniform mixed crystals, the infrared optical properties appear to behave as if determined by two nearly independent crystal lattices, one being due to the CdS, and the other to the CdSe. At present, a theoretical analysis of the experimental measurements of the transmission and reflection of the mixed crystals of CdS/Se, based upon the observations presented in this report and the classical oscillator model, is being completed.

We would like to thank Dr. S. S. Mitra, of the University of Rhode Island, and Dr. D. Reynolds, of Wright-Patterson Air Force Base, Ohio, for the samples, and to thank J. A. Kalnajs of the Center for Materials Science and Engineering, M.I.T., for the x-ray analysis.

J. F. Parrish, C. H. Perry

References

1. M. Balkanski, R. Beserman, and J. M. Besson, "Phonon Processes in Mixed Crystals of $\text{CdS}_y\text{CdSe}_{(1-y)}$," *Solid State Commun.* **4**, 201-204 (1966).
2. M. Balkanski, J. M. Besson, and R. Le Toullec, "Dispersion Curves of Phonons in Hexagonal Cadmium Sulfide Obtained by Infrared Spectroscopy," *Proc. International Union of Pure and Applied Physics*, Paris, 1965.

(VII. OPTICAL AND INFRARED SPECTROSCOPY)

3. Y. S. Chen, W. Shockley, And G. I. Pearson, "Lattice Vibration Spectra of $\text{GaAs}_x\text{P}_{1-x}$ Single Crystals," *Phys. Rev.* 151, 648-656 (1966).
4. R. Geick and C. H. Perry, "Lattice Vibrational Properties of Hexagonal CdSe," *J. Appl. Phys.* 37, 1994-1997 (1966).
5. P. J. Gielisse, J. N. Plendl, L. C. Mausar, R. Marshall, S. S. Mitra, R. Mykolajewycz, and A. Smakula, "Infrared Properties of NiO and CoO and Their Mixed Crystals," *J. Appl. Phys.* 36, 2446-2450 (1965).
6. R. Marshall, S. S. Mitra, P. J. Gielisse, and J. N. Plendl, "Optical Properties of Transition Metal Oxides," *Proc. International Union of Pure and Applied Physics*, Paris, 1965.
7. Jeanne H. Fertel, Private communication.
8. S. S. Mitra and R. Marshall, "Multiphonon Infrared Absorption in II-VI Semiconductors," *Proc. International Union of Pure and Applied Physics*, Paris, 1965.
9. R. F. Potter and D. L. Stierwalt, "Reststrahlen Frequencies for Mixed $\text{GaAs}_y\text{Sb}_{1-y}$ System," *Proc. International Union of Pure and Applied Physics*, Paris, 1965.
10. H. W. Verleur and A. S. Barker, "Optical Phonons in Mixed Crystals of $\text{CdSe}_x\text{S}_{1-x}$," Ph. D. Thesis, New York University, 1965 (unpublished).

PRECEDING PAGE BLANK NOT FILMED.

VIII. GEOPHYSICAL RESEARCH

B. Upper Atmospheric Physics*

Academic and Research Staff

Prof. G. Fiocco
Dr. G. W. Grams
Dr. Sharda Nand

Graduate Students

J. B. DeWolf
D. F. Kitrosser
H. C. Koons

N67-27089

1. OPTICAL RADAR AND AIRGLOW OBSERVATIONS IN NORWAY DURING THE PRESENCE OF NOCTILUCENT CLOUDS

Observations of noctilucent clouds were carried out in Oslo, Norway, during the summer of 1966, to obtain information on the temporal variability of the height, structure, and other physical characteristics of noctilucent clouds. The apparatus was basically the same as the optical radar unit used in Sweden in the summer of 1964 (Fiocco and Grams¹), but many improvements were incorporated to improve the reliability and general performance of the system. In the laser unit the ruby, flashlamp, and cavity were cooled by closed-loop circulation of distilled water through a water-cooling unit. This and other improvements in the laser itself provided approximately 2-J pulses of 100- μ sec duration at a maximum p.r.f. of 0.5 sec⁻¹. To record the data at these higher rates, the apparatus utilized an automatically advanced 556-BH1 radarscope camera, modified for use on a Tektronix 555 dual-beam oscilloscope. Two traces displaying the amplified photomultiplier current were recorded simultaneously with different sweep rates: one trace recorded the echoes from 0-200 km altitude for the noctilucent cloud data, the other displayed the echoes from 0-40 km for a simultaneous study of the 20-km aerosol layer to establish latitude and time variations of the dust content of the stratosphere.

In addition to the optical radar instrumentation, a developmental airglow photometer was also mounted in our instrumentation trailer to derive simultaneous measurements of the intensity and rotational temperature of the OH emission from the mesosphere. Observed changes in temperature and water-vapor content near the mesopause inferred from these airglow measurements might provide an insight into the meteorological

*This work was supported principally by the National Aeronautics and Space Administration (Grants NGR-22-009-131 and NGR-22-009-(114)), and in part by the Joint Services Electronics Programs (U. S. Army, U. S. Navy, and U. S. Air Force) under Contract DA 28-043-AMC-02536(E).

(VIII. GEOPHYSICAL RESEARCH)

processes associated with the formation of noctilucent clouds.

The equipment was located at Kjeller, near Oslo (60.0°N, 11.0°E). Viewing conditions were excellent throughout the summer: more than half of the nights were sufficiently clear to obtain optical radar data. Noctilucent clouds of varying degrees of intensity were observed visually on approximately one-third of the nights when data could be obtained. Therefore, we have accumulated a considerable amount of data on the dust content of the mesosphere for various noctilucent cloud displays, as well as background information on the scattering properties of the mesosphere in the absence of the clouds.

Our present analysis of these data, at a rather preliminary stage, corroborates the results obtained during the summer of 1964, with definite echoes observed from altitudes between 65 km and 70 km, the strongest echoes being observed when noctilucent cloud displays had been visible overhead during twilight hours. The faster rate at which data could be gathered reduced the observation time for obtaining statistical evidence of the presence of noctilucent clouds; this increases the probability of studying transient features of the clouds that would ordinarily be lost by averaging over long observation periods.

Data obtained from the airglow photometer are available for two nights. From these data we have estimated the OH temperature to be approximately 160°K. In view of appreciable scatter of data points, it was not possible to establish a difference between the temperatures on the two nights, although the intensity in the presence of noctilucent clouds appeared to be lower. This temperature estimate is in agreement with the earlier determinations by Shefov^{2,3} and with rocket measurements of the mesospheric temperature in summer at high latitudes. The decrease in intensity of the OH lines during the noctilucent cloud display is possibly at variance with Shefov's results, and possibly could be interpreted as being due to the removal of H₂O in the vapor phase following the formation of the cloud. In view of the scarcity of data, the evidence is very limited.

G. Fiocco, G. W. Grams

References

1. G. Fiocco and G. Grams, "Observation of the Upper Atmosphere by Optical Radar in Alaska and Sweden during the Summer 1964," *Tellus* 18, 34-38 (1966).
2. N. N. Shefov, "The Upper Atmospheric Emissions and Noctilucent Clouds," in *Aurorae and Airglow, n. 11 Series, Results of the IGY* (USSR Acad. Sci., pp. 48-51, 1965) (in Russian).
3. N. N. Shefov, "OH Emission and Noctilucent Clouds," a paper presented at the International Symposium on Noctilucent Clouds, IQSY, Tallin, 1966.

IX. ELECTRODYNAMICS OF MEDIA*

Academic and Research Staff

Prof. L. J. Chu
Prof. H. A. Haus
Prof. G. C. Shu

Graduate Students

J. Glaser
T. K. Gustafson
P. W. Hoff

A. ELECTRODYNAMICS OF QUADRUPOLEAR MEDIA

N67-27090

The author has undertaken a study of quadrupolar media for two reasons. First, the availability of high-intensity electromagnetic radiation at optical frequencies makes it possible to observe quadrupolar effects in situations in which they are not swamped by dipolar effects¹ (e. g. , frequency-doubling in media with inversion symmetry). Second, the quadrupolar medium provides an interesting example of the application of Chu's postulates to formulations of electrodynamics in the presence of moving media.² The question arises as to whether it is necessary to modify Maxwell's equations of the Chu formulation for polarizable and magnetizable media when dealing with a quadrupolar medium, or whether it is sufficient to replace the polarization density \bar{P} by the divergence of the quadrupolar tensor, leaving the equations otherwise unchanged.

In this report we summarize the steps taken to obtain a self-consistent formulation of Maxwell's equations in the presence of a moving quadrupolar medium. These results are used to develop a simple nonrelativistic model of a fluid consisting of noninteracting quadrupolar particles (the particles interact solely through the macroscopic fields that they produce). We generalize the expressions for the quadrupolar fluid to a solid, taking interactions among the quadrupolar particles into account. The force density acting toward acceleration of the volume elements of the solid is obtained.

We start with Maxwell's equations as formulated by Chu,² which he has called "the Amperian formulation." The presence of the material medium is taken into account by means of source terms introduced into Maxwell's equations for free space. The reason for using the Amperian formulation, rather than the formulation based on the concept of magnetic-charge dipoles, is that a quadrupolar medium produces circulating currents analogous to the Amperian model of magnetizing currents.

$$\nabla \times \frac{\partial \bar{B}}{\partial t} = 0 \quad (1)$$

*This work was supported by the Joint Services Electronics Programs (U. S. Army, U. S. Navy, and U. S. Air Force) under Contract DA 28-043-AMC-02536(E).

(IX. ELECTRODYNAMICS OF MEDIA)

$$\nabla \times \frac{\bar{\mathbf{B}}}{\mu_0} - \epsilon_0 \frac{\partial \bar{\mathbf{E}}}{\partial t} = \bar{\mathbf{J}}_Q \quad (2)$$

$$\nabla \cdot \epsilon_0 \bar{\mathbf{E}} = \rho_Q \quad (3)$$

$$\nabla \cdot \bar{\mathbf{B}} = 0. \quad (4)$$

We start with a model of a planar quadrupole shown in Fig. IX-1. The four charges form a parallelogram, so that they do not possess a dipole moment. The charge chosen

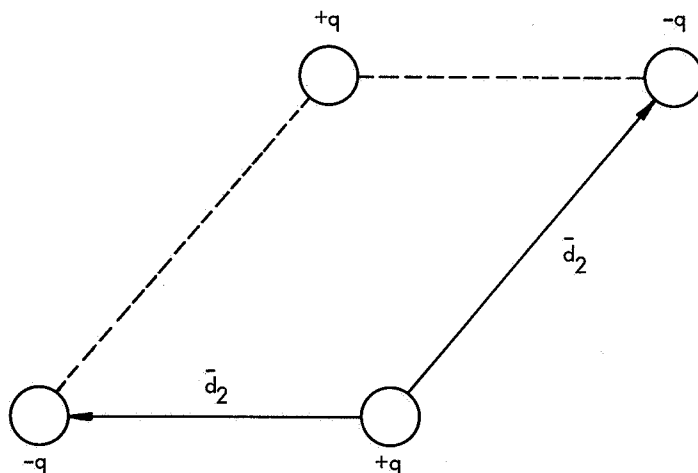


Fig. IX-1. Model of planar quadrupole.

as the origin for the measurement of the vector distances of the remaining three charges is assumed to carry the mass of the quadrupole. This assumption implies that there is no time dispersion in the constitutive law. Suppose that the mass-bearing charge is distributed with a density $n(\bar{\mathbf{r}})$ and moves with a velocity $\bar{\mathbf{v}}(\bar{\mathbf{r}})$. In order to find the source current density $\bar{\mathbf{J}}_Q$ and source charge density ρ_Q , we find the charge density and velocity of each of the four charges constituting the quadrupole and add over these. All of the evaluations have to be made to second order in the displacements, $\bar{\mathbf{d}}$, of the charges from the mass-bearing charge. The number density at point $\bar{\mathbf{r}}$ of a particle displaced a distance $\bar{\mathbf{d}}$ from its partner, the latter of which possesses a density distribution $n(\bar{\mathbf{r}})$, is given^{4,5} to second order in $\bar{\mathbf{d}}$ by

$$n - \nabla \cdot (n\bar{\mathbf{d}}) + \frac{1}{2} \nabla \nabla : (n\bar{\mathbf{d}}\bar{\mathbf{d}}). \quad (5)$$

The currents of the four charge configurations add at any particular point $\bar{\mathbf{r}}$ to produce the net current density $\bar{\mathbf{J}}_Q$. When the velocities of the four charge distributions are

evaluated, their respective current densities obtained, and then superimposed, one finds for the current density

$$\bar{J}_Q = -\nabla \cdot \left(qn \bar{d}_1 \frac{d\bar{d}_2}{dt} + qn \bar{d}_2 \frac{d\bar{d}_1}{dt} \right) + \nabla \nabla : (qn \bar{d}_1 \bar{d}_2 \bar{v}). \quad (6)$$

Similarly, one finds for the charge density

$$\rho_Q = \nabla \nabla : (qn \bar{d}_1 \bar{d}_2). \quad (7)$$

The planar quadrupole model is not sufficient to describe the most general distribution of charge with a quadrupole moment. It is easy to obtain more general expressions than those of Eqs. 6 and 7, by considering each quadrupolar particle to be made up of a superposition of planar quadrupoles. Supposing that each quadrupolar particle is made up of N planar quadrupoles, one obtains a quadrupole tensor density by superposition:

$$\bar{\bar{Q}} = \frac{1}{2} \sum_{i=1}^N q^n \left(\bar{d}_1^i \bar{d}_2^i + \bar{d}_2^i \bar{d}_1^i \right). \quad (8)$$

Equations 6 and 7 can be written in terms of $\bar{\bar{Q}}$ if one introduces the additional definition of the magnetization density

$$\bar{M} = \sum_{i=1}^N q^n \left(\bar{d}_1^i \times \frac{d\bar{d}_2^i}{dt} + \bar{d}_2^i \times \frac{d\bar{d}_1^i}{dt} \right). \quad (9)$$

One then has for the charge density and current density, as produced by moving quadrupolar particles,

$$\rho_Q = \nabla \nabla : \bar{Q} \quad (10)$$

$$\bar{J}_Q = -\nabla \cdot \left[n \frac{d}{dt} \left(\frac{\bar{\bar{Q}}}{n} \right) \right] + \nabla \nabla : (\bar{\bar{Q}} \bar{v}) + \nabla \times \bar{M}. \quad (11)$$

With these equations the formulation of Maxwell's equations for a system of quadrupolar particles is completed. In order to complete the formulation of the system, it is necessary to find the force density that acts toward acceleration of volume elements of the quadrupolar medium. If one starts with the model of a fluid of noninteracting quadrupolar particles, it is not difficult to find the amount of energy supplied by the electric and magnetic field to the fluid per unit volume, w_Q . This is accomplished by a simple application of the Lorentz law. One finds

$$n \delta \left(\frac{w_Q}{n} \right) = n \nabla \bar{E}^o : \delta \left(\frac{\bar{\bar{Q}}}{n} \right) - \bar{M} \cdot \delta \bar{B}^o. \quad (12)$$

(IX. ELECTRODYNAMICS OF MEDIA)

[The superscript o on $\bar{\mathbf{E}}$ and $\bar{\mathbf{B}}$ indicates that $\bar{\mathbf{E}}$ and $\bar{\mathbf{B}}$ are evaluated in the rest frame of the volume element under consideration.]

From the same model one may develop an energy conservation theorem that includes the rate of energy supplied to the particles per unit volume both as internal energy and as kinetic energy, the time rate of change of the energy of the electromagnetic field, and the divergence of the power flow of the electromagnetic field. Also, one finds in such a theorem the divergence of a vector that can be interpreted as the power flow associated with the quadrupolar medium.

$$\bar{\mathbf{S}}_Q^o = n \left[\frac{d}{dt} \left(\frac{\bar{\mathbf{Q}}}{n} \right) \right]^o \cdot \bar{\mathbf{E}}^o + \bar{\mathbf{Q}} \cdot \nabla \bar{\mathbf{v}} \cdot \bar{\mathbf{E}}^o - \bar{\mathbf{E}}^o \times \bar{\mathbf{M}}. \quad (13)$$

Equations 12 and 13 can be used as a starting point for the application of the principle of virtual work, or its generalization, the principle of virtual power.^{3,4} For this purpose one wants to generalize the expression for the energy density supplied to the fluid per unit volume to describe a solid, rather than a fluid of noninteracting particles. A generalization that suggests itself is

$$\text{nd} \left(\frac{w_m}{n} \right) = n \nabla \bar{\mathbf{E}}^o : \frac{d}{dt} \left(\frac{\bar{\mathbf{Q}}}{n} \right) - \bar{\mathbf{M}} \cdot \frac{d\bar{\mathbf{B}}^o}{dt} + \bar{\mathbf{t}} : \nabla \bar{\mathbf{v}}. \quad (14)$$

Here we have introduced an electromechanical stress tensor $\bar{\mathbf{t}}$, in order to take the microscopic interactions among the particles of the medium into account. It should be emphasized that the introduction of this tensor is not simply an addition of a mechanical stress tensor because $\bar{\mathbf{t}}$ may depend upon the magnetic flux density $\bar{\mathbf{B}}$ and the quadrupole tensor per particle $\bar{\mathbf{Q}}/n$. Furthermore, we assume that the power flow density associated with the quadrupolar medium is still properly represented by Eq. 13, which was obtained from the model of the quadrupolar fluid. With this information and with the additional statement that the power-conversion density in the rest frame of the material medium is given by $(\bar{\mathbf{E}} + \bar{\mathbf{v}} \times \bar{\mathbf{B}}) \cdot \bar{\mathbf{J}}_Q^o$, where $\bar{\mathbf{J}}_Q^o$ is the current density in the rest frame, one can apply the principle of virtual power to obtain the force density that accelerates the volume elements of the quadrupolar fluid. The force density is found to be

$$\bar{\mathbf{f}} = \bar{\mathbf{Q}} : \nabla \nabla \bar{\mathbf{E}} + \bar{\mathbf{v}} \times (\bar{\mathbf{Q}} : \nabla \nabla) \bar{\mathbf{B}} + n \frac{d}{dt} \left(\frac{\bar{\mathbf{Q}}}{n} \right) \cdot \times \nabla \bar{\mathbf{B}} + (\nabla \bar{\mathbf{B}}) \cdot \bar{\mathbf{M}}. \quad (15)$$

Two facts should be noted in the preceding results. First of all, Maxwell's equations for a quadrupolar medium are not simple applications of Maxwell's equations for dipolar media, in the sense that it is not possible to replace the polarization density $\bar{\mathbf{P}}$, as it appears in equations of motion for the dipolar medium, by the divergence of $\bar{\mathbf{Q}}$. In Maxwell's equations for a dipolar medium only first-order derivatives of the

velocity field \bar{v} appear. We find that the current density \bar{J}_Q of Eq. 11 contains second-order derivatives of the velocity field. It should also be noted that the quadrupolar medium under consideration has the relatively complicated power-flow density vector of Eq. 13. Hence the quadrupolar medium leads to a novel application of the principle of virtual work. The author's study of the quadrupolar medium was motivated partly by the fact that a quadrupolar medium provided an interesting new application and test of the principle of virtual power.

H. A. Haus

References

1. P. S. Pershan, "Nonlinear Optical Properties of Solids," *Phys. Rev.* 130, 919-929 (1963).
2. R. M. Fano, L. J. Chu, and R. B. Adler, Electromagnetic Fields, Energy and Forces (John Wiley and Sons, Inc., New York, 1960), Chaps. 9 and 10 and Appendix I.
3. L. J. Chu, H. A. Haus, and P. Penfield, Jr., "The Force Density in Polarizable and Magnetizable Fluids," *Proc. IEEE* 54, 920-935 (1966).
4. E. L. Chu, "On the Concept of Fictitious Surface Charges of an Electron Beam," *J. Appl. Phys.* 31, 381-388 (1960); see Eqs. (9a) and (9b).
5. P. A. Sturrock, "Generalization of the Lagrange Expansion with Applications to Physical Problems," *J. Math. Phys.* 1, 405-408 (Sept.-Oct. 1960); see Eq. (5.8).
6. P. Penfield, Jr. and H. A. Haus, Electrodynamics of Moving Media (to be published by The M. I. T. Press, Cambridge, Mass.).

(IX. ELECTRODYNAMICS OF MEDIA)

B. PULSE DISTORTION IN NONLINEAR OPTICS

A study of the interaction of intense optical radiation with materials that respond nonlinearly has led to recent investigations of the possibility into obtaining electromagnetic shock waves in non-polar liquids such as carbon di-sulfide.¹⁻³ These would result from a dependence of the phase velocity of light upon the local internal energy density of the closed system containing the pulse and the liquid.

In this report an energy equation is derived, and the Debye approach adapted to a non-polar liquid, reviewed qualitatively. The results are then used to deduce thermodynamic quantities that describe the physical mechanisms of the nonlinear interaction. Computational results are presented, illustrating the interplay between the nonlinear response, and the relaxation of the medium.

1. Energy Equation

It is assumed that the field of the optical pulse can be described in terms of a central frequency, ω , a propagation vector, k , pointing in the z -direction, and complex amplitudes, all of which are slowly varying functions of space and time. Assuming a plane wave, we write

$$\bar{H} = \text{Re } \underline{H}(t, z) e^{-\left(i \int_0^z k dz - i\omega t\right)}; \quad \underline{H}(t, z) = H(t, z) \hat{iy}$$

$$\bar{D} = \text{Re } \underline{D}(t, z) e^{-\left(i \int_0^z k dz - i\omega t\right)}; \quad \underline{D}(t, z) = D(t, z) \hat{ix}$$

$$\bar{E} = \text{Re } \underline{E}(t, z) e^{-i\left(i \int_0^z k dz - i\omega t\right)}; \quad \underline{E}(t, z) = E(t, z) \hat{ix}$$

for the \bar{H} , \bar{D} , and \bar{E} fields, respectively. \hat{ix} , \hat{iy} , and \hat{iz} refer to unit vectors pointing in the x , y , and z directions of a right-handed system.

Maxwell's equations can be employed to obtain a "Poynting theorem" relating the amplitudes and the propagation vector. The real part involving only the amplitudes is

$$\nabla \cdot (\underline{E} \times \underline{H}^* + \underline{E}^* \times \underline{H}) + \mu_0 \frac{\partial}{\partial t} (\underline{H} \cdot \underline{H}^*) + \underline{E} \cdot \frac{\partial \underline{D}^*}{\partial t} + \underline{E}^* \cdot \frac{\partial \underline{D}}{\partial t} = 0. \quad (1)$$

The theory of polar molecules can be shown to be consistent with the constitutive relationship³

$$\begin{aligned} \underline{D} &= \epsilon \{ \{ \underline{E} \cdot \underline{D}^* + \underline{E}^* \cdot \underline{D} \}, t \} \underline{E} \\ &= \epsilon \underline{E}. \end{aligned} \quad (2)$$

Furthermore, if the envelope of the pulse is slowly varying with respect to the inverse

of the optical frequency, we can write

$$\bar{k} \times \underline{H} - \left(\int_0^z \frac{\partial k}{\partial t} dz - \omega \right) \underline{D} = 0 \quad (3)$$

$$\bar{k} \times \underline{E} + \rho_0 \left(\int_0^z \frac{\partial k}{\partial t} dz - \omega \right) \underline{H} = 0 \quad (4)$$

which shows that the phase velocity of the pulse is given by

$$\frac{\left(\omega - \int_0^z \frac{\partial k}{\partial t} dz \right)}{k} = \frac{1}{\sqrt{\mu_0 \epsilon}} = v. \quad (5)$$

Moreover, (3) shows that

$$\underline{H} \cong v \underline{D}. \quad (6)$$

Together with (2), (6) allows the energy propagation equation (1) to be written

$$\frac{\partial \rho}{\partial t} + \frac{\partial \rho v}{\partial z} + \frac{1}{2} \left(\frac{\rho}{\epsilon} \right) \frac{\partial \epsilon}{\partial t} = 0, \quad (7)$$

where

$$\rho \triangleq \frac{\underline{E} \cdot \underline{D}^*}{2}. \quad (8)$$

The explicit formula for the dielectric constant can be deduced from the Debye theory, under the assumption of an anisotropic molecular polarizability. For axially symmetric molecules that polarize instantaneously, this gives to lowest order

$$\frac{\partial}{\partial t} (\epsilon - \epsilon_0) = - \left(\frac{\epsilon - \epsilon_0}{\tau} - \frac{\beta \rho}{\tau} \right); \quad \beta = \frac{K}{kT}, \quad (9)$$

where ϵ_0 is the linear dielectric constant. K is a constant depending upon the polarizabilities and the density, k is Boltzmann's constant, T is the temperature in degrees Kelvin, and τ is the relaxation time associated with viscous damping.

Because $v = \frac{1}{\sqrt{\mu_0 \epsilon}}$, if we let $v_0 = \frac{1}{\sqrt{\mu_0 \epsilon_0}}$, (7) and (9) can also be written

$$\frac{\partial \rho}{\partial t} + v_0 \frac{\partial \rho}{\partial z} + (v - v_0) \frac{\partial \rho}{\partial z} + \rho \frac{\partial}{\partial z} (v - v_0) - \left(\frac{\rho}{v} \right) \frac{\partial v}{\partial t} = 0 \quad (10)$$

$$\frac{\partial}{\partial t} (v - v_0) = - \left(\frac{(v - v_0)}{\tau} + \frac{a \rho}{\tau} \right); \quad a = \left(\frac{v_0 \beta}{2} \right). \quad (11)$$

(IX. ELECTRODYNAMICS OF MEDIA)

For $\tau = 0$, $(v-v_0) = \delta v = -a\rho$, so that the energy equation (7), with the term $\delta v^2 \frac{\partial \rho}{\partial z}$ neglected, becomes

$$\frac{\partial \rho}{\partial t} + (v_0 + 3\delta v) \frac{\partial \rho}{\partial z} = 0. \quad (12)$$

In this particular case, the propagation of the quantity ρ is three times as sensitive to the nonlinearity as is the phase.⁴

Equation 12, according to the theory of characteristics, implies that ρ is a constant along the lines

$$z = (v_0 - 3a\rho_0)t$$

where $\rho = \rho_0$ and $z = z_0$, for $t = 0$. If ρ'_0 is infinitesimally greater than ρ_0 and corresponds to z'_0 , its corresponding characteristic crosses that corresponding to ρ_0 at the point z , for a value of t equal to

$$t = \frac{1}{3a} \left\{ \frac{\partial \rho}{\partial z} \right\}^{-1}$$

This equation for $\frac{\partial \rho}{\partial z}$, having its maximum value in space along the initial ρ curve, gives the time of shock formation.

2. Thermodynamics of Pulse Evolution

Even though the system exhibits changes at the optical frequency, the particular form of the dielectric constant, as well as that of the energy flow equation, indicates that with respect to the interaction of the field with the medium such rapid changes are absent. This is true as long as the envelope changes are slow compared with the inverse of the optical frequency. If these changes are much slower than the relaxation time of the medium, too, the latter does achieve a thermodynamic equilibrium with the field. Reversible thermodynamics can then be applied.

The electromagnetic work done on the medium, dL , as obtained from (1), noting from (7) that the spatial flow of energy as given by the Koynting vector is simply $\frac{\partial \rho v}{\partial z}$; is given by

$$dL' = \mu_0 d \left(\frac{HH^*}{2} \right) + \frac{E dD^*}{2} + \frac{E^* dD}{2} = d\rho + \frac{1}{2} \left(\frac{\rho}{\epsilon} \right) d\epsilon \quad (13)$$

Choosing ρ and T as independent variables, the differential heat change for the thermodynamic system is given by

$$dQ = dU - L = d(U-\rho) - \frac{1}{2} \left(\frac{\rho}{\epsilon} \right) \frac{\partial \epsilon}{\partial \rho} d\rho - \frac{1}{2} \left(\frac{\rho}{\epsilon} \right) \frac{\partial \epsilon}{\partial T} dT. \quad (14)$$

For a reversible process $dQ = TdS$, and thus we may write

$$\frac{\partial}{\partial \rho} (U-\rho) = \frac{1}{2} \rho \frac{\partial}{\partial \rho} (\ln \epsilon) + T \frac{\partial S}{\partial \rho}. \quad (15)$$

The appropriate Maxwell relationship can be obtained from the differential of the free energy, which for the reversible process is

$$\begin{aligned} dF &= -SdT + dL \\ &= \left(-S + \frac{1}{2} \frac{\rho}{\epsilon} \frac{\partial \epsilon}{\partial T} \right) dT + \left(1 + \frac{1}{2} \frac{\rho}{\epsilon} \frac{\partial \epsilon}{\partial \rho} \right) d\rho. \end{aligned} \quad (16)$$

The differentiability condition then implies that

$$\left. \frac{\partial S}{\partial \rho} \right|_T = \frac{1}{2} \left(\left. \frac{\partial}{\partial T} (\ln \epsilon) \right|_T \right). \quad (17)$$

The total internal energy from (15) is then equal to

$$U = \rho + \int_0^\rho \frac{d\rho'}{2} \left(\rho' \frac{\partial}{\partial \rho'} (\ln \epsilon) + T \frac{\partial}{\partial T} (\ln \epsilon) \right) + C_o (T - T_o), \quad (18)$$

where C_o is the heat capacity at constant B and D, for B and D equal to zero, and T_o is a reference temperature.⁵

The entropy is given by (17):

$$S = \frac{1}{2} \int_0^\rho d\rho' \frac{\partial}{\partial T} (\ln \epsilon) + C_o \ln \left(\frac{T}{T_o} \right). \quad (19)$$

In the Debye approach, ϵ is a function of $\frac{\rho}{kT}$ ($\tau = 0$) so that the integral in (18) is zero, which implies that the internal energy increase in the interacting system is equal to ρ plus the internal energy increase attributable to a temperature increase.

From (18) and (19), other thermodynamic functions can be obtained. For instance, the free energy, which is equal to $U - TS$, is

$$F = \rho - \int_0^\rho d\rho' \left(\rho' \left. \frac{\partial \ln \epsilon}{\partial \rho'} \right|_T \right) + C_o \left((T - T_o) - T \ln \left(\frac{T}{T_o} \right) \right). \quad (20)$$

To lowest order in ρ , S and F are

$$S = C_o \ln \left(\frac{T}{T_o} \right) - \frac{1}{4} \frac{K}{kT^2 \epsilon_o} \rho^2 \quad (21)$$

(IX. ELECTRODYNAMICS OF MEDIA)

$$F = \frac{1}{2} \left(2 + \frac{\epsilon - \epsilon_0}{2\epsilon_0} \right) \rho + C_0 \left((T - T_0) - T \ln \left(\frac{T}{T_0} \right) \right). \quad (22)$$

These can be expressed in terms of the variables H , B , D , and E by employing the constitutive relationship for $(\epsilon - \epsilon_0)$ in terms of ρ , and by attributing half of the linear ρ terms that arise to the magnetic stored energy. Noting that the electromagnetic variables have at most a constant phase (ϵ is real), which can be assumed to be zero, thereby making these variables real, we get

$$\left. \frac{\partial F}{\partial \frac{D}{\sqrt{2}}} \right|_{B, T} = \left(\frac{E}{\sqrt{2}} \right) \quad \left. \frac{\partial F}{\partial T} \right|_{B, D} = -S.$$

$$\left. \frac{\partial F}{\partial \frac{B}{\sqrt{2}}} \right|_{D, T} = \left(\frac{H}{\sqrt{2}} \right)$$

In the light of these results, the optical interaction can be described as follows. As the pulse begins to penetrate the medium, it polarizes the molecules and tends to align them along the field direction. This alignment under isothermal conditions ($T = T_0$), according to (20), is equivalent to a decrease in the entropy of the system, and thus represents a heat flow out of the system. The resultant loss in internal energy, $T \int dS$, is compensated for by a portion of the electromagnetic work done on the system. The remainder of the work, which just turns out to be ρ , contributes to an increase in the internal energy.

Positions located on the lagging wing of the pulse are behaving oppositely. Because of a decreasing torque, molecular alignment is decreasing. Heat is being absorbed, which, in turn, contributes to an increase in the internal energy. The electromagnetic work done on the system is also decreasing, however, and the internal energy increase resulting from a decreasing alignment compensates for a portion of this decreasing electromagnetic work; once again, ρ is left as the internal energy.

Thus, while the pulse is within the medium, a portion of the electromagnetic energy contributes to an increase in the internal energy, while the remainder is stored in molecular alignment. As the pulse leaves the medium, the electromagnetic field has once again retrieved the energy stored in alignment; consequently, in this case no loss can occur. Only a change in shape of the pulse profile is possible.

This implies that at any point the total energy available for electromagnetic work is given by $U - T \int ds$ under isothermal conditions. This is precisely the free energy when T equals T_0 .

Now when relaxation is present, the basic relationship

$$\Delta U = \Delta Q + \Delta W$$

must still apply, since it expresses a conservation of energy, even for an irreversible process. Moreover, the internal energy of the system must still be a function of state of the system. Thus, as before, u must be equal to ρ . Q and W need not be functions of the state, however, although the entropy is. Thus it is reasonable to assume that the entropy is still given by (21), and that the energy available for electromagnetic work is given by the free energy, in the case of an isothermal process.

In order to justify these claims, consider the electromagnetic work done on the medium, $\int dL$. Upon substitution of (ρ/ϵ) from (9) in (13) and integrating where possible, keeping only lowest order terms in ρ , we obtain

$$W \approx \rho + \frac{1}{4\epsilon_0\beta} \{\epsilon - \epsilon_0\}^2 + \frac{\tau}{2\beta} \int_1^{(\epsilon/\epsilon_0)} \left\{ \frac{\partial}{\partial t} \left(\ln \left(\frac{\epsilon}{\epsilon_0} \right) \right) \right\} d \left(\frac{\epsilon}{\epsilon_0} \right). \quad (24)$$

The second term is just the reversible heat of alignment considered previously. The last term is the electromagnetic work done to overcome viscous forces. β is positive for a passive material. In this case there must also be a term in ΔQ representing the generation of heat arising from viscous damping, which compensates for the work done against viscous forces. Consequently,

$$\Delta Q = T\Delta S - \frac{\tau}{2\beta} \int_1^{(\epsilon/\epsilon_0)} \left\{ \frac{\partial}{\partial t} \left(\ln \left(\frac{\epsilon}{\epsilon_0} \right) \right) \right\} d \left(\frac{\epsilon}{\epsilon_0} \right). \quad (25)$$

As postulated, then, we have

$$U = \rho. \quad (26)$$

Returning to the energy flow equation (7); it can be written, by using (24),

$$\frac{\partial \rho}{\partial t} + \frac{\partial \rho v}{\partial z} + \frac{1}{2} \frac{(\epsilon - \epsilon_0)}{\beta \epsilon_0} \frac{\partial \epsilon}{\partial t} + \frac{\tau}{2\beta} \frac{1}{\epsilon} \left(\frac{\partial(\epsilon - \epsilon_0)}{\partial t} \right) = 0. \quad (27)$$

Consider a small control volume of the system. Equation 27 implies that the flow of the electromagnetic contribution to the internal energy is equal to its rate of increase within the small-volume element, minus the rate of heat extraction attributable to electromagnetic alignment of the molecules, plus the rate of dissipation within the volume. If the process is isothermal, this can be written

$$\frac{\partial \rho v}{\partial x} + \frac{\partial F}{\partial t} + (\text{Rate of Loss}) = 0. \quad (28)$$

Furthermore, if the loss is zero, the rate of heat extraction resulting from alignment

(IX. ELECTRODYNAMICS OF MEDIA)

can be written in terms of the internal energy term that results in (12). This shows that the internal energy decrease resulting from the alignment causes an effective decrease in the speed of propagation of the internal energy, changing it to $(v_0 + 3\delta v)$. In this case the effective flow velocity of the internal energy through the boundary of a control element obeys the continuity equation

$$\frac{\partial \rho}{\partial t} + \frac{\partial}{\partial x} \left\{ \left(v_0 + \frac{3}{2} \delta v \right) \rho \right\} = 0. \quad (29)$$

3. Computational Results

Figures IX-2, IX-3, and IX-4 show numerical solutions for the two equations (10) and (11). These bear out the theoretical results obtained above. Figure IX-2 shows that as a Gaussian pulse penetrates the nonlinear medium, a portion of the electromagnetic work goes into alignment and the remaining increases the internal energy. The decrease in phase velocity causes the internal energy pulse to steepen on the lagging wing and a shock is eventually formed. Even though relaxation is present, steepening occurs indefinitely, although at a slower rate than when τ is zero. The total electromagnetic contribution to the internal energy is also seen to decrease as the pulse traverses the medium, and electromagnetic energy is dissipated as heat.

Figures IX-3 and IX-4 illustrate pulse deformation for the case of an initial modulating amplitude formed by the beating of two frequencies, thereby obtaining a periodic pulse profile. They indicate that the behavior is highly dependent upon the ratio of the relaxation time to the period of the initial amplitude. For a small ratio, a sequence of sawteeth which gradually merge is obtained. For a larger ratio, however, in which case the relaxing velocity from one cycle can dominate the initial portion of the succeeding cycle, pulse steepening occurs both at the beginning and at the end of each cycle, pulse steepening occurs both at the beginning and at the end of each cycle. In the latter, the velocity profile tends to a constant and therefore a state of zero dissipation.

Kelly has calculated that in the case of Cs_2 in the self-trapped^{5,6} region of a mode-locked laser pulse, the steepening should occur in the order of a centimeter or two.

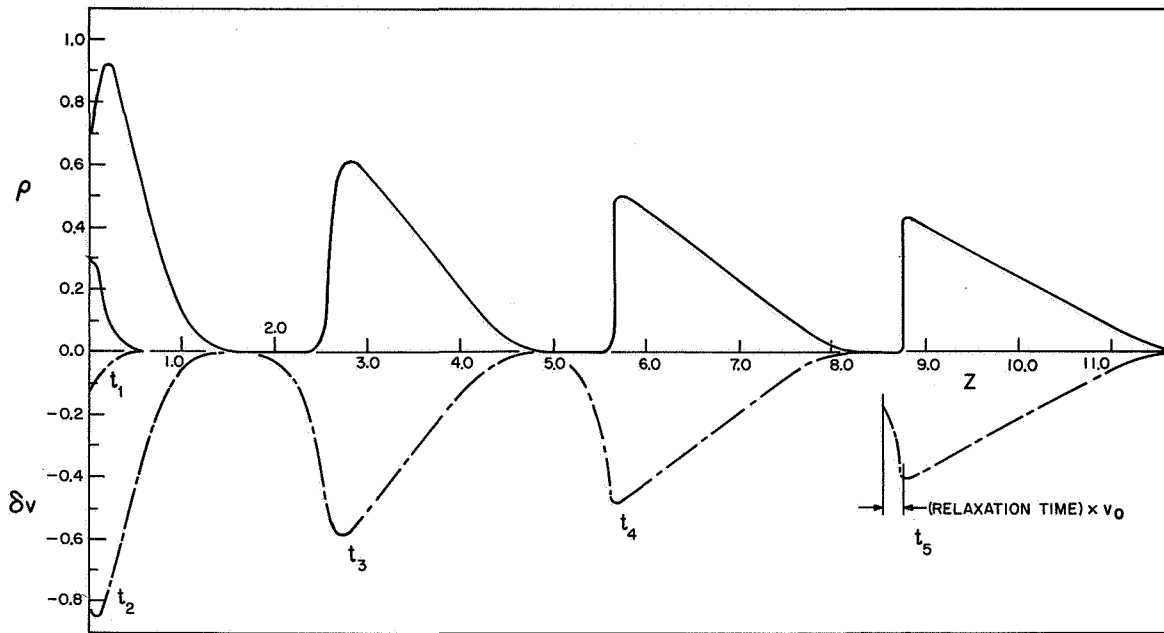
4. Acknowledgement

The results of this report were obtained from work carried out jointly with Dr. F. De Martini,^{*†} Professor C. H. Townes of the Department of Physics, M. I. T.,^{*} and Dr. P. L. Kelley, of Lincoln Laboratory, M. I. T.^{**}

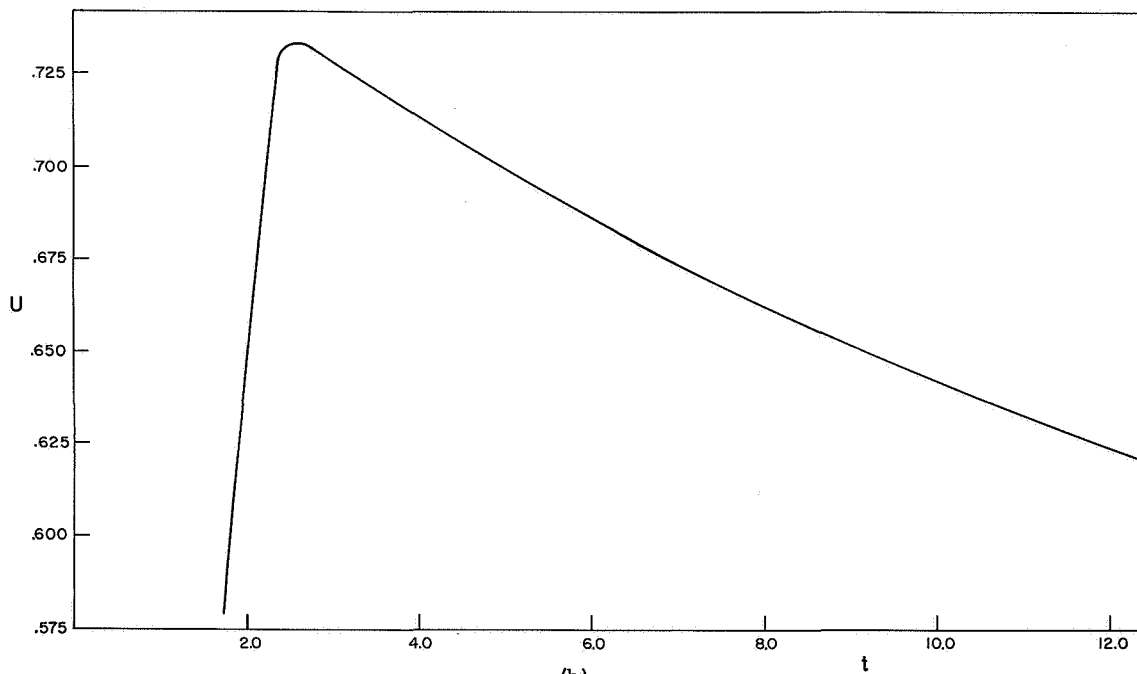
^{*}Work supported by the National Aeronautics and Space Administration under Contract NsG-330 and the U. S. Air Force Cambridge Research Laboratories.

[†]Present address: Institut d'Optique, Faculté des Sciences, Orsay (S.-et-O.), France.

^{**}Operated by the Massachusetts Institute of Technology with support from the U. S. Air Force.

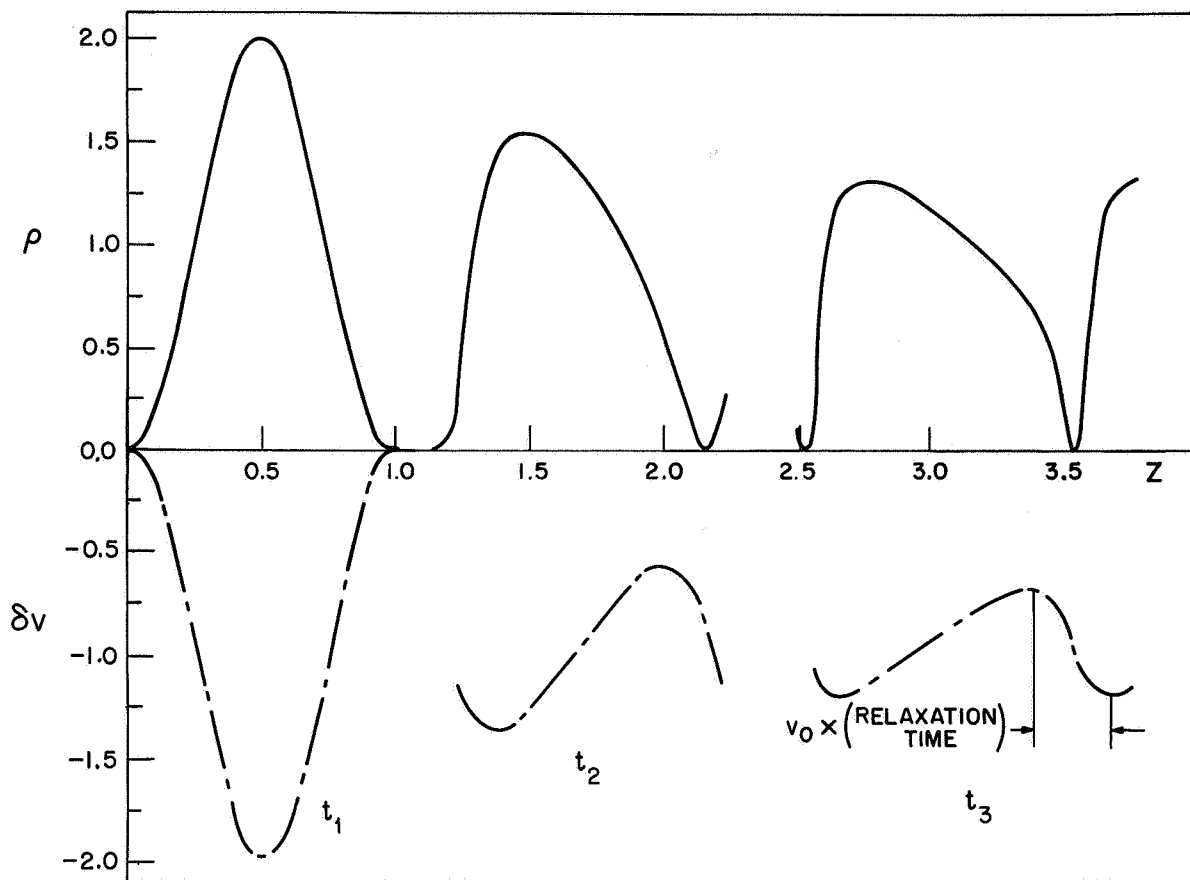


(a)

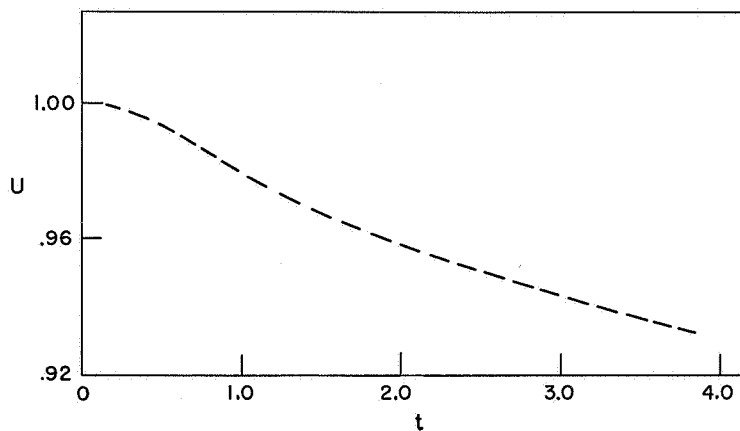


(b)

Fig. IX-2. (a) Propagation of a pulse in the stationary frame. The initial pulse just before entering the medium is Gaussian, with the height and width normalized to unity. $\frac{v_2 \rho_0}{v_0} = .2$, $\left(\frac{t_s v_0}{l} = .291\right) \cdot \tau = .229$, $t_s \cdot T_1 = .89 t_s$, $T_2 = 1.77 t_s$, $T_3 = 5.22 t_s$, $T_4 = 8.72 t_s$, $T_5 = 12.29 t_s$.
 (b) Integrated energy density, $u = \int_{-\infty}^{\infty} \rho \, dz$, as a function of time (normalized to the shock time).



(a)



(b)

Fig. IX-3. (a) Propagation of a pulse in the stationary frame. The initial pulse is sinusoidal, of the form $(1 + \sin 2\pi z)$. Distance is normalized to modulation wavelengths. $\frac{v_2^{\rho_0}}{v_0} = .075$, $\left(\frac{t_s v_0}{l} = .707\right) \cdot \tau = .354 t_s$, $T_1 = 0$, $T_2 = 1.74 t_s$, $T_3 = 4.56 t_s$.

(b) Integrated energy density as a function of time (normalized to the shock time).

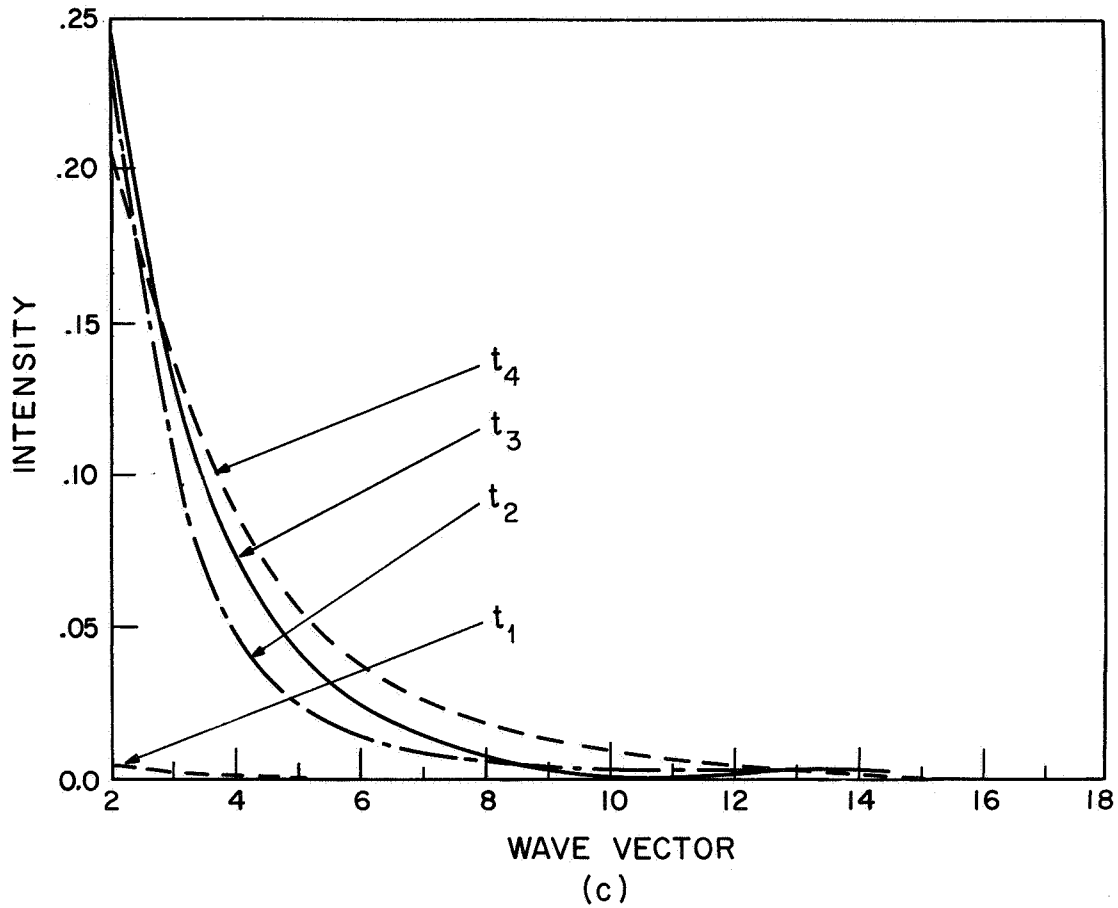
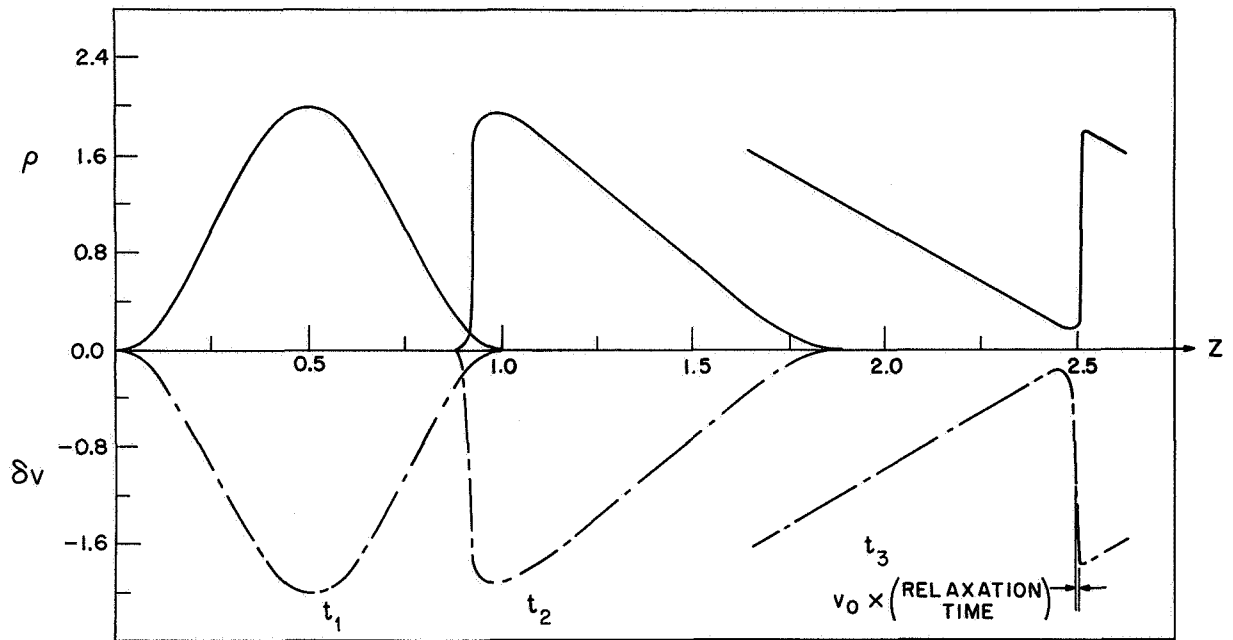
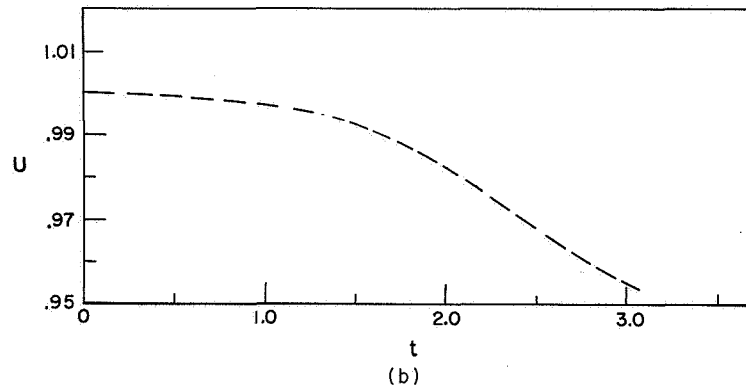


Fig. IX-3. (c) Absolute value of the Fourier transform of the pulse at various times. The wave vector is in units of the initial modulation wave vector. Amplitudes are normalized to the initial amplitude of the fundamental. $T_1 = 3.65^{-3} t_s$, $T_2 = 1.79 t_s$, $T_3 = 2.55 t_s$, $T_4 = 3.39 t_s$.



(a)



(b)

Fig. IX-14. (a) Propagation of a pulse in the stationary frame. Initial pulse in sinusoidal. of the form $(1 + \sin 2\pi z)$. Distance is given in modulation wavelengths. $\frac{v_2 \rho_0}{v_0} = .1 \left(\frac{t_s v_0}{l} = .531 \right) \cdot \tau = .0094 t_s$, $T_1 = 0$, $T_2 = 1.66 t_s$, $T_3 = 3.13 t_s$.
 (b) Internal energy increase contributed by the electromagnetic stored energy as a function of time (normalized to the shock time).

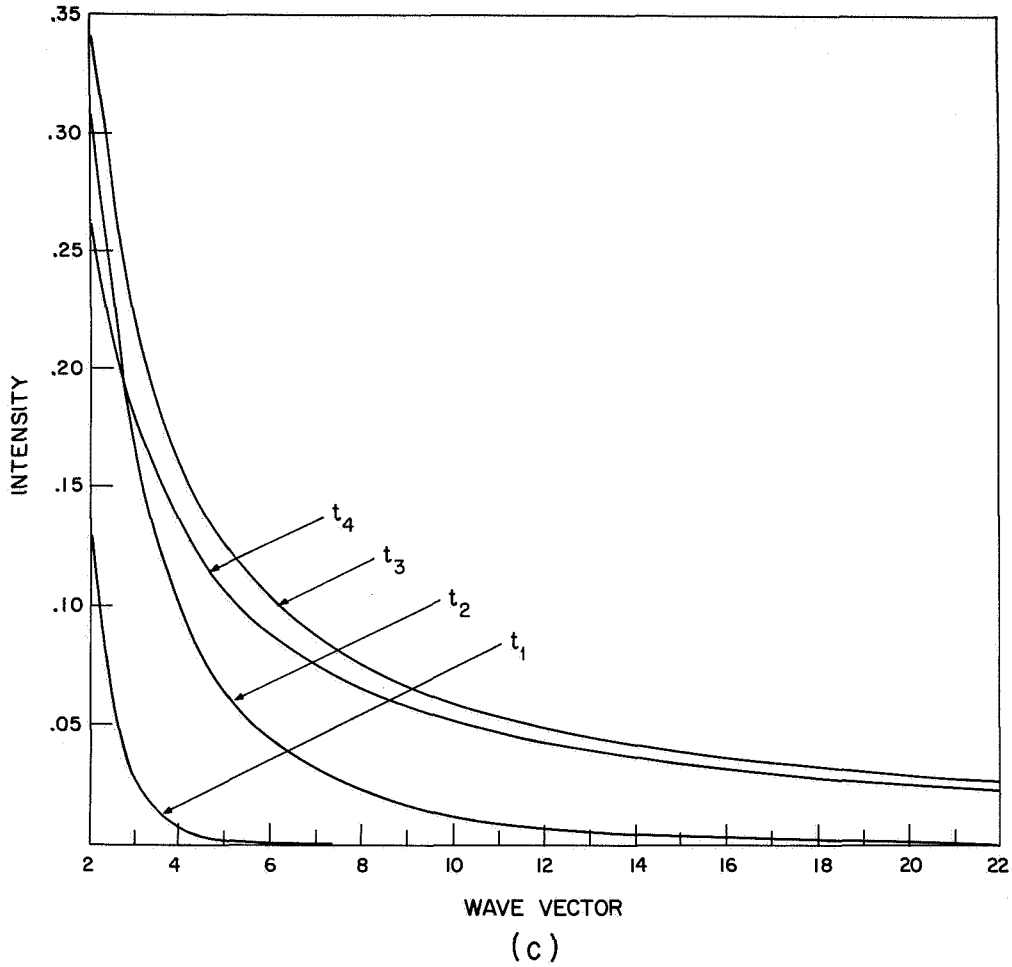


Fig. IX-4. (c) Absolute value of the Fourier transform of the pulse at various times. The wave vector is in units of the initial modulation wave vector. Amplitudes are normalized to the initial amplitude of the fundamental. $T_1 = .367 t_s$, $T_2 = 1.10 t_s$, $T_3 = 1.85 t_s$, $T_4 = 3.13 t_s$.

(IX. ELECTRODYNAMICS OF MEDIA)

The author is especially appreciative of the encouragement and the basic ideas provided by Professor H. A. Haus.

K. T. Gustafson

References

1. I. G. Katayer, Electromagnetic Shock Waves (Sovietskoye Raido, Moscow 1963) (Translation, Iliffe Books Ltd., London 1966).
2. K. Iduta and T. Taniuti, Research Report IPPJ-31, Nagoya University, Japan 1964 (unpublished).
3. G. Rosen, Phys. Rev. 139, A539 (1965).
4. R. J. Joenk and R. Landauer, Bull. Am. Phys. Soc. 12, 178 (1967).
5. R. Y. Chiao, E. Garmire, and C. H. Townes, Phys. Rev. Letters 14, 479 (1964).
6. R. Y. Chiao, P. L. Kelley, and E. Garmire, Phys. Rev. Letters 17, 1158 (1966).

X. PHYSICAL OPTICS OF INVERTEBRATE EYES*

Academic and Research Staff

Prof. G. D. Bernard
Dr. W. H. Miller

Graduate Students

J. L. Allen
F. Beltran-Barragan

N67-27091

A. OPTICS OF THE TOBACCO HORNWORM MOTH

We have made two apparently closely related observations regarding the structure and functioning of the cornea and crystalline cone portion of the optics of the compound eye of the Tobacco Hornworm Moth. (These components presumably form the focusing elements of the optical tract.)

First, we have observed, as shown in Fig. X-1, that the cone and the cornea appear

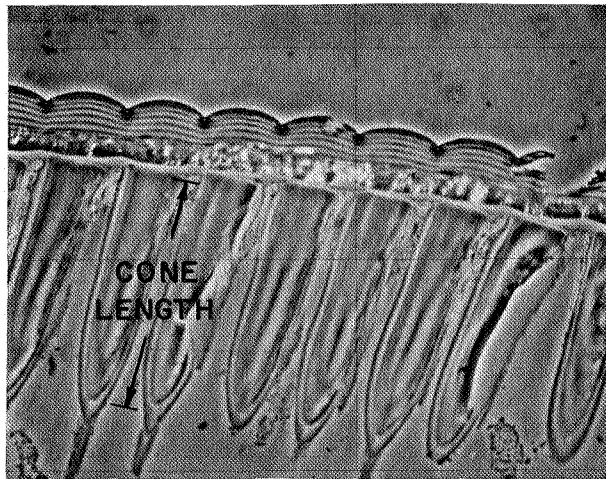


Fig. X-1. Thin ($\sim 2 \mu$), unstained normal section of Hornworm Moth eye as observed by using Zernike phase contrast. Magnification 350X.

structured when observed by phase contrast in the light microscope, thereby suggesting a varying index of refraction (n) with position. The sections show shadowing that is suggestive of a series of thin convex-concave lenses whose radii of curvature increase monotonically as one penetrates into the eye. The outer "lens" has the curvature of the front surface of the cornea; the innermost appears quite flat.

*This work is supported by the Joint Services Electronics Programs (U. S. Army, U. S. Navy and U. S. Air Force) under Contract DA 28-043-AMC-02536(E).

(X. PHYSICAL OPTICS OF INVERTEBRATE EYES)

Second, we have found that if one ray traces through the cornea and cone under the assumption of a uniform \underline{n} of 1.5 (the nominal value for chitinous cuticle), the focal point falls approximately half way through the cone – a rather unlikely focal point for efficient use of the remainder of the optical tract. The discrepancy seems too large to be attributable simply to use of an inexact value of \underline{n} .

These two observations suggest that the cornea and cone gradations substantially alter the focal length from that predicted by the simple constant- \underline{n} model. We have confirmed by experiment that the focal length is different. We observed the focussing action of a cleaned-out cornea through the microscope and found that the corneal lens alone has a focal length (measured from its outer surface) of approximately 110 μ , contrasted with a predicted focal length for a constant index model of the corneal lens alone (with the cone removed) of approximately 56 μ . It remains to be confirmed that the observed structure is a change in index of refraction and that such a variation can account for the observed focussing action. We shall make quantitative measurements on \underline{n} as a function of position, using interference microscopy to verify our hypothesis that the change in \underline{n} is the explanation for the observed long focal length.

J. L. Allen

PLASMA DYNAMICS

32M3

XI.3 PLASMA PHYSICS*8

Academic and Research Staff

Prof. S. C. Brown
Prof. W. P. Allis

Prof. G. Bekefi
Prof. J. C. Ingraham

J. J. McCarthy
W. J. Mulligan

Graduate Students

M. L. Andrews
A. J. Cohen
D. L. Flannery

V. G. Forrester, Jr.
E. V. George
P. W. Jameson
R. L. Kronquist

G. L. Rogoff
J. K. Silk
D. W. Swain
J. H. Vellenga

A. COMPUTER PROGRAMMED "BASIC DATA OF PLASMA PHYSICS"

N67-27092

As mentioned in Quarterly Progress Report No. 80,¹ an attempt has been made to revise the 1959 edition of "Basic Data of Plasma Physics" (Special Technical Report Number 2 of the Research Laboratory of Electronics, M. I. T., published by The Technology Press, Cambridge, Mass., and John Wiley and Sons, Inc., New York) by using the information retrieval service of the Library TIP Program. Details of the operation of this experiment have been published,² and therefore will not be outlined again here.

This step in the project has now been completed with the publication of the book Basic Data of Plasma Physics, 1966.³ The production of this volume was accomplished completely from a remote compatible time-sharing system console, and therefore, in principle, could have been done at any distance from the computer connected (as it was) by an ordinary telephone line. To simulate a completely remote access endeavor, we avoided going to the library in the process of collecting these data. When a relevant reference appeared on the teletype output, we checked the teletype record and mailed it to the library, and the library returned to us a Xerox copy of the paper. The overall average of extra material that was thus delivered came out to be approximately 10 per cent; that is, 90 per cent of the called-for Xerox copies of the entire paper were actually used. Drawings of the data were then made to be included in the book as illustrations, and the references are shown in standard TIP nomenclature, so that the material in the book may be updated by further use of the citation technique inherent in information retrieval from the TIP library.

It should be emphasized that this information retrieval system completely by-passes the standard abstracting. One goes directly from title and bibliography search to the paper itself. The abstract is not a useful step in this procedure.

The index was also prepared with the aid of an IBM 7094 computer, the program for doing this being at the M. I. T. Computation Center. Items indexed are subject and author reference, which consists of one word or more. The computer produces a list

*This work was supported by the United States Atomic Energy Commission under Contract AT(30-1)-1842.

(XI. PLASMA PHYSICS)

of cyclic permutations of each reference, successive permutations being with the different words of four or more letters appearing in the reference. Words originally to the left of the "key word" appear at the right end of the line, while the page number of the reference is placed to the left of the line. After forming permutations of all entries, the computer alphabetizes them according to the key word. Permutations of multiple-author listings follow the same form. Because the index is a reproduction of the computer printout, subscripts and superscripts are not used. Thus H_2O appears as H2O. The number of charge units on an ion is indicated by an equal number of plus or minus signs following the chemical symbol for the atom or molecule. The index is unusually complete and consists of an author index, a subject index, and an index of chemicals.

S. C. Brown

References

1. S. C. Brown, "Computer Programmed 'Basic Data of Plasma Physics,'" Quarterly Progress Report No. 80, Research Laboratory of Electronics, M. I. T., January 15, 1966, pp. 83-85.
2. S. C. Brown, *Physics Today* 19, 59-64 (May 1966).
3. S. C. Brown, Basic Data of Plasma Physics, 1966 (The M. I. T. Press, Cambridge, Mass., 2d edition (revised), 1967).

B. FAR INFRARED PLASMA DIAGNOSTICS

1. Introduction – Quantities Measured

A wide-bandwidth Michelson interferometer has been used to measure phase shifts caused by a repetitively pulsed plasma over the spectral range from $k = 1/\lambda = 8.55 \text{ mc}^{-1}$. Line densities NL (where N is the electron density, and L the length of the plasma) in the vicinity of 3×10^{14} electrons cm^{-2} have been measured with an accuracy of a few per cent.

The observed phase shift, $\Delta\phi$, is given by

$$\Delta\phi(\omega) = \frac{\omega}{c} \int_0^{2L} |1 - \text{Re } \mu(x, \omega)| dx \text{ radians,} \quad (1)$$

where $\mu(x, \omega)$ is the complex refractive index of the plasma at a frequency ω . It is given by¹

$$\mu^2 = 1 - \left(\frac{\omega_p}{\omega}\right)^2 \left[\frac{1}{1 + \left(\frac{\nu}{\omega}\right)^2} + \frac{j \frac{\nu}{\omega}}{1 + \left(\frac{\nu}{\omega}\right)^2} \right]$$

and approximated, in the limits $\left(\frac{\nu}{\omega}\right)^2 \ll 1$ and $\left(\frac{\omega_p}{\omega}\right)^4 \ll 1$, by

$$\mu = 1 - \frac{1}{2} \left(\frac{\omega_p}{\omega}\right)^2 - j \left[\frac{1}{2} \frac{\nu}{\omega} \cdot \left(\frac{\omega_p}{\omega}\right)^2 \right],$$

where ν is the electron collision frequency for momentum transfer,² and ω_p the plasma frequency.

In this approximation the phase shift is given by

$$\begin{aligned} \Delta\phi(\omega) &= \frac{1}{2\omega c} \int_0^{2L} \omega_p^2(x) dx \\ &= \frac{(5.65 \times 10^4)^2}{2\omega c} \int_0^{2L} N(x) dx \\ &= \frac{5.32 \times 10^{-2}}{\omega} \langle N \rangle 2L \text{ radians} \end{aligned}$$

$$\therefore \langle N \rangle = \frac{\omega}{5.32 \times 10^{-2} \times 2L} \Delta\phi(\omega) \text{ cm}^{-3}.$$

In connection with the present experiment, it is convenient to express ω in terms of

(XI. PLASMA PHYSICS)

the free-space number $k = 1/\lambda \text{ cm}^{-1}$.

Thus the average electron density is given by

$$\begin{aligned} \langle N \rangle &= \frac{2\pi ck}{5.32 \times 10^{-2} \times 2L} \\ &= \frac{3.54 \times 10^{12}}{2L} k\Delta\phi(k) \text{ cm}^{-3}. \end{aligned} \quad (2)$$

In the present case, $2L = 15 \text{ cm}$

$$\therefore \langle N \rangle = 2.36 \times 10^{11} k\Delta\phi(k) \text{ cm}^{-3}. \quad (3)$$

As the beam traverses radially through a cylindrical discharge of radius R , the radial dependence of N is probably close to that of a zero-order Bessel function,² that is,

$$N(r) = N_0 J_0\left(2.405 \frac{r}{R}\right),$$

where N_0 is the electron density at the center of the discharge.

$$\begin{aligned} \therefore \langle N \rangle &= \frac{N_0}{2.405} \int_0^{2.405} J_0(r) dr \\ &\approx 0.6N_0 \end{aligned}$$

$$\therefore N_0 \approx 1.7 \langle N \rangle. \quad (4)$$

It is also convenient in the present experiment to express the density in terms of $k_{2\pi}$, the wave number at which the phase shift caused by the plasma is exactly 2π . From Eq. 3, it is found that

$$\langle N \rangle = 1.48 \times 10^{12} k_{2\pi}. \quad (5)$$

2. Interferometric Method

It is well known that Fourier transform spectroscopy³ is the most efficient of available methods for examining a wide spectrum when resolution is energy-limited, as is the case in the far infrared region. For this reason, it is the method used throughout the studies described here. A description of the principles involved may be found in a previous report,⁵ and comprehensive discussions have been published.^{3, 4, 6}

The interferometer used here has also been discussed in detail elsewhere.⁷ It is a simple Michelson interferometer that has been demonstrated to be capable of a spectroscopic resolution, Δk , of less than 0.3 cm^{-1} when used for Fourier transform spectroscopy. The spectrum for the present experiments ranges from 8 cm^{-1} to 55 cm^{-1} .

The fundamental principle of this method is the same as that of a Rayleigh

refractometer,⁸ or of other far infrared refractometers used to make such phase-shift measurements.^{9,10} Two mutually coherent beams of light interfere to produce a fringe pattern. Introduction of a refractive sample into one of the two beams produces a displacement of the fringe pattern which is proportional to the path difference created by the sample. In Rayleigh's case the radiation is monochromatic and the fringe shift easily observable. In the present case, the radiation is not monochromatic and, moreover, the fringe shift is a strong function of frequency and not directly observable. By comparing the Fourier transforms of the shifted and unshifted fringe patterns (interferograms), it will be shown that it is easy to find those wave numbers at which the fringe shift is an exact multiple of the half-wavelength.

Owing to the low signal-to-noise ratios found in the far infrared region, it is usually necessary to use synchronous detection to observe the infrared signal. This means that the signal observed from the lock-in amplifier is the difference between two signal levels (usually "on" and "off"). Consider the effect of chopping the infrared signal in one arm of the interferometer with a refractive medium. If the signal is detected synchronously with the chopper, the resulting signal is the difference between the unperturbed interferogram and the phase-shifted interferogram. If at any given frequency the phase shift is an even multiple of π , this difference signal becomes zero, and if the phase shift is an odd multiple of π , the signal attains a maximum. The location of the wave numbers at which these maxima and minima occur is equivalent to measuring discrete phase shifts at specific frequencies.

This argument can be expressed quantitatively. When a power spectrum $\mathcal{I}(k)$ passes through the interferometer, the detector signal $I_0(x)$ (where x is path difference) is given by

$$I_0(x) = \int_0^K \mathcal{I}(k) \cos [2\pi kx + \phi_1(k)] dk, \quad (6)$$

where K is a value of k above which $\mathcal{I}(k)$ is negligible, and $\phi_1(k)$ is a phase shift, of no direct physical interest, depending upon such factors as beam-splitter and mirror misalignment and, more importantly, the crystal quartz windows to the discharge tube in one of the interferometer arms.

Normally, $I_0(x)$ is Fourier transformed by digital computer to obtain

$$\mathcal{I}'(k) = \mathcal{I}(k') * \chi(k-k'), \quad (7)$$

where "*" denotes "convolved with," and $\chi(k)$ is the scanning function or linewidth that is described in section 5 of this report.

When a plasma is present in one of the two beams, the phase shift ϕ_1 becomes ϕ_2 , so that

(XI. PLASMA PHYSICS)

$$\Delta\phi(k) = |\phi_1(k) - \phi_2(k)|,$$

where $\Delta\phi(k)$ is the phase shift caused by the plasma, given by Eq. 2.

The difference signal thus becomes

$$I_{\text{diff}}(x) = \int_0^K \mathcal{I}(k) \{ \cos [2\pi kx + \phi_1(k)] - T(k) \cos [2\pi kx + \phi_2(k)] \} dk, \quad (8)$$

where $T(k)$ is the effective transmission coefficient of the plasma. After some algebraic manipulations, Eq. 8 becomes

$$I_{\text{diff}} = \int_0^K \mathcal{I}(k) R(k) \cos [2\pi kx + \gamma(k)] dk \quad (9)$$

where $R(k)$ may be called the response function of the interferometer. It is given by

$$R(k) = \sqrt{1 + T^2(k) - 2T(k) \cos [\Delta\phi(k)]} \quad (10)$$

and may easily be determined from the ratio of the transforms of $I_0(x)$ and $I_{\text{diff}}(x)$. The phase term in Eq. 9 is given by

$$\gamma(k) = \frac{\sin \phi_1(k) - T(k) \sin \phi_2(k)}{\cos \phi_1(k) - T(k) \cos \phi_2(k)}$$

but it is not observed, as is explained in connection with the scanning function in this report.

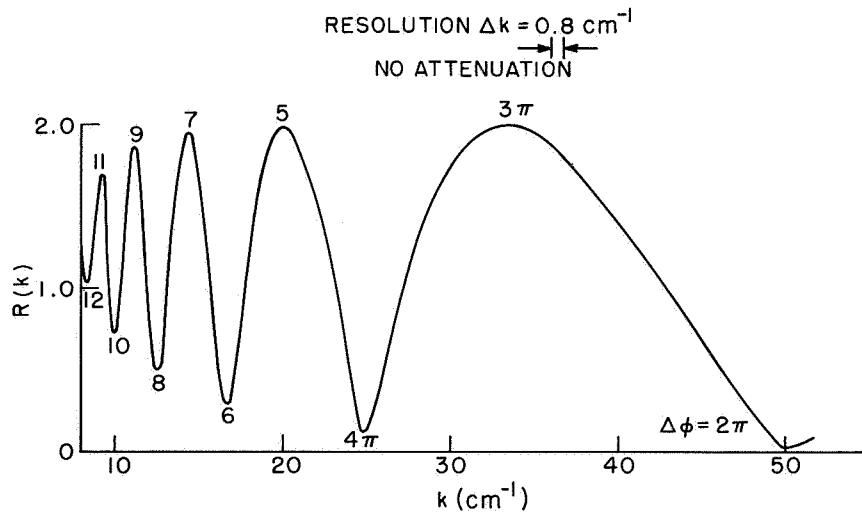


Fig. XI-1. Theoretical interferometer response for electron line density. $NL = 1.11 \times 10^{15} \text{ electron cm}^{-2}$.

It is obvious from Eq. 10 that $R(k)$ will pass through minima when $\Delta\phi(k) = 2n\pi$ and maxima when $\Delta\phi(k) = (2n+1)\pi$ for $n = 0, 1, 2, \dots$.

$R(k)$ is illustrated in Fig. XI-1 for the particular case of a plasma, where $\Delta\phi(k)$ is given by Eq. 2, and of such a line density that $k_{2\pi} = 50$, that is, $\Delta\phi(50) = 2\pi$ radians. The effect of the finite instrumental linewidth (discussed below) is also taken into account in the numerical calculation for Fig. XI-1. A resolving power of 0.8 cm^{-1} was approximated by setting $\chi(k-k')$ of Eq. 7 equal to unity for $(k-k') < 0.4$ and zero elsewhere. If the instrumental linewidth were infinitely narrow, $R(k)$ would oscillate everywhere between 0 and 2.0; Fig. XI-1 gives a more realistic expectation.

The maxima and minima of $R(k)$ can now be located and each one can now be converted to a data point for a plot of $\Delta\phi(k)$ against k , in the manner that will be demonstrated below.

3. The Electronic System

The plasma is pulsed 30 times a second, this rate is determined chiefly by conveniently available power sources for the plasma pulse. The detector signal is sampled by a gated amplifier 60 times a second, alternately in the presence and absence of the plasma, in the manner commonly used for the examination of weak transient repetitive signals.¹¹ Following this standard procedure, the gate signals are fed to a pulse stretcher which converts the series of gate spikes to a square wave. The square wave, whose amplitude is proportional to the difference in height between alternate spikes, is fed to a lock-in amplifier. Figure XI-2 is a simplified block diagram of the entire system. The plasma is fired by discharging a two-stage 2- μfd delay line by means of a thyatron switch. The resulting current pulse (shaped by the delay line) is approximately rectangular, 50 μsec long, with a rise time of approximately 5 μsec and decay time of approximately 20 μsec . A peak current of 200 amps is obtainable. The trigger to the thyatron comes from the central timing unit, which in turn is locked to the 60-cps AC power line. At a variable but well-determined delay time following the plasma pulse, the gated amplifier is opened (for 3, 10, or 20 μsec) and opened again one half-cycle later. The trigger for the gated amplifier comes from the central timing unit, which also generates a 30-cps reference signal (which is always in phase with the sampling pulses, not with the thyatron triggers) for the lock-in amplifier. The central timing unit also coordinates the behavior of the pulse stretcher with that of the gated amplifier.

The data must be collected in such a way that it can easily be fed to a digital computer. The signal (voltage level) leaving the lock-in amplifier is fed to an analog-to-digital converter (in this case a digital voltmeter, DVM), thence to a digital printer. The resulting printed list of numbers is fed to the "Project MAC" time-shared computer¹² via a teletype console upon which the processed data from the computer are also displayed.

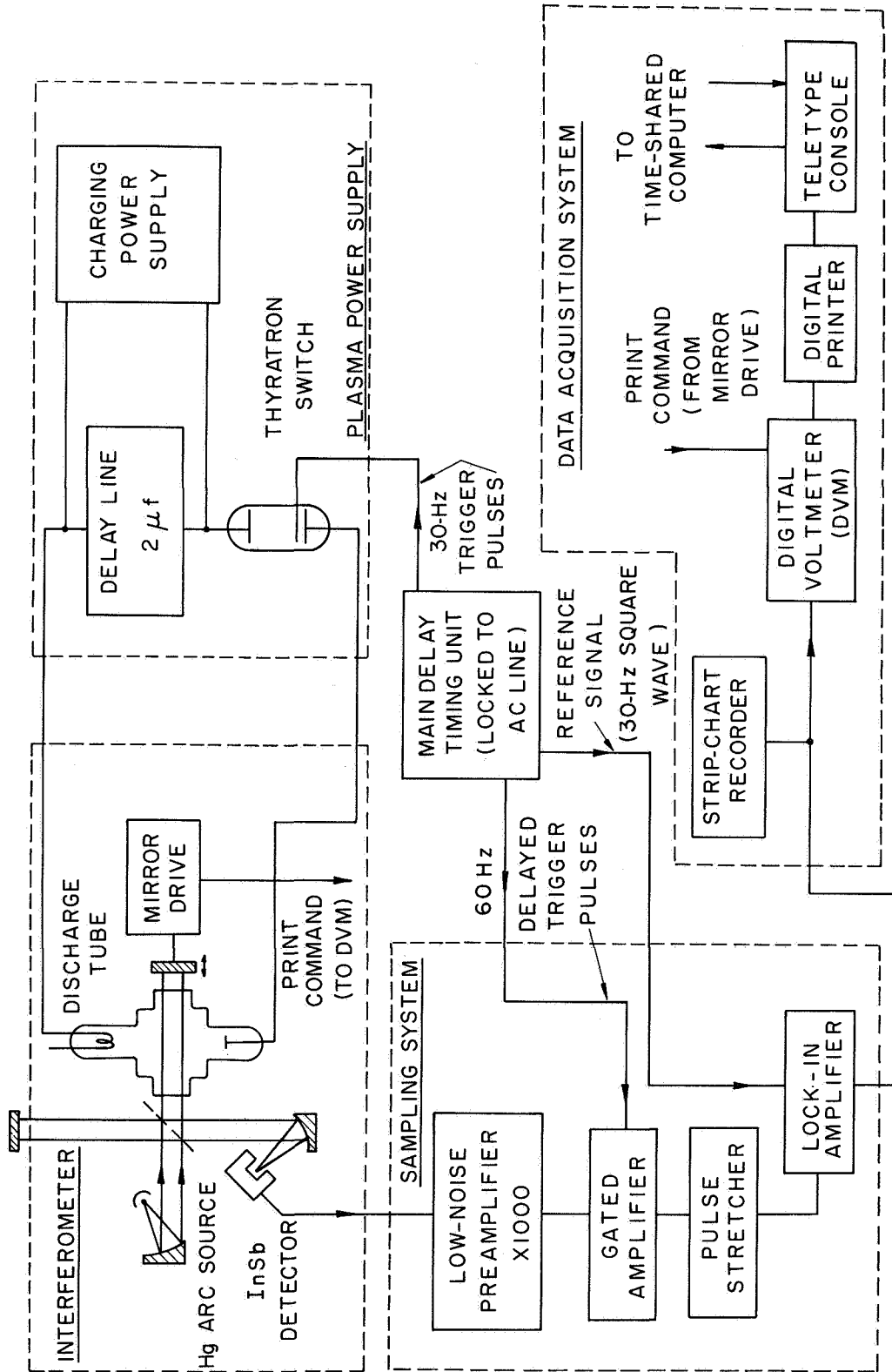


Fig. XI-2. Experimental arrangement.

Each data point represents the signal from the "lock-in" which corresponds to a given value of path difference in the interferometer. Therefore, the D. V. M. is commanded (by means of a cam in the mirror drive mechanism) to record the voltage presented to it every time the path difference has changed by $42.3 \mu\text{sec}$. (This sampling interval will be discussed further below.)

4. Performance of the System

Initially, the method was tested by simulating the pulsed plasma with a polyethylene chopper blade, 1 mm thick, which chopped one of the interferometer beams at 30 cps.

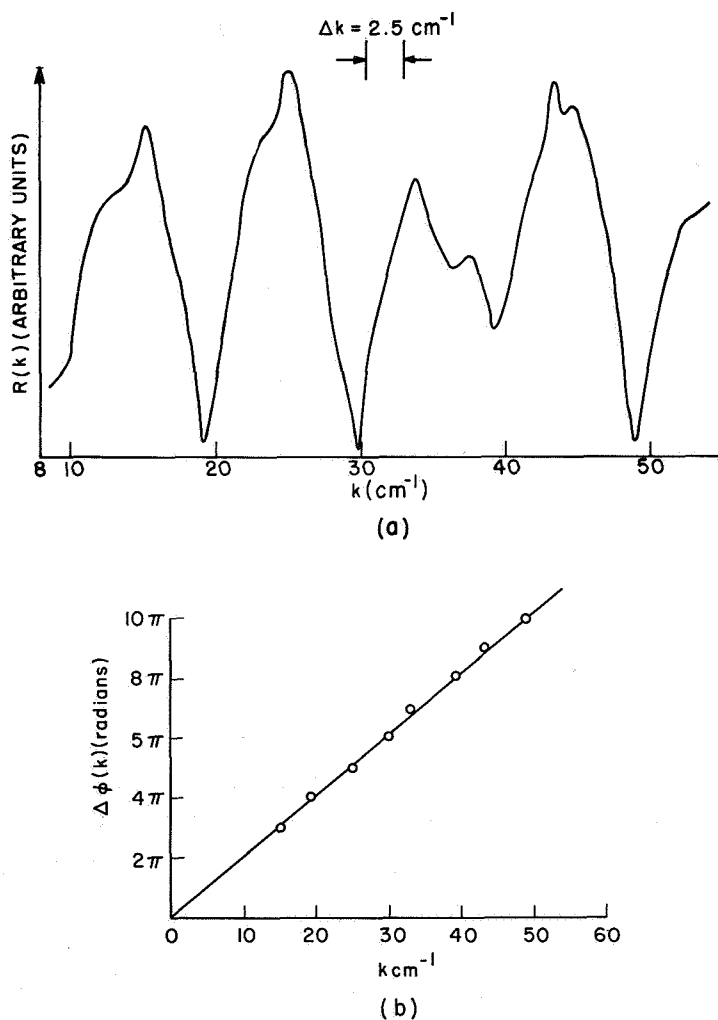


Fig. XI-3. (a) Typical interferometer response for polyethylene sample.
(b) Interpretation of (a).

(XI. PLASMA PHYSICS)

Polyethylene was used because it is refractive, but not very strongly reflective, and has a fairly high transmission coefficient in this region.

The response of the interferometer, $R(k)$, is obtained approximately by taking the ratio of the spectrum $[R(k') \mathcal{J}(k)] * \chi(k-k')$ obtained by transforming $I_{\text{diff}}(x)$ to the "normal" spectrum, $\mathcal{J}(k') * \chi(k-k')$, obtained by chopping the infrared source mechanically.

The $R(k)$ obtained in this way is shown in Fig. XI-3a. The expected maxima and minima are easily seen. With the a priori knowledge that the refractive index of polyethylene is a weak function of k , it is to be expected that the phase shift increases with k , thus the minimum close to $k = 10^{-1}$ probably corresponds to $\Delta\phi = 2\pi$, the minimum close to 19 cm^{-1} to 4π , and so on.

Thus a plot may be made of phase-shift wave number, as is shown in Fig. XI-3b. The closeness of the data points to a straight line indicates that the refractive index of polyethylene is constant within a few per cent in the spectral angle of $k = 15\text{-}50 \text{ cm}^{-1}$. From the slope of the line, the refractive index may be deduced because

$$\Delta\phi(k) = 2\pi |1 - \text{Re } \mu| kL,$$

and the slope of Fig. XI-3b is given by

$$\frac{d}{dk} \Delta\phi(k) = 2\pi |1 - \text{Re } \mu| L.$$

From Fig. XI-3b,

$$\frac{1}{2\pi} \frac{d}{dk} \Delta\phi(k) = \frac{5.0}{49.0} \text{ radian cm},$$

and $2L = 0.213 \text{ cm}$,

$$\begin{aligned} \therefore \text{Re } \mu &= 1 + \left[\frac{5.0}{0.213 \times 49.0} \right] \\ &= 1.48 \end{aligned}$$

which is in reasonable agreement with published values.

It should be noted that there is some deterioration in quality of the data of Fig. XI-3a in the spectral region between 30 cm^{-1} and 45 cm^{-1} . This is because of the presence of atmospheric water-vapor absorption lines that give rise to rather strong features in the spectrum, and as $R(k)$ is obtained as the ratio of two spectra, the presence of the strong features will cause distortion such as that in Fig. XI-3a. By taking the average of several successive runs, however, this distortion is eliminated, as will be seen with the plasma data.

Figure XI-4 shows a typical response curve obtained with a real plasma, corresponding to a line density $3.1 \times 10^{14} \text{ cm}^{-2}$; in this case $L = 7.5 \text{ cm}$, so $N = 4.1 \times 10^{13} \text{ cm}^{-3}$

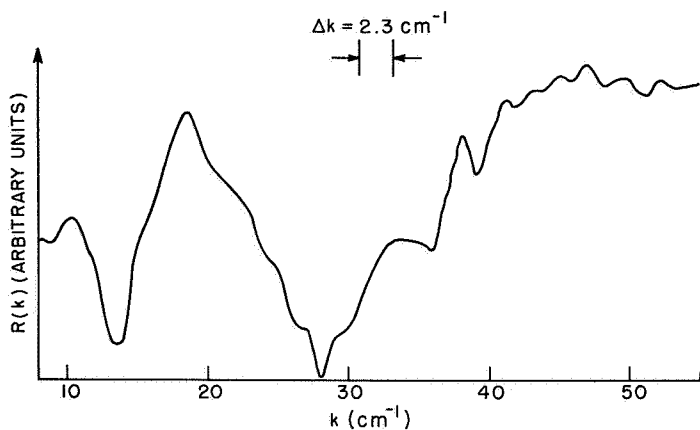


Fig. XI-4.
 Typical interferometer response
 with a plasma. $NL = 3.1 \times 10^{14}$
 cm^{-2} .

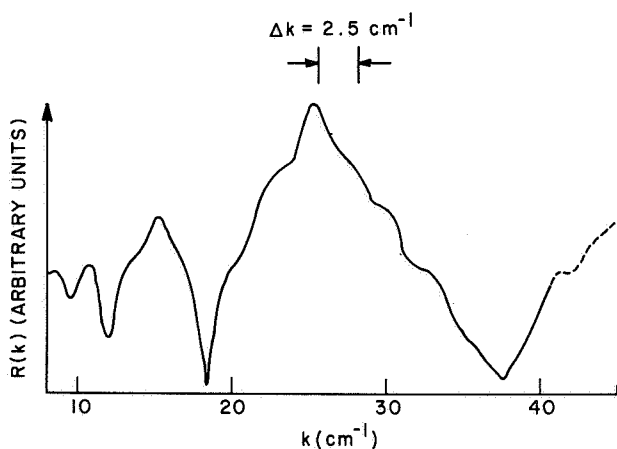
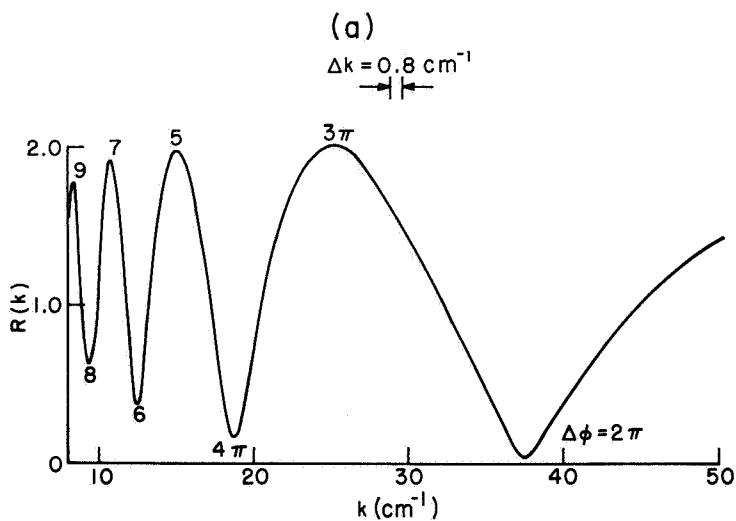


Fig. XI-5.

(a) Observed interferometer
 response resulting from
 plasma, where $NL = 4.18 \times$
 10^{14} cm^{-2} . (Average of 5
 runs.)



(b) Theoretical interferometer
 response for plasma, where
 $NL = 4.18 \times 10^{14} \text{ cm}^{-2}$.
 [Compare with (a).]

(XI. PLASMA PHYSICS)

and a central density of $N_0 = 6.9 \times 10^{13} \text{ cm}^{-3}$ can be expected. Distortion caused by water-vapor lines can also be seen in this response curve. Figure XI-5a shows a response curve attributable to a somewhat dense plasma ($NL = 4.18 \times 10^{14}$) which was obtained from the average of 5 similar interferograms. The quality of the data is substantially improved and the curve may be favorably compared with that of Fig. XI-5b, which shows the interferometer response computed from Eq. 10 which corresponds to the same value of NL , but with somewhat improved resolution and no attenuation resulting from the plasma. In this plasma $N = 5.6 \times 10^{13} \text{ cm}^{-3}$, and $N_0 = 9.3 \times 10^{13} \text{ cm}^{-3}$.

In Fig. XI-6 the observed phase shift is plotted against wavelength, $1/k$, to which it should bear a linear relationship (see Eq. 2). The fact that the data points very strongly

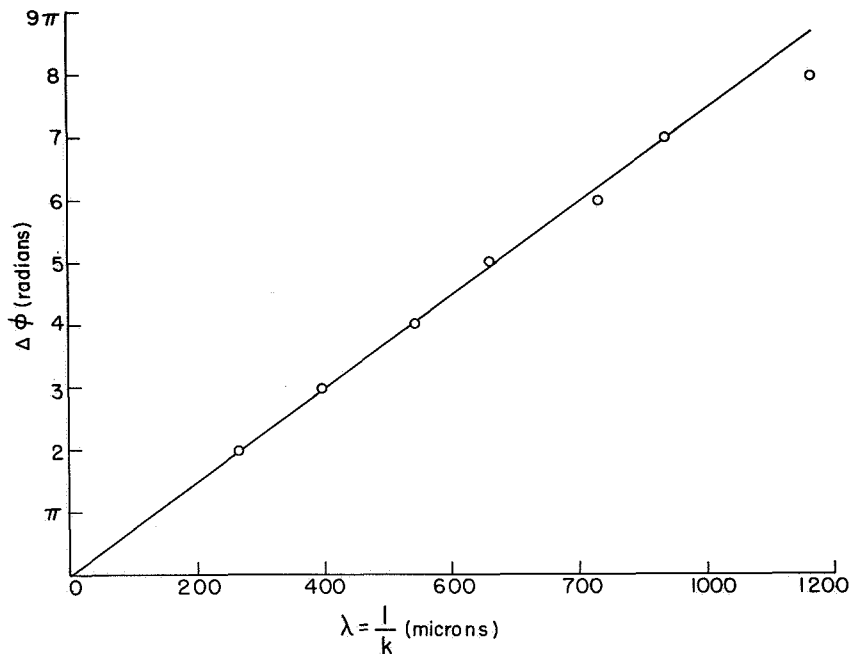


Fig. XI-6. Interpretation of Fig. XI-5a.

suggest a straight line through zero indicates that the dominant observed phase shift is due only to the plasma and not to some spurious effect such as heating of the gas. This represents a distinct advantage of far infrared techniques over optical methods. At optical frequencies, the refractive index of the plasma is usually so small that it is of the same order of magnitude as the change in refractive index of the background gas caused by heating from the plasma. Also, acoustic vibrations of the optical parts can cause effects of the same order of magnitude as that of the plasma.¹³ Figure XI-6 indicates that for density measurements alone, phase-shift measurements at one frequency are sufficient.

5. Resolution and Noise

As has been explained, the interferograms in this experiment always contain a phase term ϕ , as in Eq. 6. Thus both the sine and cosine Fourier transforms must be evaluated in order to avoid asymmetry in the final spectrum.^{3, 14, 16} In this case the spectrum is obtained as the square root of the sum of the squares of the sine and cosine transforms:

$$S(k) = \int_0^D I(x) A\left(\frac{x}{D}\right) \sin(2\pi kx) dx$$

$$C(k) = \int_0^D I(x) A\left(\frac{x}{D}\right) \cos(2\pi kx) dx$$

$$\begin{aligned} \therefore \mathcal{I}^1(k) &= \sqrt{S^2(k) + C^2(k)} \\ &= \mathcal{I}(k') * \chi(k-k'). \end{aligned}$$

The function $A\left(\frac{x}{D}\right)$ is the apodizing function⁵ and, in this case, is a triangle:

$$A\left(\frac{x}{D}\right) = \left(1 - \frac{x}{D}\right).$$

$\chi(k-k')$ is the scanning function, or instrumental line shape first mentioned above.

The instrumental line shape for this situation has been given analytically by Lowenstein¹⁴ as

$$\begin{aligned} \chi^2(k) &= \left\{ \frac{D}{4} \frac{\sin^2 [\pi(k-k_0)D]}{[\pi(k-k_0)D]^2} \right\} \\ &+ \frac{1}{4\pi^2(k-k_0)^2} \left\{ 1 - \frac{\sin [2\pi(k-k_0)D]}{2\pi(k-k_0)D} \right\} \\ &+ [\text{small terms in } (k+k_0)] \end{aligned} \quad (11)$$

and it is illustrated in Fig. XI-7 where it was obtained by feeding 18.16 cycles of pure cosine to the computer program, simulating a monochromatic signal at $k = 30 \text{ cm}^{-1}$ with the same resolving power (that is, number of data points) that is used for the data presented in the previous section. This line shape has been discussed in detail by Connes,³ who pointed out that the procedure of taking the sum of the squares of the two transforms is nonlinear. In this case random-noise fluctuations in the interferogram, instead of cancelling themselves out in the Fourier integrals, are always added cumulatively. For this reason, in cases in which the average of several runs is desired, it is important to

(XI. PLASMA PHYSICS)

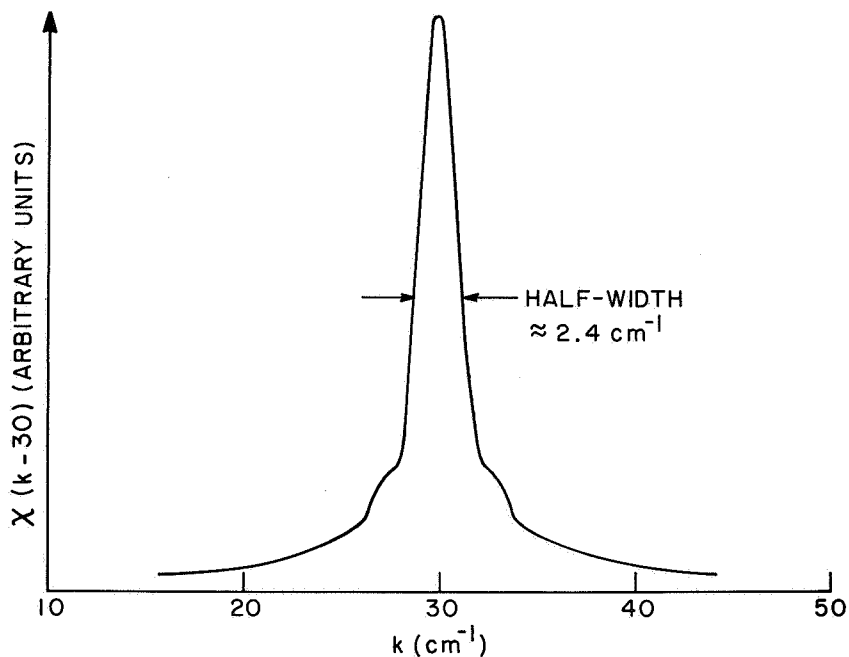


Fig. XI-7. Instrumental linewidth for $k = 30 \text{ cm}^{-1}$ (18.16 cycles of cosine at $k = 30 \text{ cm}^{-1}$).

average the interferograms before performing the transformation, rather than to average the transformed spectra, because the noise in the spectra will not average to zero.

In addition to this disadvantage, the wings of the scanning function do not decay very rapidly; thus there is always a strong "background signal" in all parts of the spectrum. The function shows, however, a high degree of symmetry, and Eq. 11 contains no reference to the phase term in the interferograms, also there are no strong ripples in the wings on account of the triangle apodization.

As the phase terms in the interferograms are not known exactly, and vary over many multiples of π throughout the spectra, it would be exceedingly difficult to employ any of the phase correction methods described by Lowenstein,¹⁴ Gibbs and Gebbie,¹⁵ and Forman, et al.¹⁵ The data presented in the previous section indicate that the scanning function is adequate in spite of its disadvantages.

The signal-to-noise ratio in the experiment is quite poor, even for a far infrared interferometer. This is because the beam is very narrow (dictating a small solid angle at the source); also the signal is sampled with a 3- μ sec gate which leads to a further reduction of signal-to-noise ratio from that of a conventional chopping technique. A double RC filter (12 db/octave, $\tau = 3$ sec) was necessary to reduce the noise to an acceptable level. It has been mentioned that the signal was sampled at intervals of $\delta = 42.3$ microns path difference; this places certain requirements on the filtering system.

When the path difference is varied at a rate of v cm sec⁻¹, it is clear that the infrared signal of wave number k becomes a signal of frequency $\omega = 2\pi vk$, and this is subject to filtering by the double RC filter which has a frequency response of

$$\frac{E_{\text{out}}}{E_{\text{in}}} = \frac{1}{1 + (\omega\tau)^2}$$

It is also clear that electronic noise of frequency, ω , will also be "seen," after the Fourier transformation, as infrared noise at $k = \frac{\omega}{2\pi v}$.

The sampling theorem of information theory¹⁷ stipulates that no frequency must be present (in the sampled signal) greater than

$$\begin{aligned}\omega_{\text{max}} &= \pi \frac{v}{\delta} \\ &= \frac{\pi}{t}\end{aligned}$$

where t secs is the sampling interval. In the present case,

$$\delta = 42.3$$

$$\begin{aligned}\therefore k_{\text{max}} &= \frac{1}{2 \times \delta} \\ &= 118 \text{ cm}^{-1}.\end{aligned}$$

This topic is treated with great thoroughness by Connes.³

The result is illustrated in Fig. XI-8 where the filter response has been translated

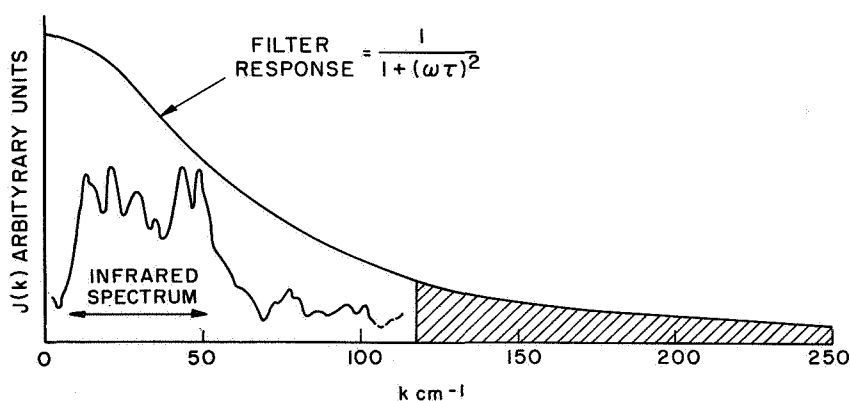


Fig. XI-8.

Frequency response of the double RC filter related to the observed spectrum (in wave numbers).

$$\tau = 3 \text{ sec.}$$

$\omega = \frac{2\pi v}{R}$, where v is the rate of change of path difference (in this case, $v = 8.6$ microns sec⁻¹).

to k -space by the transformation $\omega = 2\pi vk$, and superimposed upon the observed infrared spectrum between $k = 8$ and 55 cm^{-1} and the noise, which extends to wave numbers

(XI. PLASMA PHYSICS)

greater than 55 cm^{-1} . It can be seen that the filtering is quite heavy for $k = 118 \text{ cm}^{-1}$ and suppresses the noise in this (shaded) region quite adequately for the data taken here, although part of the spectrum is also suppressed by the filter.

This technique is described in more detail, and its usefulness assessed, in the Author's doctoral thesis.¹⁸

D. T. Llewellyn-Jones

References

1. M. A. Heald and C. B. Wharton, Plasma Diagnostics with Microwaves (John Wiley and Sons, Inc., New York, 1965).
2. S. C. Brown, Basic Data of Plasma Physics (The Technology Press of M.I.T., Cambridge, Mass., and John Wiley and Sons, Inc., New York, 1959).
3. J. Connes, *Rev. Opt.* **40**, **45**, 116, 171, 231 (1961). An English Translation of this fundamental text is available to Government Contractors as a U.S. Navy Publication NAV-WEPS Report No. 8099, NOTS TP 3157, published by the U.S. Naval Ordnance Test Station, China Lake, California.
4. P. L. Richards, *J. Opt. Soc. Am.* **54**, 1474 (1964).
5. D. T. Llewellyn-Jones, Quarterly Progress Report No. 74, Research Laboratory of Electronics, M.I.T., July 15, 1964, pp. 81-89.
6. E. V. Lowenstein, *Appl. Opt.* **5**, 845 (1966).
7. D. T. Llewellyn-Jones, S.M. Thesis, Department of Physics, Massachusetts Institute of Technology, June 1964.
8. F. A. Jenkins and H. E. White, Fundamentals of Optics (McGraw-Hill Book Company, New York, 1963).
9. S. C. Brown, G. Bekefi, and R. E. Whitney, *J. Opt. Soc. Am.* **53**, 448 (1963).
10. D. T. Llewellyn-Jones, Quarterly Progress Report No. 80, Research Laboratory of Electronics, M.I.T., January 15, 1966, pp. 85-89.
11. J. C. Ingraham and J. J. McCarthy, Quarterly Progress Report No. 64, Research Laboratory of Electronics, M.I.T., January 15, 1962, pp. 76-79.
12. P. A. Crisman and others, "The Compatible Time-Sharing System, A Programmer's Guide" (The M.I.T. Press, Cambridge, Mass., 1965).
13. E. B. Hooper, Ph.D. Thesis, Department of Physics, Massachusetts Institute of Technology, September 1965.
14. E. V. Lowenstein, *Appl. Opt.* **2**, 491 (1963).
15. M. L. Forman, W. H. Steel, and G. A. Vanasse, *J. Opt. Soc. Am.* **56**, 59 (1966).
16. J. E. Gibbs and H. A. Gebbie, *Infrared Phys.* **5**, 187 (1965).
17. S. Goldman, Information Theory (Prentice-Hall, Inc., Englewood Cliffs, N. J., 1962).
18. D. T. Llewellyn-Jones, Ph.D. Thesis, Department of Physics, Massachusetts Institute of Technology, February 1967.

C. ELECTRON DENSITY MEASUREMENTS WITH A NARROW-BAND FAR INFRARED INTERFEROMETER

In order to measure the electron concentration in high electron density plasmas, a narrow-band far infrared interferometer has been constructed to operate in the wavelength region of a few hundred microns. The initial instrument was conceived by Sanborn C. Brown,¹ and requires only a simple analysis of the output to obtain the desired data. Now, a new interferometer has been designed to operate with repetitively pulsed plasmas, retaining the same analysis for the data and a wavelength range of 200-400 microns. It is constructed in an open U frame to accommodate different plasma vacuum systems, and has a narrower bandwidth, which permits measurement of the increased electron densities that are found in pulsed, as compared with steady-state, plasmas.

The interferometer can be viewed schematically as in Fig. XI-9; it is a symmetric two-beam instrument that can be compared roughly to a Rayleigh interferometer, except for the beam-splitting and recombining method. Far infrared radiation emitted from the high-pressure Hg arc source is focused by the entrance mirror at a distance equal to the path length to the far mirrors. This radiation falls first on grating No. 1 normal to its surface and is diffracted so that the plus and minus first orders of the desired radiation fall on the far mirrors. Thus the tunable lamellar reflection grating² and far mirrors form a monochromator, or filter, the operating frequency being determined by the grating spacing and angle of the far mirrors with the grating normal. Radiation incident on the far mirrors is now returned to grating No. 2, that from the sample arm having passed twice through the plasma. Since the concave far mirrors have a radius of curvature equal to their distance from the gratings, the first grating is imaged on the second. Both the phase difference between the two beams returning to grating No. 2, which fixes the radiation pattern on the grating surface, and the lateral (direction indicated by arrow in Fig. XI-9) displacement of grating No. 2 with respect to grating No. 1 determine the output normal to grating No. 2. This output is then focused by the exit mirror on the detector. The important relation of output as a function of phase difference between the two arms and lateral movement of grating No. 2, which allows the phase shift by the plasma to be measured by moving this grating can be found through the following analysis of the optical system.

For simplicity, the optical system of the interferometer can be represented as the lens system in Fig. XI-10. When making actual calculations the proper geometry of the mirror system will be used. Now the modified Kirchhoff formulation of Bekefi,³ which gives a good representation of the wave in the intermediate and far fields by microwave measurements, can be utilized. Under the assumption of an exponential $(-i\omega t)$ time dependence of the wave, the spatial magnitude

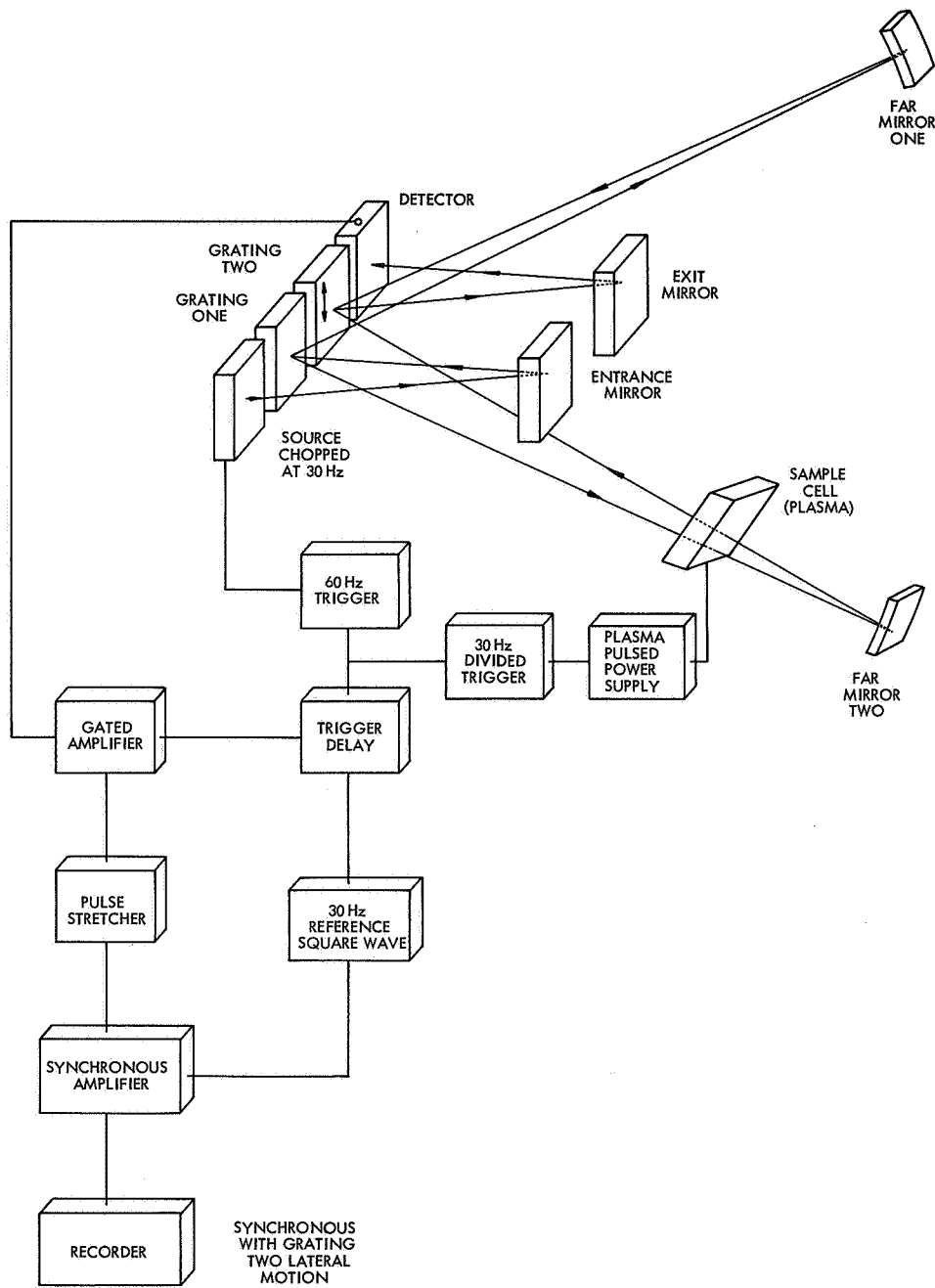


Fig. XI-9. Schematic representation of the interferometer and associated electronics equipment.

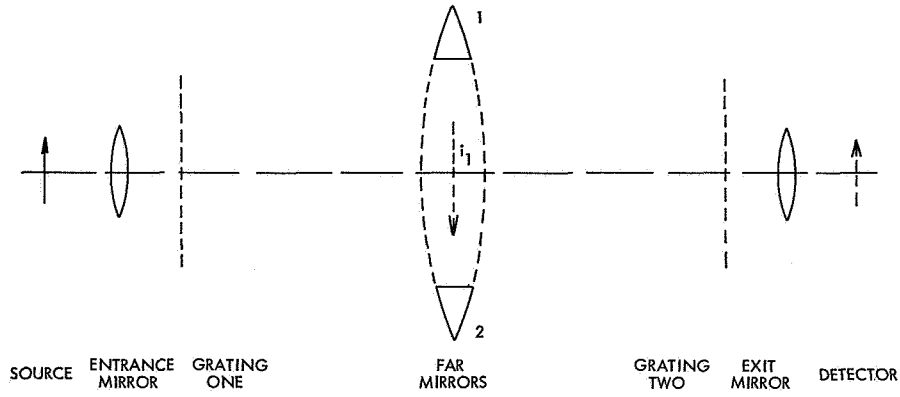


Fig. XI-10. Simplified lens approximation to the interferometer optics.

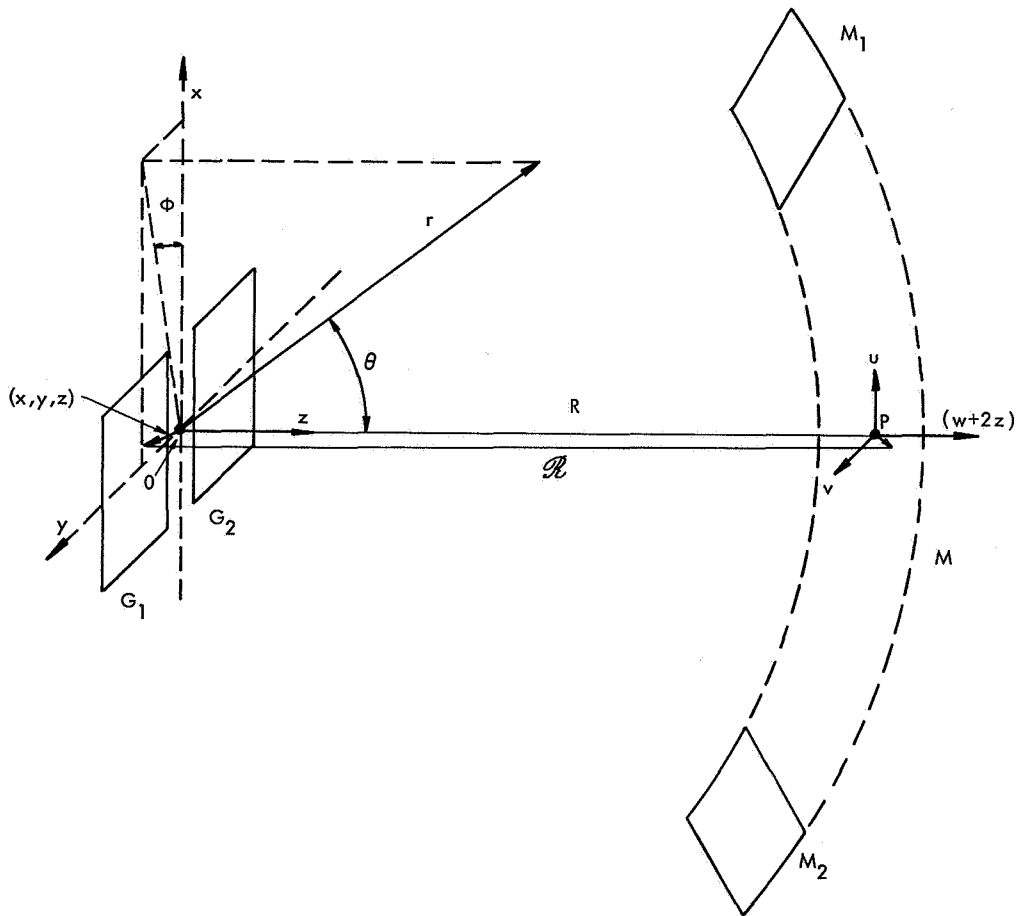


Fig. XI-11. Coordinate systems for the actual geometry of the interferometer, where G_1 and G_2 are the gratings, and the spherical surface of the far mirrors, M , has radius R and center O .

(XI. PLASMA PHYSICS)

and phase at observation point Q is given by

$$U(Q) = \frac{1}{2\pi} \int_A U_i \frac{\partial}{\partial n} \frac{e^{iks}}{s} dS,$$

where A is the surface at which diffraction is occurring, dS is an element in that surface, $\partial/\partial n$ is the normal derivation with the unit vector normal to A at dS used, U_i is the phase and magnitude of the wave front incident on dS, k is the propagation constant ω/c , and s is the distance from dS to Q. Henceforth the complex U will be called the amplitude of the wave containing both phase and magnitude. Under the assumption that diffraction effects from the entrance mirror are negligible, there is a converging spherical wave front incident on grating 1 directed as if to converge at the far mirror surface (dotted image i_1 in Fig. XI-10). By entering the amplitude of this wave at grating 1 into the equation above, the amplitude at the surface of the far mirror can be found, and, by iterating again with this new amplitude, the radiation amplitude falling on grating 2 can

be determined. This process could be continued right up to the detector but instead a simplification that obviates the complications of diffraction from the exit mirror can be employed, which should have negligible effects, and the integrated amplitude at the detector can be found directly.

Now, carrying out these steps with the actual mirror geometry of the interferometer and utilizing the standard coordinates indicated in Fig. XI-11, we find that the incident amplitude of the converging spherical wave from the source and entrance mirror at the grating plane G_1 is

$$U_{G_1} = u \frac{e^{-ikR}}{R},$$

where u is an constant proportional to the magnitude of the incident radiation, and R is the distance from grating 1 to the point of convergence. In the case of the center point of the source and where

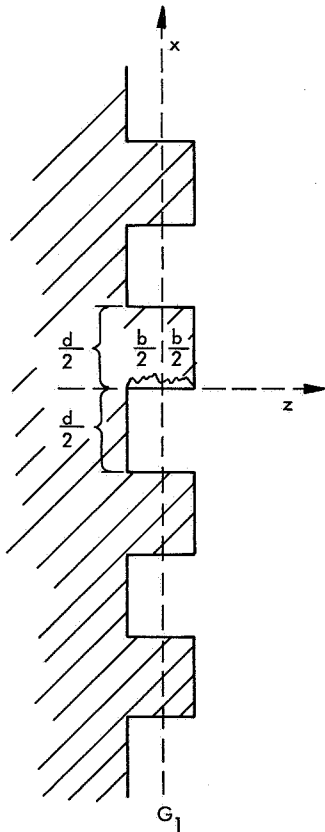


Fig. XI-12. Cross section of the grating profile.

the surface lies on G_1 (the x-y plane of the gratings) the point of convergence is P lying on the spherical surface M of the far mirror. Actually, the grating surface has grooves so that the reflected convergence point of the incoming wave changes, and this must be accounted for in \mathcal{R} . Therefore,

$$\mathcal{R} = [(u-x)^2 + (v-y)^2 + (\omega+R+z)^2]^{1/2},$$

where (u, v, ω) is the point in the undistorted image of the source, and (x, y, z) is the point on the grating surface defined relative to the plane G_1 as indicated in Fig. XI-12.

The first step gives the amplitude at the far mirror,

$$U_M = \frac{1}{2\pi} \int_{G_1} U_{G_1} \frac{d}{dz} \frac{e^{iks}}{s} dx dy,$$

where s is the distance from a point on the far mirror (R, θ, ϕ) and a point on grating 1, that is,

$$s = [(R \cos \phi \sin \theta - x)^2 + (R \sin \phi \sin \theta - y)^2 + (R \cos \theta - z)^2]^{1/2}.$$

To differentiate between the two far mirrors, a phase shift from the plasma is included by multiplying U_{M_2} by $e^{i\Phi}$. Next, from U_M the amplitude at the second grating is determined, again including the plasma phase shift:

$$U_{G_2} = -\frac{1}{2\pi} \int_{M_1} U_{M_1} \frac{d}{dR} \frac{e^{iks'}}{s'} R^2 \sin \theta d\theta d\phi \\ - \frac{e^{i\Phi}}{2\pi} \int_{M_2} U_{M_2} \frac{d}{dR} \frac{e^{iks'}}{s'} R^2 \sin \theta d\theta d\phi,$$

where

$$s' = [R \cos \phi \sin \theta - x']^2 + [R \sin \phi \sin \theta - y']^2 + [R \cos \theta - z']^2]^{1/2},$$

the coordinates (x', y', z') define a point on G_2 , and

$$\Phi = k \int_0^L \left[1 - \left(1 - \frac{\omega_p^2(\ell)}{\omega^2} \right)^{1/2} \right] d\ell,$$

ω_p being the plasma frequency proportional to the square root of the electron density.

In the final step, diffraction by the exit mirror is neglected. Since the exit mirror is positioned to focus radiation on the center of the detector head, as if it came from P

(XI. PLASMA PHYSICS)

and reflected off the grating plane, any radiation from G_2 that goes to the detector will look as if it came from P (correcting, of course, for the grating groove depth). Now radiation from P focused on D must all travel the same optical path length so that for radiation concentrated on the detector the path length PG_2 plus G_2D equals a constant. The amplitude at the detector can be found by summing all of the amplitudes of the radiation from G_2 multiplied by their phase shifts resulting from path length G_2D (or minus PG_2 and dropping the constant phase shift). Therefore,

$$U_D = \frac{1}{A_{G_2}} \int_{G_2} U_{G_2} e^{-ikR'} dx'dy',$$

where A_{G_2} is the illuminated area of G_2 , and

$$R' = [(u-x')^2 + (v-y')^2 + (\omega + R + z')^2]^{1/2}.$$

The total integral now is

$$U_D = -\frac{1}{4\pi^2 A_{G_2}} \int_{G_2} e^{-ikR'} dx'dy' \left\{ \int_{M_1} \frac{d}{dR} \left(\frac{e^{iks'}}{s'} \right) R^2 \sin \theta d\theta d\phi \int_{G_1} \frac{e^{-ikR}}{R} \frac{d}{dx} \left(\frac{e^{iks}}{s} \right) dx dy \right. \\ \left. + e^{i2\Phi} \int_{M_2} \frac{d}{dR} \left(\frac{e^{iks'}}{s'} \right) R^2 \sin \theta d\theta d\phi \int_{G_1} \frac{e^{-ikR}}{R} \frac{d}{dz} \left(\frac{e^{iks}}{s} \right) dx dy \right\}.$$

Carrying out the differentiation and dropping additive terms smaller by $\frac{\lambda}{R} \approx 3 \times 10^{-4}$, we obtain

$$U_D = \frac{1}{4\pi^2 A_{G_2}} \left\{ \int_{M_1} R^2 \sin \theta d\theta d\phi \int_{G_2} e^{ik(s'-R')} \frac{ik}{s'^2} \right. \\ \cdot [R - (x' \cos \phi \sin \theta + y' \sin \phi \sin \theta + z' \cos \theta)] dx'dy' \int_{G_1} e^{ik(s-R)} \frac{ik}{Rs^2} [R \cos \theta - z] dx dy \\ + e^{i2\Phi} \int_{M_2} R^2 \sin \theta d\theta d\phi \int_{G_2} e^{ik(s'-R')} \frac{ik}{s'^2} \\ \left. \cdot [R - (x' \cos \phi \sin \theta + y' \sin \phi \sin \theta + z' \cos \theta)] dx'dy' \int_{G_1} e^{ik(s-R)} \frac{ik}{Rs^2} [R \cos \theta - z] dx dy \right\}.$$

By including a z dimension in R , R' , s and s' , the surfaces G_1 and G_2 really become

the grating surfaces, so that each G integral can be broken up into an integral over the front flat surfaces of the grating and the depressed surfaces. Thus

$$\int_{G_1} e^{ik(s-\mathcal{R})} \frac{ik}{\mathcal{R}s^2} [R \cos \theta - z] dx dy = \sum_{\substack{n=-N/2 \\ (z=b/2)}}^{N/2} \int_{nd}^{(n+1/2)d} dx \int_{y_1}^{y_2} dy e^{ik(s-\mathcal{R})} \frac{ik}{\mathcal{R}s^2} \left[R \cos \theta - \frac{b}{2} \right] \\ + \sum_{\substack{n=-N/2 \\ (z=-b/2)}}^{N/2} \int_{(n-1/2)d}^{nd} dx \int_{y_1}^{y_2} dy e^{ik(s-\mathcal{R})} \frac{ik}{\mathcal{R}s^2} \left[R \cos \theta + \frac{b}{2} \right]$$

where the grating is positioned relative to the z -axis, as indicated in Fig. XI-12, N is the number of grooves in the grating, d is the grating spacing, and $(y_2 - y_1)$ is the grating width. For the G_2 integral, the lateral, or x , position of the grating relative to G_1 must be taken into account and, since the image of G_1 on G_2 from the far mirror is inverted, the zero position for G_2 will be the inverse of Fig. XI-12.

$$\int_{G_2} e^{ik(s'-\mathcal{R}')} \frac{ik}{s'^2} [R - (x' \cos \phi \sin \theta + y' \sin \phi \sin \theta + z' \cos \theta)] dx' dy' \\ = \sum_{\substack{n=-N/2 \\ (z'=b/2)}}^{N/2} \int_{(n-1/2)d+\Delta}^{nd+\Delta} dx' \int_{-y_2}^{-y_1} dy' e^{ik(s'-\mathcal{R}')} \frac{ik}{s'^2} \\ \cdot \left[R - \left(x' \cos \phi \sin \theta + y' \sin \phi \sin \theta + \frac{b}{2} \cos \theta \right) \right] \\ + \sum_{\substack{n=-N/2 \\ (z'=-b/2)}}^{N/2} \int_{nd+\Delta}^{(n+1/2)d+\Delta} dx' \int_{-y_2}^{-y_1} dy' e^{ik(s'-\mathcal{R}')} \frac{ik}{s'^2} \\ \cdot \left[R - \left(x' \cos \phi \sin \theta + y' \sin \phi \sin \theta - \frac{b}{2} \cos \theta \right) \right],$$

where Δ is the lateral distance G_2 is moved.

To solve these integrals analytically to first order, \mathcal{R} , \mathcal{R}' , s and s' must be expanded in decreasing powers of R . Terms of relative order $1/R^2$ and higher are neglected in the exponential, and other integrated terms of $1/R$ and higher are neglected. From the symmetry of the interferometer about the (y, z) -plane the two far mirror integrals can be combined by letting ϕ in the M_2 integral go to $(\phi' + 180^\circ)$, so that the limits

(XI. PLASMA PHYSICS)

of integration for the two integrals are identical. Dropping constant phase factors and the prime on the dummy ϕ variable,

$$\begin{aligned}
 U_D = & \frac{k^2(y_2 - y_1) d}{2\pi R(N+1)} \int_{M_1} \sin \theta d\theta d\phi \left\{ \frac{\sin^2 \left[(N+1) k \frac{d}{2} \cos \phi \sin \theta \right]}{\sin^2 \left[k \frac{d}{2} \cos \phi \sin \theta \right]} \times \frac{\sin^2 \left[k \frac{d}{4} \cos \phi \sin \theta \right]}{\left[k \frac{d}{4} \cos \phi \sin \theta \right]^2} \right. \\
 & \times \frac{\sin^2 \left[k \left(\frac{y_2 - y_1}{2} \right) \sin \phi \sin \theta \right]}{\left[k \left(\frac{y_2 - y_1}{2} \right) \sin \phi \sin \theta \right]^2} \times \cos [k\Delta \cos \phi \sin \theta + \Phi] \\
 & \left. \times \cos \left[k \frac{d}{4} \cos \phi \sin \theta + k \frac{b}{2} (1 + \cos \theta) \right] \times \cos \left[k \frac{d}{4} \cos \phi \sin \theta - k \frac{b}{2} (1 + \cos \theta) \right] \right\}. \quad (1)
 \end{aligned}$$

The factors in the integrand are equivalent to those of a typical Fraunhofer analysis, but it should be stressed that the approximations alone did not bring about this similarity — rather, it resulted from the fact that the symmetry of the interferometer causes the first power R terms in the exponentials to cancel exactly.

This integral cannot be easily evaluated in exact form, but by noting that the first term in the bracket of Eq. 1 is a strongly peaked function, it can be replaced by a delta function at these peaks and there by give a good idea of the solution of the integral.

$$\frac{\sin^2 \left[(N+1) k \frac{d}{2} \cos \phi \sin \theta \right]}{\sin^2 \left[k \frac{d}{2} \cos \phi \sin \theta \right]} \rightarrow \frac{(N+1)\pi}{k \frac{d}{2} \cos \phi} \delta \left(\sin \theta - \frac{2m\pi}{kd \cos \phi} \right),$$

where m is the order of diffraction.

$$\begin{aligned}
 U_D = & -\frac{8}{\pi^2 R} \cos \left[2\pi m \frac{\Delta}{d} + \Phi \right] \int_{\phi_1}^{\phi_2} \frac{\sin^2 \left[\pi m \left(\frac{y_2 - y_1}{d} \right) \tan \phi \right]}{\left[\pi m \left(\frac{y_2 - y_1}{d} \right) \tan \phi \right]^2} \pi m \left(\frac{y_2 - y_1}{d} \right) d \tan \phi \\
 & \times \begin{cases} 1, & \text{for } \theta_1 < \theta < \theta_2 \\ 0, & \text{for all other } \theta \end{cases} \times \begin{cases} \frac{1}{m^2} \sin^2 \left[k \frac{b}{2} (1 + \cos \theta) \right], & m \text{ odd} \\ \cos^2 [kb], & m = 0 \\ 0, & m \text{ even} \end{cases}
 \end{aligned}$$

where the far mirrors lie between θ_1 and θ_2 . From this and the fact that $I_D = U_D^* U_D$, it follows that the intensity at the detector is

$$I_D = \frac{2^6}{\pi^4 R^2} \cos^2 \left[2\pi m \frac{\Delta}{d} + \Phi \right] \left\{ \int_{a_1}^{a_2} \left(\frac{\sin a}{a} \right)^2 dx \right\}^2$$

$$\times \begin{cases} 1, & \text{for } \theta_1 < \theta < \theta_2 \\ 0, & \text{for all other } \theta \end{cases} \times \begin{cases} \frac{1}{m^4} \sin^4 \left[k \frac{b}{2} (1 + \cos \theta) \right], & m \text{ odd} \\ \cos^4 [kb], & m = 0 \\ 0, & m \text{ even} \end{cases}$$

where $a = \pi m \left(\frac{y_2 - y_1}{d} \right) \tan \phi$. Note that the grating depth b is so set that the first order is maximized; $k \frac{b}{2} (1 + \cos \theta) = \frac{\pi}{2}$. Now, the relation between the lateral displacement Δ and the single-pass plasma phase shift, Φ , is clear; if the grating is driven laterally as a function of time and the plasma is turned on, the shift in the sinusoidal output at this time is a measure of Φ .

Actually, I_D is not the signal seen by the detector. Since the detector integrates over frequency its signal is

$$\mathcal{I}_D = \left| \int F(k) U_D(k) dk \right|^2 = |\mathcal{U}_D|^2,$$

where $F(k)$ is the normalized frequency envelope determined by detector sensitivity, source output, window thin-film effects, and so forth.

$$\mathcal{U}_D = U_0 \int_0^\infty F'(k) \cos \left[2\pi \frac{\Delta}{d} + \Phi(k) \right] dk,$$

where U_0 equals all of U_D , except the cosine function in the integrand above and the term involving θ_1 and θ_2 , which limits the values of k accepted by the interferometer. Again, $F'(k)$ is normalized so that its integral over k is unity. Expanding $\Phi(k)$ about some k_0 by the Taylor series and considering the first two terms, if k_0 is so defined that

$$\int_0^\infty F'(k) \sin \left[\left(\frac{d\Phi}{dk} \right)_{k_0} (k - k_0) \right] dk = 0,$$

we obtain

$$\mathcal{U}_D = U_0 \cos \left[2\pi \frac{\Delta}{d} + \Phi(k_0) \right] \int_0^\infty F'(k) \cos \left[\left(\frac{d\Phi}{dk} \right)_{k_0} (k - k_0) \right] dk.$$

(XI. PLASMA PHYSICS)

The modulation will disappear with reasonable $F'(k)$ envelopes if

$$\left(\frac{d\Phi}{dk}\right)_{k_0} \delta k > \frac{\pi}{2},$$

where δk is the half-width at half-maximum. For a plasma for which the phase shift is inversely proportional to k , this limit is

$$\Phi\left(\frac{\delta k}{k}\right) > \frac{\pi}{2}.$$

Thus we see there is a limitation on the measurable phase shift, because of dispersion of the medium and the accepted bandwidth.

Turning now to the experimental measurements on the interferometer itself without a plasma, we found that when properly aligned the lateral motion of G_2 could give a 75% modulation signal. Figure XI-13 shows a run with over 60% modulation. The output

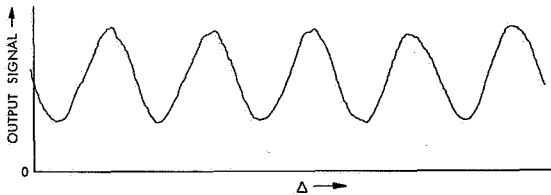


Fig. XI-13.

Typical modulation as a function of lateral motion by grating G_2 with polyethylene in one arm.

bandwidth of the interferometer was measured by placing a modified Perkin-Elmer monochromator between its output and the detector; this, with $\theta = 7^\circ$ for the center of the far mirror, gave a center wavelength of 197μ and a half-width at half-maximum or bandwidth of 5%. Using different thicknesses of the rather nondispersive medium, polyethylene, we measured the modulation magnitude as a function of phase shift (Fig. XI-14). From the index of refraction of polyethylene, $n = 1.47$ at $\lambda \approx 200 \mu$, the center frequency and bandwidth from phase shift and modulation magnitude measurements were in good agreement with those made with the monochromator.

The plasma tube that is now being used with the interferometer consists of coaxial cylindrical electrodes; the outer solid cylinder is a stainless-steel cathode, and the inner transparent grid cylinder is a stainless-steel anode. A 35 μ sec kV pulse at a 30-cycle rate produces a negative glow that fills the inside of the anode with pressures of a few Torr of helium. The Pyrex end plates of the cylinder have crystal-quartz windows set into their center, which allows the infrared to propagate through the plasma

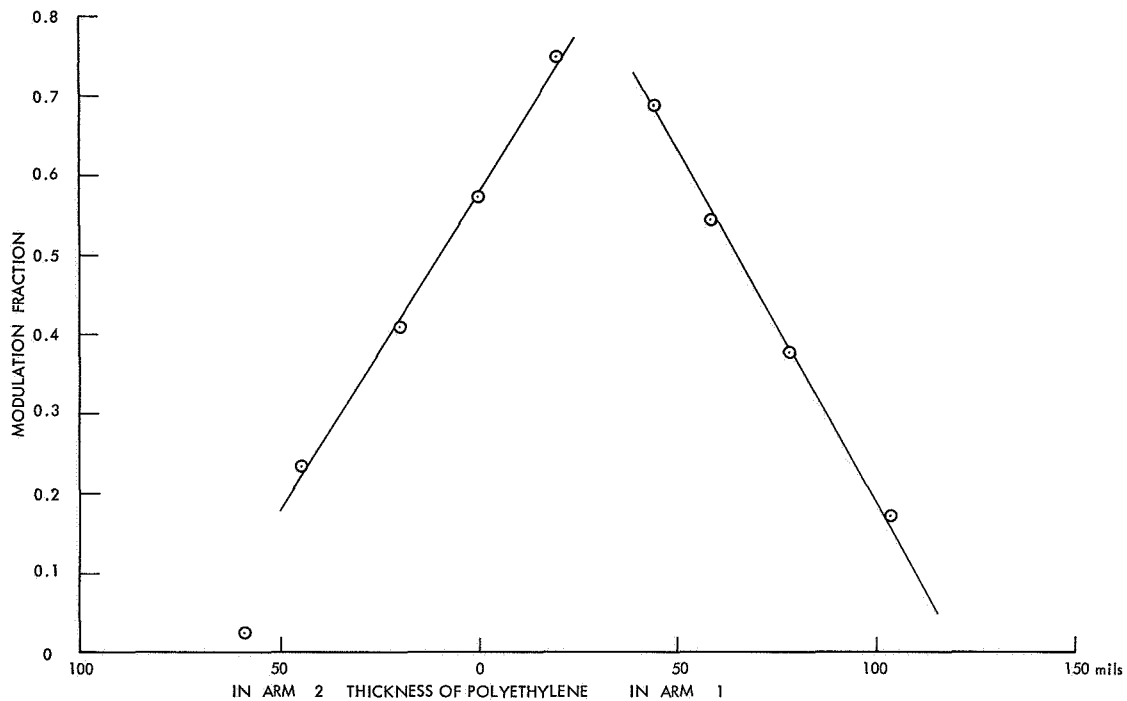


Fig. XI-14. Modulation magnitude as a function of phase shift from polyethylene sheets.

along the axis of the cylinders. As shown schematically in Fig. XI-9, the electronics part consists of a 3- μ sec sampling gate at a 60-cycle rate, which can be moved in time relative to the plasma pulse. This sampled signal is then stretched to fill the time between gates, thereby giving a square wave whose amplitude is the difference between the infrared signal in the afterglow of the plasma and the noise when there is neither plasma nor infrared (cut out by a synchronous 30-cycle chopper). Finally, synchronous detection is used to give this square-wave amplitude, which is plotted on a recorder whose drive is synchronized with the lateral movement of G_2 . A few phase-shift determinations have been made on the plasma, and average electron densities over the path length of plasma have been measured to be 5×10^{13} electrons per cubic centimeter in the early afterglow.

M. L. Andrews

References

1. S. C. Brown, G. Bekefi, and R. E. Whitney, *J. Opt. Soc. Am.* **53**, 448 (1963).
2. M. L. Andrews, *Quarterly Progress Report No. 74*, Research Laboratory of Electronics, M. I. T., July 15, 1964, pp. 74-78.
3. G. Bekefi, *Studies in Microwave Optics No. 38*, The Eaton Electronics Research Laboratory, McGill University, 1957, p. 14.

(XI. PLASMA PHYSICS)

D. MICROWAVE SCATTERING FROM WARM PLASMA WAVES NEAR THE ELECTRON CYCLOTRON FREQUENCY

We have observed microwave scattering from density oscillations in an electron-beam produced plasma. Large-amplitude emission of microwave radiation associated with these density oscillations was also observed, and the nature of the frequency spectrum of this radiation indicates that the density oscillations were associated with unstable warm plasma waves. We shall give a brief summary of previous work on these waves, after which our radiation measurements and the microwave scattering experiment will be described.

During the last few years, a great deal of theoretical and experimental work has been devoted to the study of waves that propagate in a warm plasma in a magnetic field. The effects of these waves were first observed experimentally in the form of anomalous peaks in the frequency spectrum of radiation emitted from laboratory plasmas at the electron-cyclotron frequency and its harmonics.^{1, 2} The origin of this radiation was not known at the time, but it is now generally accepted that it is due to longitudinal waves propagating in a warm plasma in a magnetic field. These waves can become unstable when a group of electrons with a large component of velocity perpendicular to the magnetic field is present in a thermal plasma. Some of the plasma wave energy can be emitted in the form of electro-magnetic radiation, but the mechanism for this coupling is not yet completely understood.

The dispersion relation for the propagation of these modes in a Maxwellian plasma was derived by Bernstein.³ It was suggested by Canobbio and Croci⁴ that fast electrons could excite these waves, and a derivation of conditions for instability and growth rates was given by Crawford and Tataronis.⁵

It was first noted by Lustig, McBee, and Kalisky⁶ that the anomalous radiation could be emitted at frequencies slightly different from the cyclotron harmonics, and the emission of radiation away from $n\omega_c$ was observed even more clearly by Tanala, Mitani, and Kubo.⁷ They measured the radiation emitted from a discharge in Neon at a pressure of 1.25×10^{-1} mm Hg. Measurements were taken at a fixed frequency of 9500 Mc, and the magnetic field was varied. They observed a peak in the microwave emission which for very small discharge currents was at a magnetic field corresponding to $\omega/\omega_c \approx 1$, where ω_c is the electron-cyclotron frequency, and ω is the receiver frequency. As the discharge current was increased, this peak shifted to lower magnetic fields, until at high discharge currents, $i_d > 0.5$ amp, the radiation peak was at $\omega/\omega_c \lesssim 2$. Thus the peak in microwave emission had shifted continuously from the cyclotron frequency to the second harmonic of the cyclotron frequency. At very low discharge currents, only this peak, $1 < \omega/\omega_c < 2$, was observed, but as the discharge current increased, peaks appeared between each of the higher harmonics and shifted upward in

frequency, approaching $\omega/\omega_c \approx n$, for large discharge currents, where $n = 3, 4, 5, \dots$, up to $n = 10$.

The data of Tanaka and co-workers can be explained in terms of Bernstein's theory³ for longitudinal waves propagating perpendicularly to the magnetic field. For very small electron densities, $\omega/\omega_c \ll 1$, his dispersion relation shows modes of propagation existing at $n\omega_c$, $n = 1, 2, 3, \dots$. As ω_p gets larger, the frequencies of propagation increase toward the next higher harmonic, $(n+1)\omega_c$.

Observations of the emission of microwave radiation at frequencies near but not exactly equal to $n\omega_c$ were also made by Bekefi and Hooper,⁸ who measured the radiation from an electron-beam produced plasma. Near each harmonic, $\omega = n\omega_c$ ($n = 1, 2, 3, \dots$), two radiation peaks were observed, one of which originated from the beam electrons and was Doppler-shifted. The other peak was not Doppler-shifted but was shifted from $\omega = n\omega_c$ toward a higher frequency by an amount proportional to the electron-beam density. This second peak seems to be related to an unstable Bernstein mode, since for each of the harmonics the peak shifts to higher frequencies with increasing electron density, as expected from the dispersion relation for these modes.

The experimental work that we wish to report here has two parts, and the two experimental geometries are shown in Fig. XI-15. Measurements of the microwave power emitted by the plasma were made with the geometry shown in Fig. XI-15a, and the scattering experiment was done with the geometry shown in Fig. XI-15b.

The plasma was produced by firing the electron beam from a focused Pierce-type gun into mercury vapor at a pressure of 2×10^{-4} mm Hg. The axis of the plasma tube was aligned along a uniform magnetic field, but the electron gun was outside the field so that the electrons in the beam acquired transverse energy as they entered the magnetic field. Measurements of the microwave power emitted by the plasma were made by passing the tube through an S-band waveguide, as shown in Fig. XI-15a, and feeding the microwaves to an S-band radiometer tuned to 3000 Mc. This experimental geometry was the same as that of Bekefi and Hooper,⁸ except that their waveguide was oriented with its axis approximately parallel to the axis of the tube. We varied the magnetic field and plotted the microwave power emitted at the fixed radiometer frequency (3000 Mc) against B . As did Bekefi and Hooper,⁸ we found peaks in the microwave radiation for frequencies in the neighborhood of $n\omega_c$ ($n = 1, 2$). Near each harmonic two peaks were observed. One was of relatively low amplitude and very nearly at $\omega = n\omega_c$; the other much larger in amplitude, was observed to shift away from $n\omega_c$ toward higher frequencies as the beam voltage was increased. (Increasing the beam voltage also increased the beam density and the plasma density.) Figure XI-16 shows the frequency shifts of these peaks for the first two harmonics. The solid lines represent the large-amplitude peaks, and the dashed lines, represent the low-amplitude peaks. Again, as in the experiments of Bekefi and Hooper,⁸ and Tanaka and co-workers,⁷ we have a radiation

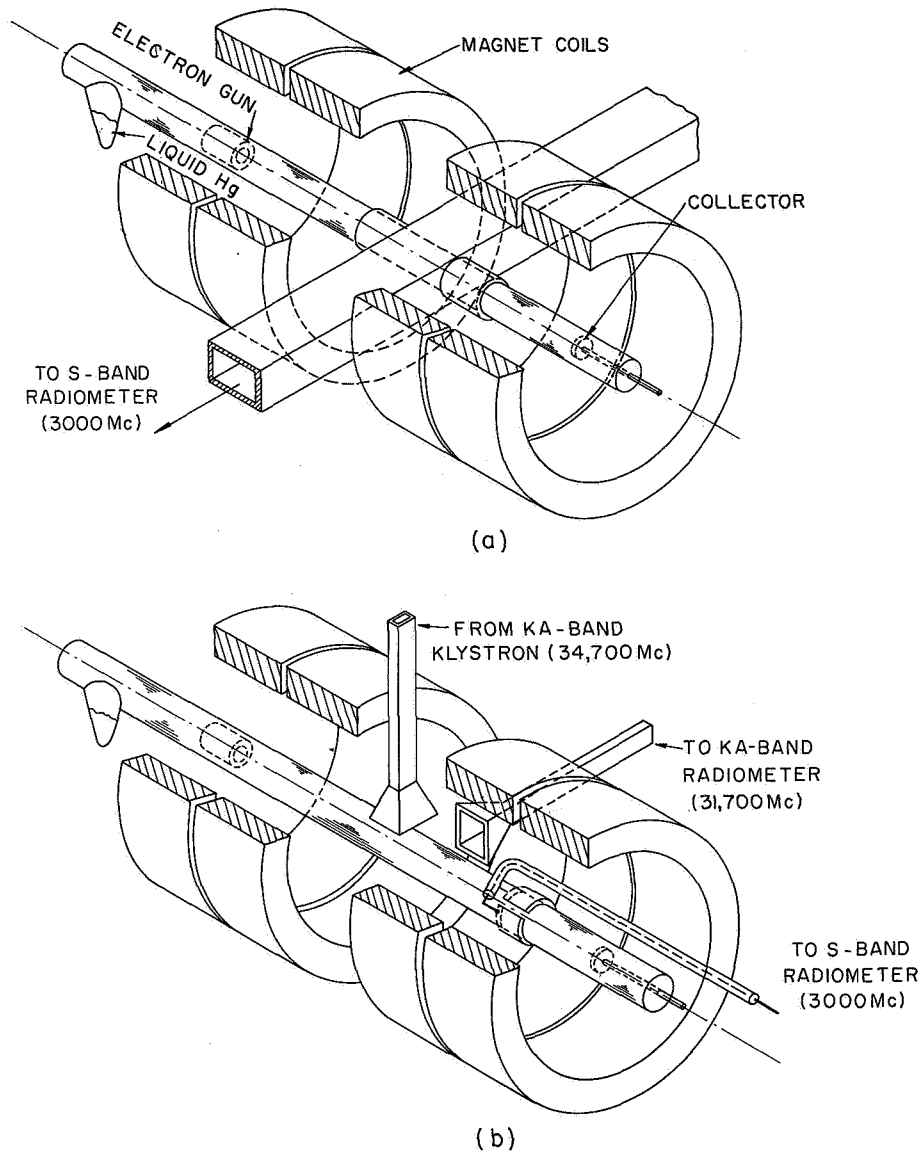


Fig. XI-15. Experimental geometry.

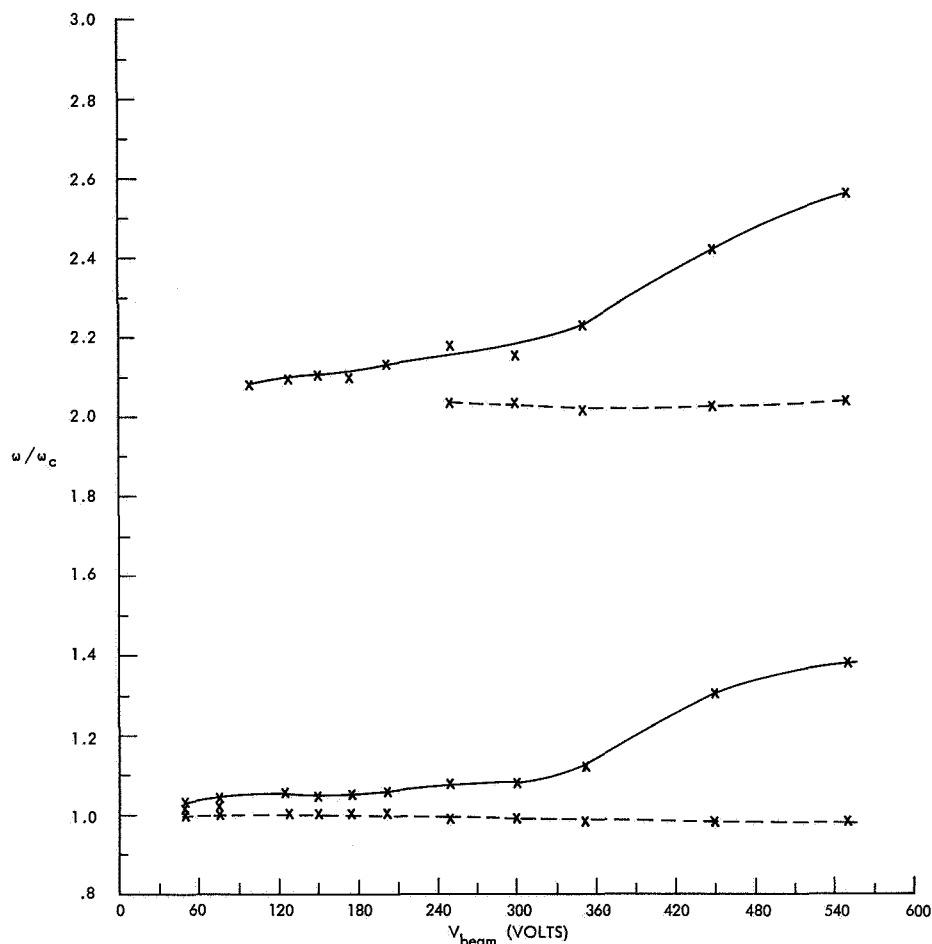


Fig. XI-16. Frequency of radiation peaks vs electron-beam voltage.

peak shifting from $n\omega_c$ toward a higher frequency as the plasma frequency is increased. The same comments regarding the similar behavior of the frequencies of the Bernstein modes for increasing plasma density apply here, too.

We now turn to the microwave scattering experiment. Since the warm plasma waves described by Bernstein³ are longitudinal waves, E parallel to k , the electron density undergoes oscillations at the wave frequency, and microwave scattering from these oscillations should be possible. (References for the theory of microwave scattering have been given in a previous report.⁹) The experimental geometry for the scattering experiment is shown in Fig. XI-15b. The S-band waveguide was removed to allow the KA-band microwave horns access to the plasma. The oscillations in the plasma that are responsible for the radiation emitted into the waveguide were picked up by means of a strip-line antenna. This antenna was connected through a coaxial cable to the S-band radiometer tuned to 3000 Mc. Microwave power at a frequency of 34,700 Mc was incident

(XI. PLASMA PHYSICS)

on the plasma from one of the horns, and radiation scattered by the plasma was received by the second horn and detected by a radiometer tuned to 31,700 Mc. Thus any scattered radiation that was detected was shifted in frequency by 3000 Mc, the frequency of the oscillations in the plasma that were detected independently by the strip-line and the S-band radiometer. The magnetic field was varied, and the outputs of the S-band and KA-band radiometers were plotted simultaneously on two X-Y recorders. Figure XI-17 shows the results. The upper trace is the microwave power picked up directly from the

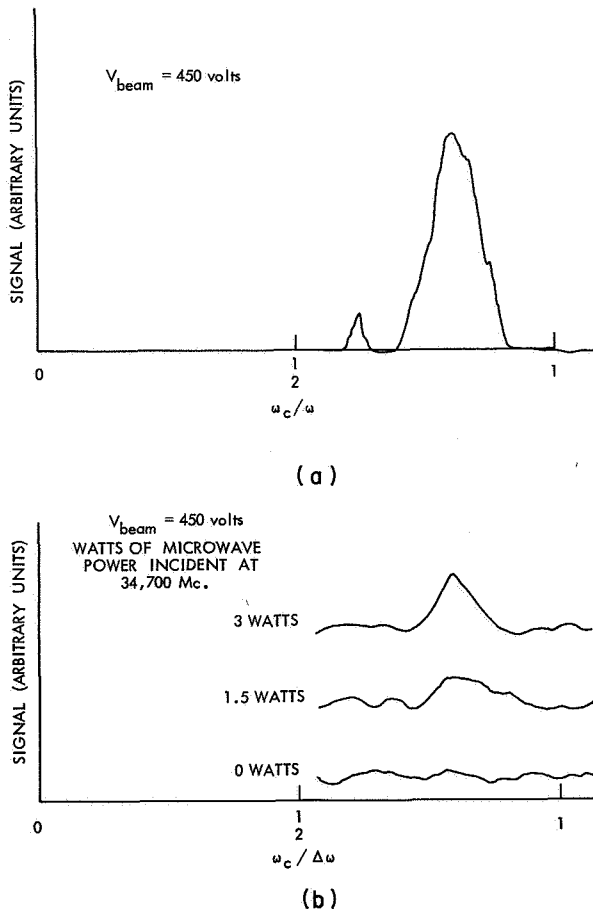


Fig. XI-17.

- (a) Signal at 3000 Mc picked up from the plasma with strip-line antenna vs normalized magnetic field ($\omega = 2\pi \times 3000$ Mc).
- (b) Scattered microwave power at 31,700 Mc vs normalized magnetic field. ($\Delta\omega$ = frequency shift between incident microwave frequency of 34,700 Mc and scattered microwave frequency of 31,700 Mc; $\Delta\omega = 2\pi \times 3000$ Mc.)

plasma by the strip-line at 3000 Mc, and the three lower traces are the scattered microwave power for three values of incident microwave power. It can be seen that the peak in the scattered power disappears when no radiation is incident on the plasma, and that the peak appears at the same value of ω_c/ω as the large peak in the signal picked up directly from the plasma at 3000 Mc. (The nature of the small peak is not understood.) From these data, it seems clear that the peak in the microwave power received by the KA-band radiometer at 31,700 Mc is due to microwave scattering from the

density oscillations associated with the waves that were observed directly at 3000 Mc. These waves seem to be the warm plasma waves described by Bernstein,³ which become unstable, because of the presence of the beam electrons with a large component of velocity perpendicular to the magnetic field. No scattering was observed from the second harmonic, $\omega/\omega_c \gtrsim 2$, since the amplitude of the oscillations associated with it was much lower than the amplitude of the oscillations near the fundamental.

R. L. Kronquist

References

1. G. Bekefi, J. D. Coccoli, E. B. Hooper, Jr., and S. H. Buchsbaum, *Phys. Rev. Letters* 9, 6 (1962).
2. G. Landauer, Proc. Fifth International Conference on Ionization Phenomena in Gases, Munich, Germany, July 1961 (North-Holland Publishing Co., Amsterdam), Vol. 1, pp. 389-394.
3. I. B. Bernstein, *Phys. Rev.* 109, 10-21 (1958).
4. E. Canobbio and R. Croci, Proc. Sixth International Conference on Ionization Phenomena in Gases, Paris, July 1963 (SERMA Publishing Co., Paris), Vol. 3, pp. 269-271.
5. F. W. Crawford and J. A. Tataronis, Seventh International Conference on Ionization Phenomena in Gases, Belgrade, 1965.
6. C. D. Lustig, W. D. McBee, and A. Kalisky, Sperry-Rand Research Center Report No. RR-645, Sudbury, Mass., January 1964; C. D. Lustig, *Bull. Am. Phys. Soc.* 9, 313 (1964).
7. S. Tanaka, K. Mitani, and H. Kubo, Institute of Plasma Physics Report No. 13, Nagoya University, Nagoya, Japan, July 1963; K. Mitani, H. Kubo, and S. Tanaka, *J. Phys. Soc., Japan* 19, 211 (1964); H. Kubo, K. Mitani, S. Tanaka, and Y. Terumichi, *J. Phys. Soc. Japan* 19, 221 (1964).
8. G. Bekefi and E. B. Hooper, Jr., *Appl. Phys. Letters* 4, 135 (1964).
9. R. L. Kronquist, Quarterly Progress Report No. 82, Research Laboratory of Electronics, M. I. T., July 15, 1966, p. 109.

E. NONLINEAR HARMONIC GENERATION AT PLASMA RESONANCE

The subject of this report is the generation of harmonics of an RF signal applied to a probe immersed in the sheath between the probe and the plasma. Harmonic generation is particularly copious at frequencies corresponding to resonances of the probe-plasma system. One such resonance, the geometrical resonance, is a manifestation of an oscillation of the sheath-plasma system.¹ This resonance frequency is near but below electron plasma frequency, ω_p . At geometrical resonance, sheath nonlinearities, in addition to generating harmonics, cause both the probe's RF admittance and the DC current collected by the probe to peak. These effects will be discussed here.

If a probe is inserted into a plasma, its RF admittance characteristic will show a

(XI. PLASMA PHYSICS)

resonance at a frequency somewhat below plasma frequency. This is attributed to a series resonance between the capacitive sheath and the inductive plasma. (A plasma acts as an inductance below plasma frequency, since the conduction current exceeds the displacement current for ω less than ω_p .) At series resonance, the electric fields in the sheath and plasma become large, and consequently large currents flow for a given voltage on the probe.

If the probe is now biased to collect DC current and an RF voltage is applied to the probe, more DC current is observed to flow than if there were no RF voltage. This effect can be explained approximately by considering the nonlinear current-voltage characteristic of the sheath surrounding the probe.

$$I = ne \left(\frac{kT_e}{2\pi m_e} \right)^{1/2} e^{-eV/kT_e}. \quad (1)$$

Here, n is the electron density, and V is the voltage drop across the sheath. When $V = V_0 + V_1 \sin \omega t$,

$$I_{DC} = ne \left(\frac{kT_e}{2\pi m_e} \right)^{1/2} e^{-eV_0/kT_e} \left[\frac{1}{2\pi} \int_0^{2\pi} e^{-eV_1/kT_e \sin \omega t} d(\omega t) \right]. \quad (2)$$

The extra DC current that flows due to the RF voltage V_1 across the sheath is

$$\Delta I_{DC} = I_{DC} \left[I_0 \left(\frac{eV_1}{kT_e} \right) - 1 \right], \quad (3)$$

where I_0 is the zero-order Bessel function of imaginary argument.

At series resonance, V_1 becomes large and ΔI_{DC} attains a maximum. It has been shown by Harp and Crawford that the incremental DC and RF admittance peak at the same frequency.²

If we now derive an equation for the instantaneous current by expanding the exponential in Eq. 3 and keep only the dominant contribution to each harmonic, we obtain³

$$\begin{aligned} I(t) &= I_{dc} \left[1 + \left(\frac{eV_1}{kT_e} \right) \sin \omega t - \left(\frac{eV_1}{kT_e} \right)^2 \frac{\cos 2 \omega t}{4} - \left(\frac{eV_1}{kT_e} \right)^3 \frac{\sin 3 \omega t}{24} + \left(\frac{eV_1}{kT_e} \right)^4 \frac{\cos 4 \omega t}{192} + \dots \right] \\ &= I_{DC} + I_1(\omega) + I_2(2\omega) + I_3(3\omega) + I_4(4\omega) + \dots \end{aligned} \quad (4)$$

$I_1(\omega)$, $I_2(2\omega)$, etc. are the harmonics with which this report is concerned.

ΔI_{DC} in Eq. 3 is the time average of the harmonic current components. The RF admittance peak occurs because $I_1(\omega)$ attains a maximum at resonance. A schematic diagram of the experiment is shown in Fig. XI-18. The discharge, probe, and method of determining geometrical resonance were described in Quarterly Progress Report No. 79 (pages 95-98) and in a paper by Waletzko and Bekefi.⁴

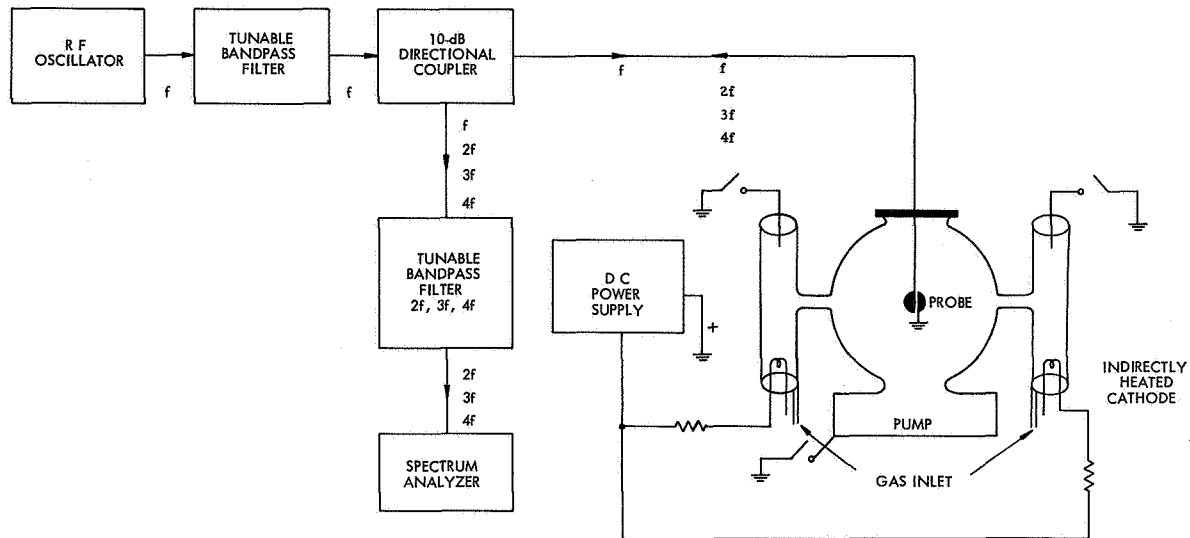


Fig. XI-18. Schematic diagram of the experiment.

Measurements of harmonic power were taken both on and off resonance. The amplitude of each harmonic peaked at resonance as expected. The harmonic power received as a function of the applied power for a fixed frequency and discharge conditions is shown in Fig. XI-19. These measurements were made on resonance.

It should be noted that V_1 is the voltage across the sheath and equals V_{applied} only for ω much less than ω_p .⁴ Nevertheless, for fixed discharge conditions and frequency, V_1 is proportional to V_{applied} and the observed dependences shown in Fig. XI-19 are

Table XI-1. $\frac{I_4 I_2}{I_3^2}$ for various runs.

	f_{inc} (MHz)	f_{res} (MHz)	$\frac{I_4 I_2}{I_3^2}$
Approximate Theory			$\frac{3}{4}$
a)	50	50	2.2
b)	60	60	1.1
c)	60	60	2
d)	60	<60 Mc	1.1
e)	60	>60 Mc	8
f)	60	>>60 Mc	16

(XI. PLASMA PHYSICS)

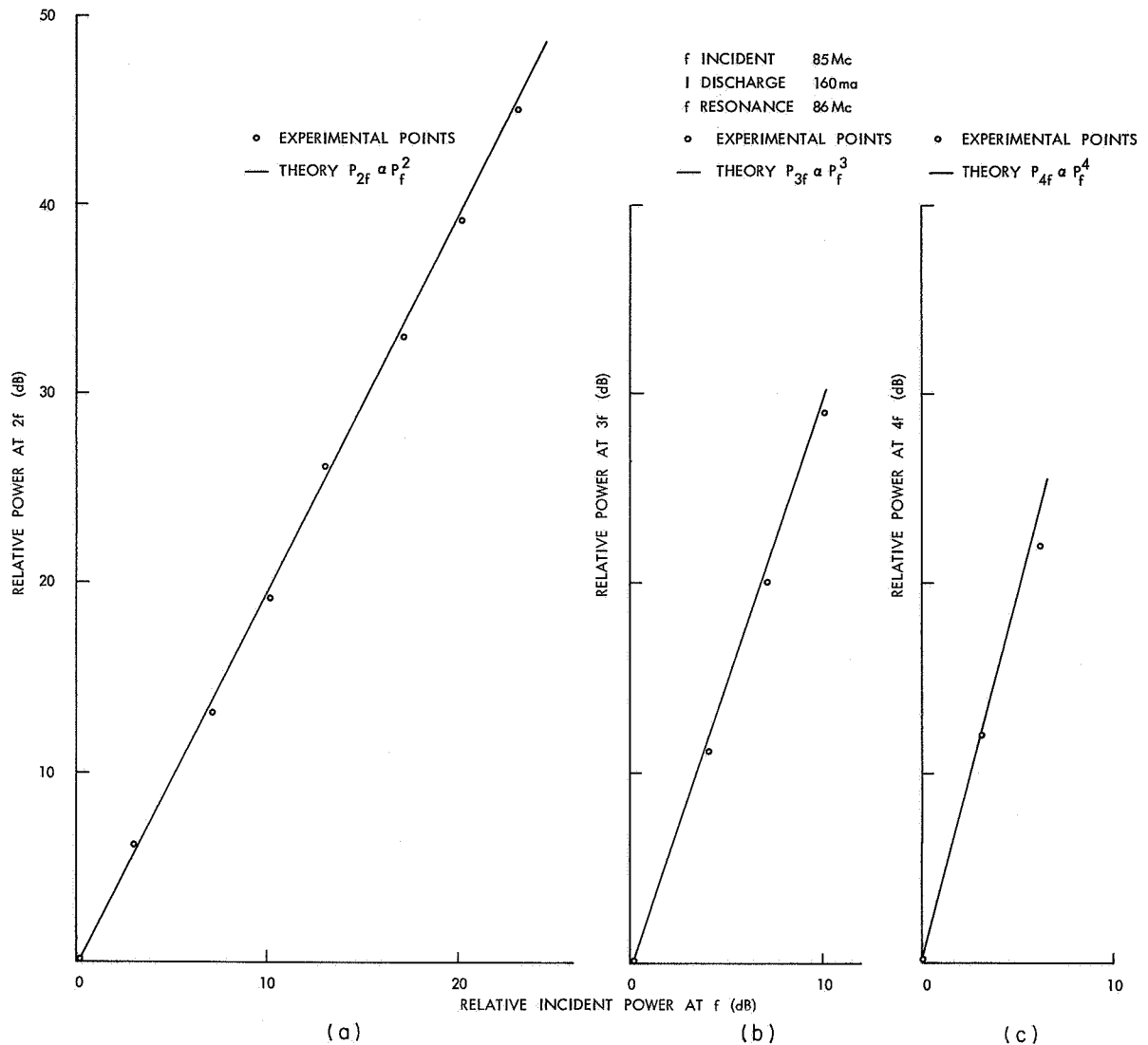


Fig. XI-19. (a) Relative power in the second harmonic vs relative fundamental power.
 (b) Relative power in the third harmonic vs relative fundamental power.
 (c) Relative power in the fourth harmonic vs relative fundamental power.

as expected from the approximate theory of Eq. 4.

We now wish to compare the relative magnitudes of observed harmonic emission with that predicted from Eq. 4. Since we do not know V_1 ,⁵ we must look for a quantity independent of this parameter. From Eq. 4, one such quantity is $I_4 I_2 / I_3^2 = 3/4$. Table XI-1 shows the preliminary experimental results. Values a, b, c were taken at resonance. values d, e, f were taken off resonance, At f less than f-resonance, there is considerably more fourth harmonic than expected. The agreement for $f \sim f_{\text{resonance}}$ is fair. All measurements were made with a

slotted-sphere antenna approximating a dipole.

The experiment is being refined in several ways. A monopole probe will be used so that a theory of harmonic amplitudes will be tractable. Since monopole fields are purely radial, there is hope of solving the Vlasov equation for the monopole harmonic amplitudes. The voltage on the probe will be monitored so as to keep V_{applied} constant as the frequency is swept. Knowledge of the DC voltage and electron density in the sheath permits one to predict V_{RF} across the sheath in terms of V_{applied} . The DC bias on the probe will be varied to determine the effect of a varying sheath size on the harmonic generation.

A. J. Cohen

Footnotes and References

1. K. Takayama, H. Ikegami, and S. Miyasaki, *Phys. Rev. Letters* **5**, 238 (1960); S. M. Levitskii and J. P. Shashurin, *Sov. Phys. - Tech. Phys.* **8**, 319 (1963); R. Buckley, *Proc. Roy. Soc. (London)* **A290**, 186 (1966); D. Lepechinsky, A. Messian, and P. Rolland, Centre D'Etudes Nucleares de Saclay Rapport CEA-R 2945; J. A. Waletzko, "Radiofrequency Dipole Resonance Probe," Quarterly Progress Reports No. 79, Research Laboratory of Electronics, M.I.T., October 15, 1965, pp. 95-98; No. 80, January 15, 1966, pp. 103-108; R. S. Harp and F. W. Crawford *J. Appl. Phys.* **35**, 3436-3446 (1964).
2. R. S. Harp and F. W. Crawford, *J. Appl. Phys.* **35**, 3444 (1964).
3. Equation 4 is valid for $eV_1/kT \leq 1$, This criterion is not necessarily satisfied at resonance, since V_1 can become very large there.
4. J. A. Waletzko and G. Bekefi (submitted to *Journal of Radio Science*).
5. $V(n\omega) = K_n [V_1(\omega)]^n$ theory. The aim of the theory is to calculate the harmonic conversion efficiency constant K_n . But V_1 is not known experimentally. $V_1 = f(\omega) V_{\text{applied}}$ where $f(\omega)$ is determined by the resonance (see Buckley, Lepechinsky et al.¹) V_{applied} is not yet known, only V_{output} and the probe impedance at frequency ω are known. V_{applied} cannot be simply determined by transmission-line theory because the oscillator output is a strong function of its loading. For example, at resonance the probe impedance is small so V_{applied} is small but $f(\omega)$ is large. Off resonance, the impedance is high, V_{applied} is large, and although $f(\omega)$ is small, V_1 can be large. Only if V_{applied} is held constant can the effect of any resonances on the harmonic generation be clearly observed.

(XI. PLASMA PHYSICS)

F. LASER BREAKDOWN EXPERIMENT

This report presents a further analysis of the laser breakdown experiment.^{1,2}

1. Absorption Coefficient

The absorption coefficient of the plasma for the light of the HeNe gas laser can be readily calculated from the transmission of the laser beam through the plasma and the radius of the cylindrical spark. The diameter of the laser beam is 2 mm and the diameter of the plasma is greater than 2 mm from 110 nsec on, after the beginning of the Gaunt pulse.

The first experimental point of the transmission curve is at 130 nsec. Figure XI-20 shows the arrangement that was adopted. The volume, V_e , of the plasma crossed at

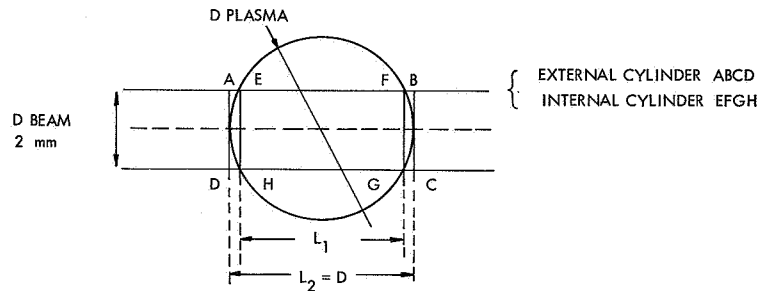


Fig. XI-20. Model for calculating the absorption coefficient of the plasma for the light of the gas laser (6328 Å).

90° by the gas laser beam is limited by the volume of the two cylinders, and for its lateral surface it has the surface of the gas laser beam itself.

$$Vol_{\text{external}} > Vol_{\text{plasma crossed}} > Vol_{\text{internal}}.$$

Thus, for a given diameter of the plasma, the true absorption coefficient will be between the values a_1 and a_2 , satisfying the equations

$$T_r = e^{-a_1 L_1} \quad T_r = e^{-a_2 L_2},$$

where L_1 and L_2 are the lengths of the two cylinders, and T_r is the transmission, at time t , of the gas laser beam through the plasma. Applying this technique to the points and extreme values of the error bars of T_r , we obtained the absorption coefficient at 6328 Å (Fig. XI-21). For times between 130 nsec and 600 nsec, the

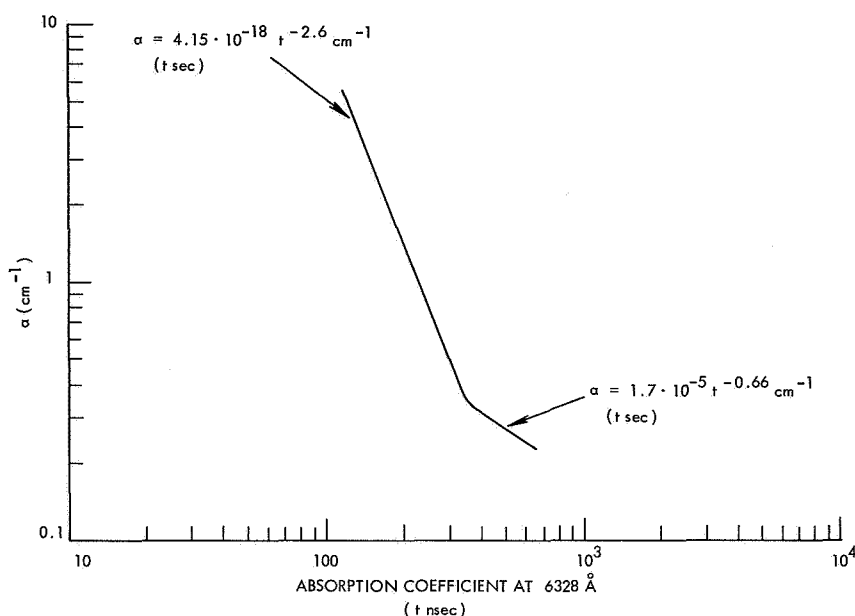


Fig. XI-21. Absorption coefficient at 6328 Å.

absorption coefficient drops from 4 cm^{-1} to $\sim 0.25 \text{ cm}^{-1}$. At approximately 300 nsec, the behavior of α changes from

$$\alpha = 4.15 \times 10^{-18} t^{-2.62} \text{ cm}^{-1} \text{ (t sec)} \quad (1)$$

to

$$\alpha = 1.7 \times 10^{-5} t^{-0.66} \text{ cm}^{-1} \text{ (t sec)}. \quad (2)$$

Since α and R versus time are known, the optical thickness of the plasma $\tau = 2\alpha R$ can be obtained immediately. The approximation that is used is very good, within the uncertainty of experimental error. The change in slope of absorption coefficient occurs when the plasma emits the axial and radial shock waves.

2. Density

The measured electron density, recording the spreading of the gas laser beam, caused by the lens effect of the plasma, is shown in Fig. XI-22. The density slope changes when the subsonic regime is reached.

It has to be kept in mind that, for every time, the density measured by this method is not the average density across the circular section of the plasma. The density has a profile across the section and it is the density corresponding

(XI. PLASMA PHYSICS)

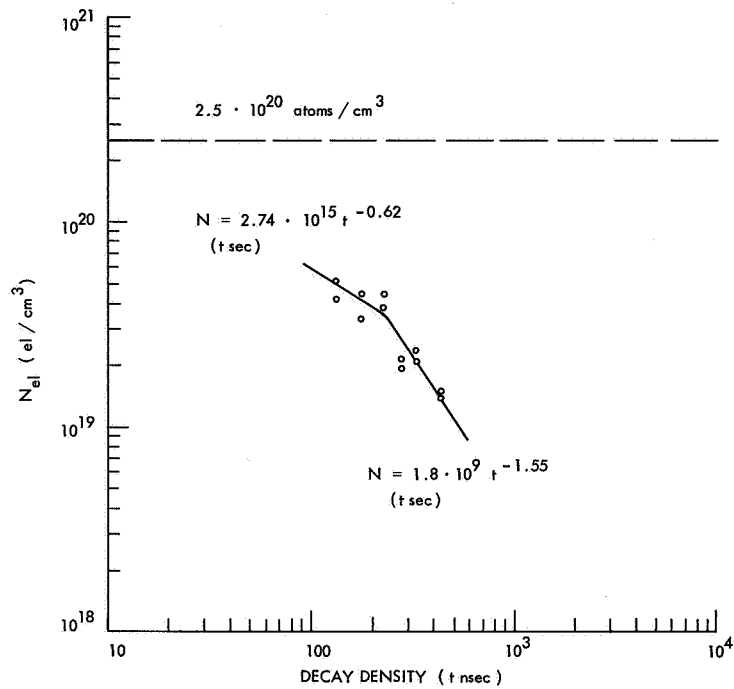


Fig. XI-22. Electron density measurement.

to the central higher part of this profile that gives the maximum angular scattering. The lens and the adjustable diaphragm detect this maximum solid angle of scattering, and so the measured density is not the average value across the circular section of the plasma. The density behavior from 100 nsec to approximately 250 nsec is

$$N = 2.74 \times 10^{15} t^{-0.62} \frac{\text{electrons}}{\text{cm}^3}. \quad (3)$$

From ~250 nsec to ~600 nsec the density (always measured in the central part of the plasma) is

$$N = 1.8 \times 10^9 t^{-1.55} \frac{\text{electrons}}{\text{cm}^3}. \quad (4)$$

The profile of the density will be obtained from the "knee curves"² that describe the transmission of the gas laser beam through the plasma.

By subtracting the transmission between two consecutive diaphragm apertures and correcting with the known absorption coefficient, averaged through the plasma, a scattering profile for the gas laser beam will be obtained. The profile of the refraction index through the plasma that modifies the initial gas laser beam profile in the scattered profile will thus be obtained for every time. Further work is in progress on this point.

3. Shock Velocity

From previous work,⁴ which has shown the behavior of the longitudinal and radial expansion of the plasma, a full description of the size of the plasma and of the shock wave emission can be obtained.^{5,6} Between 50 nsec and 200 nsec the growth of the radius of the plasma from the initial value is

$$R = 1.7 \times 10^6 t^{1.04} \text{ cm (t sec).} \quad (5)$$

When the shock wave starts to be emitted, the radius growth slows down and the radius is (from 300 nsec to 32 μ sec)

$$R = 7.4 \times 10^{-1} t^{.09} \text{ cm (t sec).} \quad (6)$$

The shock radius from \sim 500 nsec to 5 μ sec is

$$R = 2.29 \times 10^2 t^{.46} \text{ cm (t sec).} \quad (7)$$

Figure XI-4 shows the behavior of the velocity of the plasma radius and of the shock. The plasma radius shock slows down to the velocity of sound in the unperturbed gas, and so do the axial velocities.

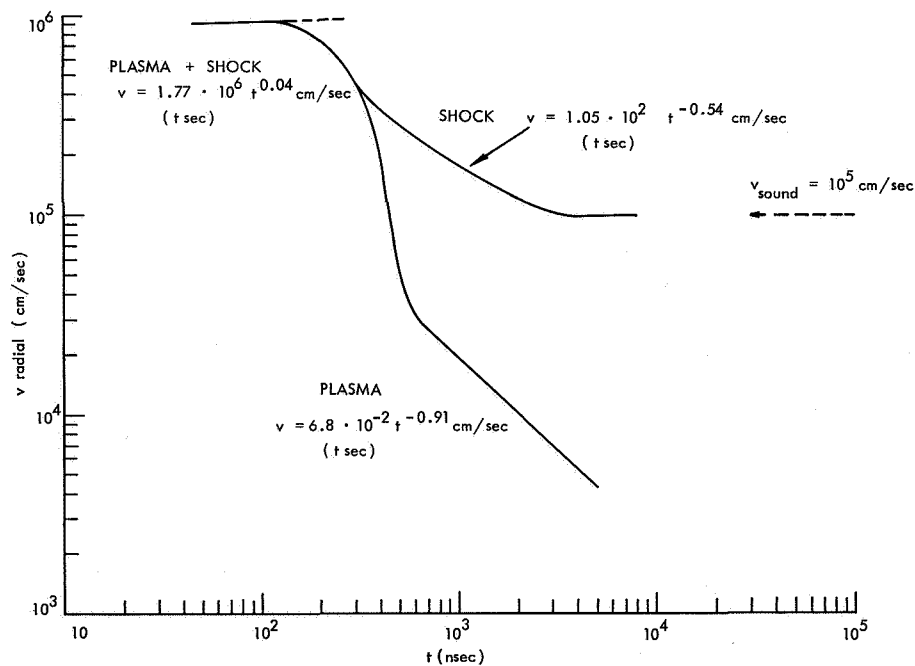


Fig. XI-23. Plasma radial velocity.

(XI. PLASMA PHYSICS)

$$V_{\text{sound}} = \sqrt{\frac{\gamma p}{\rho}}. \quad (8)$$

That is, for $\gamma = 1.66$ and $p = 10.25 \frac{\text{kg}}{\text{cm}^2}$, $\rho = 1.67 \times 10^{-3} \frac{\text{gr}}{\text{cm}^3}$, and $V = 10^5 \frac{\text{cm}}{\text{sec}}$. The shoulder plasma dragged by the radial shock wave is found up to a radius $R = 5$ mm ($t = 8 \mu\text{sec}$).^{7,8} The longitudinal growth of the plasma toward the ruby beam is shown in Fig. XI-24. Figure XI-25 gives the velocity behavior in the same direction. Figures XI-26 and XI-27 give the longitudinal growth and velocity in the direction of the beam. In the direction toward the ruby beam the growth in plasma length from the initial size of 4.5 mm is

$$L = 80 t^{.41} \text{ cm (t sec)} \quad (9)$$

for times from 30 nsec to the beginning of the separation of the shock wave from the plasma (500 nsec). The shock, measured between 500 nsec and 10 μsec is given by

$$L = 1.5 \times 10^3 t^{.61} \text{ cm (t sec)}. \quad (10)$$

The plasma slows down and its growth in length, measured between 500 nsec and 25 μsec , is

$$L = 5.1 \times 10^{-1} t^{.068} \text{ cm (t sec)}. \quad (11)$$

The motion of the exploding front against the ruby is in good agreement with Taylor's blast-wave theory.^{5,6} The front position, according to this theory, is given by

$$L = \left(\frac{E}{\rho}\right)^{.2} t^{.4} \text{ cm (t sec)}, \quad (12)$$

where E is the energy in the explosion, and ρ is the mass density. For times between 30 μsec and 500 μsec , when the shock front is still inside the plasma, introducing into (12) the values $E = 1.8$ joules (which, as we shall see, is a reasonable estimate for the energy left in the plasma after the ionization) and $\rho = 1.67 \times 10^{-3} \frac{\text{gr}}{\text{cm}^3}$, we find

$$L = 101 t^{.4} \text{ cm (t sec)},$$

which agrees with (9), within 20 per cent. The behavior in the direction following the ruby beam, is quite different. The plasma front before the separation of the shock (400 nsec) is

$$L = 2.59 \times 10^6 t^{1.14} \text{ cm (t sec)}. \quad (13)$$

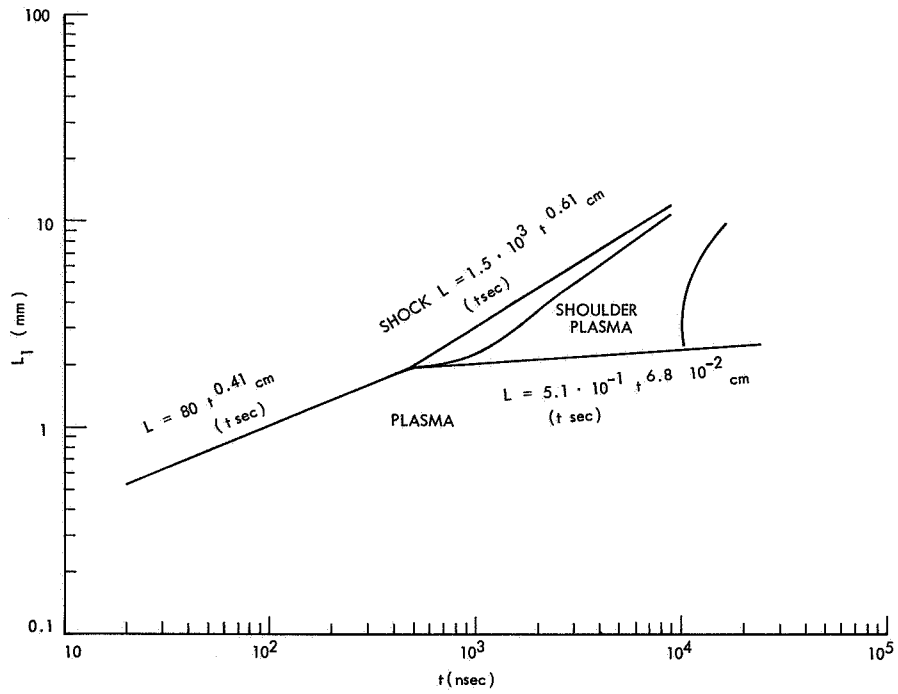


Fig. XI-24. Axial growth toward the ruby.

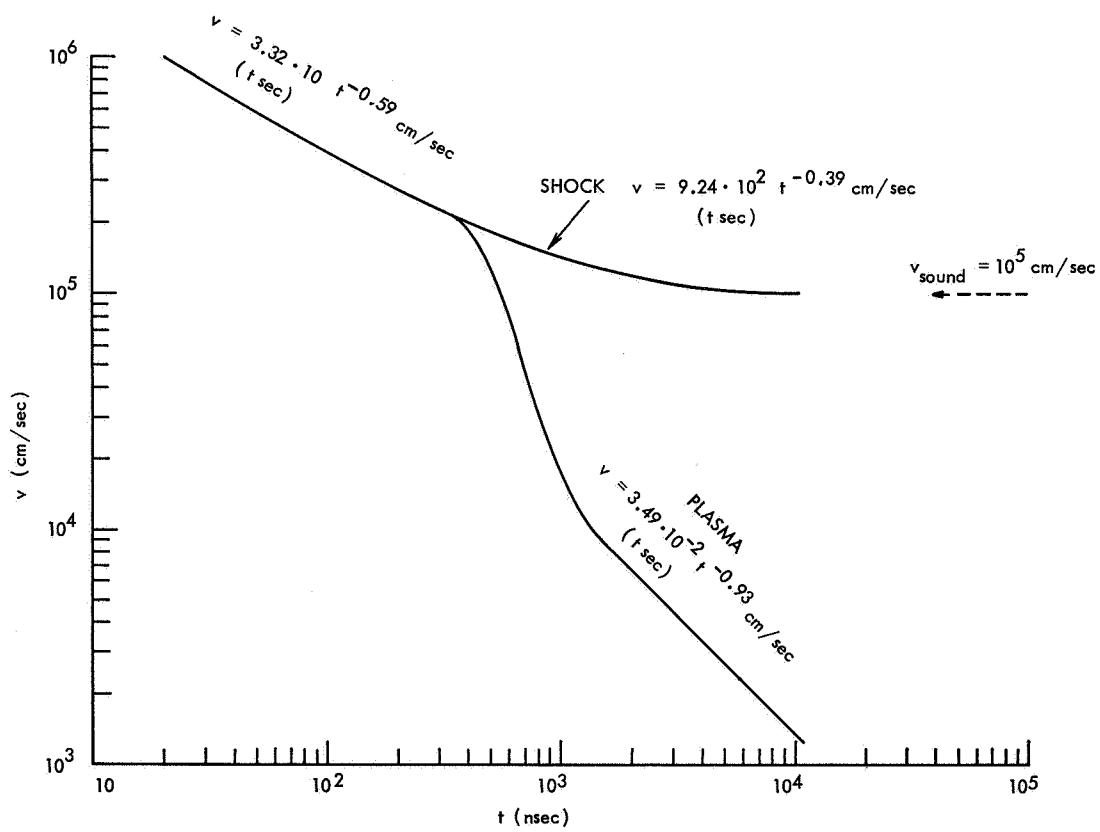


Fig. XI-25. Axial velocity toward the ruby.

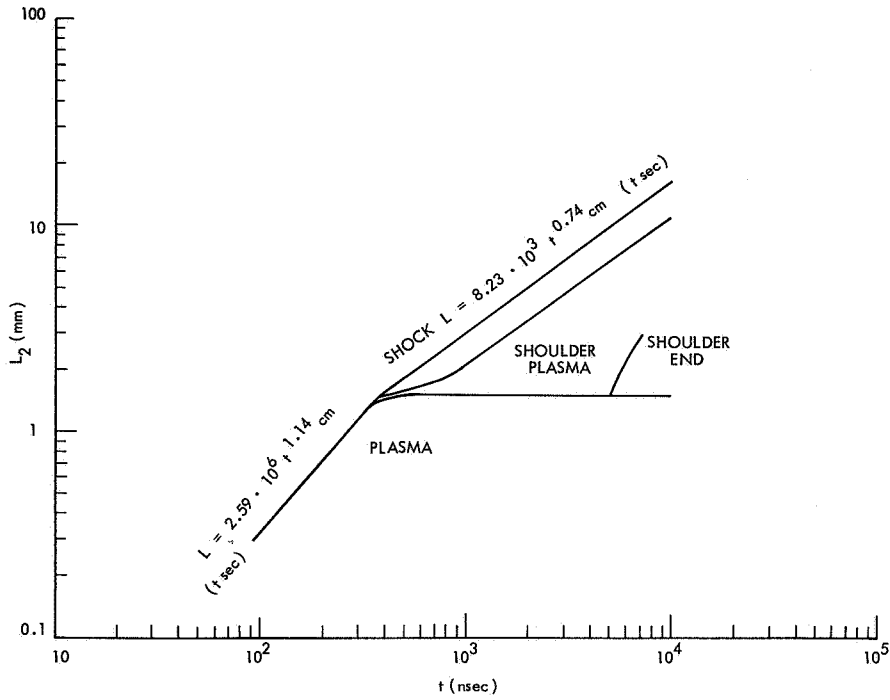


Fig. XI-26. Axial growth in the direction of the ruby.

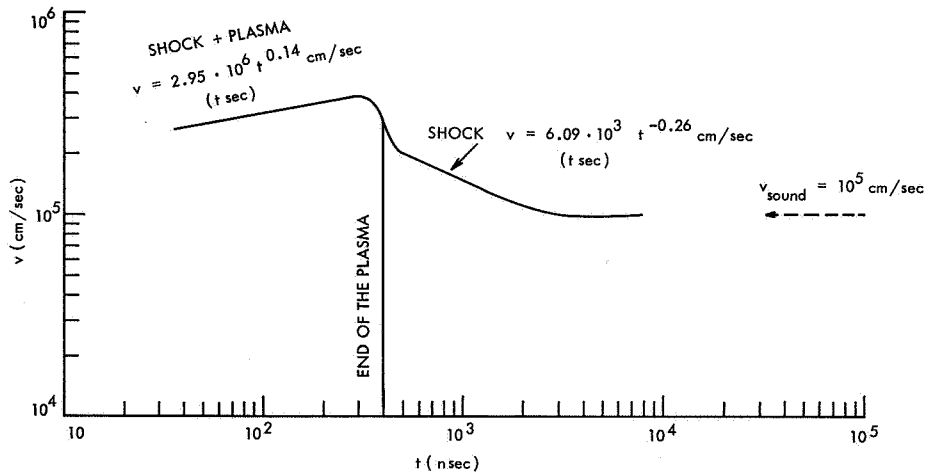


Fig. XI-27. Axial velocity in the direction of the ruby.

After the beginning of the separation, the shock is given by

$$L = 8.23 \times 10^3 t^{.74} \text{ cm (t sec).} \quad (14)$$

The plasma, after the beginning of the separation from the shock, slows greatly and does not expand farther beyond 1.4 mm than the initial position. This confirms the fact that the plasma explodes mainly towards the focussing lens. Under the assumption that the plasma has the shape of a cylinder, the volume is immediately found from the radius and length. Figures XI-28 and XI-29 give the volume and the volume velocity of the plasma. The volume velocity is growing before 200 nsec. More detailed work is in the course of interpretation of the axial expansion data in the direction of the ruby beam.

4. Temperature Measurement

The measurement of the average temperature of the plasma during the afterglow between 130 nsec and 600 nsec is made with the experimental arrangement previously reported.² To avoid directional effects on the transmission of the sharp interference filter I with respect to the emission beams coming from the plasma through the lens G, the diaphragm H was kept at a relatively small diameter $f/22$, that is, 16.35 mm; the solid angle from which the points of the plasma (distant 183 cm from the diaphragm) see the aperture of the diaphragm itself is $\Delta\Omega = 6.26 \times 10^{-5}$ steradian. The gas laser beam, when the plasma is not present, passes through the aperture of the diaphragm. The method of measurement of the temperature consists in calibrating, with the DC signal of the gas laser, the emission signal of the plasma, which the two interference filters in cascade receive in a resulting 10 Å bandwidth centered at 6328 Å; this wavelength is far from the radiation lines of Helium (the nearest lines are 5876 Å and 6678 Å) and the emission of the plasma at 6328 Å is entirely due to Bremsstrahlung. When the plasma is produced, no gas laser is on, and the photomultiplier tube receives the emission of the plasma through the interference filters D and I, the sharp cutoff filter B, and the polarizer C. Many emission curves are taken in the same situation to keep account of the nonexact repetitiveness of the plasma (Fig. XI-30). Then, when no plasma is present, the gas laser is put into operation and, in this way, a steady-state signal

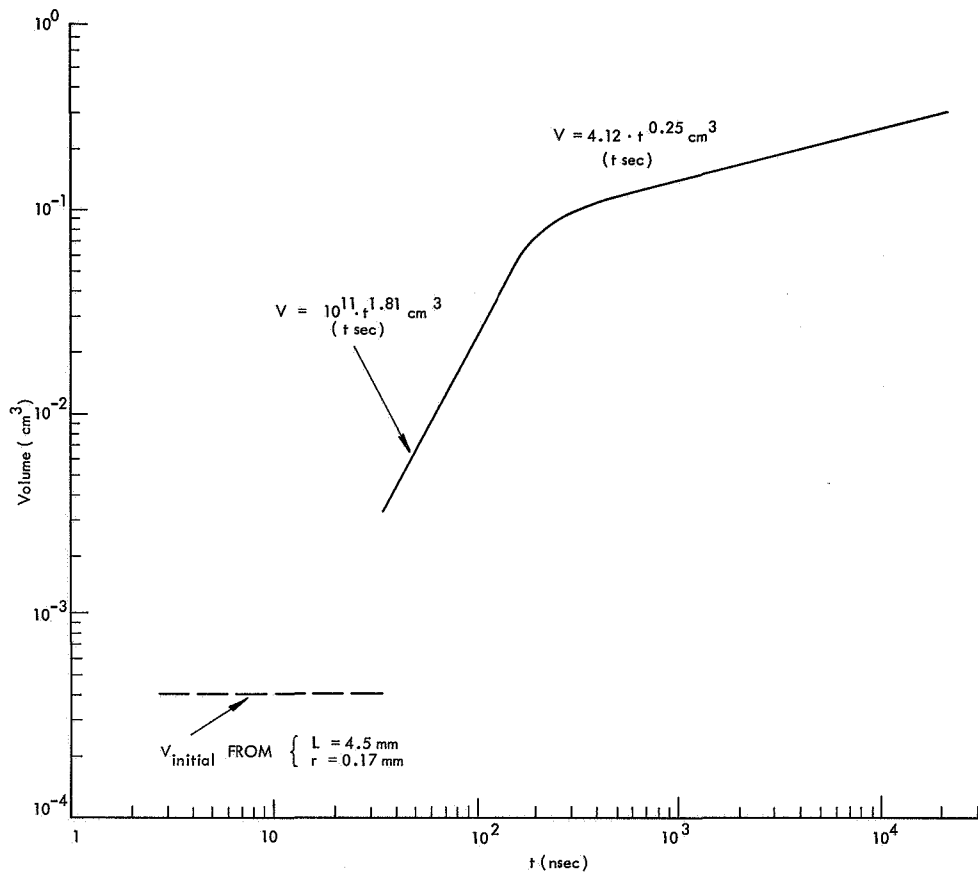


Fig. XI-28. Volume of the plasma.

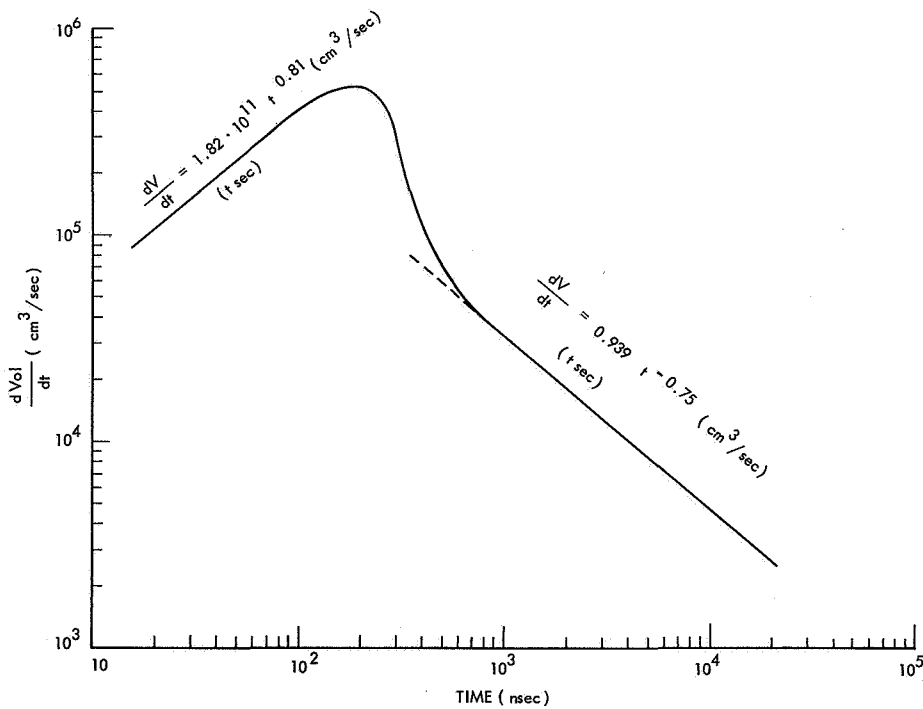


Fig. XI-29. Volume velocity of the plasma.

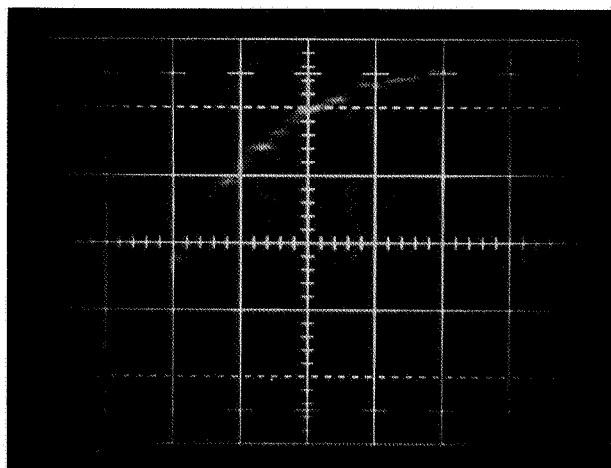


Fig. XI-30. Plasma emission (f/22) for measurement of temperature.
Scales: Vertical, 5 mV/cm; horizontal 100 nsec/cm.

is received by the detector that works always in its linear regime. A Spectra-Physics Type 401B calorimetric power meter is then used for measuring the power of the gas laser in two points: before entering the plasma chamber (immediately after diaphragm A), and before the interference filter I. In this way, the gas laser DC signal is calibrated in power. We make use of the following notation.

$\Gamma(t)$: the power (varying in time) that the diaphragm H receives from the plasma per unit radian frequency.

$$\Gamma = \frac{\text{erg}}{\left(\frac{\text{rad}}{\text{sec}}\right) \text{ sec}}$$

$\xi_{\text{sharp cut}}$: the transmission of the sharp cutoff filter at $6328 \text{ \AA} = 90\%$.

$\xi_{\text{IF}} \Delta\omega_{\text{IF}}$: the product of the bandwidth of the cascade of the two interference filters for the average transmission of the cascade itself

$$\xi_{\text{IF}} \Delta\omega_{\text{IF}} = 8.4 \times 10^{11} \frac{\text{rad}}{\text{sec}}$$

$$\Delta\omega_{\text{IF}} = 7.26 \times 10^{12} \frac{\text{rad}}{\text{sec}}.$$

ξ_{pol} : the transmission of the polarizer for unpolarized light = 34%.

ξ_{silv} : the reflectivity of each silvered mirror, E and F, for light at 6328 \AA (80%).

(XI. PLASMA PHYSICS)

ξ_{PM} : the efficiency of the photomultiplier at 6328 Å.

L: the load of the photomultiplier tube (38Ω).

Then we can write

$$\Gamma(t) \xi_{\text{sharp cut}} \xi_{IF} \Delta\omega_{IF} \xi_{\text{pol}} \xi_{\text{silv}}^2 \xi_{PM} L = V_{\text{plasma emission}}^{(t)} \quad (15)$$

where $V_{\text{plasma emission}}^{(t)}$ is the signal from the plasma (see Fig. XI-30) given by the photomultiplier. The transmittance of the lens and the quartz windows is not included. Equation 15 is the emission equation. We then introduce the following notation.

$P_L = \frac{\text{erg}}{\left(\frac{\text{rad}}{\text{sec}}\right) \text{sec}}$, the gas-laser power entering the plasma chamber during the calibration.

$\xi_{\text{POL. GL}}$: the transmittance of the polarizer for the polarized and parallel gas laser light = 70%.

$\xi_{IF \text{ PEAK SHARP}}$: the peak transmittance of the interference filter, I, for the gas laser light at 6328 Å = 50%.

$\xi_{IF \text{ PEAK NONSHARP}}$: the peak transmittance of the IF filter, D (20 Å bandwidth).

$\Delta\omega_L$: the bandwidth of the gas-laser light. (Keep in mind that an attenuator neutral filter with transmittance $\xi_{ATT} = 18.5\%$ was put in front of the photomultiplier tube during the calibration to have the tube working in the linear regime.)

Then we can calibrate the optical system.

$$P_L \xi_{\text{sharp cut}} \xi_{\text{POL. GL}} \xi_{IF \text{ PEAK SHARP}} \xi_{IF \text{ PEAK NONSHARP}} \Delta\omega_L \xi_{\text{silv}}^2 \xi_{ATT} \xi_{PM} L = V_{\text{steady}}, \quad (16)$$

where V_{steady} is the signal (in volts) from the DC gas laser on the oscilloscope during the calibration. Indicating, with M, the power of the gas-laser beam, measured in milliwatts by the calorimeter before the interference filter, I, we can write

$$P_L \xi_{\text{SHARP CUT}} \xi_{\text{POL. GL}} \xi_{IF \text{ PEAK NONSHARP}} \Delta\omega_L \xi_{\text{silv}}^2 = M. \quad (17)$$

With the use of Eq. 17, Eq. 16 becomes

$$M \xi_{IF \text{ PEAK SHARP}} \xi_{ATT} \xi_{PM} L = V_{\text{steady}} \quad (18)$$

Calling $\frac{V(t)}{V_{\text{steady}}} = K(t)$ and using Eq. 18, we can rewrite Eq. 15 as follows:

$$\Gamma(t) \xi_{\text{SHARP CUT}} \xi_{\text{IF}} \Delta\omega_{\text{IF}} \xi_{\text{POL}} \xi_{\text{silv}}^2 \xi_{\text{PM}}^L = K(t) M \xi_{\text{IF PEAK SHARP}} \xi_{\text{ATT}} \xi_{\text{PM}}^L$$

from which we get

$$\Gamma(t) = K(t) \frac{\xi_{\text{IF PEAK SHARP}} \xi_{\text{ATT}}}{\xi_{\text{SHARP CUT}} \xi_{\text{IF}} \Delta\omega_{\text{IF}} \xi_{\text{POL}} \xi_{\text{silv}}^2} \cdot M$$

$$\Gamma(t) = K(t) M 5.6 \times 10^{-13}.$$

The presence of the quartz window of the plasma chamber and of a quartz slab used to set the gas laser beam in position bring the factor 5.6×10^{-13} to the value 6.4×10^{-13} . We finally obtain

$$\Gamma(t) = K(t) M 6.4 \times 10^{-13}. \quad (19)$$

By calibrating with the gas laser at a value $V_{\text{steady}} = 20$ mV on the oscilloscope, a power $M = 0.078$ mW was measured with the calorimeter. Equation 19 then becomes

$$\Gamma(t) = K(t) 5 \times 10^{-10}, \quad (20)$$

where $\Gamma(t)$ is measured in $\frac{\text{erg}}{\left(\frac{\text{rad}}{\text{sec}}\right) \text{sec}}$, and $K(t)$ is a pure number directly obtained from the emission signal of the plasma. The problem now is to relate the emission power, per unit radian frequency, $\Gamma(t)$, collected by the diaphragm H to the source function S_{ω} of the plasma, that is, the well-known Planck function

$$S_{\omega} = \frac{\hbar\omega^3}{4\pi^3 c^2} \frac{1}{e^{\left(\frac{\hbar\omega}{kT}\right)} - 1} \frac{\text{erg}}{\left(\frac{\text{rad}}{\text{sec}}\right) \text{sterad cm}^2 \text{sec}}. \quad (21)$$

Figure XI-31 shows the model for calculating $\Gamma(t)$, that is, the radiation power per unit frequency received by diaphragm H from the plasma cylinder situated 183 cm away. The angle ψ is practically zero. The radiation received by the diaphragm H and emitted by the elementary surface centered in P comes

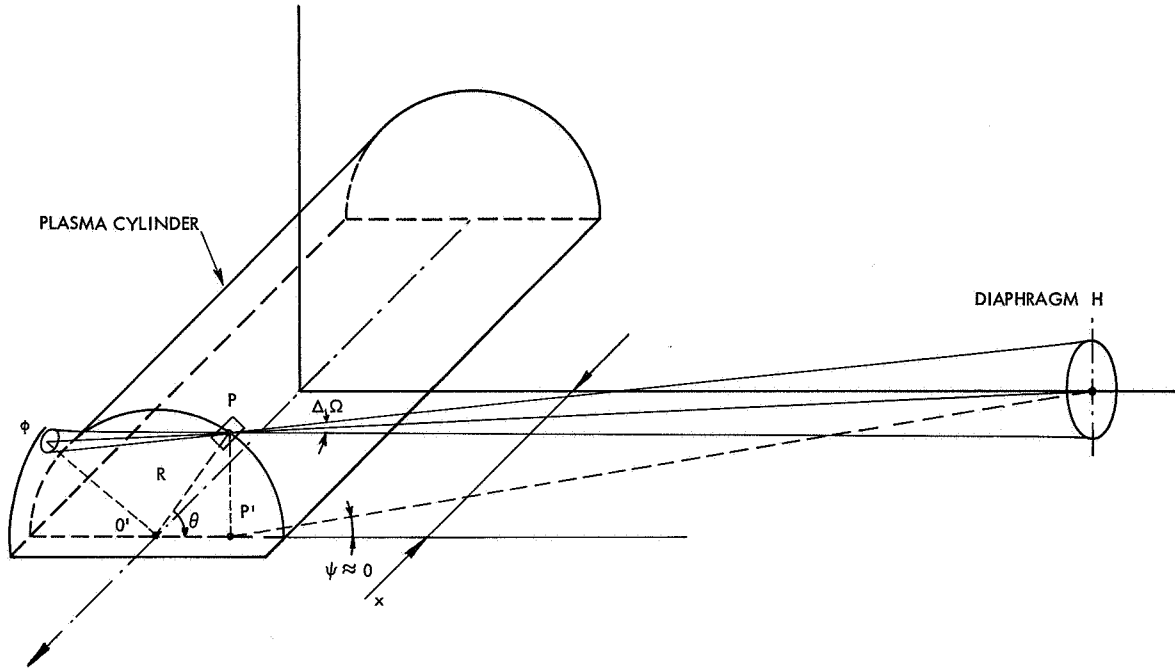


Fig. XI-31. Plasma model for calculating the radiation received from diaphragm H.

from the cone of the plasma with vertex in P and base in Q that sees the aperture of H.

$$\Gamma(t) = \Delta\Omega S_{\omega} LR \int_{-\pi/2}^{\pi/2} [1 - e^{-2R\alpha \cos \theta}] \cos \theta \, d\theta, \quad (22)$$

where $\Delta\Omega$ is the solid angle through which P sees the diaphragm H, L is the length of the plasma (cm) at time t, R is the radius of the plasma at time t, that is,

$$\Gamma(t) = \Delta\Omega S_{\omega} LR [2 - I(z)],$$

where

$$I(z) = \int_{-\pi/2}^{\pi/2} e^{z \cos \theta} \cos \theta \, d\theta$$

and $z = -2\alpha R$.

By developing the exponential in a series of Bessel functions

$$e^{z \cos \theta} = I_0(z) + 2 \sum_{K=1}^{\infty} I_K(z) \cos(K\theta)$$

the integral is solved and becomes

$$I = 2I_0(z) + \pi I_1(z) + 4 \sum_{n=1}^{\infty} \frac{I_{2n}(z)(-1)^{n+1}}{4n^2 - 1}. \quad (23)$$

Equation 22 then becomes

$$\Gamma(t) = \Delta\Omega S_{\omega}(t) L(t) R(t) 2 \left[1 - I_0(z) - \frac{\pi}{2} I_1(z) - 2 \sum_{n=1}^{\infty} \frac{I_{2n}(z)(-1)^{n+1}}{4n^2 - 1} \right],$$

where z is the reciprocal of the optical thickness of the plasma whose behavior, in

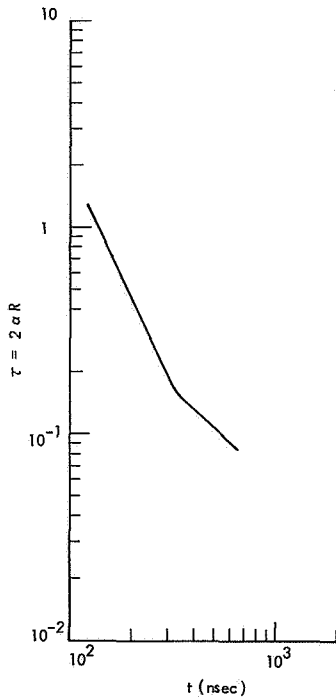


Fig. XI-32. Radial plasma optical thickness.

time, is known (Fig. XI-32). Calling $f(z)$ the quantity enclosed in square brackets, we have

$$\Gamma(t) = \Delta\Omega S_{\omega}(t) L(t) R(t) 2f[z(t)]. \quad (24)$$

Developing the Bessel functions in series

$$I_r(z) = \left(\frac{z}{2}\right)^r \sum_{K=0}^{\infty} \frac{\left(\frac{z^2}{4}\right)^K}{K! \Gamma(r+K+1)},$$

changing $-z$ in τ (optical thickness of the plasma), we get

(XI. PLASMA PHYSICS)

$$f(z) = \phi(\tau) = \tau(0.785) - \tau^2(0.333) + \tau^3(9.8 \times 10^{-2}) - \tau^4(2.22 \times 10^{-2}) + \tau^5(4.08 \times 10^{-3}) - \tau^6(6.35 \times 10^{-4}). \quad (25a)$$

Figure XI-33 is a plot of $f(z)$; the straight line is the approximated $f(z)$ obtained by developing the exponential $e^{z \cos \theta}$ as $1 + z \cos \theta$ and neglecting higher order terms. The

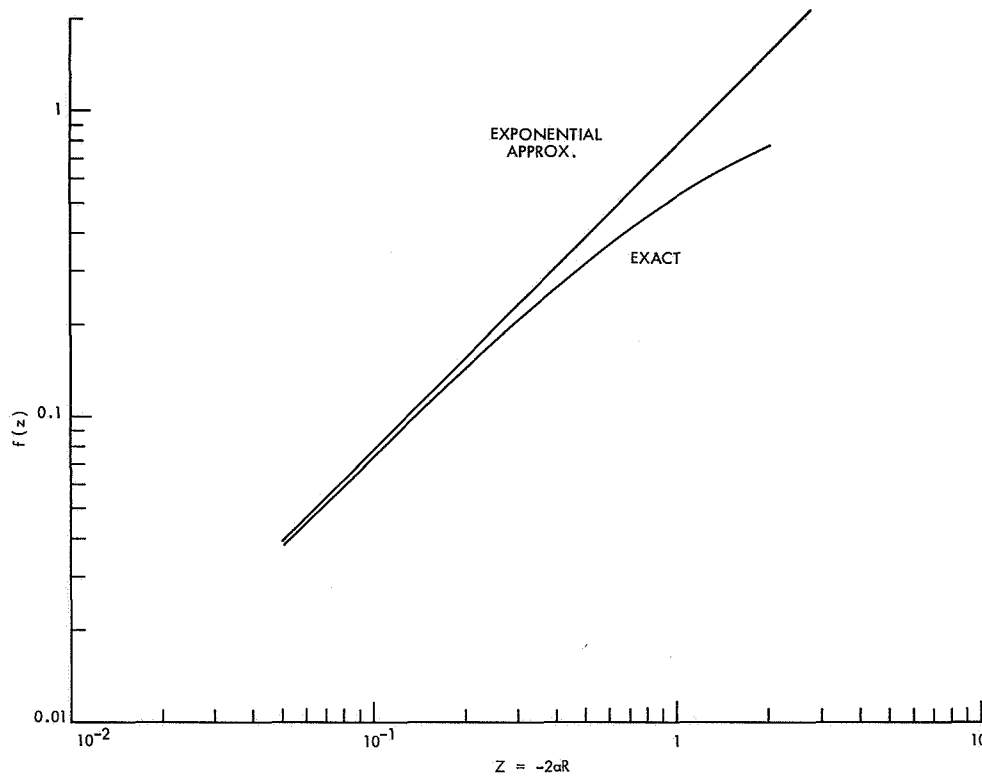


Fig. XI-33. Integrated absorptivity.

corresponding $\phi(\tau)$ is just the first-order term of $f(z)$ complete.

The source function S_ω is now readily known. Reading from three emission curves like the one in Fig. XI-30 (for calculating the error bars), the values of $K(t)$ versus time, $\Gamma(t)$ is known immediately from (20) and (24). Remembering that $2\Delta\Omega = 1.25 \times 10^{-4}$ steradian, we get

$$S_\omega(t) = 4 \times 10^{-6} \frac{K(t)}{L(t) R(t) f[z(t)]} \text{ (CGS System)}. \quad (25b)$$

Introducing in (25b) the known quantities $K(t)$, $L(t)$, $R(t)$ $f[z(t)] = \phi[\tau(t)]$, we finally get $S_\omega(t)$ (Fig. XI-31). From $S_\omega(t)$ known at the frequency of the HeNe gas-laser line at

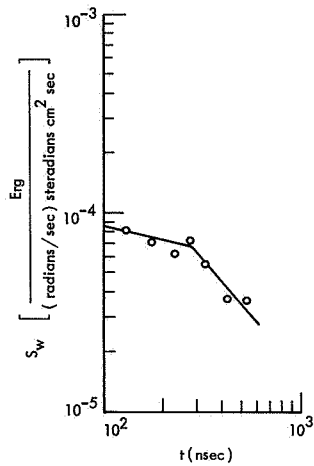


Fig. XI-34. Planck function $S_{\omega} = \frac{\hbar\omega^3}{4\pi^3 c^2} \frac{1}{e^{\frac{\hbar\omega}{kT}} - 1}$.

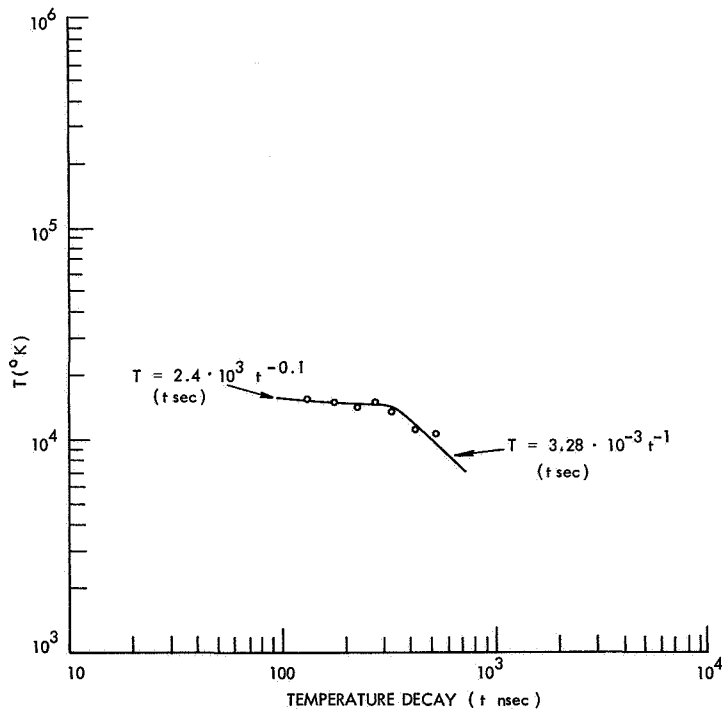


Fig. XI-35. Temperature decay.

(XI. PLASMA PHYSICS)

$\omega = 2.975 \times 10^{15}$ rad/sec, the temperature is immediately obtained (Fig. XI-35). The decay is practically isothermal up to the time when the shock wave in the radial direction starts to be emitted; the decay then goes as t^{-1} up to ~600 nsec.

5. Temperature Density Dependence

Plotting the density (in the central part of the plasma) against the temperature, we find (Fig. XI-36) that, for times larger than 300 nsec, the temperature goes as $T \propto N^{2/3}$,

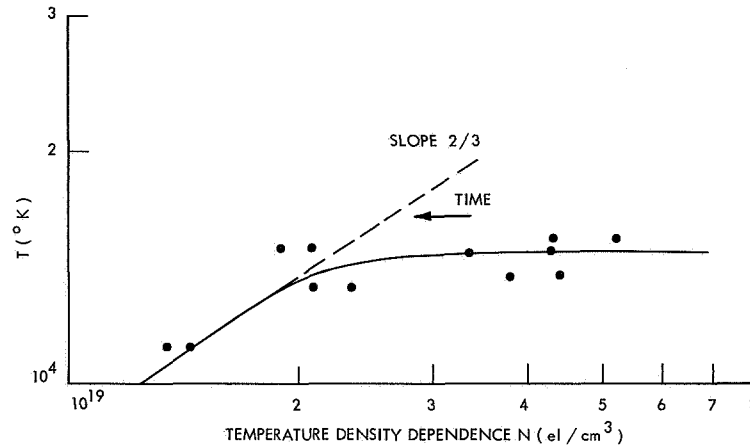


Fig. XI-36. Density vs temperature.

that is, the dependence is adiabatic during the shock wave emission.⁹ This fact can be shown better if we calculate the entropy per electron from the Sackur-Tetrode formula for a perfect gas.¹⁰

$$\frac{S}{N_{\text{total}}} = k \ln \left[\frac{1}{N} e \left(\frac{2\pi M}{h^2} \right)^{3/2} (kT)^{3/2} \right] + \frac{3}{2} k \quad (26)$$

where

h is Planck's constant

M is the mass of the electron

k is Boltzmann's constant

N is the density of the electrons

N_{total} is the total number of electrons in the plasma

e is the base of natural logarithms.

The function $\frac{S}{N_{\text{total}}}$ is plotted against the time in Fig. XI-37, in which it is clearly seen that the entropy per single electron, which before the shock emission is

$$\frac{S}{N_{\text{total}}} = 0.6 \times 10^{-23} \ln(t) + \text{constant}, \quad (27)$$

changes to a constant value, when the radial shock starts to come out from the plasma. This change of slope is found also in the density; a possible explanation is that the plasma while exploding and not starting to emit the shock wave is strongly shock-ionizing the gas met by its explosive front. When the shock starts to emerge from the plasma

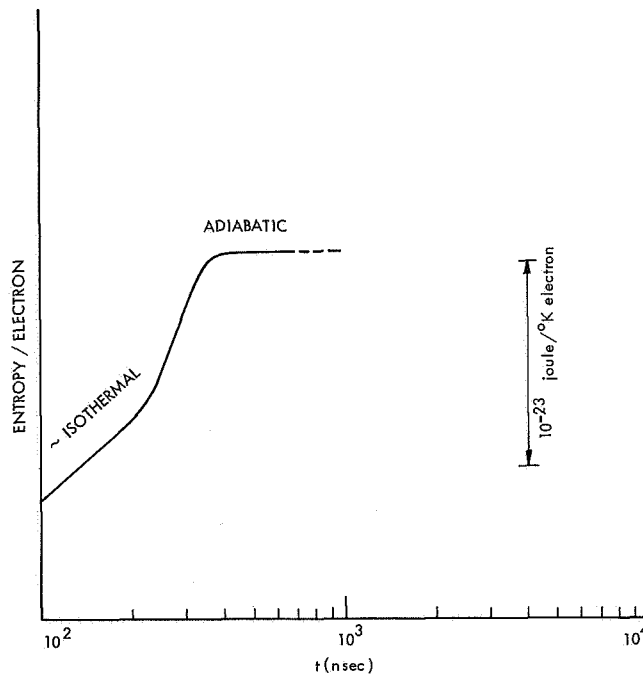


Fig. XI-37. Entropy per electron.

surface, the expansion is strongly slowed down and the shock ionization stops and does not compensate any more for the recombination loss; the dependence on time of the density then drops from $t^{-0.62}$ to $t^{-1.55}$. The fact that the measured density corresponds to the central high part of the density profile and so is not the average density through the plasma section is confirmed by the fact that the measured values of the absorption coefficient over the square of the density α/N^2 are lower by a factor of ~ 100 with respect to the theoretical value of α/N^2 calculated by Brussard¹¹ from the theory of inverse Bremsstrahlung absorption, where both free-free and free-bound collisions are kept in view. The contribution attributable to electron-neutral collisions is negligible. The

(XI. PLASMA PHYSICS)

Brussard approximated formula gives

$$\frac{a}{N^2} = 2.31 \times 10^{-38} y^{1/2} (e^y - 1) G_{ff} (\text{cm}^5), \quad (28)$$

where $y = \frac{\hbar\omega}{kT} = \frac{2.247 \times 10^4}{T}$, for the HeNe laser frequency, and G_{ff} is the Gaunt factor for free-free collision. A density profile like $N = N_o \left[1 - \left(\frac{r}{R} \right)^2 \right]^3$ would give a peak-average ratio of 8 which is fairly satisfying. More experimental data are needed to justify such a profile-shape analysis. A more detailed study of the plasma transmission should be done for this purpose.

From knowledge of the volume of the plasma, it is possible to know the energy that is spent by the plasma in expanding against the gas and in emitting the shock wave, just by multiplying the volume of the plasma by the external unperturbed gas pressure. For time up to 200 nsec the work is given by

$$L = 1.1 \times 10^{11} t^{1.8} \text{ Joules (t sec)}. \quad (29)$$

The corresponding power is immediately calculated by deriving the energy. A peak value of 6×10^5 watts is found at 200 nsec.

6. Initial Temperature Estimate

Starting from the volume of the plasma at very short times, when the giant pulse is still on, and when total ionization is supposed to be achieved, we can calculate the initial electron temperature. From the initial length of the plasma (4.5 mm) and the initial diameter, $D = f\theta$, where f is the focal length of the lens ($f = 68$ mm), and θ is the divergence of the ruby beam (f mrad), we get $D = 3.4 \times 10^{-2}$ cm, and $V_{\text{initial}} = 4.1 \times 10^{-4} \text{ cm}^3$. Supposing reasonably total ionization when the giant pulse is on, we get an initial number of electrons $N_{\text{initial}} = 10^{17}$ electrons. Knowing the ionization energy of Helium $E_{\text{ion}} = 24.58 \text{ eV} = 3.93 \times 10^{-18}$ joule, we get immediately the energy spent in breaking down the initial crowd of atoms $E_{\text{ion initial}} = 3.9 \times 10^{-1}$ joules $\approx 4 \times 10^{-1}$ joules. Assuming that, of the 2.5 joules emitted by the laser, approximately 10% is reflected back by the entry window, we find available immediately after the breakdown approximately 1.8 joules. Extrapolating the volume curve, we find the initial volume $V = 4.1 \times 10^{-1} \text{ cm}^3$ at a time of ~ 10 nsec. In doing a pessimistic calculation of the temperature, we keep in mind that at 10 nsec after breakdown $\sim 25\%$ of the energy from the ruby has been emitted. Then the energy available for heating the plasma at a time of ~ 10 nsec is 0.45 joule. The absorption coefficient measured at 6328 \AA is not very far away from the absorption coefficient for the ruby light at 6943 \AA ; at 100 nsec the measured absorption coefficient at 6328 \AA is $\sim 6 \text{ cm}^{-1}$. Assuming this value also for shorter time and using as a value for the length

of the plasma the initial length 4.5 mm, we get an optical longitudinal thickness of 2.7. The absorbed fraction of the initial ruby energy is then, at least, $1 - e^{-2.7} = 93\%$, and so the initial crowd of electrons and ions has a total thermal energy of ~ 0.4 joule. The corresponding temperature is immediately found. Assuming thermal equilibrium between ions and electrons, we have

$$E = \frac{0.4}{2 \times 10^{17}} = 2 \times 10^{-18} \text{ joule/electron.}$$

Since $E = 3/2 kT$, we find $T = 9.6 \times 10^4 \approx 10^5$ °K corresponding to 12.4 eV. The radiation loss and the extremely fast expansion cause a very fast drop of the temperature before 100 nsec. The experiment cannot give information on the temperature before 130 nsec, because of the impossibility of measuring the absorption coefficient for shorter times. In doing this measurement the experimenter should use a powerful gas laser (power of the order of 10-50 mW), so that, by bringing the lens G closer to the plasma, a larger solid angle of scattered gas-laser light could be detected by the diaphragm H; in this way, a larger emission power would be received by H. This fact would necessitate having a very powerful gas laser, since the signal must be attenuated in order not to saturate the photomultiplier tube. A weak gas-laser signal would be lost in the noise.

G. Lampis

References

1. G. Lampis, Quarterly Progress Report No. 81, Research Laboratory of Electronics, M.I.T., April 15, 1966, pp. 58-61.
2. G. Lampis, Quarterly Progress Report No. 83, Research Laboratory of Electronics, M.I.T., October 15, 1966, pp. 41-52.
3. *Ibid.*, see Fig. VII-4, p. 45.
4. *Ibid.*, see Fig. VII-8, p. 48, and Fig. VII-12, p. 52.
5. S. A. Ramsden and P. Savic, *Nature*, p. 1217, September 1964.
6. Yu. P. Raizer, *Soviet Phys. - JETP* 21, 1009 (1965).
7. G. V. Ostrovskaya, Yu. I. Ostrovskii, *JETP Letters* 4, No. 4 (1966).
8. G. A. Askar'yam, M. S. Rabinovich, et al., *Soviet Phys. - JETP* 1, 162 (1965).
9. M. M. Litvak and D. F. Edwards, "Electron Recombination in Laser Produced Hydrogen Plasma," Lincoln Laboratory, M.I.T., 1965.
10. C. Kittel, Elementary Statistical Physics (John Wiley and Sons, Inc., New York, 1965), p. 35.
11. P. J. Brussard and H. C. van de Hulst, *Rev. Modern Phys.* 34, 507 (1962).

(XI. PLASMA PHYSICS)

G. MICROWAVE EMISSION FROM n-TYPE INDIUM ANTIMONIDE
AT 422°K AND 77°K*

Larrabee¹ and Hicinbothem² were the first to observe microwave emission from n-type InSb when a sample was subjected simultaneously to DC magnetic and electric fields. The threshold values of B and E for onset of the emission were approximately 3000 Gauss and 200 V/cm, respectively. At these high electric fields, electron-hole avalanche occurs, and Steele³ attributes the microwave emission to photoconductive mixing of band-gap radiation associated with this avalanche breakdown.

Buchsbaum, Chynoweth, and Feldmann,⁴ and others,⁵⁻⁷ have found another regime of microwave emission at relatively low electric fields ($E \approx 10$ V/cm), well below values of E required for avalanche breakdown, where the sample exhibits nearly linear current-voltage characteristics. This report is concerned exclusively with this low-field regime.

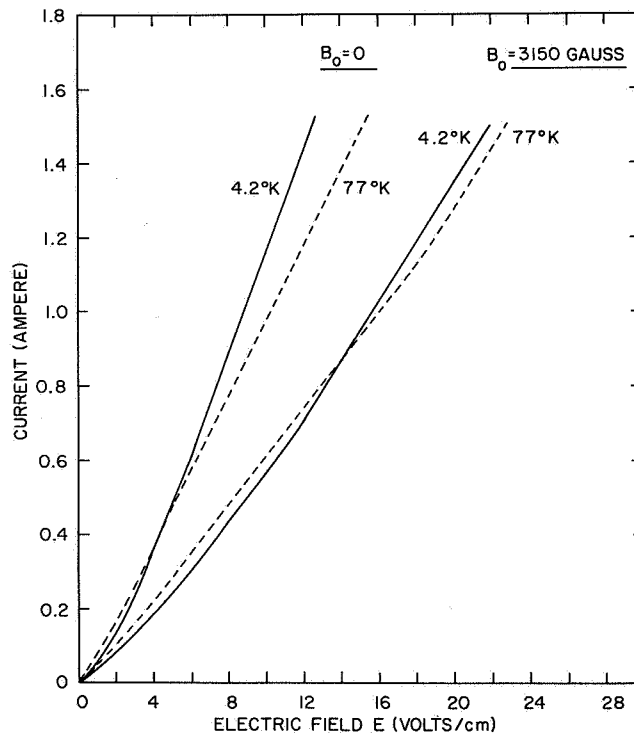


Fig. XI-38. Voltage-current characteristics of a sample of InSb.

Figure XI-38 illustrates the current-voltage characteristics as measured at 77°K and 4.2°K for the range of parameters in which studies of the microwave emission were

* This work was supported in part by the Joint Services Electronics Programs (U. S. Army, U. S. Navy, and U. S. Air Force) under Contract DA 28-043-AMC-02536(E).

made. In this, as in all succeeding experiments, the static magnetic field was parallel to the electric field.

The specific instability that gives rise to the microwave emission at low DC electric fields is not known. It has been suggested^{8,9} that the instability arises from phonons that are excited by the drifting electrons. The unstable longitudinal wave then couples to an electromagnetic wave at the boundary of the sample. If this is indeed

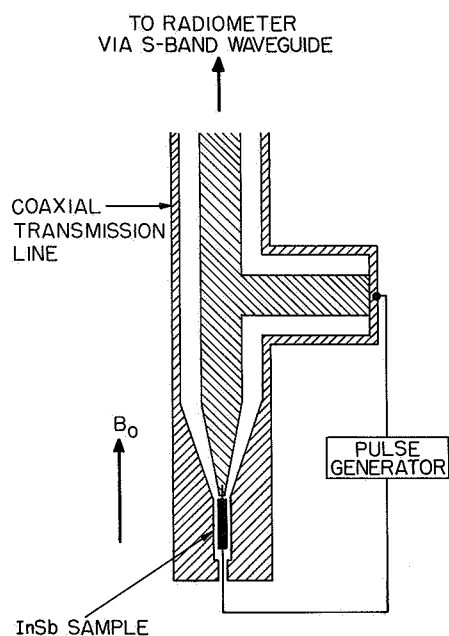


Fig. XI-39. Experimental arrangement used in the measurements of microwave noise.

the mechanism, the phonon lifetime plays a crucial role in the determination of the threshold magnetic and electric fields for onset of instability. Theory^{8,9} indicates that the threshold in electric field requires that the electron drift velocity exceed the sound velocity, while the threshold in magnetic field decreases as the phonon lifetime increases. Since the phonon lifetime at 4.2°K is much longer¹⁰ than at 77°K, the microwave emission at 4.2°K (if, in fact, it exists at this temperature) should set in at a lower value of B . To see this change in threshold was one of the motivations for the experiments described here.

A bar of InSb, $1 \times 1 \times 10 \text{ mm}^3$, cut along the (110) crystal axis, was mounted near a shorted coaxial transmission line as shown in Fig. XI-39.

All samples were cut from one block. For our block, the Hall mobility at 77°K and 4.2°K was in the range $2-5 \times 10^5 \text{ cm}^2 \text{ Volts}^{-1} \text{ sec}^{-1}$, and the carrier concentration was in the range $1-2 \times 10^{14} \text{ cm}^{-3}$. The surface of the sample was lapped and then etched in a Bromine-Ethanol solution. The coaxial line was tapered to allow for better RF impedance matching between the sample and a standard 50-ohm line. The entire assembly was immersed in liquid nitrogen or liquid helium kept at a constant level. The sample was bathed continuously by the coolant and good circulation of the liquid was insured by a number of holes drilled in the coaxial line. The axis of the sample and the DC current flow were parallel to the static magnetic field (with uncertainties in angle of less than $\pm 2^\circ$ of arc) in all the experiments reported here. The magnetic field was uniform to better than 0.5 per cent over the volume of the sample. Current pulses of 2.5- μsec duration were applied to the sample (at a repetition rate of 200 pulses/sec) through

(XI. PLASMA PHYSICS)

indium soldered contacts. Tin solder was also used with no observable changes in the voltage-current or microwave emission characteristics. It was also ascertained that no changes occurred when the pulse length was increased from 2.5 μ sec to 7 μ sec, thereby indicating that no significant heating of the crystal occurred.

The microwave signal was led through the coaxial transmission line, past a double-stub tuner and S-band waveguide to a time-resolved radiometer¹¹ that operated at a fixed frequency of 3000 Mc/sec, with an IF bandwidth of 10 Mc/sec. The IF amplifier was gated with a 2- μ sec gate so that the noise emission was received only during the central portion of the 2.5- μ sec current pulse. The noise power from the sample was compared repetitively with the noise power emitted by a standard noise source that had an equivalent noise temperature of 18,500°K. Thus the absolute noise power from the sample could be measured.

Figure XI-40 is a plot of the threshold magnetic field as a function of the threshold

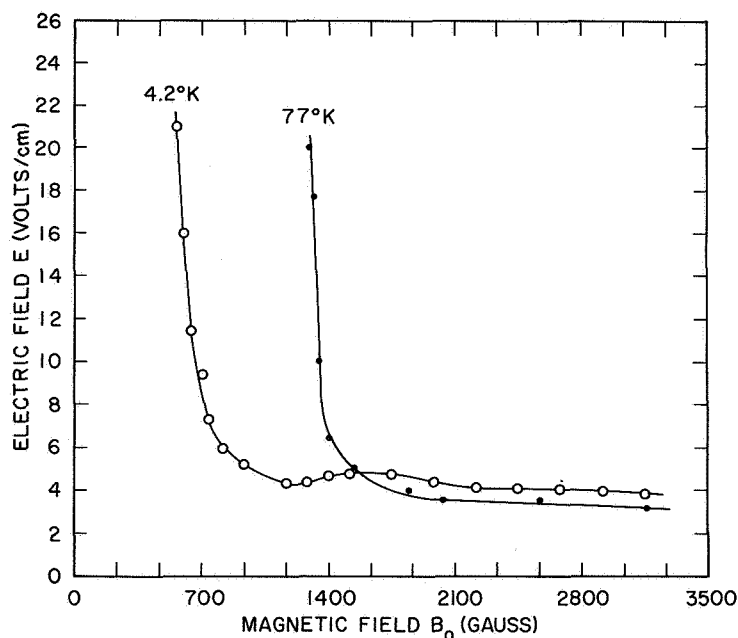


Fig. XI-40. Threshold electric field vs threshold magnetic field. Emission occurs above and to the right of a given line.

electric field for measurements on a given sample at 4.2°K and 77°K. Threshold is defined as that value of B and E for which the emitted noise power had an equivalent temperature of 100°K. This value of temperature is near the limit of sensitivity of our radiometer. The results shown for 77°K agree qualitatively with observations of Musha et al.⁵ We see from Fig. XI-40 that the threshold magnetic field for onset of

emission at 4.2°K is approximately half that at 77°K.

The dependence of the radiation intensity on magnetic field (above threshold) is illustrated in Fig. XI-41 for different values of electric field. These measurements made at

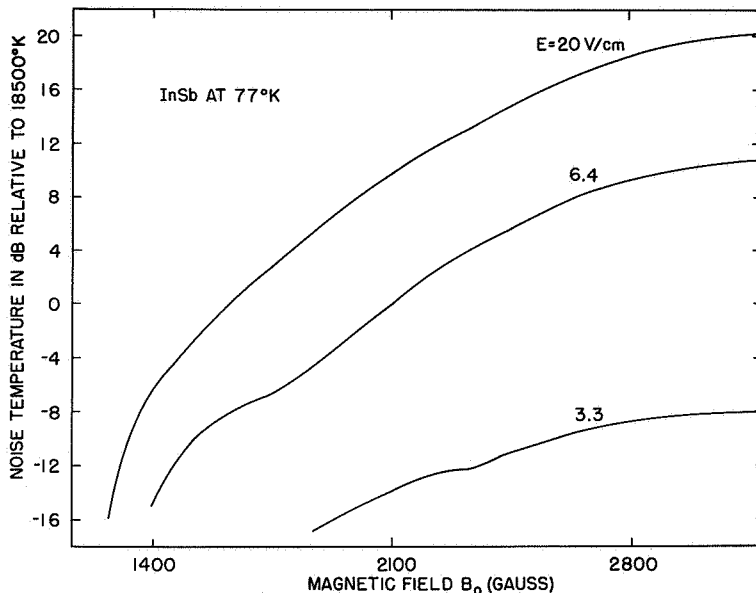


Fig. XI-41. Noise-power output as a function of magnetic field for various values of applied electric field, at 77°K.

77°K are qualitatively the same as those obtained by Buchsbaum et al.⁴ Figure XI-42 shows how the emitted intensity varies with electric field at constant magnetic field. This and the previous figure exhibit clearly the sharp threshold values of E and B. Data such as these were used in plotting the threshold curves of Fig. XI-40.

Measurements of the emission as a function of magnetic field made at 4.2°K differ quite dramatically from those shown in Fig. XI-41. We now see in Fig. XI-43 that superposed on the monotonically increasing background emission are resonant spikes. Such spikes do not occur at 77°K.

We have labeled the spikes with a series of integers n from 1 to 11. As the electric field on the sample is decreased, a given spike moves to higher values of magnetic field. This increase in B is very nearly the same as the corresponding increase in the threshold value of B shown in Fig. XI-40 for the monotonic "continuum" radiation. Indeed, at some values of E, the first spike occurs precisely at the threshold of the "continuum" radiation (see spike n=1 of Fig. XI-43). These observations suggest that the "spikey" and "continuum" emission processes are coupled to one another.

A given spike n is sometimes not excited or it is too small to be resolved. This is

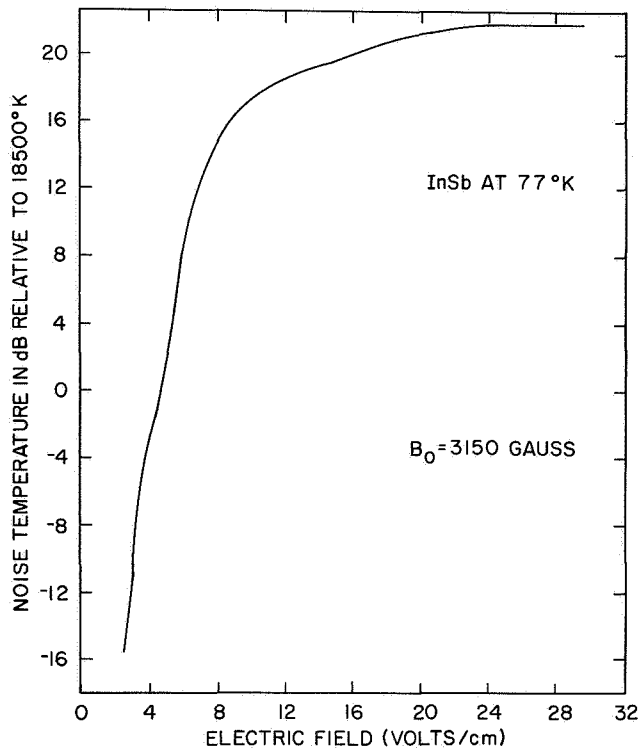


Fig. XI-42. Noise power as a function of electric field measured at 77°K.

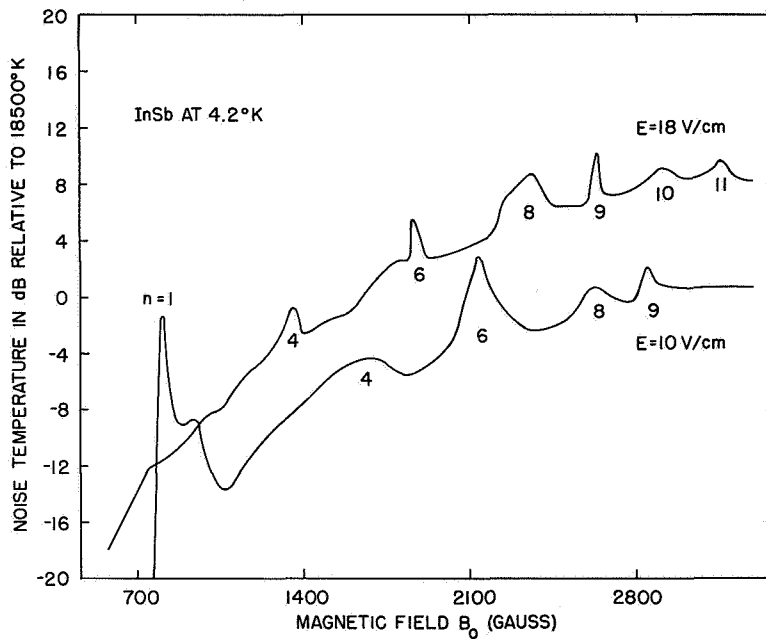


Fig. XI-43. Noise-power output as a function of magnetic field, as measured at 4.2°K. (This figure should be compared with Fig. XI-41.)

indicated in Fig. XI-43. For example, for $E = 18 \text{ V/cm}$, spikes 1, 2, 3, 5, 7 are missing. If we accept this possibility of missing spikes, we are led to the conclusion that the spikes are nearly equally spaced with a spacing of approximately 255 Gauss. This fact is confirmed in Fig. XI-44 where the magnetic field value of a given spike n is plotted as a function of n .

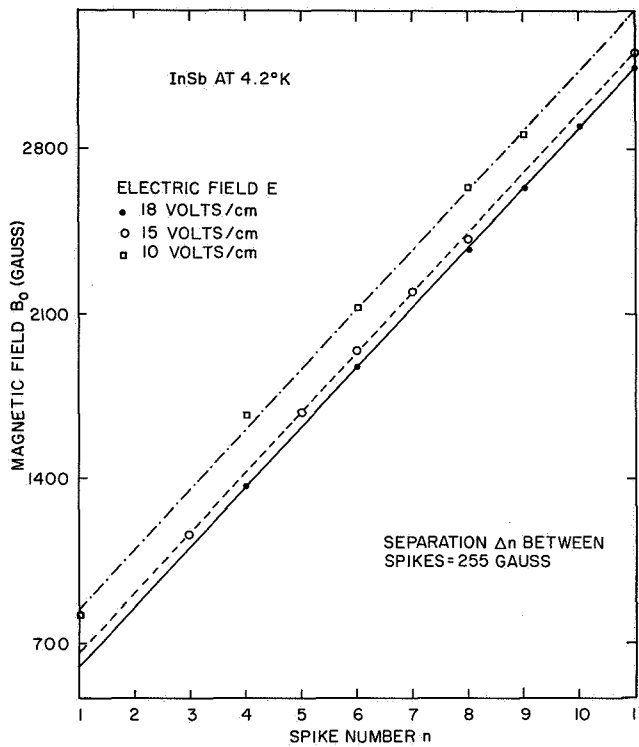


Fig. XI-44.

Position in magnetic field of a given spike, n , as a function of n . The labeling of the spikes is as shown in Fig. XI-43. Note that whether or not a spike is missing appears to be a random event.

All of the observations above refer to measurements made on a single sample of InSb and for one polarity of the applied electric field. When the polarity was reversed the only significant change was in the over-all power level of the continuum radiation. Changes as high as 5 db were noted. Different samples exhibited variations of power level by as much as 10 db. The separation between spikes from sample to sample varied, however, less than 5 per cent.

G. Bekefi, A. Bers

References

1. R. D. Larrabee, Bull. Am. Phys. Soc. 9, 258 (1964).
2. R. D. Larrabee and W. A. Hicinbothem, Proc. Symposium on Plasma Effects in Solids, Paris, 1964, Vol. 2, p. 181.
3. M. C. Steele, RCA Review 27, 263 (1966).

(XI. PLASMA PHYSICS)

4. J. Buchsbaum, A. G. Chynoweth, and W. L. Feldmann, *Appl. Phys. Letters* 6, 67 (1965).
5. T. Musha, F. Lindvall, and J. Hagglund, *Appl. Phys. Letters* 8, 157 (1966).
6. D. K. Ferry, R. W. Yound, and A. A. Dougal, *J. Appl. Phys.* 36, 3684 (1965).
7. J. C. Eidson and G. S. Kino, *Appl. Phys. Letters* 8, 183 (1966).
8. A. Bers and T. Musha, Quarterly Progress Report No. 79, Research Laboratory of Electronics, M. I. T., October 15, 1965, pp. 99-109.
9. T. Musha and A. Bers, *Bull. Am. Phys. Soc.* 11, 569 (1966).
10. K. W. Nill, Ph.D. Thesis, Department of Electrical Engineering, M. I. T., May 1966; Proc. Int. Conf. Phys. of Semiconductors, Kyoto, Japan, 1966, p. 755.
11. G. Bekefi, Radiation Processes in Plasmas (John Wiley and Sons, Inc., New York, 1966), p. 334.
12. S. R. J. Brueck and A. Bers, Quarterly Progress Report No. 83, Research Laboratory of Electronics, M. I. T., October 15, 1966, pp. 72-76.

1-23
XII.3 GASEOUS ELECTRONICS* P 13 P

Academic and Research Staff

Prof. S. C. Brown
Prof. W. P. Allis

Prof. G. Bekefi
Prof. J. C. Ingraham

J. J. McCarthy
W. J. Mulligan

Graduate Students

W. B. Davis
G. A. Garosi

L. D. Pleasance

T. T. Wilheit, Jr.
B. L. Wright

A. ELECTRON COLLISIONAL EFFECTS ON WAVE PROPAGATION
IN A NONMAGNETIZED PLASMA

N67-27093

To account properly for the effect of electron-atom collisions on the propagation of waves in plasmas, it is necessary to utilize the Boltzmann collision integral.¹ This integral assumes only two-body collisions, and therefore is valid only for collisions involving short-range forces such as those occurring in electron-atom collisions.

Our treatment utilizes the Boltzmann collision integral and assumes that the electrons collide with particles of much greater mass. Thus, this treatment applies to electron-atom collisions. The calculation determines the form of the dispersion relation for the electron plasma wave in the presence of electron-atom collisions, and is a direct application of the method developed by Allis.¹

Generally, the Krook model^{2,3} is used to account for collisions when studying collisional effects on the electron plasma wave. The advantage of this method is that it can be applied readily to problems in which the electron temperature is high; for example, when the Larmor orbit is comparable with the wavelength perpendicular to \vec{B} , the mean-free path is long compared with the wavelength parallel to \vec{B} , and the thermal motion of the electrons parallel to \vec{B} introduces a significant Doppler shift of the plasma-wave frequency. It has the disadvantage that it is only an approximation to the collisional effect and, although it can be so formulated that it does not violate the conservation of plasma particles, it cannot be readily formulated in such a way that it also conserves plasma particle energy and accounts correctly for the angular and velocity dependence of the electron-atom scattering cross section. The method used in this report is cumbersome to apply to plasmas with high electron temperatures, but it does account exactly for the collisional effects. The results of the two methods will be compared at the end of the calculation.

The Boltzmann equation for the electron distribution function, f , in the absence of an applied magnetic field is

*This work was supported by the Joint Services Electronics Programs (U. S. Army, U. S. Navy, and U. S. Air Force) under Contract DA 28-043-AMC-02536(E).

(XII. GASEOUS ELECTRONICS)

$$\frac{\partial f}{\partial t} + \vec{v} \cdot \vec{\nabla}_r f - \frac{e}{m} \vec{E} \cdot \vec{\nabla}_v f = \left(\frac{\partial f}{\partial t} \right)_c, \quad (1)$$

where e/m is the electron charge-to-mass ratio, \vec{E} is the electric field, and $\left(\frac{\partial f}{\partial t} \right)_c$ represents the Boltzmann collision integral. The distribution function is expanded in Legendre polynomials, $P_\ell(\cos \theta)$, where θ is the angle between \vec{E} and the electron velocity, \vec{v} :

$$f = \sum_{\ell=0}^{\infty} f^\ell(r, v, t) P_\ell(\cos \theta). \quad (2)$$

This expression is substituted in both the right- and left-hand sides of (1), and the terms comprising the coefficients of each P_ℓ on each side of the equation are equated separately; this generates an infinite set of equations for the f^ℓ (the ratio of the electron-to-atom mass is set equal to zero, also):

$$\frac{\partial f^0}{\partial t} + v \frac{\partial f^1}{\partial z} - \frac{eE}{3mv^2} \frac{\partial}{\partial v} v^2 f^1 = 0 \quad (3)$$

$$\frac{\partial f^1}{\partial t} + v \frac{\partial}{\partial z} \left[f^0 + \frac{2}{5} f^2 \right] - \frac{eE}{m} \left[\frac{\partial f^0}{\partial v} + \frac{2}{5v^3} \frac{\partial}{\partial v} v^3 f^2 \right] = -\nu_{c1} f^1$$

...

$$\begin{aligned} \frac{\partial f^\ell}{\partial t} + v \frac{\partial}{\partial z} \left[\frac{\ell}{2\ell-1} f^{\ell-1} + \frac{\ell+1}{2\ell+3} f^{\ell+1} \right] - \frac{eE}{m} \left[\frac{\ell}{2\ell-1} v^{\ell-1} \frac{\partial}{\partial v} \frac{f^{\ell-1}}{v^{\ell-1}} \right. \\ \left. + \frac{\ell+1}{2\ell+3} \frac{1}{v^{\ell+2}} \frac{\partial}{\partial v} v^{\ell+2} f^{\ell+1} \right] = -\nu_{c\ell} f^\ell. \end{aligned}$$

It has been assumed that the perturbed distribution function does not depend on the x and y spatial coordinates, and the E field is assumed to be parallel to the z -axis. This is consistent with the effect of plasma wave propagation ($\vec{E} \parallel \vec{k}$) on the distribution function, in the absence of a magnetic field. The quantities $\nu_{c\ell}$ are weighted collision frequencies arising from the Boltzmann collision integral. They are given by

$$\nu_{c\ell} = 2\pi v n_g \int_{\theta=0}^{\theta=\pi} \sigma(\theta) (1 - P_\ell(\cos \theta)) \sin \theta \, d\theta, \quad (4)$$

where $\sigma(\theta)$ is the differential scattering cross section, v the electron velocity, and n_g the volume density of the gas atoms.

In the absence of the perturbing wave only the spherically symmetric, time-independent part of f , $f^0_O(v)$, is nonzero. The unperturbed distribution function, f^0_O , is so normalized that $\int f^0_O d^3v = n_O$, where n_O is the unperturbed electron density. Denoting

the time-dependent part of f^0 by f_1^0 , we obtain the linearized form of Eqs. 3:

$$\frac{\partial f_1^0}{\partial t} + \frac{v}{3} \frac{\partial f_1^0}{\partial z} = 0 \quad (5)$$

$$\frac{\partial f_1^1}{\partial t} + v \frac{\partial}{\partial z} \left[f_1^0 + \frac{2}{5} f_1^2 \right] - \frac{eE}{m} \frac{\partial f_1^0}{\partial v} = -v_{c1} f_1^1$$

...

$$\frac{\partial f_1^l}{\partial t} + v \frac{\partial}{\partial z} \left[\frac{l}{2l-1} f_1^{l-1} + \frac{l+1}{2l+3} f_1^{l+1} \right] = -v_{cl} f_1^l \quad (l > 1).$$

We next assume that all of the perturbed quantities and the electric field vary as $e^{-i(\omega t - kz)}$; thus we obtain for Eqs. 5

$$-i\omega f_1^0 + \frac{ikv}{3} f_1^0 = 0 \quad (6)$$

$$(-i\omega + v_{c1}) f_1^1 + ikv \left(f_1^0 + \frac{2}{5} f_1^2 \right) = + \frac{eE}{m} \frac{\partial f_1^0}{\partial v}$$

...

$$(-i\omega + v_{cl}) f_1^l + ikv \left[\frac{l}{2l-1} f_1^{l-1} + \frac{l+1}{2l+3} f_1^{l+1} \right] = 0 \quad (l > 1).$$

This infinite set of equations can be solved for f_1^0 to obtain

$$f_1^0 = \frac{-i \frac{eE}{m} \frac{kv}{3} \frac{\partial f_1^0}{\partial v}}{i\omega(i\omega - v_{c1}) + \frac{(kv)^2}{3} - \frac{4}{15} \frac{i\omega(kv)^2}{(-i\omega + v_{c2} + D)}}, \quad (7)$$

where D is a fraction of the form

$$D = \frac{9(kv)^2}{35 \left(-i\omega + v_{c3} + \frac{16(kv)^2}{63(-i\omega + v_{c4} + \dots)} \right)}, \quad (8)$$

and the general term in the fraction is

$$-i\omega + v_{cl-1} + \frac{l^2(kv)^2}{(4l^2 - 1) \left(-i\omega + v_{cl} + \frac{(\ell+1)^2(kv)^2}{(4(\ell+1)^2 - 1)(-i\omega + v_{cl+1} + \dots \text{etc.})} \right)}$$

(XII. GASEOUS ELECTRONICS)

We may now calculate the electron density perturbation, n_1 , which is due to the wave:

$$n_1 = n_o \int_0^\infty f_1^o 4\pi v^2 dv. \quad (9)$$

Poisson's equation for the electric field is

$$\nabla \cdot E = ikE = -\frac{n_1 e}{\epsilon_o}, \quad (10)$$

and combining (9) and (10), we obtain the dispersion relation for the wave

$$1 = \frac{4\pi}{3} \omega_p^2 \int_0^\infty \frac{v^3 \frac{\partial f_o^o}{\partial v} dv}{i\omega(i\omega - \nu_{c1}) + \frac{(kv)^2}{3} - \frac{4}{15} \frac{i\omega(kv)^2}{(-i\omega + \nu_{c2} + D)}}, \quad (11)$$

where $\omega_p = \sqrt{\frac{n_o e^2}{m\epsilon_o}}$ is the electron plasma frequency.

If f_o^o is Maxwellian, it follows that $\frac{\partial f_o^o}{\partial v} = -\frac{v}{v_o} f_o^o$, where $v_o^2 = \frac{kT}{m}$, and is of the order of the mean-square electron velocity. In this case Eq. 11 becomes

$$1 = -\frac{4\pi}{3} \frac{\omega_p^2}{v_o^2} \int_0^\infty \frac{v^4 f_o^o dv}{i\omega(i\omega - \nu_{c1}) + \frac{(kv)^2}{3} - \frac{4}{15} \frac{i\omega(kv)^2}{(-i\omega + \nu_{c2} + D)}}. \quad (12)$$

For a cold plasma in which $(kv)^2 \ll \omega(\omega^2 + \nu_{c1}^2)^{1/2}$, only the collision frequency ν_{c1} enters significantly into the damping. To account correctly for first-order temperature effects, it is seen from the denominator of (12) that the collision frequency ν_{c2} is also important. The last of the three terms in the denominator (see Eqs. 6) is absent if f^2 is assumed to be negligible and, therefore, f^2 must not be neglected in this treatment if the dispersion relation is to be correct to first order in temperature. It is seen that this treatment does not converge rapidly unless $\frac{(kv)^2}{\omega(\omega^2 + \nu_{c1}^2)^{1/2}} \ll 1$ and, therefore,

is not readily applied to cases in which the wave phase velocity is not much greater than the electron thermal velocity. Setting $D = 0$ is equivalent to assuming $f^l = 0$ for $l \geq 3$

in Eqs. 6, and will give us the correct first-order dependence on temperature of Eq. 12.

By setting $f_0^0 = \left(\frac{1}{2\pi v_0^2}\right)^{3/2} e^{-v^2/2v_0^2}$ and $D = 0$, Eq. 12 becomes

$$1 = -\frac{4\pi}{3} \frac{\omega_p^2}{v_0^2} \left(\frac{1}{2\pi v_0^2}\right)^{3/2} \int_0^\infty \frac{e^{-v^2/2v_0^2} v^4 dv}{(kv)^2 \left(i\omega(i\omega - \nu_{c1}) + \frac{3}{5} \left(1 + \frac{4}{5} \frac{i\omega}{i\omega - \nu_{c2}}\right) \right)}. \quad (13)$$

Bers and Musha⁴ have calculated the plasma wave dispersion relation, using the Krook model and assuming a collisional relaxation rate, ν_c , that is independent of velocity. Their result for zero magnetic field is

$$1 = -\frac{\frac{\omega_p^2}{k^2 v_0^2} [1 + \xi_0 Z(\xi_0)]}{1 + \frac{i\nu_c}{\omega + i\nu_c} \xi_0 Z(\xi_0)}, \quad (14)$$

where $\xi_0 = \frac{\omega + i\nu_c}{kv_0 \sqrt{2}}$, and $Z(\xi_0)$ is the plasma dispersion function.⁵ For low temperature, the asymptotic expansion of $Z(\xi_0)$ may be used. With Landau damping neglected, this is

$$Z(\xi_0) = -\frac{1}{\xi_0} \left(1 + \frac{1}{2\xi_0^2} + \frac{3}{4\xi_0^4} + \dots \right). \quad (15)$$

Substituting (15) in (14) and saving terms to first order in temperature in the numerator and denominator, we obtain, after some algebraic manipulations,

$$1 = \frac{\frac{\omega_p^2}{\omega(\omega + i\nu_c)} \left[1 + \frac{3k^2 v_0^2}{(\omega + i\nu_c)^2} \right]}{1 - \frac{i\nu_c}{\omega} \frac{k^2 v_0^2}{(\omega + i\nu_c)^2}}. \quad (16)$$

To first order in temperature Eq. 16 becomes

$$1 = \frac{\omega_p^2}{\omega(\omega + i\nu_c)} \left[1 + \frac{3k^2 v_0^2}{(\omega + i\nu_c)^2} \left(1 + \frac{i\nu_c}{3\omega} \right) \right]. \quad (17)$$

(XII. GASEOUS ELECTRONICS)

It is only possible to check Eq. 17 against Eq. 13 if we assume v_{c1} and v_{c2} to be velocity-independent in Eq. 13. Making this assumption, evaluating Eq. 13 to first order in temperature, and again neglecting the effect of Landau damping gives

$$1 = \frac{\omega_p^2}{\omega(\omega + iv_{c1})} \left[1 + \frac{3(kv_0)^2}{(\omega + iv_{c1})(\omega + iv_{c2})} \left(1 + \frac{5}{9} \frac{iv_{c2}}{\omega} \right) \right]. \quad (18)$$

If we consider a gas for which the scattering is isotropic, then $v_{c1} = v_{c2}$. For this case, Eqs. 17 and 18 agree very closely. For low-temperature plasmas and for $v_c \ll \omega$, this small error in the Krook model will not be important. In a plasma for which the electron scattering cross section is not isotropic and is strongly velocity-dependent, for instance, in an argon plasma, a deviation from the Krook model predictions of measured wave lengths and collisional damping effects might be observable.

J. C. Ingraham

References

1. W. P. Allis, "Motions of Ions and Electrons," Technical Report 299, Research Laboratory of Electronics, M. I. T., June 13, 1956, see Chap. III.
2. P. L. Bhatnagar, E. P. Gross, and M. Krook, *Phys. Rev.* 94, 511 (1954).
3. A. Bers and T. Musha, Quarterly Progress Report No. 79, Research Laboratory of Electronics, M. I. T., October 15, 1965, p. 104.
4. B. D. Fried and S. D. Conte, The Plasma Dispersion Function (Academic Press, Inc., New York, 1961).

A. Active Plasma Systems*

Academic and Research Staff

Prof. L. D. Smullin
Prof. A. Bers

Prof. R. J. Briggs
Prof. J. G. Siambis

Graduate Students

R. R. Bartsch
S. R. J. Brueck
S-L. Chou
J. A. Davis

F. N. Herba
B. R. Kusse
O. Lopez
J. A. Mangano
R. R. Parker

D. M. Perozek
H. M. Schneider
R. E. Tremain, Jr.
R. N. Wallace

1. SYSTEM C: EXCITATION OF AN ION-CYCLOTRON RESONANCE **N67-27094**

A method of exciting ion-cyclotron resonance by modulation of the electron beam normally used to create a beam-plasma discharge has been proposed.¹ This method of excitation is being investigated experimentally in System C. An RF pulse transformer has been used to modulate the 8-kV DC beam pulse with 4-kV peak-to-peak of

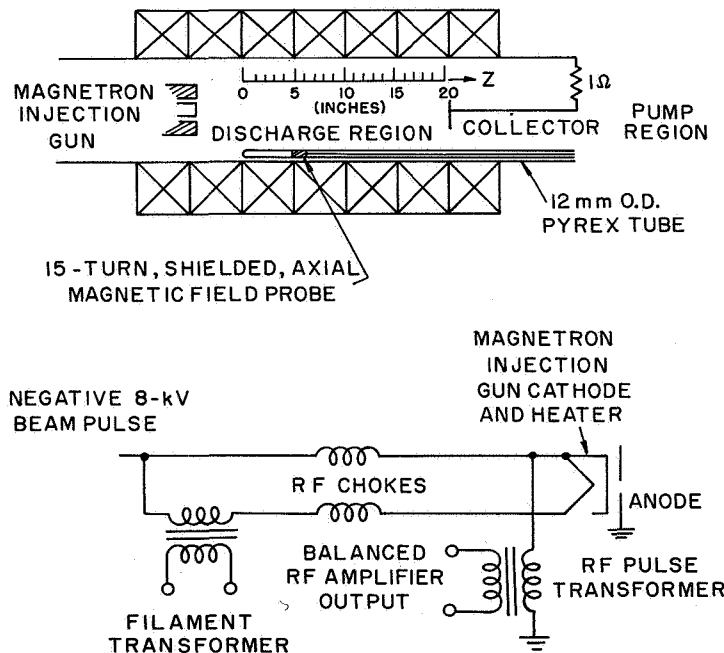


Fig. XIII-1. Upper: drift tube showing probe position and coordinate system. Lower: beam-pulse modulation circuit.

*This work was supported by the National Science Foundation (Grants GK-57 and GK-1165).

(XIII. PLASMAS AND CONTROLLED NUCLEAR FUSION)

RF voltage. The circuit is shown schematically in Fig. XIII-1. The driver and balanced output stages of an RF amplifier (10 kW) is keyed to provide an RF pulse of variable width and starting time. Under normal operating conditions, an RF pulse of 350- μ sec duration is turned on 150 μ sec after the beginning of the DC beam pulse (Fig. XIII-2). The width of the negative DC beam pulse is 700 μ sec, with a repetition rate of 2/sec. The modulation frequency may be varied continuously over the range 1-4 MHz. With the present magnet coil configuration, the axial static magnetic field may be adjusted smoothly from a 2000-Gauss uniform field to a mirror field with a midplane intensity of 1000 Gauss and a mirror ratio of 2. For the experimental data reported, the beam-plasma discharge is generated in hydrogen gas at pressures from 7×10^{-5} Torr to 2×10^{-4} Torr.

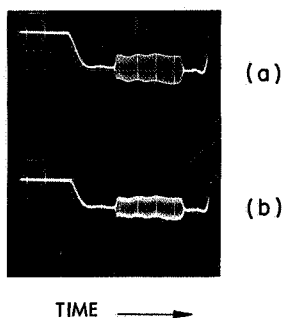


Fig. XIII-2.

Beam voltage with and without a beam-plasma discharge. Voltage scale, 4 kV/cm; time scale, 0.1 msec/cm; modulation frequency, 2.0 MHz. (a) V_b no plasma discharge. (b) V_n with beam-plasma discharge.

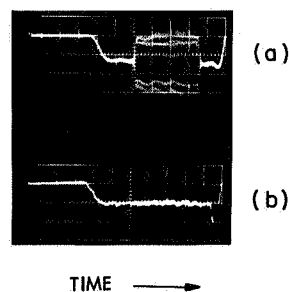


Fig. XIII-3.

Current scale, 2 amps/cm; time scale, 0.1 msec/cm. (a) Collector current with no hydrogen gas in the system (no beam-plasma discharge). (b) Collector current with 1.0 Torr of hydrogen gas in the system (with beam-plasma discharge).

With no hydrogen gas admitted into the system, a measurement of the collector current indicates nearly 100% RF modulation of the DC current pulse of 7 amps (Fig. XIII-3). When gas is admitted to the system and a beam-plasma discharge created, the RF modulation of the cathode current is substantially unchanged, but the collector RF current is reduced by approximately a factor of 15.

Since we are looking for a resonance of the cyclotron motion of the plasma ions, relatively large azimuthal currents are expected. These currents will produce an axial RF magnetic field that should be resonant at the ion-cyclotron frequency. Therefore a movable, electrostatically shielded, magnetic-field probe has been inserted near the drift tube wall to measure resonance effects in the axial RF field (Fig. XIII-1). The

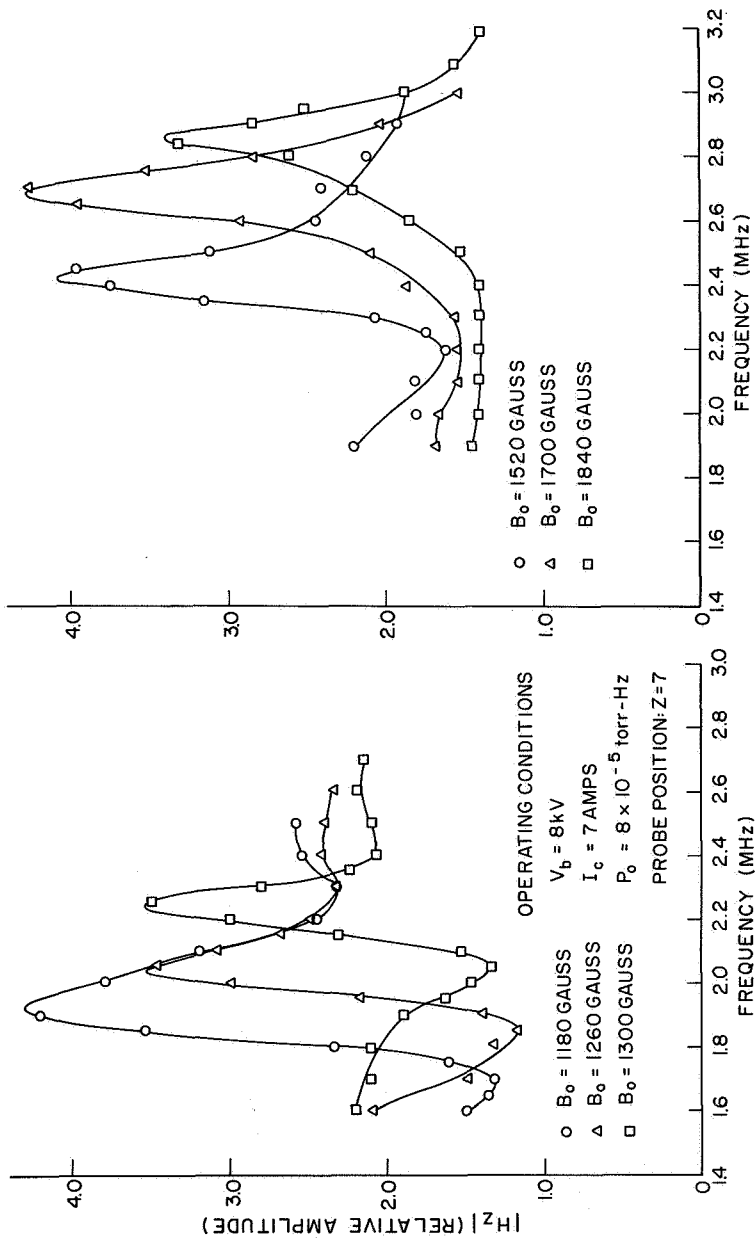


Fig. XIII-4. Axial magnetic probe signal as a function of frequency.

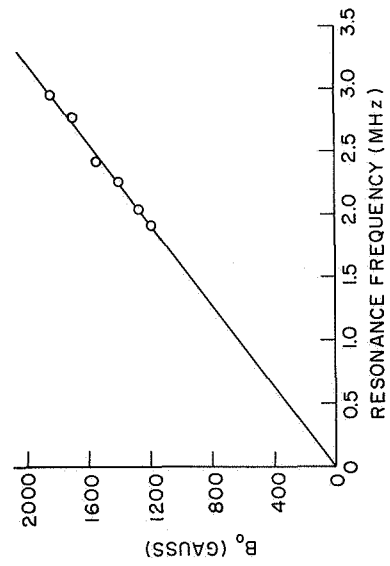


Fig. XIII-5. Known magnetic field at $z = 7$ inches, vs measured resonant frequencies.

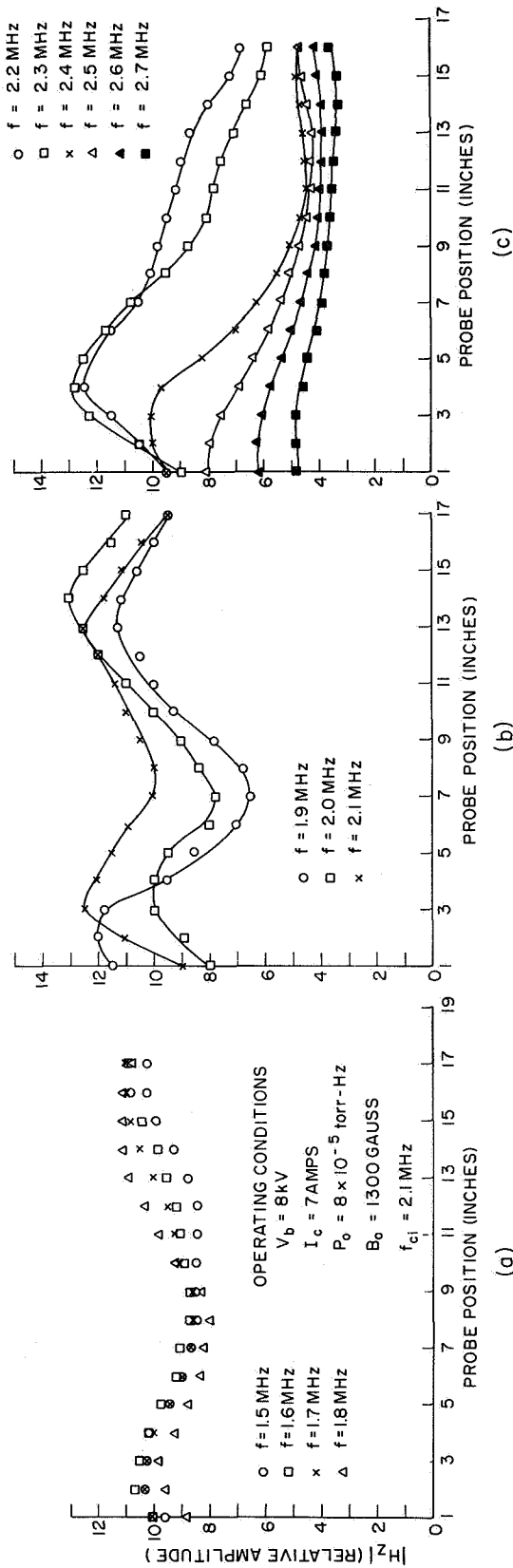


Fig. XIII-6. Axial variation of $|H_z|$. (a) at frequencies below f_{ci} . (b) at frequencies near f_{ci} . (c) at frequencies above f_{ci} .

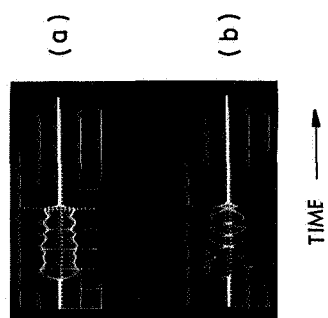


Fig. XIII-7. Filtered H_z probe signal. Vertical scale, 0.05 volts/cm; time scale, 0.1 msec/cm.
 (a) Typical signal away from resonance.
 (b) Typical signal just before resonance is reached.

(XIII. PLASMAS AND CONTROLLED NUCLEAR FUSION)

output of the probe is filtered, peak-detected, and integrated. Basically, two types of measurements have been made with this probe. The amplitude of H_z has been measured in two ways: (a) at a fixed position in the drift tube with the magnetic field and frequency as varying parameters, and (b) in a fixed magnetic field with the frequency and probe position as parameters.

The results of these measurements are shown in Figs. XIII-4, XIII-5, and XIII-6. Figure XIII-4 is a plot of the H_z probe signal, taken at a fixed position, as a function of frequency. The magnetic field at the probe position is varied over a range from 1180 Gauss to 1840 Gauss. In this experiment, the region from $z = 1$ to $z = 15$ (see (Fig. XIII-1) has an essentially uniform field; however, the current in the magnets at each end of the system is chosen to maintain a field of 1900 Gauss under these magnets. Therefore as the magnetic field at the probe position is increased, the mirror ratio is reduced. When a uniform field over the entire length of the system is used, the magnitude of the resonance is reduced by a factor of 2. Figure XIII-5 is a plot of the observed resonance frequencies versus the known magnetic field. These data are taken from Fig. XIII-4. Figure XIII-6 is a plot of the axial variation of the H_z probe signal for frequencies from 1.5 MHz to 2.7 MHz. The magnetic field is essentially uniform and equal to 1300 Gauss from $z = 1$ to $z = 15$. Again, the current in the end magnet was chosen to operate with a field of 1900 Gauss directly under these magnets. Figure XIII-7 illustrates the change in the structure of the RF H_z field as the resonant frequency is approached.

The method by which the modulated electron beam couples energy to the plasma ions is, at present, not understood. Theoretical work is being done which may explain the central role played by the nonuniform field in the excitation of the resonance, and the axial variation of the H_z signal.

J. A. Mangano

References

1. L. D. Smullin, "Beam-Plasma Discharge: Excitation of Ions at the Ion-Cyclotron Frequency," Quarterly Progress Report No. 80, Research Laboratory of Electronics, M. I. T., January 15, 1966, pp. 111-113.

(XIII. PLASMAS AND CONTROLLED NUCLEAR FUSION)

2. BEAM-PLASMA DISCHARGE: SYSTEM D

The x-ray Bremsstrahlung spectrum has been measured during the afterglow of the beam-plasma discharge. A thin-window sodium iodide scintillation crystal, 2 inches in diameter, has been used with an RIDL pulse-height analyzer and photomultiplier. The detection crystal is shielded and collimated so that only the emission of the core of the discharge is observed. The vacuum window between the scintillation crystal and the discharge is a thin beryllium disc (~5 mils).

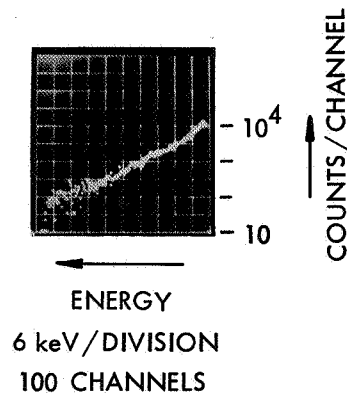


Fig. XIII-8. X-ray spectrum, 0.4-2.7 msec after the beam-plasma discharge (30 minutes at 30 discharges/minute).

The pulse-height analyzer is gated at various times during the afterglow. A typical x-ray spectrum is shown in Fig. XIII-8. We have used the Fessenden's model for Bremsstrahlung in nonrelativistic Coulomb collisions to determine the electron density during the afterglow (the plasma temperature can be read directly from the observed spectrum).¹ The plasma energy density ($n_e T_e$) as determined from the x-ray measurements is shown in Fig. XIII-9, where we have also shown the decay of the diamagnetism (transverse energy density) as observed by a pickup coil inside the discharge tube. Data are shown for pressures up to 10 times the normal operating pressure. The diamagnetic and x-ray measurements of the plasma energy density are in agreement at the higher pressures. We interpret the disagreement at the lower pressures as being attributable to enhancement of the x-ray emission by electron-impurity collisions. The atomic number of the impurity is estimated to be approximately 10 times that of H₂, based on the known pressure of H₂ at the time when the x-ray emission is too high by a factor of 2, the base pressure of the system, and the dependence of the x-ray emission on atomic number. Likely impurities are H₂O, O₂, N₂, and CO₂.

The temperature is shown in Fig. XIII-10 as a function of time in the afterglow. The plasma temperature is observed to rise with time as the plasma is lost from the mirror

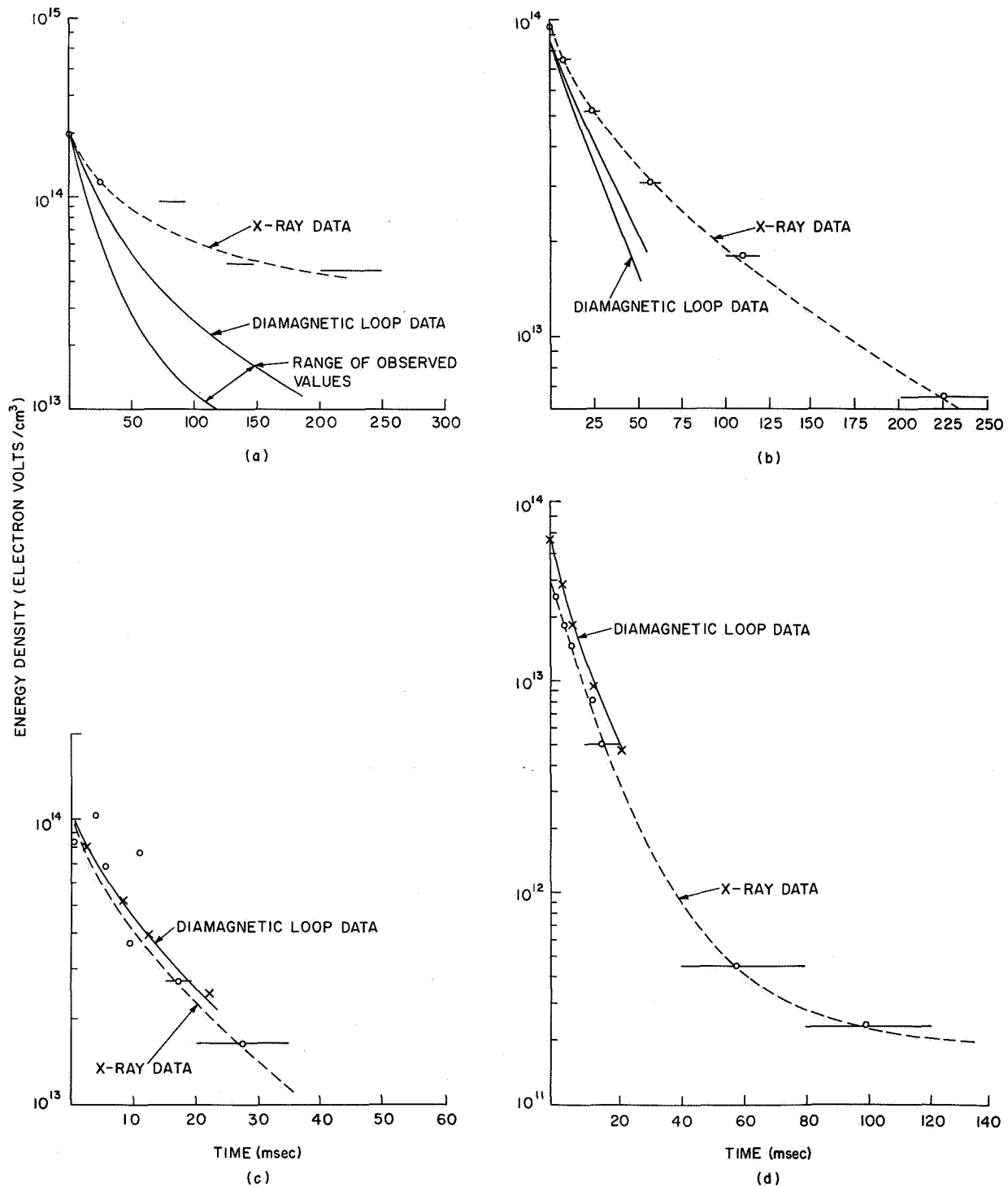


Fig. XIII-9. Plasma energy density decay determined from x-ray spectra and plasma diamagnetism. (a) Normal operation. (b) 2 times normal gas pulse. (c) 5 times normal gas pulse. (d) 10 times normal gas pulse.

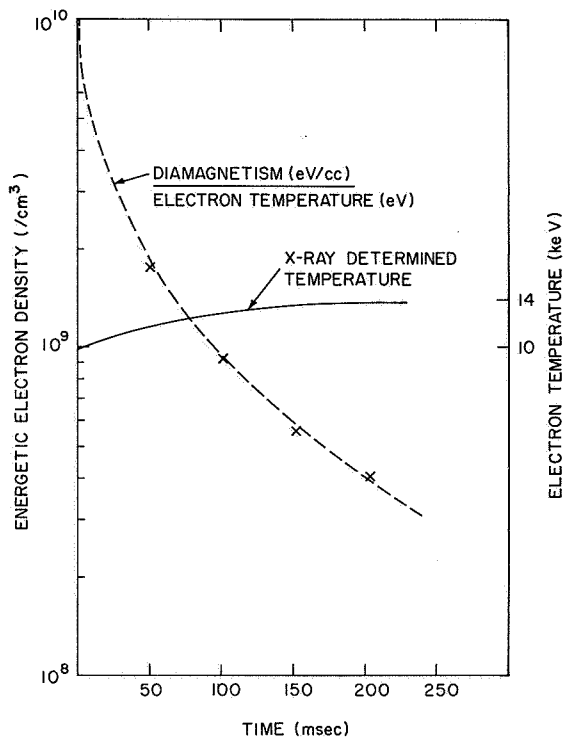


Fig. XIII-10. Temperature and density of the hot component of the plasma.

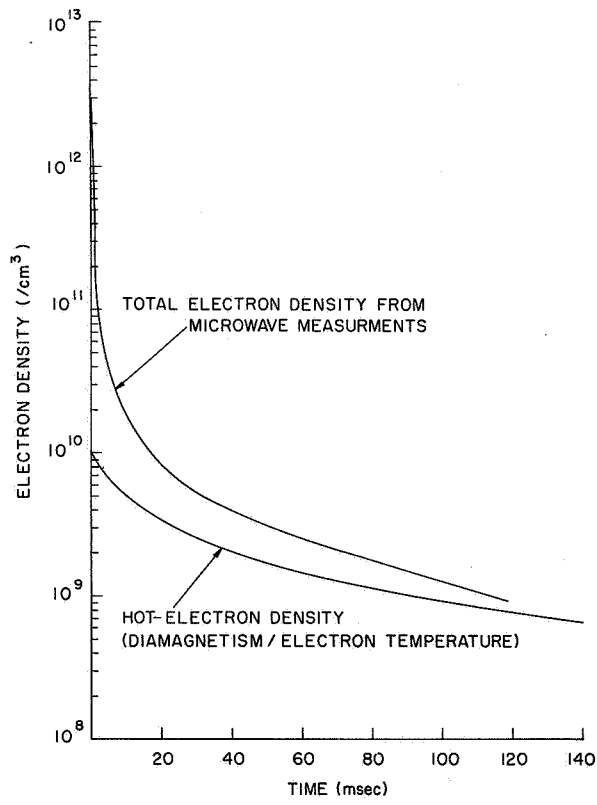


Fig. XIII-11. Decay of total electron density and hot component of electron density.

(XIII. PLASMAS AND CONTROLLED NUCLEAR FUSION)

system. The high-energy electron density is shown in Figs. XIII-10 and XIII-11, as determined by dividing the transverse energy density (diamagnetism) by the mean electron energy determined from the x-ray spectra. Figure XIII-11 illustrates the decays of the total electron density and the hot component of the electron density.

A low-level beam pulser is being used, at present, with the electron gun to excite oscillations in the afterglow following a beam-plasma discharge.

The author wishes to acknowledge the use of the facilities of the National Magnet Laboratory for the experimental work reported here.

R. R. Bartsch

References

1. T. J. Fessenden, "Pulsed Electron-Cyclotron Resonance Discharge," Technical Report 442, Research Laboratory of Electronics, M.I.T., Cambridge, Mass., March 15, 1966.

(XIII. PLASMAS AND CONTROLLED NUCLEAR FUSION)

3. CROSS-FIELD BEAM-PLASMA EXPERIMENTS

The cross-field beam-plasma experiment previously described^{1, 2} has been operated with a hollow, axially flowing beam and a hollow spiraling beam. These beams have not been pulsed but operated continuously. Observations have been made as these beams passed through a background gas. Various beam densities and gas pressures have been used. The initial observations are presented in this report.

a. Low Gas Pressure, Weak Beam

Low-frequency oscillations have been observed as an axially flowing, hollow beam of approximately 300 volts and 3.5 μ pervs passed through a background gas of pressure $1-5 \times 10^{-7}$ mm Hg. Under these conditions, a plasma was formed by the beam only in the region of the beam particles. These low-frequency oscillations have been observed as a modulation of the collector current and on a radial probe placed near the beam. For a low perveance beam (3 μ pervs) these oscillations were essentially pure sine waves in the neighborhood of 100-200 kHz. Their frequency increased when the ion mass was decreased and as the beam density was increased. Increasing the beam density also caused these oscillations to spread in frequency. First harmonics were observed. Then the spectrum spread and became continuous. At a beam perveance of approximately 30 μ pervs, the spectra appeared as shown in Fig. XIII-12. This particular perveance

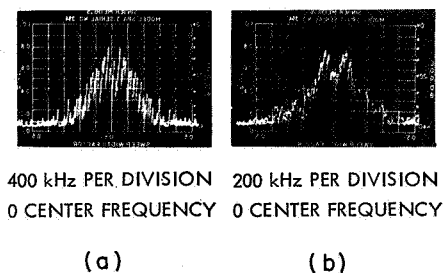


Fig. XIII-12.

Low-frequency Spectrum.

- (a) 400 kHz per division, center frequency = 0.
(b) 200 kHz per division, center frequency = 0.

(30 μ pervs) was also characteristic of beam breakup which is described here.

When a spiraling beam was employed a low-frequency behavior similar to the one described above was observed. The perveances for this beam are also similar to the axially flowing beam if only the axial voltage is used.

b. Low-Pressure, Strong Beam

With a weak (~ 3.00 μ pervs) axially flowing hollow beam, a sharp, well-defined ring of light was formed just in front of the collector (Fig. XIII-13a). Increasing the beam perveance by increasing the beam density caused an increase in the collector current until ~ 30 μ pervs. At this point, the beam current made a drop (Fig. XIII-14) and the pattern

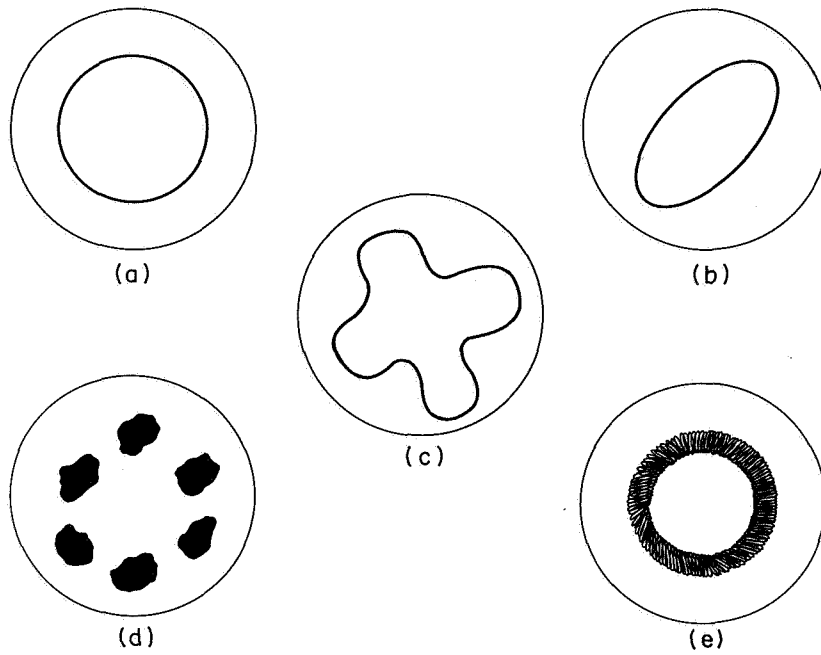


Fig. XIII-13. Beam breakup.

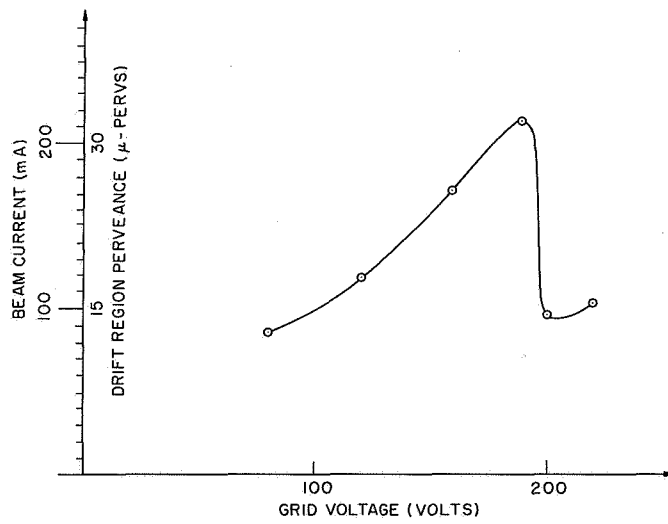


Fig. XIII-14. Beam current vs gun grid voltage at fixed beam voltage.

(XIII. PLASMAS AND CONTROLLED NUCLEAR FUSION)

at the collector takes on one of the shapes shown in Figs. XIII-13b-d. If ℓ is the azimuthal wave number, Fig. XIII-13b is an $\ell = 2$ mode, Fig. XIII-13c, an $\ell = 4$ mode, and Fig. XIII-13d, an $\ell = 6$ mode. An $\ell = 1$ mode would correspond to a shift of the circular pattern in a particular direction, and has not been observed. The different ℓ modes were obtained for different values of magnetic field and beam voltage, and were treated as fixed variables in the experiment.

By using a spiraling beam, the breakup appeared to be different. The beam current also behaved as shown in Fig. XIII-14. For low perveances the spiraling beam hit the collector in a well-defined ring as in Fig. XIII-13a. At the critical perveance ($\sim 30 \mu\text{pervs}$), however, where the current dropped, the pattern at the collector smeared, as shown in Fig. XIII-13e. With the spiraling beam, no stationary patterns were observed, which occurred for the straight flowing beam.

c. Intermediate Pressure, Weak Beams

Operating the system at a background gas pressure of approximately 3×10^{-5} mm Hg and using a weak beam resulted in oscillations in the neighborhood of the electron-cyclotron frequency. These oscillations were also seen on the collector current and the radial probe. An oscillation first set in at a beam perveance of $\sim 4.35 \mu\text{pervs}$ at an approximate frequency of 65 mHz. The frequency of this oscillation appeared to have a dependence only on the magnetic field and was linearly proportional. Increasing the beam perveance destroyed this oscillation, until it reached a value of 5 μpervs . At this value, an oscillation set in at approximately 95 mHz. This frequency increased with increasing magnetic field and also with increasing beam density.

These oscillations at and above the electron-cyclotron frequency could be observed on both the spiraling and straight flowing beams.



Fig. XIII-15. Beam spiraling through the axis.

(XIII. PLASMAS AND CONTROLLED NUCLEAR FUSION)

At the present time, we continue the investigation of the low-frequency oscillations and the beam breakup.

d. Beam

Our experiments have dealt with a hollow cylindrical beam, either straight-flowing or spiraling. It is possible to create many other types of beams in our experiment.¹ Fig. XIII-15 shows the beam that results when there is no magnetic field in the gun region. The beam particles then spiral synchronously through the axis of symmetry. Here the gun is on the left. The collector and a screen grid are on the right.

B. Kusse

References

1. B. Kusse and A. Bers, "Cross-Field Beam-Plasma Interactions," Quarterly Progress Report No. 82, Research Laboratory of Electronics, M. I. T., July 15, 1966, pp. 154-157.
2. B. Kusse and A. Bers, "Cross-Field Beam-Plasma Experiment," Quarterly Progress Report No. 84, Research Laboratory of Electronics, M. I. T., January 15, 1967, p. 144.

(XIII. PLASMAS AND CONTROLLED NUCLEAR FUSION)

4. EXPERIMENTAL INVESTIGATION OF A BEAM-PLASMA INTERACTION IN A MINIMUM-B FIELD

This experiment is designed to study (a) the hydromagnetic stability properties of a plasma produced in a beam-plasma interaction in an axisymmetric mirror confinement field stabilized by the addition of a hexapole field, and (b) any possible effects of the minimum B field on the beam-plasma interaction.

Charged particles tend to attach themselves to magnetic field lines, by virtue of the conservation of magnetic moment. The radial confinement of the plasma away from the material walls is achieved by means of a static magnetic field. The axial confinement along the field lines is achieved by shaping the uniform static field into an axisymmetric mirror field. The collective behavior of the charged particles in the plasma may give rise, however, to instabilities that destroy the confinement.

The experiment described in this report is being carried out in a slightly modified version of system A. In a series of experiments that were carried out in the same experimental device by H. Y. Hsieh and B. Hartenbaum (in System B), a number of instabilities were observed that led to the eventual loss of confinement of the plasma. We suspect that one of these instabilities is the hydromagnetic interchange instability.

The interchange instability is driven by the negative radial gradient in the magnetic field at the center region of the axisymmetric mirror.¹ The radial gradient of the magnetic field can be reversed in the region of interest by superimposing a multipole cusp magnetic field. A minimum-B magnetic field that is stable against the interchange instability is thus obtained.

a. Experimental Arrangement

A description of the present experimental system can be found in H. Y. Hsieh's doctoral thesis.² For this experiment, glass tubing, 3 3/4 in. in diameter and 16 in. long, was installed in system A in the interaction region. This is illustrated in Fig. XIII-16. The magnetic mirror is formed by two coils separated by a distance of ~10.5 in. between their mirror faces, with iron cylinders as magnetic shields placed in front of the electron gun and the collector to produce a field of almost parabolic shape. Magnetic fields in the center region are approximately 400 and 250 Gauss for a current in the coils of 18 and 10 Amps, respectively, with a mirror ratio of approximately 3.

An oxide-coated cathode assembly of a VA-220 gun gives an electron beam of a width approximately 0.2 cm at the center region. The beam flows to a water-cooled copper collector. Neutral gas is admitted continuously into the system through a needle valve.

The minimum-B field is generated by a hexapole configuration. This was accomplished by placing 6 hard-drawn copper strips at intervals of 60° on the periphery of the interaction region inside the glass tubing. The stabilizing field is pulsed during the

(XIII. PLASMAS AND CONTROLLED NUCLEAR FUSION)

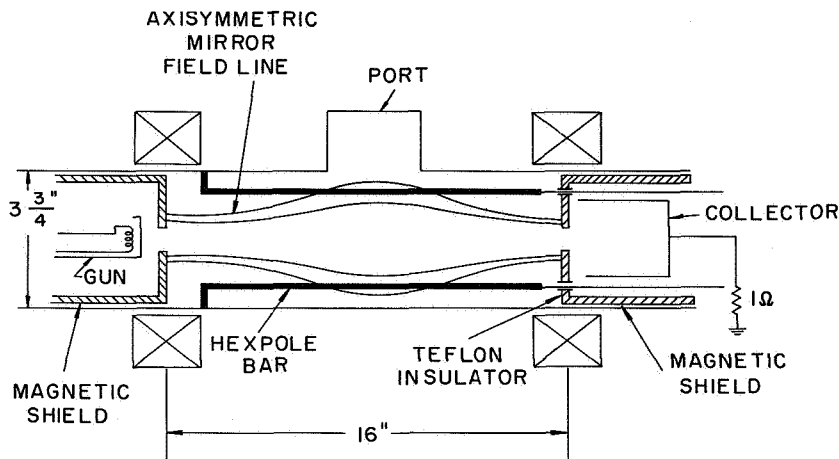


Fig. XIII-16. Experimental apparatus.

discharge at a fixed time, which can be adjusted by a delay circuit connected to the beam pulser.

A simple computation, based on the hexapole's stored magnetic energy in the interaction region, shows that a current pulse with a peak value of 1 k amp is required to generate the stabilizing minimum-B field. Before the discharge, the magnetic energy is stored in electric form in a 60 μ Fd low-inductance capacitor bank. The current is fed to the bars through the inner conductor of a high-voltage coaxial cable. The bank is fired with an ignitron, with a second ignitron crowbaring the bars some time later when the current in the bars has reached its peak value. Fig. XIII-17 is a diagram of the circuit.

The current through the bars can be monitored with a Rogowski coil. The waveform that is obtained is a damped sinusoid with a period of 120 μ sec and a rise time to its peak of 30 μ sec. Preliminary measurements show that the resulting currents are

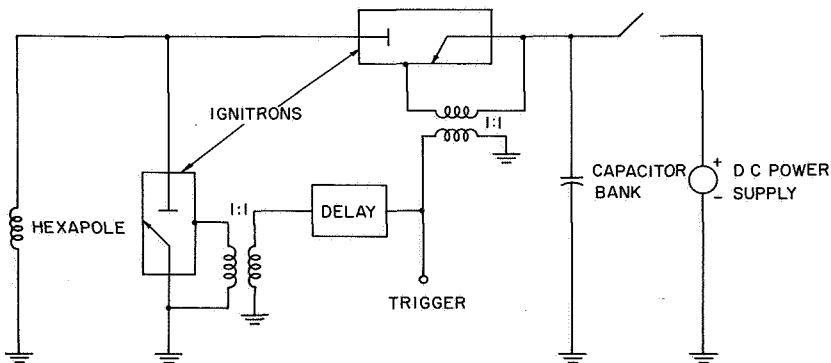


Fig. XIII-17. Hexapole's excitation circuit.

(XIII. PLASMAS AND CONTROLLED NUCLEAR FUSION)

approximately 20% below the theoretical values computed from the stored magnetic energy in the hexapole field.

b. Present Status of Experiment

The experimental arrangement has been built and most of the components tested. In order to study the behavior of the plasma under various experimental conditions, the following diagnostic tools will be used.

- (i) RF probe to measure plasma density and to detect plasma oscillations.
- (ii) Collector current and, in particular, its time variation that indicates the period of rotation of the unstable plasma.
- (iii) Diamagnetic signal to determine the plasma temperature.

c. Combined Minor Multipole Field

Starting from the center of the axisymmetric mirror configuration, the magnetic field increases toward the plane of the mirrors, but decreases radially away from the axis. The multipole field is produced by $2n$ rods, placed symmetrically around a cylinder with its axis coincident with that of the axisymmetric mirror field. The multipole field has the property that its magnitude remains constant along a line parallel to the axis and increases radially away from the axis. In order to obtain as uniform a field as possible over the path of the electron beam, we use a hexapole, or higher multipole field, rather than a quadrupole field.

The components of the multipole field² are

$$\frac{B_r}{B_\theta} \sim \sum_{k=0}^{\infty} r^{n(2k+1)-1} \frac{\sin n(2k+1)\theta}{\cos n(2k+1)\theta}$$

Near the axis (small r),

$$|B| \sim r^{n-1}.$$

For a quadrupole, $n = 2$ and $|B| \sim r$.

For a hexapole, $n = 3$ and $|B| \sim r^2$.

This shows that variations in $|B|$ around the beam are smaller for the hexapole.

F. N. Herba, J. G. Siambis

References

1. H. Y. Hsieh, "Experimental Study of Beam Plasma Discharge," Ph.D. Thesis, Department of Electrical Engineering, M. I. T., September, 1964.
2. J. Siambis, "Guiding Center Motion of Charged Particles in Combined Mirror-Cusp Magnetic Field," Electronics Research Laboratory, University of California, 1965.

5. ANOMALOUS MILLIMETER MICROWAVE PLASMA DENSITY MEASUREMENTS

We have been concerned with the validity of recent 4-mm interferometric plasma density measurements.¹ Plasma density information is derived from the phase shift observed resulting from the presence of the plasma in a propagation path between two antennas. Such phase-shift measurements are usually interpreted by applying a geometrical optics approximation which, in this application, requires that the size of the plasma be large compared with a wavelength of the probing microwaves.² Further, the plasma is usually considered to be a planar slab having sides that are large compared with the size of the probing microwave beam, in order to avoid the difficulty of interpreting the effect of diffraction fields. Hence, the validity of such an interpretation of observed phase shift for small cylindrical plasma columns may be seriously in question.

The interpretation of such microwave phase-shift measurements made recently on the beam-plasma discharge, System C, is subject to difficulties. When this machine is operated with a uniform axial magnetic field, the plasma produced is essentially a long cylinder having a diameter of approximately 2.5 cm. There is some evidence that it is annular in cross section. The plasma, therefore, may be only several wavelengths in thickness and because the microwave beam is of the order of an inch in effective cross section, the validity of the slab approximation is doubtful.

It has been found that an analytic treatment of the relevant propagation problem is impractical within the scope of the present work. Such a problem must accommodate such factors as the finite microwave beam, the near field patterns of the horns, and the presence of a reflective drift tube around the propagation path. An experimental approach was adopted. We shall describe the basic experiment for establishing the validity of the geometrical optics slab approximation.

a. Microwave Propagation Analog

An analog for the microwave propagation, similar to that described by B. B. Rosen,³ has been built. Since the refractive index of a plasma is less than one, the model for the microwave propagation was constructed by replacing vacuum regions of the path and surrounding geometry with a dielectric ($\kappa = 1.19$) and representing the plasma column by an air-filled hole ($\kappa = 1.0$). The construction is shown in Fig. XIII-18. The dielectric constant ratio corresponds to a plasma density of $0.16 n_{\text{crit}}$, a typical value in System C ($n \approx 10^{13}$ electrons/cc).

Cross section dimensions of beam-plasma discharge System C were scaled smaller by a factor of $\sqrt{\kappa} = 1.09$, thereby preserving the electrical lengths of the actual system. The model measures 10 cm along the dimension parallel to the axis of the cylinder, which represents a length of 26 wavelengths at 70.4 GHz. The steel drift tube of the discharge was modeled by a copper sheet wrapped around the dielectric. Horns and

(XIII. PLASMAS AND CONTROLLED NUCLEAR FUSION)

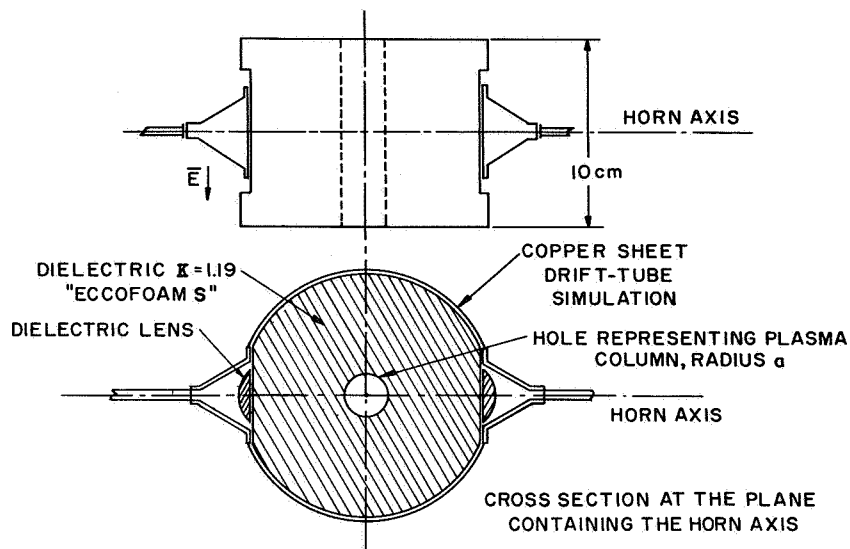


Fig. XIII-18. Microwave propagation analog for scattering from long plasma cylinders.

their lenses were those used in the actual plasma measurements, and were not filled with the dielectric or dimensionally scaled.

The dielectric was "Eccofoam S," a dense, small-celled, polyurethane foam manufactured by Emerson and Cuming, Inc. This material can be shaped by common machining and is available in a variety of dielectric constants with very small loss tangent at millimeter frequencies. Properties of this dielectric at 70.4 GHz were obtained by measuring the amplitude and phase shift of transmission through large slabs, of various thicknesses, using a circuit similar to that shown in Fig. XIII-19.

Amplitude and phase shift caused by the presence of cylindrical holes of various diameters in the model were measured by standard techniques, using phase change

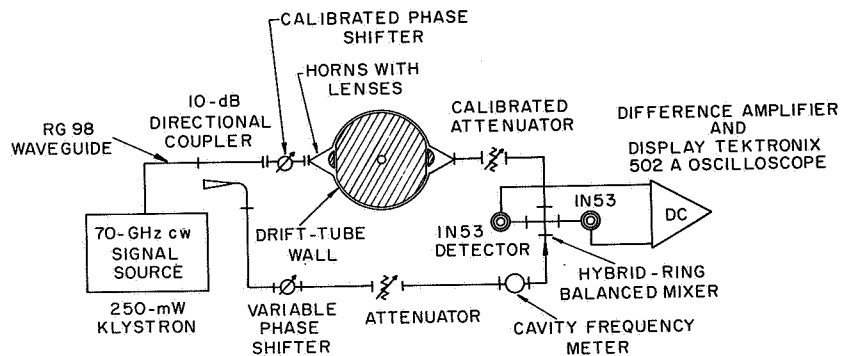


Fig. XIII-19. Microwave bridge circuit.

(XIII. PLASMAS AND CONTROLLED NUCLEAR FUSION)

interferometer circuit of Fig. XIII-19. Polarization was parallel to the cylinder axis. The phase-measuring bridge was adjusted to a null, with a dielectric calibrating cylinder filling the hole. Calibrating cylinders were machined from the same dielectric from which the model was made; hence, their presence represented the "no plasma" condition of zero phase shift and attenuation. We have found that tight dielectric-dielectric interfaces produce no error in this calibration. After calibration and removal of the calibrating cylinder, phase shift was measured by renulling the bridge with a calibrated phase shifter. Similarly, attenuation caused by refraction was measured, by using a precision calibrated attenuator.

b. Results

To examine the geometrical optics, infinite slab approximation phase shift was measured as a function of cylinder radius, a . These data are shown in Fig. XIII-20 compared with the slab approximation for the range of values of interest. Cylinder radii are measured in wavelengths in Eccofoam, $\lambda_E = \lambda_O \kappa^{-1/2} = 3.92$ mm. We have found that the measured phase shift reaches excellent agreement with the slab approximation at a cylinder radius of 2.5 wavelengths, and it is surprisingly close for cylinders as small as 1 wavelength in radius. Note that no phase-shift reversal as observed by Rosen⁴ occurs at any point in this range, thereby indicating that the effects of interference of waves around the column is not significant.

Attenuation resulting from refraction for this same range of cylinder sizes is shown in Fig. XIII-21. The large peak occurring at approximately $1.5 \lambda_E$ is due to the sharp refractive lens effect of the column. This is also in agreement with the experimental work of Rosen.

These results indicate that the slab approximation is applicable to plasmas observed in System C. This appears to be due in part to the good phase correction provided by the horn lenses.

c. Effects of Microwave Beam Misalignment

In an effort to explain an apparent inconsistency of interferometric density measurements on System C the effects of misalignment between the plasma column and the microwave beam were studied. Here, the position of the cylindrical hole representing the plasma was displaced from the center of the model by a distance δ . Phase-shift and attenuation information was obtained for both homogeneous and annular "plasma" cylinders. Annular radial density distributions (hollow-plasma columns) were represented in the model by placing a smaller dielectric cylinder concentrically within a larger hole. Three such annular configurations were considered.

Figure XIII-22 displays the error in phase measurement resulting from column displacement in a direction perpendicular to the horn axis. It appears that displacement

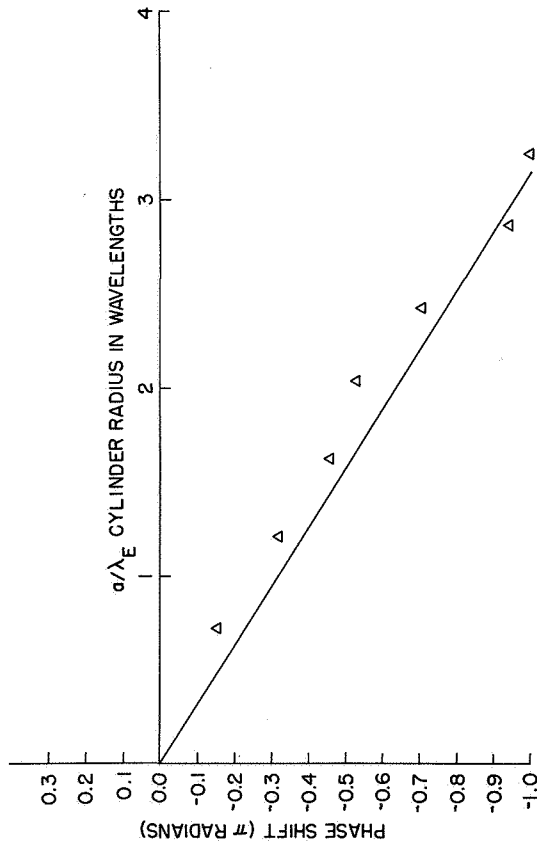


Fig. XIII-20. Measured phase shift vs simulated plasma cylinder radius measured in wavelengths in Eccofoam. Solid Line: geometrical optics slab approximation.

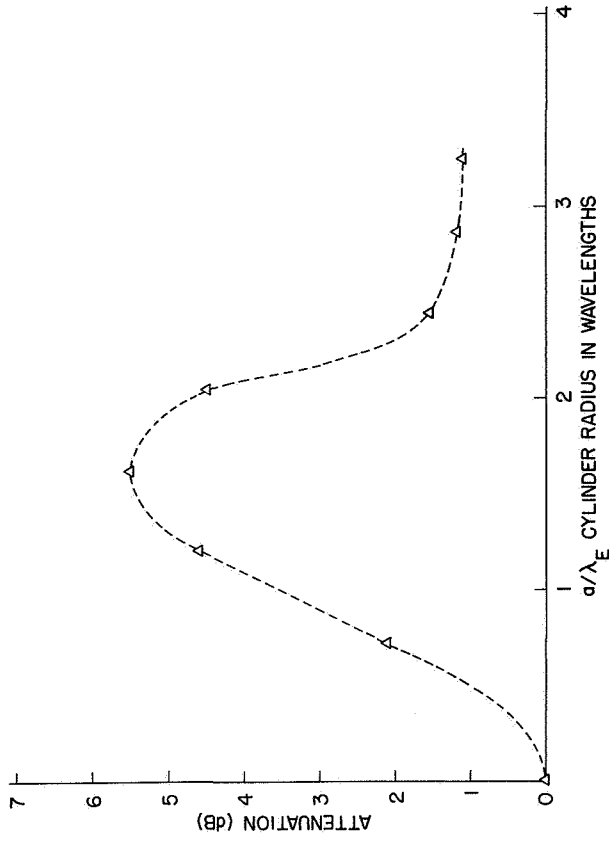


Fig. XIII-21. Measured attenuation vs cylinder radius measured in wavelengths.

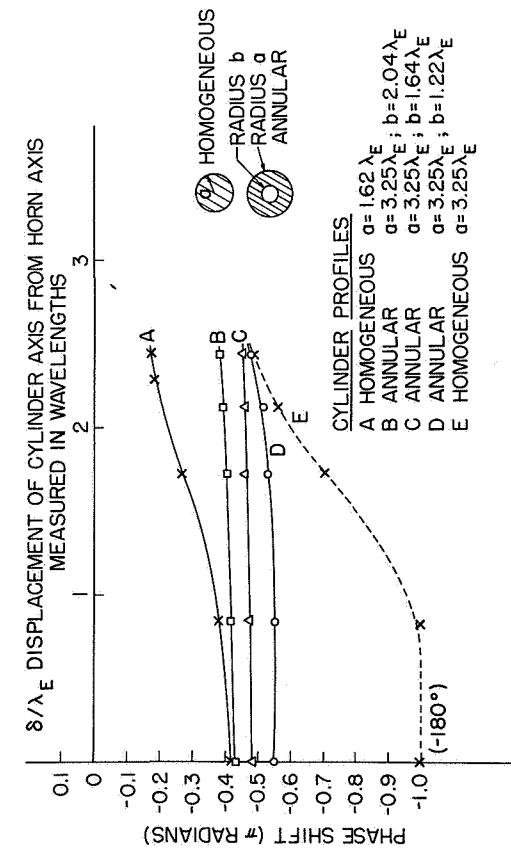


Fig. XIII-22. Measured phase shift vs displacement of simulated plasma cylinder from axis of the horn path.

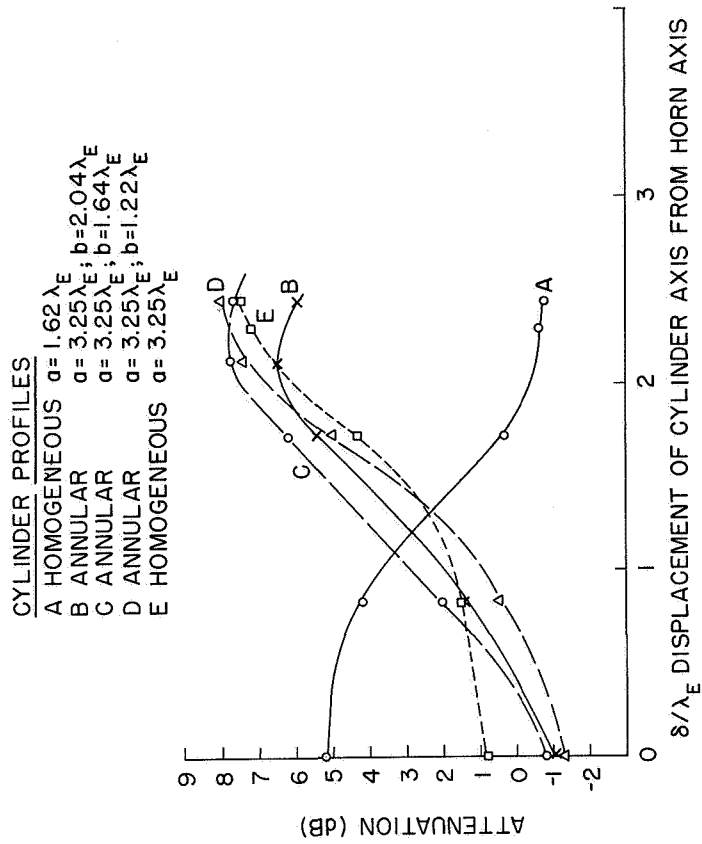


Fig. XIII-23. Measured attenuation vs displacement of cylinder from the axis of the horn path.

(XIII. PLASMAS AND CONTROLLED NUCLEAR FUSION)

from the center of the propagation path in a direction parallel to the horn axis over the range of $3 \lambda_E$ does affect observed amplitude or phase shift.

For the same range of displacement, Fig. XIII-23 shows the variation of the attenuation resulting from refraction.

The strong sensitivity of the amplitude or phase to displacement perpendicular to the horn axis for particular sizes and cross sections suggests a possible method for radial-profile diagnosis. For example, a relative insensitivity of the phase-to-horn alignment, together with an amplitude gain through a centered column, would reasonably be interpreted as due to an annular plasma. A technique such as this is of particular value for beam-plasma discharge studies, because of the impracticability of using Langmuir probes within the electron-beam region.

D. M. Perozek

References

1. D. M. Perozek and W. D. Getty, Quarterly Progress Report No. 82, Research Laboratory of Electronics, M. I. T., July 15, 1966, pp. 138-143.
2. M. A. Heald and C. B. Wharton, Plasma Diagnostics with Microwaves (John Wiley and Sons, Inc., New York, 1965), p. 119.
3. B. B. Rosen, The "Inverted Universe" Plasma Analog for Microwaves, Project Matterhorn Technical Memo 85, Princeton University, Princeton, N. J., 1959.
4. Ibid., p. 3.

6. THEORY OF BEAM-PLASMA INTERACTIONS

In studies of small-signal beam-plasma interactions the common approach is to describe both the beam and the plasma by an equivalent dielectric tensor. Such a formulation is convenient for studying interactions with characteristic wavelengths that are short compared with the dimensions of the plasma or beam (which is usually smaller), so that boundary effects are relatively unimportant. When boundary effects become important the dielectric tensor formulation imposes a restrictive description of the particles at the boundary, which may not be consistent with their true dynamics.^{2,3} Thus, for example, the surface-charge model for the dynamics at a beam-plasma boundary is of questionable validity. Recent computer experiments on a similar boundary problem indicate that the particle motion is highly nonlaminar.⁴

We shall outline a new approach to describing beam-plasma interactions that should be particularly suited for thin beams and wavelengths large compared with beam thickness. In this development we first study the excitation of the plasma by beam-density perturbations, and then describe the dynamics of the beam perturbations in the average fields over the beam cross section. The thin beam is allowed to have an arbitrary unperturbed density distribution, and moves rigidly. We use the electrostatic approximation throughout.

a. Excitation of Plasma Waves by an External Charge Source

Consider a plasma consisting of s -types of charged carriers and an external charge density distribution ρ_{ext} . In the electrostatic approximation we describe this by

$$\nabla \cdot \epsilon_0 \bar{\mathbf{E}} - \sum_s e_s n_s = \rho_{\text{ext}} \quad (1)$$

$$\bar{\mathbf{E}} = -\nabla \Phi \quad (2)$$

and

$$\begin{aligned} n_s &= \int f_s(\bar{\mathbf{r}}, \bar{\mathbf{w}}, t) d^3w \\ &= F_{s \text{ op}}(\bar{\mathbf{r}}, t) \Phi, \end{aligned} \quad (3)$$

where f_s is the perturbed distribution function for the particles of species s , and Eq. 3 represents the formal solution of the Vlasov equation. For a homogeneous plasma in a magnetic field, and fields with dependence $\exp[-i\omega t + i\bar{\mathbf{k}} \cdot \bar{\mathbf{r}}]$,

$$F(\omega, \bar{\mathbf{k}}) = \frac{k^2 \epsilon_0}{e_s} [1 - K_\ell(\omega, \bar{\mathbf{k}})], \quad (4)$$

(XIII. PLASMAS AND CONTROLLED NUCLEAR FUSION)

where

$$K_{\ell}(\omega, \bar{k}) = \frac{\bar{k} \cdot \bar{K}(\omega, \bar{k}) \cdot \bar{k}}{k^2} \quad (5)$$

is the longitudinal dielectric coefficient. Three examples of this follow.

(a) Collisionless plasma with unperturbed distribution function $f_0(w_{\perp}, w_{\parallel})$:

$$K_{\ell} = 1 + \int d^3w \frac{\omega_p^2}{k^2} \sum_n \frac{J_n^2\left(\frac{k_{\perp} w_{\perp}}{\omega_c}\right) \left[\frac{n\omega_c}{w_{\perp}} \frac{\partial f_0}{\partial w_{\perp}} + k_{\parallel} \frac{\partial f_0}{\partial w_{\parallel}} \right]}{(\omega - k_{\parallel} w_{\parallel} - n\omega_c)} \quad (6)$$

(ii) If f_0 is a Maxwellian with $v_T^2 = \kappa T/m$,

$$K_{\ell} = 1 + \frac{\omega_p^2}{k^2 v_T^2} \left[1 + \sum_n I_n(\lambda) e^{-\lambda} \xi_n Z(\xi_n) \right] \quad (7)$$

where

$$\lambda = \left(\frac{k_{\perp} v_T}{\omega_c} \right)^2$$

$$\xi_n = \frac{\omega - n\omega_c}{k_{\parallel} v_T \sqrt{2}}$$

Z is the plasma dispersion function

I_n is the modified Bessel function.

(iii) For a cold plasma,

$$K_{\ell} = \frac{1}{k^2} \left[k_{\perp}^2 K_{\perp} + k_{\parallel}^2 K_{\parallel} \right] \quad (8)$$

where K_{\perp} and K_{\parallel} are the usual relative dielectric coefficients of a cold plasma in a magnetic field.

With the external source density ρ_{ext} the problem becomes inhomogeneous, and $F(\omega, \bar{k})$ must be converted to an operator. Formally, we can let $-ik_{\perp} \rightarrow \partial/\partial x$ and $-ik_{\parallel} \rightarrow \partial/\partial z$, and obtain

$$\left\{ \nabla^2 + \sum_s \left[k^2 (1 - K_{s\ell}) \right]_{\text{op}} \right\} \Phi = -\frac{\rho_{\text{ext}}}{\epsilon_0} \quad (9)$$

b. Electron-Beam Perturbations as a Charge Density Source

The external source in Eq. 9 will now be described in terms of perturbations of a thin electron beam.

$$\rho_{\text{ext}} = en, \quad (10)$$

where n is the first-order perturbation in the beam particle density. The unperturbed density of the beam is assumed to be a function of position in the beam cross section

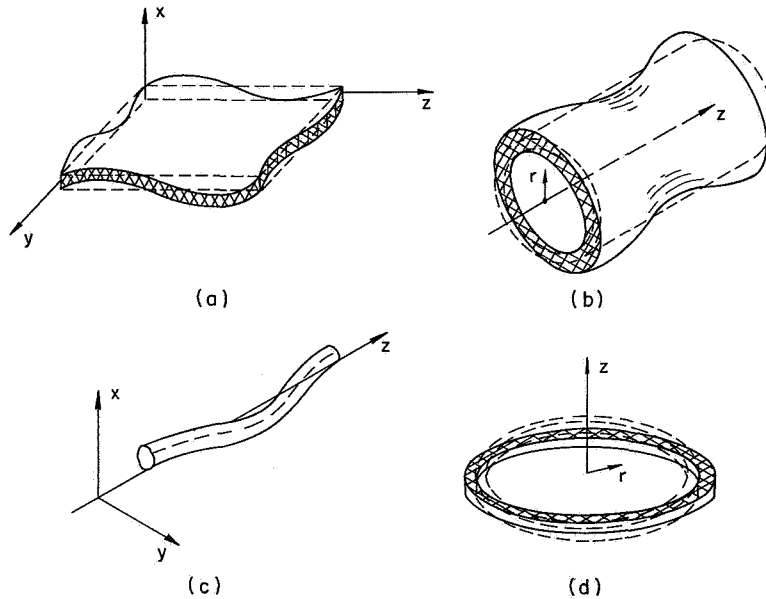


Fig. XIII-24. Examples of thin beams and their perturbations.
 (a) Sheet beam, with rigid motion in x .
 (b) Hollow beam, with rigid motion in r .
 (c) Pencil beam, with rigid motion in x and y .
 (d) Ring beam, with rigid motion in r and z .

$n_0(\bar{r}_{\text{CS}})$. The beam perturbations are characterized by a displacement vector $\bar{\delta}$ which is rigid in the direction of \bar{r}_{CS} . The beam particle density perturbation then is

$$\begin{aligned} n &= -\nabla \cdot (n_0 \bar{\delta}) \\ &= -n_0 \nabla \cdot \bar{\delta} - \bar{\delta} \cdot \nabla n_0. \end{aligned} \quad (11)$$

Four examples follow.

(i) Sheet beam (Fig. XIII-24a).

(XIII. PLASMAS AND CONTROLLED NUCLEAR FUSION)

$$n_o(x)$$

$$\bar{\delta} = \bar{\delta}_o e^{-j\beta_y y} e^{-j\beta_z z}$$

$$n = -n_o(-j\beta_y \delta_y - j\beta_z \delta_z) - \delta_x \frac{\partial n_o}{\partial x}. \quad (12)$$

(ii) Hollow beam (Fig. XIII-24b).

$$n_o(r)$$

$$\bar{\delta} = \bar{\delta}_o e^{-j\beta_z z} e^{-jm\theta}$$

$$n = -n_o(-jm\delta_\theta - j\beta_z \delta_z) - \delta_r \frac{\partial n_o}{\partial r}. \quad (13)$$

(iii) Pencil beam (Fig. XIII-24c).

$$n_o(x, y)$$

$$\bar{\delta} = \bar{\delta}_o e^{-j\beta_z z}$$

$$n = -n_o(-j\beta_z \delta_z) - \delta_x \frac{\partial n_o}{\partial x} - \delta_y \frac{\partial n_o}{\partial y} \quad (14)$$

(iv) Ring beam (Fig. XIII-24d).

$$n_o(r, z)$$

$$\bar{\delta} = \bar{\delta}_o e^{-jm\theta}$$

$$n = -n_o(-jm\delta_\theta) - \delta_r \frac{\partial n_o}{\partial r} - \delta_z \frac{\partial n_o}{\partial z}. \quad (15)$$

c. Beam Dynamics in Fields Averaged over the Beam Cross Section

We define an average over the beam cross section

$$\langle \rangle = \frac{1}{A_b} \int_{A_b} da, \quad (16)$$

where A_b is the beam cross section. The equation of motion for the first-order beam displacements then is

$$\frac{d^2}{dt^2} \langle mn_o \bar{\delta} \rangle = e \left[\langle -n_o \nabla \Phi \rangle + \left\langle n_o \frac{d\bar{\delta}}{dt} \times \bar{B}_o \right\rangle \right] \quad (17)$$

or, for the nonrelativistic case,

$$\frac{d^2}{dt^2} \bar{\delta} = \frac{e}{m} \left[\frac{\langle -n_o \nabla \Phi \rangle}{\langle n_o \rangle} + \frac{d\bar{\delta}}{dt} \times \bar{B}_o \right]. \quad (18)$$

d. Beam-Plasma System

The small-signal dynamics of the beam-plasma system may now be described (in the electrostatic approximation) by Eqs. 9, 10, 11, and 17 or 18. From Eqs. 9, 10, and 11, we can find $\Phi(\bar{\delta})$, which when substituted in Eq. 18 allows one to study the stability of the beam perturbations, δ .

A. Bers

References

1. R. J. Briggs, Electron-Stream Interaction with Plasmas (The M. I. T. Press, Cambridge, Mass., 1964).
2. D. L. Bobroff, H. A. Haus, and J. W. Kluver, *J. Appl. Phys.* 33, 2934 (1962).
3. W. P. Allis, S. J. Buchsbaum, and A. Bers, Waves in Anisotropic Plasmas (The M. I. T. Press, Cambridge, Mass., 1963).
4. H. M. Schneider, *Phys. Fluids* 9, 2298 (1966).

(XIII. PLASMAS AND CONTROLLED NUCLEAR FUSION)

7. DISPERSION RELATIONS FOR BEAM-PLASMA INTERACTIONS

We shall present the detailed formulation of some beam-plasma interactions that were outlined in Section XIII-A. 6. We restrict ourselves to a cold-plasma model and consider, first, a pencil beam, and then a thin-sheet beam. In the first case the plasma is assumed to be unbounded, and in the second case the effects of boundaries on the plasma are included.

a. Pencil Beam in an Unbounded Plasma

Consider an electron beam with an unperturbed density distribution $n_0(x, y)$ and velocity $v_0 \hat{i}_z$ immersed in a uniform, infinite, cold plasma. A longitudinal (z -directed) static magnetic field \vec{B} is applied (Fig. XIII-25).

The beam is assumed to be neutralized in its unperturbed state, and the beam density is small compared with the plasma density.

The displacement $\vec{\delta}(z, t)$ of the beam is assumed to be a function of z only, that is, it is independent of position in a given transverse plane. This "rigid-beam" approximation allows for great simplification of the analysis.

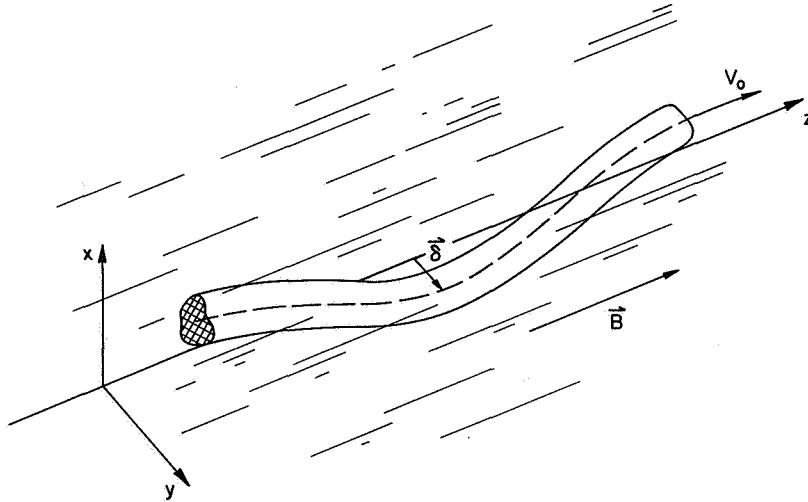


Fig. XIII-25. Pencil beam and its rigid perturbation δ .

For convenience, Cartesian coordinates will be used in the following treatment. This permits Fourier analysis of the beam density and electric potential. If cylindrical coordinates are used, Fourier-Bessel analysis must be employed.

Wave solutions of the form $\exp j(\omega t - \beta z)$ are assumed for the electrostatic potential ϕ , the beam displacement $\vec{\delta}$, and the perturbed beam electron density n_1 .

(XIII. PLASMAS AND CONTROLLED NUCLEAR FUSION)

Poisson's equation¹ then reads

$$K_{\perp} \left(\frac{\partial^2}{\partial x^2} + \frac{\partial^2}{\partial y^2} \right) \phi(x, y) - \beta^2 K_{\parallel} \phi(x, y) = \frac{e}{\epsilon_0} \left[\delta_x \frac{\partial n_0}{\partial x} + \delta_y \frac{\partial n_0}{\partial y} + n_0 (-j\beta) \delta_z \right], \quad (1)$$

where K_{\perp} and K_{\parallel} are components of the dielectric tensor as introduced previously.

The Lorentz equation² written out in Cartesian components, gives

$$\begin{aligned} -\Omega^2 \delta_x &= \frac{e}{m} \frac{\langle -n_0 \frac{\partial \phi}{\partial x} \rangle}{\langle n_0 \rangle} - j \omega_c \Omega \delta_y \\ -\Omega^2 \delta_y &= \frac{e}{m} \frac{\langle -n_0 \frac{\partial \phi}{\partial y} \rangle}{\langle n_0 \rangle} + j \omega_c \Omega \delta_x \\ -\Omega^2 \delta_z &= \frac{e}{m} \frac{\langle j\beta n_0 \phi \rangle}{\langle n_0 \rangle}, \end{aligned} \quad (2)$$

where $\omega_c \equiv -\frac{eB}{m}$ is the cyclotron frequency for an electron, and $\Omega \equiv (\omega - \beta v_0)$ is the Doppler-shifted frequency for the moving beam. The quantities in angular brackets are to be averaged over the cross section of the beam. Thus

$$\langle n_0 \rangle \equiv \frac{1}{\tau^2} \iint_{-\infty}^{\infty} n_0(x, y) dx dy, \quad (3)$$

where τ^2 is some suitably defined cross-section beam area; it is introduced merely for normalization purposes.

The beam profile $n_0(x, y)$ and the transverse potential distribution $\phi(x, y)$ can be expressed in terms of their spatial Fourier transforms:

$$\begin{aligned} n_0(x, y) &= \iint_{-\infty}^{\infty} n_0(k_x, k_y) e^{-jk_x x - jk_y y} \frac{dk_x}{2\pi} \frac{dk_y}{2\pi} \\ \phi(x, y) &= \iint_{-\infty}^{\infty} \phi(k_x, k_y) e^{-jk_x x - jk_y y} \frac{dk_x}{2\pi} \frac{dk_y}{2\pi}. \end{aligned} \quad (4)$$

Substituting these in Eq. 1, we obtain

$$\phi(k_x, k_y) = \frac{e n_0(k_x, k_y) (jk_x \delta_x + jk_y \delta_y + j\beta \delta_z)}{\epsilon_0 K_{\perp} (k_x^2 + k_y^2 + q^2)}, \quad (5)$$

(XIII. PLASMAS AND CONTROLLED NUCLEAR FUSION)

where $q^2 = \beta^2 \frac{K_{\parallel}}{K_{\perp}}$ is the transverse wave number in the plasma. The averages of products in Eq. 2 can be written

$$\begin{aligned} \langle j\beta n_o \phi \rangle &\equiv \frac{j\beta}{\tau^2} \iint_{-\infty}^{\infty} n_o(x, y) \phi(x, y) dx dy \\ &= \frac{j\beta}{\tau^2} \iint_{-\infty}^{\infty} n_o^* (k_x, k_y) \phi(k_x, k_y) \frac{dk_x}{2\pi} \frac{dk_y}{2\pi} \\ \langle -n_o \frac{\partial \phi}{\partial x} \rangle &= \frac{1}{\tau^2} \iint_{-\infty}^{\infty} jk_x n_o^* (k_x, k_y) \phi(k_x, k_y) \frac{dk_x}{2\pi} \frac{dk_y}{2\pi} \\ \langle -n_o \frac{\partial \phi}{\partial y} \rangle &= \frac{1}{\tau^2} \iint_{-\infty}^{\infty} jk_y n_o^* (k_x, k_y) \phi(k_x, k_y) \frac{dk_x}{2\pi} \frac{dk_y}{2\pi} \end{aligned} \quad (6)$$

where the star indicates a complex conjugate.

Substituting (5) in (6), and then in (2), we obtain the following form for the force equations:

$$-\Omega^2 \delta_x = -\frac{1}{K_{\perp}} \frac{e^2 \langle n_o \rangle}{\epsilon_o m} F_x(q\tau) \delta_x - j\omega_c \Omega \delta_y \quad (7a)$$

$$-\Omega^2 \delta_y = -\frac{1}{K_{\perp}} \frac{e^2 \langle n_o \rangle}{\epsilon_o m} F_y(q\tau) \delta_y + j\omega_c \Omega \delta_x \quad (7b)$$

$$-\Omega^2 \delta_z = -\frac{1}{K_{\perp}} \frac{e^2 \langle n_o \rangle}{\epsilon_o m} (\beta\tau)^2 F_z(q\tau) \delta_z, \quad (7c)$$

where F_x , F_y , and F_z are dimensionless quantities defined by

$$\begin{aligned} F_x(q\tau) &= \frac{1}{\langle n_o \rangle^2 \tau^4} \iint_{-\infty}^{\infty} \frac{(k_x\tau)^2 |n_o(k_x, k_y)|^2}{(k_x\tau)^2 + (k_y\tau)^2 + (q\tau)^2} \frac{d(k_x\tau)}{2\pi} \frac{d(k_y\tau)}{2\pi} \\ F_y(q\tau) &= \frac{1}{\langle n_o \rangle^2 \tau^4} \iint_{-\infty}^{\infty} \frac{(k_y\tau)^2 |n_o(k_x, k_y)|^2}{(k_x\tau)^2 + (k_y\tau)^2 + (q\tau)^2} \frac{d(k_x\tau)}{2\pi} \frac{d(k_y\tau)}{2\pi} \\ F_z(q\tau) &= \frac{1}{\langle n_o \rangle^2 \tau^4} \iint_{-\infty}^{\infty} \frac{|n_o(k_x, k_y)|^2}{(k_x\tau)^2 + (k_y\tau)^2 + (q\tau)^2} = \frac{d(k_x\tau)}{2\pi} \frac{d(k_y\tau)}{2\pi}. \end{aligned} \quad (8)$$

(XIII. PLASMAS AND CONTROLLED NUCLEAR FUSION)

Here, τ can be interpreted as a measure of the thickness of the beam.

Equations 7 show that the transverse displacements of the beam are related to each other, but not to the longitudinal displacement. The reason for this is that the field structure associated with longitudinal displacements, when weighted with the beam density and averaged over the beam, yields no net force in the transverse direction.

A case of frequent interest occurs when $n_o(x, y)$ is symmetric with respect to x and y (this includes the circularly symmetric beam). In this case, Eq. 8 shows that

$$F_x(q\tau) = F_y(q\tau) \equiv F_T(q\tau), \quad (9)$$

where the subscript T is used to indicate association with transverse displacements.

In the case of a one-dimensional Gaussian density variation $n_o(x)$, we have in closed form

$$F_T = \frac{1}{\langle n_o \rangle^2 \tau^2} \int_{-\infty}^{\infty} \frac{(k\tau)^2 |n_o(k)|^2}{(k\tau)^2 + (q\tau)^2} \frac{d(k\tau)}{2\pi}$$

$$= \frac{-Z'(jq\tau/2)}{2\sqrt{\pi}}$$

$$F_Z = \frac{1}{\langle n_o \rangle^2 \tau^2} \int_{-\infty}^{\infty} \frac{|n_o(k)|^2}{(k\tau)^2 + (q\tau)^2} \frac{d(k\tau)}{2\pi}$$

$$= \frac{-jZ(jq\tau/2)}{2\sqrt{\pi} (q\tau)},$$

where Z is the plasma dispersion function, and Z' its derivative.

The force equations (7) now become

$$\left[\Omega^2 - \frac{\langle \omega_{pb}^2 \rangle}{K_{\perp}} F_T(q\tau) \right] \delta_x = j\omega_c \Omega \delta_y \quad (10a)$$

$$\left[\Omega^2 - \frac{\langle \omega_{pb}^2 \rangle}{K_{\perp}} F_T(q\tau) \right] \delta_y = -j\omega_c \Omega \delta_x \quad (10b)$$

$$\left[\Omega^2 - \frac{\langle \omega_{pb}^2 \rangle}{K} (\beta\tau)^2 F_Z(q\tau) \right] \delta_z = 0, \quad (10c)$$

in which we have defined an average of the square of the beam-plasma frequency:

(XIII. PLASMAS AND CONTROLLED NUCLEAR FUSION)

$$\langle \omega_{pb}^2 \rangle \equiv \frac{e^2 \langle n_0 \rangle}{\epsilon_0 m}.$$

Equations 10a and 10b give the dispersion relation for the transverse modes:

$$\left[\Omega^2 - \frac{\langle \omega_{pb}^2 \rangle}{K_{\perp}} F_T(q\tau) \right]^2 - \omega_c^2 \Omega^2 = 0. \quad (11)$$

The dispersion relation for the longitudinal modes follows immediately from Eq. 10c:

$$\Omega^2 - \frac{\langle \omega_{pb}^2 \rangle}{K_{\perp}} (\beta\tau)^2 F_z(q\tau) = 0. \quad (12)$$

This is readily identified as the dispersion for space-charge beam waves coupled to the plasma (through K_{\perp} and $F_z(q\tau)$).

The transverse waves are more easily interpreted if the roots to Eq. 11 are expressed in the form

$$\begin{aligned} \Omega_1 &\equiv (\omega - \beta v_0)_1 = -\frac{\omega_c}{2} - \left[\left(\frac{\omega_c^2}{2} \right) + \frac{\langle \omega_{pb}^2 \rangle}{K_{\perp}} F_T(q\tau) \right]^{1/2} \\ \Omega_2 &\equiv (\omega - \beta v_0)_2 = \frac{\omega_c}{2} - \left[\left(\frac{\omega_c^2}{2} \right) + \frac{\langle \omega_{pb}^2 \rangle}{K_{\perp}} F_T(q\tau) \right]^{1/2} \\ \Omega_3 &\equiv (\omega - \beta v_0)_3 = -\frac{\omega_c}{2} + \left[\left(\frac{\omega_c^2}{2} \right) + \frac{\langle \omega_{pb}^2 \rangle}{K_{\perp}} F_T(q\tau) \right]^{1/2} \\ \Omega_4 &\equiv (\omega - \beta v_0)_4 = \frac{\omega_c}{2} + \left[\left(\frac{\omega_c^2}{2} \right) + \frac{\langle \omega_{pb}^2 \rangle}{K_{\perp}} F_T(q\tau) \right]^{1/2}. \end{aligned} \quad (13)$$

In the absence of the plasma ($K_{\perp} = 1$, $K_{\parallel} = 1$), and for a very thin beam ($q\tau \approx 0$; $F(q\tau) \approx F(0)$), Eq. 13 describes the well-known waves on a filamentary beam (Fig. XIII-26).

The transverse waves are circularly polarized, as can be seen by substituting the roots (13) in the force equation (10) to obtain

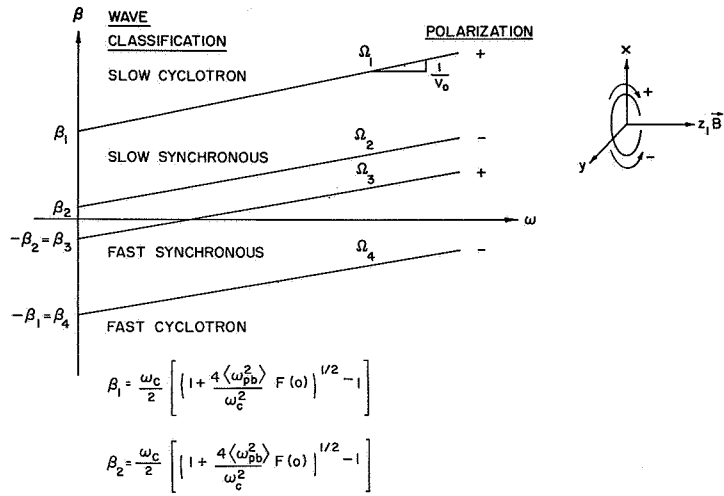


Fig. XIII-26. Waves on a filament — any beam in the absence of a plasma.

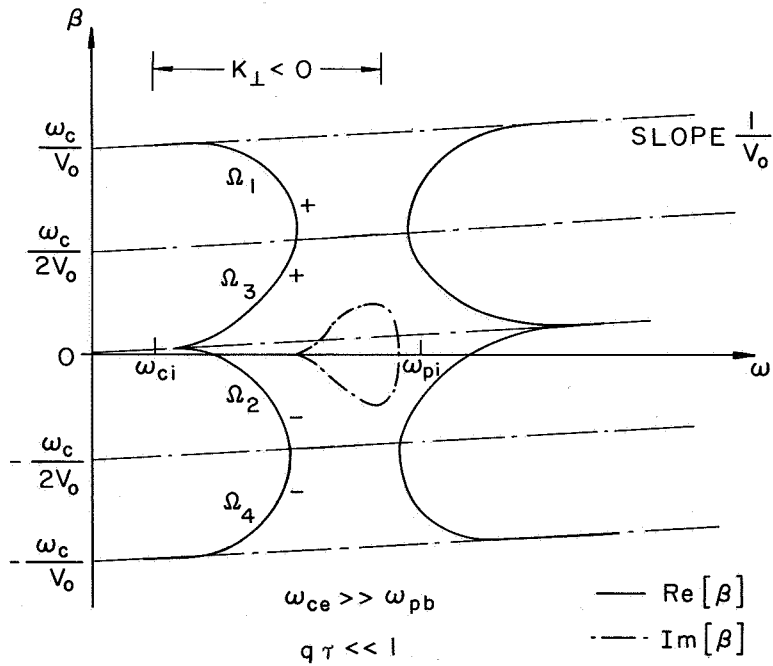


Fig. XIII-27. Low-frequency beam-plasma interactions for a filamentary beam.

(XIII. PLASMAS AND CONTROLLED NUCLEAR FUSION)

$$\frac{\delta_x}{\delta_y} = \begin{cases} -j & (\Omega = \Omega_1, \Omega_3) \\ +j & (\Omega = \Omega_2, \Omega_4) \end{cases} \quad (14)$$

It may be shown that roots Ω_1 and Ω_3 represent waves rotating in the sense of ions in the magnetic field (+ polarization). The other two waves rotate in the opposite sense (- polarization).

As an example of unstable modes that can arise when the plasma is present, Fig. XIII-27 illustrates reactive medium amplification, which arises when K_{\perp} is negative.

Note, at the onset of amplification, that the waves of similar polarization merge and have the same phase velocities.

b. Sheet Beam in a Bounded Cold Plasma

Finally, consider a sheet beam, infinite and uniform in the y direction, traveling with velocity $v_0 \bar{i}_z$ through a cold plasma bounded by two perfectly conducting plates (Fig. XIII-28). A longitudinal magnetic field $B \bar{i}_z$ is applied to the system.

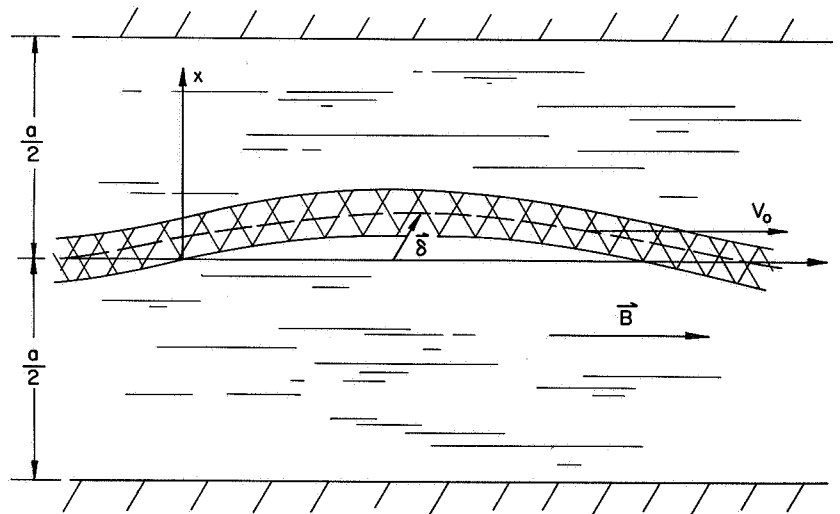


Fig. XIII-28. Sheet beam, and its rigid perturbation δ , in a bounded plasma.

The unperturbed beam is neutralized, with a symmetric density profile $n_0(x)$. The beam displacement $\bar{\delta}$ is independent of both x and y.

If we assume wave solutions of the form $\exp[j(\omega t - \beta z)]$ for the electrostatic potential $\bar{\delta}$, the perturbed density n_1 , and the displacement ϕ , Poisson's equation yields

$$\frac{\partial^2 \phi(x)}{\partial x^2} + p^2 \phi(x) = \frac{e}{\epsilon_0 K_{\perp}} \left[\delta_x \frac{\partial n_0}{\partial x} - j\beta n_0 \delta_z \right], \quad (15)$$

where

$$p^2 \equiv -\beta^2 \frac{K_{\parallel}}{K_{\perp}}$$

is the transverse wave number in the plasma. The force equations are

$$-\Omega^2 \delta_x = \frac{e}{m} \frac{\left\langle -n_0 \frac{\partial \phi}{\partial x} \right\rangle}{\left\langle n_0 \right\rangle} - j\omega_c \Omega \delta_y \quad (16a)$$

$$-\Omega^2 \delta_y = j\omega_c \Omega \delta_x \quad (16b)$$

$$-\Omega^2 \delta_z = \frac{e}{m} \frac{\left\langle j\beta n_0 \phi \right\rangle}{\left\langle n_0 \right\rangle}, \quad (16c)$$

where the quantities in angular brackets are to be averaged over the transverse dimensions of the plasma.

$$\left\langle n_0 \right\rangle = \frac{1}{a} \int_{-a/2}^{a/2} n_0(x) dx. \quad (17)$$

The procedure now is to expand $\phi(x)$ in terms of the eigenfunctions of Laplace's equation, obtained from Eq. 1 by setting the right hand side to zero. These eigenfunctions $\phi_m(x)$ are simply the natural plasma modes in the absence of the beam. Let

$$\phi(x) = \sum_{m=0}^{\infty} A_m \phi_m(x). \quad (18)$$

The eigenfunctions (natural modes) are

$$\phi_m(x) = \begin{cases} \cos \frac{m\pi z}{a} & m = 1, 3, 5 \dots \\ \sin \frac{m\pi x}{a} & m = 2, 4, 6 \dots \end{cases} \quad (19)$$

and the corresponding wave numbers are

$$p_m = \frac{m\pi}{a}. \quad (20)$$

(XIII. PLASMAS AND CONTROLLED NUCLEAR FUSION)

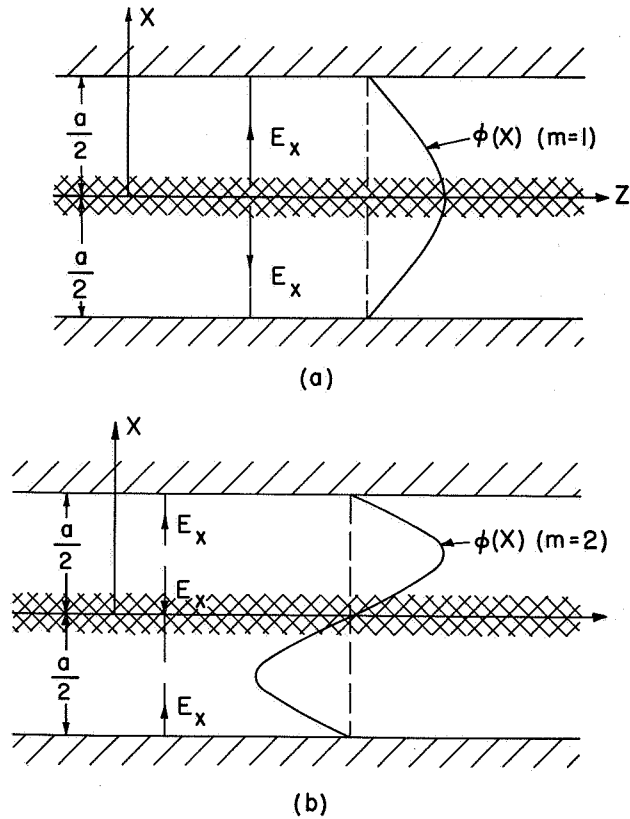


Fig. XIII-29. Field distributions for a sheet beam in a bounded plasma.
 (a) Transverse fields for longitudinal displacements.
 (b) Transverse fields for transverse displacements.

The two lowest natural modes and associated fields are shown in Fig. XIII-29. Equation 18 can now be written

$$\phi(x) = \sum_{m \text{ odd}} A_m \cos \frac{m\pi x}{a} + \sum_{m \text{ even}} A_m \sin \frac{m\pi x}{a}. \quad (21)$$

Substituting Eq. 21 in Eq. 15 and evaluating coefficients A_m , we obtain

$$\phi(x) = -\frac{2e}{\epsilon_0 K_{\perp}} \left\{ \sum_{m \text{ odd}} \frac{j\beta n_m \delta_z}{p^2 - \left(\frac{m\pi}{a}\right)^2} \cos\left(\frac{m\pi x}{a}\right) + \sum_{m \text{ even}} \frac{\left(\frac{m\pi}{a}\right) n_m \delta_x}{p^2 - \left(\frac{m\pi}{a}\right)^2} \sin\left(\frac{m\pi x}{a}\right) \right\}, \quad (22)$$

where

$$n_m = \frac{1}{a} \int_{-a/2}^{a/2} n_0(x) \cos \frac{m\pi x}{a} dx.$$

(XIII. PLASMAS AND CONTROLLED NUCLEAR FUSION)

It can be seen that longitudinal displacements excite only symmetric fields and transverse displacements only antisymmetric fields. This is obvious because of the beam symmetry. Substitution of Eq. 12 in Eq. 16 results in the following form for the force equations:

$$\left\{ \Omega^2 + \frac{1}{K_{\perp}} \frac{e^2 \langle n_o \rangle}{m \epsilon_o} \left[\sum_{m \text{ even}} \frac{2 \left(\frac{m\pi}{a} \right)^2}{p^2 - \left(\frac{m\pi}{a} \right)^2} \frac{n_m^2}{\langle n_o \rangle^2} \right] \right\} \delta_x = j \omega_c \Omega \delta_y \quad (23a)$$

$$\Omega^2 \delta_y = -j \omega_c \Omega \delta_x \quad (23b)$$

$$\left\{ \Omega^2 + \frac{1}{K_{\perp}} (\beta \tau)^2 \frac{e^2 \langle n_o \rangle}{m \epsilon_o} \left[\sum_{m \text{ odd}} \frac{2 \frac{n_m^2}{\langle n_o \rangle^2}}{\tau^2 \left[p^2 - \left(\frac{m\pi}{a} \right)^2 \right]} \right] \right\} \delta_z = 0, \quad (23c)$$

where τ is a characteristic beam thickness introduced for normalization purposes.

Notice in Eq. 23 that the transverse displacements are again uncoupled from the longitudinal displacements. The physical reason for this should be clear from Fig. XIII-29. Longitudinal displacements excite symmetric fields, which when averaged over the beam give no net transverse force. Similarly, transverse displacements do not give rise to a net longitudinal force.

The dispersion relation for the transverse modes is derived from Eqs. 23a and 23b.

$$\Omega^2 \left\{ \Omega^2 - \omega_c^2 + \frac{1}{K_{\perp}} \frac{e^2 n_o}{m \epsilon_o} \left[\sum_{m \text{ even}} \frac{2 \left(\frac{m\pi}{a} \right)^2}{p^2 - \left(\frac{m\pi}{a} \right)^2} \frac{n_m^2}{\langle n_o \rangle^2} \right] \right\} = 0. \quad (24)$$

The double root, $\Omega^2 = 0$, has no physical significance and corresponds to arbitrary displacements in the y direction. The other two roots give cyclotron-type waves.

For longitudinal modes, the dispersion equation is simply given by Eq. 23c.

The stability of this and other dispersion relations pertinent to our experiments are under study at present.

S-L. Chou, A. Bers

References

1. See Eq. 9 in Section XIII-A. 6.
2. See Eq. 18 in Section XIII-A. 6.

(XIII. PLASMAS AND CONTROLLED NUCLEAR FUSION)

8. SHEET MODELS OF THE BEAM-PLASMA DISCHARGE

We have continued the study of the beam-plasma discharge, using superparticles to represent the beam, and the fluid equations to represent the plasma. We are now studying the effects of finite beam diameter on the interaction, by representing the beam with disks. An analytic, linear, finite-diameter beam theory is presented here, for later comparison with computer experiments. The electrostatic approximation will be used throughout ($H=0$).

We assume: (i) no transverse beam motion; (ii) plasma transverse motion is unhindered; (iii) no radial variation in v_{bz} ; (iv) a cold infinite plasma with a linear density gradient along the beam; and (v) a uniform beam of radius b .

To evaluate assumptions (i) and (ii), we see, from Allis, Buchsbaum, and Bers,¹

$$\mathbf{v} = \frac{e}{m} \begin{pmatrix} \frac{\omega_{1,2}}{j(\omega_{1,2}^2 - \omega_c^2)} & \frac{-\omega_c}{\omega_{1,2}^2 - \omega_c^2} & 0 \\ \frac{\omega_c}{\omega_{1,2}^2 - \omega_c^2} & \frac{\omega_{1,2}}{j(\omega_{1,2}^2 - \omega_c^2)} & 0 \\ 0 & 0 & \frac{1}{j\omega_{1,2}} \end{pmatrix} \begin{pmatrix} E_x \\ E_y \\ E_z \end{pmatrix} \quad (1)$$

where

$$\omega_c = \frac{eB_0}{m}$$

$$\omega_1 = \omega - kv_0 \quad \text{for beam electrons}$$

$$\omega_2 = \omega \quad \text{for plasma electrons.}$$

In System A,

$$\omega \approx \omega_p = 2\pi \times 1.5 \times 10^{10} \text{ Hz}$$

$$\omega_c = 2\pi \times 2.8 \times 10^6 \text{ Hz/Gauss}$$

$$0 < B_0 < 700 \text{ Gauss.}$$

Since $\omega_2 \approx \omega_p^2 \gg \omega_c^2$, assumption (ii) is valid. Assumption (i) requires $\omega_1^2 \ll \omega_c^2$ if the transverse fields are of the same magnitude as the longitudinal field. But

$\omega_1^2 = (\omega - \text{Re } kv_0 - j\text{Im } kv_0)^2 \approx -(\text{Im } kv_0)^2 \approx -\left(\frac{\omega_p}{5}\right)^2$, which we obtain by anticipating the results of Fig. XIII-30. Hence the transverse beam motion would be reduced by less

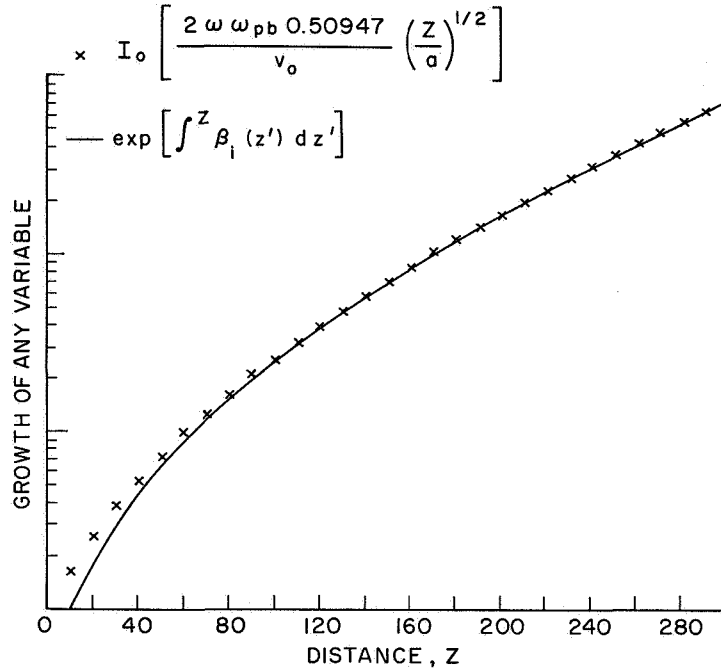


Fig. XIII-30. W K B approximation to the growth of any variable in a finite-diameter beam-plasma interaction, with a linear plasma density gradient. This is compared with the growth of the first-order beam velocity in a one-dimensional beam. Distances normalized to $0.4 v_{ob} \omega_{po}^{-1}$.

than a factor of 2. For a symmetric mode, however, the transverse field on the axis is zero, and might be expected to be small over the beam. The quantitative effects of assumptions (i) and (iii) are not completely understood.

We assume a cold plasma with a linear density gradient given by

$$\omega_p^2 = \omega^2 + az. \quad (2)$$

For quasi-statics, the pertinent equations are

$$\nabla \cdot (\bar{K}_{11} \cdot \nabla \phi) = -\frac{en_b}{\epsilon_0} \quad (3)$$

$$K_{11} = \bar{I} \left(1 - \frac{\omega_p^2(z)}{\omega^2} \right) = -\frac{az}{\omega^2} \bar{I}. \quad (4)$$

(XIII. PLASMAS AND CONTROLLED NUCLEAR FUSION)

We make Fourier-Bessel transforms in the transverse direction.

$$\Phi_r = \frac{1}{(2\pi)^2} \int_0^\infty dk \int_0^{2\pi} d\phi k e^{ikr \cos(\theta-\phi)} \Phi_k,$$

under the assumption of θ - symmetric modes, or

$$\Phi_r = \frac{1}{2\pi} \int_0^\infty dk J_0(kr) \Phi_k, \quad (5)$$

and

$$\Phi_k = 2\pi \int_0^\infty dr r J_0(kr) \Phi_r, \quad (6)$$

Equation 3 becomes

$$\frac{az}{\omega^2} k^2 \Phi_k - \frac{a}{\omega^2} \frac{\partial \Phi_k}{\partial z} - \frac{az}{\omega^2} \frac{\partial^2 \Phi_k}{\partial z^2} = - \frac{en_{bk}}{\epsilon_0}. \quad (7)$$

The conservation equation can be written

$$n_b = -\nabla \cdot [n_{ob}(r) \delta]$$

or, by using assumption (i),

$$n_{bk} = -n_{ok} \frac{\partial \delta}{\partial z}, \quad (8)$$

where δ is the displacement from equilibrium. We use assumption (iii) in the force equation, so that

$$\left[j\omega + v_0 \frac{\partial}{\partial z} \right]^2 n_{ob} \delta_z = \frac{e}{m} \left\langle n_{ob} \frac{\partial \Phi}{\partial z} \right\rangle. \quad (9)$$

We define the average as

$$\langle \rangle \equiv \lim_{r_0 \rightarrow \infty} \frac{2\pi}{\pi r_0^2} \int_0^{r_0} dr r. \quad (10)$$

Hence

$$\langle n_o \Phi \rangle = \lim_{r_0 \rightarrow \infty} \frac{2\pi}{\pi r_0^2} \int_0^{r_0} dr r \int_0^\infty \frac{dk}{2\pi} k n_{ok} J_0(kr) \int_0^\infty \frac{dk'}{2\pi} k' \Phi_{k'} J_0(k'r)$$

or

(XIII. PLASMAS AND CONTROLLED NUCLEAR FUSION)

$$\langle n_o \Phi \rangle = \frac{1}{\pi r_o^2} \int_0^\infty \frac{dk}{2\pi} k n_{ok} \Phi_k. \quad (11)$$

To proceed further, we use the W K B approximation ($\frac{\partial}{\partial z} = -j\beta$). We combine Eqs. 7, 8, 9, and 11 to obtain

$$(\omega - \beta v_o)^2 \frac{-e^2 \beta^2 \omega^2}{m \epsilon_o \langle n_o \rangle \pi r_o^2 a 2\pi} \int_0^\infty \frac{dk k n_{ok}^2}{[z(\beta^2 + k^2) + j\beta]}, \quad (12)$$

since

$$\begin{aligned} n_o(r) &= n_o & r \leq b \\ &= 0 & r > b \end{aligned} \quad (13)$$

$$n_{ok} = \frac{2\pi n_o b J_1(kb)}{k}. \quad (14)$$

We know that

$$\langle n_o \rangle \pi r_o^2 = \pi b^2 n_o, \quad (15)$$

and hence we define

$$\omega_{pb}^2 = \frac{e^2 n_o}{m \epsilon_o}. \quad (16)$$

Then

$$(\omega - \beta v_o)^2 = \frac{-\omega_{pb}^2 \beta^2 \omega^2}{a} \int_0^\infty \frac{dk J_1^2(kb)}{k [z(\beta^2 + k^2) + j\beta]} \quad (17)$$

or

$$(\omega - \beta v_o)^2 = \frac{-\omega_{pb}^2 \beta^2 \omega^2}{az(\beta^2 + j\beta/z)} \left[1 - 2I_1 \left(b \sqrt{\beta^2 + j\beta/z} \right) K_1 \left(b \sqrt{\beta^2 + j\beta/z} \right) \right] \quad (18)$$

If the plasma were homogeneous, we would replace az with $\omega_p^2 - \omega^2$, and drop the

$j\beta/z$ terms, which arose from the fact that $\frac{\partial \omega_p^2}{\partial z} \neq 0$. Then Eq. 19 becomes

$$1 - \frac{\omega_p^2}{\omega^2} - \frac{\omega_{pb}^2}{(\omega - \beta v_o)^2} [1 - 2I_1(\beta b) K_1(\beta b)] = 0. \quad (19)$$

(XIII. PLASMAS AND CONTROLLED NUCLEAR FUSION)

This can be contrasted with the calculations done under the assumption of transverse beam motion.²

$$1 - \frac{\omega_p^2}{\omega^2} - \frac{\omega_{pb}^2}{(\omega - \beta v_o)^2} \beta b I_1(\beta b) K_0(\beta b) = 0. \quad (20)$$

Equations 19 and 20 have different limits as $b \rightarrow \infty$. Equation 19 goes to the correct one-dimensional limit, but Eq. 20 becomes

$$1 - \frac{\omega_p^2}{\omega^2} - \frac{\omega_{pb}^2/2}{(\omega - \beta v_o)^2} = 0. \quad (21)$$

Crawford³ has concluded that the fields of Eq. 20 are due entirely to surface charge at the beam edge, whereas in the one-dimensional limit the fields are due to volume charge. The fields of Eq. 19 are due entirely to volume charge, so that correct limit as $b \rightarrow \infty$ is physically reasonable.

We have solved Eq. 18 on the computer, using normalized beam and plasma parameters as given in a previous report,⁴ corresponding to typical values in System A.

$$\begin{aligned} (\omega_{pb}) &= 0.1 & \omega &= (0.15)^{1/2} \\ a &= 0.001 & (v_o) &= 2.5 \end{aligned}$$

$$b_n = 4.69.$$

Distances are normalized to $0.4 v_o / \omega_{po}$, times to ω_{po}^{-1} . ω_{po} corresponds to the peak density in System A.

In the WKB approximation, all first-order plasma and beam parameters grow at the same rate. This growth is shown in Fig. XIII-30. It is compared with $I_o \left[\frac{2\omega_{pb}'}{v_o} \left(\frac{z}{a} \right)^{1/2} \right]$, the growth of the first-order beam velocity in one dimension. The two curves have been matched at $z = 250$ and $z = 300$. We found that $\omega_{pb}' = 0.50947 \omega_{pb}$ for a match, or an effective beam density reduction factor of approximately 0.25.

J. A. Davis

References

1. W. P. Allis, S. Buchsbaum, and A. Bers, *Waves in Anisotropic Plasmas* (The M.I.T. Press, Cambridge, Mass., 1963), p. 19.
2. E.E. Abraham and F.W. Crawford, "Comparison of Experimental and Theoretical Results of the Beam-Plasma Interaction," Stanford University SU-IPR Report No. 24, August 1965.
3. F. W. Crawford, *J. Electronics and Control* 19, 217 (1965).
4. J. A. Davis, Quarterly Progress Report No. 84, Research Laboratory of Electronics, M.I.T., January 15, 1967, pp. 145-148.

9. EFFECT OF ESSENTIAL SINGULARITIES ON STABILITY CRITERIA

The interaction of a monoenergetic beam with a cold collisionless plasma, as described by the dispersion relation

$$\frac{\omega_{pb}^2}{(\omega - kv_0)^2} + \frac{\omega_p^2}{\omega^2} = 1, \quad (1)$$

is often cited as a classical example of a convective instability.¹ The purpose of this note is to point out that this is not strictly correct, and to show why caution should be exercised in other examples in which the dispersion relation has roots $k(\omega)$ for which $k \rightarrow \infty$ at some real ω . (That is, cases for which there are essential singularities of $F(\omega, z)$ on the real ω axis.²)

The response $\psi(z, t)$, which is due to an excitation at the plane $z = 0$, has the form

$$\psi(z, t) = \int_{-\infty - j\sigma}^{\infty - j\sigma} \int_{-\infty}^{+\infty} \frac{e^{j(\omega t - kz)} s(\omega)}{\left(k - \frac{\omega}{v_0} - K(\omega)\right) \left(k - \frac{\omega}{v_0} + K(\omega)\right)} \frac{dk d\omega}{(2\pi)^2}, \quad (2)$$

where

$$K(\omega) = \frac{\omega_{pb}}{v_0} \left(1 - \omega_p^2/\omega^2\right)^{-1/2}. \quad (3)$$

The source considered here is of the form $s(t, z) = \delta(z) \exp(j\omega_0 t)$ for $t > 0$, for which $s(\omega) \sim (\omega - \omega_0)^{-1}$. The k integration can be readily done, and yields

$$\psi(z, t) = - \int_{-\infty - j\sigma}^{+\infty - j\sigma} s(\omega) e^{j\omega(t - z/v_0)} \frac{\sin K(\omega) z}{K(\omega)} \frac{d\omega}{2\pi} \quad (4)$$

for $z > 0$. The integrand in Eq. 4 has an essential singularity at $\omega = \omega_p$ in addition to the simple pole at $\omega = \omega_0$, and this fact complicates its asymptotic evaluation. We shall consider both t and z to be fairly large, and evaluate the integral asymptotically by a saddle-point method. Let $\tau = t - z/v_0$ and

$$\phi(\omega) \equiv \omega\tau - K(\omega)z. \quad (5)$$

The saddle points are determined by $\partial\phi(\omega)/\partial\omega = 0$. For $\omega_p\tau \gg k_b z$ (where $k_b \equiv \omega_{pb}/v_0$), there is a saddle point at

$$\omega_s = \omega_p \left[1 + \frac{1}{2} \left(\frac{k_b z}{\omega_p \tau} \right)^{2/3} e^{-j2\pi/3} \right] \quad (6)$$

(XIII. PLASMAS AND CONTROLLED NUCLEAR FUSION)

for which

$$\phi(\omega_s) = \omega_p \tau + \frac{3}{2} (k_b z)^{2/3} (\omega_p \tau)^{1/3} e^{-j2\pi/3}. \quad (7)$$

The saddle-point integration leads to the asymptotic response

$$\psi(z, t) \sim \exp \left\{ j \omega_p \tau + \frac{3\sqrt{3}}{4} (k_b z)^{2/3} (\omega_p \tau)^{1/3} \right\} \quad (8)$$

for $z > 0$ ($\psi = 0$ for $z < 0$), independent of the source frequency ω_0 . The intuitive reason why this model predicts continued growth in time, and not steady-state amplification at ω_0 , is quite clear: The cold collisionless model of the beam-plasma interaction predicts infinite amplification rate at ω_p , and therefore the spectral components of the source very near ω_p head for this level (∞) as $t \rightarrow \infty$. It is interesting to contrast the form of the growth in Eq. 8 with the more usual absolute instability formed from pinching poles. In the latter case, the asymptotic growth with time is as $\exp(\alpha t)$, with the same α at every position z ; in the present case, the response grows in time at a rate that depends on z .

The present refinements on stability criteria are chiefly of theoretical, as opposed to practical, significance, since a realistic plasma model should include temperature and/or collisional effects if the one-dimensional assumption is retained. As an example, in the limit of a very small collision frequency, γ_c , and zero plasma temperature, we can carry over the previous results by replacing ω_p with $\omega_p (1 + j\gamma_c/2\omega)$ everywhere in the equation above. The essential singularity is now displaced into the upper-half ω -plane, and we can show that $\psi(t, z)$ remains bounded as $t \rightarrow \infty$. It is interesting to note, however, that the saddle-point evaluation of $\psi(z, t)$ in Eq. 8 now shows that

$$\psi_s(z, t) \sim \exp \left(-\frac{\gamma_c}{2} \tau + \frac{3\sqrt{3}}{4} (k_b z)^{2/3} (\omega_p \tau)^{1/3} \right). \quad (9)$$

That is, $\psi_s(t, z)$ grows for a (relatively) long time at the "collisionless" rate before the collisional damping sets in. The maximum of $\psi_s(z, t)$ is reached when

$$\tau_m = \left(\frac{\sqrt{3}}{2} \right)^{3/2} \frac{k_b z \left(\omega_p^{1/2} \right)}{(\gamma_c)^{3/2}}, \quad (10)$$

and is

$$\psi_{\max}(z) \sim \exp \left[\left(\frac{\sqrt{3}}{2} \right)^{3/2} \left(\frac{\omega_p}{\gamma_c} \right)^{1/2} k_b z \right]. \quad (11)$$

This maximum of the response, ψ_{\max} , can be shown to be identical to the maximum

(XIII. PLASMAS AND CONTROLLED NUCLEAR FUSION)

steady-state amplification for small γ_c . A more detailed investigation of the transient aspects of this problem shows that the saddle-point contribution to ψ (ψ_s as given in Eq. 9) is the dominant part of the response until the time τ_m given in Eq. 10 (when $\psi_s = \psi_{\max}$ as given in Eq. 11). For $\tau > \tau_m$, the pole at $\omega = \omega_0$ (which we have not yet discussed explicitly) becomes important at the time when ψ_s drops below the steady-state amplification level at the same source frequency, ω_0 . That is, it can be shown that τ_m represents the minimum time for steady-state conditions to be reached at any position z .

In other physical situations, the effects of plasma temperature might be more important than collisions. It can be shown that the instability is again convective for small but finite plasma temperature and zero collision frequency. Finally, we should mention that Sturrock³ pointed out some time ago that if one considers a cold drifting plasma interacting with a beam, then the point of zero plasma drift is the critical point between convective and nonconvective behavior.

To summarize, it has been illustrated by one example how caution must be exercised in stability criteria when an essential singularity of $F(\omega, z)$ exists on the real ω -axis. In these cases, the resolution of the convective or absolute nature of the instability may often rest on the inclusion of additional physical parameters in the model.

The importance of the essential singularities was first pointed out to the author by B. R. Kusse in a different example.

R. J. Briggs

References

1. The notation in this report follows R. J. Briggs, Electron-Stream Interaction with Plasmas (The M.I.T. Press, Cambridge, Mass., 1964), p. 32.
2. Ibid., p. 22.
3. P. A. Sturrock, "Kinematics of Growing Waves," Phys. Rev. **112**, 1488-1503 (1958).

(XIII. PLASMAS AND CONTROLLED NUCLEAR FUSION)

10. MOTION OF CHARGED PARTICLES IN MAGNETIC MIRROR FIELD IN THE PRESENCE OF A RADIAL TIME-VARIANT ELECTRIC FIELD

The presence of a uniform RF electric field affects the gyrating motion of a charged particle in a uniform magnetic field perpendicular to the RF electric field according to the frequency of the RF field (ω). For $\omega \gg \omega_B$ (ω_B is the frequency of gyration) and $\omega \ll \omega_B$, there is no time-average exchange of energy between the electromagnetic field and the particle. But for $\omega = \omega_B$, the particles gain energy from the field, because of the cyclotron resonance. Those particles that start in phase with the field will gain energy indefinitely, until radiation losses and relativistic effects become significant. Those starting out of phase will lose energy until they are brought into phase with the RF field.

If the magnetic field is nonuniform, the resonance interaction will be modified. Transverse gradients of the magnetic field produce a frequency of gyration that depends on radial position. Longitudinal gradients add an acceleration along the field lines and, as in the case of a magnetic mirror, may cause reflections (see Appendix A). The acceleration experienced by a particle will also depend on its radial position, because of the radial gradients of the electric field. The phase relationship between the gyrating particle and the applied RF field is thus altered from the uniform field case.

In general, there are many mechanisms in a plasma which change the phase relationship between the particles and the field. It is our interest to study the effect of the nonuniformity of the fields on the energy exchange between the RF field and a single particle.

The trajectories of the particles are obtained by numerical integration of the normalized nonrelativistic equations of motion. The fields that are used are a magnetic mirror field and an electric field, attributable to an oscillating line charge. The frequency of the electric field corresponds to an average cyclotron frequency at the midplane of the mirror. The trajectories to be studied can be classified as follows: Class I, Particles that stay in the midplane; Class II, Particles that stay close to the midplane; and Class III, Particles that move far from the midplane.

Results

A measure of the inhomogeneity of the magnetic field is given by the mirror ratio (the ratio of the maximum to the minimum value of the field along the axis) and the aspect ratio (L/L_0 - the ratio of the distance between the points of maximum field strength along the axis to the maximum radial distance of interest). The ratio of characteristic Larmor radius for the particle motion to the radial dimension of the system $\left(R_L = \frac{mV}{qB_0} \frac{1}{L_0} \right)$ gives a measure of the portion of space that the particle samples. The

(XIII. PLASMAS AND CONTROLLED NUCLEAR FUSION)

ratio of the energy in the electric field to the initial energy of the particle is given by \tilde{K}/R_L , where \tilde{K} is the normalized constant associated with the field (see Appendix A). The frequency of the applied electric field is the controlling parameter for the exchange of energy between particle and field. The corresponding values are given in Appendix B.

Trajectories of Class I

See Fig. XIII-31. (Also, see Appendix B.) The initial velocity is in phase with the field. The energy increases monotonically with time. The normalized radial position

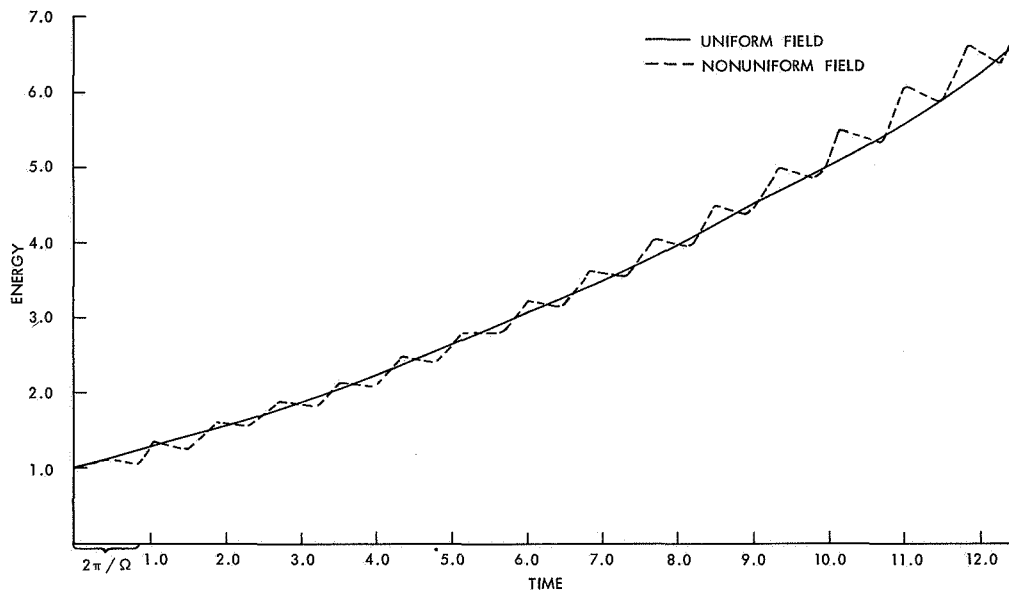


Fig. XIII-31. Energy as a function of time for a particle that stays in the midplane and starts in phase with the electric field, compared with a particle starting in phase (for the cyclotron-resonance case) in uniform electric and magnetic fields.

of the guiding center oscillates about a value of approximately 0.44, and the amplitude of this oscillation reaches values of approximately 0.1. After $T \approx 8.26$ (approximately 10 cyclotron periods), the particle has completed one revolution around the axis. As time increases, the energy gained by the particle becomes larger than that predicted for the uniform fields.

See Fig. XIII-32. The initial velocity is out of phase with the electric field. The energy decreases up to a time $T = 7.05$ (~ 8.5 cyclotron periods). For times greater than this the energy increases, since the particle has been brought into phase with the field. The normalized radial position of the guiding center moves inward from an initial

(XIII. PLASMAS AND CONTROLLED NUCLEAR FUSION)

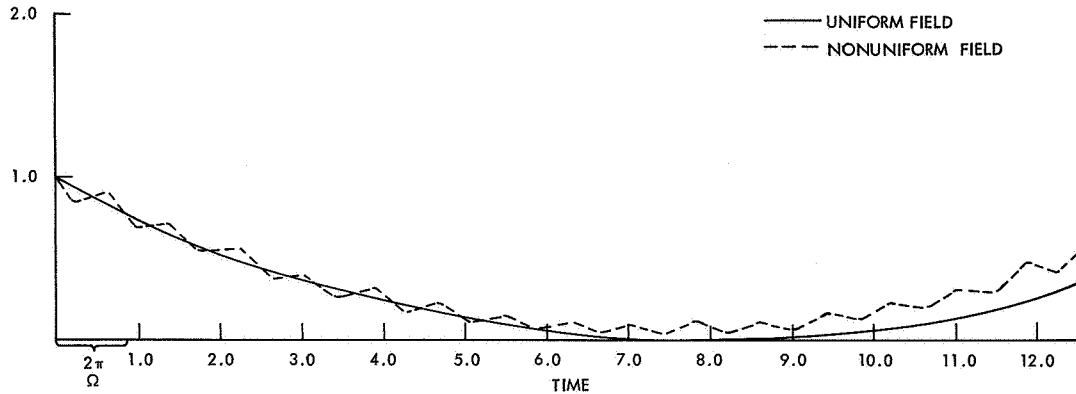


Fig. XIII-32. Energy as a function of time for a particle that stays in the midplane out of phase with the electric field, compared with the corresponding case in uniform fields.

position ~ 0.428 to an average value of approximately 0.4061. The variations about this value decrease as the energy decreases, and start to increase as the energy increases. After approximately 25.5 cyclotron periods, the particle has completed one revolution around the axis.

Trajectories of Class II

See Fig. XIII-33. The initial velocity is in phase with the field. The energy and the magnetic moment increase. The normalized radial position of the guiding center has an initial value of 0.428, and moves out to an average value of 0.45. The variations about this position reach values of approximately 0.1. The particle reflects at ~ 2.41 cyclotron periods ($T = 5.0566$), ~ 9.12 cyclotron periods, ~ 11.9 cyclotron periods, and 14.05 cyclotron periods. The z coordinate of the reflection points moves inward as the energy increases. For the first reflection the guiding center is located at $z \approx 0.0866$. By the time of the third reflection, the particle has completed one revolution around the axis.

See Fig. XIII-34. The initial velocity is out of phase with the field. The energy and the magnetic moment decrease until ~ 7.5 cyclotron periods ($T = 5.778$). For times greater than this, the energy and the magnetic moment increase. The normalized radial position of the guiding center is initially ~ 0.428 , goes down to an average of 0.405 as the energy goes down, and increases back to an average of ~ 0.415 as the energy starts to increase. The particle is brought into phase between the first and second reflections. Thus, the z coordinate for the first reflection is farther away from the midplane than the others, since it corresponds to the reflection of lowest energy. The z coordinates of the reflection points move toward the midplane as energy increases. At ~ 17.05 cyclotron periods, the third reflection occurs, and the guiding center is at $z = 0.1203$, while

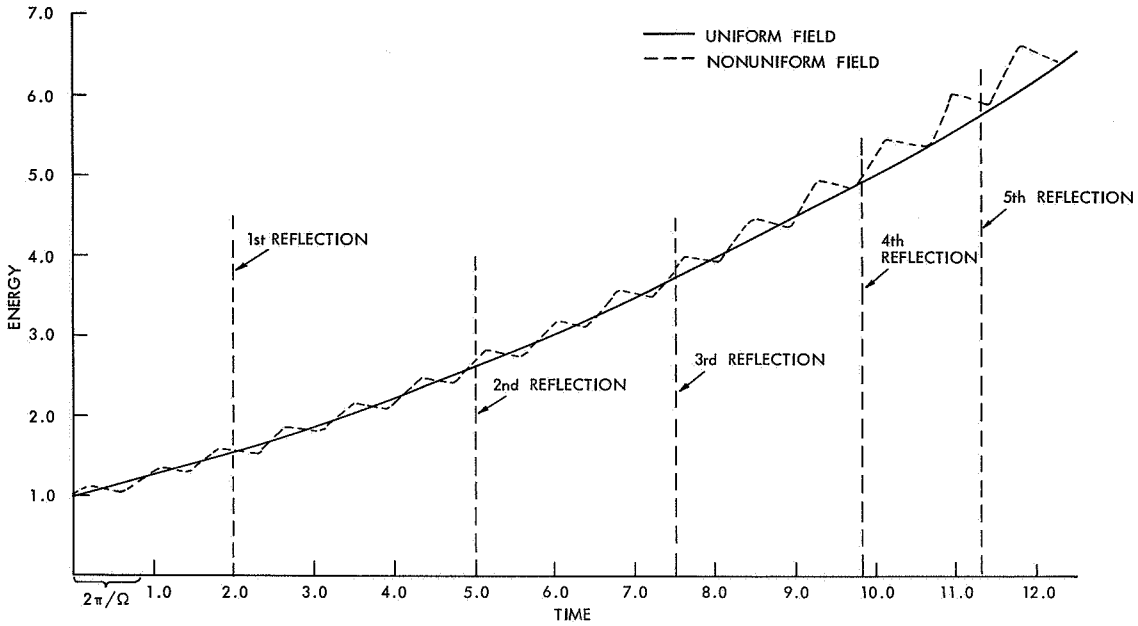


Fig. XIII-33. Energy as a function of time for a particle that stays close to the midplane and starts in phase with the electric field, compared with the corresponding case in uniform fields.

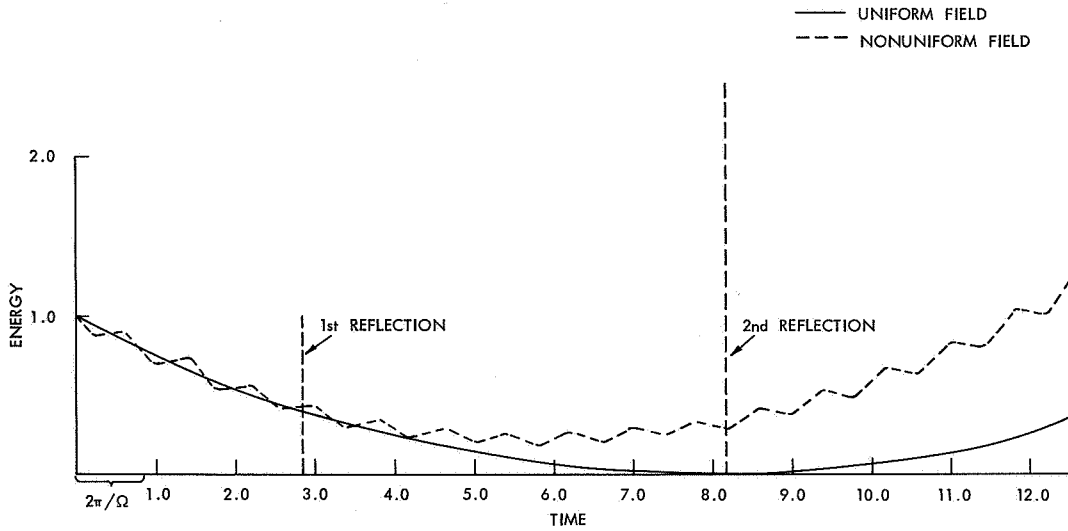


Fig. XIII-34. Energy as a function of time for a particle that stays close to the midplane and starts out of phase with the electric field, compared with the corresponding case in uniform fields.

(XIII. PLASMAS AND CONTROLLED NUCLEAR FUSION)

for the first reflection it was at $z = 0.167$. At ~ 20.65 cyclotron periods, the particle's angular position is 5.81 radians (not having completed one revolution around the axis). The trajectories of particles that move far away from the midplane are now under study.

Appendix A. The Fields and Their Normalization in Computations

The magnetic field used for the calculations is of the form

$$B_r = -B_0 a I_1 \left(\frac{2\pi r}{L} \right) \sin \left(\frac{2\pi z}{L} \right)$$
$$B_z = B_0 \left[1 - a I_0 \left(\frac{2\pi r}{L} \right) \cos \left(\frac{2\pi z}{L} \right) \right],$$

where the mirror ratio $R_m = (1+a)/(1-a)$, L is the distance between the mirrors, and B_0 is the field at $r = 0$, $z = \pm L/4$. The electric field is given by

$$E_r = \frac{K}{r} (1 + \cos \omega t) \quad r \geq 0.1 R_{\max}$$
$$= \frac{K}{0.1 R_{\max}} (1 + \cos \omega t) \quad r \leq 0.1 R_{\max}$$

A way of producing an electric field of this type has been proposed by L. D. Smullin.¹

The equations of motion are normalized by using as variables $\vec{V} = \vec{v}/v_0$, $\vec{B} = \vec{B}/B_0$, $\vec{E} = \vec{E}/v_0 B_0/c$, $T = v_{0t}/L_0$, $\vec{R} = \vec{r}/L_0$, where L_0 is a characteristic length (R_{\max}), B_0 is a characteristic value of the magnetic field ($B(r=0, z=\pm L/4)$), and v_0 is a characteristic velocity (the initial velocity). Then the equations of motion are

$$R_L \frac{d\vec{V}}{dT} = \vec{E} + \vec{V} \times \vec{B}, \quad (1)$$

where $R_L = \frac{mv_0}{qB_0} \frac{1}{L_0}$ is the ratio of the characteristic Larmor radius to the characteristic length. The normalized fields are

$$\vec{B}_r = -a I_1 \left(2\pi R \frac{L_0}{L} \right) \sin \left(2\pi Z \frac{L_0}{L} \right)$$
$$\vec{B}_z = 1 - a I_0 \left(2\pi R \frac{L_0}{L} \right) \cos \left(2\pi Z \frac{L_0}{L} \right)$$
$$\vec{E}_r = \frac{K}{R} (1 + \cos \Omega t),$$

where

$$\tilde{K} = \frac{K}{\frac{L_0 V_0 B_0}{C}}, \quad \Omega = \frac{\omega}{(v_0/L_0)}$$

$$\tilde{\Omega}_B = \frac{\omega_B}{(v_0/L_0)} = \frac{B}{R_L}$$

For the uniform fields,

$$\tilde{E}_r = \frac{E_0}{\frac{v_0 B_0}{C}} (1 + \cos \Omega T); \quad \tilde{B} = \frac{B}{B_0}$$

The solution to Eq. 1, with uniform fields and $\Omega = \Omega_B$, is

$$V_R = V_r(0) \cos \Omega_B T + \left(V_0(0) + \frac{3}{2} \frac{E_0}{\tilde{B}} \right) \sin \Omega_B t + \frac{E_0}{2R_L} t \cos \Omega_B t$$

$$V_\theta = -V_r(0) \sin \Omega_B T + \left(V_\theta(0) + \frac{E_0}{\tilde{B}} \right) \cos \Omega_B t + \frac{E_0}{2R_1} t \sin \Omega_B T - \frac{E_0}{\tilde{B}}$$

When $V_\theta(0) = 0$. The energy in the uniform field case can be approximated by

$$EN = V_R^2(0) + V_R(0) \frac{E_0}{R_L} t + \frac{E_0^2}{4R_L} 2t^2.$$

When $V_R = 0$, this approximation is not useful because the cross terms become important in carrying the information about the initial phase difference.

Appendix B. Parameters Used in the Computation

All computations have been done by using the following values.

Mirror Ratio = 1.5

$R_L = 0.1$

$K = 0.01$ (which corresponds to an E_0 (in the uniform case) of 0.025)

$\frac{L}{L_0} = 3.0$

$\Omega = 7.6$.

The following trajectories have been studied.

Class I. Particles that stay in the midplane. Initial position - $R_0 = 4$

(XIII. PLASMAS AND CONTROLLED NUCLEAR FUSION)

$$\theta_0 = 0.0, \quad z_0 = 00$$

- (a) $V_0 = 1.0 i_r$ - in phase with the RF field
- (b) $V_0 = -1.0 i_r$ - out of phase with the RF field
- (c) $V_0 = 1.0 i_\theta$ - out of phase with the RF field
- (d) $V_0 = -1.0 i_\theta$ - out of phase with the RF field.

Class II. Particles that stay close to the midplane. Same initial position.

- (a) $V_0 = 0.9949874 i_r + 0.1 i_z$
- (b) $V_0 = -0.9949874 i_r + 0.1 i_z$
- (c) $V_0 = 0.9949874 i_\theta + 0.1 i_z$
- (d) $V_0 = -0.9949874 i_\theta + 0.1 i_z$.

O. Lopez, J. G. Siambis

References

1. L. D. Smullin, Quarterly Progress Report No. 80, Research Laboratory of Electronics, January 15, 1966, pp. 111-113.

XIII. PLASMAS AND CONTROLLED NUCLEAR FUSION*

B. Applied Plasma Physics Related to Controlled Nuclear Fusion

Academic and Research Staff

Prof. D. J. Rose
Prof. T. H. Dupree

Prof. L. M. Lidsky
Prof. E. P. Gyftopoulos

Prof. S. Yip
Dr. K. Chung

Graduate Students

K. R-S. Chen
H. Ching
D. G. Colombant
R. W. Flynn

R. A. Hill
M. Hudis
W. H. Manheimer
G. R. Odette

L. C. Pittenger
A. Sugawara
C. E. Wagner
A. Watanabe

1. EXPERIMENTAL STUDY OF HOLLOW-CATHODE DISCHARGE ARC PLASMA

We have continued the study of the highly ionized Argon plasma produced by the hollow-cathode discharge arc (HCD).¹ This study includes measurement of the ion temperature, and observation of the plasma oscillations with correlation techniques used.

Ion Temperature

We have measured the ion temperature by observing the Doppler broadening of a singly ionized Argon spectral line at 4806 Å. A Fabry-Perot interferometer was designed and built which has a resolving power of 7.57×10^5 . During the operation of the interferometer, the spacing between the plates was fixed, and the pressure of gas (N_2) of the interferometer cell was varied to change the index of refraction. A typical profile of the spectral line is shown in Fig. XIII-35, in which the phototube output is traced simultaneously with the pressure of the cell. Analyzing the spectral profile according to the expression for the Doppler half-width,

$$\delta\lambda_D = \lambda_0 (\ln 2) \left(\frac{2kT_i}{mc^2} \right)^{1/2}, \quad (1)$$

where λ_0 is 4806 Å for our case, we obtained the experimental ion temperature. In the actual analysis, we included the Zeeman splitting of the spectral line caused by the presence of a strong axial magnetic field. The typical datum shown in Fig. XIII-35 represents an ion temperature of 0.41 eV, as compared with the electron temperature of 5.82 eV measured by the Langmuir probe.

Estimating the charge transfer cross section by extrapolating the available values (for $20 \text{ eV} \geq kT_i \geq 1 \text{ eV}$) into the energy range for this experiment, we computed the

*This work was supported by the National Science Foundation (Grant GK-1165).

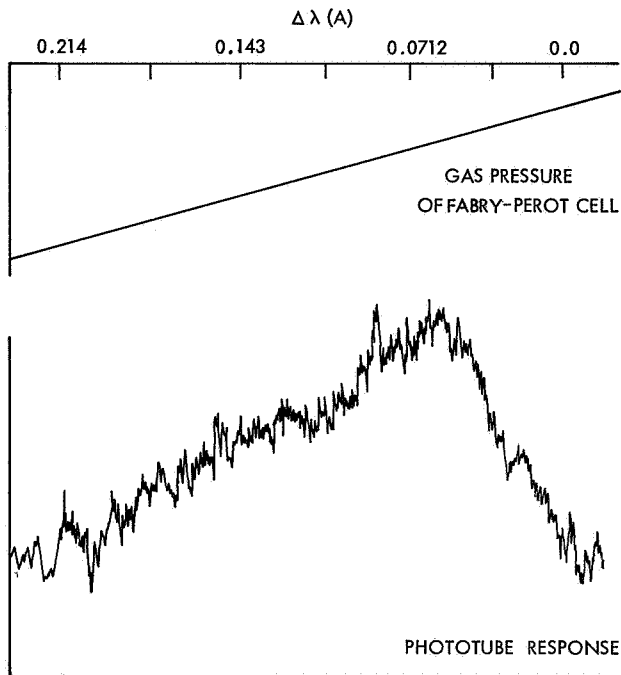


Fig. XIII-35.
Spectral-line profile obtained by a Fabry-Perot interferometer. ($r = 0 \pm 0.2$ cm, $T_e = 5.28$ eV, $T_i = 0.41$ eV).

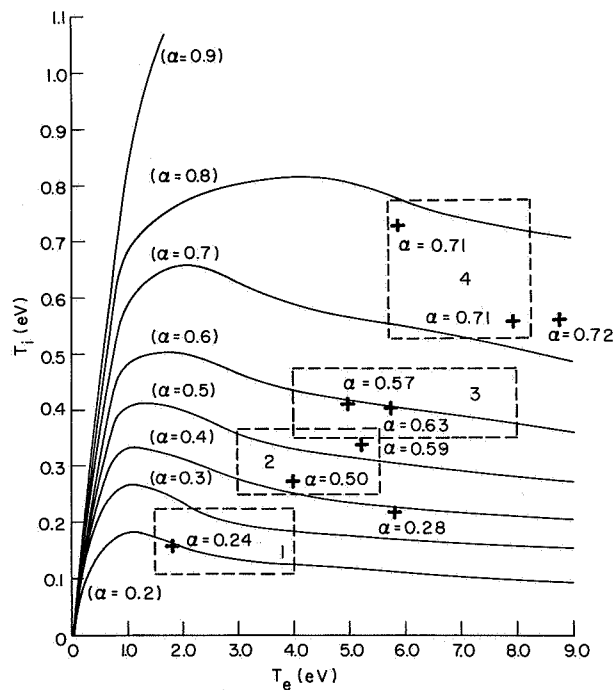


Fig. XIII-36. Ion temperature vs electron temperature with different values of α (degree of ionization). The typical experimental points are represented by + and corresponding α values. In region 1, $B = 1.4$ kGauss, $r = 0.8 \pm 0.2$ cm; in region 2, $B = 2.8$ kGauss, $r = 0.8 \pm 0.2$ cm; in region 3, $B = 1.4$ kGauss, $r = 0 \pm 0.2$ cm, and in region 3, $B = 2.8$ kGauss, $r = 0 \pm 0.2$ cm.

degree of ionization, α , as a function of the ion and electron temperatures.

$$\alpha = \frac{n_i}{n_i + n_o} = \left\{ 1 + \left(\frac{kT_e}{kT_i} - 1 \right) \frac{\sigma_{ie}}{\sigma_{io}} \right\}^{-1}, \quad (2)$$

where the collision cross section for energy transfer to ions from electrons, σ_{ie} , was replaced by $26/T_e^{3/2} T_i^{1/2} \text{ \AA}^2$, and σ_{io} is the charge transfer cross section.

The direct experimental values of α can be obtained through the plasma density measurement by the probe and the background pressure reading. In Fig. XIII-36 we show a comparison between the values of α by plotting the experimental points in the $(T_i - T_e)$ -plane. On the other hand, we can estimate the ion temperature by using the experimental value of α with the aid of relation (2). Within some restricted operation conditions of the HCD, we obtained an excellent agreement between the experimental and calculated ion temperatures (within 10% difference).

Plasma Oscillations

We have investigated the nature of the oscillations² when the plasma is unstable. Langmuir probe data are analyzed by obtaining autocorrelations and crosscorrelations electronically in quasi-real time. In Fig. XIII-37 we show an oscilloscope picture of the oscillations, and the autocorrelogram of the oscilloscope picture taken by the correlator. The autocorrelation of a signal $f_A(t)$,

$$R_A(\tau) = \frac{1}{T} \int_0^T f_A(t) f_A(t+\tau) dt, \quad (3)$$

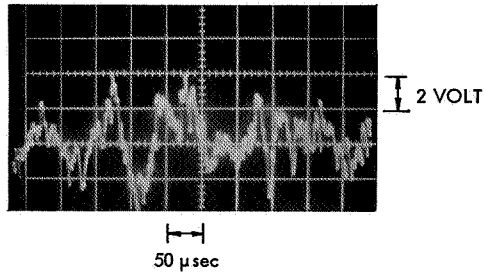
can be used to get the power spectrum through the Fourier transformation. Figure XIII-37 shows the power spectrum (c) obtained by the Fourier transformation of (b). The averaging time, T , in this case is 5 seconds.

The crosscorrelation between two signals $f_A(t)$ and $f_B(t)$,

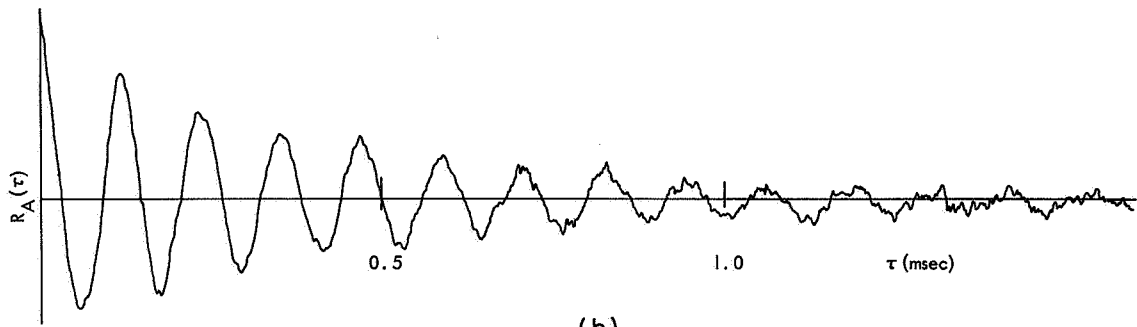
$$R_{AB}(\tau) = \frac{1}{T} \int_0^T f_A(t) f_B(t+\tau) dt, \quad (4)$$

can be used to get not only the extent of signal f_A in signal f_B , or vice versa, but also the clear phase lag between them.

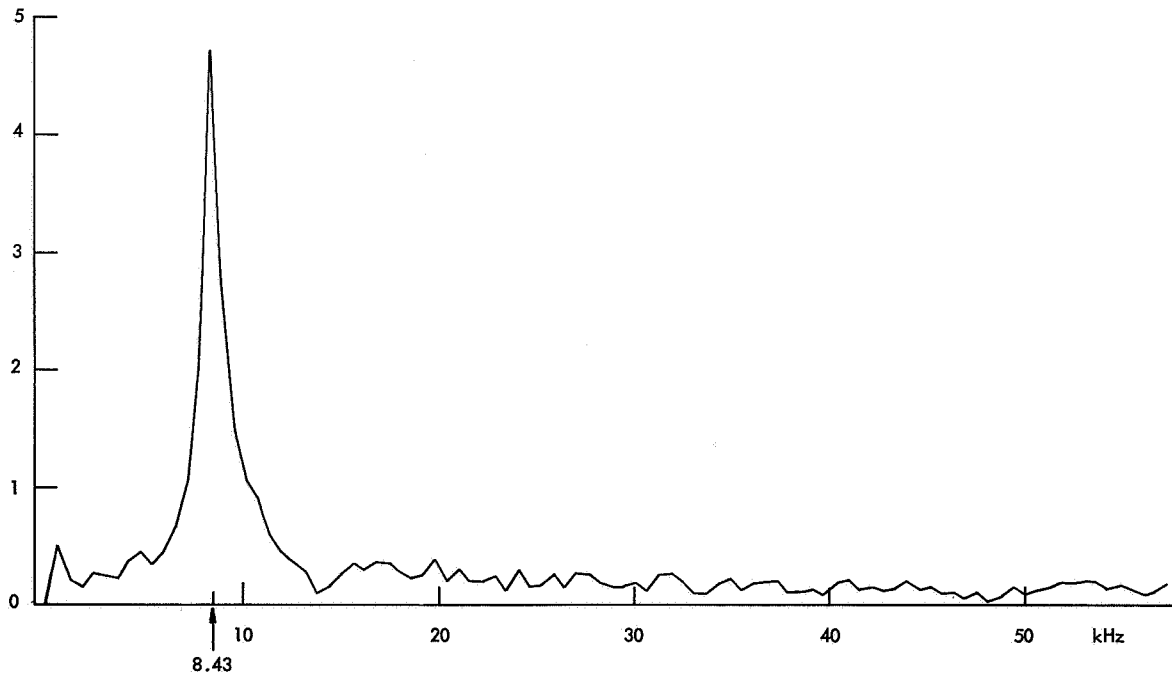
In Fig. XIII-38 we show (a) the oscilloscope traces, (b) the crosscorrelogram, and (c) the Fourier transform of (b) of signals detected by two probes separated by 90° azimuthally. We note that in Fig. XIII-38c we have a single strong peak at 50.7 kHz, which indicates that the signals are due to an unstable rotating mode. The phase lag between the two signals shown in Fig. XIII-38b is clearly 180°, and thus we conclude that this particular oscillation is an $m = 2$ mode, and the fundamental frequency is 25.3 kHz,



(a)



(b)



(c)

Fig. XIII-37. (a) Oscilloscope picture of the oscillation ($f_{app} \approx 9$ kHz).
 (b) Autocorrelogram of (a).
 (c) Power spectrum of (b).

(XIII. PLASMAS AND CONTROLLED NUCLEAR FUSION)

instead of 50.7 kHz. We also biased the probes near the electron-saturation and ion-saturation regions, and obtained the signals. By employing many probes azimuthally

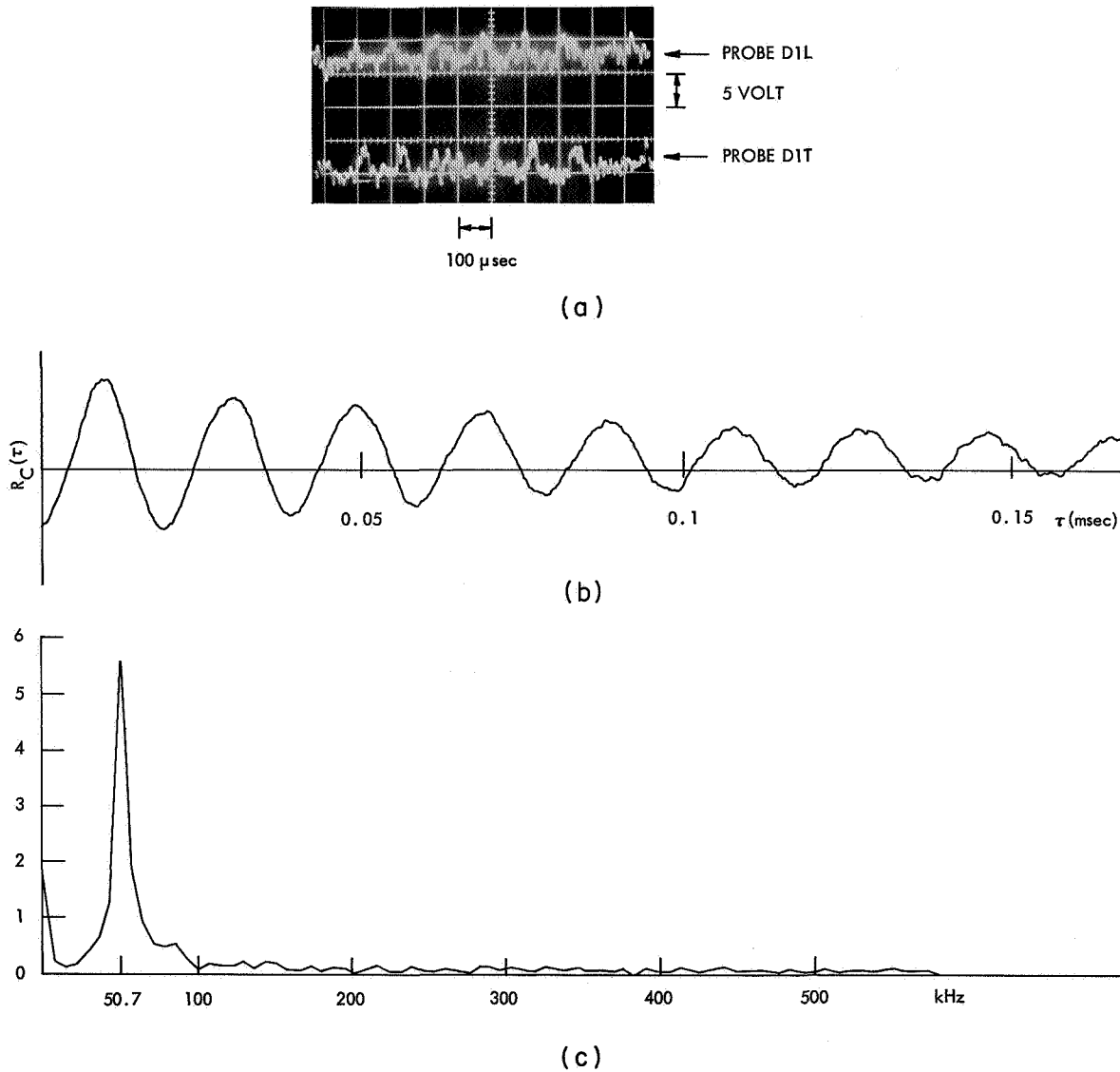


Fig. XIII-38. (a) Oscilloscope pictures of the oscillation ($f_{app} \approx 50$ kHz) picked up by two probes separated by 90° azimuthally. (b) Crosscorrelogram of (a). (c) Fourier transform of (b).

and axially separated, and moving the probes radially, we have obtained further information about the oscillations in the unstable plasma.

(XIII. PLASMAS AND CONTROLLED NUCLEAR FUSION)

In Table XIII-1 we summarize data from the crosscorrelograms. Because of the strong dependency of the oscillations on the source magnetic field, we list the current

Table XIII-1. Characteristics of oscillations in HCD.

I_s (A)	r (in)	Azimuthal Probe Separation	Probe Bias	f_{app} (kHz)	m (experimental)
120	3/8	90°	Floated	8.9	0.92
120	6/8	90°	Floated	8.8	-1.0
150	6/8	45°	Ion Saturated	8.6	-0.87
137	1	45°	Floated	9.0	-0.82
137	1	90°	Floated	9.0	-1.1
50	3/8	45°	Floated	53.0	-2.1
50	3/8	90°	Floated	53.0	-2.0
50	6/8	90°	Floated	52.3	0
50	7/8	90°	Floated	50.0	0
50	9/8	90°	Floated	53.5	0

to the source magnetic coils, I_s . The apparent frequency is f_{app} , and r represents the radial positions of the Langmuir probes.

In Table XIII-1 we have chosen the positive direction of θ as the counter-clockwise direction looking along the axial magnetic field, that is, from the anode to the cathode. To determine the helicity of the mode, we obtained crosscorrelations between probes separated along the magnetic field lines. We could not detect any phase lag between them. From Table XIII-1 we construct the following model for the unstable modes: (a) the low-frequency oscillation ($f_{app} \approx 9$ kHz) has mode $m = 1$, and reverses azimuthal direction at an intermediate plasma radius, and is stronger at the boundary; (b) the high-frequency oscillation ($f_{app} \approx 50$ kHz), mode $m = 2$, is strong near the center of the plasma column, and is weak and nonrotating in the outer region. The reversal of azimuthal direction of the low-frequency oscillation agrees with the $\vec{E} \times \vec{B}$ direction obtainable from the space potential measurement,³ which is reproduced in Fig. XIII-39. In Fig. XIII-40 we

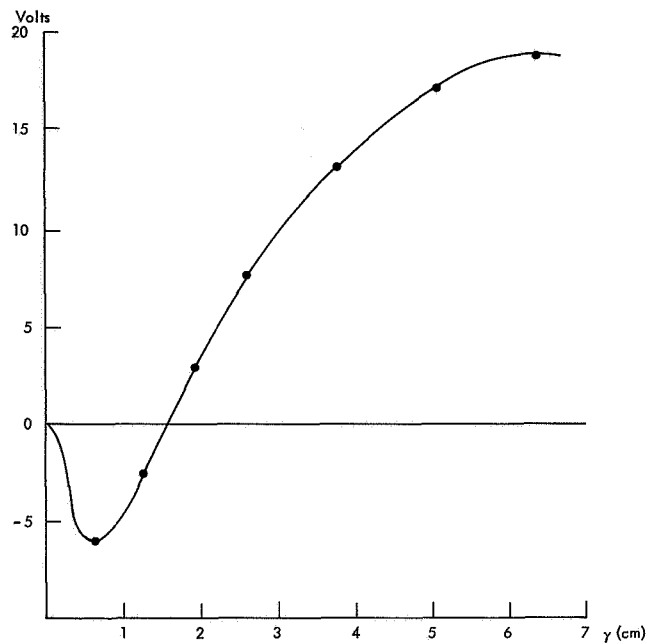
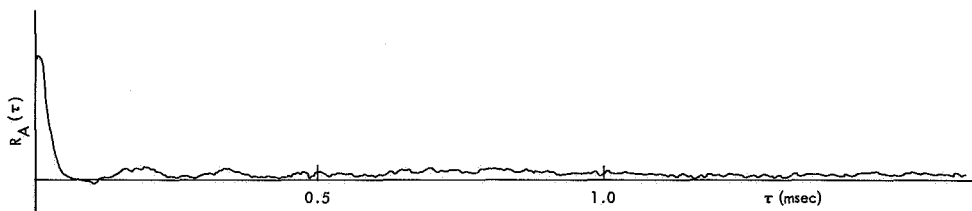
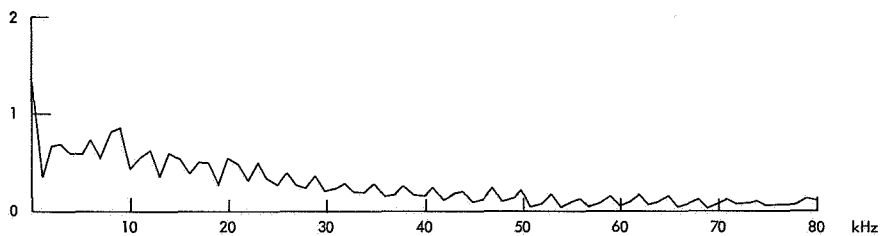


Fig. XIII-39. Radial profile of the plasma potential in an unstable regime.



(a)



(b)

Fig. XIII-40. (a) Autocorrelogram in a "quiet" plasma.
(b) Power spectrum of (a).

(XIII. PLASMAS AND CONTROLLED NUCLEAR FUSION)

show the remarkably clear autocorrelogram, and the power spectrum in the "quiet" plasma. In Fig. XIII-40 we see no oscillations except the noise.

M. Hudis, D. J. Rose, J. Small, K. Chung

References

1. J. C. Woo, L. M. Lidsky, and D. J. Rose, Quarterly Progress Report No. 76, Research Laboratory of Electronics, M. I. T., January 15, 1965, pp. 130-133.
2. K. Chung, Quarterly Progress Report No. 84, Research Laboratory of Electronics, M. I. T., January 15, 1967, pp. 159-163.
3. J. C. Woo, Ph. D. Thesis, Department of Nuclear Engineering, M. I. T., 1966, p. 89.

XIII. PLASMAS AND CONTROLLED NUCLEAR FUSION

C. Plasma Magnetohydrodynamic Flows, Waves, and Instabilities

Academic and Research Staff

Prof. W. P. Allis

Prof. H. A. Haus

Graduate Students

C. A. McNary

K. R. Edwards

1. MAGNETOHYDRODYNAMIC WAVE PROPAGATION TRANSVERSE TO MAGNETIC FIELD

When a magnetic field exists in a compressible fluid with a finite electric conductivity, the evolution of magnetic field disturbances can be strongly coupled to fluid-motion fluctuations if these events occur with time scales that are shorter than the magnetic field relaxation time for the fluid. In such an electromechanically coupled medium, an increase in apparent fluid stiffness occurs with an increase in magnetic field strength. This causes an increase in the phase velocity of compressional wave modes traveling transverse to the magnetic field – commonly called magnetoacoustic waves. These waves are described by a combination of the quasi-static Ampère law for a magnetic system, Faraday's law, Ohm's law (with $\omega_c \ll \nu$), conservation laws for mass and momentum, and a thermodynamic equation of state. For a highly conductive, homogeneous, isotropic, ideal gas approximately described by an adiabatic equation of state, the aforementioned combination yields the magnetoacoustic wave equation

$$\frac{\partial^2 \psi}{\partial t^2} = c^2 \frac{\partial^2 \psi}{\partial \chi^2} \tag{1}$$

$$c^2 = s^2 + a^2, \quad s^2 = \gamma \frac{p_0}{\rho_0} \quad \text{and} \quad a^2 = \frac{B_0^2}{\rho_0 \mu}.$$

But this equation does not hold for a collision-dominated, partially ionized plasma where fluid motions occur with a time scale comparable with the magnetic field relaxation time, where fluctuations in conductivity accompany wave motion, and an equilibrium current density exists. This report is concerned with such a medium and the waves that it can support.

Physical assumptions incorporated in the mathematical model to be developed are

*This work was supported principally by the National Science Foundation (Grant GK-1165).

Table XIII-2. Physical assumptions, coordinate system, and glossary of symbols.

Assumptions

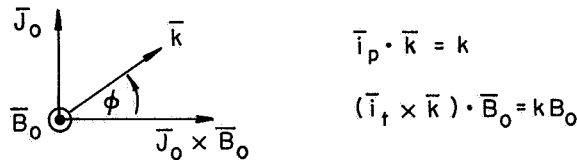
Homogeneous, isotropic, one-fluid model. Knudsen number $\ll 1$.

$$\frac{\omega}{\nu}, \frac{\nu\omega}{\omega_p^2}, \frac{\mu_i}{\mu_e}, c[\mu\epsilon]^{1/2}, \frac{\rho_o k^2 \nu_k}{\sigma_o B_o^2}, \frac{k^2 K_\sigma T_o}{\alpha(J_o^2/\sigma_o)} \ll 1$$

$$\frac{\nu}{\nu_{ee}} < 1$$

The equilibrium (uniform) current density flowing in the plasma is assumed to be returned back through the plasma by evenly distributed wires, infinite in number and infinitesimal in thickness so as not to disturb the plasma flow and so as to ensure a uniform magnetic field.

Coordinate System



The natural and constituent laws are linearized for small amplitude one-dimensional perturbations about an equilibrium state. Equilibrium variables have a zero subscript unless otherwise noted.

Glossary

<u>Symbol</u>	<u>Definition</u>	<u>Symbol</u>	<u>Definition</u>
B	magnetic field	α_o	n_{e0}/n_o
C_v, C_p	specific heats	γ	C_p/C_v
E_p, E_t	parallel, transverse electric fields	ϵ_i	ionization potential
i	$(-1)^{1/2}$	ϵ	permittivity
\bar{i}_p, \bar{i}_t	unit vectors $\perp B_o$	λ	wavelength
J	current density	μ	permeability
K_σ	thermal conductivity	μ_e, μ_i	electron, ion mobility
k	wave number	ν	$\nu_{ei} + \nu_{en}$
k_B	Boltzmann's constant	$\nu_{ee}, \nu_{ei}, \nu_{en}$	electron-electron, electron-ion, electron-neutral collision frequency
n	heavy-gas number density	ν_k	kinematic viscosity
n_e	electron number density	ρ	mass density
p	pressure	σ	conductivity
q	charge density	ϕ	angle of propagation
R	gas constant	Ω	Hall parameter
T	temperature	ω	wave frequency
t	time	ω_c	electron-cyclotron frequency
v_p, v_t	parallel, transverse velocity	ω_p	plasma frequency

(XIII. PLASMAS AND CONTROLLED NUCLEAR FUSION)

given in Table XIII-2 along with a description of the coordinate system embedded in the moving plasma and a list of symbol meanings. The linearized equations of motion are Laplace-analyzed in space and time. Equivalently, the linearized natural and constituent laws are considered for one particular Laplace frequency and wave-number dependence. The variables are chosen to have the space-time dependence:

$$\text{Re } \zeta \exp(\omega t - \bar{k} \cdot \bar{r}).$$

In this report the wave number will be chosen as a real number, and the angular frequency will be sought analytically and numerically.

Conservation of Mass

$$\frac{\rho}{\rho_0} = \frac{k}{\omega} v_p. \quad (2)$$

Without equilibrium current density, these waves are of a purely compressional nature with $v_t = 0$.

Conservation of Momentum

$$\left(\frac{k}{\omega}\right) v_p = \left(\frac{k}{\omega}\right)^2 \gamma^{-1} s^2 \frac{p}{\rho_0} + i \frac{k J_0 B_0}{\rho_0 \omega^2} \left(\frac{J}{J_0} - \cos \phi \frac{B}{B_0}\right) \quad (\text{parallel component}) \quad (3a)$$

$$\left(\frac{k}{\omega}\right) v_t = -i \frac{k J_0 B_0 \sin \phi}{\rho_0 \omega^2} \frac{B}{B_0}. \quad (\text{transverse component}) \quad (3b)$$

Except for propagation in the $\bar{J}_0 \times \bar{B}_0$ direction, the velocity is rotational for a finite equilibrium current density. The rotational component of velocity results from the perturbation magnetic field interacting with the equilibrium current density so as to produce a force density that, in general, is unaligned with \bar{k} .

Ampère's Law

$$\frac{B}{B_0} = iI \frac{J}{J_0}; \quad \bar{B} = \frac{\bar{B}_0}{B_0} B; \quad I = \frac{\mu_0 J_0}{k B_0}. \quad (4)$$

The current perturbation is in the transverse direction. The perturbation magnetic field is always aligned with the equilibrium magnetic field for plane wave propagation transverse to the equilibrium field.

Faraday's Law

$$\frac{\sigma_0}{J_0} E_t = - \frac{\sigma_0 B_0 (\omega/k)}{J_0} \frac{B}{B_0}. \quad (5)$$

(XIII. PLASMAS AND CONTROLLED NUCLEAR FUSION)

Modified Ohm's Law

$$\Omega_0 \cos \phi \frac{\Omega}{\Omega_0} - \Omega_0 \frac{J}{J_0} = \frac{\sigma_0}{J_0} E_p - \frac{\sigma_0 B_0}{J_0} v_t + (\Omega_0 \cos \phi + \sin \phi) \frac{\sigma}{\sigma_0} \quad \begin{array}{l} \text{(parallel} \\ \text{component)} \end{array} \quad (6a)$$

$$\frac{J}{J_0} + \Omega_0 \sin \phi \left(\frac{\Omega}{\Omega_0} \right) = \frac{\sigma_0}{J_0} E_t + \frac{\sigma_0 B_0}{J_0} v_p + [\Omega_0 \sin \phi - \cos \phi] \frac{\sigma}{\sigma_0} \quad \begin{array}{l} \text{(transverse} \\ \text{component)} \end{array} \quad (6b)$$

Equation 6b expresses the resistive-inductive nature of the medium. By using Eqs. 4 and 5, Eq. 6b can be rewritten in the form

$$\frac{J}{J_0} [1 + iR_m] = -\Omega_0 \sin \phi \left(\frac{\Omega}{\Omega_0} \right) + \frac{\sigma_0 B_0}{J_0} v_p + [\Omega_0 \sin \phi - \cos \phi] \frac{\sigma}{\sigma_0}. \quad (6c)$$

The right-hand side of (6c) represents a change in the electromotive force in the plasma continuum. The current variation lags this emf, as it would in a lossy inductor. The first term on the right of (6c) produces current variations as a result of changes in Hall parameter. That is, changes in the magnetic field and mass density cause the ratio of ω_c and v to change, with the result that there is a repositioning of the equilibrium current density vector with respect to the electric field vector. The second term on the right of (6c) represents the conventional current variation associated with wave motion and produces wave damping. The last term on the right of (6c) is a current variation attributable to conductivity fluctuations. If the first and third terms more than cancel out the damping effects of the second term, wave growth may result — but not necessarily.

Thermodynamic Equation of State

$$\frac{P}{P_0} = \frac{\rho}{\rho_0} + \frac{T}{T_0}. \quad (7)$$

Conservation of Energy

$$\frac{T}{T_0} = \frac{R}{C_v} \left(\frac{k}{\omega} \right) v_p + i \left(\frac{k}{\omega} \right) c_{yH} \left[2 \cos \phi \frac{J}{J_0} - \frac{\sigma}{\sigma_0} \right]; \quad H = \frac{J_0^2 / \sigma_0}{kc\rho_0 C_p T_0}. \quad (8)$$

The second and third terms on the right of Eq. 8 represent small changes in Joule heating. If these changes are in phase with temperature, wave growth may result — but again not necessarily.

Conductivity

$$\frac{\sigma}{\sigma_0} = \frac{n_e}{n_{e0}} - \frac{\nu}{\nu_0}. \quad (9)$$

Collision Frequency

$$\frac{\nu}{\nu_0} = \frac{\nu_{ei0}}{\nu_0} \left(1 - \frac{1}{2 \ln \Lambda_0}\right) \frac{n_e}{n_{e0}} + \frac{\nu_{en0}}{\nu_0} \frac{\rho}{\rho_0} + \left[\frac{3}{2} \frac{\nu_{ei0}}{\nu_0} \left(1 - \frac{1}{\ln \Lambda_0}\right) - \frac{1}{2} \frac{\nu_{en0}}{\nu_0} \right] \frac{T}{T_0} \quad (10)$$

$$\Lambda_0 = 12\pi \left(\frac{\epsilon_k B T_0}{e^2} \right)^{3/2} n_{e0}^{-1/2}$$

Cross sections for electron-neutral collisions are assumed to be constant.

Saha's Equation

$$\frac{n_e}{n_{e0}} = \left(\alpha + \frac{3}{4} \right) \frac{T}{T_0} + \beta \frac{\rho}{\rho_0} \quad (11)$$

$$\alpha = \frac{\epsilon_i}{2k_B T_0} \left(1 - \alpha_0^2\right) - \frac{3}{4} \alpha_0^2; \quad \beta = \frac{1}{2} \left(1 + \alpha_0^2\right).$$

Equation 11 represents the balance between production and removal of free electrons for a Maxwellianized gas.

Hall Parameter

$$\frac{\Omega}{\Omega_0} = \frac{B}{B_0} - \frac{\nu}{\nu_0}. \quad (12)$$

Since, for the case at hand, the perturbation and equilibrium magnetic fields are vectorially aligned, the small amplitude changes in Hall parameter and magnetic field are also aligned, and thus the Hall parameter changes can be described here in a single scalar equation.

The thirteen linearized equations of motion and state presented above govern the thirteen small amplitude perturbations ($v_p, v_t, p, \rho, T, J, E_p, E_t, B, n_e, \nu, \sigma, \Omega$). Also, there is a fourteenth equation representing Gauss's law for small-amplitude charge density, but it is coupled to the other thirteen equations only through one of its two variables.

Gauss' Law

$$\frac{\sigma_0 E_p}{J_0} = i \left(\frac{q_0 \sigma_0 / \epsilon_0}{J_0 k} \right) \frac{q}{q}. \quad (13)$$

Table XIII-3. Dispersion relation.

$$\begin{aligned}
 & \omega_n^4 + \omega_n^3 \{-iH\gamma C_4 - iR_m^{-1} + \Omega_o R_m^{-1} \sin \phi\} \\
 & + \omega_n^2 \{-iI(1-R) \cos \phi - HR_m^{-1} \Omega_o \gamma C_4 \sin \phi - 1 + HR_m^{-1} (X_{21} - \Omega_o X_{22})\} \\
 & + \omega_n \left\{ iH[\Omega_o X_{11} + \Omega X_{12} + \gamma C_4] + iR_m^{-1} R + IR_m^{-1} [(1-R)(X_{14} + \Omega_o) - \Omega_o \sin \phi] \right. \\
 & \quad \left. + HR[\gamma C_4 \cos \phi - I^{-1} X_{16}] \right\} \\
 & + \omega_n^0 \left\{ iH\Omega_o R_m^{-1} F \Omega_o [X_{o4} + \left(\frac{R}{1-R}\right) \gamma^{-1} \xi_{13} \sin \phi] + HR[R_m^{-1} (X_{o1} + \Omega_o X_{o2}) + H\Omega_o X_{o3}] \right\} \\
 & = 0
 \end{aligned}$$

$$\begin{aligned}
 C_1 &= -\beta / \cos \phi \\
 C_4 &= \left[1 - \frac{v_{ei_o}}{v_o} \left(1 - \frac{1}{2 \ln \Lambda_o} \right) \right] \left(\alpha + \frac{3}{4} \right) - \left[\frac{1}{2} \left(\frac{v_{en_o}}{v_o} \right) - \frac{3}{2} \left(\frac{v_{ei_o}}{v_o} \right) \left(1 - \frac{1}{\ln \Lambda_o} \right) \right] \\
 C_5 &= \frac{1}{2} - \frac{v_{ei_o}}{v_o} - \frac{1}{2} \frac{v_{ei_o}}{v_o} \left(1 - \frac{1}{2 \ln \Lambda_o} \right) \\
 \xi_{13} &= 2C_4 - C_5 \\
 \xi_{14} &= 2 \left(\alpha + \frac{3}{4} \right) - \beta \\
 X_{o1} &= \xi_{13} (1 - 2 \cos^2 \phi) \\
 X_{o2} &= 2\xi_{14} \sin \phi \cos \phi \\
 X_{o3} &= \frac{-C_p}{R} C_4 \xi_{14} \sin \phi \cos \phi + \frac{C_p}{R} \xi_{13} \left(\alpha + \frac{3}{4} \right) \sin \phi \cos \phi \\
 X_{o4} &= \left(\alpha + \frac{3}{4} \right) \xi_{13} \sin \phi - C_4 \xi_{14} \sin \phi \\
 X_{11} &= \left[\left(1 + \frac{C_v}{R} \right) \left(\alpha + \frac{3}{4} \right) - \frac{C_v}{R} \xi_{14} \right] \sin \phi \cos \phi \\
 X_{12} &= \left[\xi_{13} - \frac{C_v}{R} C_5 - C_4 \right] \cos^2 \phi + \xi_{13} \sin^2 \phi - \gamma C_4 \\
 X_{14} &= \left[\gamma C_4 - 2 \frac{R}{C_v} \right] \cos \phi \\
 X_{15} &= \frac{C_v}{R} \xi_{14} \sin \phi - \left(1 + \frac{R}{C_v} \right) \left(\alpha + \frac{3}{4} \right) \sin \phi \\
 X_{16} &= \frac{C_v}{R} \xi_{13} \cos \phi \\
 X_{21} &= 2\gamma C_4 \cos^2 \phi - \gamma C_4 \\
 X_{22} &= 2\gamma \left(\alpha + \frac{3}{4} \right) \sin \phi \cos \phi \\
 \omega &= \omega / kc \\
 H &= \frac{R}{C_p} FR_m^{-1} I = \frac{(J_o^2 / \sigma_o)}{kc(\rho_o C_p T_o)} \\
 R &= \left(\frac{S}{c} \right)^2 \\
 F &= \gamma I \left(\frac{1-R}{R} \right) = \frac{J_o B_o}{p_o k}
 \end{aligned}$$

(XIII. PLASMAS AND CONTROLLED NUCLEAR FUSION)

The dispersion equation formed from the set of homogeneous equations (2) through (12) is of fourth degree in wave frequency. It is given in Table XIII-3. Analytic solutions of the dispersion equation are stated for two limiting cases which are motivated by physical insight. First, analytic solutions for the characteristic frequencies are obtained in the limit of low current density. This limit is suggested by the fact that parameter variations have a negligible effect for low current density and are uncoupled from the magnetoacoustic roots. Second, analytic solutions are obtained in the limit of slight fluid compressibility. This limit is motivated by a desire to uncouple the two magnetoacoustic roots in such a manner that the two remaining modes can be examined.

Low-Current Density Limit

This limit considers solutions to first order in current density such that $\frac{J_o B_o}{p_o k}, \frac{\mu J_o}{k B_o} \sim \mathcal{O}(\epsilon), \epsilon \ll 1$. Furthermore, solution is facilitated by choosing a large magnetic Reynolds number, $R_m^{-1} = \frac{k}{\mu_o \sigma_o c} \sim \mathcal{O}(\epsilon)$, with the Alfvén and acoustic speeds of the same order of magnitude. The result is that for $-\pi/2 \leq \phi \leq \pi/2$:

$$\omega_1 = kc + i \left[\left(\frac{k^2}{2\mu\sigma_o} \right) \left(\frac{a}{c} \right)^2 - \frac{1}{2} \frac{(\bar{J}_o \times \bar{B}_o)}{k\rho_o c^2} \cdot \bar{k}c \right] \quad \text{(positive magnetoacoustic mode)} \quad (14a)$$

$$\omega_2 = -kc + i \left[\left(\frac{k^2}{2\mu\sigma_o} \right) \left(\frac{a}{c} \right)^2 + \frac{1}{2} \frac{(\bar{J}_o \times \bar{B}_o)}{k\rho_o c^2} \cdot \bar{k}c \right] \quad \text{(negative magnetoacoustic mode)} \quad (14b)$$

$$\omega_3 = i \left(\frac{k^2}{\mu_o \sigma_o} \right) \left(\frac{s}{c} \right)^2 \quad \text{(magnetic diffusion mode)} \quad (14c)$$

$$\omega_4 = 0 \quad \text{(parameter variations mode)} \quad (14d)$$

Only the positive magnetoacoustic mode exhibits an instability, and this occurs whenever

$$iR_m \cos \phi > 1, \quad (15)$$

where the most unstable direction of propagation is along $\bar{J}_o \times \bar{B}_o$. This instability results from the fact that the small amplitude Lorentz force density is less than $\pi/2$ radians out of phase with the velocity perturbation of the wave. Joule-heating effects have no influence in this limit; $H \sim \mathcal{O}(\epsilon^3), \epsilon \ll 1$. By way of elaboration, consider the case in which $\phi = 0$. For near perfect conductivity, $v_p B_o \cong \frac{\omega}{k} B$. Some phase relationships of the positive magnetoacoustic wave ($\phi=0$) are demonstrated in Fig. XIII-41. But if the effects of finite conductivity are accounted for, then $E_t - v_p B_o = J/\sigma$,

(XIII. PLASMAS AND CONTROLLED NUCLEAR FUSION)

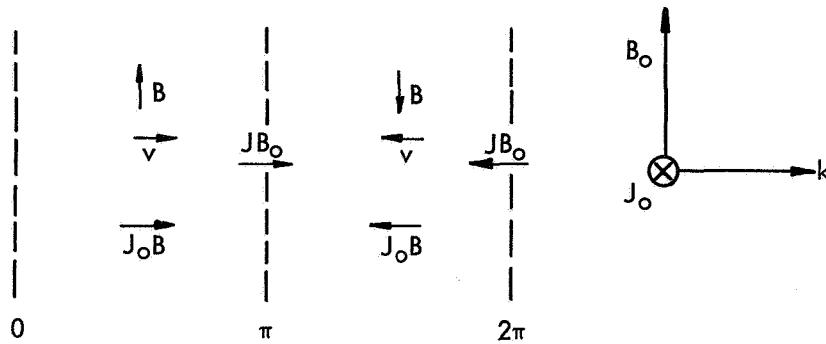


Fig. XIII-41. Phase relationships for positive magnetoacoustic mode for $\phi = 0$ and negligible resistivity.

or $v_p B = \left(\frac{a}{k}\right) B - i\left(\frac{k}{\mu\sigma_0}\right) B$, and then B leads v somewhat, as shown in Fig. XIII-42. The greater I becomes, the larger is the magnitude of $J_0 B$ relative to $J B_0$. It is the

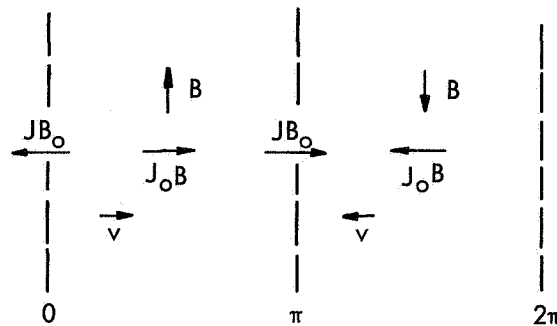


Fig. XIII-42. Phase relationships for positive magnetoacoustic mode for $\phi = 0$ and finite resistivity.

$J_0 B$ component of the Lorentz force density that is destabilizing. Furthermore, the larger R_m is, the less is the phase difference between velocity and magnetic field perturbations. To understand the inequality for some arbitrary angle ($|\phi| \leq \pi/2$), consider $\phi = \pi/2$. Here the inequality cannot be satisfied. In fact, the third term on the right side of (14a) disappears. This results from the fact that for $\phi = \pi/2$, $J_0 B$ acts in a direction orthogonal to v_p , and only serves to produce small amplitude motion transverse to the direction of propagation. With a more detailed analysis, it can be shown that this instability mechanism persists even when the criterion for the low-current-density limit is not met (with the same inequality (15) almost satisfied at a state of marginal stability). In summary, a physical mechanism for the instability of the positive magnetoacoustic mode has been exposed. Its existence depends upon the presence of a

finite current density, and does not depend upon parameter variations (though it may be influenced by them).

Slight Fluid Compressibility Limit

First, only incompressible phenomena are considered.

$$\omega_{1,2} \rightarrow \pm\infty \quad \begin{array}{l} \text{(positive, nega-} \\ \text{tive magneto-} \\ \text{acoustic mode)} \end{array} \quad (16a, b)$$

$$\omega_3 = -\bar{k} \cdot \bar{s}_d + i(\zeta_1 + \zeta_2); \quad \bar{s}_d = \frac{\bar{J}_0}{n_{e0}e}, \quad e = \text{electron charge} \quad \begin{array}{l} \text{(magnetic diffusion} \\ \text{mode)} \end{array} \quad (16c)$$

$$\omega_4 = i(\zeta_1 - \zeta_2)$$

$$\zeta_1 = \frac{1}{2} \frac{k^2}{\mu\sigma_0} + \frac{1}{2} \left[2 \frac{(\bar{k} \times \bar{J}_0) \cdot \bar{B}_0}{kJ_0 B_0} - 1 \right] \frac{aJ_0^2/\sigma_0}{\rho_0 C_p T_0} \quad \begin{array}{l} \text{(parameter variations} \\ \text{mode)} \end{array}$$

$$\zeta_2 = \left\{ \zeta_1^2 + \left[2 \frac{(\bar{k} \times \bar{J}_0) \cdot \bar{B}_0}{kJ_0 B_0} - 1 \right] \frac{aJ_0^2/\sigma_0}{\rho_0 C_p T_0} \frac{k^2}{\mu\sigma_0} \right\}^{1/2} \quad (16d)$$

The physical meaning of (16c) and (16d) becomes more apparent in the limit of small magnetic Reynolds number, $R_m \sim \mathcal{O}(\epsilon)$.

$$\omega_3 = -\bar{k} \cdot \bar{s}_d + i \frac{k^2}{\mu\sigma_0} \quad (17a)$$

$$\omega_4 = -i \left[\frac{2(\bar{k} \times \bar{J}_0) \cdot \bar{B}_0}{kJ_0 B_0} - 1 \right] \frac{aJ_0^2/\sigma_0}{\rho_0 C_p T_0} \quad (17b)$$

The propagation of the magnetic diffusion mode simply represents the effect of electron drift, and therefore does not appear for $\phi = 0$. Magnetic field disturbances are swept along with the moving electron gas. The parameter variations mode indicates growth for $\phi = 0$ and decay for $\phi = \pi/2$. This is a result of having small-amplitude Joule-heating changes, respectively, in phase and out of phase with small temperature variations. For spatial variations along the $\bar{J}_0 \times \bar{B}_0$ direction, the second term on the right of (8) dominates the third term, and growth results. For variations along the \bar{J}_0 direction, however, the second term does not contribute, since \bar{J} is orthogonal to \bar{J}_0 and the third term, representing conductivity fluctuations, produces decay.

(XIII. PLASMAS AND CONTROLLED NUCLEAR FUSION)

The solutions (17a) and (17b) can be further altered to include slight compressibility. For simplicity, assume $\phi = 0$ and also that $I, R_m, a^{-1} \sim \mathcal{O}(\epsilon)$ and $\frac{s^2}{a^2} \sim \mathcal{O}(1)$. Then, the slightly compressible solutions for the magnetic diffusion and parameter variations modes are

$$\omega_3^1 = a(\gamma-1) IR_m(1-i) kc + i \frac{k^2}{\mu_0 \sigma_0} \quad (18a)$$

$$\omega_4^1 = \frac{a^2 J_0^2 / \sigma_0}{\rho_0 C_p T_0} (\gamma-1) \left(\frac{a}{c}\right)^2 I - i \frac{a J_0^2 / \sigma_0}{\rho_0 C_p T_0} \quad (18b)$$

The two unpaired modes, ω_3^1 and ω_4^1 take on wave propagation characteristics that reflect the existence of preferential directions in the medium. The physical effect causing propagation is similar for the two modes. For instance, in the parameter variations mode some relative phases of variables are indicated in Fig. XIII-43, with ΔT and $\Delta \sigma$

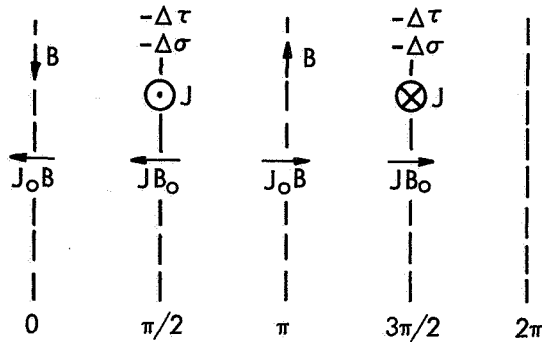


Fig. XIII-43. Dynamics of the parameter variations mode for $\phi = 0$ and slight compressibility.

indicating a positive small change in temperature and conductivity. The small changes in current density caused by conductivity fluctuations (which result from temperature changes) interact with the magnetic field. These forces, in turn, set up pressure gradients with peak pressure out of phase with the original conductivity fluctuations. These pressure gradients are accompanied by new temperature fluctuations, and so on, causing the pattern to shift in the $+\bar{J}_0 \times \bar{B}_0$ direction. In (18b) the direction of propagation changes if either \bar{J}_0 or \bar{B}_0 is reversed, thereby reversing the preferential direction $\bar{J}_0 \times \bar{B}_0$.

By means of a more extensive investigation, it can be shown that the basic concept of a magnetic diffusion mode and parameter variations mode that propagate remains valid even when the assumptions of Eqs. 18a and 18b are not met. Furthermore, it can

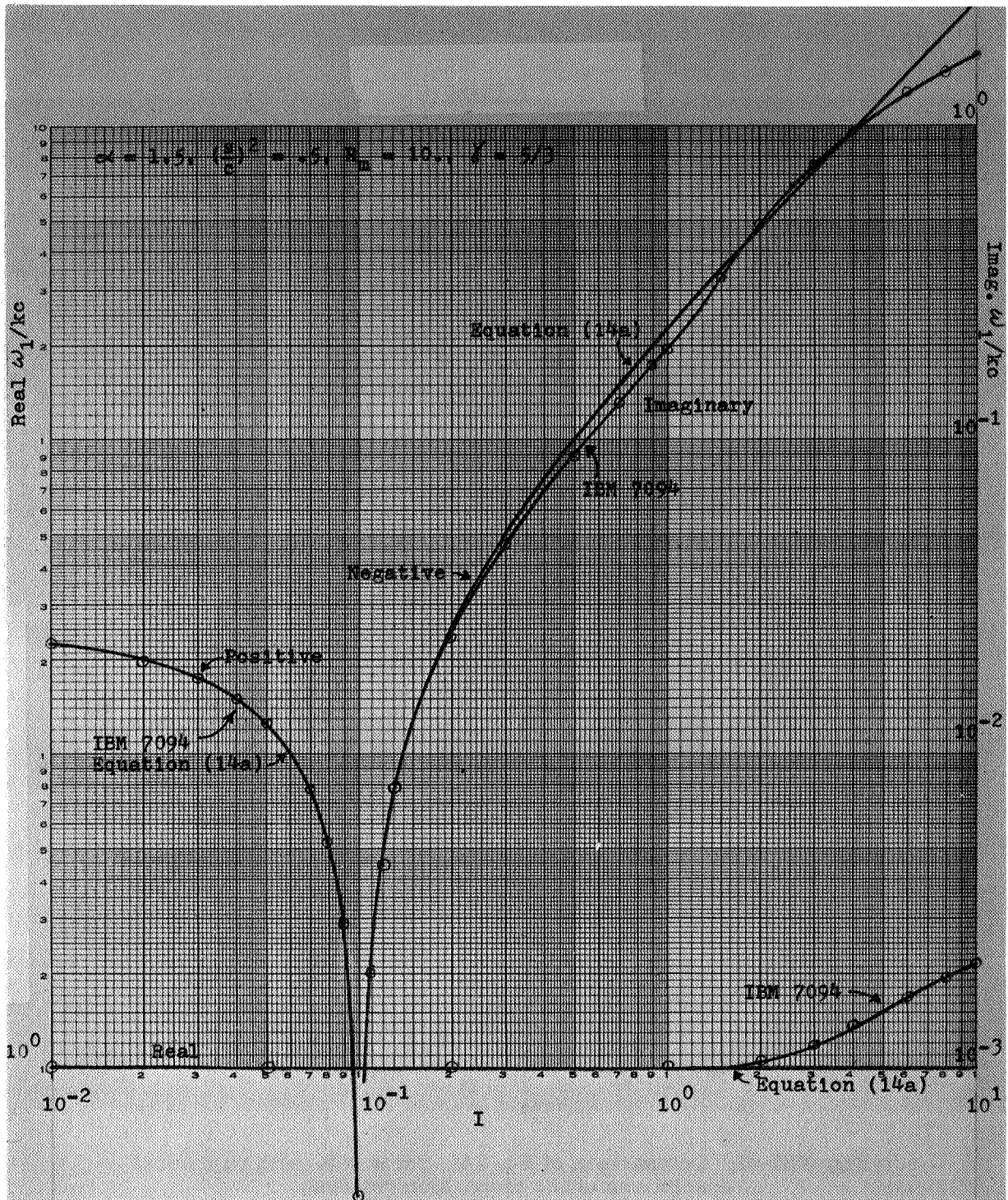


Fig. XIII-44. Comparison of Eq. 14a, for $\phi = 0$, with numerical solutions of the dispersion relation.

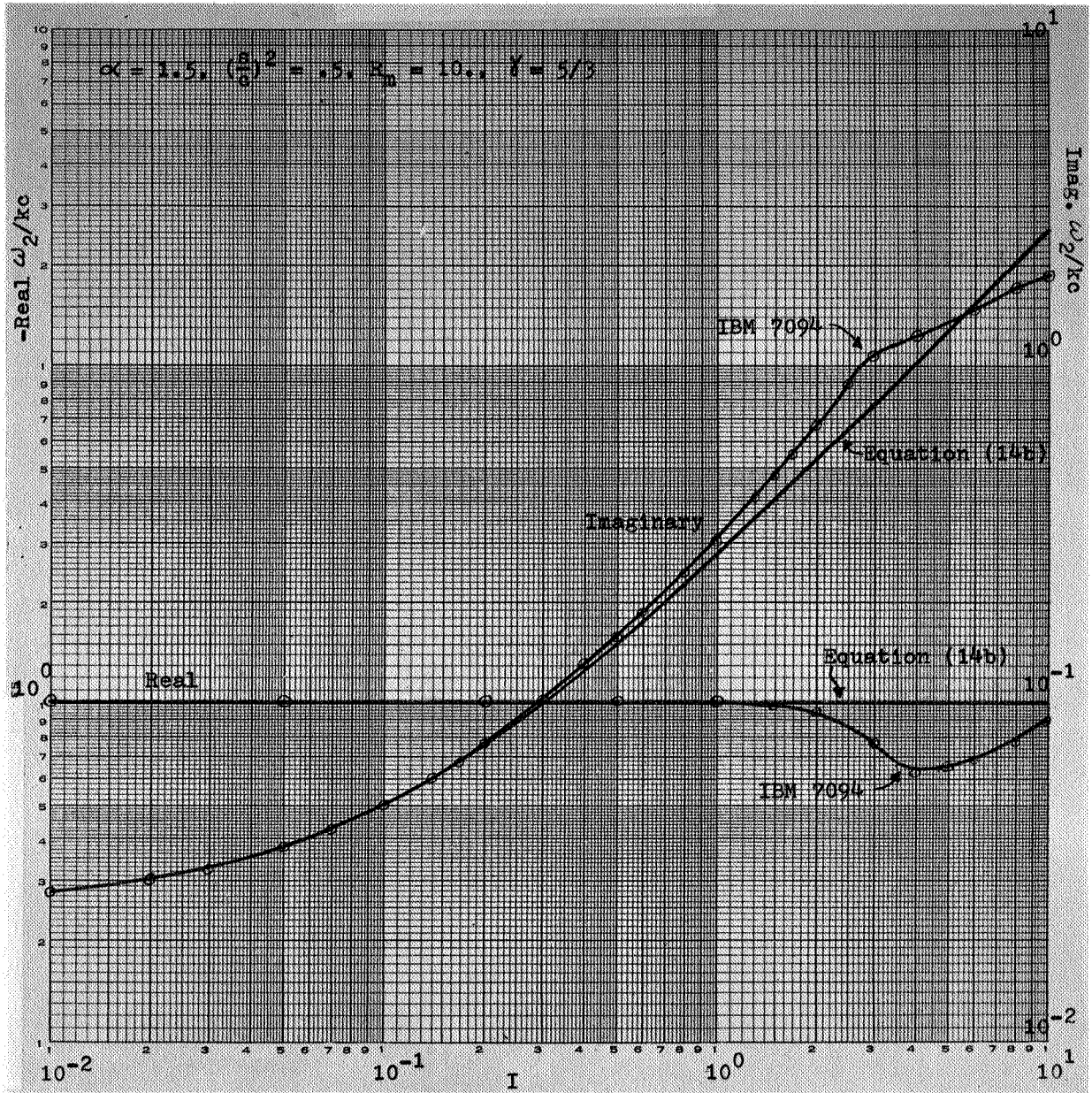


Fig. XIII-45. Comparison of Eq. 14b, for $\phi = 0$, with numerical solutions of the dispersion relation.

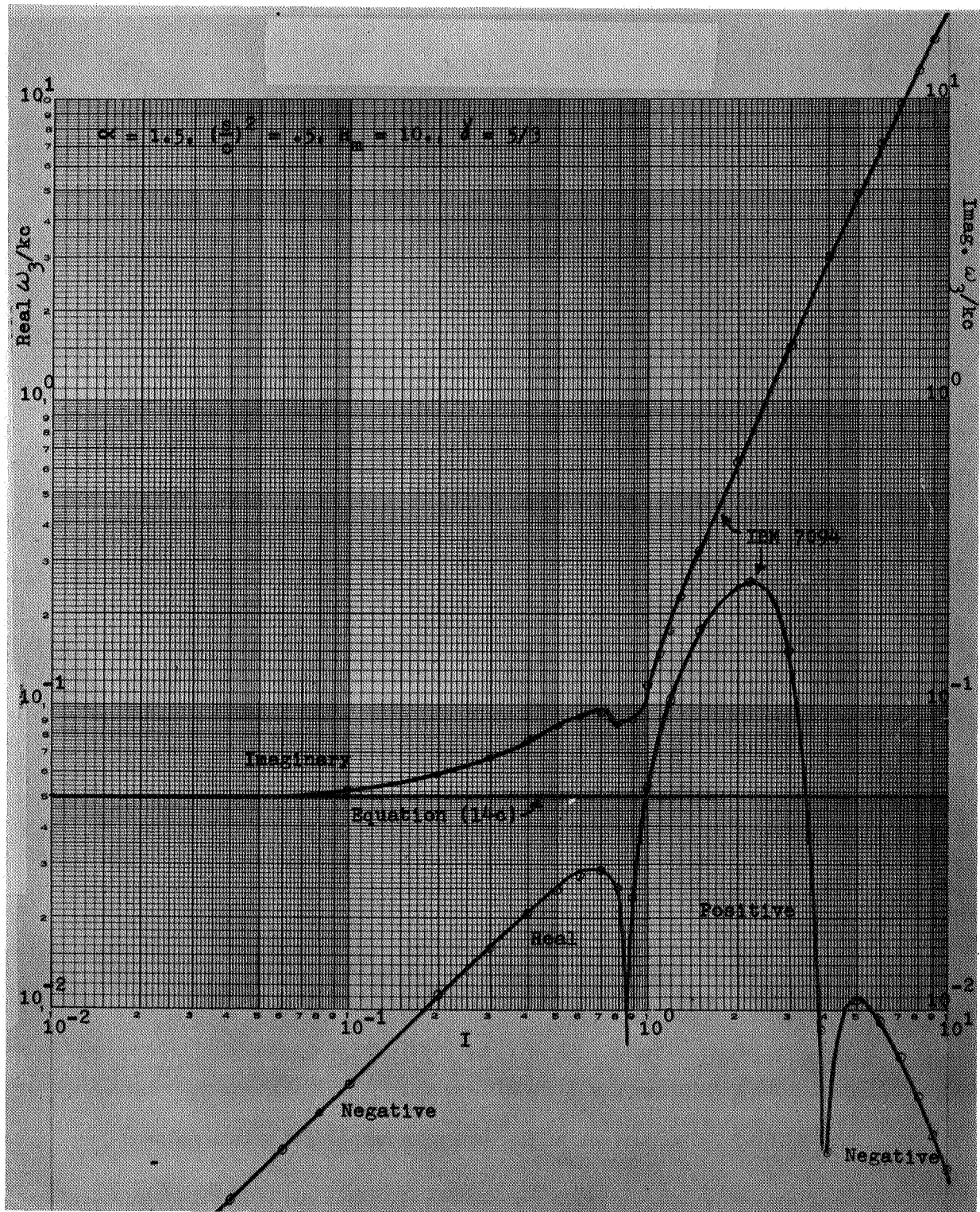


Fig. XIII-46. Comparison of Eq. 14c with numerical solutions of the dispersion relation.

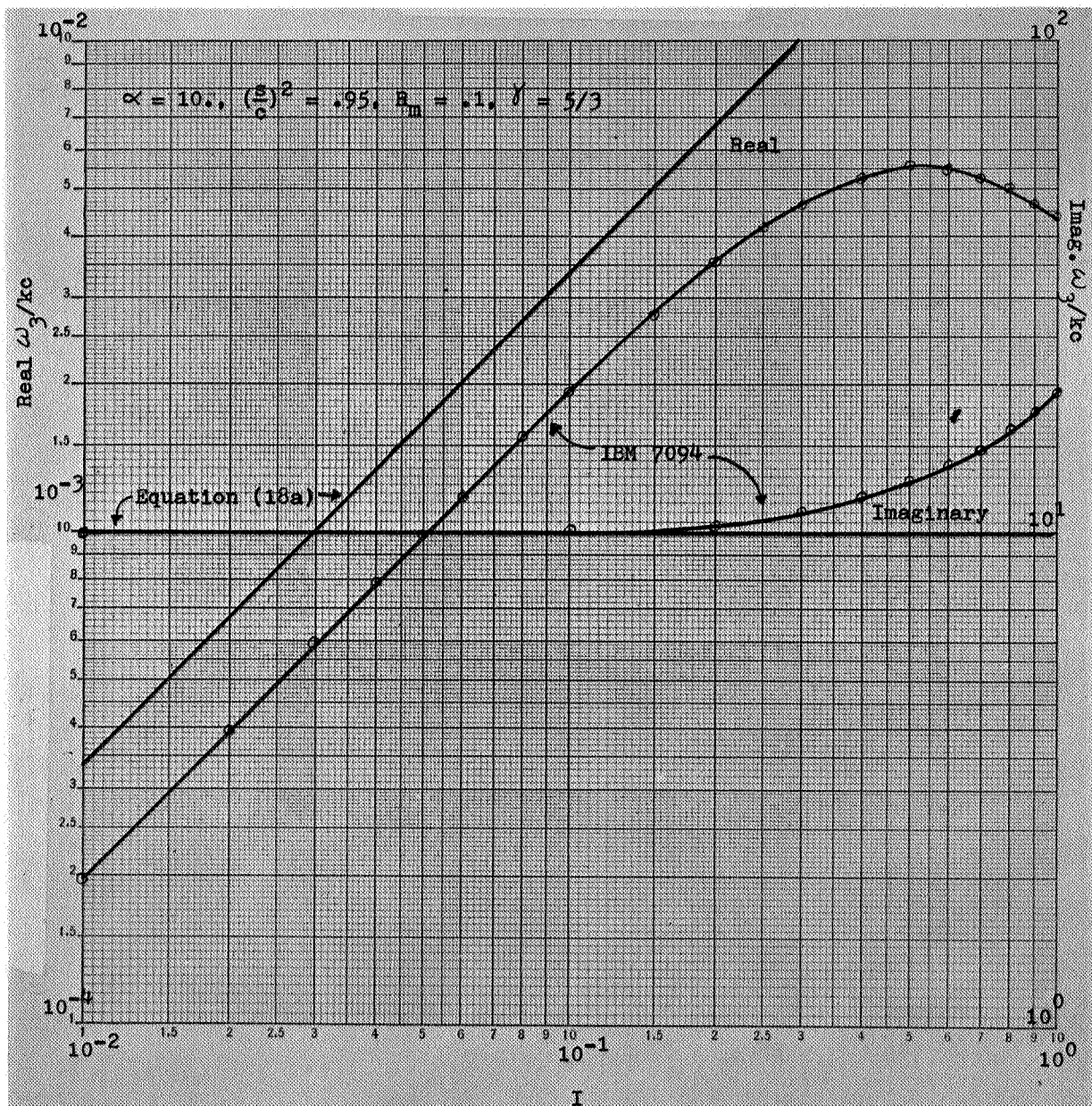


Fig. XIII-47. Comparison of Eq. 18a with numerical solutions of the dispersion relation.

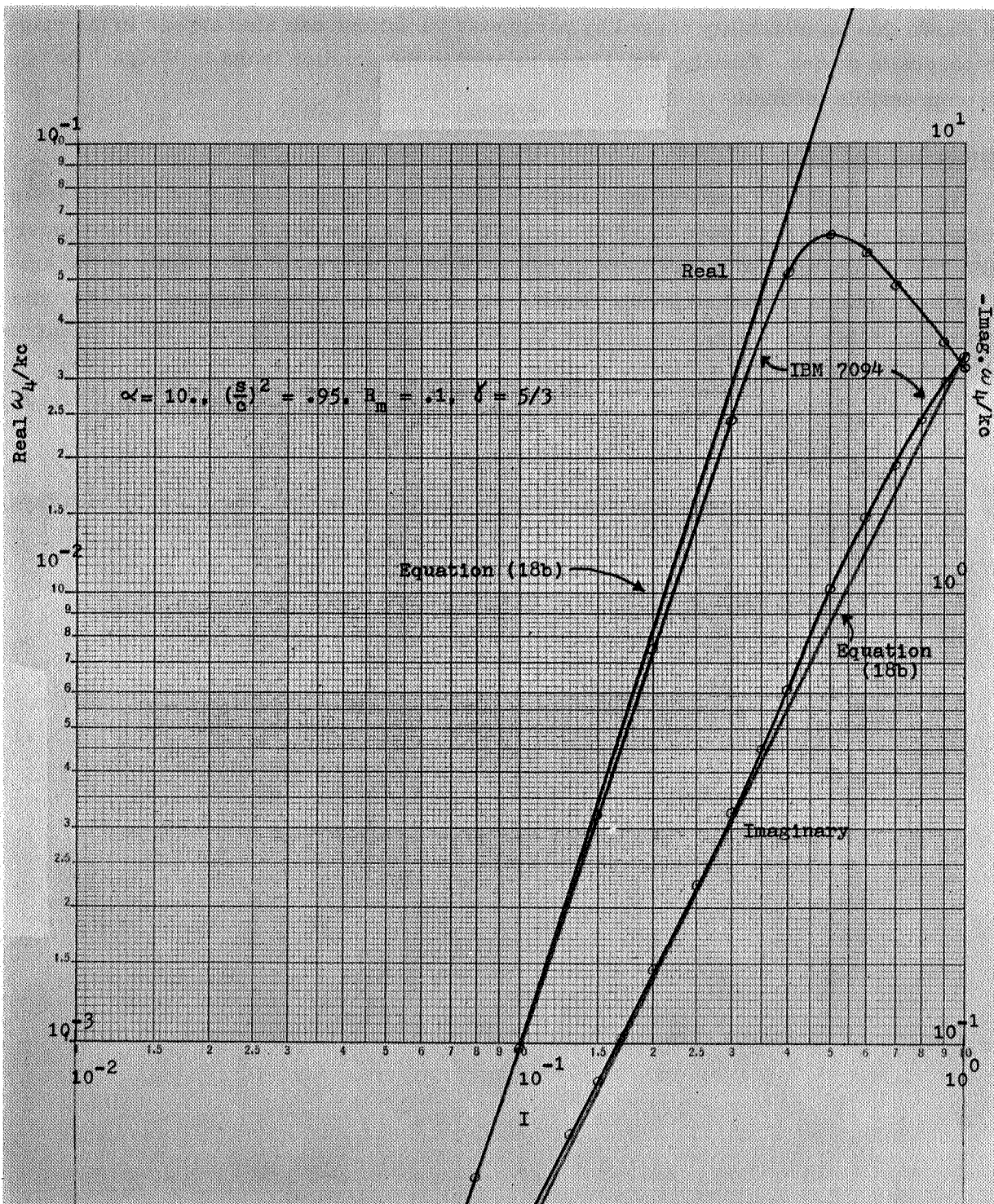


Fig. XIII-48. Comparison of Eq. 18b with numerical solutions of the dispersion relation.

(XIII. PLASMAS AND CONTROLLED NUCLEAR FUSION)

be shown that an instability caused by parameter variations can also appear in the magnetoacoustic modes. Finally, Eq. 17b is related to the solution found by Wright¹ for an incompressible medium.

Numerical Solutions

The characteristic roots of the complete one-fluid dispersion equation derived from homogeneous Eqs. 2-12 were found numerically by using the M.I.T. Computation Center's IBM 7094 computer. Solutions were sought in order to ascertain the validity of the analytic descriptions presented in this report. Some critical comparisons of analytic and numerical solutions are plotted in Figs XIII-44 through XIII-48. In these figures analytic solutions are valid for $I = \mathcal{O}(0.1)$, or less.

H. A. Haus, J. E. McCune, K. R. Edwards

References

1. J. K. Wright, "A Temperature Instability in Magnetohydrodynamic Flow," Proc. Phys. Soc. (London) 81, 498 (1963).

102 793
XIV. ENERGY CONVERSION RESEARCH* 8/10/70

Academic and Research Staff

Prof. J. L. Kerrebrock
Prof. G. C. Oates

Graduate Students

R. Decher
M. L. Hougen
G. W. Zeiders, Jr.

A. STATUS OF RESEARCH

1. ALKALI-METAL VAPOR STUDIES

N67-27095

Our studies of the condensing plasma, both theoretical and experimental, indicate that probably it will not be feasible to maintain a state of nonequilibrium ionization in a wet vapor. This conclusion follows from two facts.

a. At moderate current densities, the moisture increases the slope of the curve of $\log \sigma$ versus $\log j$ to greater than unity. With this characteristic, the plasma is unstable to current concentration.

b. At higher current densities, the flux of energy to the liquid droplets is such as to evaporate them quite rapidly.

Thus we are forced to the conclusion that an alkali-vapor MHD generator should operate with dry vapor. Our evaluation of the system potential will proceed on this basis.

2. LARGE NONEQUILIBRIUM GENERATOR

During this quarter, the large generator was operated twice with a pre-ionizer. In the first run, load resistances from 100 to 3 ohms per electrode pair were used. Pressure distributions along and across the channel were taken. Although the data are still being analyzed two points can be made.

a. When the pre-ionizer was operating, the pressure distribution in the channel was nearly independent of load resistance. When the pre-ionizer was turned off, the pressure rose throughout the channel, the increase being approximately 30% at the entrance and a factor of two at the exit. This may indicate a large increase in dissipation when the pre-ionizer is off.

b. The performance of the channel appeared to improve slightly with time during

*This work was supported by the U.S. Air Force (Research and Technology Division) under Contract F33615-67-C-1148 with the Air Force Aero Propulsion Laboratory, Wright-Patterson Air Force Base, Ohio.

(XIV. ENERGY CONVERSION RESEARCH)

the run. Because of this, the second run was made with a fixed-load resistance of 3 ohms, in an attempt to define the time dependence of the performance. The data from this run have not yet been analyzed.

3. INSTABILITIES

A general theoretical study of MHD instabilities is being made, which encompasses both magnetoacoustic and electrothermal waves, and accounts for interaction between the two. It also includes the effects of radiative heat loss.

J. L. Kerrebrock

1/2 m s
XV. SPONTANEOUS RADIOFREQUENCY EMISSION
FROM HOT-ELECTRON PLASMAS*

Academic and Research Staff

Prof. A. Bers

Graduate Students

C. E. Speck

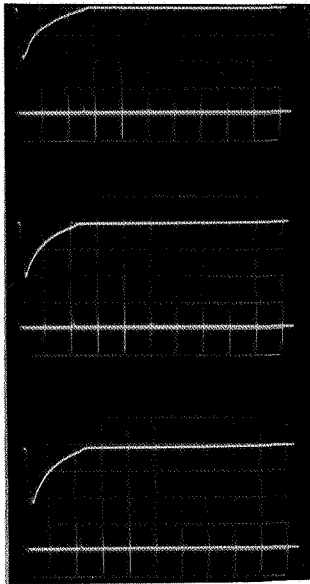
A. ENHANCED CYCLOTRON RADIATION FROM AN ELECTRON-CYCLOTRON
RESONANCE DISCHARGE

N67-27096

Previously, we have reported preliminary observations of an instability occurring in the afterglow of a pulsed electron-cyclotron resonance discharge.¹ This instability was characterized by bursts of radiation at frequencies near that of the RF microwave field which generates the plasma. The bursts are normally observed, however, as occurring several hundred microseconds after the removal of this RF heating field. We have continued this investigation in order to gain sufficient information about the plasma so that an appropriate theoretical model might be formulated.

Above a background pressure of approximately 2×10^{-5} Torr H_2 , the plasma is observed to be stable. Below this pressure, the plasma is unstable, in that the parameters of the plasma do not normally repeat themselves after each RF heating pulse. This critical pressure appears to be independent of the magnetic field over a wide range. It is in this low-pressure region that the intense bursts of microwave radiation are observed. The number of bursts, the most probable time of their occurrence, and their intensity are all complicated functions of the magnetic field strength or the background pressure. The radiation observed in a 30-Mc band near the RF heating frequency generally occurs later in the afterglow as the pressure is lowered. Just below the critical pressure, bursts are seen as early as 25 μ sec after the heating power is removed. At a pressure of 5×10^{-6} Torr and a central magnetic field of 880 Gauss, however, the most probable time for these bursts of radiation is more than 800 μ sec after the end of the heating pulse. Below approximately 4×10^{-6} Torr, it is impossible to form a discharge with the available microwave power. The dependence of the most probable time of occurrence on the magnetic field strength is extremely complicated. No typical trend is evident. Below a central field of approximately 690 Gauss, the bursts are absent. Increasing the field results in bursts whose amplitudes increase until the magnetic field reaches 830 Gauss. The amplitudes of these bursts are estimated to be of the order of 500 watts peak, with a duration of approximately 5 μ sec.

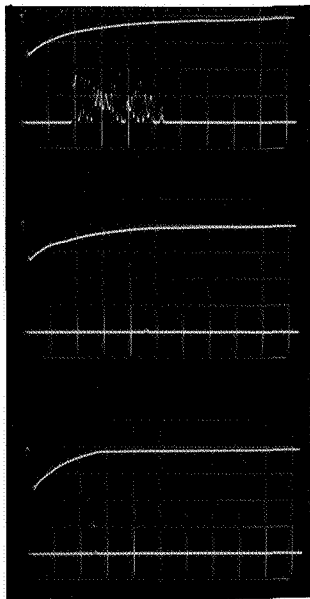
*This work is supported by the United States Atomic Energy Commission under Contract AT(30-1)-3581.



← TIME

Fig. XV-1.

Afterglow behavior of the pulsed electron-cyclotron discharge under repeatable operating conditions. Top trace: radiated power near 2850 Mc. Bottom trace: decay of the stored plasma energy. Time scale: 50 μ sec/division. Conditions: pressure 1.5×10^{-5} Torr; magnetic field at mirror center, 1030 Gauss.



← TIME

Fig. XV-2.

Typical behavior under nonrepeatable operating conditions. Top trace: radiated power near 2850 Mc. Bottom trace: decay of the stored plasma energy. Time scale: 50 μ sec/division. Conditions: pressure 1.5×10^{-5} Torr; magnetic field at mirror center, 1050 Gauss.

(XV. SPONTANEOUS RF EMISSION FROM HOT-ELECTRON PLASMAS)

Increasing the field strength results, first, in an appreciable decrease in burst amplitude, followed by a slight increase at even higher fields. The occurrence of multiple bursts does not appear to be limited to either extreme in pressure or magnetic field. Typical oscilloscope traces of these multiple bursts have been previously reported.¹

The most encouraging result of this preliminary investigation is that there are several critical combinations of magnetic field and pressure for which the instability is repeatable. At a central magnetic field of 1030 Gauss and a pressure of 1.5×10^{-5} Torr, a single intense burst of radiation occurs consistently 120 ± 20 μ sec after each RF heating pulse. Correlated in time with the burst is a sudden drop to zero of the measured energy density of the plasma. Figure XV-1 illustrates this behavior. Comparison of the energy radiated in the burst with the change in the stored energy in the plasma indicates that an appreciable fraction of the kinetic energy of the hot electrons is converted into coherent radiation by the instability. Figure XV-2 illustrates the more general behavior occurring at pressures and field strengths other than these special ones. Note that while the first shot is similar to the behavior illustrated in Fig. XV-1, the second shot does not indicate a change in stored energy when the burst occurs. The bottom shot exhibits a very intense period of microwave radiation which has no apparent effect on the stored energy. This behavior is still not understood. The behavior of the bursts at the critical values of fields and pressures, however, should make possible a thorough investigation of the repeatable operation.

Measurement of the frequencies radiated by the discharge has been complicated by the presence of the high-power heating pulses. In order to protect the detectors from these pulses, it has been necessary to use a narrow-band transmit/receive switch. Retuning this switch has indicated that under some operating conditions more than one band of frequencies is being radiated. These separate bands each have their own characteristic intensity and most probable time of occurrence. Although these bands are all near the frequency of the RF heating power, the narrow-band switch discriminates against part of the radiated energy, and thus makes time-resolved frequency measurements impossible. We plan to replace this transmit/receive switch in the near future with a wideband PIN diode switch. This will allow time-resolved spectra to be determined easily.

We shall continue the investigation of this intense instability. Experiments are to be directed toward a thorough study of the time-dependent plasma parameters both before and after the occurrence of the repeatable bursts.

C. E. Speck

References

1. C. E. Speck and A. Bers, "Observation of Enhanced Cyclotron Radiation from an Electron-Cyclotron Resonance Discharge," Quarterly Progress Report No. 82, Research Laboratory of Electronics, M. I. T., July 15, 1966, pp. 187-189.

XVI. INTERACTION OF LASER RADIATION WITH PLASMAS AND NONADIABATIC MOTION OF PARTICLES IN MAGNETIC FIELDS* 8/10/72

Academic and Research Staff

Prof. D. J. Rose
Prof. T. H. Dupree

Prof. L. M. Lidsky
Prof. S. Yip

Graduate Students

T. S. Brown
J. D. Callen
H. Ching

D. E. Crane
M. D. Lubin

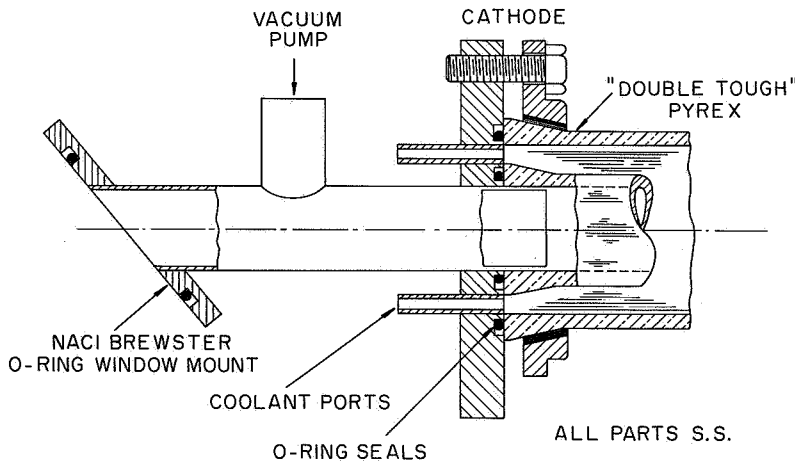
R. W. Moir
M. Murakami
A. A. Offenberger

N67-27097

A. INCOHERENT SCATTERING OF LIGHT FROM A PLASMA IV

The N₂-CO₂ laser development for the plasma scattering experiment¹⁻³ has been completed; the optical detecting scheme has been finalized; and, after delivery of a 0.14-μ bandpass filter centered at 10.6 μ, noise measurements were made to determine the NEP of our mercury-doped Ge detector.

The final, and greatly simplified, laser design is indicated in Fig. XVI-1. Two



NOTE: ENDS SYMMETRICAL EXCEPT FOR GAS INLET AND VACUUM PORT SIZES

Fig. XVI-1. Detail of laser discharge tube.

coaxially mounted equal lengths of "Double Tough" Pyrex tubing, 10 ft long and 1 in. and 2 in. I. D., with compressive O-ring sealing to the end flanges, form the discharge region and coolant channel. The flanges incorporate the O-ring mounted NaCl Brewster

* This work was supported by the United States Atomic Energy Commission (Contract AT(30-1)-3285).

(XVI. INTERACTION OF LASER RADIATION WITH PLASMAS)

windows, vacuum fitting and gas inlet ports, cathode and anode for the discharge, and are directly cooled by passing the cooling water through them. The discharge tube and mirrors are mounted on a 4-in. Al H-beam.

The discharge conditions are 100 mA at 12 kV in a gas mixture of 1 Torr CO_2 , 1 Torr N_2 , and 4 Torr He. The mirrors have a separation of 4 m; one being an Au-coated B.S.C. glass, the other a flat Ge mirror. The Au mirror has a 1-mm central hole for alignment purposes when using an He-Ne laser. The Ge mirror, 2-mm thick, has a front surface reflectivity of 36% (index of refraction $n=4$) and the back surface has a ZnS antireflection coating. The output power is ~ 100 watts at 10.59μ , with essential stability on a single rotational transition. At lower power levels, or with slightly detuned mirrors, other rotational lines ($\sim 200 \text{ \AA}$ separation) appear. The output is multi-mode longitudinally and transversely, but this is of no consequence in our scattering experiment. Using a Au-coated mirror with 1-cm hole coupling yields an even higher power level, but does not give the single rotational line stability that the Ge mirror affords. The optics for detecting the scattered radiation from the plasma is indicated in Fig. XVI-2, with the exception of substituting mirrors for lenses in collecting and

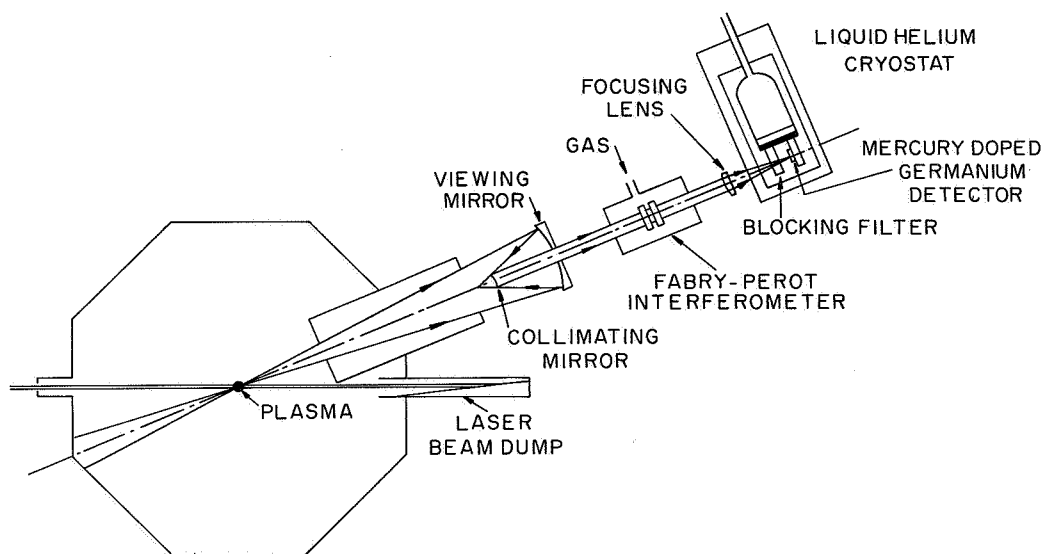


Fig. XVI-2. Laser-plasma scattering-detection optics.

rendering the scattered radiation parallel for wavelength analysis. We found that spherical aberration in the KCl lenses was the limiting factor in utilizing all available scattered light. A redesign, with mirrors substituted for lenses, indicates far less spherical aberration and hence much better collection efficiency. The large mirror subtends $\pi \times 10^{-2}$ sr at the scattering point in the plasma. The mirror assembly

(XVI. INTERACTION OF LASER RADIATION WITH PLASMAS)

is under construction.

The Fabry-Perot interferometer uses Ge plates with 96% ZnS reflective coatings, which affords a 20 Å bandpass. The central wavelength is to be pressure-tuned by using ethane, which will afford a spectral scan of 1400 Å. This range will enable measurement of the plasma-frequency satellite resonances, as well as temperature measurements from the Doppler-shifted intensity spectrum.

An NaCl lens with small spherical aberration focuses the spectrally analyzed radiation onto an Hg-doped Ge detector cooled to 4°K. A Ge substrate blocking filter of 0.14-μ bandpass mounted in the 4°K cryostat blocks all orders from the Fabry-Perot, except one, and additionally limits the 300°K black-body radiation seen by the detector.³ The measured NEP is 2×10^{-14} with a responsivity of 8×10^8 volts watt⁻¹ and watt cps^{-1/2}, source impedance of 1.5 M, compared with an unblocked detector of NEP = 8×10^{-13} watt cps^{-1/2} and responsivity = 2.5×10^6 volt watt⁻¹. A considerable improvement has been achieved. The anticipated scattered power levels are 4×10^{-15} watt; this indicates detection bandwidths of 1/25 cps for a S/N = 1.

The laser radiation is chopped before focusing into the scattering volume, and the scattered signal is detected synchronously by using an FET impedance-matching pre-amplifier and Princeton Applied Research HR-8 lock-in amplifier. The detector noise is well above pre-amplifier noise, and is the limiting factor in this experiment.

The scattered light collecting mirrors are being set up and the only outstanding question will be that of laser beam dump efficiency.

A. A. Offenberger

References

1. A. A. Offenberger, Quarterly Progress Report No. 78, Research Laboratory of Electronics, M.I.T., July 15, 1965, pp. 131-135.
2. A. A. Offenberger, Quarterly Progress Report No. 79, Research Laboratory of Electronics, M.I.T., October 15, 1965, pp. 145-147.
3. A. A. Offenberger, Quarterly Progress Report No. 81, Research Laboratory of Electronics, M.I.T., April 15, 1966, pp. 139-141.

B. ELECTRON DIFFUSION IN THE HELICALLY PERTURBED MAGNETIC FIELD OF THE M.I.T. STELLARATOR

Electrons of 1500 volts are being injected and trapped in a torus for an average of 100 transits. The trapped electrons diffuse outward toward the walls of the torus and are collected in an azimuthally symmetric charge detector. After an initial transient, the current at the collector decays exponentially after the injection current is switched off. This type of behavior implies a random walk of the electrons toward the walls. The

(XVI. INTERACTION OF LASER RADIATION WITH PLASMAS)

average number of transits $N = \frac{R}{\langle(\Delta r)^2\rangle}$, where R is the radius of the vacuum wall, and $\langle(\Delta r)^2\rangle$ is the average square change in the particle's radial position in one transit. $\langle(\Delta r)^2\rangle$ is produced by perturbation fields (waves), as well as gas scattering, scattering from the Stellarator fields in the U-bends, and noncancellation of the toroidal drifts. The perturbing fields are varied while the others are kept as constant as possible; thus their effects can be subtracted out.

The electrons diffuse to the torus in real space, but the perturbing fields produce velocity-space diffusion and almost no real-space diffusion of the guiding centers. The drift cancellation in the U-bends is velocity-dependent and hence converts velocity diffusion into real-space diffusion.

The average number of transits then becomes

$$N = \frac{v_{\perp}^2 \text{ loss cone}}{\langle(\Delta v)^2\rangle}$$

in velocity coordinates, where $v_{\perp} \text{ loss cone}$ is the perpendicular (to \vec{B}) velocity at which the electron will be lost rapidly. $\langle(\Delta v_{\perp})^2\rangle$ is the squared change in perpendicular velocity in one transit averaged over all possible initial entrance velocity-space angle (phase average).

The loss cone ($v_{\perp} \text{ loss cone}$) in a torus is not simply defined as in a mirror device, and depends on the drift-cancellation method that is used; however, it does not vary with a change in perturbation field strength, and hence we can measure the dependence of $\langle(\Delta v_{\perp})^2\rangle$ on perturbation field strength, keeping $v_{\perp} \text{ loss cone}$ constant. We plan to measure the loss cone ($v_{\perp} \text{ loss}$), but, at present, we use it as an adjustable parameter to fit the data.

The perturbation field used for this experiment was a static transverse magnetic field rotating in space with a varying pitch length.

A theoretical prediction of the lifetime for weak perturbations is the following.¹

$$N = \left\{ \frac{A \left(\frac{B_{\perp}}{B_0} \right)^2 F(z_0)}{\frac{v_{\perp}^2 \text{ loss cone}}{v_0^2}} \right\}^{-1}, \quad (1)$$

where

$$A = \frac{2}{\pi} \frac{LP_0}{a^2 r_0^2}$$

(XVI. INTERACTION OF LASER RADIATION WITH PLASMAS)

$$F(z_0) = \tan \frac{\pi z_0}{2L} \left(1 - a^2 \cos^4 \frac{\pi z_0}{2L} \right)^{3/2}$$

B_0 = field for resonance for 1.5 kV electrons

= 61.2 Gauss

r_0 = Larmor radius at the resonant field for $v_z = 0$

= 2.13 cm

a^2 = Percentage of electron energy for which the perturbed field has been designed to convert parallel (to \vec{B}) energy to transverse energy (or vice versa)

= 80%

L = length of perturbed-field region = 1 meter

P_0 = resonant pitch length for $v_{\perp} = 0$, = 13.4 cm

z_0 = position at which an electron with $v_{\perp} = 0$ is in resonance for a given B_z ,
 $0 \leq z_0 \leq L$.

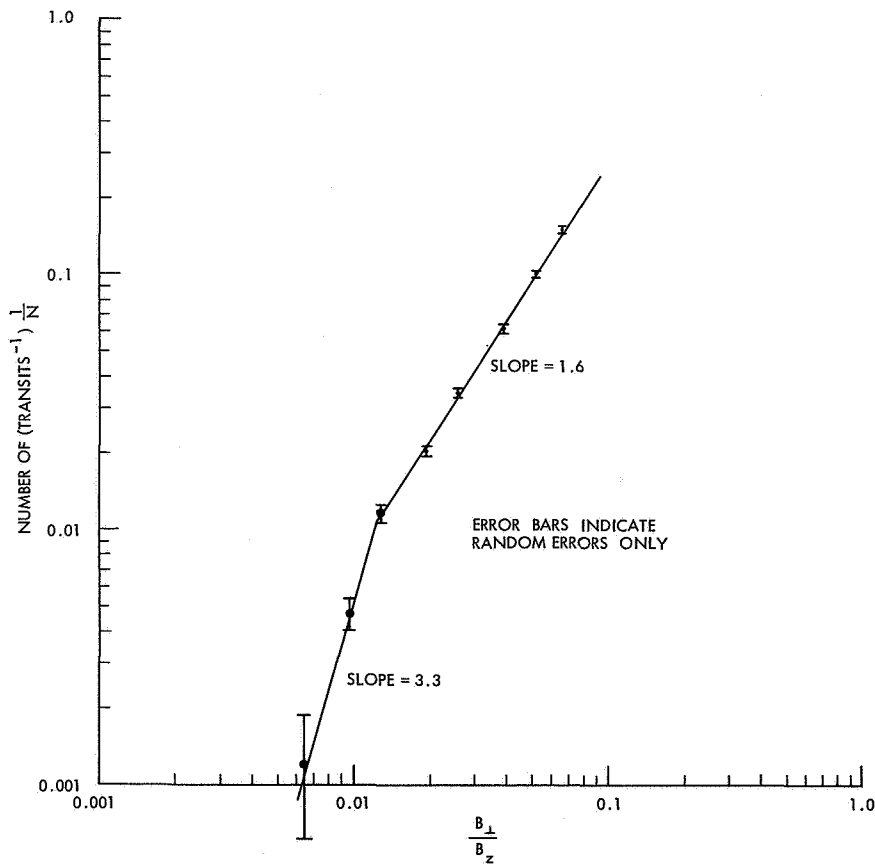


Fig. XVI-3. Diffusion coefficient vs perturbation field strength.

(XVI. INTERACTION OF LASER RADIATION WITH PLASMAS)

The raw data from the experiment was the average number of transits, $N(B_{\perp})$.

$$\frac{1}{N} = \frac{1}{N(B_{\perp})} - \frac{1}{N(o)}$$

where N is the average number of transits attributable to the perturbation field with $N(o) = \infty$.

Figure XVI-3 shows experimental results for Eq. 1, with B_{\perp} varied and all else fixed. Equation 1 predicts a square-law dependence of the number of transits on perturbation field strength. The dependence goes from a 1.6 power law to something higher (possible square law) at fields below $B_{\perp}/B_z = 1.3\%$. The large error bars

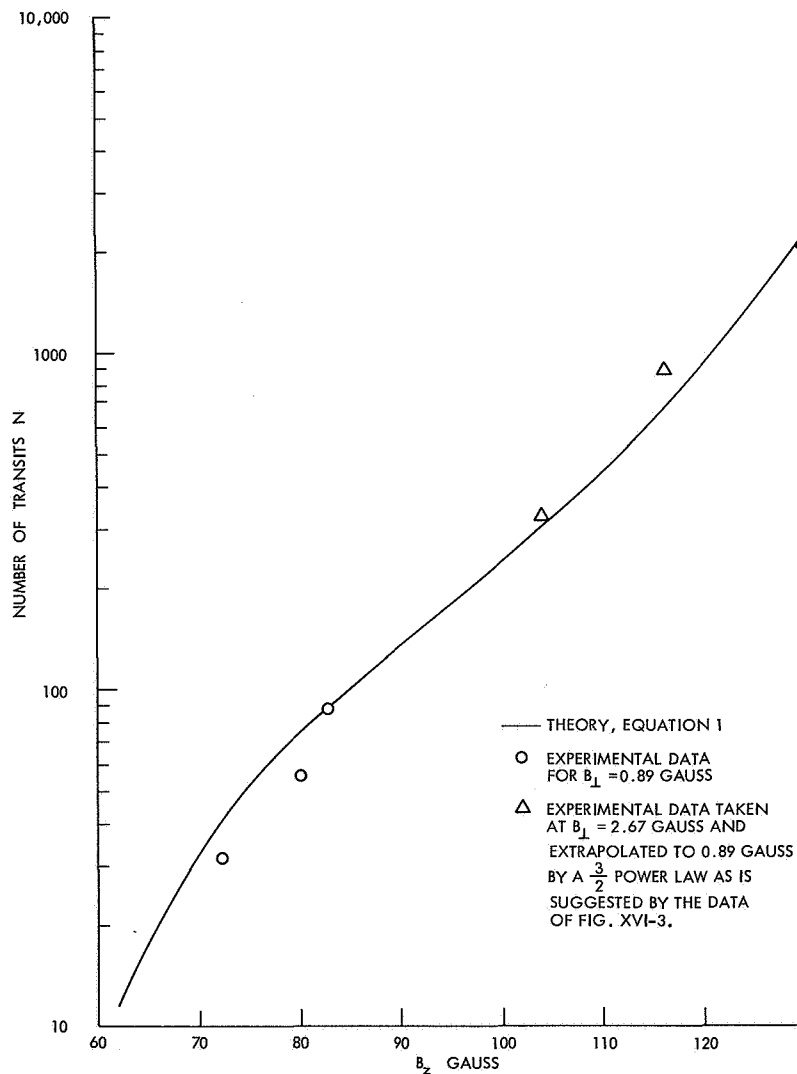


Fig. XVI-4. Lifetime vs magnetic field strength.

(XVI. INTERACTION OF LASER RADIATION WITH PLASMAS)

result from the small difference of large numbers in Eq. 2 for weak perturbation (that is, $N(B_{\perp}) \approx N(0)$).

Clark and Lidsky² predict $N \propto [B^{3/2}]^{-1}$ for sufficiently large B_{\perp} , which is in agreement with the region of Fig. XVI-3 above $B_{\perp}/B_z = 1.3\%$.

The dependence of Eq. 1 on \bar{B} was checked experimentally; it is given in Fig. XVI-4 for a constant value of $B_{\perp} = 0.89$ Gauss. By changing B_z , the resonance point was shifted. $B_z = 61.2$ Gauss corresponds to resonance at the left of Fig. XVI-4 ($z_0 = 100$ cm), while $B_z = 137$ Gauss corresponds to resonance at $z_0 = 0$ for electrons with $v_{\perp} = 0$. An approximate fit to the data was found for $v_{\perp \text{ loss}}/v_0 = 1$.

Researchers have proposed the use of perturbation fields for nonadiabatic traps, whereby molecular ions are trapped by a resonant field. Before that are lost by the inverse trapping process, collisions can break up an appreciable fraction of the molecular ions into atomic ions with half the mass, for instance. Figure XVI-4 gives experimental results that are equivalent to changing the mass of the particles. A molecular ion, H_2^+ say, would behave like an electron in resonance at 61.2 Gauss. An atomic ion of half the mass would be in resonance at 122.4 Gauss and, from Fig. XVI-4, we see that the atomic ion would have a lifetime 100 times longer than the molecular ion. In this perturbed field the pitch changed by more than a factor of 2, so the atomic ion equivalent electrons were still in resonance with a portion of the perturbed field.

During the next quarter we shall investigate diffusion from perturbed fields in the transition region between resonant and nonresonant fields. Also, we plan to measure the size of the loss cone in our torus.

R. W. Moir, L. M. Lidsky

References

1. R. C. Wingerson, T. H. Dupree, and D. J. Rose, *Phys. Fluids* 7, 1475 (1964); see Eq. (58).
2. L. M. Lidsky, J. F. Clarke, and D. J. Rose, "Experimental and Numerical Investigations of Velocity Diffusion in a Nonadiabatic Injection System," Paper No. 5L-9, Eighth Annual Meeting of the Division of Plasma Physics, Boston, Mass., November 1966; J. F. Clarke and L. M. Lidsky, "Nonclassical Diffusion Produced by a Resonant Helical Magnetic Field Perturbation," Paper No. 51-10; J. F. Clarke, Ph.D. Thesis, Department of Nuclear Engineering, M. I. T., June 1967.

COMMUNICATION SCIENCES
AND
ENGINEERING

XVII. STATISTICAL COMMUNICATION THEORY*

Academic and Research Staff

Prof. Y. W. Lee
Prof. A. G. Bose

Prof. J. D. Bruce
Prof. A. V. Oppenheim

Prof. D. E. Nelsen
G. Gambardella

Graduate Students

T. Huang
D. J. Matthiessen
M. F. Medress
V. Nedzelnitsky
A. D. Pitegoff

E. M. Portner, Jr.
L. R. Poulo
A. E. Roland
S. K. Samson
R. W. Schafer
J. E. Schindall

F. P. Tuhy
J. L. Walker
J. J. Wawzonek
C. J. Weinstein
D. H. Wolaver

A. DISCRETE ANALYSIS OF HOMOMORPHIC DECONVOLUTION

N67-27098

A method for separating convolved signals based on the canonic system of Fig. XVII-1 has been previously discussed.¹ Some preliminary analytical results for continuous signals and a brief discussion of the problems involved in implementing such a system have

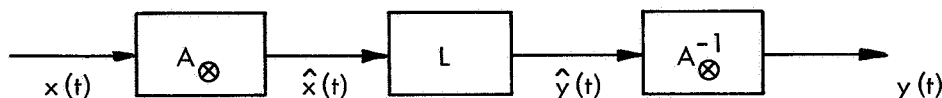


Fig. XVII-1. Canonic form for deconvolution filter.

also been given.² Since such a system must be implemented by using a digital computer, it is of importance to consider the characterization of the system of Fig. XVII-1 when all of the signals are discrete time functions.

In this report we shall discuss the discrete characterization of the system A_{\otimes} . This is a nonlinear system that is characterized by the property that if $x = x_1 \otimes x_2$, then $\hat{x} = \hat{x}_1 + \hat{x}_2$, with \otimes denoting discrete convolution. If $X(z)$ and $\hat{X}(z)$ denote the two-sided z-transforms of $x(n)$ and $\hat{x}(n)$, respectively, this property can be realized through the requirement that

$$\hat{X}(z) = \log X(z),$$

provided that when $z = e^{j\omega}$, $\arg[X(z)]$ is continuous in the interval $-\pi < \omega < \pi$. Since the z-transform is periodic in ω , $\arg[X(z)]$ must also be periodic in ω . It is not necessary to associate the region of convergence of $X(z)$ with $\hat{X}(z)$.

We shall make use of just two choices for the region of convergence of $\hat{X}(z)$. One

* This work was supported principally by the Joint Services Electronics Programs (U. S. Army, U. S. Navy, and U. S. Air Force) under Contract DA 28-043-AMC-02536(E), and in part by the National Aeronautics and Space Administration (Grant NsG-496).

(XVII. STATISTICAL COMMUNICATION THEORY)

choice is the region outside all poles and zeros of $X(z)$. This results in a sequence, $\hat{x}(n)$, which is zero for $n < 0$. The other choice is an annular region that includes the unit circle. This choice results in a sequence, $\hat{x}(n)$, which always approaches 0 as n approaches $\pm\infty$.

It will be assumed that $X(z)$ is of the form

$$X(z) = Az^r \frac{\prod_{k=1}^m (1-a_k z^{-1})}{\prod_{i=1}^p (1-b_i z^{-1})} \quad (1)$$

which can be rewritten in the form

$$X(z) = \frac{z^{r-m_o+p_o} A(-1)^{m_o-p_o} \prod_{k=1}^{m_o} a_k \prod_{k=1}^{m_o} (1-a_k^{-1}z) \prod_{k=m_o+1}^m (1-a_k z^{-1})}{\prod_{i=1}^{p_o} b_i \prod_{i=1}^{p_o} (1-b_i^{-1}z) \prod_{i=p_o+1}^p (1-b_i z^{-1})},$$

where the first m_o zeros and p_o poles are assumed to be outside the closed contour that is used for determining $\hat{x}(n)$, and the rest inside. For $X(z)$ of the form of Eq. 1 and for which the angle is computed as discussed above, it can be shown by integrating by parts that

$$\hat{x}(0) = \log \left[\frac{A \prod_{k=1}^{m_o} |a_k|}{\prod_{i=1}^{p_o} |b_i|} \right] + \sigma(r-m_o+p_o), \quad (2a)$$

and

$$\hat{x}(n) = Ke^{\frac{\sigma n \cos \pi n}{n}} + c(n) \quad n = \pm 1, \pm 2, \dots \quad (2b)$$

The function $c(n)$ is defined by

$$c(n) = -\frac{1}{2\pi j} \oint_C z \frac{X'(z)}{X(z)} z^{n-1} dz, \quad (3)$$

where C is a circular contour defined by $z = e^{\sigma+j\omega}$, which lies in the region of convergence of $\hat{X}(z)$. The constant K in Eq. 2b is given by

$$K = r + p_o - m_o.$$

It can also be shown that

$$K = r + m_i - p_i + p - m,$$

where m_i and p_i are the number of nonzero zeros and poles inside the contour C .

By applying the properties of z -transforms, it can be shown that $c(n)$ also satisfies the equation

$$c(n) = \frac{1}{n} \sum_{k=-\infty}^{\infty} kc(k) \frac{x(n-k)}{x(0)} \quad n \neq 0.$$

In the special case for which $x(n) = 0$ for $n < 0$, $x(0) \neq 0$, and the contour C in Eq. 3 encloses all of the poles and zeros of $X(z)$, so that $\hat{x}(n) = 0$, $n < 0$, the constant K in Eq. 2 is zero and therefore $\hat{x}(n) = c(n)$. Under these conditions, $\hat{x}(n)$ satisfies the recursion formula

$$\hat{x}(n) = \frac{x(n)}{x(0)} - \frac{1}{n} \sum_{k=0}^{n-1} k\hat{x}(k) \frac{x(n-k)}{x(0)} \quad n > 0 \quad (4a)$$

$$\hat{x}(0) = \log A = \log x(0). \quad (4b)$$

It should also be noted that the inverse operation, corresponding to the characterization of the system A_{\otimes}^{-1} , can easily be obtained simply by solving Eqs. 4 for $x(n)$.

If $x(n) = 0$, $n < 0$ and $x(0) \neq 0$, Eq. 4 can be used to compute $\hat{x}(n)$. The computation is practical only in the case in which $X(z)$ has no poles or zeros outside the unit circle because if this is not true, $\hat{x}(n)$ will grow at least as fast as $\frac{a^n}{n}$, where a is some number greater than 1. It should be mentioned, however, that multiplication of $x(n)$ by β^n ($\beta < 1$) will sometimes result in a new function whose transform has no poles or zeros outside the unit circle. It can also be shown that if $X(z)$ is a rational function, the effect of multiplying $x(n)$ by β^n is simply to multiply the output $\hat{x}(n)$ by β^n .

In many cases of interest it may not be possible or desirable to use Eq. 4 in the calculation of $\hat{x}(n)$. In such cases, the inverse discrete Fourier transform of the logarithm of the discrete Fourier transform of $x(n)$ must be computed. If N denotes the number of points in the discrete Fourier transform, then the resulting sequence, $\tilde{\hat{x}}(n)$, is related to $\hat{x}(n)$ by the equation

$$\tilde{\hat{x}}(n) = \sum_{a=-\infty}^{\infty} \hat{x}(n+aN) \quad n = 0, 1, \dots, N-1,$$

corresponding to aliasing of the sequence $\hat{x}(n)$. This aliasing can be made less

(XVII. STATISTICAL COMMUNICATION THEORY)

noticeable by exponentially weighting $x(n)$ or by augmenting the sequence $x(n)$ by terminating in zeros.

R. W. Schafer, A. V. Oppenheim

References

1. A. V. Oppenheim, "Nonlinear Filtering of Convolved Signals," Quarterly Progress Report No. 80, Research Laboratory of Electronics, M. I. T., January 15, 1966, pp. 168-175.
2. R. W. Schafer, "A New Approach to Echo Removal," Quarterly Progress Report No. 84, Research Laboratory of Electronics, M. I. T., January 15, 1967, pp. 194-201.

B. UNITY FEEDBACK TWO-STATE MODULATOR CONFIGURATIONS

1. Introduction

The transfer function for the two-state modulation configuration described by Bose¹ has been derived in detail.² It has been shown that the dynamic ramp response, within an error term, is of the form

$$\bar{y}(t) = -x(t) - \tau x'(t). \tag{1}$$

The frequency response of the modulator, then, as inferred from the ramp response, goes as

$$\frac{\bar{Y}(s)}{X(s)} = -(1 + \tau s) \tag{2}$$

which, as in the case of a continuous amplifier with feedback, is the inverse of the feedback network response.

The system frequency response can be made flat by placing an RC filter identical to the feedback network in front of the modulator loop.

The same effect is achieved in the circuit of Fig. XVII-2, in which the RC feedback filter has been located in the place where it also acts to filter the input waveform.

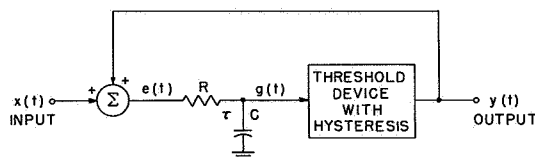


Fig. XVII-2. Unity feedback two-state modulation system.

In Fig. XVII-2 the hysteresis switch with delay, previously used as the forward element of the modulator loop, has been replaced by an arbitrary threshold device with hysteresis. This has been done to

permit application of the analysis to more general effects that are present in a physical realization, such as switching transients and variations in the switching levels. The

threshold device has two states or modes of operation: the charge state, entered when its input $g(t)$ drops below w_c , during which the output will be designated $y_c(t)$; and the discharge state, entered when $g(t)$ rises above w_d , during which the output will be designated $y_d(t)$. The only constraints on the device behavior to insure recurrent alternation of states or cyclic operation of the modulator are that $x(t)$ plus $y_c(t)$ be sufficiently positive that $g(t)$ tends to increase or "charge," eventually reaching w_d , and that $x(t)$ plus $y_d(t)$ be sufficiently negative that $g(t)$ tends to decrease or "discharge," eventually reaching w_c . A switch with hysteresis and delay, for example, meets this requirement, provided the input is bounded by $h_d - w_c < x < h_c - w_d$.

A general transfer expression for this system configuration will be derived. For static input, the system is shown to be identical to the RC feedback configuration² if ideal hysteresis with delay is assumed. For dynamic inputs – again, under the assumption of ideal hysteresis with delay – it can be shown that a flat frequency response is obtained with error equivalent to the static error. Finally, an improved system will be introduced for which the transfer function predicts zero error, even for the arbitrary threshold device described above.

2. Analysis

The transfer function for the circuit of Fig. XVII-2 will now be derived. For the RC circuit,

$$e(t) = g(t) + \tau g'(t). \quad (3)$$

The input to the nonlinear element has the form sketched in Fig. XVII-3. As long as this waveform is cyclic, the desired modulation will obtain.

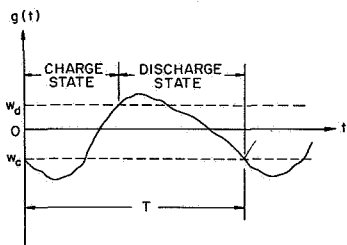


Fig. XVII-3. Typical input to the threshold device.

Define a cycle of operation to be from one w_c state transition to the next. Then, choosing $t = 0$ at the start of a cycle, we have

$$g(T) = g(0). \quad (4)$$

From (3), since $e(t) = x(t) + y(t)$,

(XVII. STATISTICAL COMMUNICATION THEORY)

$$\int_0^T [x(t)+y(t)] dt = \int_0^T g(t) dt + \tau g(t) \Big|_0^T. \quad (5)$$

Rearranging terms, using (4), and dividing by the period T yields

$$\frac{1}{T} \int_0^T y(t) dt = -\frac{1}{T} \int_0^T x(t) dt + \frac{1}{T} \int_0^T g(t) dt. \quad (6)$$

The output mean over the cycle is equal to the negative of the input mean over the cycle to an error term in $g(t)$, independently of the form of $x(t)$ and $y(t)$, as long as cyclic behavior is maintained. For efficiency, $y(t)$ should be a switching waveform, and, to enable accurate reconstruction of the input waveform, the modulator parameters should be such that the cycle time is short compared with the rate of change of $x(t)$; however, neither of these considerations is involved in the derivation of Eq. 6.

As indicated by Eq. 6, the modulator output in the unity feedback configuration is referenced to the mean of the input during a cycle, rather than depending only on the input values at the switching instants as was the case with the RC feedback configuration. The RC network continuously looks at the input waveform and effectively stores its behavior over the entire cycle in $g(t)$.

3. Investigation of the Error Term

In the preceding development arbitrary parameters that were appropriate for cyclic operation were assumed. It is intuitively clear that a narrow hysteresis window, bounded input and output, and small delays will limit the excursion of $g(t)$ to a restricted range and permit a bound on the error term. For typical operation this bound is exceedingly loose because the approximate symmetry of $g(t)$ reduces the value of its integral over a cycle. Expressions for the modulator error term have been developed for the case in which the forward path is an ideal switch with hysteresis and delay, and the input is static or characterized by its midpoint and slope over the cycle.

A typical error waveform $g(t)$ over a cycle with static input is sketched in

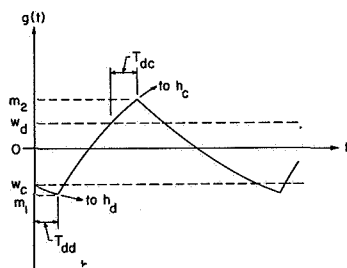


Fig. XVII-4. Error waveform, static input.

Fig. XVII-4. Notice that $g(t)$ is precisely the static error waveform evaluated in a previous report,² in which the RC feedback modulator configuration was discussed. The average of $g(t)$ was shown to be equal to its midpoint, which can be evaluated in terms of the modulator parameters, plus a term expressing the discrepancy between mean and midpoint. This

result, for the symmetric case, is reproduced in Eq. 7.

$$\bar{y} = -x_0 e^{-\frac{T_d}{\tau}} \left\{ 1 + \frac{2}{3} \frac{\left[\left(1 - e^{-\frac{T_d}{\tau}} \right) + \frac{w}{h} e^{-\frac{T_d}{\tau}} \right]^2}{1 - \left[\frac{x_0 e^{-\frac{T_d}{\tau}}}{h} \right]^2} \right\}. \quad (7)$$

The error function for ramp input can be derived by characterizing the ramp as altering the effective midpoint and half-width of the exponential window function $g(t)$, which is the same procedure previously used to discuss the ramp response of the RC modulator configuration.² The detailed mathematics will be omitted here; the result supports our intuitive claim that the device should exhibit flat frequency response by predicting the same transfer expression as for the static case. The "static" input value of Eq. 7 is simply replaced by the mean of the ramp during the modulator cycle.

4. Integral Modulator

In the derivation presented in this report, the error term was found to be the integral of $g(t)$ over a cycle. If the RC network is replaced by an integrator, as drawn in Fig. XVII-5,

$$e(t) = \tau g'(t), \quad (8)$$

and the error term in the derivation vanishes! Equation 6 becomes simply

$$\frac{1}{T} \int_0^T y(t) dt = -\frac{1}{T} \int_0^T x(t) dt. \quad (9)$$

Independent of the form of $y(t)$ — as long as it is appropriate to produce cyclic operation — and independent of the parameters of the hysteresis element and the nature

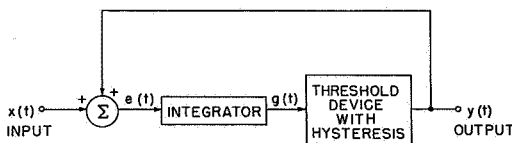


Fig. XVII-5. Integral two-state modulation system.

of the input, the average of the output over a cycle is precisely the negative of the mean of the input over the cycle.

A qualitative explanation of this type of modulator operation is easy to provide. The output of the integrator represents the input mean plus the output mean, and the hysteresis element guarantees that this output is cyclic. Then, over a cycle, the sum of the

(XVII. STATISTICAL COMMUNICATION THEORY)

means, the output error, is brought to zero.

In practice, the realization of the integrator may not be ideal. The transfer function of the integrator may then be represented in the form.

$$e(t) = Ag(t) + \tau g'(t), \quad (10)$$

where A is zero ideally, approximately .001 for a typical operational amplifier realization of an integrator, and equal to one for the simple RC approximation to an integrator. We have shown that the modulator error resulted from the integral of $g(t)$ over a cycle. In the analysis of this error, A was taken as unity (an RC approximation) and error expressions were derived. These same error expressions can be applied to the case of incomplete realization of the integrator in an integral modulation scheme simply by multiplying the error expressions by the factor A . Of course, for an ideal integrator A is zero and there will be no error, and for most practical realizations A is sufficiently small that the error may be neglected.

J. E. Schindall

References

1. A. G. Bose, Quarterly Progress Reports No. 66 and No. 67, Research Laboratory of Electronics, M. I. T., July 15 and October 15, 1962, pp. 187-189 and 115-119.
2. J. E. Schindall, Quarterly Progress Report No. 84, Research Laboratory of Electronics, M. I. T., January 15, 1966, pp. 184-194.

Academic and Research Staff

Prof. P. Elias
 Prof. R. M. Gallager
 Prof. M. M. Goutmann
 Prof. E. V. Hoversten

Prof. D. A. Huffman
 Prof. R. S. Kennedy
 Prof. J. L. Massey

Prof. E. Mortenson
 Prof. C. E. Shannon
 Prof. R. N. Spann
 Prof. J. T. Wagner

Graduate Students

D. S. Arnstein
 E. A. Bucher
 D. Chase
 R. L. Greenspan
 H. M. Heggestad

J. A. Heller
 M. Khanna
 Jane W-S. Liu
 J. Max
 J. C. Moldon
 J. T. Pinkston III

E. M. Portner, Jr.
 J. S. Richters
 A. H. M. Ross
 S. Thongthammachat
 D. A. Wright

A. SHIFT-REGISTER SYNTHESIS AND APPLICATIONS

N67-27099

The general form of a linear feedback shift-register (FSR) is shown in Fig. XVIII-1. The register is completely described by its length and its connection polynomial

$$C(D) = 1 + c_1D + \dots + c_tD^t.$$

Given a finite sequence s_1, \dots, s_N of digits from some number field (for example, the field of binary numbers), the problem is posed of finding (one of) the shortest

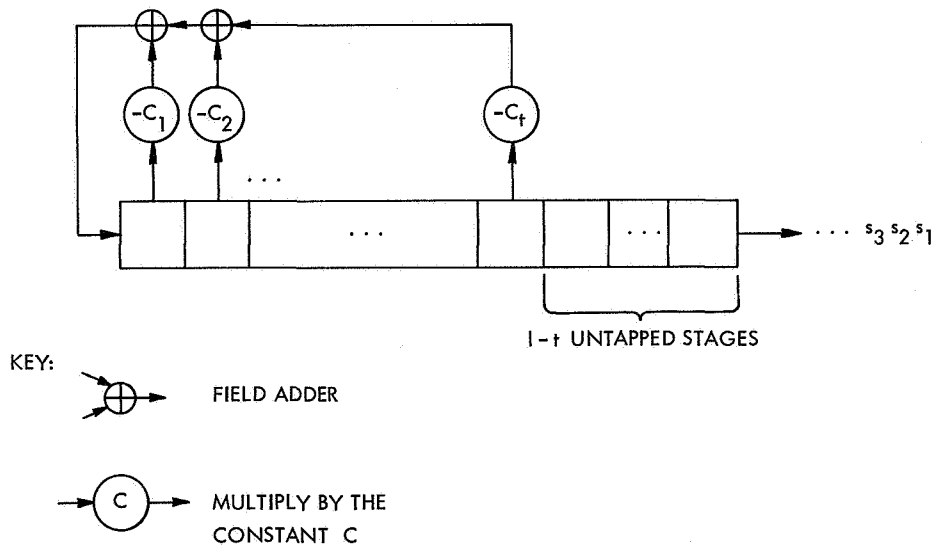


Fig. XVIII-1. General linear feedback shift register.

*This work was supported principally by the National Aeronautics and Space Administration (Grant NSG-334); and in part by the Joint Services Electronics Programs (U.S. Army, U.S. Navy, and U.S. Air Force) under Contract DA 28-043-AMC-02536(E).

(XVIII. PROCESSING AND TRANSMISSION OF INFORMATION)

linear FSR that could generate this sequence when loaded initially with $s_1, s_2, \dots, s_{\ell}$. The following algorithm, which solves this problem by a recursive technique, has been obtained. Defining

$$d_n = s_{n+1} + \sum_{i=1}^{\ell_n} c_i^{(n)} s_{n+1-i},$$

where

$$C^{(n)}(D) = 1 + c_1^{(n)}(D) + \dots + c_{\ell_n}^{(n)} D^{\ell_n},$$

gives a linear FSR of length ℓ_n , the shortest possible one for a linear FSR that generates s_1, s_2, \dots, s_n . Initializing with $n' = -1$, $n = 0$, $\ell_{n'} = \ell_n = 0$, $d_{n'} = 1$, $C^{(n')}(D) = 1$, $C^{(n)}(D) = 1$, we compute the registers for $n = 1, 2, \dots, N$ by the following recursion:

1. If $d_n = 0$, set $C^{(n+1)}(D) = C^{(n)}(D)$, $\ell_{n+1} = \ell_n$, and leave all other quantities unchanged.

2. If $d_n \neq 0$, set

$$C^{(n+1)}(D) = C^{(n)}(D) - d_n d_{n'}^{-1} D^{n-n'} C^{(n')}(D)$$

and

$$\ell_{n+1} = \max[\ell_n, n - n' + \ell_{n'}].$$

If $n - \ell_n \leq n' - \ell_{n'}$, leave all other quantities unchanged. But if $n - \ell_n > n' - \ell_{n'}$, replace n' , $\ell_{n'}$, $d_{n'}$, and $C^{(n')}(D)$ with n , ℓ_n , d_n , and $C^{(n)}(D)$, respectively.

Among the applications for this algorithm are (a) solving Newton's identities, which is the fundamental problem in decoding the Bose-Chaudhuri-Hocquenghem codes, (b) finding simple digital devices to produce a specified binary sequence, and (c) compressing the output of certain data sources with memory.

J. L. Massey

References

1. J. L. Massey, "Shift-Register Synthesis and BCH Decoding" (submitted to IEEE Transactions on Information Theory).

B. CODING THEOREMS FOR SOURCE-CHANNEL PAIRS

In a recently completed thesis,¹ we have studied the communication system shown in Fig. XVIII-2 when the capacity of the communication channel is not sufficiently high to allow perfect transmission of the source. The resulting (nonzero) distortion is measured by a non-negative distortion function, $d(w, z)$, which gives the distortion in the event that the source letter w has occurred at the source output but been reproduced at the decoder output as the letter z . It is assumed that both the source and channel are discrete, constant, and memoryless, and that the channel is available for use at a rate of once per source output. It is also assumed that the encoder and decoder are allowed to operate on blocks of letters; the encoder maps n -letter source output words into n -letter channel

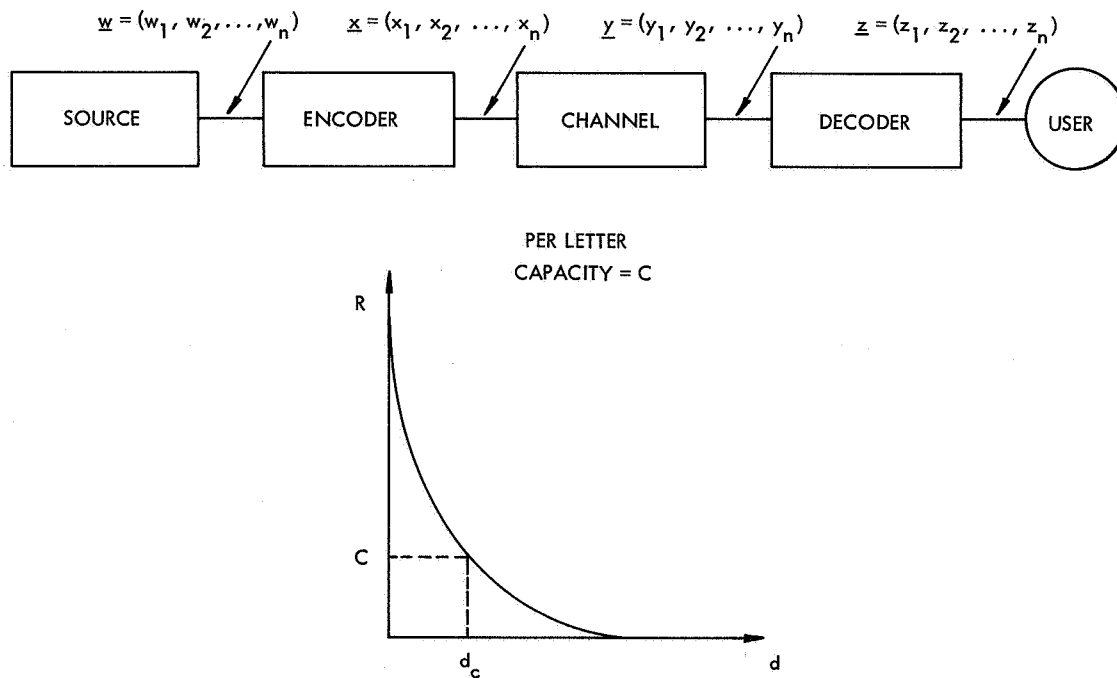


Fig. XVIII-2. Rate-distortion curve for the source.

input words, and the decoder maps n -letter channel output words into n -letter decoder output words. When block operators of this type are used, and one "transmission" contains n information letters from the source, the system performance is measured by the normalized sum of the n letter distortions, or

$$d(\underline{w}, \underline{z}) = \frac{1}{n} \sum_{i=1}^n d(w_i, z_i).$$

(XVIII. PROCESSING AND TRANSMISSION OF INFORMATION)

For such transmission systems, Shannon has introduced a rate-distortion function² that specifies the minimum attainable transmission distortion, d_c , in terms of the channel capacity, C . In general, though, the distortion level d_c is attainable only in the limit as the encoder and decoder are allowed to be arbitrarily complex, that is, the block lengths on which they operate are arbitrarily long. In this work, the block length was included as a variable, and upper and lower bounds were found to the minimum attainable transmission distortion as a function of this block length. Particular emphasis was placed on finding the asymptotic form of these bounds.

Even before these bounds are found, several interesting situations are known to exist. For instance, there are some source-channel pairs for which the minimum attainable transmission distortion is independent of the encoding block length; therefore, it is possible to attain the distortion level d_c even with $n = 1$. An example of such a pair is the binary symmetric source (equally-likely binary letters with $d(i, j) = 1 - \delta_{ij}$, $i, j = 1, 2$) used with a binary symmetric channel, where the optimum encoder is a direct connection. Another example is a Gaussian source used with an additive Gaussian noise channel, where the optimum encoder is simply an amplifier. When the source-channel pair is such that the minimum attainable distortion is independent of the coding block length, we shall say that the source and channel are "matched." For the more common situation, wherein the minimum attainable transmission distortion decreases with increasing encoding block length to asymptotically approach the distortion level d_c , we say that there is a "mismatch" between the source and channel, and suggest as a measure of this mismatch the "slowness" of the approach of the distortion to the asymptote d_c . Examples illustrating mismatches between source and channel are given in the author's thesis.¹

Another interesting situation occurs when there is a choice of using one of several channels of different capacity. Although the channel of highest capacity would be the best choice when one is willing to use infinite block-length coding, it might not be the best choice with finite-length coding. This could easily happen if the high capacity channel were very much more mismatched to the source than some lower-capacity channel.

1. Lower Bound

A generalization of the sphere-packing concept is used to derive the lower bound. The idea involved can be described with the following simple, but poor, bound. It is first assumed that the source word \underline{w} has occurred at the source output and that the channel input word \underline{x} is used for transmission. We list all possible received words, \underline{y} , ordered in decreasing conditional probability, $p(\underline{y}|\underline{x})$, and pair with each the decoder output word, $\underline{z}(\underline{y})$, to which it is decoded. The transmission distortion,

$$d(\underline{w}) = \sum_{\underline{y}^n} p(\underline{y}|\underline{x}) d(\underline{w}, \underline{z}(\underline{y})), \quad (1)$$

can be seen to equal the sum of conditional probability-distortion products on this list. If the set of distortion values that appear on this list are now rearranged (with the list of conditional probabilities fixed) to be ordered in increasing distortion values, the resulting sum of conditional probability-distortion products must be smaller, or at most equal to, the sum in Eq. 1. It therefore provides a lower bound.

An improved lower bound employs the same sort of orderings and rearrangements but includes a probability function, $f(\underline{y})$, in the ordering of the channel output words. This function is defined over the set of all channel output words, denoted by \underline{y}^n , and is later chosen to optimize the result. The channel output words are now ordered according to increasing values of the information difference $I(\underline{x}, \underline{y}) = \ln f(\underline{y})/p(\underline{y}|\underline{x})$, and each is again paired with the decoder output word $\underline{z}(\underline{y})$ to which it is decoded. The rearrangement of decoder output words is also slightly different. To describe this rearrangement, we visualize each channel output word, \underline{y} , as "occupying" an interval of width $f(\underline{y})$ along the line $[0, 1]$. The decoder output word, $\underline{z}(\underline{y})$, that is paired with a particular channel output word, \underline{y} , is also viewed as occupying the same region along $[0, 1]$ as \underline{y} , but, since any particular word \underline{z}_0 might be the decoding result of several channel output words, the region along $[0, 1]$ occupied by \underline{z}_0 could be a set of separated intervals. The arrangement of decoder output words is, this time, a rearrangement of occupancies in $[0, 1]$ toward the desired configuration, wherein the decoder words are ordered in increasing distortion (along this line), and each occupies the same total width in $[0, 1]$ as it did before the ordering. Thus two monotone nondecreasing functions can be defined along the line $[0, 1]$; one, $I(h)$, giving the information difference $I(\underline{x}, \underline{y})$ at the point h , $0 \leq h \leq 1$, and the other, $d(h)$, giving the distortion $d(\underline{w}, \underline{z})$ at h . The distortion $d(\underline{w})$ in Eq. 1, can be lower-bounded in terms of these functions by

$$d(\underline{w}) \geq \int_0^1 d(h) e^{-nI(h)} dh. \quad (2)$$

The lower bound to the total average transmission distortion is then the average of this bound over all possible source events.

If the probability function $f(\underline{y})$ and the probability function, $g(\underline{z})$, induced on Z^n by $f(\underline{y})$ through the optimum decoder function, are used to define the quantities $I(\underline{x}, \underline{y})$ and $d(\underline{w}, \underline{z})$ as random variables, the functions $I(h)$ and $d(h)$ can be seen to be the "inverses" of their cumulative distribution functions. By using estimates to these distribution functions,^{3, 5} the lower bound in Eq. 2 can be simplified considerably. When the (unknown) $g(\underline{z})$ is approximated by a probability function factorable into blocks of arbitrary but constant size and then varied to minimize the bound, and $f(\underline{y})$ is also varied to optimize the bound,

(XVIII. PROCESSING AND TRANSMISSION OF INFORMATION)

it can be shown that the asymptotic form of this approximated lower bound to distortion is

$$d(S) \geq d_c + \frac{a}{n} + o\left(\frac{1}{n}\right), \quad (3)$$

where

$$a = \frac{1}{2|s|} \left\{ \frac{\gamma''}{s^2 \mu''} - 1 - \ln \frac{\gamma''}{s^2 \mu''} + \frac{\sigma^2}{s^2 \mu''} \right\}$$

d_c = distortion at $R = C$ on the rate-distortion curve for the source

C = capacity of the channel

$$\mu(s) = \sum_i q_i \ln \sum_j g_j e^{s d_{ij}} \equiv \sum_i q_i \mu_i(s)$$

$$\gamma(t) = \sum_k C_k \ln \sum_l f_l^{1+t} p_{kc}^{-t}$$

$$\underline{q} = \underline{p}$$

\underline{p} = source output probabilities

\underline{g} = output probability on the test channel for the source at the point (d_c, C) on the rate-distortion curve

$\underline{c}, \underline{f}$ = input and output probabilities on the channel when it is used to capacity

σ^2 = variance of $\mu_i(s) - s\mu'_i(s)$ according to \underline{p}

$$t = -1$$

s satisfies: $\mu(s) - s\mu'(s) = -C$.

The coefficient a can be shown to be a non-negative function of the source and channel statistics that interrelates these statistics in such a way that the particular channel (among those of capacity C) for which a has its minimum value depends upon the source that is used. The reverse is also true. Among those sources that have a common point (d_c, C) on their rate-distortion curves, the particular source that minimizes a is different for different channels. Also, the coefficient a is precisely zero when the source and channel are matched. These properties of a suggest its utility as a measure of "mismatch" between the source and channel; the larger the mismatch, the slower is the approach of the lower bound to its asymptote. Several examples of different types of mismatch have been provided, and a strict lower bound, including the specification of the low-order terms, are to be found in the author's thesis.¹

2. Upper Bound

A random-coding argument is used to derive the upper bound. That is, an ensemble of encoders and decoders are defined over which the ensemble average transmission distortion is calculated. This, then, upper-bounds the minimum individual average (over source and noise events) transmission distortion in the ensemble and, in turn, upper-bounds the minimum average transmission distortion attainable with any encoding and decoding method.

First, two distortion values, d_R and d^* , are chosen to satisfy

$$d_c < d_R < d^* \leq d_{\max}. \quad (4)$$

Since a valid upper bound results for any two such choices, d_R and d^* are considered as parameters to be optimized later. The monotonicity of the rate-distortion curve and the inequalities in Eq. 4 provide the following inequalities among the corresponding values of rate on this curve:

$$C > R > R^*. \quad (5)$$

For each choice of d_R and d^* , and each coding block length n , the ensemble of codes is generated by picking, according to some probability distribution $p(\underline{x}, \underline{z})$, M independent pairs $(\underline{x}, \underline{z})$ from $X^n Z^n$. Thus, if in X there are J channel input letters and in Z there are K decoder output letters, there is a total of $(JK)^{nM}$ codes, each with the associated probability

$$\Pr(\text{code}) = \prod_{i=1}^M p(\underline{x}_i, \underline{z}_i).$$

The particular distribution that was used factors as $p(\underline{x}, \underline{z}) = p(\underline{x}) g(\underline{z})$, in which $p(\underline{x})$ is the channel input probability distribution that uses the channel to capacity, and $g(\underline{z})$ is the output probability distribution on the test channel for the source at the point (d^*, R^*) on its rate-distortion curve.

The encoding and decoding is done in the following way. When a source output \underline{w} occurs, the encoder chooses any member in its set of M permissible decoder words, say \underline{z}_0 , which satisfies

$$d(\underline{w}, \underline{z}_0) \leq d^*. \quad (6)$$

If there is no such member, it chooses any word in the set, say \underline{z}_1 . Because in each ensemble member there is a particular pairing defined between the M decoder output words and the M channel input words, there corresponds to \underline{z}_0 , or \underline{z}_1 , a particular channel input word, \underline{x}_0 , which is used for transmission. From the received channel output word, \underline{y} , the decoder first decodes to one of the M possible channel input words, and

(XVIII. PROCESSING AND TRANSMISSION OF INFORMATION)

from this, through the pairings defined by the code, to a decoder output word.

Clearly, if no channel error occurs and if the set of decoder words does contain a member satisfying Eq. 6, the transmission distortion must be upper-bounded by d^* . In any other event, the distortion can be upper-bounded by d_{\max} . By using the union bound, the total average (the average over source events, noise events, and the ensemble) can therefore be upper-bounded by

$$\bar{d}(\text{ens.}) \leq d^* + (d_{\max} - d^*) [\Pr(\exists' \underline{z}_0 \text{ in code}) + \Pr(\text{channel error})], \quad (7)$$

in which the symbol \exists' is used for "there does not exist."

The first probability in Eq. 7 was calculated by conditioning events on the occurrence of \underline{w} , finding the probability of codes lacking a decoder word satisfying Eq. 6, and then averaging over the source space W^n . The result is an exponentially decreasing function of n , with the exponent starting from zero and increasing monotonically in the difference $R - R^*$. This is analogous to the second probability, which is known also to be an exponentially decreasing function of n , but has an exponent starting from zero and increasing monotonically in the difference $C - R$. Thus the upper bound in Eq. 7 converges exponentially to the level d^* which, from Eq. 4, is strictly greater than d_c . This bound alone would not be satisfactory, since Shannon has shown that the level d_c can be approached.

As the bound in Eq. 7 is valid for each d^* and R satisfying Eqs. 4 and 5, the lower envelope to the set of bounds corresponding to all such choices of d^* and R is also a valid upper bound. It can be seen that the optimum choice of d^* (corresponding to that bound to which the lower envelope is tangent) must decrease toward d_c with increasing n and, from Eqs. 4 and 5, that R^* (and R) must increase toward C . The result of this is that the exponents in the probabilities of Eq. 7 must decrease toward zero, with the further consequence that the exponential terms in this equation decay more slowly as n increases. (For this reason, a choice of d^* marginally above d_c is not optimum for all block lengths.) The asymptotic form of the lower envelope, which is our upper bound to the average transmission distortion, is found to be

$$d(S) \leq d_c + b \sqrt{\frac{\ln n}{n}} [1 + o(1)], \quad (8)$$

in which

$$f(n) \stackrel{\Delta}{=} o(1) \quad \text{if } \lim_{n \rightarrow \infty} f(n) = 0$$

$$b = \frac{1}{|S|} \left[E_S''(R^*)^{-1/2} + E''(C)^{-1/2} \right].$$

In Eq. 8, $E(R)$ is the reliability function for the channel, and $E_S(R)$ is given by

$$E_S(R) = \min_i \ln \left[\left(\frac{p_i}{p_i \pm \Delta} \right)^{p_i \pm \Delta} \left(\frac{1 - p_i}{1 - p_i \mp \Delta} \right)^{1 - p_i \mp \Delta} \right],$$

where Δ is the largest number for which

$$\mu(s) - s\mu'(s) \geq -R$$

$$\mu'(s) = d^*$$

$$q_i = p_i \pm \Delta$$

$$\sum_i q_i = 1$$

are all satisfied. Another form of the function $E_S(R)$, which is more difficult to work with but provides a tighter bound, has been found.¹

In this derivation, we were forced to use a coding ensemble in which the signal set in each ensemble member is limited to $M < e^{nC}$ points, since no more general code could be found that provided the correct asymptote, d_c . The restriction to such a signal set, in effect, introduces an interface between the source and channel. This causes the coefficient b not to reveal the mismatch properties that the coefficient a brings about in the lower bound, since the set of source and channel statistics that minimize b are each independent of the other. We can, though, interpret b as (the reciprocal of) a type of stretch factor similar to those studied by Shannon⁶ and by Wozencraft and Jacobs.⁷

With the restriction to a signal set with $M < e^{nC}$, we have also found a lower bound to distortion that (for noisy channels) has the asymptotic form

$$d(S) \geq d_c + a_1 n^{-1/2}.$$

Thus one can conclude that it is necessary to have a signaling set larger than e^{nC} if one is to attain the $1/n$ rate of approach to d_c that appears in the lower bound in Eq. 3. Although we cannot exhibit such a coding scheme, the author conjectures that one does exist, and that the lower bound in Eq. 3 more correctly expresses the behavior of the performance curve.

For the special case of a noiseless channel, upper and lower bounds to the average transmission distortion have been found which, asymptotically, behave the same. Their form is

$$d_c + \frac{1}{2} \frac{\ln n}{|s|n} [1+0(1)] \leq d(s) \leq d_c + \left(\frac{1}{2} + \epsilon\right) \frac{\ln n}{|s|n} [1+0(1)],$$

(XVIII. PROCESSING AND TRANSMISSION OF INFORMATION)

in which s is equal to the slope of the rate-distortion curve at (d_c, C) , and ϵ is an arbitrarily small positive constant. The lower bound is similar to one derived by Gobllick⁸ (the bound in Eq. 3 is not applicable as $a = \infty$). The upper bound is derived by using essentially the same procedure as that used to obtain the noisy-channel upper bound. The significant difference is the replacement of the threshold encoder (Eq. 6) with an optimum encoder, that is, choosing for \underline{z}_0 that permissible decoder output word which minimizes $d(\underline{w}, \underline{z})$.

R. J. Pilc

References

1. R. J. Pilc, "Coding Theorems for Discrete Source-Channel Pairs," Ph. D. Thesis, Department of Electrical Engineering, M. I. T., 1966.
2. C. E. Shannon, "Coding Theorems for a Discrete Source with a Fidelity Criterion," IRE National Convention Record, Part 4, 1959, p. 142.
3. C. E. Shannon, "Notes for Seminar in Information Theory at M. I. T.," 1956 (unpublished).
4. R. M. Fano, The Transmission of Information (The M. I. T. Press, Cambridge, Mass., 1961).
5. R. G. Gallager, "Lower Bounds on the Tails of Probability Distributions," Quarterly Progress Report No. 77, Research Laboratory of Electronics, M. I. T., April 15, 1965, p. 277.
6. C. E. Shannon, "Communication in the Presence of Noise," Proc. IRE 37, 10 (1949).
7. J. M. Wozencraft and I. M. Jacobs, Principles of Communication Engineering (John Wiley and Sons, Inc., New York, 1965).
8. T. J. Gobllick, "Coding for a Discrete Information Source with a Distortion Measure," Ph. D. Thesis, Department of Electrical Engineering, M. I. T., 1962.

32 m)
3
XIX. DETECTION AND ESTIMATION THEORY* 8/10/68

Academic and Research Staff

Prof. H. L. Van Trees
Prof. D. L. Snyder

Graduate Students

M. E. Austin
A. B. Baggeroer

L. D. Collins
T. J. Cruise

R. R. Kurth
A. P. Tripp, Jr.

A. NONLINEAR MAP INTERVAL ESTIMATION

N67-27100

We shall consider two problems related to the equations specifying the nonlinear interval estimator. In the first part, we shall discuss a method for solving these equations which involves the optimum nonlinear realizable filter. In the second part, we shall present a technique for determining the optimum nonlinear realizable filter from the equations specifying the nonlinear interval estimator.

We shall assume that the following equations describe the system of interest:

$$\frac{d\mathbf{x}(t)}{dt} = \mathbf{f}(\mathbf{x}(t), t) + \mathbf{g}(\mathbf{x}(t), t) \mathbf{u}(t) \quad \text{nonlinear state equation} \quad (1)$$

$$E[\mathbf{u}(t)\mathbf{u}^T(\tau)] = Q\delta(t-\tau) \quad (2)$$

$$E[\mathbf{x}(T_0)] = \bar{\mathbf{x}}_0 \quad \text{initial condition assumption} \quad (3)$$

$$E[(\mathbf{x}(T_0) - \bar{\mathbf{x}}_0)(\mathbf{x}(T_0) - \bar{\mathbf{x}}_0)^T] = P_0 \quad (4)$$

$$\mathbf{r}(t) = \mathbf{s}(\mathbf{x}(t), t) + \mathbf{w}(t) \quad \text{nonlinear observation equation} \quad (5)$$

$$E[\mathbf{w}(t)\mathbf{w}^T(\tau)] = R\delta(t-\tau) \quad T_0 < t, \tau < T_f \quad (6)$$

For this system, the equations^{1, 2} describing the MAP interval estimate of the state vector $\mathbf{x}(t)$ are

$$\frac{d\hat{\mathbf{x}}(t)}{dt} = \mathbf{f}(\hat{\mathbf{x}}(t), t) + \mathbf{g}(\hat{\mathbf{x}}(t), t) Q \mathbf{g}^T(\hat{\mathbf{x}}(t), t) \mathbf{p}(t) \quad (7)$$

$$\frac{d\mathbf{p}(t)}{dt} = - \left. \frac{\partial \mathbf{f}^T}{\partial \mathbf{x}} \right|_{\mathbf{x} = \hat{\mathbf{x}}(t)} \mathbf{p}(t) + \mathbf{C}^T(\hat{\mathbf{x}}(t), t) R^{-1} (\mathbf{r}(t) - \mathbf{s}(\hat{\mathbf{x}}(t), t)), \quad (8)$$

where

*This work was supported by the Joint Services Electronics Programs (U. S. Army, U. S. Navy, and U. S. Air Force) under Contract DA 36-039-AMC-03200(E).

(XIX. DETECTION AND ESTIMATION THEORY)

$$C(\underline{x}(t), t) \triangleq \frac{\partial s(\underline{x}(t), t)}{\partial \underline{x}(t)}. \quad (9)$$

There is also a two-point boundary-value restriction on the equations. The boundary conditions are required to satisfy

$$\hat{\underline{x}}(T_0) - \bar{\underline{x}}_0 = P_0 \underline{p}(T_0) \quad (10)$$

$$\underline{p}(T_f) = 0. \quad (11)$$

The difficulty in solving these equations is the two-point boundary condition associated with the problem. We note that if we could obtain the value $\underline{x}(T_f)$, that is, the state estimate at the end point of the interval, we would have a complete set of boundary conditions at this time. We could then solve these equations backwards in time from this end point as if it were an initial or, more precisely, final-value problem. The estimate at the end point of the interval, however, is identical to the realizable filter estimate, since it involves only an operation upon past data, that is, the data before the end point time, T_f . Therefore, one method that we propose for solving the nonlinear smoothing problem may be outlined as follows:

a. Determine a complete set of boundary conditions at the end point of the interval by obtaining the realizable filter estimate.

b. Solve the MAP interval estimation equations backwards in time from the end point of the observation interval, using this set of boundary conditions.

This method is not the only algorithm for solving the MAP estimation equations. Another technique is the method of quasi-linearization. With this technique, the estimation equations are linearized around some a priori estimate of the solution. Then these linear equations are solved exactly, by use of the transition matrix associated with this system. This new solution provides the next estimate around which the nonlinear equations are linearized. This technique is repeated until a satisfactory convergence criterion has been satisfied.

The equivalence of the two methods has not been shown. It is suspected that in the high signal-to-noise case they produce identical estimates. In the low signal-to-noise case, however, the quasi-linearization procedure is probably better. This is because the realizable filter estimate that we obtain is an approximate estimate. Probably, the best procedure is some combination of the two techniques.

We shall now present a derivation of the optimum nonlinear realizable filter by the use of the technique of invariant imbedding. Our derivation is a modified version of that given by Detchmendy and Shridar.^{3, 4}

A fundamental difference between the interval estimator and the realizable filter is the time variable involved. In the interval estimator the important time variable is the time within the fixed observation interval, whereas in the realizable filter the important

time variable is the end-point time of the observation interval, which is not fixed but increases continually as the data are accumulated. For the realizable filter we want the estimate at the end point of the observation interval as a function of the length of the interval.

Let us now consider a more general class of solutions to the MAP equations. Instead of imposing the condition of Eq. 11, let us consider the class of solutions for the boundary condition

$$\underline{p}(T_f) = \underline{\eta}. \quad (12)$$

In general, the solution to Eq. 7 at the end point of the observation interval is now a function of the end-point time of the interval and the parameter $\underline{\eta}$. Let us denote the solution to Eq. 7 at the end point of the interval by $\underline{\xi}(T_f, \underline{\eta})$, where we emphasize the dependence noted above. We also note that

$$\underline{\xi}(T_f, \underline{\eta}) \Big|_{\underline{\eta}=0} = \hat{\underline{x}}(T_f). \quad (13)$$

We now state that it can be shown that the function satisfies the following partial differential equation:⁴

$$\frac{\partial \underline{\xi}(T_f, \underline{\eta})}{\partial T_f} + \frac{\partial \underline{\xi}(T_f, \underline{\eta})}{\partial \underline{\eta}} \underline{\pi}(\underline{\xi}, \underline{\eta}, T_f) = \Phi(\underline{\xi}, \underline{\eta}, T_f), \quad (14)$$

where

$$\Phi(\underline{\xi}, \underline{\eta}, T_f) = \underline{f}(\underline{\xi}, T_f) + \underline{g}(\underline{\xi}, T_f) \underline{Q} \underline{g}^T(\underline{\xi}, T_f) \underline{\eta} \quad (15)$$

$$\underline{\pi}(\underline{\xi}, \underline{\eta}, T_f) = - \frac{\partial \underline{f}}{\partial \underline{x}}(\underline{x}, T_f) \Big|_{\underline{x}=\underline{\xi}} \underline{\eta} - \underline{C}^T(\underline{\xi}, T_f) \underline{R}^{-1}(\underline{r}(T_f) - \underline{s}(\underline{\xi}, T_f)). \quad (16)$$

For convenience of notation, let us define the term

$$\underline{K}(\underline{x}, \underline{r}(T_f), T_f) = \underline{C}^T(\underline{x}, T_f) \underline{R}^{-1}(\underline{r}(T_f) - \underline{s}(\underline{x}, T_f)). \quad (17)$$

We now try a solution to Eq. 14 of the form

$$\underline{\xi}(T_f, \underline{\eta}) = \hat{\underline{x}}(T_f) + \underline{P}(T_f) \underline{\eta}, \quad (18)$$

where $\hat{\underline{x}}(T_f)$ and $\underline{P}(T_f)$ are functions that are to be chosen appropriately. As indicated by the notation, the function is the desired estimate. We now substitute this trial solution in the invariant imbedding equation. Since we are interested in the solution when $\underline{\eta}$ is small, we expand the functions around $\hat{\underline{x}}(T_f)$. We want to consider terms to order $|\underline{\eta}|$. The expansions of (15) and (16) are

(XIX. DETECTION AND ESTIMATION THEORY)

$$\Phi(\underline{\xi}, \underline{\eta}, T_f) \approx \underline{f}(\hat{\underline{x}}(T_f), T_f) + \frac{\partial \underline{f}}{\partial \underline{x}}(\underline{x}, T_f) \Big|_{\underline{x}=\hat{\underline{x}}(T_f)} P(T_f) \underline{\eta} + \underline{g}(\hat{\underline{x}}(T_f), T_f) Q g^T(\hat{\underline{x}}(T_f), T_f) \quad (19)$$

$$\pi(\underline{\xi}, \underline{\eta}, T_f) = - \frac{\partial \underline{f}}{\partial \underline{x}}(\underline{x}, T_f)^T \Big|_{\underline{x}=\hat{\underline{x}}(T_f)} \underline{\eta} - \frac{\partial \underline{K}}{\partial \underline{x}}(\underline{x}, \underline{r}, T_f) \Big|_{\underline{x}=\hat{\underline{x}}(T_f)} P(T_f) \underline{\eta} - \underline{K}(\hat{\underline{x}}(T_f), \underline{r}(T_f), T_f). \quad (20)$$

Substituting (19) and (20) in (14) yields

$$\left\{ \frac{d\hat{\underline{x}}(T_f)}{dT_f} - \underline{f}(\hat{\underline{x}}(T_f), T_f) + P(T_f) \underline{K}(\hat{\underline{x}}(T_f), \underline{r}(T_f), T_f) \right\} \\ + \left\{ \frac{dP(T_f)}{dT_f} - \frac{\partial \underline{f}}{\partial \underline{x}}(\underline{x}, T_f) \Big|_{\underline{x}=\hat{\underline{x}}(T_f)} P(T_f) - P(T_f) \frac{\partial \underline{f}}{\partial \underline{x}}(\underline{x}, T_f) \Big|_{\underline{x}=\hat{\underline{x}}(T_f)} \right. \\ \left. - P(T_f) \frac{\partial \underline{K}}{\partial \underline{x}}(\hat{\underline{x}}, \underline{r}(T_f), T_f) \Big|_{\underline{x}=\hat{\underline{x}}(T_f)} P(T_f) + \underline{g}(\hat{\underline{x}}(T_f), T_f) Q g^T(\hat{\underline{x}}(T_f), T_f) \right\} + O(\eta^2) = 0. \quad (21)$$

We require that the functions $\underline{x}(T_f)$ and $P(T_f)$ be so chosen that the terms within the first and second braces of Eq. 21 vanish identically. This specifies the solution to the invariant imbedding equation to $O(|\underline{\eta}|^2)$. The term within the first brace specifies the estimation equation. This is given by

$$\frac{d\hat{\underline{x}}(T_f)}{dT_f} = \underline{f}(\hat{\underline{x}}(T_f), T_f) - P(T_f) C^T(\hat{\underline{x}}(T_f), T_f) R^{-1}(\underline{r}(T_f) - \underline{s}(\hat{\underline{x}}(T_f), T_f)). \quad (22)$$

The term within the second brace specifies part of the dynamics of the estimation equation. This is given by

$$\frac{dP(T_f)}{dT_f} = \frac{\partial \underline{f}}{\partial \underline{x}}(\underline{x}, T_f) \Big|_{\underline{x}=\hat{\underline{x}}(T_f)} P(T_f) + P(T_f) \frac{\partial \underline{f}}{\partial \underline{x}}(\underline{x}, T_f) \Big|_{\underline{x}=\hat{\underline{x}}(T_f)}^T \\ - P(T_f) \frac{\partial \underline{K}}{\partial \underline{x}}(\underline{x}, \underline{r}, (T_f), T_f) \Big|_{\underline{x}=\hat{\underline{x}}(T_f)} P(T_f) + \underline{g}(\hat{\underline{x}}(T_f), T_f) Q g^T(\hat{\underline{x}}(T_f), T_f), \quad (23)$$

where (see Eq. 17)

$$\underline{K}(\underline{x}; \underline{r}, T_f) = C^T(\underline{x}, T_f) R^{-1}(\underline{r}(T_f) - \underline{s}(\underline{x}, T_f)).$$

The initial conditions to these differential equations are found by setting T_f equal to T_0 and using Eq. 10. This gives

$$\hat{\underline{x}}(T_0) = \underline{\bar{x}}_0 \quad (24)$$

$$P(T_0) = P_0. \quad (25)$$

Equations 22 and 23 are identical to those derived by Snyder by approximating the solution to the Fokker-Planck equation describing the a posteriori density.⁵ We note that we obtain the same result – that the optimum nonlinear realizable filter may not be equivalent to successively linearizing the system under consideration and then applying the Kalman-Bucy filtering equations.⁶ We also note that our solution is an approximate one because we only approximated the solution to the invariant imbedding equation.

A. B. Baggeroer

References

1. A. E. Bryson and M. Frazier, "Smoothing for Linear and Non-Linear Dynamic Systems," Proc. Optimum Synthesis Conference, Wright-Patterson Air Force Base, Ohio, September 1962.
2. A. Baggeroer, "Maximum a posteriori Interval Estimation," WESCON/66 Technical Papers, Paper 7/3, August 23-26, 1966.
3. R. Bellman, Invariant Imbedding (Academic Press, New York, 1964).
4. D. Detchmندی and R. Shridar, "Sequential Estimation of States and Parameters in Noisy Nonlinear Dynamical Systems," ASME J. Basic Engineering, Vol. 88, pp. 362-368, June 1966.
5. D. Snyder, "A Theory of Continuous Nonlinear Recursive-Filtering with Application to Optimum Analog Demodulation," WESCON/66 Technical Papers, Paper 7/2, August 23-26, 1966.
6. R. E. Kalman and R. Bucy, "New Results in Linear Filtering and Prediction Theory," ASME J. Basic Engineering, Vol. 83, pp. 95-108, March 1961.

B. PERFORMANCE BOUNDS FOR OPTIMUM DETECTION FOR GAUSSIAN SIGNALS

In this report, we shall apply the technique of tilted probability distributions to the problem of evaluating the performance of optimum detector for Gaussian signals received in additive Gaussian noise.

Stated in mathematical terms, we shall consider the following binary detection problem.

$$\left. \begin{array}{l} H_1: r(t) = s_{r_1}(t) + m_1(t) + w(t) \\ H_2: r(t) = s_{r_2}(t) + m_2(t) + w(t) \end{array} \right\} \quad 0 \leq t \leq \tau \quad (1)$$

where $s_{r_1}(t)$ and $s_{r_2}(t)$ are sample functions from zero-mean Gaussian random

(XIX. DETECTION AND ESTIMATION THEORY)

processes with known covariance functions $K_1(t, \tau)$ and $K_2(t, \tau)$, respectively; $m_1(t)$ and $m_2(t)$ are known waveforms, $w(t)$, in a sample function of white Gaussian noise of spectral density $\frac{N_0}{2}$.

Since the optimum detector for such problems is well known,¹⁻³ we shall not dwell upon it here. It suffices to indicate that for a large class of performance criteria, the detector bases its decision on the likelihood ratio, or some monotone function of the likelihood ratio. This is the class of detectors with which we shall be concerned.

One structure for the optimum detector is shown in Fig. XIX-1. A direct evaluation

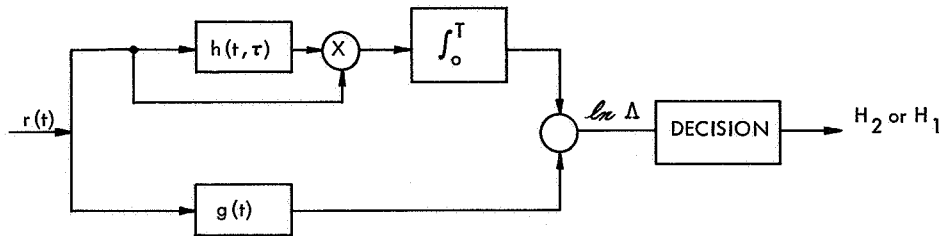


Fig. XIX-1. Optimum receiver structure.

of the error probabilities is conceptually possible, but practically it is extremely difficult, for we are faced with the problem of computing the probability distribution at the output of a time-variant nonlinear filter. It is this motivation that has led us to consider alternative methods of performance evaluation.

One alternative which is widely used is the output signal-to-noise ratio,⁴ which is valid in the so-called low-energy coherence, or threshold, case. One can show by a simple example that this performance measure can give incorrect results in some problems of interest, and therefore it must be applied with caution.

In an attempt to overcome the computational difficulties associated with an exact computation of error probabilities, while at the same time having a performance measure that is of wider applicability than the output signal-to-noise ratio, we have been investigating bounds on error probabilities, and, in particular, we have been seeking bounds that become asymptotically exact as the transmitted signal energy becomes large.

1. Tilted Probability Distribution

The technique that we employ is usually called "tilting" of probability distributions. It was introduced into information and coding theory by Shannon,^{5,6} and has been employed with great success. Earlier applications in the field of mathematical statistics are due to Chernoff⁷ and Esscher.⁸ We only summarize the notation and results

here, before proceeding to our specific problem.

All of our results center around the semi-invariant moment-generating function $\mu(s)$, which is merely the logarithm of the conditional characteristic function $M_{\ell|H_1}(s)$

$$\begin{aligned}\mu(s) &\triangleq \ln M_{\ell|H_1}(s) \\ &= \ln \int p_{\underline{r}}^s|H_2(\underline{R}) p_{\underline{r}}^{1-s}|H_1(\underline{R}) d\underline{R},\end{aligned}\quad (2)$$

where $p_{\underline{r}}|H_i(\underline{R})$ denotes the probability density for the received vector \underline{r} , conditioned on the hypothesis H_i , $i = 1, 2$. It can be readily shown that

$$\mu'(s) = \int p_{\underline{r}_s}(\underline{R}) \ell(\underline{R}) d\underline{R} \quad (3)$$

$$\mu''(s) = \int p_{\underline{r}_s}(\underline{R}) \ell^2(\underline{R}) d\underline{R} - [\mu'(s)]^2, \quad (4)$$

which are the mean and variance of $\ell(\underline{r})$ with respect to the probability density

$$\begin{aligned}p_{\underline{r}_s}(\underline{R}) &\triangleq \frac{p_{\underline{r}}^{1-s}|H_1(\underline{R}) p_{\underline{r}}^s|H_2(\underline{R})}{\int p_{\underline{r}}^{1-s}|H_1(\underline{R}') p_{\underline{r}}^s|H_2(\underline{R}') d\underline{R}'} \\ &= \exp[-\mu(s)] p_{\underline{r}}^{1-s}|H_1(\underline{R}) p_{\underline{r}}^s|H_2(\underline{R}).\end{aligned}\quad (5)$$

We shall refer to $p_{\underline{r}_s}(\underline{R})$ as the "tilted" density. The amount of "tilting" depends on the value of the parameter s . It follows from our definition that

$$p_{\underline{r}}|H_1(\underline{R}) = p_{\underline{r}_s}(\underline{R}) \exp[\mu(s) - s\ell(\underline{R})] \quad (6)$$

$$p_{\underline{r}}|H_2(\underline{R}) = p_{\underline{r}_s}(\underline{R}) \exp[\mu(s) + (1-s)\ell(\underline{R})]. \quad (7)$$

Hence the error probabilities may be expressed in terms of $\mu(s)$ and the tilted density $p_{\underline{r}_s}(\underline{R})$

$$\begin{aligned}Pr[\mathcal{E}|H_1] &= \int_{\{\underline{R}: \ell(\underline{R}) > \gamma\}} p_{\underline{r}}|H_1(\underline{R}) d\underline{R} \\ &= \int_{\gamma}^{\infty} p_{\ell_s}(L) \exp[\mu(s) - sL] dL\end{aligned}\quad (8)$$

(XIX. DETECTION AND ESTIMATION THEORY)

$$\begin{aligned} \Pr [\mathcal{E} | H_2] &= \int_{\{\underline{R}: \ell(\underline{R}) < \gamma\}} \text{pr} | H_2(\underline{R}) \, d\underline{R} \\ &= \int_{-\infty}^{\gamma} p_{\ell_s}(L) \exp[\mu(s) + (1-s)L] \, dL, \end{aligned} \quad (9)$$

where γ denotes the threshold level, and $p_{\ell_s}(L)$ is the tilted probability density for the log-likelihood ratio corresponding to the nonlinear transformation $\ell_s = L(\underline{r}_s)$.

A simple, well-known upper bound that follows immediately from Eqs. 8 and 9 is the Chernoff bound. For example, if in (7) we bound e^{-sL} by $e^{-s\gamma}$, then bound $\int_{\gamma}^{\infty} p_{\ell_s}(L) \, dL$ by unity, we obtain the following upper bounds:

$$\Pr [\mathcal{E} | H_1] \leq \exp[\mu(s) - s\gamma] \quad (10)$$

$$\Pr [\mathcal{E} | H_2] \leq \exp[\mu(s) + (1-s)\gamma]. \quad (11)$$

Then we can minimize the bound by proper choice of the parameter s . This choice is the solution to

$$\mu'(s) = \gamma. \quad (12)$$

A solution exists and is unique, provided the threshold γ lies between the means of the conditional densities $p_{\ell | H_1}(L)$ and $p_{\ell | H_2}(L)$. This condition is usually satisfied in the applications. An important step in our work consists in finding tighter bounds than Eqs. 10 and 11. After all, the arguments leading to these bounds were rather crude, and while the exponential behavior exhibited in Eqs. 10 and 11 is adequate for many applications, particularly in information and coding theory, we would like to retain the algebraic dependence for our applications to radar, sonar, and uncoded communication systems. A bound of a particularly attractive form is

$$\Pr [\mathcal{E} | H_1] \leq \frac{\exp[\mu(s) - s\mu'(s)]}{\sqrt{2\pi s^2 \mu''(s)}} \quad (13)$$

$$\Pr [\mathcal{E} | H_2] \leq \frac{\exp[\mu(s) + (1-s)\mu'(s)]}{\sqrt{2\pi(1-s)^2 \mu''(s)}} \quad (14)$$

where $\mu'(s) = \gamma$.

For large values of transmitted energy, this bound is considerably tighter than the Chernoff bound, although at the other extreme the Chernoff bound is tighter. Clearly, the bound that should be used in a given situation is the one that is the tightest.

We have not yet obtained a rigorous derivation of Eqs. 13 and 14 that is of sufficient

generality to take care of all problems of interest to us. In the sequel, when we discuss the application of these bounding techniques to the Gaussian problem, we shall discuss some preliminary results in this direction.

2. Application to the Gauss-in-Gauss Problem

We shall specialize the bounding techniques to the case in which the received vectors have Gaussian conditional probability densities with statistically independent components. Then, by interpreting the components of these vectors as coordinates in a Karhunen-Loève expansion, we shall generalize our results to the case in which the received signals are sample functions from random processes; that is, they are infinite dimensional.

The present problem is the evaluation of $\mu(s)$. We assume that on hypothesis H_j , $j = 1, 2$, \underline{r} is an N component Gaussian vector with

$$E[r_i] = m_{ij} \quad (15)$$

$$V_{\sigma}[r_i] = \lambda_{ij} + \frac{N_0}{2} \quad (16)$$

$$E[r_i r_k] = m_{ij} m_{kj}, \quad k \neq i$$

for $i, k = 1, 2, \dots, N$

$$j = 1, 2 \quad (17)$$

Substituting the N -dimensional Gaussian densities in the definition of $\mu(s)$, we find

$$\mu(s) = \frac{1}{2} \sum_{i=1}^N \left\{ s \ln \left(1 + \frac{2\lambda_{i1}}{N_0} \right) + (1-s) \ln \left(1 + \frac{2\lambda_{i2}}{N_0} \right) - \ln \left[\frac{2}{N_0} (s\lambda_{i1} + (1-s)\lambda_{i2}) + 1 \right] - \frac{(m_{i1} - m_{i2})^2}{\frac{\lambda_{i1} + \frac{N_0}{2}}{1-s} + \frac{\lambda_{i2} + \frac{N_0}{2}}{s}} \right\}$$

$0 \leq s \leq 1. \quad (18)$

Equation 18 is now in a very convenient form to let $N \rightarrow \infty$. This limiting operation is frequently used in detection and estimation theory, so we need not worry about its justification here. Furthermore, the infinite series which results is convergent in all cases of interest to us. It then remains to interpret the various terms as closed-form expressions involving the (conditional) mean and covariance functions of the random process $r(t)$, for (17) is not at all convenient from a computational point of view for the case $N \rightarrow \infty$. To illustrate the manner in which we find a closed-form expression for Eq. 18,

(XIX. DETECTION AND ESTIMATION THEORY)

consider the first term in the series,

$$\frac{s}{2} \sum_{i=1}^{\infty} \ln \left(1 + \frac{2\lambda_{i1}}{N_o} \right).$$

Now, for the moment, we wish to focus on a related problem; namely that of estimating the zero-mean Gaussian random process $s_{r_1}(t)$ when observed in additive white Gaussian noise of spectral height $N_o/2$.

Let $\hat{s}_{r_1}(t)$ denote the minimum mean-square-error point estimate of $s_{r_1}(t)$. The resulting mean-square error is

$$\xi_1 \left(t; \frac{N_o}{2} \right) = E \left[\left(\hat{s}_{r_1}(t) - s(t) \right)^2 \right], \quad (19)$$

where we have explicitly included the noise level as a parameter. Furthermore, we explicitly indicate the dependence of the Karhunen-Loève eigenvalues and eigenfunctions on the length of the interval:

$$\lambda_{i1}(\tau) \phi_i(t;\tau) = \int_0^T K_1(t, \tau) d_1(\tau) d\tau. \quad (20)$$

Then,

$$\begin{aligned} & \sum_{i=1}^{\infty} \ln \left(1 + \frac{2\lambda_{i1}}{N_o} \right) \\ &= \sum_{i=1}^{\infty} \ln \left(1 + \frac{2\lambda_{i1}(\tau)}{N_o} \right) \\ &= \int_0^T dt \frac{\partial}{\partial t} \sum_{i=1}^{\infty} \ln \left(1 + \frac{2\lambda_{i1}(t)}{N_o} \right) \\ &= \int_0^T dt \sum_{i=1}^{\infty} \frac{\lambda_{i1}(t)}{\frac{N_o}{2} + \lambda_{i1}(t)} \phi_i^2(t;t). \end{aligned} \quad (21)$$

In Eq. 21, we have used the result of Huang and Johnson⁹

$$\frac{\partial \lambda_{i1}(t)}{\partial t} = \lambda_{i1}(t) \phi_i^2(t;t). \quad (22)$$

Then we have

$$\begin{aligned} & \frac{s}{2} \sum_{i=1}^{\infty} \ln \left(1 + \frac{2\lambda_{i1}}{N_0} \right) \\ &= \frac{s}{2} \frac{2}{N_0} \int_0^T \xi_1 \left(t; \frac{N_0}{2} \right) dt. \end{aligned} \quad (23)$$

Similar results hold for the other terms in Eq. 18. The final closed-form expression for $\mu(s)$ is

$$\mu(s) = \frac{2}{N_0} \left\{ \begin{aligned} & \frac{s}{2} \int_0^T \xi_1 \left(t; \frac{N_0}{2} \right) dt + \frac{1-s}{2} \int_0^T \xi_2 \left(t; \frac{N_0}{2} \right) dt \\ & - \frac{1}{2} \int_0^T \xi_{1+2} \left(t; \frac{N_0}{2}, s \right) dt \\ & - \frac{s(1-s)}{2} \int_0^T \left[m_1(t) - m_2(t) - \int_0^T h_{1+2}(t, \tau; s) [m_1(\tau) - m_2(\tau)] h_1 \right]^2 dt \end{aligned} \right\} \quad (24)$$

The terms in Eq. 24 that have not been previously defined are the following. $\xi_{1+2} \left(t; \frac{N_0}{2}, s \right)$ is the minimum mean-square point estimation error for estimating the fictitious random process $s_{1+2}(t)$, which is defined by

$$s_{1+2}(t) = s s_{r_1}(t) + (1-s) s_{r_2}(t) \quad 0 \leq s \leq 1. \quad (25)$$

It is easy to see that this fictitious random process plays the same role as the tilted random vector \underline{r}_s in the finite-dimensional case. $h_{1+2}(t, \tau; s)$ denotes the minimum mean-square point estimator of $s_{1+2}(t)$. The important computational advantage of Eq. 24, as compared with Eq. 18, stems from the availability of techniques for efficiently solving linear estimation problems. In particular, the Kalman-Bucy formulation¹⁰ of the estimation problem provides us with a direct approach for calculating the pertinent estimation errors. Furthermore, this approach to the problem is readily implemented on a digital computer, which is an important practical advantage.

We have briefly mentioned the need for a bound that would be tighter than the Chernoff bound. We shall now indicate some results in this direction, when we make use of our Gaussian assumption.

A straightforward substitution of the appropriate Gaussian densities in Eq. 5 shows that the tilted density $\text{pr}_{\underline{r}_s}(\underline{R})$ is also a Gaussian probability density. Therefore, the tilted random variable l_s is a "generalized Chi-square" random variable, that is, it is the sum of the square of Gaussian random variables which have nonzero means and unequal variances.

(XIX. DETECTION AND ESTIMATION THEORY)

In the special case for which all variances are the same, the means are all zero, and the number of components, N , is finite, ℓ_s has a Chi-squared distribution, and we have an analytic expression for the probability density $p_{\ell_s}(L)$. This enables us to rigorously derive the following bounds by using a very simple argument.

$$P_r[\mathcal{E} | H_1] < \left(2\pi s^2 \mu''(s) \left(1 - \frac{2}{N}\right)\right)^{-1/2} \exp[\mu(s) - s\mu'(s)] \quad (26)$$

$$P_r[\mathcal{E} | H_2] < \left(2\pi(1-s)^2 \mu''(s) \left(1 - \frac{2}{N}\right)\right)^{-1/2} \exp[\mu(s) + (1-s)\mu'(s)] \quad \text{for } N > 2 \quad (27)$$

Observe that these are in the form of (12) and (13) and, in fact, for moderate values of N the factor $\left(1 - \frac{2}{N}\right)^{-1/2} \approx 1$.

Another special case of more interest to us occurs when the variances of the various components are all distinct, but occur in pairs, as is always the case for a signal transmitted at RF through some physical channel. In this case, we can obtain an expression for the probability density $p_{\ell_s}(L)$. We have shown that this density has only one maximum. Furthermore, in each of a large number of cases treated numerically, the maximum value was not found to differ appreciably from that for a Gaussian density having the same variance, namely $(2\pi\mu''(s))^{-1/2}$. Furthermore, various methods of asymptotically approximating the integrals in Eqs. 8 and 9 lead to this same dependence for the dominant behavior as $\mu''(s)$ becomes large.

Therefore, we feel confident that for the Gaussian detection problem that we have been discussing, the expressions in Eqs. 13 and 14 provide good approximations for the error probabilities.

3. Examples

We shall give a few simple examples illustrating the application of the techniques just discussed. We shall choose one example from each of the three levels of detection problems: known signal, signal with a finite number of random parameters, and random signal.

EXAMPLE 1: Known Signal

$$\begin{aligned} H_1: r(t) &= m_1(t) + n_c(t) + w(t) \\ H_2: r(t) &= m_2(t) + n_c(t) + w(t) \end{aligned} \quad 0 \leq t \leq \tau \quad (28)$$

Here the random "signal" components $n_c(t)$ are identical and represent the colored component of the noise. Substituting in Eq. 24 (or 18), we find

$$\mu(s) = -\frac{s(1-s)}{2} d^2 \quad (29)$$

where

$$d^2 \triangleq \frac{(E(\ell|H_1) - E(\ell|H_0))^2}{\sqrt{\text{Var}(\ell|H_1) \text{Var}(\ell|H_0)}} \\ = \int_0^T \left[m_1(t) - m_2(t) - \int_0^T h_{1+2}(t, \tau) [m_1(\tau) - m_2(\tau)] d\tau \right]^2 \quad (30)$$

Here, $h_{1+2}(t, \tau)$ is independent of s , since

$$s_{1+2}(t) = s_{r_1}(t) = s_{r_2}(t) = n_c(t). \quad (31)$$

And, as a matter of fact,

$$\delta(t-\tau) - h_{1+2}(t, \tau) = h_w(t, \tau), \quad (32)$$

which is a realizable whitening filter for this problem.¹³ Thus Eq. 30 is equivalent to the more familiar form

$$\theta^2 = \int_0^T \int_0^T [m_1(t) - m_2(t)] Q_n(t, \tau) [m_1(\tau) - m_2(\tau)] dt d\tau \quad (33)$$

$$\mu'(s) = d^2 \left(s - \frac{1}{2} \right) = \gamma. \quad (34)$$

Hence we can solve explicitly for s in this case, and we obtain the bounds

$$\text{Pr} [\mathcal{E} | H_1] \leq \frac{1}{\sqrt{2\pi d^2 \left(\frac{1}{2} + \frac{\gamma}{d^2} \right)^2}} \exp \left[-\frac{d^2}{2} \left(\frac{1}{2} + \frac{\gamma}{d^2} \right) \right] \quad (35)$$

$$\text{Pr} [\mathcal{E} | H_1] \leq \frac{1}{\sqrt{2\pi d^2 \left(\frac{1}{2} - \frac{\gamma}{d^2} \right)^2}} \exp \left[-\frac{d^2}{2} \left(\frac{1}{2} - \frac{\gamma}{d^2} \right) \right]. \quad (36)$$

These are exactly the same results that we would obtain using the familiar bound

$$\int_x^\infty \frac{1}{\sqrt{2\pi}} e^{-y^2/2} dy \leq \frac{1}{\sqrt{2\pi} x} e^{-x^2/2} \quad (37)$$

in the exact error expression for this problem.

(XIX. DETECTION AND ESTIMATION THEORY)

EXAMPLE 2: Slow Rayleigh Fading with Diversity

This is another case in which analytical results are available for comparison purposes.¹¹

One of two orthogonal signals, $s_1(t)$ or $s_2(t)$, is received in additive white Gaussian noise after transmission through a fading channel in which the signal undergoes a random attenuation and phase shift. The attenuation is a Rayleigh random variable, and the phase shift is uniform $0 \leq \theta < 2\pi$. We assume that there are N such channels operating in space, time, or frequency diversity. We also assume that the average received energy is the same in each channel on either hypothesis. Substitution in (17) yields

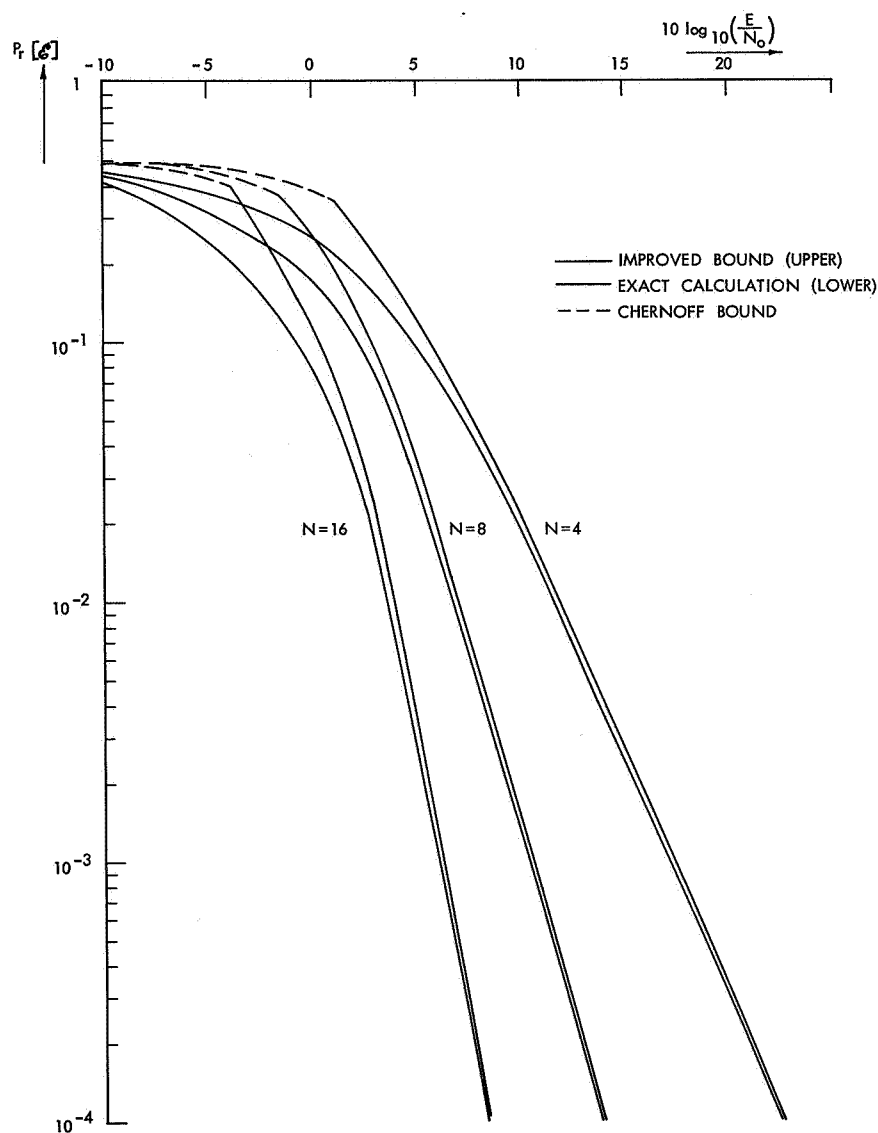


Fig. XIX-2. Error probabilities for slow Rayleigh fading with diversity.

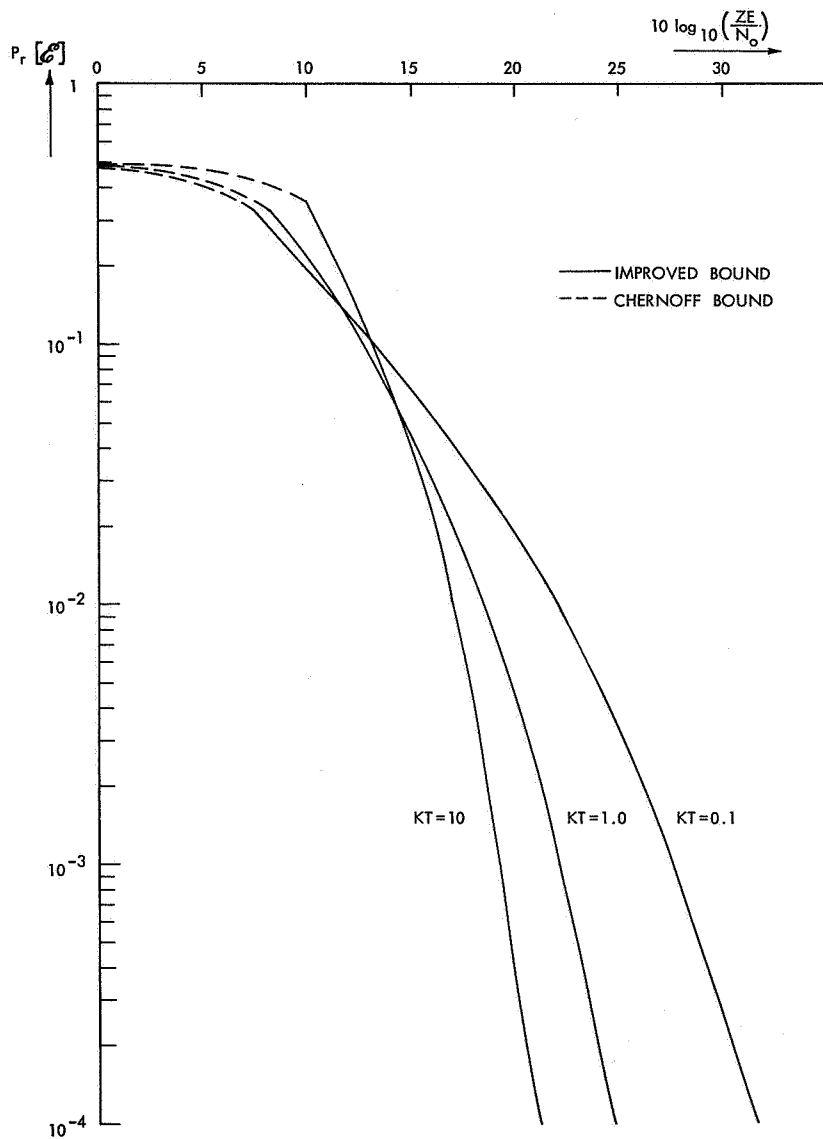


Fig. XIX-3. Upper bounds on error probability for single-pole Rayleigh fading.

(XIX. DETECTION AND ESTIMATION THEORY)

$$\mu(s) = N \begin{cases} \ln \left(1 + \frac{E}{N_0} \right) - \ln \left(1 + \frac{sE}{N_0} \right) \\ - \ln \left[1 + (1-s) \frac{E}{N_0} \right] \end{cases} \quad (38)$$

where E is the average received signal energy in each diversity channel.

Figure XIX-2 shows the bound

$$\Pr [\mathcal{E}] \leq \frac{1}{\sqrt{\frac{\pi}{4} \mu''\left(\frac{1}{2}\right)}} \exp\left[\mu\left(\frac{1}{2}\right)\right], \quad (39)$$

as well as the exact results for several values of N .

EXAMPLE 3: Rayleigh Fading, Single-Pole Spectrum

This simple example illustrates the application of our results to a problem for which it would be extremely difficult to obtain error probabilities in any other manner. The model is the same as that of the previous case, except that, now the channel attenuation is a sample function from a random process.

For purposes of illustration, we assume only one Rayleigh channel (that is, no explicit diversity) and a single-pole spectrum for the fading.

The upper bound on the probability of error is shown in Fig. XIX-3. To our knowledge, no other calculations are available for comparison. It is interesting to observe that this optimum receiver does not exhibit the irreducible error probability of one sub-optimum receiver that has been analyzed.¹²

4. Summary

We have discussed the application of tilted probability distributions to the evaluation of the performance of optimum detectors for Gaussian signals in Gaussian noise. Two main points were covered: (i) obtaining bounds that are tighter than the Chernoff bound and ones that are asymptotically exact; (ii) obtaining closed-form expressions for $\mu(s)$ in terms of minimum mean-square estimation errors, which may be readily computed by using Kalman-Bucy filtering techniques. We concluded with three simple examples.

L. D. Collins

References

1. C. W. Helstrom, Statistical Theory of Signal Detection (Macmillan Company, New York, 1960).
2. H. L. Van Trees, Detection and Estimation Theory (John Wiley and Sons, Inc., New York, 1967).

(XIX. DETECTION AND ESTIMATION THEORY)

3. R. Price, "Optimum Detection of Random Signals in Noise with Application to Scatter-Multipath Communication, I," IRE Trans., Vol. IT-2, pp. 125-135 (December 1956).
4. R. Price, "Output Signal-to-Noise Ratio as a Criterion in Spread-Channel Signaling," Technical Report 388, Lincoln Laboratory, M. I. T., May 13, 1965.
5. C. E. Shannon, "Notes for Seminar on Information Theory at M. I. T.," 1956 (unpublished).
6. R. Fano, Transmission of Information (The M. I. T. Press, Cambridge, Mass., 1961).
7. H. Chernoff, "A Measure of Asymptotic Efficiency for Tests of a Hypothesis Based on a Sum of Observations," Ann. Math. Stat. 23, 493-509 (1952).
8. F. Esscher, "On the Probability Function in the Collective Theory of Risk," Skandinavisk Akluarietidskrift, Vol. 15, pp. 175-195, 1932.
9. R. Y. Huang and R. A. Johnson, "Information Transmission with Time-Continuous Random Processes," IEEE Transactions, Vol. IT-9, No. 2, pp. 84-95, April, 1963.
10. R. E. Kalman and R. S. Bucy, "New Results in Linear Filtering and Prediction Theory," Trans. ASME, Journal of Basic Engineering, pp. 95-108, March, 1961.
11. J. N. Pierce, "Theoretical Diversity Improvement in Frequency-Shift Keying," Proc. IRE 46, 903-910 (1958).
12. P. A. Bello and B. Nelin, "The Influence of Fading Spectrum on the Binary Error Probabilities of Noncoherent and Coherent Matched Filter Receivers," IRE Trans., Vol. CS-1, No. 1, pp. 160-168, June, 1962.
13. L. D. Collins, "Realizable Whitening Filters," Internal Memorandum IM-LDC-5, Research Laboratory of Electronics, M. I. T., April 1, 1966 (unpublished).

XX. SPEECH COMMUNICATION* 8 10 10

Academic and Research Staff

Prof. K. N. Stevens
 Prof. M. Halle
 Prof. W. L. Henke
 Prof. D. H. Klatt

Prof. A. V. Oppenheim
 Dr. Margaret Bullowa
 Dr. Paula Menyuk

Dr. J. Suzuki†
 C.-W. Kim
 N. Benhaim
 J. S. Perkell

Graduate Students

J. K. Frediani
 A. J. Goldberg

L. R. Rabiner
 R. S. Tomlinson

M. Y. Weidner
 J. J. Wolf

A. ON THE MECHANISM OF GLOTTAL VIBRATION FOR VOWELS
 AND CONSONANTS

N67-27101

In the study of speech it has been assumed that glottal vibration is independent of the configurations of the supraglottal cavity or, at least, that the effects of different configurations are negligible. In connection with the word saving, for example, it is usually stated that the entire utterance is voiced except for the initial consonant; no distinction is made between the kind of voicing that occurs during the vowels and during the voiced consonant v.

There is some evidence to suggest, however, that the positioning of the vocal cords and the manner in which they vibrate may be quite different, the difference depending upon whether the supraglottal tract is unconstricted, as in a vowel, or is constricted to some degree, as in stops, fricatives, and certain semivowels. This evidence comes in part from an analysis of the mechanism of larynx vibration, and in part from measurements of air-flow events during speech.

Analysis of the mechanism of vocal-cord vibration has shown that the process involves the interaction of several forces. In the beginning of the time interval in which the vocal folds are moving apart, the principal force tending to separate the folds is due to the positive subglottal pressure. During the time interval in which the glottis is closing, on the other hand, the principal force is the Bernoulli force, which is a consequence of the rapid air flow in the glottis.

High-speed motion pictures and other kinds of data have indicated that during vowel production the glottal opening as a function of time is roughly triangular in form, and the glottis is closed over part of the cycle. A typical open time for a male voice might be approximately 4 msec, with a closed interval of comparable duration. The subglottal pressure for normal stressed vowels is typically ~10 cm H₂O, and each glottal pulse

*This work was supported principally by the U.S. Air Force (Electronic Systems Division) under Contract AF19(628)-5661; and in part by the National Institutes of Health (Grant 5 ROI NB-04332-04).

†On leave from Radio Research Laboratories, Tokyo, Japan.

(XX. SPEECH COMMUNICATION)

generates a flow of the order of 1 cm^3 .

Let us examine now what would happen if the vocal tract becomes constricted at some point along its length, and let us suppose, for the moment, that the vocal cords continue to vibrate as before, generating the same volume flow for each cycle. It is possible to make an approximate calculation of the sound pressure immediately above the glottis by convolving the triangular volume-velocity pulse with the impulse response of the vocal tract as seen from the glottis. When the first-formant frequency is low, the response is approximately that of a simple resonant circuit tuned to the frequency of the first formant. This calculation shows that, for a resonant frequency of approximately 250 cps, and an assumed bandwidth of ~ 100 cps, a 1-cm^3 air pulse of 4-msec duration would give rise to a peak sound pressure above the glottis of the order of $10 \text{ cm H}_2\text{O}$. For higher first-formant frequencies, i. e., for first-formant frequencies that are normally found in vowels, the sound pressure would be considerably less, but for resonant frequencies lower than 250 cps, as found in consonants, this peak sound pressure would be substantially greater. Under the latter conditions, the peak supra-glottal sound pressure would be of the order of the steady subglottal pressure, and the pressure drop across the glottis would undergo extreme fluctuations. Flow conditions through the glottis would be greatly modified, and the vocal-cord vibrations would become highly erratic. Regular vocal-cord vibration could be maintained with a constricted vocal tract only under one or both of two conditions: the width of the glottal pulse must increase considerably, and the damping of the first formant must be increased substantially, probably by creating a larger average glottal opening.

In addition to this effect of increased driving-point impedance of the vocal tract at low resonant frequencies, a second consequence of the constricted vocal tract associated with consonantal articulation is that the resistance to air flow at the constriction may become appreciable, thereby causing a rise in average pressure in the mouth. As a result of the heightened mouth pressure, there will be an increase in the net pressure force tending to separate the vocal cords. Furthermore, the air flow through the open glottis will decrease as a consequence of the reduced pressure across the glottis (under the assumption that the subglottal pressure does not change appreciably), thereby causing a reduction of the Bernoulli force. Thus there will be a tendency for the pattern of vibration to change, with the open time being longer, and possibly with the vocal cords remaining separated during the entire cycle. In fact, if vocal-cord vibration is to continue through the constricted consonant, it is reasonable to suppose that an overt adjustment in vocal-cord position toward a more open state is made in order to accommodate vibration with reduced pressure across the glottis. (It is known that this kind of adjustment is made when a vocal-cord vibration is to be maintained during a vowel that is generated with low subglottal pressure.¹⁻³

From this simple analysis it is evident that there are rather drastic adjustments in

vocal-cord positioning and in the manner in which the vocal cords vibrate when voicing is to be maintained during certain consonants. Further evidence for this change in laryngeal operation comes from studies of air flow for vowels and for voiced fricative consonants.⁴ During a voiced fricative, the air flow tends to be somewhat greater than during a vowel. At first glance, this increased flow is contrary to expectation; one might expect that the supraglottal consonantal constriction would cause an increased resistance to flow and hence a reduction in flow, under the assumption that the subglottal pressure does not change appreciably. The fact that flow is greater during the fricative suggests that the glottal resistance must be less in the consonant than in the vowel, and thus indicates that the open time of the glottis is increased or, more likely, that the vocal cords are separated so that the glottis remains open during the entire vibratory cycle. A similar adjustment of the vocal cords would probably also be made for the production of a voiced-stop consonant in English. In such a consonant, vocal-cord vibration often occurs in the stopped interval before the release of the consonant, and the effects of increased supraglottal pressure and decreased resonant frequency of the supraglottal cavity are even more pronounced than for a voiced fricative.

During the production of a voiceless consonant, the vocal cords are also separated, of course, so that the resistance to air flow at the glottis is small and, under normal circumstances, there is little or no glottal vibration. The vocal-cord separation is much greater for a voiceless consonant than for a voiced consonant. In the case of a voiceless consonant the mouth pressure tends to be higher or to rise more rapidly than during a voiced consonant; this increased mouth pressure would presumably act on the vocal cords to produce a still greater separation.

In the air-flow trace for a vowel preceding a voiced or voiceless consonant there tends to be an increase in air flow in the latter part of the vowel in anticipation of the consonant.⁵ It appears that 100 msec or more before the time when the consonantal constriction is achieved an adjustment of vocal-cord positioning is initiated in preparation for the production of the constricted consonant. Likewise, there is a similar time interval following a voiceless consonant before the air flow drops to a value appropriate for a steady vowel. These observations would suggest, therefore, that the rate at which vocal-cord positioning can be achieved is relatively slow, and that a talker must compensate for this slow response in timing his commands to the larynx musculature. In the case of a voiceless consonant following a vowel, it might be argued that the necessary wide separation of the vocal cords can be achieved more rapidly than the more finely adjusted smaller separation for a voiced consonant. Furthermore, the abduction maneuver for a voiceless consonant can be assisted or speeded up by the increased mouth pressure that occurs in such a consonant. This line of reasoning would lead, then, to a logical explanation for the difference in vowel length in English before voiced and voiceless consonants. The longer laryngeal adjustment time required for a voiced

(XX. SPEECH COMMUNICATION)

consonant would necessitate an increased duration of the preceding vowel; the consonantal constriction cannot be effected before the vocal cords are positioned in a way that will guarantee uninterrupted vocal-cord vibration during the constricted interval.

Table XX-1. Average vowel durations for symmetrical consonant-vowel-consonant syllables in English. Data for each consonant represent averages over 36 utterances (12 vowels, 3 speakers).

Consonantal Environment	Vowel Duration (msec)
b	270
m	240
d	310
n	260

Partial support for this explanation is found by comparing vowel length before voiced stops and nasals in English. Before a nasal consonant, which presumably does not require the special vocal-cord adjustment, a vowel is found to be consistently shorter than before a voiced-stop consonant. Table XX-1 summarizes measurements of vowel length in symmetrical CVC syllables, averaged over three talkers.

It is evident, then, that during a consonant the vocal cords may be positioned with various degrees of spacing between them. Adjustment of vocal-cord spacing is, however, only one parameter that determines whether or not the vocal cords will vibrate during the consonantal interval. It is important that an adequate glottal air flow be provided if vibration is to be maintained. The amount of air flow is determined both by the subglottal pressure and by the configuration of the supraglottal articulators. The supraglottal tract must have an adequate constriction through which air can flow (as in voiced fricatives, liquids, glides, and nasals) or, in the case of a stopped configuration, continuously increasing volume of the cavities must be provided (as in voiced-stop consonants in English).⁶ Thus a talker has under his control a variety of independent or quasi-independent parameters that he can use to generate voiced and voiceless consonants of various types. Any inventory of phonetic features which purports to describe the various stop and fricative consonants in different languages must specify these parameters, which include the subglottal pressure, vocal-cord positioning, and the means by which air is allowed to flow into the supraglottal cavities.

M. Halle, K. N. Stevens

References

1. J. L. Flanagan, Speech Analysis, Synthesis and Perception (Academic Press, New York, 1965), p. 44.
2. A. Bouhuys, D. F. Proctor, and J. Mead, "Kinetic Aspects of Singing," *J. Appl. Physiol.* 21, 483 (1966).
3. A. Bouhuys, J. Mead, D. F. Proctor, and K. N. Stevens, "Pressure-Flow Events during Singing," *Ann. N. Y. Acad. Sci.* (in press).
4. D. H. Klatt, K. N. Stevens, and J. Mead, "Studies of Articulatory Activity and Air Flow during Speech," *Ann. N. Y. Acad. Sci.* (in press).
5. D. H. Klatt, "Articulatory Activity and Air Flow during the Production of Fricative Consonants," Quarterly Progress Report No. 84, Research Laboratory of Electronics, M.I.T., January 15, 1967, pp. 257-260.
6. J. Perkell, "Studies of the Dynamics of Speech Production," Quarterly Progress Report No. 76, Research Laboratory of Electronics, M.I.T., January 15, 1956, pp. 253-257.

B. HOMOMORPHIC SPEECH PROCESSING*

It is generally accepted that an approximate model for the speech waveform consists of a cascade of a system G whose impulse response $g(t)$ has the form of a single glottal pulse, a system V whose impulse response $v(t)$ corresponds to the response of the vocal tract, and a system R representing the radiation characteristics. The excitation to this system is an impulse train whose spacing corresponds to the fundamental frequency of the resulting waveform.

Both for speech bandwidth compression and basic studies of the nature of the speech wave, it is desirable to attempt to isolate the effects of each of these systems. If we consider that, on a short-time basis, each of these systems is representable as a linear, time-invariant system, then we may represent $s(t)$, the speech waveform, as

$$s(t) = p(t) \otimes w(t) \tag{1}$$

with

$$w(t) = g(t) \otimes v(t) \otimes r(t),$$

where \otimes denotes convolution. The work reported here represents the application of a previously proposed technique for the separation of convolved signals¹ to separation of the effects of $p(t)$, which represents the fine structure in the spectrum of $s(t)$, and $w(t)$, which represents the spectral envelope of $s(t)$. The motivation for this study lies both in the notion of what could conveniently be termed homomorphic deconvolution, and the

*This work was supported in part by Lincoln Laboratory, a center for research operated by the Massachusetts Institute of Technology, with support of the U.S. Air Force.

success of cepstral pitch detection as considered by Noll.²

Since the processing illustrated here was simulated on a digital computer, it is convenient to rewrite Eq. 1 in terms of a set of equally spaced samples of $s(t)$. Under the assumption that the pitch period is an integer multiple of the sampling period, it follows from Eq. 1 that

$$s(k) = p(k) \otimes w(k), \quad (2)$$

where $s(k)$, $p(k)$, and $w(k)$ are the k^{th} samples of $s(t)$, $p(t)$, and $w(t)$, respectively, and \otimes now denotes a discrete convolution. To separate $p(k)$ and $w(k)$ from $s(k)$, we wish to operate on $s(k)$ with a transformation D defined by

$$z[D(s(k))] = \log [z(s(k))],$$

where z denotes the Z-transform of the sequence. After linear filtering, the result is then transformed by the inverse of the transformation D . If $p(k)$ contains N unit samples spaced by r and starting at $k = 0$, then it can be shown that

$$D[p(k)] = \frac{r}{k} \sum_{m=1}^{\infty} \delta(k-mr) - \frac{Nr}{k} \sum_{m=1}^{\infty} \delta(k-mNr) \quad k \neq 0$$

where

$$\begin{aligned} \delta(k-j) &= 1 & k &= j \\ &= 0 & k &\neq j. \end{aligned}$$

Under certain conditions, we may write $w(k)$ approximately as

$$w(k) = v(k) \otimes h(k),$$

where $v(k)$ are samples of $v(t)$, and $h(k)$ are samples of $g(t) \otimes r(t)$. If we represent $v(t)$ by the impulse response of a simple acoustic cavity with small loss, so that the transfer function of $v(t)$ is

$$|V(j\omega)| = \left| \frac{1}{\cosh \left[a + j\frac{\omega}{c} \right] \ell} \right|,$$

then

$$v(k) = \sum_{m=0}^{\infty} (-1)^m e^{-2a\ell m} \delta\left(k - \frac{2m\ell}{c}\right) \quad k \neq 0$$

and

$$D[v(k)] = \frac{2\ell}{kC} \sum_{m=1}^{\infty} (-1)^m e^{-2a\ell m} \delta\left(k - \frac{2\ell m}{C}\right). \quad k \neq 0$$

Under the idealization that $g(t)$ is a symmetrical triangular pulse of duration $T\Delta$, where Δ is the sampling rate, and that $r(t)$ can be represented by a differentiator,

$$D[h(k)] = \frac{1}{k} - \frac{T}{k} \sum_{m=0}^{\infty} \delta\left(k - \frac{mT}{2}\right). \quad k \neq 0$$

We observe, in this case, that $D[h(k)]$ and $D[v(k)]$ provide their primary contribution for small values of k , as compared with $D[p(k)]$. By multiplying the sequence $D[s(k)]$ by unity up to some value of k , and zero thereafter, we should, to some approximation, have retained only values relevant to $h(k)$.

The processing described above was carried out on the Lincoln Laboratory TX-2 computer. To determine the response of the system D , the inverse transform of the logarithm of the discrete Fourier transform was computed. The use of the discrete transform, rather than the Z-transform, introduces an aliasing effect into the expressions derived previously, although it is usually possible to minimize this effect. For the present studies, phase information was not included; this means working with the autocorrelation function of the speech sample, rather than with the speech sample itself. In this case, the sequence $D[\phi_{ss}(k)]$, with $\phi_{ss}(k)$ denoting the autocorrelation function of $s(k)$, is equivalent to the cepstrum.

To illustrate the result of this processing, consider the sample of the vowel "ah" in father as shown in Fig. XX-1, representing 41 msec sampled at 25 kHz. The spectrum

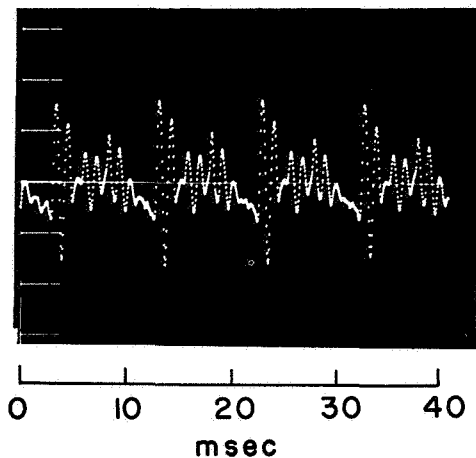


Fig. XX-1. 41 msec of "ah" spoken in isolation sampled at 25 kHz.

of this sample was computed by weighting the speech sample with a raised cosine window, 41 msec long, followed by 41 msec of zero. The logarithm of the magnitude of

(XX. SPEECH COMMUNICATION)

the spectrum obtained in this way is shown in Fig. XX-2.

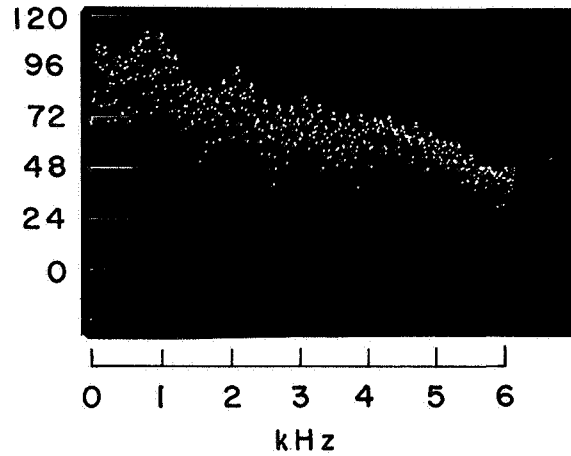


Fig. XX-2. Log magnitude of the spectrum of Fig. XX-1 after weighting with a raised cosine window and terminating in 41 msec of zero.

Figure XX-3 represents the inverse transform of the spectrum of Fig. XX-2, with a pronounced peak occurring at a time corresponding to the pitch period.

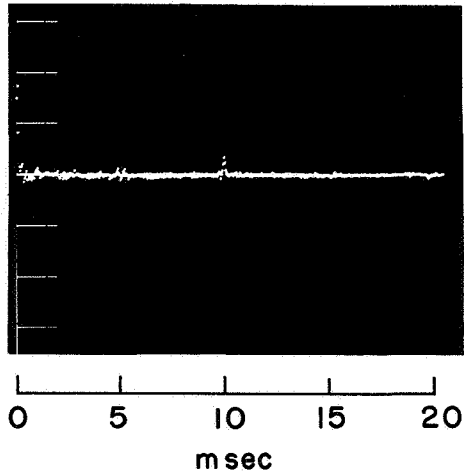


Fig. XX-3. Inverse transform of the spectrum of Fig. XX-2.

As described above, filtering of the logarithmic spectrum is carried out by multiplying the series of Fig. XX-3 by unity until some time τ and zero thereafter. Figures XX-4, XX-5, and XX-6 represent the result of filtering and transforming for $\tau = 7.7$ msec,

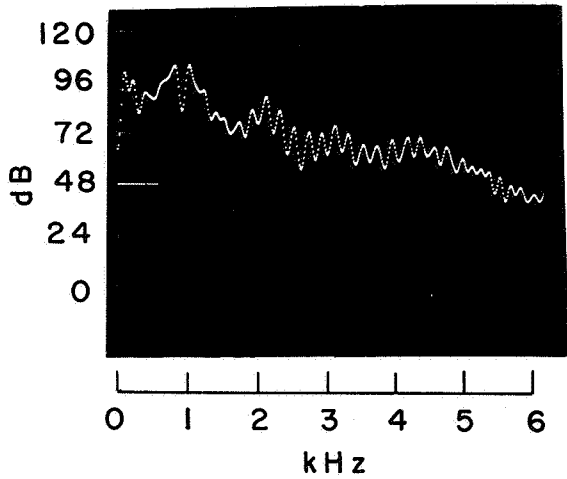


Fig. XX-4. Low-time filtered log magnitude spectrum with filter cutoff time, $\tau = 7.7$ msec.

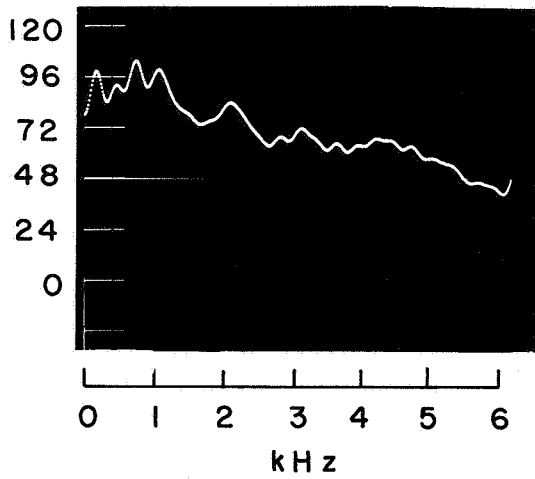


Fig. XX-5. Low-time filtered log magnitude spectrum with filter cutoff time, $\tau = 3.8$ msec.

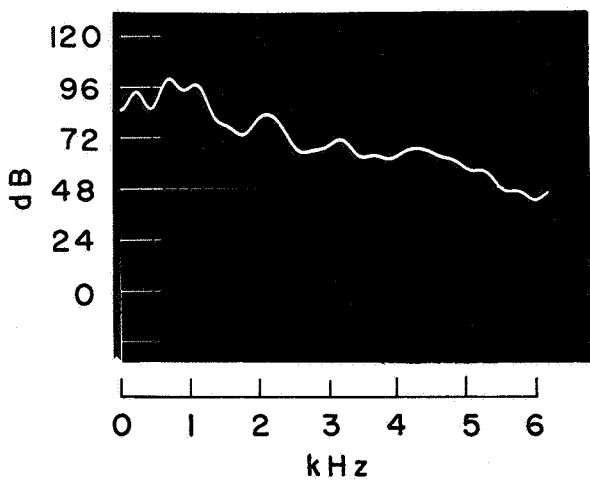


Fig. XX-6. Low-time filtered log magnitude spectrum with filter cutoff time, $\tau = 2.6$ msec.

(XX. SPEECH COMMUNICATION)

$\tau = 3.8$ msec, and $\tau = 2.6$ msec, respectively. Figure XX-7 shows the superposition of the spectra of Fig. XX-2 and Fig. XX-5.

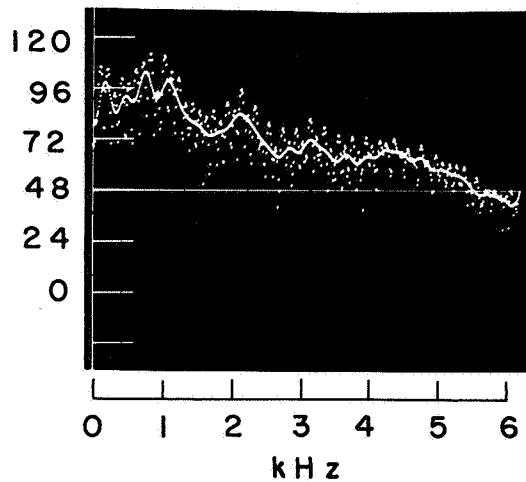


Fig. XX-7. Series of Fig. XX-2 and Fig. XX-5 superimposed.

To implement the inverse of the system D, the filtered spectrum will, in general, be operated on by an exponential transformation, and then the inverse Fourier transform will be taken. The result of an exponential transformation on the spectrum of Fig. XX-6 is shown in Fig. XX-8.

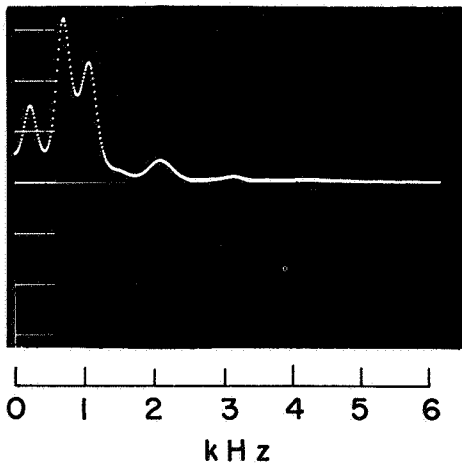


Fig. XX-8. Spectrum of Fig. XX-5 after an exponential transformation. Vertical scale is linear.

In a case for which high-frequency emphasis of this smoothed spectrum is desired, the series of Fig. XX-3 can be "band-time filtered" rather than "low-time filtered." The result of introducing high-frequency emphasis for the spectrum of Fig. XX-8 is shown in Fig. XX-9.

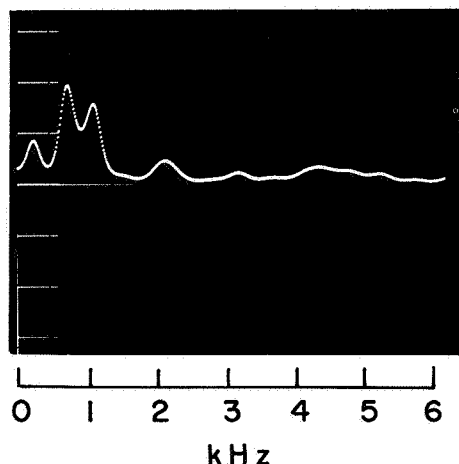


Fig. XX-9. Spectrum of Fig. XX-5 after an exponential transformation with high-frequency emphasis obtained by band-time filtering. Vertical scale is linear.

In comparing the spectra of Figs. XX-4, XX-5, and XX-6, we observe that for values of τ slightly less than the pitch period, a ripple is apparent in the spectrum. As τ decreases the ripple disappears, bringing more into evidence the individual formants, while apparently broadening the resonance bandwidths. The ripple for larger values of τ is apparently contributed by the terms that are due to the glottal pulse, the spacing of the peaks being related to glottal pulse duration.

In continuing this study, the objective is to isolate the effects of pitch, glottal pulse, and vocal-tract impulse response. Although for constant pitch, the pitch period can be measured directly from the series of Fig. XX-3, the contribution from pitch is generally more pronounced after "long-time" filtering and operating on the resulting series with the inverse of the system, D. To recover the glottal pulse, the log spectrum corresponding to a series of resonators will be subtracted from the smoothed log spectrum of Fig. XX-4 and the result operated on with the inverse of the system, D. In order to recover the glottal pulse, rather than its minimum phase counterpart, phase information must be included in the determination of the series corresponding to Fig. XX-3. This procedure for recovering the glottal pulse is similar to inverse filtering; the parameters of the inverse filter are obtained by a spectral matching procedure on the smoothed log spectrum.

A. V. Oppenheim

References

1. A. V. Oppenheim, "Nonlinear Filtering of Convolved Signals," Quarterly Progress Report No. 80, Research Laboratory of Electronics, M.I.T., January 15, 1966, pp. 168-175.
2. A. M. Noll, "Short-time Spectrum and Cepstrum Techniques for Vocal-Pitch Detection," J. Acoust. Soc. Am. 36, 296-302 (1964).

Academic and Research Staff

Prof. R. Jakobson /	Prof. J. R. Ross	Dr. J-C. G. Milner
Prof. M. Halle /	Prof. J. H. Sledd	Dr. A. Schwartz
Prof. N. A. Chomsky -	Dr. J. V. Canfield	Dr. N. V. Smith
Prof. S. Bromberger	Dr. J. B. Fraser	Dr. D. E. Walker
Prof. J. A. Fodor	Dr. M. F. Garrett	Dr. Anna Wierzbicka
Prof. J. J. Katz	Dr. J. S. Gruber	C-J. N. Bailey
Prof. R. P. V. Kiparsky	Dr. C. Heeschen	N. R. Cattell
Prof. G. H. Matthews		J. J. Viertel

N67-27102

Graduate Students

A. Akmajian	R. C. Dougherty	R. Kirk
S. R. Anderson	J. E. Emonds	J. R. Lackner
J. S. Bowers	J. L. Fidelholtz	Amy E. Myers
M. K. Brame	R. Goldfield	A. J. Naro
E. W. Browne III	L. N. Gross	D. M. Perlmutter
R. J. Carter	J. W. Harris	J. T. Ritter
S. W-C. Chan	T. R. Hofmann	M. S. Snow
P. G. Chapin	I. J. Howard	R. J. Stanley
P. W. Culicover	R. S. Jackendoff	C. L. Thiersch
Janet P. Dean	R. S. Kayne	F. J. Vandamme
R. P. G. De Rijk	J. P. Kimball	Nancy Woo

A. ON NONCYCLIC TRANSFORMATIONAL GRAMMARS

The conventions concerning the applications of the transformations in the transformational component of a generative grammar which are proposed by Chomsky¹ are as follows: The only recursive symbol in the phrase structure base is S; in processing a deep structure the transformations all apply within the domain of each S bracket of the deep structure, and they apply from the most deeply embedded S-dominated substrings of the deep structure upward until the entire deep structure has been processed. As all the transformations are available for application within each S-dominated substring, and there may be more than one such substring in a given deep structure, one speaks of this form of application of the transformations as the transformational cycle. (For the motivations for this proposal, see Chomsky.²) We shall refer to grammars in which the transformations apply as described above as cyclic transformational grammars, or cyclic grammars.

On the basis of research conducted with G. Lakoff, John R. Ross has advanced for consideration a change in the convention under which transformations apply to deep

*This work was supported principally by the U. S. Air Force (Electronics Systems Division) under Contract AF 19(628)-2487; and in part by the Joint Services Electronics Programs (U.S. Army, U.S. Navy, and U.S. Air Force) under Contract DA 28-043-AMC-02536(E), the National Science Foundation (Grant GK-835), the National Institutes of Health (Grant 2 PO1 MH-04737-06), and the National Aeronautics and Space Administration (Grant NsG-496).

(XXI. LINGUISTICS)

structures in the course of derivations. Under the changes considered, the transformational component of a grammar would consist of a linearly ordered finite set of transformations, as before, but each transformation would apply to the whole deep structure processing S-dominated substrings from the bottom up. After a transformation had applied, it would not be available for further processing of a given deep structure. We shall call grammars in which the transformations apply in the manner described here noncyclic transformational grammars.

We will not give a formal definition of either of the kinds of grammars discussed above, but for purposes of exposition we shall carry out transformational derivations of a given deep structure in a particular grammar according to the cyclic and noncyclic conventions. The rules for the grammar are as follows:

Phrase structure: $S \rightarrow abc S$
 $S \rightarrow abc s$

Transformations: $T_1 X a b Y \rightarrow X b+a \emptyset Y$
 $T_2 X a c Y \rightarrow X \emptyset c+a Y$

A cyclic derivation in this grammar would go as follows:

$[a b c [a b c [a b c s]_S]_S]_S$	Base string
$[a b c [a b c [b a c s]_S]_S]_S$	T_1 - first cycle
$[a b c [a b c [b c a s]_S]_S]_S$	T_2 - first cycle
$[a b c [b a c [b c a s]_S]_S]_S$	T_1 - second cycle
$[a b c [b c a [b c a s]_S]_S]_S$	T_2 - second cycle
$[b a c [b c b a [c a s]_S]_S]_S$	T_1 - third cycle
$[b c a [b c b [c a a s]_S]_S]_S$	T_2 - third cycle

The noncyclic derivation of the same base string is as follows:

$[a b c [a b c [a b c s]_S]_S]_S$	Base string
$[a b c [a b c [b a c s]_S]_S]_S$	T_1 - within lowest <u>S</u>
$[a b c [b a c [b a c s]_S]_S]_S$	T_1 - within second lowest <u>S</u>
$[b a c [b a c [b a c s]_S]_S]_S$	T_1 - within highest <u>S</u>
$[b a c [b a c [b c a s]_S]_S]_S$	T_2 - within lowest <u>S</u>

$$[b a c [b c a [b c a s]_S]_S]_S \quad T_2 - \text{within second } \underline{S}$$

$$[b c a [b c a [b c a s]_S]_S]_S \quad T_2 - \text{within highest } \underline{S}$$

Thus, in general, in a grammar G with transformations $T_1 \dots T_k$ a cyclic derivation of a deep-structure string will have a transformational history which is some word in the regular language $(T_1 \cup T_2 \cup \dots \cup T_k)^*$, whereas a noncyclic derivation will have a transformational history which is some work in the regular language $(T_1)^* \dots (T_k)^*$.

Note that in the grammar specified above, the language generated by the grammar when the transformations are applied cyclically is different from the language generated when the transformations are applied noncyclically. Thus, in giving a formal treatment of noncyclic grammars we want to compare the generative capacity of noncyclic grammars with that of cyclic grammars. It has been shown³ that a context-free based cyclic grammar with filter and post cyclic transformations can generate any recursively enumerable language. This result has been extended,⁴ in that it has been shown that a regular-based cyclic grammar with filter and post cyclic transformations can generate any recursively enumerable language. In this report we shall modify the methods of proof of these earlier reports to show that a context-free based noncyclic grammar with filter transformations can generate any recursively enumerable language; and, although the details of the proof are not given here, it is clear that a regular-based noncyclic grammar with filter transformations can generate any recursively enumerable language. We can then conclude that any language generated by a cyclic grammar can be generated by a noncyclic grammar, and conversely.

In the statement of the following theorem we intersect the language generated by the noncyclic grammar with a regular language in producing the r. e. (recursively enumerable) language. The reader is referred to previous work^{3, 4} to see how the operation of filter and post cyclic transformations is effected by such intersection. In fact, since the notion 'post cyclic transformation' has no obvious application for noncyclic grammars, the proof that follows shows that a noncyclic grammar with filter transformations can generate any r. e. language. (All grammars discussed in this report are assumed to meet the condition on recoverability of deletions.)

Theorem: There exists a fixed regular language H such that for any r. e. set of positive integers N there exists a context-free based noncyclic grammar G over the terminal alphabet $\{a\}$ such that $\underline{n} \in N$ iff $a^n \in L(G) \cap H$.

The proof relies on a lemma that is due to Leonard Haines.

Lemma: There exists a fixed context-free language L_1 and a fixed homomorphism λ such that for any r. e. set of positive integers N there exists a context-free language L_2 such that $\lambda(L_1 \cap L_2) = \{a^n / n \in N\}$.

We do not repeat the proof of this lemma here; it will suffice to remark that the

terminal alphabet of L_1 is the set $\{a, b, \dots, g\}$, and that λ is defined as follows:

$$\lambda(a) = a, \quad \lambda(b) = e, \dots, \lambda(g) = e; \quad \text{where } \underline{e} \text{ is the null string.}$$

The outline of the Proof is as follows: Given the set N , we are given L_2 by Haines' lemma. In the base P of the noncyclic grammar G that 'generates' N is generated strings of the form (STV) , where $S \in L_1$, $T \in L_2$, and V is an arbitrary string over the alphabet $\{a, \dots, g\}$. The first transformation checks, one symbol at a time, that $S = T = V$, and progressively deletes S and T simultaneously. The second transformation checks that V is not merely a proper initial part of both S and T . The third transformation performs the operation of λ on the string V . If either of the first two transformations fails to apply, the string is filtered out by virtue of the construction of the regular language H . All deletions are in accordance with the principle of recoverability, since we delete symbols in S and T only as they are equal to symbols in V , and the third transformation deletes symbols in V in effecting the operation of λ by virtue of equality with one of a finite number of terminal strings.

Given N , and therefore L_2 , the grammar that 'generates' N is constructed as follows: The base P of the grammar has the following rules in addition to the rules generating L_1 and L_2 :

$$S \rightarrow S \begin{Bmatrix} a \\ \vdots \\ g \end{Bmatrix} \beta_1$$

$$S \rightarrow S_1 S_2 \begin{Bmatrix} a \\ \vdots \\ g \end{Bmatrix} \beta_1 \beta_2$$

where S_1 and S_2 are the initial symbols of the context-free grammars that generate L_1 and L_2 , respectively. The transformations of the grammar are

T_1	Analysis:	$[x X]_{S_1} [y Y]_{S_2} Z z \beta_1 (\beta_2)$
	such that	(i) x, y , and z are single terminal symbols (ii) X, Y , and Z are any strings, including \underline{e} . (iii) $x = y = z$.
	Operation:	delete x, y and β_1 .
T_2	Analysis:	$z \beta_2$
	such that	(i) z is a single-terminal symbol
	Operation:	delete β_2 .

T_3	Analysis:	$Z z$
	such that	(i) z is a single-terminal symbol in the set $\{b \dots g\}$
		(ii) Z is any string, possibly \underline{e}
	Operation:	delete z .

Let H consist of all strings of the form a^n , $n > 0$.

The language generated by the base is of the form $[\dots [[x_1 \dots x_n]_{S_1} [y_1 \dots y_m]_{S_2} z_1 \beta_1 \beta_2]_S z_2 \beta_1]_S \dots z_k \beta_1]$. T_1 checks within each S that $x_i = y_i = z_i$, and erases the first two and β_1 . If the equality fails at some point or if either $n < k$ or $m < k$, then T_1 will fail to apply, β_1 will be left in the interior of the string, and the string will be excluded by nonmembership in H . If either $n > k$ or $m > k$, then T_2 will fail to apply on the lowest S as its structural description will not have been satisfied, β_2 will be left in the interior of the string, and the string will be excluded by nonmembership in H . T_3 then operates, deleting just those symbols deleted by λ . It is evident, then, that for all strings x , $x \in \lambda(L_1 \cap L_2)$ iff $x \in L(G) \cap H$.

The result of this theorem and of those remarked upon above is that any language weakly generated by a noncyclic grammar can be weakly generated by a cyclic grammar, and vice versa. The linguistic interest of this kind of gross comparison, however, is quite limited. But what is striking about certain current formulations of the transformational grammar of English is that, modulo some reorderings, the languages generated when the transformations are applied cyclically and noncyclically are essentially the same. In general, the language generated by a transformational grammar is not invariant under cyclic and noncyclic applications of the transformations. Thus, we should like to make precise the empirical claims about language which are involved in stating that the transformations apply either cyclically or noncyclically. One avenue of investigation is to give a formal characterization of those grammars whose languages remain invariant under cyclic and noncyclic application of transformations. Having specified the defining features of such grammars, we will know that it is just these features which are relevant to the empirical questions involved in cyclic or non-cyclic application of transformations.

J. P. Kimball

References

1. N. A. Chomsky, Aspects of the Theory of Syntax (The M. I. T. Press, Cambridge, Mass., 1965).
2. Ibid., see Chap. 3.
3. J. P. Kimball, "On the Intersection of Regular Languages and Languages Generated by Transformational Grammars," Quarterly Progress Report No. 83, Research Laboratory of Electronics, M. I. T., October 15, 1966, pp. 117-128.
4. J. P. Kimball, "Predicates Definable over Transformational Derivations by Intersection with Regular Languages" (forthcoming, Information and Control).

(XXI. LINGUISTICS)

B. LITHUANIAN MORPHOPHONEMICS

I shall present and discuss briefly some phonological rules of Lithuanian. They are by no means all that are needed for a complete account of Lithuanian morphophonemics. I think, however, that they permit us to derive the paradigms of at least the primary verbs and nouns (that is, those with monosyllabic stems).

I assume that no long vowels occur in lexical representations. Vowels that appear as long in their final phonetic form are represented in the lexicon as sequences of two identical short vowels that are contracted to a single long vowel by a comparatively late rule. Thus a short vowel is meant wherever the symbol V appears.

For accent rules two conventions apply:

1. The accent can fall on any vowel and on l, m, n, r – on the latter, however, only when they stand immediately before a consonant and are not preceded by more than one vowel. The symbol M is used to represent all segments capable of bearing the accent.

2. When an M is accented, all preceding M's in the same word are accented also. This convention makes possible certain simplifications in the formulation of accent rules. A late rule, not stated here, will erase all accent specifications, except the rightmost in each word. Other rules, likewise not discussed here, will have to introduce what in traditional grammar is known as Silbenton or Wortintonation; in other words, they must interpret sequences MM as rising (~ in the normal orthography) and sequences MM as falling (´ in the normal orthography). It is clear that these rules must apply before the operation of the contraction rule.

For the accent rules to apply, grammatical morphemes must be specified for the lexical feature strong, and stems must be specified for the lexical feature strong susceptible. Furthermore, stems must be specified for the feature post stem (a term used here for the traditional oxytone). It is a fact about verb stems that the features strong susceptible and post stem are not independent: a verb stem may only be $\begin{bmatrix} +\text{strong susceptible} \\ +\text{post stem} \end{bmatrix}$ or $\begin{bmatrix} -\text{strong susceptible} \\ -\text{post stem} \end{bmatrix}$. In noun stems, on the other hand, no such restrictions obtain.

The order of the rules given here cannot be considered as fully established at the present stage. Although the ordering of a given rule with respect to some others can often be strictly motivated, its placement relative to the remaining rules is, to some extent, arbitrary. Some of the considerations relevant to the ordering will be briefly discussed in connection with individual rules.

The rules:

(1) Palatalization:

All consonants (including l, m, n, r) are palatalized before front vowels.

(2) Assimilation:

An n is completely assimilated to a preceding vowel when followed by word boundary or a sibilant (s, š, z, ž) or the sonorants l, m, r. Although there is, to the best of my

knowledge, no example for the occurrence of the sequence Vn before an n, we may include the n in the environment specification in order to gain greater generality. The vowel sequence resulting from the application of the assimilation rule is nasalized. If two identical vowels precede the n, both are nasalized.

$$V_1(V_1)n \rightarrow V_{31}(V_{31})V_{31} / \left. \begin{array}{l} [+sonorant] \\ -sonorant \\ +strident \\ \# \end{array} \right\}$$

Typical examples are the verbs with nasal infix in the present tense (banla → ba₃a₂la, finally bā₃la) and the accusative singular (e. g., uuir + a + an → uuir + a₃ + a₃a₃, finally vī₃rā).

The rule does not apply before the future tense marker si.

As for the ordering, assimilation must operate before the final shortening rule (8), because a vowel derived from an n by rule (2) can be subject to rule (9).

(3) i/y:

The glides y and w will be treated as the prevocalic realizations of the vowels i and u. The latter are converted by the following rule:

$$i, u \rightarrow y, w / \text{---} V$$

Examples: 1. sing. pret. buu + a + au → buw + a + au (finally buvaũ)

1. sing. pret. lii + a + au → liy + a + au (finally lijau)

It seems that two further restrictions apply to rule (3): i does not go to y before i, and u does not go to w before u or when preceded by certain consonants.

The rule must apply before metathesis, (rule 4), as can be seen in the nom. plur. of the pronoun jis:

iei → (3) → yei → (4) → yie, not: iei → (4) *iie with rule (3) now being inapplicable.

(4) Metathesis (this rule does not operate across formative boundary):

au and ei go to ua and ie, respectively.

A majority of stems with au as their root vocalism, and a substantial minority of stems with ei are exceptions to this rule. I know of only one grammatical morpheme, however, that is an exception – the gen. sing. of u-stems:

suun + u + au + sV → sū₃aus.

Metathesis must operate before the accent rules and before the e/a rule (5) because an au resulting from the application of rule (5) is not metathesized.

(5) e/a:

An e goes to a before u:

$$e \rightarrow a / \left. \begin{array}{l} [+voc.] \\ +grv. \\ +diff. \end{array} \right\}$$

Since e never occurs before a at the stage in the derivation where this rule applies, we can make the rule more general by omitting the feature specification [+diff.]. It now applies before all back vowels, though nonvacuously only before u.

The following rules deal with the assignment of the accent. Recall that, by the convention mentioned above, all M's preceding the M that receives the accent by one of the accent rules are also accented.

- (6) The accent is placed on the second M from the left in stems specified as [-post stem].
- (7) For stems specified as [+post stem] the accent is placed on the M immediately following the stem.
- (8) The accent is retracted by one M.
- (10) If an ending is [+strong] and the preceding stem is [+strong susceptible], then the accent is placed on the rightmost M of the ending (that is, rightmost at this stage in the derivation).

To show in greater detail how these rules operate, I shall select examples from nouns of the a-declension. All nouns are divided into four classes determined by the two features [post stem], [strong susceptible]:

[-post stem]	{	[-strong susceptible] (e. g., vyras)	(a)
	}	[+strong susceptible] (e. g., langas)	(b)
[+post stem]	{	[-strong susceptible] (e. g., pir ^ˇ stas)	(c)
	}	[+strong susceptible] (e. g., dievas)	(d)

(a) corresponds to the traditional class 1, (b) to class 3, (c) to class 2, and (d) to class 4. The first two accent rules differentiate [-post stem] and [+post stem]-stems. The former receive an accent on the stem, the latter after the stem by rules (6) and (7), respectively.

e. g., Nom. plur. (after operation of metathesis and i/y)	[-post stem]	{	viir + a + ie	}	→ (6) →	{	viir' + a + ie	}
			lang + a + ie				láng + a + ie	
	[+post stem]	{	pir ^ˇ st + a + ie	}	→ (7) →	{	pir ^ˇ st + á + ie	}
			diew + a + ie				diéw + á + ie	

Note that there are no [-post stem]-stems with fewer than two M's in their stem syllable. This is a regularity of morpheme structure still to be accounted for.

The accent retraction rule (8), which follows, is not conditioned by feature specifications as are (6) and (7), but operates in all environments. It yields the following results: All [-post stem]-stems have the accent on the first M of the stem throughout the

paradigm. This can later be interpreted as acute on the stem. All [+post stem]-stems have the accent on the last M of the stem. This can later be interpreted as circumflex or grave, depending on whether the stem syllable is long or short.

The nominative plural forms now become:

$$\begin{aligned} [-\text{post stem}] & \left\{ \begin{array}{l} \text{viir} + a + ie \\ \text{lang} + a + ie \end{array} \right\} \\ [+ \text{post stem}] & \left\{ \begin{array}{l} \text{pir}^{\check{v}}\text{st} + a + ie \\ \text{diew} + a + ie \end{array} \right\} \end{aligned}$$

The results just described are not quite correct; it is a well-known fact that in the [+post stem]-paradigm the endings of the instr. sing., loc. sing., and acc. plur. retain the accent. This can easily be accounted for by assigning to these three case endings the exception feature [-Rule (8)]. The derivation of the acc. plur., for example, is now as follows:

$$[+ \text{post stem}] \left\{ \begin{array}{ll} \text{pir}^{\check{v}}\text{st} + \text{aus} \longrightarrow (4) + \text{uas} \longrightarrow (7) & + \acute{\text{u}}\text{as} \longrightarrow (8) \text{ inapplicable} \\ \text{diew} + \text{aus} \longrightarrow (4) + \text{uas} \longrightarrow (7) & + \acute{\text{u}}\text{as} \longrightarrow (8) \text{ inapplicable} \end{array} \right\}$$

After rule (8) a rule of segmental phonology intervenes, namely the final shortening rule, which drops an unaccented final vowel before a word boundary or when separated from a word boundary only by an s:

$$(9) \quad \begin{array}{l} V \longrightarrow \emptyset / \text{---} (s) \# \\ [-\text{acc.}] \end{array}$$

(A certain problem associated with this rule will be discussed below.)

Our example, the nom. plur., is now represented:

$$\begin{array}{l} \text{viir} + a + i \\ \text{lang} + a + i \\ \text{pir}^{\check{v}}\text{st} + a + i \\ \text{diew} + a + i \end{array}$$

As we have seen, both the [-post stem] and [+post stem]-classes are further divided into [-strong susceptible] and [+strong susceptible]-subclasses. The strong case rule (10) now assigns an accentual interpretation to this subdivision by accenting the final (after application of (9)) M of strong endings preceded by strong susceptible stems. The endings of the a-declension specified as strong are:

$$\begin{array}{ll} \text{Loc. sing.} & (eV \rightarrow (9) \rightarrow e) \\ \text{Nom. plur.} & (a + ei \rightarrow (4) \rightarrow a + ie \rightarrow (9) \rightarrow a + i) \end{array}$$

(XXI. LINGUISTICS)

Gen. plur.	(a + uun → (2) → a + u ₃ u ₃ → (9) → a + u ₃ u ₃)
Dat. plur.	(a + ms)
Instr. plur.	(a + isV → (9) → a + is)
Loc. plur.	(au + seV → (4) → ua + seV → (9) → ua + se).

It should be pointed out that there is no general way to predict whether an ending is strong or not. There is variation from declension to declension; the nom. plur., for example, is [+strong] in the a-declension, but [-strong] in the aa-declension.

Rule (10) brings about two accent shifts: in stem specified as [-post stem, +strong susceptible] the accent goes from the first M of the stem to the last M of the ending; in stems specified as [+post stem, +strong susceptible] from the last M of the stem to the last M of the ending:

e. g., lánġ + a + i	lánġ + á + í (finally langáĩ)
[+strong]	
diēw + a + i	diēw + á + í (finally dieváĩ)
[+strong]	

An interesting case is the loc. sing., which is both [-Rule (8)] and [+strong]. The loc. sing. of dievas is derived as follows (after i/y and metathesis):

diēw + eV → (7) → diēw + éV → (8) inapplicable → (9) → diēw + é → (10) → diēw + é.

It can be seen that the strong case rule (10) applies vacuously here. The loc. sing., incidentally, was crucial to my ordering of the final shortening rule with respect to the accent rules. It is easy to see that for all other cases the same correct results could be arrived at with the ordering: (6), (7), (10), (8), (9). Note, however, that this alternative ordering would give us an incorrect result for the loc. sing.:

diēw + eV $\xrightarrow{\left[\begin{array}{l} +\text{strong} \\ -\text{Rule (8)} \end{array} \right]}$ (7) → diēw + éV → (10) → diēw + éV →
 (8) inapplicable → (9) inapplicable (that is, finally something like *dievē).

To summarize: The accent rules yield the fourfold paradigm:

- 1) [-post stem, -strong susceptible] e. g., v́yras – accent on the first M of the stem throughout the paradigm.
- 2) [-post stem, +strong susceptible] e. g., lánġas – accent on the first M of the stem, but on the ending in strong cases.
- 3) [+post stem, -strong susceptible] e. g., pírstas – accent on the last M of the stem, except in the case of endings with the exception feature [-Rule (8)], where the accent is on the first M after the stem.
- 4) [+post stem, +strong susceptible] e. g., diēvas – accent as in pírstas, but with accent on the last M of the ending in strong cases.

Now let us return to the final shortening rule. If my analysis of certain verb forms

is correct, this rule requires a further specification. Consider the following reflexive forms (after application of metathesis):

1. sing. a-pres.: pin + ug + si pin + ua E si (finally pinuosi)
3. sing. a-pres.: pin + a + \check{V} + si \rightarrow pin + a + \emptyset + si (finally pinasi)
4. sing. aa-pres.: \check{z} valg + a + ug + si \rightarrow \check{z} valg + a + u \emptyset + si (finally \check{z} valgaūsi)

The dropping of the vowel of the personal ending before the reflexive particle si in pinasi and \check{z} valgausi, as well as the retention of the final vowel in the reflexive particle itself, is not immediately explainable by rule (9). Both cases seem to be exceptions. But a certain regularity may be observed: the final vowel of the personal ending is dropped before si when the personal ending itself begins with a vowel and is immediately preceded by a vowel. This suggests the following modification in the environment specification of rule (9):

$$\begin{array}{l} V \rightarrow \emptyset / \langle V+(V) \rangle \text{ ______ } (s \langle i \rangle) \# \\ [-\text{acc.}] \end{array}$$

But even this formulation leaves at least one problem unsolved, the treatment of the final i of the reflexive particle.

- (11) After the application of the i/y rule and the final shortening rule the sequence Vy can occur at the end of a word. This sequence is converted to a true diphthong, that is, y is revocalized as i:

$$[-\text{cons.}] \rightarrow [+voc.] / [\text{ ______ }] \#$$

E.g., Dative singular of the aa-stems:

$$\begin{array}{l} \text{dein} + a + ia \rightarrow (3) \rightarrow \text{dein} + a + ya \rightarrow (4) \rightarrow \text{dien} + a + ya \rightarrow (9) \rightarrow \text{dien} + a + y \\ \rightarrow (11) \rightarrow \text{dien} + a + i \text{ (finally diēnai).} \end{array}$$

Note that the rule as stated above also covers the parallel case of $w \rightarrow u$ in this position, although no examples are known to me at the moment.

For the ordering of (11) see below.

- (12) Sequences of more than two consecutive vowels are not permitted in Lithuanian. If after the final shortening rule such a sequence still occurs, the following rule applies:

$$V \rightarrow \emptyset / \text{ ______ } VV$$

Halle and Zeps (Quarterly Progress Report No. 83, pages 105-112) have established for Latvian rules similar to (9) and (12) which can be combined into a single rule. I believe it can be shown, however, that such a combination is impossible in Lithuanian, where both rules can apply to a single string with (11) necessarily intervening. Consider the dative singular of a-stems:

(XXI. LINGUISTICS)

- stem + a + u + ia
- stem + a + u + ya by rule (3)
- stem + a + u + y by rule (9)
- stem + a + u + i by rule (11)
- stem + ~~o~~ + u + i by rule (12)

Note that unless (11) operates before (12), the environment conditions of rule (12) are not met. Furthermore, it is impossible for rule (11) to operate before the final a has been dropped by rule (9).

(13) Through the operation of the palatalization rule (1) and the i/y rule (3) sequences Cjy can arise. Such sequences are realized phonetically simply as palatalized consonants, that is, y is dropped after Cj.

(14) The palatalized dentals t_j and d_j are affricated before back vowels: t_j, d_j → č' dz' / _____ back vowel.

(15) Sequences of two identical vowels are contracted to a single long vowel, which is always tense.

The rules which, as mentioned above, interpret VV̇ as rising and V̇V as falling, will have to apply before (15).

(16) Long non-nasalized ā goes to ō in all environments. The underlying representation of phonetic ō as aa is required by morphophonemic considerations (e. g. , parallelism in ablaut pattern u:ū, a:ō).

(17) All vowels, whether long or short, are denasalized.

In the sequel I shall give the abstract phonemic representation of the paradigms of primary nouns and verbs, together with the rules that must apply to them. The final results are given in their orthographic form.

	aa-stems	(example dein)
		[+post stem	
		[+strong susceptible]	
Nom.	dein + aa	(1, 4, 7, 9, 10)	dienà
	[+strong		
	[-R(8)]		
Gen.	dein + aa + sV	(1, 4, 7, 8, 9, 10, 15, 16)	dienõs
	[+strong]		
Dat.	dein + a + ia	(1, 3, 4, 7, 8, 9, 11)	diēnai
Acc.	dein + a + an	(1, 2, 4, 7, 8, 9, 15, 17)	diena _s

Instr.	dein + a + n [-R(8)]	(1, 2, 4, 7, 9, 17)	dienà
Loc.	dein + aa + ieV [+strong]	(1, 3, 4, 7, 8, 9, 10, 15, 16)	dienojè
Plural			
Nom.	dein + aa + sV	(1, 4, 7, 8, 9, 15, 16)	diēnos
Gen.	dein + a + uun [+strong]	(1, 2, 4, 7, 8, 9, 10, 12, 15, 17)	dienũ̃
Dat.	dein + aa + ms [+strong]	(1, 4, 7, 8, 10, 15, 16)	dienóms
Acc.	dein + a + ns [-R(8)]	(1, 2, 4, 7, 9, 17)	dienàs
Instr.	dein + aa + meis [+strong]	(1, 4, 7, 8, 9, 10, 15, 16)	dienomís
Loc.	dein + aa + seV [+strong]	(1, 4, 7, 8, 9, 10, 15, 16)	dienosè

The ee-stems parallel the aa-stems more or less exactly. Only the nominative singular demands special attention: unlike aa-stems, the ee-stems in the nominative singular require that an additional vowel be attached to the ending ee, in order to account for the final phonetic length of this ending, as well as for the phonetic circumflex.

a-stems (example lang)
[-post stem
[+strong susceptible]]

Singular

Nom.	lang + a + sV	(6, 8, 9)	lángas
Gen.	lang + a + aa	(6, 8, 9, 15, 16)	lángo
Dat.	lang + a + u + ia	(3, 6, 8, 9, 11, 12)	lángui
Acc.	lang + a + an	(2, 6, 8, 9, 15, 17)	lánga,
Instr.	lang + au	(4, 6, 8, 9)	lángu
Loc.	lang + eV [+strong]	(1, 6, 8, 9, 10)	langè

Plural

Nom.	lang + a + ai [+strong]	(4, 6, 8, 9, 10)	langaĩ
Gen.	lang + a + uun [+strong]	(2, 6, 8, 9, 10, 12, 15, 17)	láng
Dat.	lang + a + ms [+strong]	(6, 8, 10)	lángams
Acc.	lang + au + s [-R(8)]	(4, 6, 8, 9)	lángus

(XXI. LINGUISTICS)

Instr.	lang + a + isV [+strong]	(6, 8, 9, 10)	langaĩs
Loc.	lang + au + seV [+strong]	(1, 4, 6, 8, 9, 10)	languosè

The locative singular is somewhat exceptional, insofar as the ending shows no trace of the stem vowel a. Nevertheless, I see no possibility for an alternative representation.

i-stems (example \check{s} ird
[-post stem
[+strong susceptible])

Masculine and feminine substantives of the i-declension differ only in the dative and instrumental singular. I give one example for each case. The genitive plural of certain substantives is formed without the stem vowel i. This irregularity must be accounted for in some way either in the lexicon or in the morphological component.

Singular			
Nom.	\check{s} ird + i + sV [+strong]	(1, 6, 8, 9, 10)	\check{s} irdìs
Gen.	\check{s} ird + i + ei + sV [+strong]	(1, 3, 4, 6, 8, 9, 10, 13)	\check{s} irdiēs
Dat.	fem. \check{s} ird + i + a + ia	(1, 3, 6, 8, 9, 11, 13, 14)	\check{s} irdžiai
	masc. dant + i + u + ia [+post stem [+strong susceptible]]	(1, 3, 7, 8, 9, 11, 13, 14)	danciui
Acc.	\check{s} ird + i + in	(1, 2, 6, 8, 9, 15, 17)	\check{s} ird ₃
Instr.	fem. \check{s} ird + i + mei [+strong]	(1, 4, 6, 8, 9, 10)	\check{s} irdimi
	masc. dant + i + au [+post stem][-R(8)]	(1, 3, 4, 7, 9, 13, 14)	danciù
Loc.	\check{s} ird + ii + ieV [+strong]	(1, 3, 6, 8, 9, 10, 15)	\check{s} irdyjè
Plural			
Nom.	\check{s} ird + ii + sV	(1, 6, 8, 9, 15)	\check{s} irdys
	\check{s} ird + i + uun [+strong]	(1, 2, 3, 6, 8, 9, 10, 13, 14, 15, 17)	\check{s} irdžiu ₃
Gen.	irregular dant + uun [+post stem] [+strong] [+strg. susc.]	(2, 7, 8, 9, 10, 15, 17)	dantū ₃
Dat.	\check{s} ird + i + ms [+strong]	(1, 6, 8, 10)	\check{s} irdims
Acc.	\check{s} ird + i + ns [-R(8)]	(1, 2, 6, 8, 9, 17)	\check{s} irdis

(XXI. LINGUISTICS)

Loc. sing. masc.	staar + ameV [+strong]	→	storame [˘]
Nom. plur. masc.	staar + ei [+strong]	→	stori [˘]
Dat. pl. masc.	staar + eims [+strong]	→	storiems [˘]

The corresponding forms of adjectives with u or ia as stem vowel are quite parallel.

On the whole, the definite forms of adjectives can be represented as the simple forms plus the correspondings forms of the pronoun jis, e. g., gen. sing. masc.: stem + a + aa + i + aa → stem + ojo. Note that with the suffixation of the pronoun the final shortening rule will no longer apply to the endings of the adjective proper. The accusative plural, for example, is [˘]saltuosius, and not *[˘]saltusius.

As far as their accentuation is concerned, the long forms of the adjective follow the short forms exactly; the accent never falls on the pronominal element. This is explained by a restriction on the domain of the accent rules.

A further peculiarity of the definite declension should be mentioned: the apparent merger of classes 3 and 4 in the acc. pl. ([˘]saltuosius, geruosius) and instr. sing. ([˘]saltuojū, geruojū). We would expect *[˘]saltuosius (cf. indefinite [˘]saltus) and *[˘]saltuojū (cf. [˘]saltu). The obvious solution, the introduction of a readjustment rule saying that a [-post stem]-adjective becomes [+post stem] when suffixed with the pronoun, is impossible, since forms with the accent on the stem always bear an acute in adjectives [˘]saltas. The only way to account for this peculiarity is to specify the acc. plur. and the instr. sing. as [+strong] in the environment in question; that is, we have to add a rule to the morphological component of roughly this form:

$$\left\{ \begin{array}{l} \text{Instr. sing.} \\ \text{Acc. Plur.} \end{array} \right\} \longrightarrow [+strong] /]_A + \text{---} + \text{pronoun.}$$

To be sure, this solution seems a bit ad hoc, but as can be seen in any case, the feature strong is not in general predictable for case endings.

The Verb:

There are 3 markers of the present tense and 2 of the preterite; their distribution must be specified in the morphological component. For our present purposes this problem can be disregarded. There is one peculiarity associated with the present and preterite markers, which, interestingly enough, has been observed in Latvian also. Except in the i-present, the tense marker is, in general, shorter by one vowel before the personal endings of the 1. and 2. sing. than before the remaining personal endings, that is, the present marker a does not appear at all in the 1. and 2. sing., and the present markers aa, ia and the preterite markers aa, ee appear as a, i, a, e, respectively.

In the verb forms given below the tense marker has been affixed directly to the stem; at the moment, it is not clear whether this treatment is correct or whether a special verbalizing suffix should be set up between the stem and the tense marker.

a-present (example pin[+post stem, +strong susceptible])

1. sing.	pin + au [+strong]	(1, 4, 7, 8, 9, 10)	pinù
2. sing.	pin + ei [+strong]	(1, 4, 7, 8, 9, 10)	pini
3. pers.	pín + a + V	(1, 7, 8, 9)	pína
1. plur.	pin + a + mee	(1, 7, 8, 9)	piname
2. plur.	pin + a + tee	(1, 7, 8, 9)	pinate

aa-present (example valg[-post stem, -strong susceptible])

1. sing.	ualg + a + au [+strong]	(3, 4, 6, 8, 9)	valgau
2. sing.	ualg + a + ei [+strong]	(3, 4, 6, 8, 9)	valgai
3. pers.	ualg + aa + V	(3, 6, 8, 9, 15, 16)	valgo
1. plur.	ualg + aa + mee	(1, 3, 6, 8, 9, 15, 16)	valgome
2. plur.	ualg + aa + tee	(1, 3, 6, 8, 9, 15, 16)	valgote

ia-present (example dur[+post stem, + strong susceptible])

1. sing.	dur + i + au [+strong]	(1, 3, 4, 7, 8, 9, 10, 13)	duriù
2. sing.	dur + i + ei [+strong]	(1, 3, 4, 7, 8, 9, 10, 13)	duri
3. pers.	dur + ia + V	(1, 3, 7, 8, 9, 13)	dùria
1. plur.	dur + ia + mee	(1, 3, 7, 8, 9, 13)	dùriame
2. plur.	dur + ia + tee	(1, 3, 7, 8, 9, 13)	dùriate

i-present (example tur[+post stem, +strong susceptible])

1. sing.	tur + i + au [+strong]	(1, 3, 4, 7, 8, 9, 10, 13)	turiù
2. sing.	tur + i + ei [+strong]	(1, 3, 4, 7, 8, 9, 10, 13)	turi
3. pers.	tur + i + i	(1, 7, 8, 9)	tùri
1. plur.	tur + i + mee	(1, 7, 8, 9)	tùrime
2. plur.	tur + i + tee	(1, 7, 8, 9)	tùrite

aa-preterite (example pin[+post stem, +strong susceptible])

1. sing.	pin + a + au [+strong]	(1, 4, 7, 8, 9, 10)	pinaũ
----------	---------------------------	---------------------	-------

(XXI. LINGUISTICS)

2. sing.	pin + a + ei [+strong]	(1, 4, 7, 8, 9, 10)	pináĩ
3. pers.	pin + aa + V	(1, 7, 8, 9, 15, 16)	pino
1. plur.	pin + aa + mee	(1, 7, 8, 9, 15, 16)	pinome
2. plur.	pin + aa + tee	(1, 7, 8, 9, 15, 16)	pinote

ee-preterite (example valg[-post stem, -strong susceptible])

1. sing.	ualg + e + au [+strong]	(1, 3, 4, 5, 6, 8, 9)	valgiau
2. sing.	ualg + e + ei [+strong]	(1, 3, 4, 6, 8, 9)	valgei
3. pers.	ualg + ee + V	(1, 3, 6, 8, 9, 15)	valgẽ
1. plur.	ualg + ee + mee	(1, 3, 6, 8, 9, 15)	valgẽme
2. plur.	ualg + ee + tee	(1, 3, 6, 8, 9, 15)	valgẽte

The future is formed by affixation of si to the stem of the verb that appears in the infinitive. Note two peculiarities of the future: 1.) The assimilation rule (2) does not operate before the future marker si, as already mentioned above; and 2.) in the third person the si always attracts the accent, except when it is preceded by a [-post stem]-stem plus derivational suffix (e. g., máák + ii + si → finally mókys, but ráś + ii + si → finally raśys). This peculiarity of the third person provides an explanation for what in traditional grammars is referred to as Metatonie.

Example: lauk[-post stem, -Rule (4), -strong susceptible]

1. sing.	lauk + si + au	(1, 3, 4, 6, 8, 9, 13)	lauksiu
2. sing.	lauk + si + ei	(1, 3, 4, 6, 8, 9, 13)	lauksi
3. pers.	lauk + si → lauk + sí	(1, 8, 9)	lauks
1. plur.	lauk + si + mee	(1, 6, 8, 9)	lauksime
2. plur.	lauk + si + tee	(1, 6, 8, 9)	lauksite

Note that the personal endings au and ei are not [+strong] in the future.

C. Heeschen

C. INWARD AND UPWARD – DIRECTIONALS IN ENGLISH

We have in present-day English several small wordlike elements; in, out, up, down, and others, which we may call "directionals."¹ Any one of these formatives may alternatively be called a preposition, as in (1); a part of a compound preposition, as in (2); part of an adverb of direction, as in (3); and in (4), various analyses call it a "dangling" preposition (in analogy with (1)), an adverb (in analogy with (3)), or even a verbal particle (in analogy with "he blew up (became angry)" or "the teacher bawled him out").

- (1a) at this point the smoke travels up the chimney.
 b) this piece of paper just blew in the window.
- (2a) but first, the smoke must travel up to the ceiling.
 b) so he pushed it into the center.
- (3a) after being released, the balloon floated upward.
 (3b) in a hurricane, the surface wind blows inward.
- (4a) the air travels up for a few minutes before taking on a rotational motion.
 b) after traveling in, it starts moving up the eye of the storm.

Thus we have 4 uses of each of several directionals (Di's). In discussing them, let us use up for examples, since it is a typical one.

The semantic contribution offered to the sentence by any Di (e.g., up) is at least roughly the same, regardless of which construction it is used in. For this reason, it would be desirable to relate them in the syntax, thereby allowing a single lexical reading to be applied in these different cases. But it is not only desirable to do so but also necessary, because of the following considerations. First, a Di in any of these usages is found only after a verb of motion.² Second, after a Di, there may be only one of 4 possibilities; either a nominal phrase as in (1), or the formative-ward(s) as in (3) (Is this a nominal of sorts?), or a prepositional phrase as in (2), or else nothing, by which I mean that it can be followed by any and everything that can follow any of the other 3 possibilities. These 4 constructions are syntactically equivalent; they play the same role in the syntactic structure of the sentence, as is seen by the fact that whatever can follow (precede) one such usage can follow (precede) the other, and whatever cannot follow (precede) one cannot follow (precede) another. But the most binding consideration is that if a sentence contains an occurrence of a particular directional in any usage, it cannot contain a second occurrence of the same directional, as seen in the impossibility of the constructions in (5).

- (5) *he climbed { up up the flagpole
 up upward
 upward up the flagpole
 up up to the top
 upward up to the top
 etc.

(XXI. LINGUISTICS)

(The same usage of a Di may apparently be repeated, however, for emphasis, as is typical of simple adverbs "? he flew up up and away," like "have you ever ever done that?") The only reasonable way to disallow multiple occurrences of each Di is to derive the different usages from a common underlying structure, which can become one or another of its realizations but not several. And the reduplicated cases (if they occur) can be handled by a low-level rule, which works only on single words.

We may note that many of the so-called "2-word verbs" or "verb particle combinations" are formed from a verb of motion and an accompanying directional, e. g. , "blow up" (explode), "put up" (preserve), and as is expected from directionals, they cannot co-occur with another occurrence of the same directional. There is nothing further to be said here, except that these must be essentially verb-directional idioms.

Thus we see that any satisfactory grammar of English must have these underlying directionals which are realized in the various ways (1) to (4). This fact will serve to explain the other properties of directionals noted above. Accepting, then, that a unified analysis of all of these usages is necessary, let us examine an example of such an analysis.

First, it seems clear that the bare Di of (4) is derived by deleting the -ward(s) of (3). Semantic and syntactic constance,³ along with a designated element for deletion, makes this a clear case of a simple deletion transformation. The conditions to be met for deletion to occur are perhaps more interesting, but to a rough approximation they merely require that there be something to the right of the -ward in the same clause. While (6) and (8) are permitted, (7) is not.

- (6a) the electrons are moving upward.
- b) he was climbing upward.
- c) helium balloons go upward.

- (7a) *the electrons are moving up.
- b) *he was climbing up.
- c) *helium balloons go up.

- (8a) the electrons are moving up in order to avoid the negative charge here.
- b) he was climbing up when it happened.
- c) a helium balloon goes up if you release it.

Next, we note that in the compound preposition cases, the Di may have -ward attached without any semantic change, except perhaps a loss of the concept of completion (necessarily submerged if the preposition carried this meaning also), as in (9). The same explanation as that above given will suffice here.

- (9) he walked up(ward) to the top.
- she looked up(ward) through the conduit.
- the wires pass up(ward) along this joist.
- he climbed up(ward) from the bottom.

Finally, turning to the prepositional⁴ cases of (1), if we distinguish between 'goal' prepositions (from, to) and 'path' prepositions (along, through), we may observe that whenever a Di is used as a preposition, there is a path preposition (but never an end preposition) which can be inserted without changing the meaning of the sentence (10), and which makes these constructions parallel to the ones just examined. Because the prepositional

- (10a) he climbed up (along) the path.
 b) it fell down (through) the tube.
 c) it rolled down (along) the crack.

cases must be related to the other directionals, we are, at present, forced to accept the analysis that these putative prepositional Di's are really Di's followed by deleted path prepositions.⁵

Thus we have a clean, tight analysis.⁶ There is a -ward (or something similar) deletion transformation, and there is a preposition deletion transformation applying to its output which depends in an interesting way upon the object of that preposition. If prepositions are analyzed as a spelling-out of features from a nominal phrase, then the effect of the second transformation can presumably be obtained by inhibiting that spelling-out process.

There is, however, a joker left in the deck. If the directionals really are adverbial in nature, as they must be from the arguments above, they must also be prepositions, at least they must be so considered by some transformations. Besides (11) we have the word questions (12), and also the alternate word question (13), which is possible only for prepositional phrases. The same problem appears in relative clauses (14).

- (11a) Lincoln climbed up the flagpole.
 b) he pushed it up the tube.

- (12a) what did Lincoln climb up?
 b) what did he push it up?

- (13a) up what did Lincoln climb?
 b) up what did he push it?

- (14a) the flagpole up which Lincoln climbed fell down last year.
 b) the tube up which he pushed the wire ended on the second floor.

Thus we are faced with a contradiction. We must either give up this analysis of directionals and consequently try to explain the distributional facts noted above in diverse ways or give up the restriction of the question-word fronting transformation(s) to prepositions only (it does not work on ordinary adverbs, e.g., *accidentally whom did he hit?), or, as I am inclined to believe, we must have a process by which directional is attached to a prepositional phrase in such a way that is is indistinguishable from a true preposition.⁷ For the last alternative, other hints of support may be found in examining the relationship of prepositions to verbal prefixes in

German, Greek, and Russian (especially zu in German).

T. R. Hofmann

Footnotes

1. I am indebted to G. H. Matthews and J. S. Gruber, who have discussed the issues raised here.
2. Either a verb of physical motion, e. g., fly, move, travel or go, or a verb of metaphorical motion, e. g., look, shout; see J. Gruber, "Look and See" (to appear in Language).
3. We might want to delete some other element that expresses completion and contrasts with -ward (which expresses noncompletion). This contrast of completeness is emphasized by the perfect auxiliary as in:
 he has climbed upward.
 he has climbed up.
This explanation may also figure in the explanation of the completive interpretation of many verb-Di idioms (2-word verbs) such as "burn up," "wrap up," etc.
4. We notice that the putative preposition can often be deleted, sometimes leaving the nominal phrase looking like an object of the verb, but sometimes not.
 he climbed (up) the flagpole
 he walked (down) the road
 he crawled (down) the length of the hallway.
5. The real situation is somewhat more involved than the one described here; we have been looking only at nonvolumetric nominal phrases figuratively denoting planes, lines, and points). If we look at volumetric nominal phrases (denoting 3-dimensional objects, e. g., room, box, etc.), to is deletable and path prepositions are not. Generally speaking, what can be deleted after a directional depends on the following nominal phrase.
6. We may note that, besides the common directionals discussed herein, there are proper directionals ('proper' in the sense found in 'proper noun'). The names of the cardinal directions, north, south, east, west, behave just as common directionals, except that preposition deletion is forbidden.
 he walked north.
 he walked northward.
 *he walked north the road.
 he walked north along the road.
 ?north along what road did he walk?
7. There are phonologically identical and semantically similar locative prepositions which any complete analysis would presumably relate to these directionals. We shall not attempt to do so here.

D. ON PROBLEMS IMPLIED BY THE CONCEPT 'PERFORMANCE'

In Susumo Kuno's¹ works we find a tendency to construct a system, by means of an algorithm on the basis of a particular transformational grammar without applying inverse transformations, to directly determine the deep structure of a given sentence. Let us call this position A. Kuno intends this approach to be a hypothetical approximation to 'performance'.^{2, 3}

The possible generalizations of this approach are clear. The problem, of course, is to prove that each generalization can be constructed. First, there could be construction of a system that goes immediately from the deep structure to the sentence (a kernel or derived sentence in the terminology of Chomsky⁴). A condition is proposed, however, that this system be formed by an algorithm on the basis of transformational grammar (position B, which is the inverse of A).

The second generalization (position C) is a system that immediately determines the meaning(s) of a received sentence. This system also has to be constructed by an algorithm on the basis of the syntax and the semantics of a transformational grammar.

The third generalization (position D) is the inverse of C.

In this report we shall not take into account possible generalizations on a phonological level.

The last generalization that we make (position E) differs qualitatively from the previous ones. It is the construction of a system on the basis of linguistic data to directly determine the meaning(s) of a given sentence, and vice versa. The qualitative difference between this generalization and the previous ones is the following: The previous generalizations are all dependent on a competence (a transformational grammar); this generalization is not.

Let us now ask to what extent approaches A-E (if they can be constructed) are approaches to 'performance.' In these theories an attempt is made to achieve recognition or production procedures for each grammatical sentence and only for this kind.

Therefore, it seems possible to argue that these systems are approaches to a 'competence' model for speech production and speech recognition. The limitations and individual differences in speech production and speech recognition are the result of (a) psychophysical realizations of this kind of competence (performance-competence, which itself is dependent on 'competence' in approaches A-D); and (b) use of this realization (a and b can be called performance-performance).⁵

There is room for discussion about the use of the concepts 'performance-competence' and 'performance-performance.' We shall not discuss the pros and cons here. We shall only try to indicate a few problems that are implied by accepting this kind of distinction in the performance.

The first problem is the origin of the 'performance-competence.' Is it innate or is it

learned? If it is made by an algorithm from a particular competence grammar, is this algorithm learned or innate?

The second problem, "Is it possible to construct a 'performance competence' independently of a competence?" (generalization E⁶). If it can be proved that it is not possible, or possible only under conditions that cannot be met by a human being, then, I think, there would be strong confirmation of the 'competence' hypothesis and the transformational grammar, which is a competence grammar. If, however, it could be proved that such a construction is possible, then the problem arises, "How can we confirm the evidence for the competence hypothesis?" (competence grammar as a psychological and biological reality and necessity⁷).

A psychological proof or another proof of the dichotomy between competence and performance, independently of a proof of the possibility or impossibility of generalization E, would be very decisive. As long as no such proof is available, however, a proof of the possibility (or impossibility) of generalization E seems to be important.⁸

We feel that it is useful for future developments to make explicit certain problems to which contemporary approaches to 'performance' lead.

We wish to thank Professor H. Putnam, Professor S. Kuno, Dr. Rubenstein, M. De May, and Dr. W. Vereecke for discussing various topics that gave rise to some of these problems. Of course, only the author is responsible for the point of view taken here.

F. J. Vandamme

Footnotes and References

1. S. Kuno, "The Predictive Analyzer," in Readings in Automatic Language Processing, edited by D. G. Hays, p. 83.
2. The term 'performance' is used to denote the actual speech-production and speech-recognition systems of mankind. It is generally assumed to be based on a 'competence.' The difference between the two is mainly a difference in function (a theory of competence is not a theory for speech recognition or speech production; see N. Chomsky, "Current Issues in Linguistic Theory," in The Structure of Language, edited by J. A. Fodor and J. J. Katz (Prentice-Hall, Inc., Englewood Cliffs, N. J., 1966), p. 52; N. Chomsky, Aspects of the Theory of Syntax (The M. I. T. Press, Cambridge, Mass., 1965), p. 9). Possibly there is a difference in formal qualities. For a more intensive discussion about the concepts 'competence and performance' in linguistics, see N. Chomsky, Aspects of the Theory of Syntax, op. cit.
3. Another proposal for approximation to 'performance' has been made by R. S. Petrick, "Recognition Procedure for Transformational Grammars," Ph. D. Thesis, Department of Modern Languages and Linguistics, M. I. T., June 1965.
4. N. Chomsky, "A Transformational Approach to Syntax," in The Structure of Language, edited by J. A. Fodor and J. J. Katz, op. cit., p. 223.
5. This 'performance-performance' corresponds closely, we think, to F. de Saussure's 'parole' in, "Course in General Linguistics," translated by M. Baskin (McGraw-Hill Book Company, New York, 1966). We read: "Speaking ... is an individual act Within the act, we should distinguish between: (1) the combinations by which the

speaker uses the language code for expressing his own thought; and (2) psychophysical mechanism that allows him to exteriorize those combinations." (p. 14). Does de Saussure's "langue" correspond (with a few reservations) more to the concept 'competence' than to the concept 'performance-competence'?

6. Even if the distinction 'performance-competence' and 'performance-performance' is not accepted, the generalization E can be stated, "Is a performance system possible without a preconstruction of a competence grammar?". Two interpretations seem possible: (a) a competence grammar is not explicitly used, but is not implicitly required for the construction of a performance system; (b) a competence grammar is not at all needed. The discussion that follows seems to us to be valid in this case, too.
7. N. Chomsky, Aspects of the Theory of Syntax, *op. cit.*, p. 8. "Obviously, every speaker of a language has mastered and internalized a generative grammar that expresses his knowledge of language." (=competence).
8. More about that can be found in "A Discussion about a Possible Approach to a Model for Speech Recognition and Speech Production," (preprint, December 1966) by F. Vandamme. There we give arguments that seem to indicate very strongly that position E is possible. The value of the proposed system for 'analyse by analyse' and 'synthese by analyse' is crucial.

Academic and Research Staff

Prof. W. L. Black
Prof. M. Eden
Prof. T. S. Huang
Prof. F. F. Lee
Prof. S. J. Mason

Prof. W. F. Schreiber
Prof. D. E. Troxel
Dr. K. R. Ingham
Dr. P. A. Kolers

Dr. P. H. Liss
Dr. O. J. Tretiak
C. L. Fontaine
E. R. Jensen
G. L. Wickelgren

Graduate Students

G. B. Anderson
T. P. Barnwell III
A. K. Bhushan
B. A. Blesser
A. L. Citron
R. W. Cornew
D. P. De Wan
H. D. Evans III
A. Gabrielian

R. V. Harris III
D. W. Hartman
H. P. Hartmann
G. R. Kalan
R. W. Kinsley, Jr.
W. H. Lee
J. I. Makhoul
L. C. Ng

D. L. Peterson
D. S. Prerau
G. M. Robbins
A. H. M. Ross
C. L. Seitz
D. Sheena
R. M. Strong
G. A. Walpert
J. A. Williams

N67-27103

A. ACQUIRED ASYMMETRY OF SHAPE LEARNING

Using geometrically transformed texts, we have been able to show that humans learn to decode them differentially.¹ Mathematically equivalent transformations impose different burdens, both with respect to speed of decoding (as measured by the amount of time taken to read pages in a single geometrical transformation), and with respect to the rate of learning. The order of difficulty of the transformations shows that rotation in the plane of the page is easiest to master, while inversion on a horizontal axis and reflection about a vertical axis are far more difficult. Furthermore, there is a negative correlation between speed of initial learning and rate of acquisition of skill – the easiest transformation shows the least improvement.

These results imply that learned sequences of visual scanning, in conjunction with learned preferences for shapes of differing orientation, powerfully affects the subjects' ability to decode the texts. To learn whether the asymmetrical preferences are specific characteristics of the nervous system or reflect special learning was the motivation for the following experiment.

The experiment was performed in Israel with native speakers of Hebrew who had virtually no familiarity with languages read from left to right. Their reading skill with Hebrew (and for some of them with Arabic, too) was at or near the level of college freshmen. For reasons that are irrelevant to this report, it was difficult to obtain

*This work was supported in part by the Joint Services Electronics Programs (U. S. Army, U. S. Navy, and U. S. Air Force) under Contract DA 38-43-AMC-02536(E), and in part by the National Science Foundation (Grant GK-835), the National Institutes of Health (Grant 2 PO1 MH-04737-06), and the National Aeronautics and Space Administration (Grant NsG-496).

(XXII. COGNITIVE INFORMATION PROCESSING)

subjects, and the few whom we finally got could be tested only on a restricted set of materials, because of various time commitments. The array of 8 transformations that we have used previously was therefore reduced to 6, and testing time itself reduced to 5 days. Despite the small number of subjects, the results are quite clear.

The geometrical operations performed on the text were identical with those previously performed with English,¹ except for the 2 missing examples. Hebrew, as all Semitic languages, is read from right to left. A rotation in the plane of the page of Hebrew, consequently, yields a geometry that is opposite, but symmetrical, to that of English, and similarly with all other transformations that we have used. That is, identical geometrical transformations were performed on different bases (English and Hebrew) which are left-right inversions of each other. On each of the 5 days, each of the 6 students read aloud one page of Hebrew text in each of the 6 transformations. The results of the testing are shown in Fig. XXII-1, time being represented in minutes on

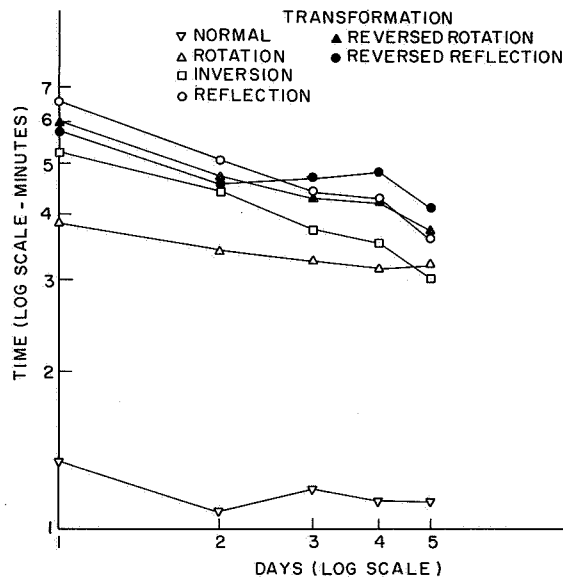


Fig. XXII-1. Results of tests.

the ordinate, and successive pages (days) on the abscissa. Very little improvement occurs in the reading of normally oriented Hebrew; rotation in the plane of the page is the easiest of the transformations, followed by inversion and reflection. In these respects, the data are identical with those obtained from native readers of English for the same transformations. The results show clearly, therefore, that the relative difficulty with the transformations, which had previously been found with native readers of English is not due to specific biases for orientation in the visual system. The difficulties rather seem to be due to biases induced by a well-practiced scanning "program" upon the ability to utilize other such "programs" (decoding strategies). If the biases were

specific to orientations, the results from the Hebrew readers would have shown inversion to be far easier than reflection, in order for them to be consistent with those obtained from English readers. The fact that it is the relative orientation that orders the difficulty with the transformations reveals clearly that the biases are acquired.

P. A. Kolars

References

1. P. A. Kolars, A. C. Boyer, and K. F. Rosenthal, "Protracted Practice on Decoding Spatially Transformed Text," Quarterly Progress Report No. 78, Research Laboratory of Electronics, M.I.T., July 15, 1965, pp. 229-231.

B. TRANSMISSION AND CODING OF COLOR PICTURES

Efficient schemes for transmission and coding of color pictures have been investigated by real-time processing of color television signals.¹ Subjective effects of random noise, PCM quantization noise, delta-modulation noise, and sampling and filtering degradations in color signals were evaluated by direct viewing of kinescope displays.² Such real-time displays are not only superior in quality to photographs obtained by computer simulation process but also show frame-to-frame degradations, thereby making evaluation more meaningful.

The blocks of a color picture transmission system are shown in Fig. XXII-2. The

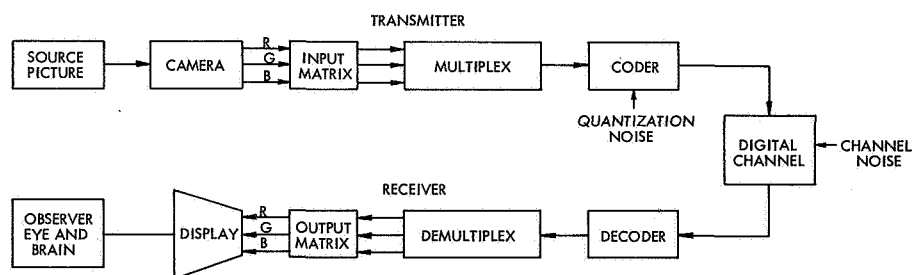


Fig. XXII-2. Color picture transmission system.

source pictures (standard SMPTE and other color transparencies) are scanned by the RCA TK-27 color camera to generate Red (R), Green (G), and Blue (B) signals of 2-MHz bandwidth. These signals may be matrixed, if desired, and multiplexed suitably to give a single analog signal. The analog signal is encoded into a digital stream and transmitted. At the receiver, the digital signal is decoded back to its original analog form, demultiplexed, and displayed on the TM21-B RCA color monitor to reconstruct the

(XXII. COGNITIVE INFORMATION PROCESSING)

original picture. This picture is viewed by the human observer through his eye and evaluated in his brain.

Time-division multiplexing may be more efficient and convenient if the signal is to be transmitted digitally. Thus sequential transmission of color television signals was considered as an alternative approach to matrixing and subcarrier multiplexing. For this purpose, a time-division multiplexing unit was constructed for sampling and multiplexing the color signals at variable bit rates. The two codecs (coder and decoder) that were used primarily in the experiments were the 111 Mb/sec solid-state PCM facility³ of the High Speed PCM Terminal Department of Bell Telephone Laboratories, Inc., for standard PCM, and the Ball Brothers Research Corporation Codec⁴ for the delta modulator. The performance of the codecs and the multiplexing equipment was checked and insured by appropriate noise-loading tests. The noise performance of the multiplexer was at least 10 dB better than a 9-bit PCM coder.

Figure XXII-3 compares the bound on signal-to-quantization-noise ratio for

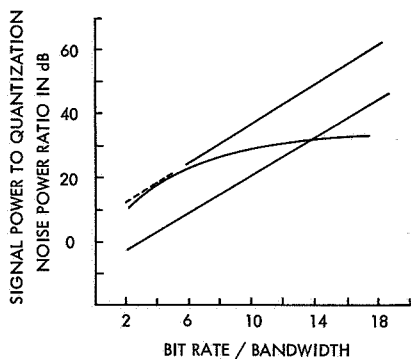


Fig. XXII-3. Comparison of DPCM, ΔM , and standard PCM systems for Gaussian signals.

differential PCM (DPCM), delta modulation (ΔM), and standard PCM systems for Gaussian signal inputs.⁵ This figure indicates how efficient the coding scheme is at the desired signal-to-noise ratio (SNR), or alternatively the best SNR obtainable at the desired bit rate. The SNR given is the rms signal-to-rms noise ratio. To calculate the peak-to-peak signal-to-rms-noise ratio, we have to add 18-20 dB, the amount depending on the statistics of the television signal.⁶ Thus to obtain $(SNR)_{pp}$ of 54, 46, 38, and 29 dB by ΔM , we need bit rates of 16, 8, 4, and 2 times the bandwidth; for standard PCM this figure is approximately 12, 10, 7, and 4 times the bandwidth, respectively. Although for standard PCM, the SNR in dB increases linearly with bit rate, for ΔM it increases only logarithmically. Thus for higher SNR standard PCM would be more efficient than ΔM , and for lower SNR, ΔM would be superior. The quality of a television picture cannot be judged, however, by its SNR alone. Though these analytical results and physically measurable tests are often helpful in making gross judgments, it is the perceptual significance of transmission distortion that is the

(XXII. COGNITIVE INFORMATION PROCESSING)

crucial factor in determining the merit of a transmission system. Only a subjective test can lead to a meaningful judgment in the final evaluation of picture quality.

Evaluation and subjective tests consisted of assigning a comment on the degradation perceived on a high-quality color monitor display. The comments were chosen from a comment scale ranging from 'not perceptible' to 'extremely objectionable,' as indicated in Figs. XXII-5, XXII-7 and XXII-8. The results were viewed by several trained observers in a dark studio with a viewing distance of 4 times the picture height (5 ft). The screen highlight brightness was kept at 25 ft L (85 cd/m^2), and from ten to twelve slides with widely varying color, tones, content, and details were used for the tests. The arithmetic mean of comments from all observers and on all pictures was taken for the final results. The standard deviation in comments for observers was, on the average, 0.5, while that for pictures was 1.0. Thus for accurate evaluation of color picture-transmission schemes not only a large number of observers but also a large number of widely varying pictures should be used.

To study subjective effects of random noise in the three color channels, the experimental arrangement of Fig. XXII-4 was used. The SNR can be varied by the attenuators

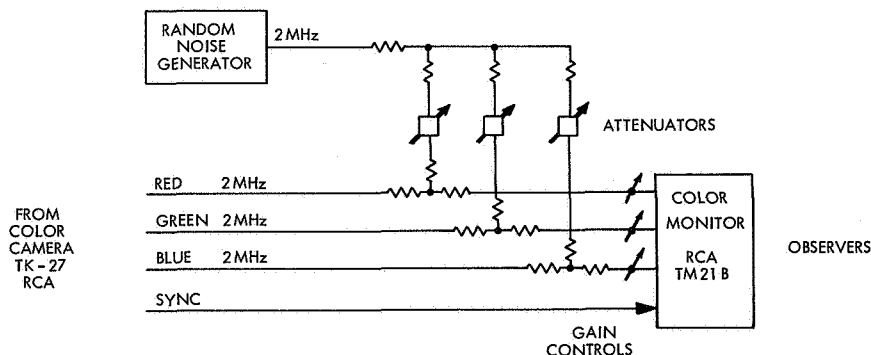


Fig. XXII-4. Experimental arrangement for evaluating the effects of random noise.

for each of the channels. Noise added in this form is perfectly correlated. To observe the effects of uncorrelated noise, delays of 20 and 40 μsec ($1/3$ and $2/3$ of line scanning time) were added to the noise path of two of the channels. For evaluating the subjective effects of degradation by random noise for the channels individually, the SNR in two of the channels were maintained at a level of 55 dB, while the SNR of the third channel varied. The results are shown graphically in Fig. XXII-5. There is an approximate 10-dB difference in the SNR required for the blue, red, and green signals for the same transmission objective (just perceptible, not objectionable, etc.). With noise present in all three channels together, correlated noise, which appears more as luminance

(XXII. COGNITIVE INFORMATION PROCESSING)

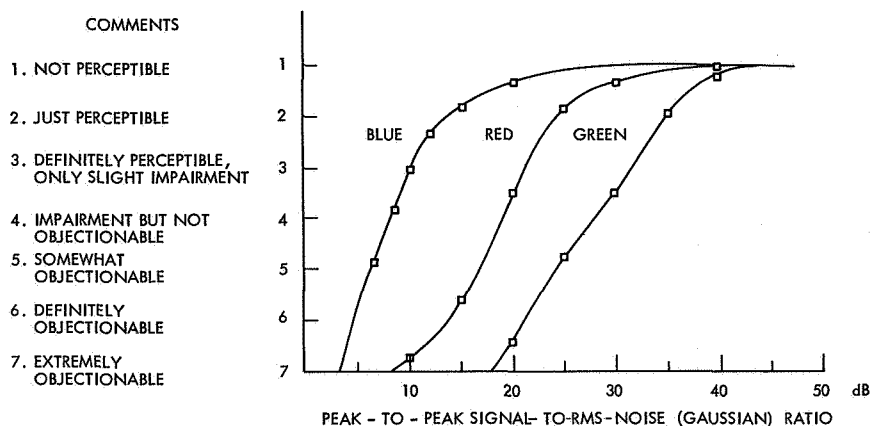


Fig. XXII-5. Subjective effects of random noise in color channels.

degradations, is slightly more degrading than uncorrelated noise, which appears more as true degradations (see Table XXII-1).

Subjective effects of delta-modulation noise and PCM quantization noise in the three color channels were evaluated by individually coding and decoding each of the color

Table XXII-1. Effects of correlated and uncorrelated random noise.

Source	SNR (db)			Mean Comment
	Green	Red	Blue	
Correlated	35	25	15	3.5
Correlated	37	27	17	3.1
Correlated	40	30	20	2.1
Uncorrelated	39	28	10	4.1
Uncorrelated	36	25	14	4
Uncorrelated	40	30	18	2.3
Uncorrelated	40	30	20	1.8
Uncorrelated	42	31	21	1.4
Uncorrelated	43	32	24	1

signals while directly transmitting the other two (unimpaired analog signals) (see Fig. XXII-6). The results for delta modulation are summarized in Fig. XXII-7. The bit rates for transmission by ΔM that are required for a given transmission objective may be determined from Fig. XXII-7. For a transmission objective of 4 (impairment but not objectionable) the bit rates required by the green, red, and blue signals are 9, 8, and 4 mB/sec, respectively. ΔM is slightly more degrading subjectively than

(XXII. COGNITIVE INFORMATION PROCESSING)

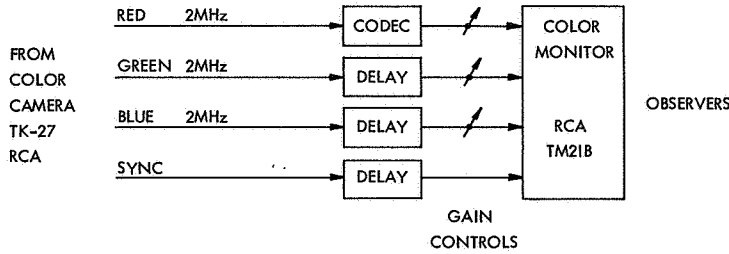


Fig. XXII-6. Experimental arrangement for evaluating the effects of modulation noise and quantization noise.

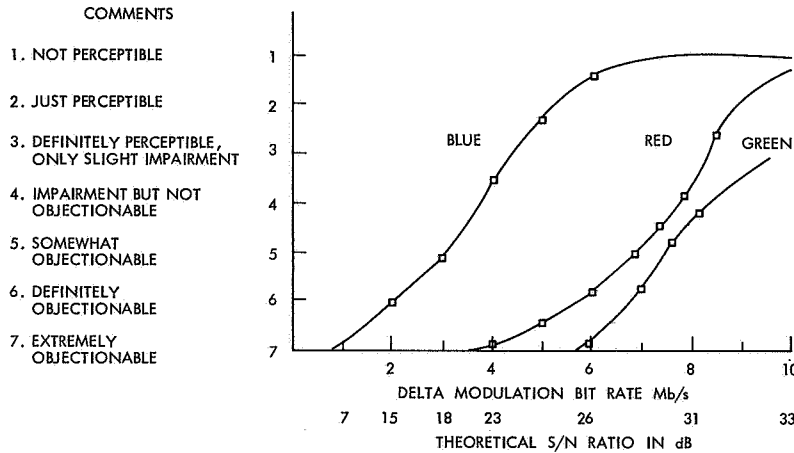


Fig. XXII-7. Subjective effects of ΔM noise in color channels.

random noise for the same SNR.

In transmission of signals by standard PCM much higher SNR are required, as PCM quantization noise is subjectively most annoying. The subjective effects of PCM quantization noise are shown graphically in Fig. XXII-8. For a comment of 4 the quantization bits required for the green, red, and blue signals are 5, 5, and 4, respectively. This corresponds to SNR of 40, 40, and 34 dB, which is much higher than the 32, 31, and 23 dB required by delta modulation. Not only is delta modulation more efficient in terms of SNR but also at the low SNR involved delta modulation requires a lower bit rate for transmission than standard PCM, as shown in Fig. XXII-3. The crossover point when standard PCM becomes more efficient than delta modulation for the same SNR is at 50 dB peak-to-peak signal-to-rms noise ratio.

Three different kinds of filters were used for bandlimiting the color signals, and the subjective effect on the composite picture was evaluated. The filters were the Thomson and the overshoot filters which were identified by their 20-dB down point, and

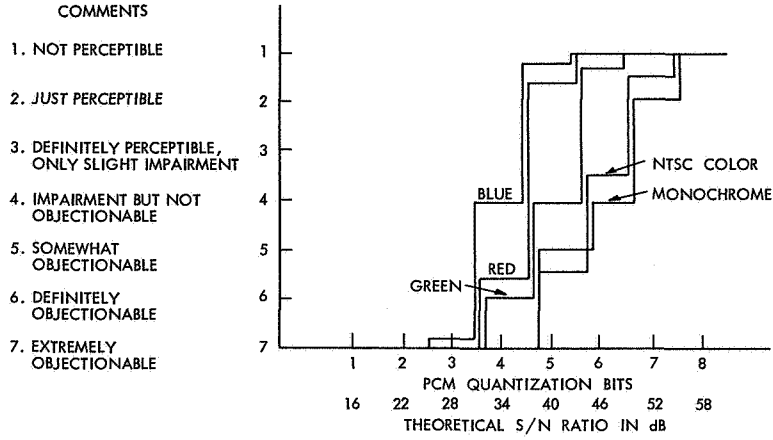


Fig. XXII-8. Subjective effects of PCM quantization noise in color signals.

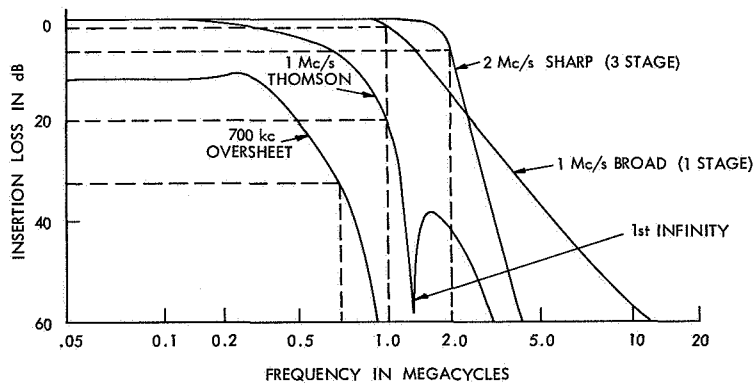


Fig. XXII-9. Filter characteristics.

Table XXII-2. Lowpass filtering of color signals.

	Blue	Red	Green	Mean Comment
Thomson	0.7 MHz	Thomson 1.5 MHz	Original 2 MHz	4
Thomson	1	Thomson 1.5	Original 2	2
Thomson	1	Thomson 1	Original 2	2.5
Thomson	1	Broad 1	Original 2	2
Overshoot	0.7	Broad 1	Original 2	2.5
Overshoot	0.7	Overshoot 1.5	Original 2	4.5

the broad filter, which was identified by its design frequency, f_c . The filter characteristics are shown in Fig. XXII-9. The overshoot filter acts as a crispener, by overemphasizing the steepness of transition at edges. It achieves edge enhancement by addition of the inverted second derivative (or approximate) of the image signal to the image signal.⁷ The overshoot filter also produces a ring, because of its sharp cutoff characteristics. The comments obtained about the composite picture when the indicated filters were used are shown in Table XXII-2. The ringing caused by the overshoot filter is not perceptible in the blues, but is objectionable in the reds and results in a false chroma edge.

To determine the subjective effects of degradations introduced during sampling, the color signals were sampled at variable rates by the time-division multiplexing unit built for this purpose. Fig. XXII-10 shows the results of sampling the individual color channels at different sampling rates. In these experiments only one signal was sampled and the other two transmitted directly. The filter losses at the sampling rate and half the sampling rate were computed and the results are shown in Table XXII-3.

The efficiency of transmission by standard PCM can be improved by judicious choice of sampling frequency. The idle bands generated in the spectrum of a television signal, because of the scanning process, can be shared by frequency-interleaving⁸ it with the image band around the sampling frequency, thereby minimizing foldover distortion. When such is the case, we no longer need to sample at the Nyquist rate of twice the bandwidth, but at a much lower rate. Thus an 800-kHz blue signal can be sampled at a frequency of 1.15 MHz (see Fig. XXII-10) with almost no perceptible degradations. The filter losses required for the blue, red, and green signals are indicated to be approximately 4, 7, and 12 dB at half the sampling frequency, and 16, 36, and 44 dB at the sampling frequency. For monochrome signals comparable results are 16-19 dB at half the sampling rate, and 38 dB at the sampling rate.⁹ A comparison of bit rates required for sequential transmission of color signals by delta modulation and standard PCM is shown in Table XXII-4 for different transmission objectives.

For the NTSC signal transmitted by standard PCM (quantized to 6 bits and sampled at 9 MHz) the bit rate required is 54 Mb/sec. This represents a transmission objective of 3-4. Taking into account the fact the combined degradation in the picture from all three signals will make it subjectively worse (this effect is approximately one step on the comment scale), we need approximately 26 Mb/sec for transmission by delta modulation and 33 Mb/sec for transmission by standard PCM for the same transmission objective in a sequential transmission system. The picture in the last case will not be as sharp, however, because the green signal transmitted is of 2-MHz quality. For a sharper picture a bit rate only slightly higher would be required. Thus for digital transmission of color signals, time-division multiplexing would be more efficient than frequency-division multiplexing by a considerable amount. The bit rate required

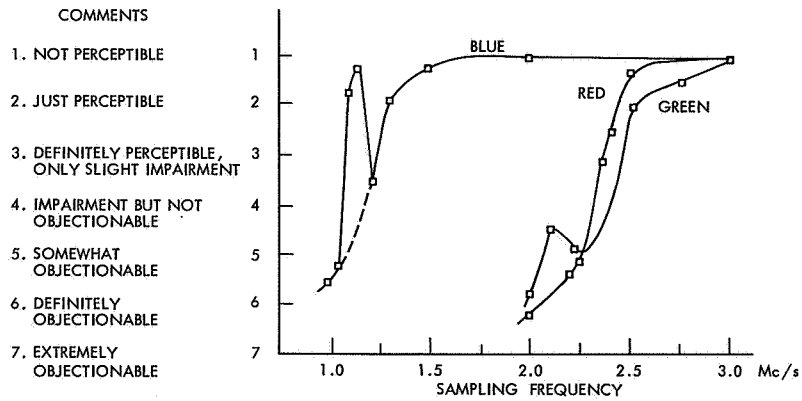


Fig. XXII-10. Subjective effects of sampling degradations in color channels.

Table XXII-3. Sampling of signals and filter insertion losses.

Signal	Sampling Rate (Mc/sec)	Combined Filter Loss at Half Sampling Rate	Output Filter Loss at Sampling Rate	Mean Comment
Blue	1.0	1.5	7	5.5
	1.05	1.8	8.5	5.2
	1.10	2.0	10	1.7
	1.15	2.2	10.5	1.2
	1.20	2.3	11	3.6
	1.30	2.6	12	1.8
	1.50	4	16	1.2
	2.0	17	26	1
Red	2.0	7	11	6.2
	2.20	8	22	5.4
	2.25	9	27	5.1
	2.35	9.5	30	3.1
	2.40	10	34	2.5
	2.50	11	36	1.3
	3.0	16	66	1
	Green	2.0	7	11
2.10		7.5	17	4.5
2.25		9	28	4.8
2.5		11	36	2
2.75		12	44	1.5
3.0		16	50	1

Table XXII-4. Comparison of standard PCM and delta modulation.

Trans- mission Objective	Delta Modulation				Standard PCM										Total Bit Rate		
	Green	Red	Blue	Total Bit Rate	Green		Red		Blue		S.R.		Q.B.			B.R.	
					S.R.	Q.B.	B.R.	S.R.	Q.B.	B.R.	S.R.	Q.B.	B.R.	S.R.	Q.B.	B.R.	
1-2	16	10	6	32	3	6	18	2.5	5	12.5	1.5	5	7.5	38			
2-3	12	8.5	5	25.5	2.5	6	15	2.35	5	11.75	1.25	5	6.25	33			
3-4	9	8	4	21	2.4	6	14.4	2.30	5	11.50	1.2	5	6	31.9			
4-5	8	7	3	18	2.3	5	11.5	2.25	5	11.25	1.1	4	4.4	27.2			
5-6	7	6	2.5	15.5	2.25	5	11.25	2.0	4	8	1	4	4	23.3			

S.R. - Sampling rate in MHz

Q.B. - Quantization bits

B.R. - Bit rate in Mb/sec

(XXII. COGNITIVE INFORMATION PROCESSING)

for transmission of the NTSC signal by delta modulation was not determined, but it is suspected to be much higher, as the NTSC signal is very sensitive to the phase and amplitude errors that delta modulation will introduce.

A great amount of frame-to-frame redundancy exists in the color television signal, and this can be exploited by using delays that can store entire frames. The highlight brightness for the blue and red signals is much lower, and this considerably reduces the critical flicker frequency. This fact can be exploited by transmitting fewer frames per second for these signals. Also, the vertical resolution in the color pictures is greater than necessary. It is more difficult to resolve the line structure in the Blue and Red components of the picture, than for the luminance component. Low-cost line delays may be used to further exploit the redundancy in vertical resolution. Such techniques seem to be very promising, and further investigation is called for.

The transmission of a low-resolution monochrome signal by several kinds of differential PCM schemes was also studied. We found that for the same bit rate a 3-bit DPCM system produces a picture that is less noisy than either ΔM or 2-bit DPCM pictures, but subjectively the ΔM picture is preferred, because of the sharpness resulting from the permitted higher sampling rate. For a higher quality of transmission, the 3-bit DPCM system would be more efficient, as indicated by Fig. XXII-3.

A. K. Bhushan

References

1. This work was done at Centre 321, Bell Telephone Laboratories, Inc., Holmdel, New Jersey, and was submitted as a thesis in partial fulfillment of the requirements for the degree of Master of Science, Department of Electrical Engineering, M.I.T., June 1967, with the title, "Efficient Transmission and Coding of Color Pictures."
2. A. K. Bhushan, "Efficient Transmission and Coding of Color Pictures," S.M. Thesis, M.I.T., June 1967.
3. J. O. Edson and H. H. Henning, "Broadband Codecs for an Experimental 224 Mb/s PCM Terminal," *Bell System Tech. J.* 44, 1887-1940 (1965).
4. Ball Brothers Research Corporation, Boulder, Colorado, "Technical Manual for BBRC Variable Bit Rate A/D-D/A Converter," n. d.
5. J. B. O'Neal, Jr., "A Bound on Signal to Quantizing Noise Ratio for Digital Encoding Systems," *Proc. IEEE* 55, p. 862 (1967).
6. J. B. O'Neal, Jr., "Quantizing Noise in Delta Modulation for Gaussian and Television Signals," *Bell System Tech. J.* 45, 117-142 (1966).
7. E. F. Brown, "A New Crispener Circuit for Television Images," *SMPTE J.* 72, 849 (November 1963).
8. P. Mertz and F. Gray, "A Theory of Scanning and Its Relation to the Characteristics of the Transmitted Signal in Telephotography and Television," *Bell System Tech. J.* 34, 464 (July 1934).
9. F. W. Mounts, "An Experimental Digital System for Evaluating Bandwidth Reduction Techniques," *Bell System Tech. J.* 47, 181 (January 1967).

C. SUBJECTIVE EFFECT OF ADDITIVE WHITE PICTORIAL NOISE WITH VARIOUS PROBABILITY DISTRIBUTIONS

The purpose of this study was to find out how strongly the objectionability of pictorial noise depends on its probability distribution.

The noisy pictures were generated on a digital computer. A picture with a cameraman as a central object was used as the original, to which noise with various probability distributions was added.

For the simulation on the computer the picture was divided into 256×256 points, and the intensity at these points quantized to $2^{10} = 1024$ levels. The noise was generated by using the random-number generator subroutine of the computer in conjunction with suitable transformations. To the picture samples were then added the noise samples, thus producing the output noisy picture. The noise samples were independent of each other and of the original picture samples.

The signal-to-noise ratio, S/N , is defined as

$$\frac{S}{N} = 10 \log_{10} \frac{S_{\max}^2}{\sigma^2} = 20 \log_{10} \frac{S_{\max}}{\sigma},$$

where

S_{\max} = peak signal amplitude = 1023

σ^2 = variance of the noise.

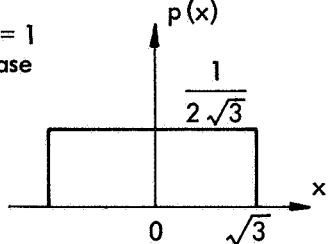
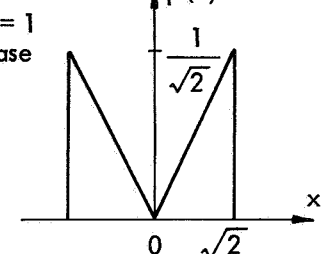
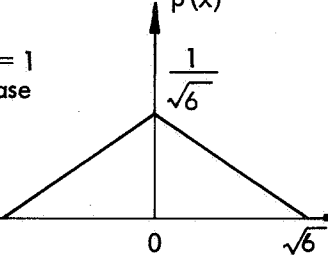
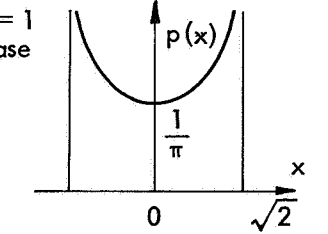
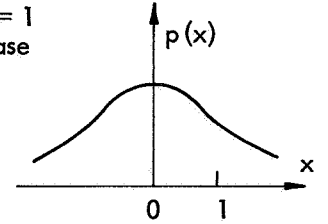
Table XXII-5 shows the signal-to-noise ratios that were used and the corresponding values of σ and σ^2 .

Table XXII-6 shows the probability distributions that were used, together with their variances.

Table XXII-5. Signal-to-noise ratios.

S/N (db)	σ	σ^2
26	51.2	2620
22	81.3	6610
20	102.3	10485
18	129	16650
14	204	41620

Table XXII-6. Probability distributions.

<p>Uniform Distribution</p>	<p>$\sigma = 1$ case</p> 	$p(x) = \begin{cases} \frac{1}{2 \cdot a} & x < a \\ 0 & x > a \end{cases}$ $\sigma^2 = \frac{1}{3} \cdot a^2$
<p>Inverse Triangular Distribution</p>	<p>$\sigma = 1$ case</p> 	$p(x) = \begin{cases} \frac{1}{a^2} \cdot x & 0 < x < a \\ -\frac{1}{a^2} \cdot x & -a < x < 0 \\ 0 & \text{otherwise} \end{cases}$ $\sigma^2 = \frac{1}{2} \cdot a^2$
<p>Triangular Distribution</p>	<p>$\sigma = 1$ case</p> 	$p(x) = \begin{cases} \frac{1}{a} - \frac{1}{a^2} \cdot x & 0 < x < a \\ \frac{1}{a} + \frac{1}{a^2} \cdot x & -a < x < 0 \\ 0 & \text{otherwise} \end{cases}$ $\sigma^2 = \frac{1}{6} \cdot a^2$
<p>"Sine" Distribution</p>	<p>$\sigma = 1$ case</p> 	$p(x) = \begin{cases} \frac{1}{\pi} \cdot \frac{1}{\sqrt{a^2 - x^2}} & x < a \\ 0 & x > a \end{cases}$ $\sigma^2 = \frac{1}{2} \cdot a^2$
<p>Gaussian Distribution</p>	<p>$\sigma = 1$ case</p> 	$p(x) = \frac{1}{\sqrt{2\pi} \cdot a} \cdot e^{-\frac{x^2}{2a^2}}$ $\sigma^2 = a^2$

(XXII. COGNITIVE INFORMATION PROCESSING)

Table XXII-7 shows the values of a (see Table XXII-6) for the various probability distributions and the different signal-to-noise ratios.

The fourth moments were also computed; their values are shown in Table XXII-8.

Table XXII-7. Values of a .

Distribution \ S/N	26	22	20	18	14
Uniform	88.8	141.0	177.8	223.9	354.0
Inverse triangular	72.4	115.0	144.9	182.4	288.8
Triangular	125.4	199	251	316	500
"Sine"	72.4	115.0	144.9	182.4	288.8
Gaussian	51.2	81.3	102.3	129	204

Table XXII-8. Values of x^4 . (These values have to be multiplied by 10^6 .)

Distribution \ S/N	26	22	20	18	14
Uniform	12.37	78.8	198.0	500.0	3120
Inverse triangular	9.13	58.1	146.3	368	2310
Triangular	1.83	11.7	29.3	74.0	462
"Sine"	10.3	65.5	165	416	2600
Gaussian	20.6	131	330	832	5200

By inspection of the noisy pictures, we found that the difference between the objectionabilities of noises having the same variance but different probability distributions was hardly noticeable, although the fourth moments of the noises were quite different. It seems therefore, that for pictures with additive white noise, the signal-to-noise ratio can be used as a good measure of picture quality for a wide class of noise probability distributions, including at least the five that we studied.

T. S. Huang, H. P. Hartmann

(XXII. COGNITIVE INFORMATION PROCESSING)

D. STOCHASTIC MODEL FOR WEATHER MAPS

An investigation was undertaken¹ to see if a two-state Markov source² was an adequate model for weather maps in the following sense. Segments of weather maps were quantized into an $n \times n$ array of 1's and 0's. The array was then scanned in line-by-line fashion. The one-dimensional sequence of zeros and ones thus generated was modeled as a stochastic source, for which line-to-line dependencies in the original picture were ignored.

The two-state Markov model implies that the run lengths are independent and geometrically distributed. Three statistical tests were performed to test the hypotheses that the one runs were independent, the zero runs were independent, and the one runs were independent of the zero runs. The results of the last two tests were consistent with the hypothesis of independence at approximately the .05 level of significance. The first hypothesis was rejected, however, at the same significance level. The test of the one runs was repeated, only those one runs being counted were preceded by a one run of length 3 or larger. This was motivated by the fact that the pictures present regions of high detail and other regions of low detail. If a different run-length density were used within each region, the resulting model might be more accurate. This test (at the .05 level) was consistent with the hypothesis of independence. The experimental probability transition functions were calculated and compared with the geometric run-length probabilities of the two-state Markov model. The Chi-Square test of significance was used in this comparison. The tests indicated a significant deviation; however, graphs of the data revealed that the geometric approximation was apparently quite good.

Sequences of run lengths from the pictures were coded by using Huffman coding. The probability of overflow and the expected amount of overflow were determined from the data. We chose to encode $T = 1800$ cells at a time. If a maximum of $RT = .575 \times 1800$ bits were used in encoding the original 1800 cells, the expected overflow would be 7 bits. The entropy of the pictures as calculated from the model was .455 bits. A bound to the probability of overflow was derived which is exponentially decreasing in T , the number of cells encoded for a given rate R (=number of bits allowed in encoding T cells/ T). From this, a bound to the expected over-flow was calculated. Both of these bounds were quite loose when compared with the actual data for $T = 1800$.

J. W. Woods

References

1. J. Woods, "Run-Length Coding of Weather Maps," S.M. Thesis, Department of Electrical Engineering, M.I.T., June 1967.
2. J. Capon, "A Probabilistic Model for Run-Length Coding of Pictures," IRE Trans., Vol. IT-5, No. 4, No. 4, pp. 157-163, December 1959.

XXIII. NEUROPHYSIOLOGY*

Academic and Research Staff

Dr. W. S. McCulloch	Dr. T. O. Binford	Dr. A. Natapoff
Prof. J. Y. Lettvin	Dr. S-H. Chung	Dr. S. A. Papert
Prof. P. D. Wall	Dr. J. L. S. da Fonseca	Dr. A. Taub
Prof. M. Blum	Dr. H. Hartman	B. Howland
Prof. J. E. Brown	Dr. Dora Jassik-Gerschenfeld	Diane Major
Prof. P. R. Gross	Dr. K. Kornacker	W. H. Pitts
Prof. B. Pomeranz	Dr. T. McLardy	Sylvia G. Rabin
	Dr. R. Moreno-Diaz	

Graduate Students

E. E. Fetz	J. I. Simpson
G. P. Nelson	W. A. Wright

N67-27104

A. CONTRAST DETECTORS[†]

Lateral subtractive inhibition may occur at the retinal bipolar level, thereby enabling a contrast-detection process in which each "contrast bipolar" cell could detect any spatial change of the intensity of light incident in its receptive field. In such a situation, the locus of the contrast bipolar cells that fire at any time gives the contour of any sharply contrasted image on the retina at this time. A contrast-detector ganglion cell receiving signals from an area that contains many contrast bipolar cells thereby senses a significant part of that contour as limited by the object size-ganglion field relationship. Its rate of firing is different for different shapes and sizes of the image and for different velocities of a moving image. It is, therefore, desirable to obtain simple expressions relating ganglion tone to the aforementioned parameters that are consistent with, and supported by, neurophysiological evidence.

In particular, we shall be concerned with the dependence of ganglion tone upon the length of the contrast, or edge, of the image and upon its velocity. By applying a process used to model a specific visual ganglion cell,¹ we can obtain one expression for such a dependence. The process to which we refer is the lateral (nonlinear) inhibition at the level of the ganglion cell dendrites. All that we require is, first, that there be a single horizontal dendritic layer for the contrast ganglion cell, and second, that signals arriving there from bipolar cells interact by lateral nonlinear inhibition. Either divisive inhibition or exponential inhibition would be adequate for this task. We chose, for simplicity, to use exponential inhibition² in our formulations.

*This work was supported by the National Institutes of Health (Grant 5 ROI NB-04985-04), and in part by the U.S. Air Force (Aerospace Medical Division) under Contract AF33(615)-3885.

[†]This work was done partly at the Instrumentation Laboratory under the auspices of DSR Project 55-257, sponsored by the Bioscience Division of National Aeronautics and Space Administration through Contract NSR 22-009-138.

(XXIII. NEUROPHYSIOLOGY)

For the sake of simplicity, we assume: First, that the contrast bipolars are uniformly distributed throughout the retina and that their number is large enough to permit the assignment of "linear density" (λ), the number of contrast bipolar cells per unit retinal length, as a constant. Second, we assume that bipolar cells give rise to pulses (action potentials) of constant amplitude (p) and constant duration (τ), and that they contain refractory periods of sorts.

If the image of a sharply contrasted object is stationary with respect to the retina, and l is the length of the edge in the contrast ganglion cell receptive field, this cell receives pulses from n_o contrast bipolar cells, in which

$$n_o = l\lambda. \quad (1)$$

If the image moves with respect to the retina, with velocity of absolute value u , the ganglion cell will receive pulses from n_e additional bipolar cells such that n_e is approximately given by

$$n_e = u \cdot \tau l \lambda^2. \quad (2)$$

The total number, n , of bipolar cells exciting the ganglion cell is given by

$$n = n_o + n_e = l\lambda(1+u\tau\lambda). \quad (3)$$

If the lateral exponential inhibition occurs, the contribution of a single bipolar cell to the activity of the ganglion cell is given by

$$p \cdot e^{-kp(n-1)}, \quad (4)$$

where k is a constant that determines the strength of the inhibitory action. Under the assumption that contributions are additive, the total activity, A_c , of the ganglion cell is given by

$$A_c = \sum p e^{-kp(n-1)}, \quad (5)$$

where the summation is over all of the bipolar cells that are firing, that is, n . Then,

$$A_c = np e^{-kp(n-1)}. \quad (6)$$

By substituting Eq. 3 in Eq. 6 and renaming the constants, we obtain

$$A_c = K_1 l (1+K_3 u) e^{-K_2 l (1+K_3 u)}, \quad (7)$$

where

$$K_1 = \lambda p e^{kp}$$

$$K_2 = k p \lambda$$

$$K_3 = \tau \lambda.$$

Let the frequency (tone), f , of the ganglion cell be linearly related to its activity; that is,

$$f = aA_c + b, \quad f \geq 0, \quad (8)$$

where b , if positive, is the spontaneous firing frequency. A negative value of b may be interpreted as threshold.

Let us define z as

$$z \equiv 1(1+K_3 u). \quad (9)$$

The maximum value of f occurs when $\frac{\partial f}{\partial z} = 0$, that is, for a value of z (represented by Z_{opt}), in which

$$Z_{opt} = \frac{1}{K_2}. \quad (10)$$

For a stationary object ($u=0$) there is an optimum edge length in the retinal field which produces a maximum response. This is

$$l_{opt} = \frac{1}{K_2}. \quad (11)$$

For moving objects of constant edge length, l_o , there is an optimum velocity, U_{opt} , which produces a maximum f and is given by

$$U_{opt} = \frac{1}{K_3} \left(\frac{1}{K_2 l_o} - 1 \right). \quad (12)$$

In any case, the maximum frequency is given by

$$f_{max} = a \frac{K_1}{K_2 e} + b. \quad (13)$$

Since only the absolute value of the velocity u appears in the expressions above, a negative value for U_{opt} has no meaning. Therefore, for a given edge length, l_o , the maximum frequency can be obtained only if

$$K_2 l_o \leq 1. \quad (14)$$

The case $K_2 l_o = 1$ corresponds to the optimum stationary edge, that is, a maximum

(XXIII. NEUROPHYSIOLOGY)

ganglion tone that is due to a stationary edge, as given by Eq. 11.

Properties that are qualitatively similar to the ones described here – and that have oriented our work – have been reported for the group 1 ganglion cells in the frog's retina.^{3,4}

R. Moreno-Diaz

References

1. R. Moreno-Diaz, "Modeling the Group 2 Ganglion Cell of the Frog's Retina," Quarterly Progress Report No. 81, Research Laboratory of Electronics, M.I.T., April 15, 1966, pp. 227-236.
2. Exponential inhibition may be formulated as follows: Let E and I be the excitatory and inhibitory signals. After inhibition, the resulting signal (activity) is $E \cdot e^{-KI}$, where K is a constant. See, for example, J. J. Shypperheyn, "Contrast Detection in Frog's Retina," *Acta Physiol. Pharmacol. Neerl.* 13, 231-277 (1965).
3. J. Y. Lettvin, H. R. Maturana, W. H. Pitts, and W. S. McCulloch, "Two Remarks on the Visual System of the Frog," in *Sensory Communication*, W. A. Rosenblith (ed.) (The M.I.T. Press, Cambridge, Mass., and John Wiley and Sons, Inc., New York and London, 1961), pp. 757-776.
4. R. Grusser-Cornehls, O. J. Grusser, and T. H. Bullock, "Unit Responses in the Frog's Tectum to Moving and Non-moving Visual Stimuli," *Science* 141, 820-822 (1963).

B. INSIGHT INTO NEURONAL CLOSED LOOPS FROM SHIFT-REGISTER THEORY*

In 1943, Pitts and McCulloch¹ produced three theorems showing that nets with circles could compute only those numbers that a Turing machine could compute with a finite tape. Recently, Minsky and Papert² have reported several theorems applicable to them, and our group has presented some in previous reports.³⁻⁶ Since Wiener's pioneering treatment of nonlinear filters, little progress has been made, until last year when Caianiello published two items in *Kybernetik*.^{7,8}

In the meantime, a theory of shift registers has grown up independently, depending on Galois Fields, initiated by Huffman's^{9,10} analysis of their use in coding, and a subsequent evolution of theorems of limited generality.¹¹⁻²⁴ It has not been recognized that all such devices were within the scope of nerve net theory, although the converse is not generally true in the present state of the art. As their theory is relatively complete²⁵⁻²⁹ (except for fully nonlinear shift registers with inputs), it is clear that shift-register theory can sometimes be extended from Boolean functions of 0 and 1 to any finite field of integers, and in some cases to the field of real numbers,³⁰⁻³² and perhaps even of complex numbers.

There is no apparent reason why these theories may not ultimately be extended to all closed-loop structures in finite automata of neuron nets of proper neuromimes. We still do not know how to extend this theory to the general problems of nonlinear anastomotic nets with inputs.

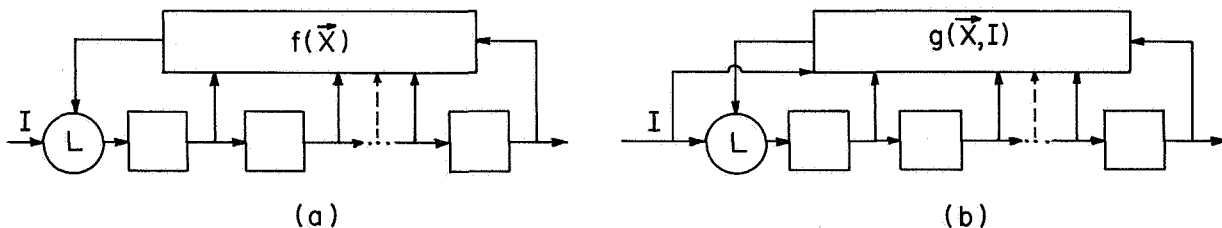


Fig. XXIII-1. Nonlinear feedback shift register for control (a) and command (b).

Even without that, the utility of these notions foreshadows a great extension of neuronal modelling in the design of circuits for command and control, as well as in the programming of commands for which shift registers are eminently suitable. We already have simple solutions for temporal sequences in nonlinear feedback shift registers.

*This work was done partly at the Instrumentation Laboratory under the auspices of DSR Project 55-257, sponsored by the Bioscience Division of the National Aeronautics and Space Administration through Contract NSR 22-009-138.

(XXIII. NEUROPHYSIOLOGY)

For example, we have found conditions for driving the state of nonlinear feedback shift registers with input through any logical gate of types (a) and (b) (see Fig. XXIII-1). In this figure

I = Input

L = Logical gate

\vec{X} = The vector that defines the state of the n delay elements of an nth-order shift register

$f(\vec{X})$ = Any Boolean function of the n components of \vec{X}

$g(\vec{X}, I)$ = Any Boolean function of the components of \vec{X} and I.

W. S. McCulloch, J. L. S. da Fonseca

References

1. W. S. McCulloch and W. H. Pitts, "A Logical Calculus of the Ideas Immanent in Nervous Activity," *Bull. Math. Biophys.* 9, 127-247 (1943).
2. M. L. Minsky and S. A. Papert, "Unrecognizable Sets of Numbers," *Project MAC Progress Report III*, Massachusetts Institute of Technology, July 1965-July 1966, pp. 18-20.
3. M. Blum, "Properties of a Neuron with Many Inputs," in *Principles of Self-Organization*, H. von Foerster and G. Zopf (eds.) (Pergamon Press, Oxford and New York, 1961), pp. 95-119.
4. C. P. J. Schnabel, "Number of Modes of Oscillation of a Net of N Neurons," *Quarterly Progress Report No. 80*, Research Laboratory of Electronics, M. I. T., January 15, 1965, p. 253.
5. R. Moreno-Diaz, "Realizability of a Neural Network Capable of All Possible Modes of Oscillation," *Quarterly Progress Report No. 82*, Research Laboratory of Electronics, M. I. T., July 15, 1966, pp. 280-285.
6. R. Moreno-Diaz, "Stability of Networks with Loops," *Quarterly Progress Report No. 83*, Research Laboratory of Electronics, M. I. T., October 15, 1966, pp. 165-171.
7. E. R. Caianiello and A. De Luca, "Decision Equation for Binary Systems. Application to Neuronal Behavior," *Kybernetik* 3, 33-40 (1966).
8. E. R. Caianiello, "Decision Equation and Reverberation," *Kybernetik* 3, 98-99 (1966).
9. D. A. Huffman, "The Synthesis of Linear Sequential Coding Networks," in *Information Theory*, C. Cherry (ed.) (Butterworths, London, 1955), pp. 77-95.
10. D. A. Huffman, "A Linear Circuit Viewpoint on Error-Correcting Codes," *IRE Trans.*, Vol. IT-2, 20-28, 1956.
11. M. Cohn, "Controllability in Linear Sequential Networks," *IRE Trans.*, Vol. CT-9, pp. 74-78, 1962.
12. B. Elspas, "The Theory of Autonomous Linear Sequential Networks," *IRE Trans.*, Vol. CT-6, pp. 45-60, 1959.
13. P. Fire, "Boolean Operations on Binary Markov Chains," Report EDL-L 27, Sylvania Electronic Defense Laboratories, 1964.
14. B. Friedland and T. E. Stern, "On Periodicity of States in Linear Modular Sequential Circuits," *IRE Trans.*, Vol. IT-5, pp. 136-137, 1959.

(XXIII. NEUROPHYSIOLOGY)

15. B. Friedland, "Linear Modular Sequential Circuits," IRE Trans., Vol. CT-6, pp. 61-68, 1959.
16. W. Golomb, "Sequences with Randomness Properties," Final Report on Contract No. W 36-039 SC-54-36611, Glenn L. Martin Co., Baltimore, Md., 1955.
17. J. Hartmanis, "Linear Multivalued Sequential Coding Networks," IRE Trans., Vol. CT-6, pp. 69-74, 1959.
18. J. Massey, "Shift-Register Synthesis and BCH Decoding" (personal communication).
19. F. J. Mowle, "Enumeration and Classification of Stable Feedback Shift Registers," Technical Report No. EE-661, Department of Electrical Engineering, University of Notre Dame, Notre Dame, Indiana, 1966.
20. W. W. Peterson, Error Correcting Codes (The M. I. T. Press, Cambridge, Mass., 1961).
21. C. V. Srinivasan, "State Diagram of Linear Sequential Machines," J. Franklin Inst. 273, 383-418 (1962).
22. T. E. Stern and B. Friedland, "The Linear Modular Sequential Circuit Generalized," IRE Trans., Vol. CT-8, pp. 79-80, 1961.
23. N. Zierler, "Several Binary-Sequence Generators," Technical Report No. 95, Lincoln Laboratory, M. I. T., 1955.
24. N. Zierler, "Linear Recurring Sequences," SIAM J. 7, 31-48 (1959).
25. S. W. Golomb, "Non-Linear Shift Register Sequences," Memorandum No. 20-149, Jet Propulsion Laboratory, California Institute of Technology, Pasadena, California, 1957.
26. S. W. Golomb, L. R. Welch, and R. M. Goldstein, "Cycles from Non-Linear Shift Registers," Jet Propulsion Laboratory, California Institute of Technology, Pasadena, California, 1959.
27. K. B. Magleby, "The Synthesis of Nonlinear Feedback Shift Registers," Technical Report No. 6207-1, Stanford Electronics Laboratories, Stanford, California, 1963.
28. J. Massey and R. Liu, "Equivalence of Nonlinear Shift Registers," IEEE Trans., Vol. IT-10, pp. 378-379, 1964.
29. K. Fukunaga, "A Theory of Nonlinear Autonomous Sequential Nets Using Z Transforms," IEEE Trans., Vol. EC-13, pp. 310-312, 1964.
30. T. Kubista and J. Massey, "Pseudo-Linear Generalized Shift-Registers," Department of Electrical Engineering, University of Notre Dame, Notre Dame, Indiana, 1966.
31. J. Massey and R. Liu, "Application of Lyapunov's Direct Method to the Error-Propagation Effect in Convolutional Codes," IEEE Trans., Vol. IT-10, pp. 248-250, 1964.
32. C. M. Rader and B. Gold, "Digital Filter Design Techniques in the Frequency Domain," Proc. IEEE 55, 149-170 (1967).

XXIV. COMPUTATION RESEARCH*

Research Staff

Martha M. Pennell
Heather S. Davis

Gail M. Fratar
Joan Harwitt

Elaine C. Isaacs
Eleanor C. River

N67-27105

A. FINDING THE ROOTS OF AN ANALYTIC FUNCTION

The root-finding method described in Quarterly Progress Report No. 84 (pages 351-352) has been implemented on the Electronic Systems Laboratory Display Console at Project MAC, using the TOCS (TACT On-Line Computing System) developed by Project TACT at Harvard University.^{1,2}

TOCS is an interpreter intended for use by the scientist with no prior programming experience. It provides a set of operators to act on variable-length real and complex vectors created by the user. TOCS has been given additional power and flexibility by the addition of display facilities, capabilities for limited algebraic manipulation, the editing facilities of TYPSET, and facilities for incorporating user-created BSS files into the TOCS. The user may write his own "console program," employing both the TOCS operators and programs written in other languages, such as MAD.

We are planning to introduce TOCS to members of the Research Laboratory of Electronics to determine its usefulness in their research. If the response is encouraging, we shall explore the possibility of using the version being developed for the 360 computer by TACT.

Eleanor C. River

References

1. K. B. Winiecki, "TACT On-Line Computing System, Version II," Manual - Technological Aids to Creative Thought Project, Harvard University, Cambridge, Massachusetts, December 13, 1966.
2. A. Ruyle, "The Status of TOCS," Memorandum 44, Technological Aids to Creative Thought Project, Harvard University, Cambridge, Massachusetts, November 10, 1966.

*This work was supported in part by the Joint Services Electronics Programs (U.S. Army, U.S. Navy, and U.S. Air Force) under Contract DA 28-043-AMC-02536(E).

PRECEDING PAGE BLANK NOT FILMED.

Author Index

Allen, J. L., 69
Andrews, M. L., 87
Babitch, D., 1
Baggeroer, A. B., 249
Barrett, A. H., 16, 23
Bartsch, R. R., 146
Bekefi, G., 128
Bell, C. M., 1
Bers, A., 128, 163, 168
Bhushan, A. K., 307
Biemann, K., 33
Bowers, K. W., 13, 14
Briggs, R. J., 183
Brown, S. C., 71
Burke, B. F., 22, 23
Chou, S-L., 168
Chung, K., 193
Cohen, A. J., 103
Collins, L. D., 253
Davis, J. A., 178
Edwards, K. R., 201
Fertel, Jeanne H., 39
Fiocco, G., 49
da Fonseca, J. L. S., 325
Gaut, N. E., 16, 19
Glaser, J. I., 36
Goff, M. E., 32
Grams, G. W., 49
Gustafson, T. K., 56
Halle, M., 267
Hartmann, H. P., 317
Haus, H. A., 51, 201
Heeschen, C., 284
Herba, F. N., 154
Hofmann, T. J., 297
Huang, T. S., 317
Hudis, M., 193
Ingraham, J. C., 135
Kerrebrock, J. L., 217
Kimball, J. P., 279
Kolers, P. A., 305
Kronquist, R. L., 98
Kusse, B., 150
Lampis, G., 108
Lidsky, L. M., 225
Llewellyn-Jones, D. T., 73
Lopez, O., 186
Lovins, R. E., 33
Mangano, J. A., 141
Massey, J. L., 239
McCulloch, W. S., 325
McCune, J. E., 201
Moir, R. W., 225
Moran, J. M., 23
Moreno-Diaz, R., 321
Offenberger, A. A., 223
Oppenheim, A. V., 231, 271
Parrish, J. F., 42
Perozek, D. M., 157
Perry, C. H., 39, 42
Pilc, R. J., 241
Rafuse, R. P., 27, 28
Reifenstein, E. C., III, 22
Reznek, S. R., 5
River, Eleanor C., 329
Rogers, A. E. E., 23
Rose, D. J., 193
Schafer, R. W., 231
Schindall, J. E., 234
Siambis, J. G., 154, 186
Small, J., 193
Solomon, A. H., 32
Speck, C. E., 219
Staelin, D. H., 15, 16
Steele, J. M., 37
Steinbrecher, D. H., 27, 28, 32, 33
Stevens, K. N., 267
Vandamme, F. J., 301
Wilson, T. L., 22
Woods, J. W., 320
Zisk, S. H., 34